

UNIVERSITÀ DEGLI STUDI DI PAVIA
Dipartimento di Scienze della Terra e dell'Ambiente

PhD Program in Earth and Environmental Sciences
Dottorato di ricerca in Scienze della Terra e dell'Ambiente
XXXIV Series

**Multidisciplinary investigations on the relationships
between deformation and metamorphism
across crustal rheological boundaries**

PhD thesis of
Stefania Corvò

Tutors

Dr. Matteo Maino,
Dr. Antonio Langone
Prof. Sandra Piazzolo

Coordinator

Prof. Roberto Sacchi

Academic year 2020/2021

*“What the eye doesn't see and
the mind doesn't know,
doesn't exist.”*

D.H. Lawrence

Acknowledgements

This is the end of another journey, the best from the academical point of view because it has given me the opportunity to dedicate myself to what I have always been passionate about and to discover more and more about the world of geology and research. There are many people inside and outside DSTA - UNIPV whom I must thank and who have contributed in many ways to the successful completion of this academic path and to making the most of it despite the difficult times.

First of all, a special thanks goes to my supervisors, Matteo Maino and Antonio Langone, who first gave me the opportunity to undertake and complete this path. For their guidance and for always following me during my personal and academic growth during the three years of my PhD. I thank them for transmitting me their passion, for always believing in me and in my skills, for always considering me at the same level by listening to my ideas, discussing them, encouraging me and addressing the way even when everything seemed to go wrong. I also owe them the lessons I have learnt for what concern the world of research at national and international level. I could not have wished for better guides.

My sincere thanks also go to Sandra Piazzolo, my tutor especially during my time abroad in Leeds (UK), but who has been a precious guide throughout all my PhD path. It was a great honour to collaborate with her. To her I owe above all the teaching of how and on which research topics and objectives to focus and how to make it readable to the geological and scientific community.

My thanks also go to the people with whom I collaborated on topics related to the thesis or during side projects and in the writing of scientific articles: Silvio Seno, Leonardo Casini, Filippo Luca Schenker, Mattia Bonazzi, Matteo Simonetti, Alberto Zanetti; because they have contributed to enrich these three years with further knowledge and experience. Consequently, thanks are also due to the financial support given by SUPSI and IGG-CNR, as well as the possibility of using their instrumentation and laboratories.

I would also like to thank my co-examiners, Prof. Daniela Rubatto, Prof. Marco Scambelluri and Prof. Matteo Alvaro, who were careful critics and expert reviewers during the various steps of the PhD path. I would also like to thank the reviewers of this thesis, Dr. Salvatore Iaccarino and Prof. Marco Scambelluri, whose comments and suggestions allow to make the thesis a complete and clear manuscript.

I would also like to thank all the technicians at the laboratories of: IGG-CNR, the Università Statale di Milano, and the University of Leeds (to name but a few), for their help in obtaining data for my research.

Special thanks are due to my friends in Pavia and in Leeds, colleagues, students and friends in Genoa (too many to list!), who have been of fundamental support and have given me unforgettable moments, without which my PhD would not have been the same.

I would also like to thank all the wonderful acquaintances I have had the pleasure of making during conferences, schools, seminars, workshops, because they have contributed to enrich these years with experiences and friendships, and hopefully collaborations in the future.

Last but not least, a huge thank you goes to my family, Federico and Daniela, for their continuous support and holy patience, who have always supported me and put up with me at all times during these years, without which I would not absolutely have reached this goal.

I apologise if I have unintentionally forgotten anyone, but there are so many of you!

Thank you all from the bottom of my heart,



Multidisciplinary investigations on the relationships between deformation and metamorphism across crustal rheological boundaries

Stefania Corvò

Abstract

The rheology of crustal rocks plays a key role in lithosphere dynamics, influencing the orogenic cycle and how plate tectonics evolve. Lithosphere deformation involves a complex interplay between metamorphic and deformation processes, whose effects tend to be enhanced in domains characterized by variable composition or inherited petrological and structural history. These variations may produce heterogeneous rheological behaviours, which allow concentrating stress or strain, finally resulting in tectonic structures, such as shear zones. Given the complexity of the relationships between deformation and metamorphism, reconstructing the reasons controlling the birth and the evolution of tectono-metamorphic structures is challenging, but of fundamental importance for understanding the initiation of geodynamic processes. The use of multidisciplinary approach is fundamental to isolate the contribution of each of the several parameters controlling the rock rheology. Rheology is expected to significantly change in correspondence of major variations in rock composition, therefore the boundaries between contrasting lithologies are the preferential location for study the role of inherited heterogeneities in the interlinked evolution of deformation and metamorphism.

In this thesis, the interplay between metamorphism and deformation is explored throughout the investigation on how different paired rock types may: 1) record contrasting metamorphic conditions despite a structural coherence, and 2) drive strain localization leading to shear zone nucleation. These purposes are addressed to two case studies from the Alps, whose topics are highly debated by the geological community as they are representative of significant processes occurring in the middle to lower crust during opposite regional tectonic regime (compressive and extensional): 1) the Alpine high pressure and high temperature (HP/HT) occurrence of Cima di Gagnone (Central Alps) and 2) the Tethyan rift-related extensional shear zone (Anzola shear zone, Ivrea-Verbano zone), respectively.

The Cima di Gagnone area (Case study 1) belongs to the Cima Lunga unit, which is part of the southern sector of the Lepontine dome of the Central Alps. It represents an example of ultrahigh-pressure and high-temperature ultramafic lenses enveloped within amphibolite-facies metasedimentary rocks

as the result of the Alpine subduction/collision deformation phases. For this case study, investigations focused on the metamorphic and deformation evolution of the metasediments, which received minor attention respect with the ultramafic lenses. The aims consisted to: i) constrain the Pressure-Temperature-time-Deformation (P - T - t - D) path of micaschists in relation with the ultramafics, ii) to investigate the geochemical exchange at the boundary of these compositionally different rock types. Results demonstrate that even though metasediments share the same structural evolution with ultramafic boudins, large differences in the P - T paths are recorded. Large part of the unit experienced middle pressure and temperature conditions ($P < 1.2$; $T < 700^{\circ}\text{C}$), whereas a few occurrences preserve higher metamorphic conditions (1.3–1.7 GPa; 750–850°C). These estimates approach the P - T peak conditions experienced by the ultramafic rocks (1.5–3.2 GPa; 740–850°C). These pressure and temperature deviations are not randomly distributed in the unit but changes systematically as a function of the distance from the strong lithology (i.e., ultramafic rocks), being maximum at the interface between the two rock pairs. Moreover, fluid-rock interaction is documented as being strongly localized at the boundary between ultramafic lenses and the metapelitic host throughout all the progressive-retrogressive subduction-exhumation path during the Alpine tectonic evolution. This study suggests that heterogeneous metamorphism conditions are locally developed, rather than locally preserved. Different local equilibria are related to the proximity to the strong lithology, suggesting that the rheological and chemical contrasts between strong and surrounding weak rocks had a significant role in modifying the local metamorphic gradients. Moreover, the chemical gradient between compositionally different lithologies combined with fluids circulations result in coexisting heterogeneous metamorphic equilibria, which are not representative of the ambient conditions.

The Anzola shear zone (Case study 2) represents a major extensional structure from one of the best-preserved cross-sections through the middle to lower continental crust, the Ivrea-Verbanò Zone (Western Alps, Italy). It is interpreted as one of the main rift-related structure of the Late Triassic-Jurassic deformation in the lower crust of the Adriatic margin. Nevertheless, the timing of its activity is still poorly constrained. Furthermore, the Anzola shear zone is believed to have developed within a rheologically hard and isotropic mafic body rather than in the surrounding weaker and anisotropic metamorphic sequence. However, a detailed characterization at the meso-microscale of its compositional and structural features is still lacking. For this case study, investigations focused on the: i) characterization of compositional and structural features and ii) identification of the protolith of the shear zone rocks,

with the aim to decipher the role of inherited rock heterogeneities as drivers of weakening and strain localization at middle/lower crustal layers. Results revealed that the Anzola shear zone developed within a multi-lithological metamorphic volcanic-sedimentary sequence that before shearing, experienced multiphase Variscan folding and late Variscan High-Temperature metamorphism, at the boundary between amphibolite and granulite facies conditions. Besides the rheological contrasts due to the compositional and structural anisotropies, strain localisation was further promoted by i) the close intrusion of a nearly isotropic mafic body and ii) the occurrence of rocks showing transitional metamorphic conditions between granulites (dominated by anhydrous minerals) to amphibolite facies (rich of hydrous minerals). This study suggests that detailed petrological, structural and geochemical investigations allow a better comprehension at the outcrop scale of the role of structural and compositional heterogeneities leading the initiation of shear zone nucleation. Moreover, trace elements analyses resulted as the most powerful tool to reconstruct the pre-shearing relationships between wall rocks and mylonites and thus determine the protoliths of the shear zone rocks. Finally, the boundaries characterized by alternated different lithologies and pre-existing structural features combined with the inherited deformation and metamorphic patterns, become the preferential loci for the nucleation of large-scale deformation structure.

In both case studies, pre-existing rock compositional and structural heterogeneities promoted highly variable rheological behaviours, producing local concentration of stress or strain, which finally resulted in local complex interaction between deformation and metamorphic processes. Overall, this PhD thesis highlights that the use of a calibrated multidisciplinary approach on complex rock assemblages is fundamental for providing key information to interpret the geodynamic evolution of the tectonic structures more carefully.

Table of Contents

Abstract

Chapter 1: Introduction	1
1.1 Research topic	3
1.2 Research topic and aims	7
1.3 Multidisciplinary approach of PhD thesis	10
1.4 Thesis Structure	11
1.5 Author Contribution	13
1.6 References	15
Chapter 2: State of the Art	23
2.1 Overview of the Alps and their geological evolution	25
2.1.1 The structure of the Alps	27
2.2 Rheology of the crust	31
2.3 Metamorphic Pressure-Temperature conditions	35
2.4 Differential stress, deviatoric stress and implications for phase equilibria	38
2.5 Mechanisms of weakening and strain localization of the middle to lower crust	40
2.5.1 Water presence	40
2.5.1 Melt presence	41
2.6 Relationships between deformation, metamorphism, and geochemistry	42
2.7 Influence of local scale-rheology in the geodynamic models	44
2.7.1 Subduction-exhumation modelling in the orogens	44
2.7.2 Rifting modelling of the fossil Adriatic margin	46
2.8 References	48
Chapter 3: Methods	55
3.1 Abstract	57
3.2 Field work and sampling strategy	58
3.2.1 Sample preparation	58

3.3 Petrography	59
3.4 Microstructural analysis	60
3.4.1 Scanning electron microscope (SEM) – BSE - EDS	60
3.4.2 Electron Backscattered Diffraction (EBSD)	63
3.4.2.1 EBSD data acquisition and processing	65
3.5. Chemical analysis	67
3.5.1 Bulk rock (XRF)	67
3.5.2 Major element (EPMA)	68
3.5.3 Trace element (LA-ICP-MS)	70
3.6 P-T estimates	72
3.6.1 Geothermobarometry	73
3.6.2 Thermodynamic modelling: <i>P-T-X</i> Pseudosection	74
3.7 Geochronology	77
3.8 References	80
Chapter 4: Case study 1 - Cima di Gagnone	87
4.1 Abstract	89
4.2 Introduction	90
4.3 Geological setting	93
4.3.1 Location and metamorphic evolution	93
4.3.2 Tectonic evolution	95
4.3.3 Geochronological background	95
4.4 Field relationships	97
4.5 Sampling strategy and analytical methods	100
4.6 Petrography and microstructure	101
4.6.1 Country rocks	101
4.6.2 Halos	106
4.7 Mineral Chemistry	110
4.7.1 Country rocks	110
4.7.2 Halos	111

4.8 P–T estimates	114
4.8.1 Geothermobarometry	114
4.8.2 <i>P–T</i> pseudosections	115
4.9 U–Pb Geochronology	119
4.9.1 Zircon Zoning and Isotopic Results	119
4.10 Discussion	122
4.10.1 <i>P–T–t–D</i> paths	122
4.10.2 Country rocks	122
4.10.3 Halos	124
4.10.4 Petrological and geochemical interferences between UM and metasediments	126
4.10.5 Inferences on the exhumation of Cima Lunga–Adula nappe	132
4.11 Conclusions	135
4.12 References	137
Chapter 5: Case study 2 - The Anzola Shear Zone	149
5.1 Abstract	151
5.2 Introduction	153
5.3 Geological setting	155
5.3.1 The Ivrea-Verbano Zone	155
5.3.2 Tectonic evolution	157
5.3.3 The Anzola shear zone	159
5.4 Field observations	162
5.5 Sampling strategy and analytical methods	165
5.6 Petrography and microstructure	165
5.6.1 Wall rocks	165
5.6.1.1 Hanging wall rocks	165
5.6.1.2 Footwall rocks	166
5.6.1.2.1 Gabbroic rocks	171
5.6.1.2.2 Felsic Granulite	171

5.6.2 Shear zone rocks	172
5.6.2.1 Amphibolites	172
5.6.2.2 Paragneisses	174
5.7 Bulk and Mineral chemistry across the shear zone	175
5.7.1 Bulk Rock	175
5.7.2 Mineral chemistry: Major elements	178
5.7.2.1 Amphibole	178
5.7.2.2 Clinopyroxene	178
5.7.2.3 Plagioclase	178
5.7.2.4 Garnet	179
5.7.2.5 Biotite	179
5.7.3 Mineral chemistry: Trace Elements	180
5.8 Geothermobarometry	183
5.9 Discussion	187
5.9.1 Pre- and syn-deformational <i>P-T</i> conditions	187
5.9.2 Protoliths within the Anzola shear zone are compositional heterogeneous	188
5.9.3 Formation of a major crustal shear zone along rheological boundaries	191
5.9.4 The role of the Anzola shear zone during the Triassic-Jurassic rifting phases	193
5.10 Conclusions	195
5.11 References	196
Chapter 6: Thesis conclusions	205
6.1 Overall conclusions	207
6.2 Current and future work	209
Appendices	211
Appendix 1: Supplementary data for case study 1	213
A.1.1 Thin sections scans of the representative studied samples	214
A.1.2 Supplementary information on methods	218
A.1.3 Figures	224
A.1.4 Tables	231
A.1.5 U-(Th)-Pb geochronology: Monazite	238

A.1.6 Integration to the discussion of Chapter 4	243
Appendix 2: Supplementary data for case study 2	249
A.2.1 Supplementary information on methods	250
A.2.2 Figures	251
A.2.3 Tables	253
Appendix 3 U-Pb titanite dating on case study 2 samples	275
Appendix 4 Microstructural characterization (SEM-EBSD) of mylonitic amphibolites from the Anzola shear zone	309
Appendix 5: Thesis related manuscripts	315
A.5.1 Triassic-Jurassic rift related deformation and temperature-time evolution of the fossil Adriatic margin: A review from Ossola and Strona di Omegna valleys (Ivrea-Verbano Zone).	316
A.5.2 Rift-related deformation in the middle continental crust: new microstructural and petrological insights from the Forno-Rosarolo shear zone (Ivrea-Verbano Zone, Western Alps)	332
A.5.3 Porphyroclasts: Source and Sink of Major and Trace Elements During Deformation-Induced Metasomatism (Finero, Ivrea-Verbano Zone, Italy)	334
Appendix 6: Side projects	367
A.6.1 HT-LP metamorphism and multi-stage anatexis of upper continental crust (N Sardinia, Italy)	368
A.6.2 Petrochronology of Late Variscan Castellaccio pluton (Asinara Isl., NW Sardinia, Italy)	370
Curriculum vitae et studiorum of Stefania Corvò	373

CHAPTER 1:

Introduction

1.1 Research topic

The structure of the Earth is the result of geodynamic processes evolving over time and space (e.g., Stüwe, 2002). The plate tectonics movements cause the break-up and drift of continents, how mountain ranges and oceanic floors raise. The most significant geological processes occur in correspondence of the plate tectonics boundaries (i.e., earthquakes, volcanic activity, detachment faults, orogeneses, rifting; e.g., Maggi et al., 2000; Handy and Brun, 2004; Bürgmann and Dresen, 2008; Groome et al., 2008). While the consequences of plate tectonic dynamic are easier to document, determining its driving causes is one of the most challenging dynamics questions in Earth science (e.g., Hacker et al., 2015; Holder et al., 2019).

In the last decades, significant progress has been made towards understanding the geodynamic forces controlling the motion of the plate boundaries (e.g., Bercovici, 2000, 2003; Jolivet and Nataf, 2001; Gerya, 2010). Since Holmes (1931), the hypothesis that thermal convection in the Earth's mantle was the force needed to drive continental motions represented a breakthrough in the understanding plate tectonics. More recently, the development of petrological, rheological, thermal and mechanical models significantly improved the knowledge of the lithosphere movements driven by mantle convection (e.g., Bercovici, 2003; Gerya, 2010). Such models raise knowledge on how lithosphere localizes important deformation structures (e.g., normal or strike-slip faults, thrusts, shear zones, etc.) at the plate boundaries in response to geodynamic processes (e.g., rifting, subduction, transtension/transpression; e.g., Tommasi and Vauchez, 2001; Stern, 2002; Cunningham and Mann, 2007). However, a still open question is how planetary-scale processes - movements of thousands of kilometres - are accomplished along very narrow structures, like faults and shear zones that usually show thickness of $1-10^2$ m. Moreover, these structures result from the combination of complex physical and chemical processes that origin at the micro-scale (e.g., Bercovici, 2003; Passchier and Trouw, 2005; Tajčmanová et al., 2015). These processes may be competing or reinforcing each other. They involve the interaction between rock deformation (i.e., fragile and ductile), metamorphic reactions and fluid flow at variable P - T conditions (e.g., White and Knipe, 1978; Brodie and Rutter, 1987; Rutter and Brodie, 1995; Tajčmanová et al., 2015). Notably, the physical and chemical processes affect all the rock volume subjected to tectonic stress but tend to localize their effects in correspondence of particular heterogeneous domains characterized by high strain density zones, usually defined as faults or shear zones, according

to whether brittle or ductile deformation mechanisms dominate (e.g., Bürgmann and Dresen, 2008). Coevally to the structural pattern's evolution, metamorphic processes take place changing the initial mineralogical assemblages to create new minerals and rock associations (e.g., Brodie and Rutter, 1987; Passchier and Trouw, 2005; Philpotts, and Ague, 2009). Given the complexity of the relationships between deformation and metamorphism, reconstructing why a certain tectonic structure develops in one area rather than another is challenging, but of fundamental importance for understanding the initiation of geodynamic processes (e.g., Handy et al., 2007; Burgmann & Dresen, 2008; Burov, 2011; Mouthereau et al., 2012; Vauchez et al., 2012; Whitney et al., 2013; Fossen, 2016; Fossen and Cavalcante, 2017; Gardner et al., 2017a, b; Kaatz et al., 2021).

The complexity of the mechanisms underlying the formation of tectonic structures firstly depends on the rheology of the lithosphere. The rheology of lithospheric layers is in turn influenced by several parameters, including: rock composition, geothermal gradient, differential and deviatoric stress, pre-existing sedimentological/structural/mineralogical anisotropies, presence of melts/fluids, geochemical gradient (e.g., Passchier and Trouw, 2005; Drury, 2005; Pennacchioni and Mancktelow 2007; Jamtveit, B., & Austrheim, 2010; Hobbs and Ord, 2017; Gardner et al., 2017b; Moulas et al., 2019; Gardner et al., 2020; Piazzolo et al., 2020; Schmalholz et al., 2020; Maino et al., 2021).

Typically, the interaction of these factors when different lithologies are coupled, creates the condition for significant rheological heterogeneity, that may act as boundaries (or thresholds) for metamorphic reactions and/or deformation processes (e.g., Brodie and Rutter, 1987; Daly et al., 1989; Passchier and Trouw, 2005; Wheeler, 2014; Hobbs & Ord, 2015). In these “anomalous” contexts, the interplay between deformation and metamorphic factors, indeed, significantly promotes the variation of the thermodynamic equilibrium system of rocks leading to metastable conditions governing both the deformation and metamorphic processes (Bucher and Frey, 2002). A complete understanding of the conditions far from the equilibrium is typically prevented by the complexity of the controlling factors, as well as the poor knowledge about the timing of the processes themselves. For this reason, it is essential to isolate the contribution of each of these agents, in order to recognise the relative impact of them in forming a certain type of deformational and metamorphic pattern. Nevertheless, the intricate interlink of the above-mentioned factors often makes it very difficult to determine individual contributions and, consequently, a priori simplifications are commonly made. Few of these consists in:

1) in considering broad geothermal gradients (averaged over large regions) without quantify any local heating effect due to, for example, advection of hot fluids/melts from the deep (e.g., hydrothermal fluids) or mechanical heat dissipation (shear heating; Zhao et al., 2008; Kohn et al., 2018).

2) Under- (or over) estimate of water/melt circulation in the system. It has been demonstrated in experimentally and naturally deformed rocks representative of the composition of the crust that the introduction of a phase with lower viscosity (water or melt) to the system decrease, indeed, the strength of rocks triggering partial melting by lowering the solidus conditions of minerals (e.g., Blenkinsop, 2000; Rosenberg and Handy 2005; Piazzolo et al., 2020). Moreover, the most important metamorphic reactions in the lower crust (i.e., the granulite – eclogite, the gabbro-eclogite and the eclogites-amphibolite transitions) are, indeed, all triggered by hydrous fluids that generally circulate in deformation structures (e.g., Jamtveit, B., & Austrheim, 2010; Austrheim, 2013).

3) A further important shortcoming is represented by ignoring the variations in rock composition (e.g., inherited sedimentary layering, block-in-matrix texture), generally due to the lack of detailed characterization both at the meso- and micro-scale. Indeed, it is demonstrated that the interaction between the deformation and metamorphic processes along heterogeneous rock boundaries (e.g., ultramafics-micaschists) facilitate (de)hydration reactions, such as related to eclogitization, serpentinization, decarbonation, amphibolite-to granulite facies transition, and thus may have a significant impact on the evolution of, for example, subduction interface processes (e.g., Guillot et al., 2015; Schorn, 2018), shear zones (e.g., Austrheim, 1987; Vauchez et al., 2012; Fossen and Cavalcante, 2017; Gardner et al., 2017a, 2020), faulting at slow-spreading ridges (e.g., Escartin et al., 1997; Casini et al., 2021), or slip-weakening of faults (e.g., Sulem & Famin, 2009; Ikari et al., 2013).

4) Ignoring the role of structural heterogeneities (e.g., pre-existing or inherited deformation structures) may be a further important simplification. At the regional scale, pre-existing inherited heterogeneities (e.g., faults, shear zones), and their position (in depth) in the continental lithosphere can have a first-order control on the development of shear zones driving the evolution of rifted margins (e.g., Michibayashi and Mainprice, 2003; Mohn et al., 2010, 2012; Manatschal et al., 2015; Petri et al., 2019). Mechanically weak boundaries were, indeed, documented to produce detachment faults and decoupling horizons, especially at mid-crustal depth in magma-poor rifted margin during major lithospheric thinning (e.g., Mohn et al., 2012).

5) Another simplification is related to the assumption that metamorphic record is only influenced by lithostatic pressure, whereas the deviatoric pressure is insignificant for the metamorphic reactions. Generally, the common way to draw the evolution of crustal rocks are largely founded on pressure (P), temperature (T) and age (t) constraints deriving from petro-chronological investigations on metamorphic rocks assuming to convert P - T estimates into depth. However, several studies have recently underlined that this approach has several shortcomings, as peak metamorphic assemblages are usually not coeval within orogenic domains (e.g., Burton & O’Nions, 1992; Schmalholz, and Podladchikov, 2014; Tajčmanová et al., 2021; Bauville and Yamato, 2021), and P - T conditions might not correspond to isotopic age derived from accessory minerals (e.g., Rubatto and Hermann, 2007; Warren, 2013). It is also highlighted that the tectonic over (or under) pressure could have a significant influence on mineral phase equilibria in deforming metamorphic rocks (e.g., Gerya, 2015; Powell et al., 2018; Moulas et al., 2019). By definition, when rocks experience deformation, deviatoric stresses drive shear deformation, and the mean stress in a deforming rock is, hence, not lithostatic, due to also the mechanically heterogeneous rheology and composition (e.g., Schmid & Podladchikov, 2003; Moulas et al., 2014; Casini and Maino, 2018; Schmalholz et al., 2020). Deviatoric pressure typically produce folding and necking in the deforming rocks across all geological scales (e.g., Schmalholz & Mancktelow, 2016), as well as pressure-solution reactions around porphyroclats within shear zones (e.g., Casini & Funedda, 2014). At present, however, quantifying the real amount of these deviations remains elusive because it is still difficult to understand whether variations in deviatoric stress can actually produce metamorphic assemblages stable over geological times (10³-6 Ma) different from those produced by lithostatic pressures (e.g., Hobbs & Ord, 2017).

Overall, a complete comprehension of the range of processes concerning the crustal rocks deformation, is limited to the understanding of single aspects as the crystal chemistry of rock forming minerals, experimental phase equilibria, theoretical petrology, physical chemistry, and textural analysis. To correctly interpret the significance of the tectono-metamorphic evolution of crustal rocks, especially from complex rheological context, multiple combined data are requested, also including knowledge on the inherited stratigraphy, structural geology (micro-, meso-, and mega-scale structures), rock mechanics, geophysical heat flow and geochronology (e.g., Spear, 1995; Passchier and Trouw, 2005). For this reason, the combination of petrographic, microstructural, geochemical, and

geochronological analyses is more and more required to detect all possible conditions where changes in rheological behaviour can occur. For these purposes, the interface between rocks with significant different compositions and/or focused strain features are the first place to investigate because they are preferential zones for the developing of anomalous deformation and metamorphic conditions. Thanks to the adoption of this multidisciplinary approach, a complete reconstruction in the Pressure-Temperature-time-Deformation-Composition (P - T - t - D - X) paths of the studied rocks should be obtained. Moreover, in this way, quantify the interplay between rock deformation, metamorphic reactions, fluid flow should become more feasible.

Summing up, the reconstruction of the evolution of the lithosphere appears to be challenging as it requires analysis of its complete i.e., physical, chemical, dynamic state through time. Further works are still needed to understand how metamorphism and deformation are interconnected in natural crustal rocks. However, recent advances in techniques provide the opportunity to apply a multidisciplinary approach to the challenging questions noted above.

1.2 Research topic and aims

The topic of this PhD thesis is to investigate the relationships between deformation and metamorphic processes in correspondence of crustal heterogeneous rheological boundaries. In particular, the study focuses on two highly debated questions in the geological community: 1) the occurrence of contrasting metamorphic records in coupled rocks assemblages (High Pressure vs Low-Middle Pressure or High Temperature vs Low-Middle Temperature); 2) the mechanisms leading to the strain localization and the formation of shear zones. The major aim is namely to understand: 1) whether/why compositional contrasts, - e.g. (ultra)mafics-micaschists - show contrasting metamorphic record (HP and/or HT rocks in medium-grade rocks) and 2) whether/how the heterogeneous rock boundaries represent preferential zones to the nucleation of large crustal faults.

The PhD study is based on natural samples, which retain a wealth of textural and chemical information that are challenging to reproduce in experimental setups. Moreover, the studied samples preserve clues of the complex processes that usually occur in the middle to lower continental crust, such as fluid-rock interaction, metamorphic reactions, geochemical variations, inherited structures and pre-existing heterogeneities, protracted weakening, strain localization in different lithologies

(e.g., Beach, 1980; Passchier, 1982; Austrheim, 1987; Brodie and Rutter, 1987; Dell'Angelo and Tullis, 1988; Treagus & Sokoutis, 1992; Austrheim and Boundy 1994; Pennacchioni and Cesare 1997; Rutter, 1999; Arbaret & Burg, 2003; Rybacki and Dresen, 2004; Passchier and Trouw, 2005; Pennacchioni and Mancktelow 2007; Burg et al., 2011; Fossen and Cavalcante, 2017; Gardner et al., 2020; Piazzolo et al. 2020; Maino et al., 2021; Osagiede et al., 2021).

The project focuses on two case studies situated in the Alpine chain and representative of tectono-metamorphic boundaries formed under compressive and extensional tectonic regime: the Alpine HP/HT Cima di Gagnone area and the Triassic Anzola shear zone, respectively (Fig. 1.1).

The Cima di Gagnone area (case study 1) belongs to the Cima Lunga unit, which is part of the southern sector of the Lepontine dome of the Central Alps (Fig. 1.1). The Cima di Gagnone represents an example of (ultra)mafic lenses enveloped within metasedimentary rocks as the result of the Alpine subduction/collision deformation phases (see Sections 4.3 for geological setting). (Ultra)mafic and metasedimentary rocks show different metamorphic-peak records, although all rock types share a

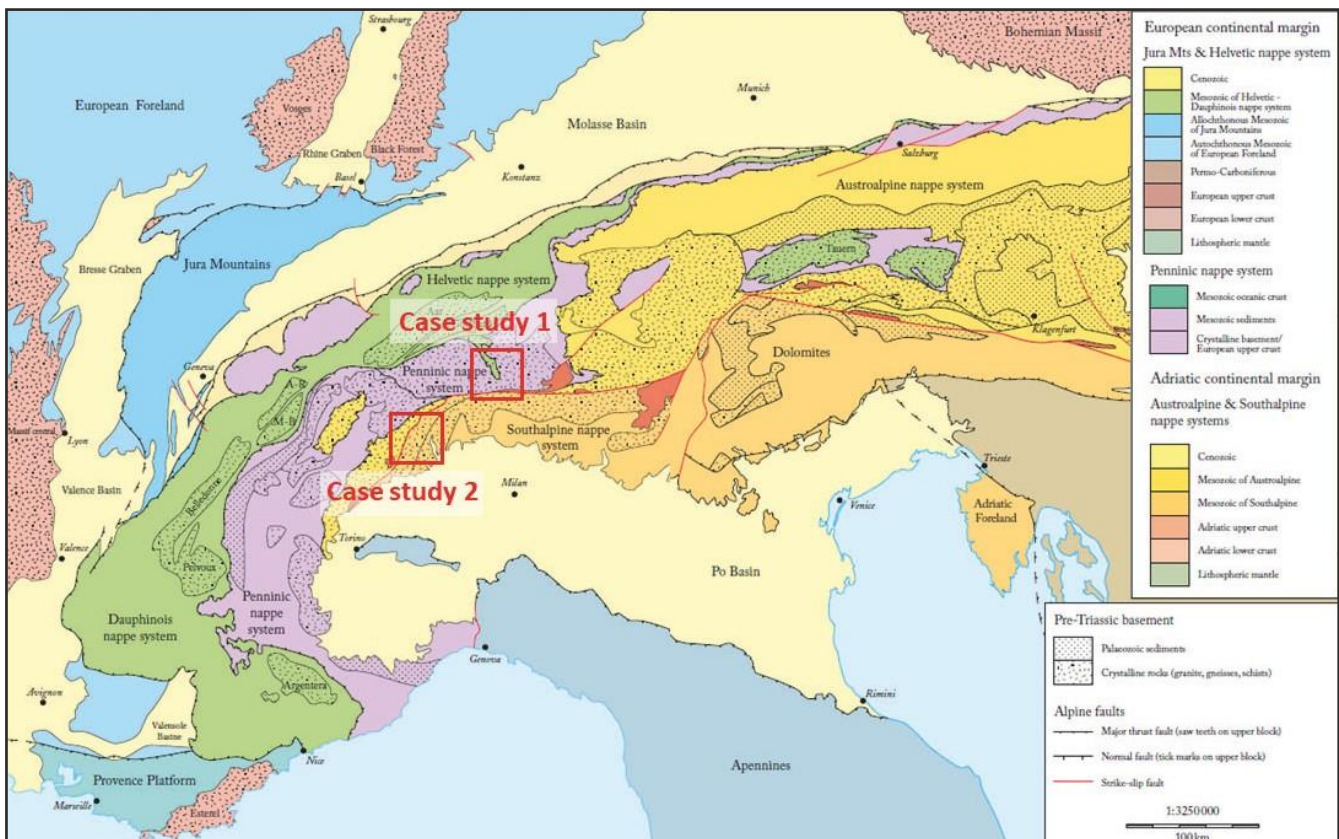


Fig. 1.1 – Simplified tectonic map of the Alps and their foreland showing the geographical locations of the two case studies (boxed, in red). The Cima di Gagnone (case study 1) is in Cima Lunga unit in Central Alps; the Anzola shear zone (case study 2) is in the Ivrea-Verbano Zone, Italian Southern Alps. Modified after Pfiffner, (2014).

continuous progressive deformation and a common amphibolite-facies equilibration. This issue is still a matter of a lively scientific debate for countless studies for what concern the evolution of this tectonic nappe system (e.g., Evans and Trommsdorff, 1974, 1978; Evans et al., 1979; Heinrich, 1982, 1986; Früh-Green, 1987; Pfeifer, 1987; Grond et al. 1995; Pfiffner and Trommsdorff, 1997, 1998; Gebauer, 1999; Nimis and Trommsdorff, 2001; Rutti et al., 2005; Schmalhoz et al., 2014; Scambelluri et al., 2014, 2015; Schenker et al., 2015; Casini and Maino, 2018; Maino et al., 2021). Moreover, examples of such rock pairings as mafic/ultramafic-metasediments, orthogneiss-micaschist, metacarbonate-micaschists occur in a range of field localities: in the European Alps - e.g., Adula-Cima Lunga, Monte Rosa, Dora-Maira, Zermatt-Saas, Ulten Zone (Chopin, 1984; Evans et al., 1979; Godard et al., 1996; Luisier et al., 2019; Tumiati et al., 2018), Western Norway (e.g., Smith, 1984), Cycladic Archipelago (e.g., Gyomlai et al., 2021), central China (e.g., Wang et al., 1989) just to give some examples. In the Cima di Gagnone area, investigations were addressed on the metamorphic and deformation evolution of the metasediments (which received minor attention respect with the (ultra)mafic lenses) with the aim to i) constrain the *P-T-D-t* path of micaschists in relation with the ultramafics, ii) to investigate the geochemical exchange at the boundary of these compositionally different rock types.

The Anzola shear zone (case study 2) is exposed in the Ossola Valley and belongs to the Ivrea-Verbano Zone (IVZ, Western Alps, Fig. 1.1), which is an example of one of the best-preserved cross-sections through the middle-lower continental crust (see Sections 5.3 for geological setting). Beside this latter peculiarity, the IVZ attracted many geoscientists since it experienced a long-lived tectono-metamorphic history going from the Variscan to the Alpine orogenesis. Recently, it has been emphasized the role of the IVZ was during extensional processes leading to the Alpine Tethys rifting (e.g., Rutter et al., 1993; Beltrando et al., Petri et al., 2019). This study investigates if the Anzola shear zone developed on monotonous or heterogeneous inherited lithological, metamorphic and structural setting. In the last decades many studies highlight that at the regional scale, pre-existing compositional/mechanical heterogeneities in the continental lithosphere have a first-order control on the development of shear zones driving the evolution of rifted margins (Michibayashi and Mainprice, 2003; Prosser et al., 2003; Lavier and Manatschal, 2006; Mohn et al., 2010, 2012; Beltrando et al., 2014, 2015; Manatschal et al., 2007, 2015; Aravadinou and Xypolias, 2017; Langone et al., 2018; Real et al., 2018; Petri et al., 2019; Simonetti et al. 2021). Therefore, tectonic structures, such as the Anzola shear zones, constitutes an excellent opportunity to investigate on rift-related tectonics across different crustal levels. For this

case, the project aims to explore the link between metamorphism and deformation focusing on which inherited compositional, metamorphic and structural heterogeneities brought to the development of the Anzola shear zone.

Despite the differences, the two geological sites represent case studies where inherited compositional heterogeneities (possibly accompanied by pre-existing variable metamorphic and structural patterns) potentially produced local divergent rheological behaviours in the rock assemblages, finally resulting in differential accumulation of stress or strain. In the Cima di Gagnone area, heterogeneous deviatoric stress is suspected to have produced contrasted metamorphic assemblages at same lithostatic pressure conditions. In the IVZ, strain localization triggering the initiation of the crustal shear zone is thought to have occurred in a rock assemblage characterized by alternating rheologically weak and hard layers.

1.3 Multidisciplinary approach of PhD thesis

To achieve the PhD project aims, the methods adopted consisted in combining field-based work observations with detailed (micro)structural, petrological, geochemical, and geochronological analyses with particular attention to quantify the time and space variations of metamorphic and deformation conditions as reply of the rheological rock behaviour.

i) The first phase consisted in field work mainly included basic geological mapping and targeted sampling. The sampling strategy adopted consisted in the collection of samples representative of the compositional and structural heterogeneous boundaries and their wall rocks, in order to compare the respective metamorphic and structural patterns.

ii) Successively, samples were accurately selected for thin sections and other preparation in function of the analytical technique to perform. After a first petrographic characterization by the optical microscope, detailed microstructural analyses were carried out at the Scanning Electron Microscope (SEM; at University of Pavia) and by acquiring electron backscatter diffraction (EBSD) analyses (at the Electron Optics Facility, University of Leeds, UK). The EBSD is a special technique that allows to quantify punctually and mapping the deformation features of main mineral phases or, more interesting, of geochronometers.

iii) Geochemical characterization consisted in determine bulk rocks composition by using the X-ray Fluorescence (XRF; Activation Laboratories Ltd., Ancaster, Canada) and mineral chemistry. This

last is usually split in the quantification of major element contents by using electron micro probe analyzer (EPMA; mainly performed at the University of Milan) and trace element concentrations by Laser Ablation Inductively Coupled Plasma Mass Spectrometry (LA-ICP-MS) technique (at C.N.R., Istituto di Geoscienze e Georisorse of Pavia).

iv) The chemical data obtained are fundamental to constrain the P - T conditions of rocks. The last step worked combining calculation of P - T pseudosections and geothermobarometers. Finally, on the base of the previously analyses, preliminary geochronological studies, i.e., U-(Th)-Pb using LA-ICP-MS technique on geochronometers such as zircon, monazite, titanite, were performed. From the data obtained by the previous analytical techniques, pressure and temperature conditions of the studied rocks were constrained applying the following methods: geothermobarometry (e.g., Fe-Mg garnet-biotite, Ti-in-Amphibole, Si in muscovites/phengites, Garnet-Aluminosilicate-Silica-Plagioclase, Zr-in-Rutile, and so on) and/or the reconstruction of P - T - X pseudosection diagrams (using PERPLE_X software).

v) As last phase, geochronological analyses consisted in U-(Th)-Pb dating of accessories minerals (zircon, monazite, titanite) were performed using different kind of instruments, commonly combining an excimer laser coupled with the ICP- (Multi collector) - MS (at C.N.R., Istituto di Geoscienze e Georisorse of Pavia).

The result is the reconstruction of the Pressure-Temperature-time-Deformation-Composition (P - T - D - X) conditions of the studied rocks. Most of analysis were conducted mainly, when possible, on polished thin sections to maintain the textural control and the link between deformation and metamorphic features. Overall, the multidisciplinary methodology had as final aim to provide key information for interpreting the tectonic evolution of rocks in correspondence of heterogeneous tectono-metamorphic rock boundaries, without ignoring the reciprocal interplay between deformation and metamorphism.

1.4 Thesis Structure

This thesis focuses on the processes occurring across tectono-metamorphic boundaries and on the compositional and structural heterogeneities responsible for stress or strain accumulation in narrow rock volumes. The investigated rocks were sampled from two distinct middle-lower crustal units: in the Cima Lunga Unit (Central Alps) and in the Ivrea-Verbano Zone (Western Alps). The peculiarities of

Chapter 1

each study area required each location to be presented, analysed, and discussed separately. Therefore, this thesis is structured as two stand-alone case studies, which together serve as natural examples of compositional and rheological heterogeneous rock boundaries at middle to lower crustal levels from two opposite geodynamic settings, i.e., subduction and rifting.

This thesis comprises six chapters: this introductory chapter (Chapter 1), one reporting a brief state of the art on relevant concepts of the research topic (Chapter 2), one related to the multidisciplinary methodology and procedures used for this thesis (Chapter 3), one chapter related to the Cima di Gagnone (Chapter 4) and another one to the Anzola shear zone (Chapter 5), a final chapter summarizing the main conclusions (Chapter 6) and Appendices.

Chapter 2 – This chapter provides the interested reader with some basic concepts on the most relevant aspects and issues related to this PhD study and applied in the two case studies that follow in Chapters 4 and 5.

Chapter 3 - This chapter reported the shared workflow used in the investigations of both case studies. The methodology consisted in a multidisciplinary approach resulting by the combination of field work observations, petrological, micro-structural, geochemical, geothermobarometry, *P-T-X* pseudosections reconstructions and preliminary geochronological investigations. The nature of this type of thesis necessitates some repetition with regards to some methods.

Chapter 4 – Here, a reconstruction of the *P-T-t-D-X* path at the interface of rocks with different composition and rheology (ultramafic lenses and metasediments host rock) is proposed. The content of this chapter is shared with the publication published on *Lithos* as Corvò et al. (2021) with title: Local variations of metamorphic record from compositionally heterogeneous rocks (Cima di Gagnone, Central Alps): Inferences on exhumation processes of (U)HP–HT rocks. Co-authors of this publication are Matteo Maino (University of Pavia), Antonio Langone (Institute of Geosciences and Earth Resources of Pavia), Sandra Piazzolo (University of Leeds), Filippo Luca Schenker (University of Applied Sciences and Arts of Southern Switzerland), Leonardo Casini (University of Sassari) and Silvio Seno (University of Pavia).

Chapter 5 - This chapter explores the lithological and structural heterogeneities and related processes across a shear zone as the reasons for the incipient of strain localisation. The content of this chapter is shared with the recently submitted manuscript on *Lithos* (actually under review) with title: Role of inherited compositional and structural heterogeneity in shear zone development at mid-low

levels of the continental crust (the Anzola shear zone; Ivrea-Verbano Zone, Western Alps). Co-authors of this work are Matteo Maino (University of Pavia), Sandra Piazzolo (University of Leeds), Silvio Seno (University of Pavia) and Antonio Langone (Institute of Geosciences and Earth Resources of Pavia).

Chapter 6 ends the thesis with some final remarks and conclusions. A section devoted to planned ongoing and future research is also presented.

The Appendices at the back of the thesis incorporate supplementary information and results that complement and support the main chapters (Appendices 1, 2). In addition, as appendices are reported also several ongoing research, published and submitted manuscripts related with the thesis's topics including those for which the candidate was a contributing author (Appendices 3-6).

1.5 Author Contribution

The direction of the PhD project was determined by the candidate in discussion with the supervisory team: Matteo Maino (MM) of the University of Pavia (Italy), Antonio Langone (AL) of the Institute of Geosciences and Earth Resources (Italy) and Sandra Piazzolo (SP) of the University of Leeds (UK). Fieldwork, data acquisition, data analysis and treatment, interpretation, figure creation, and manuscript preparation were undertaken by the candidate under supervision and reviews of MM, AL and SP unless explicitly stated otherwise below. The presented data have been acquired from laboratories at the Department of Earth and Environmental Sciences of University of Pavia, Institute of Geosciences and Earth Resources of Pavia (IGG-CNR) and School of Earth and Environment of University of Leeds. Some parts of this thesis were developed in conjunction with or with contribution by other authors, universities and laboratories, further related detailed are explicated in the chapter 3 of Methods.

Samples for chapter 4 were provided by MM, as well as most of field work and structural analysis were done by MM and Filippo Luca Schenker during the geological survey of the sheet 1293 – Osogna for the Swiss Geological Atlas – Swisstopo. Moreover, chapter 4 benefited from a discussion and a review of the manuscript by Filippo Luca Schenker (University of Applied Sciences and Arts of Southern Switzerland), Leonardo Casini (University of Sassari) and Silvio Seno (University of Pavia). Conversely, chapter 5 was completely developed by the candidate together with the supervisory team.

Overall, the PhD project involved the further acquisition of new data for both case studies whose processing is still in progress but not far to be completed for potential manuscript to be submitted. For

that reason, they are presented in short paragraphs at the back of the thesis as appendices (Appendices 3, 4).

During the PhD making, the candidate had the possibility to join in field works in geological localities inherent to the PhD project theme and aim, such as Val Strona di Omega (Ivrea-Verbano Zone), the southern adjacent valley to Val d'Ossola. There are many geological, petrological and structural similarities between the two valleys whose direct comparison results very useful for a better comprehension for this thesis case study 2. As the candidate did for case study 2 in this thesis, even in Val Strona di Omega the aim consisted in petrological, microstructural and geochronological characterization of the valley and of the Forno-Rosarolo shear zone, which is considered the prolongation of the Anzola shear zone (Rutter et al., 2007). For the Val Strona di Omega studies, the candidate collaborated in field, lab work, data acquisition and processing and writing papers (see Appendix 5.1, 5.2) with the collaborating team made by Matteo Simonetti (Servizio Geologico d'Italia, ISPRA), Mattia Bonazzi (University of Pavia) and my supervisors AL, MM. A first paper was already published on *Ofioliti* (vol.46) as Simonetti et al., (2021) with title: Triassic-Jurassic rift-related deformation and temperature-time evolution of the fossil Adriatic margin: A review from Ossola and Strona di Omega valleys (Ivrea-Verbano Zone). A second paper was recently submitted to the *Italian Journal of Geosciences* as Simonetti et al., entitle: Rift-related deformation in the middle continental crust: new microstructural and petrological insights from the Forno-Rosarolo shear zone (Ivrea-Verbano Zone, Western Alps). Another related thesis work was the published paper: Corvò, S., Langone, A., Padrón-Navarta, J. A., Tommasi, A., & Zanetti, A. (2020). Porphyroclasts: Source and Sink of Major and Trace Elements During Deformation-Induced Metasomatism (Finero, Ivrea-Verbano Zone, Italy). *Geosciences*, 10(5), 196. For this last, data were collected during Master thesis and six months of scholarship at IGG-CNR of Pavia, but the manuscript was written and published during the PhD (Appendix 5.3).

Moreover, several published papers and works in progress are presented as result of side projects carried out during the PhD (Appendix 6). In these side projects the candidate joined as first author or co-authors since she was personally involved in laboratory work, data collection and reduction methods, interpretations and discussion. In a recently submitted paper with title "HT-LP metamorphism and multi-stage anatexis of upper continental crust (N Sardinia, Italy)"; authors: Casini L., Maino M., Langone A., Oggiano G., Corvò S., Reche J., Liesa M; the candidate collaborates for the elaboration and interpretation of P - T pseudosections modelling (Appendix 6.1). Finally, the candidate personally

contributed to the development of the side project related to the Variscan evolution of the Asinara island and of the related manuscript (in preparation) entitled: “Petrochronology of Late Variscan Castellaccio pluton (Asinara Isl., NW Sardinia, Italy)”; authors: Corvo’ S., Langone A., Maino M., Oggiano G., Casini L., (Appendix 6.2)

1.6 References

- Aravadinou, E. and Xypolias P., 2017. Evolution of a passive crustal-scale detachment (Syros, Aegean region): Insights from structural and petrofabric analyses in the hanging-wall. *J. Struct. Geol.*, 103: 57-74.
- Arbaret, L., & Burg, J.P. 2003. Complex flow in lowest crustal, anastomosing mylonites: Strain gradients in a Kohistan gabbro, northern Pakistan. *Journal of Geophysical Research*, 108, 2467.
- Austrheim, H., 1987. Eclogitization of lower crustal granulites by fluid migration through shear zones. *Earth and Planetary Science Letters*, 81(2-3), 221-232.
- Austrheim, H. and Boundy, T.M. 1994. Pseudotachylytes generated during seismic faulting and eclogitization of the deep crust. *Science*, 265, 82–83.
- Bauville, A., & Yamato, P., 2021. Pressure-to-depth conversion models for metamorphic rocks: derivation and applications. *Geochemistry, Geophysics, Geosystems*, 22(1), e2020GC009280.
- Beach, A., 1980. Retrogressive metamorphic processes in shear zones with special reference to the Lewisian complex. *Journal of Structural Geology*, 2(1-2), 257-263.
- Beltrando, M., Manatschal G., Mohn G., Dal Piaz G.V., Vitale Brovarone A. and Masini E., 2014. Recognizing remnants of magma-poor rifted margins in high-pressure orogenic belts: The Alpine case study. *Earth. Sci. Rev.*, 131: 88-115.
- Beltrando, M., Stockli D.F., Decarlis A. and Manatschal G., 2015. A crustal-scale view at rift localization along the fossil Adriatic margin of the Alpine Tethys preserved in NW Italy. *Tectonics*, 34: 1927-1951.
- Bercovici, D., Ricard, Y., & Richards, M. A., 2000. The relation between mantle dynamics and plate tectonics: A primer. *Geophysical Monograph-American Geophysical Union*, 121, 5-46.
- Bercovici, D., 2003. The generation of plate tectonics from mantle convection. *Earth and Planetary Science Letters*, 205(3-4), 107-121.
- Brodie, K. H., & Rutter, E. H., 1987. Deep crustal extensional faulting in the Ivrea Zone of northern Italy. *Tectonophysics*, 140(2-4), 193-212.
- Bucher, K., & Frey, M., 2002. *Petrogenesis of metamorphic rocks*. Springer Science & Business Media.
- Bürgmann, R., & Dresen, G., 2008. Rheology of the lower crust and upper mantle: Evidence from rock mechanics, geodesy, and field observations. *Annu. Rev. Earth Planet. Sci.*, 36, 531-567.
- Burov, E. B., 2011. Rheology and strength of the lithosphere. *Marine and Petroleum Geology*, 28(8), 1402-1443.
- Burton, K. W., & O’Nions, R. K., 1992. The timing of mineral growth across a regional metamorphic sequence. *Nature*, 357(6375), 235.

Chapter 1

- Casini, L., & Funedda, A., 2014. Potential of pressure solution for strain localization in the Baccu Locci Shear Zone (Sardinia, Italy). *Journal of Structural Geology*, 66, 188-204.
- Casini, L., & Maino, M., 2018. 2D-thermo-mechanical modelling of spatial PT variations in heterogeneous shear zones. *Italian Journal of Geosciences*, 137(2), 272-282.
- Casini, L., Maino, M., Sanfilippo, A., Ildefonse, B., & Dick, H. J., 2021. High-Temperature Strain Localization and the Nucleation of Oceanic Core Complexes (16.5° N, Mid-Atlantic Ridge). *Journal of Geophysical Research: Solid Earth*, 126(9), e2021JB022215.
- Chopin, C., 1984. Coesite and pure pyrope in high grade blueschists of the Western Alps: a first record and some consequences. *Contributions to Mineralogy and Petrology*, 86(2), 107-118.
- Connolly, J.A.D., 1990. Multivariable phase-diagrams - an algorithm based on generalized thermodynamics. *Am. J. Sci.* 290, 666-718.
- Connolly, J. A. D., 2005. Computation of phase equilibria by linear programming: A tool for geodynamic modeling and its application to subduction zone decarbonation. *Earth and Planetary Science Letters*, 236(1-2), 524-541.
- Cunningham, W. D., & Mann, P., 2007. Tectonics of strike-slip restraining and releasing bends. Geological Society, London, Special Publications, 290(1), 1-12.
- Daly, J. S., Cliff, R. A., & Yardley, B. W., 1989. Evolution of metamorphic belts (Vol. 43). London: Geological Society.
- Dell'Angelo, L.N., Tullis, J., 1996. Textural and mechanical evolution with progressive strain in experimentally deformed aplite. *Tectonophysics* 256, 57-82.
- Drury, M. R., 2005. Dynamic recrystallization and strain softening of olivine aggregates in the laboratory and the lithosphere. Geological Society, London, Special Publications, 243(1), 143-158.
- Escartin, J., Hirth, G., & Evans, B., 1997. Effects of serpentinization on the lithospheric strength and the style of normal faulting at slow-spreading ridges. *Earth and Planetary Science Letters*, 151(3-4), 181-189.
- Evans, B. W., and Trommsdorff, V., 1974. Stability of Enstatite + Talk, and CO₂-Metasomatism of Metaperidotite, Val d'Efra, Lepontine Alps. *American Journal of Sciences*, 274, 274-296.
- Evans, B. W., and Trommsdorff, V., 1978. Petrogenesis of garnet lherzolite, Cima di Gagnone, Lepontine Alps. *Earth and Planetary Science Letters*, 40(3), 333-348.
- Evans, B. W., Trommsdorff, V., and Richter, W., 1979. Petrology of an eclogite-metarodingite suite at Cima di Gagnone, Ticino, Switzerland. *American Mineralogist*, 64(1-2), 15-31.
- Fossen, H., 2016. Structural geology. Cambridge university press
- Fossen, H., & Cavalcante, G. C. G., 2017. Shear zones-A review. *Earth-Science Reviews*, 171, 434-455.
- Früh-Green, G. L., 1987. Stable isotope investigations of fluid rock of eclogite-facies rocks: case studies from the Swiss and Italian Alps. PhD Thesis, ETH Zurich.
- Gardner, R., Piazzolo, S., Evans, L., & Daczko, N., 2017a. Patterns of strain localization in heterogeneous, polycrystalline rocks-a numerical perspective. *Earth and Planetary Science Letters*, 463, 253-265.

- Gardner, R. L., Piazzolo, S., & Daczko, N. R., 2017b. Determining relative bulk viscosity of kilometre-scale crustal units using field observations and numerical modelling. *Tectonophysics*, 721, 275-291
- Gardner, R. L., Piazzolo, S., Daczko, N. R., & Trimby, P., 2020. Microstructures reveal multistage melt present strain localisation in mid-ocean gabbros. *Lithos*, 366, 105572.
- Gebauer, D., 1999. Alpine geochronology of the Central Alps and Western Alps: new constraints for a complex geodynamic evolution. *Schweizerische Mineralogische und Petrographische Mitteilungen*, 79, 191-208.
- Gerya, T., 2010. *Introduction to Numerical Geodynamic Modelling*-Cambridge University Press.
- Gerya, T., 2015. Tectonic overpressure and underpressure in lithospheric tectonics and metamorphism. *Journal of Metamorphic Geology*, 33(8), 785-800.
- Gyomlai, T., Agard, P., Marschall, H. R., Jolivet, L., and Gerdes, A., 2021. Metasomatism and deformation of block-in-matrix structures in Syros: The role of inheritance and fluid-rock interactions along the subduction interface. *Lithos*, 105996.
- Godard, G., Martin, S., Prosser, G., Kienast, J. R., and Morten, L., 1996. Variscan migmatites, eclogites and garnet-peridotites of the Ulten zone, Eastern Austroalpine system. *Tectonophysics*, 259(4), 313-341.
- Grond, R., Wahl, F., and Pfiffner, M., 1995. Mehrphasige alpine Deformation und Metamorphose in der Nördlichen Cima-Lunga-Einheit, Zentralalpen (Schweiz) = Polyphase Alpine deformation and metamorphism in the northern Cima Lunga unit, Central Alps (Switzerland). *Schweizerische Mineralogische und Petrographische Mitteilungen*, 75, 371-386.
- Groome, W. G., Koons, P. O., & Johnson, S. E., 2008. Metamorphism, transient mid-crustal rheology, strain localization and the exhumation of high-grade metamorphic rocks. *Tectonics*, 27(1).
- Guillot, S., Schwartz, S., Reynard, B., Agard, P., & Prigent, C., 2015. Tectonic significance of serpentinites. *Tectonophysics*, 646, 1-19.
- Hacker, B. R., Kelemen, P. B., & Behn, M. D., 2015. Continental lower crust. *Annual Review of Earth and Planetary Sciences*, 43, 167-205.
- Handy, M. R., & Brun, J. P., 2004. Seismicity, structure and strength of the continental lithosphere. *Earth and Planetary Science Letters*, 223(3-4), 427-441.
- Handy, M. R., Schmid, S. M., Bousquet, R., Kissling, E., & Bernoulli, D., 2010. Reconciling plate-tectonic reconstructions of Alpine Tethys with the geological-geophysical record of spreading and subduction in the Alps. *Earth-Science Reviews*, 102(3-4), 121-158.
- Heinrich, C. A., 1982. Kyanite-eclogite to amphibolite facies evolution of hydrous mafic and pelitic rocks, Adula nappe, Central Alps. *Contributions to Mineralogy and Petrology*, 81(1), 30-38.
- Heinrich, C. A., 1986. Eclogite facies regional metamorphism of hydrous mafic rocks in the Central Alpine Adula Nappe. *Journal of Petrology*, 27(1), 123-154.
- Hobbs, B.E., Ord, A., 2017. Pressure and equilibrium in deforming rocks. *J. Metamorph. Geol.*, 35 (9), 967-982.
- Holder, R. M., Viete, D. R., Brown, M., & Johnson, T. E., 2019. Metamorphism and the evolution of plate

- tectonics. *Nature*, 572(7769), 378-381.
- Holmes, A., 1931. Radioactivity and earth movements. *Nature*, 128(3229), 496-496.
- Jamtveit, B., & Austrheim, H., 2010. Metamorphism: the role of fluids. *Elements*, 6(3), 153-158.
- Jolivet, L., & Nataf, N. C., 2001. *Geodynamics*. CRC Press.
- Kaatz, L., Zertani, S., Moulas, E., John, T., Labrousse, L., Schmalholz, S. M., & Andersen, T. B., 2021. Widening of hydrous shear zones during incipient eclogitization of metastable dry and rigid lower crust—Holsnøy, western Norway. *Tectonics*, 40.
- Kohn, M. J., Castro, A. E., Kerswell, B. C., Ranero, C. R., & Spear, F. S., 2018. Shear heating reconciles thermal models with the metamorphic rock record of subduction. *Proceedings of the National Academy of Sciences*, 115(46), 11706-11711.
- Ikari, M. J., Marone, C., Saffer, D. M., & Kopf, A. J., 2013. Slip weakening as a mechanism for slow earthquakes. *Nature geoscience*, 6(6), 468-472.
- Langone A., Zanetti A., Daczko N.R., Piazzolo S., Tiepolo M. and Mazzucchelli M., 2018. Zircon U-Pb dating of a lower crustal shear zone: A case study from the northern sector of the Ivrea-Verbano Zone (Val Cannobina, Italy). *Tectonics*, 37: 322-342.
- Lavier, L. L., & Manatschal, G., 2006. A mechanism to thin the continental lithosphere at magma-poor margins. *Nature*, 440(7082), 324-328.
- Luisier, C., Baumgartner, L., Schmalholz, S. M., Siron, G., and Vennemann, T., 2019. Metamorphic pressure variation in a coherent Alpine nappe challenges lithostatic pressure paradigm. *Nature communications*, 10(1), 1-11.
- Maggi, A., Jackson, J. A., Mckenzie, D., & Priestley, K., 2000. Earthquake focal depths, effective elastic thickness, and the strength of the continental lithosphere. *Geology*, 28(6), 495-498.
- Maino, M., Adamuszek, M., Schenker, F. L., Seno, S., & Dabrowski, M., 2021. Sheath fold development around deformable inclusions: Integration of field-analysis (Cima Lunga unit, Central Alps) and 3D numerical models. *Journal of Structural Geology*, 144, 104255.
- Manatschal, G., Müntener, O., Lavier, L. L., Minshull, T. A., & Péron-Pinvidic, G., 2007. Observations from the Alpine Tethys and Iberia–Newfoundland margins pertinent to the interpretation of continental breakup. *Geological Society, London, Special Publications*, 282(1), 291-324.
- Manatschal, G., Lavier, L., & Chenin, P., 2015. The role of inheritance in structuring hyperextended rift systems: Some considerations based on observations and numerical modeling. *Gondwana Research*, 27(1), 140-164.
- Michibayashi, K., & Mainprice, D., 2004. The role of pre-existing mechanical anisotropy on shear zone development within oceanic mantle lithosphere: an example from the Oman ophiolite. *Journal of Petrology*, 45(2), 405-414.
- Mohn, G., Manatschal, G., Müntener, O., Beltrando, M., & Masini, E., 2010. Unravelling the interaction between tectonic and sedimentary processes during lithospheric thinning in the Alpine Tethys margins. *International Journal of Earth Sciences*, 99(1), 75-101.

- Mohn, G., Manatschal, G., Beltrando, M., Masini, E. and Kuszniir, N., 2012. Necking of continental crust in magma-poor rifted margins: Evidence from the fossil Alpine Tethys margins: neck-ing of continental crust. *Tectonics*, 31 (1): TC1012. <https://doi.org/10.1029/2011TC002961>.
- Moulas, E., Burg, J. P., & Podladchikov, Y., 2014. Stress field associated with elliptical inclusions in a deforming matrix: Mathematical model and implications for tectonic overpressure in the lithosphere. *Tectonophysics*, 631, 37-49.
- Moulas, E., Schmalholz, S.M., Podladchikov, Y., Tajčmanová, L., Kostopoulos, D., Baumgartner, L., 2019. Relation between mean stress, thermodynamic, and lithostatic pressure. *J. Metamorph. Geol.* 37 (1), 1–14.
- Mouthereau, F., Lacombe, O., & Vergés, J., 2012. Building the Zagros collisional orogen: timing, strain distribution and the dynamics of Arabia/Eurasia plate convergence. *Tectonophysics*, 532, 27-60.
- Nimis, P., and Trommsdorff, V., 2001. Revised thermobarometry of Alpe Arami and other garnet peridotites from the Central Alps. *Journal of Petrology*, 42(1), 103-115.
- Osagiede, O., Haehn, D. A., Spaulding, A. C., Otto, N., Cochuyt, J. J., Lemini, R., ... & Colibaseanu, D. T., 2021. Influence of surgeon specialty and volume on the utilization of minimally invasive surgery and outcomes for colorectal cancer: a retrospective review. *Surgical endoscopy*, 35(10), 5480-5488.
- Passchier, C.W., 1982. Pseudotachylyte and the development of ultramylonite bands in the Saint-Barthelemy Massif, French Pyrenees. *Journal of Structural Geology*, 4.
- Passchier, C. W., & Trouw, R. A., 2005. *Microtectonics*. Springer Science & Business Media.
- Pennacchioni, G. and Cesare, B., 1997. Ductile–brittle transition in pre-Alpine amphibolite facies mylonites during evolution from water-present to water deficient conditions (Mont Mary nappe, Italian Western Alps). *Journal of Metamorphic Geology*, 15, 777–791.
- Pennacchioni, G. and Mancktelow, N.S., 2007. Nucleation and initial growth of a shear zone network within compositionally and structurally heterogeneous granitoids under amphibolite facies conditions. *Journal of Structural Geology*, 29, 1757–1780.
- Petri, B., Duretz, T., Mohn, G., Schmalholz, S. M., Karner, G. D., & Müntener, O., 2019. Thinning mechanisms of heterogeneous continental lithosphere. *Earth and Planetary Science Letters*, 512, 147-162.
- Pfeifer, H. R., 1987. A Model for Fluids in Metamorphosed Ultramafic Rocks: IV. Metasomatic Veins in Metaharzburgites of Cima di Gagnone, Valle Verzasca, Switzerland. In *Chemical Transport in Metasomatic Processes* (pp. 591–632). Springer Netherlands.
- Pfiffner, M., and Trommsdorff, V., 1997. Evidence for high–pressure metamorphosed ophicarbonate rocks, Cima di Gagnone, Central Alps. *Terra Nova*, 9(1), 26.
- Pfiffner, M., and Trommsdorff, V., 1998. The high–pressure ultramafic–mafic–carbonate suite of Cima Lunga–Adula, central Alps: excursions to Cima di Gagnone and Alpe Arami. *Schweizerische Mineralogische Und Petrographische Mitteilungen*, 78(2), 337–354.
- Pfiffner, O. A., 2014. *Geology of the Alps*. John Wiley & Sons.
- Piazolo, S., Daczko, N.R., Silva, D., Raimondo, T., 2020. Melt–present shear zones enable intracontinental

- orogenesis. *Geology* 48 (7), 643–648.
- Powell, R., Evans, K. A., Green, E. C., & White, R. W., 2018. On equilibrium in non-hydrostatic metamorphic systems. *Journal of Metamorphic Geology*, 36(4), 419-438.
- Prosser, G., Caggianelli, A., Rottura A., Del Moro, A., 2003. Strain localisation driven by marble layers: the Palmi shear zone (Calabria-Peloritani terrane, Southern Italy). *GeoActs*, 2, 155-166.
- Real, C., Froitzheim N., Carosi R. and Ferrando S., 2018. Evidence of large-scale Mesozoic detachments preserved in the basement of the Southern Alps (northern Lago di Como area). *Italy. J. Geosci.*, 137: 283-293.
- Rybacki, E., & Dresen, G., 2004. Deformation mechanism maps for feldspar rocks. *Tectonophysics*, 382(3-4), 173-187.
- Rubatto, D., and Hermann, J., 2007. Zircon behaviour in deeply subducted rocks. *Elements*, 3(1), 31–35.
- Rutter, E. H., 1999. On the relationship between the formation of shear zones and the form of the flow law for rocks undergoing dynamic recrystallization. *Tectonophysics*, 303(1-4), 147-158.
- Rutter, E. H., & Brodie, K. H., 1995. Mechanistic interactions between deformation and metamorphism. *Geological Journal*, 30(3-4), 227-240.
- Rutter, E.H., Brodie K.H. and Evans P.J., 1993. Structural geometry, lower crustal magmatic underplating and lithospheric stretching in the Ivrea-Verbano zone, northern Italy. *J. Struct. Geol.*, 15: 647-662.
- Rutter, E. H., Holdsworth, R. E., & Knipe, R. J., 2001. The nature and tectonic significance of fault-zone weakening: an introduction. *Geological Society, London, Special Publications*, 186(1), 1-11.
- Rutter, E., Brodie, K., James, T., & Burlini, L., 2007. Large-scale folding in the upper part of the Ivrea-Verbano zone, NW Italy. *Journal of Structural Geology*, 29(1), 1-17.
- Scambelluri, M., Pettke, T., Rampone, E., Godard, M., and Reusser, E., 2014. Petrology and trace element budgets of high-pressure peridotites indicate subduction dehydration of serpentized mantle (Cima di Gagnone, Central Alps, Switzerland). *Journal of Petrology*, 55(3), 459-498.
- Scambelluri, M., Pettke, T., and Cannà, E., 2015. Fluid-related inclusions in Alpine high-pressure peridotite reveal trace element recycling during subduction-zone dehydration of serpentized mantle (Cima di Gagnone, Swiss Alps). *Earth and Planetary Science Letters*, 429, 45–59.
- Schenker, F. L., Schmalholz, S. M., Moulas, E., Pleuger, J., Baumgartner, L. P., Podladchikov, Y., Müntener, O., 2015. Current challenges for explaining (ultra)high-pressure tectonism in the Pennine domain of the Central and Western Alps. *Journal of Metamorphic Geology*, 33(8), 869–886.
- Schmalholz, S. M., & Podladchikov, Y., 2014. Metamorphism under stress: The problem of relating minerals to depth. *Geology*, 42(8), 733–734.
- Schmalholz, S. M., & Mancktelow, N. S., 2016. Folding and necking across the scales: a review of theoretical and experimental results and their applications. *Solid Earth*, 7(5), 1417-1465.
- Schmalholz, S. M., Moulas, E., Plümper, O., Myasnikov, A. V., & Podladchikov, Y. Y., 2020. 2D Hydro-Mechanical-Chemical Modeling of (De) hydration Reactions in Deforming Heterogeneous Rock: The Periclase-Brucite Model Reaction. *Geochemistry, Geophysics, Geosystems*, 21(11), e2020GC009351.

- Schmid, D. W., & Podladchikov, Y. Y., 2003. Analytical solutions for deformable elliptical inclusions in general shear. *Geophysical Journal International*, 155(1), 269-288.
- Schorn, S., 2018. Dehydration of metapelites during high-P metamorphism: The coupling between fluid sources and fluid sinks. *Journal of Metamorphic Geology*, 36(3), 369-391.
- Simonetti, M., Langone, A., Corvò, S., Bonazzi, M., 2021. Triassic-Jurassic rift-related deformation and temperature-time evolution of the fossil Adriatic margin: A review from Ossola and Strona di Omegna valleys (Ivrea-Verbano Zone). *Ophioliti*, 46(2), 147-161.
- Smith, D. C., 1984. Coesite in clinopyroxene in the Caledonides and its implications for geodynamics. *Nature*, 310(5979), 641-644.
- Spear, F. S., 1995. Metamorphic phase equilibria and pressure-temperature-time paths.
- Stern, R. J., 2002. Subduction zones. *Reviews of geophysics*, 40(4), 3-1.
- Stüwe, K., 2002. *Geodynamics of the Lithosphere* (p. 449). Berlin: Springer.
- Sulem, J., & Famin, V., 2009. Thermal decomposition of carbonates in fault zones: Slip-weakening and temperature-limiting effects. *Journal of Geophysical Research: Solid Earth*, 114(B3).
- Tommasi, A., & Vauchez, A., 2001. Continental rifting parallel to ancient collisional belts: an effect of the mechanical anisotropy of the lithospheric mantle. *Earth and Planetary Science Letters*, 185(1-2), 199-210.
- Warren, C.J., 2013. Exhumation of (ultra-)high-pressure terranes: concepts and mechanisms. *Solid Earth* 4, 75–92.
- Tajčmanová, L., Vrijmoed, J., & Moulas, E., 2015. Grain-scale pressure variations in metamorphic rocks: implications for the interpretation of petrographic observations. *Lithos*, 216, 338-351.
- Treagus, S. H., & Sokoutis, D., 1992. Laboratory modelling of strain variation across rheological boundaries. *Journal of Structural Geology*, 14(4), 405-424.
- Tumiati, S., Zanchetta, S., Pellegrino, L., Ferrario, C., Casartelli, S., and Malaspina, N. (2018). Granulite-facies overprint in garnet peridotites and kyanite eclogites of Monte Duria (Central Alps, Italy): clues from srilankite-and sapphirine-bearing symplectites. *Journal of Petrology*, 59(1), 115-151.
- Wang, X., Liou, J. G., and Mao, H. K., 1989. Coesite-bearing eclogite from the Dabie Mountains in central China. *Geology*, 17(12), 1085-1088.
- Wheeler J., 2014. Dramatic effects of stress on metamorphic reactions. *Geology*, v. 42; no. 8; p. 647–650.
- White, S. T., & Knipe, R. J., 1978. Transformation-and reaction-enhanced ductility in rocks. *Journal of the Geological Society*, 135(5), 513-516.
- Whitney, D. L., Teyssier, C., Rey, P., & Buck, W. R., 2013. Continental and oceanic core complexes. *Bulletin*, 125(3-4), 273-298.
- Vauchez, A., Tommasi, A., & Mainprice, D., 2012. Faults (shear zones) in the Earth's mantle. *Tectonophysics*, 558, 1-27.
- Zhao, C., Hobbs, B. E., & Ord, A., 2008. *Convective and advective heat transfer in geological systems*. Springer Science & Business Media.

CHAPTER 2:

State of the Art

2. State of the Art

This chapter aims to provide the interested reader with some basic concepts on the most relevant topics related to this PhD research.

2.1 Overview of the Alps and their geological evolution

The Alps are the typical example of a collisional belt. Important geological concepts were established with the study of the rock formations of the Alps in the 18th century. The formation of the Alps was an episodic process that began about 300 Ma ago involving different types of rocks – sedimentary, igneous and metamorphic – all of different ages and with multiple deformation phases. Due to its multifaceted geology, the Alps represent one of the best places for investigations on the metamorphic and deformation processes occurring during the orogenic evolution. This section briefly summarizes some main aspects of the Alpine evolution (Dal Piaz et al., 2003).

The plate tectonic processes during the break-up of the supercontinent, Pangaea, had several effects on the Alps. The small ocean basins and microcontinents that originated during this process resulted in a intricate juxtaposition of different sedimentary environments whose facies are now visible in the Alps juxtaposed vertically and laterally, in apparent complete disorder. The palaeogeographical shapes of the sedimentary basins affected the architecture of the Alps when these basins were closed during their formation (Schmid et al., 2004; Pfiffner, 2014).

A number of collisions between continents, or orogenies, have occurred before the geological evolution of Alps. Among these, the Variscan orogenesis (or Hercynian orogeny) was one of the most important in the contribution to the formation of the European mountains, and thus in the Alps (Handy et al., 1999). It originated in the Carboniferous (380-280 Ma) as a consequence of the collision between the continents North America–Baltica (Laurasia) and the South America–Africa (Gondwana). In the Early Permian (280 Ma) intense magmatic activity is evidenced by a widespread distribution of magmatic products now documented in the Southern and Eastern Alps domains (Pfiffner, 2014).

In the Early Triassic (230 Ma), Pangaea broke up along a rift that opened up between Gondwana and Laurasia (Fig. 2.1). The rift originated in the Jurassic (200-150 Ma) in the Tethys and extended along an arm of the Tethys between the continental masses of Arabia and Greece–Italy (Fig. 2.1). The eastern part of the rift shifted to the north and separated the landmass Greece–Italy from Laurasia. This small

ocean basin is referred to as the Ligurian or Piemont Ocean in Alpine geology. The rift expanded to the west and separated Africa–South America from North America and was the precursor to the Atlantic Ocean (Beltrando et al., 2015; Pfiffner, 2014 and references therein).

In the Early Cretaceous (120 Ma), North America and Africa drifted further apart, and the Central Atlantic was born (Figs. 2.1, 2.2). A transform fault separated Iberia from Europe and acted as a local plate boundary during the drift of Iberia away from North America. The spreading of mid-oceanic ridge of the Atlantic in the west and the occurrence of a transform fault to the opposite sides (north and south) of Iberia, promoted the movement of the Iberia itself. Here, a continental fragment composed of Corsica–Sardinia–Briançon extended from Iberia in a north-easterly direction becoming separated from Iberia (Fig. 2.2). The Corsica–Sardinia–Briançon continental fragment corresponds to the so-called Briançon microcontinent, a submarine rise that can be traced nowadays from the Western Alps through to the Swiss Alps (Schmid and Kissling, 2000). The sea basin to the northwest of the Briançon microcontinent corresponds to the Valais Basin, and that in the southeast corresponds to the Penninic Ocean. Another transform fault connects the Ligurian-Piemont with the Penninic Ocean. The opening up of the Atlantic occurred simultaneously with an oblique opening up of the Ligurian–Piemont and Penninic oceans. The Ligurian-Piemont Ocean had a mid-oceanic ridge that led to the formation of oceanic crust. The Adriatic continental margin and the Austroalpine microcontinent were stretched in an east–west direction by the opening up of the Ligurian-Piemont and the Penninic oceans (Fig. 2.2). The normal faults in the future Austroalpine and Southalpine realms are evidence of this (Zingg et al., 1990; Pfiffner, 2014).

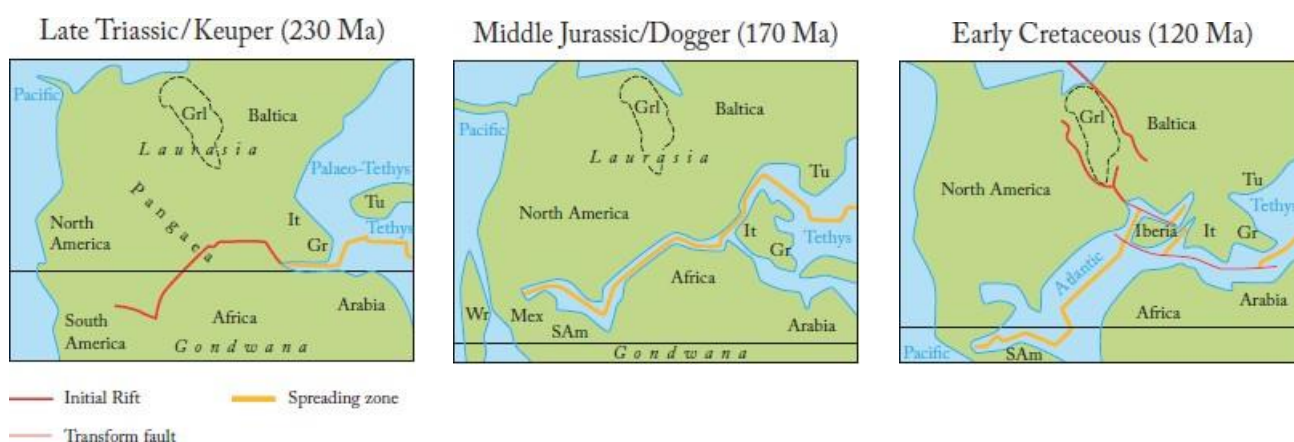


Fig. 2.1 - The break-up of Pangaea shown in three time slices. Grl, Greenland; It, Italy; Gr, Greece; Tu, Turkey; SAm, South America; Wr, Wrangellia; Mex, Mexico; (from Pfiffner, 2014).

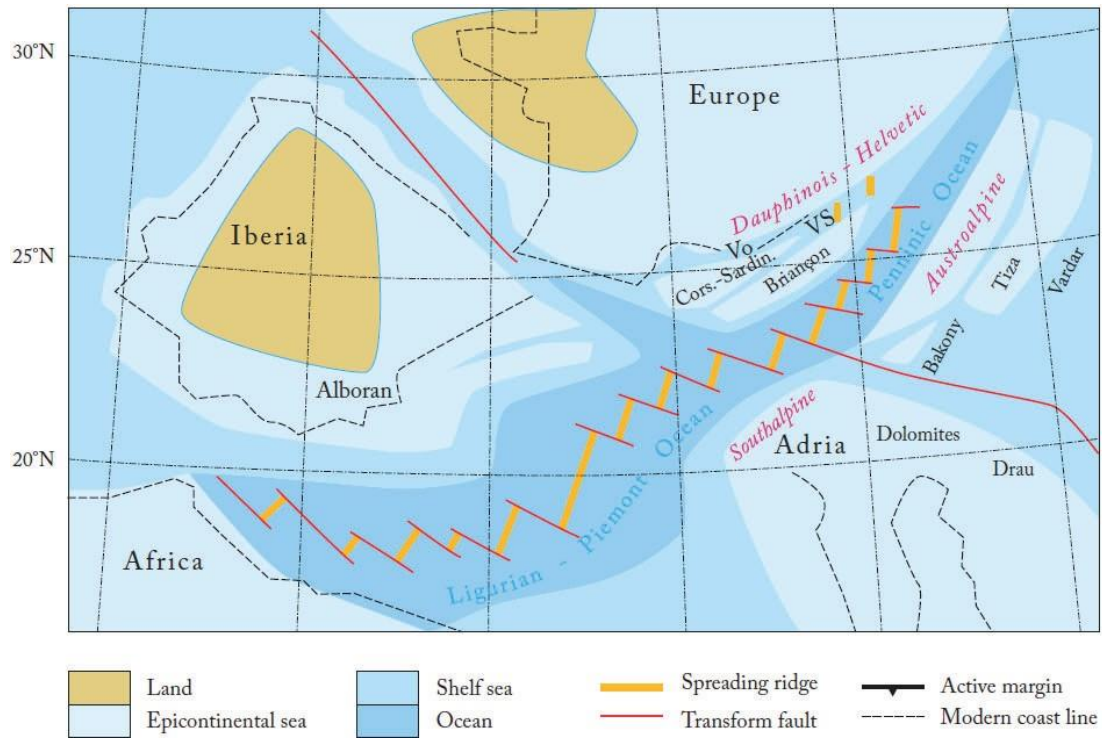


Fig. 2.2 - Plate reconstruction for the Barremian (ca. 125 Ma), from Pfiffner (2014). The Ligurian–Piemont Ocean is now wider and aligned with the Penninic Ocean. Similarly, the Southalpine and Austroalpine domains are now aligned. Cors-Sard, Corsica–Sardinia continental fragment; Vo, Vocontian basin; VS, Valais basin.

The formation of the European Alps *sensu stricto* started in the Mesozoic in the Late Mesozoic (130–65 Ma) as a result of convergent plate movements between Baltica/Europe and Africa–Arabia. During this process, the sea basins that lay between, the Piemont Ocean and the Valais Basin, were closed by subduction. This occurred in two separate stages. The Piemont–Penninic ocean was closed by subduction proceeding in a westerly direction in the Cretaceous, the Valais Basin by a collision in the Cenozoic between the Briançon microcontinent and the Adriatic continental margin, proceeding in a more north–south direction and, later, between the Briançon microcontinent and the European continental margin. The subduction and the collision process led to an even more complex geometry in the Alpine chain that was being uplifted (e.g., Schmid and Kissling; Dal Piaz et al., 2003; Pfiffner, 1993; 2014).

2.1.1 The structure of the Alps

The Alps extends in a wide arc from Nice to Vienna (Fig. 2.3A). The Po Basin lies within the arc. Along this mountain chain, the Alps are geographically subdivided into the Western Alps, Central Alps and Eastern Alps (Pfiffner, 1993). From a geological point of view, the Alps are divided into two portions by an important tectonic line, the Insubric line, which runs east-west (Schmid et al., 1987; Fig. 2.3A). To the north of it we find the Pennine and Austroalpine domains, and to the south the Southalpine domain. The Penninic domain is the deepest part of the Alpine chain laid bare by erosion. It is mainly made up of a nappe system characterised by high grade metamorphic rocks of different paleogeographic origins (Pfiffner et al., 1997; Rutti, 2003). The Austroalpine comprises the highest structural units of the Alpine chain, as they overlie the Penninic ones. This domain consists of Mesozoic sediments and predominantly pre-Permian basement materials, already metamorphosed before the Alpine orogeny. The Southalpine domain is very similar to the Austroalpine domain and is considered paleogeographically as a large fragment of a continent (paleo-Africa) originally located to the south of the Ligurian–Piemont ocean (Fig. 2.3B; Handy et al., 1999). The Southalpine domain is predominantly made up of a continental metamorphic basement, on which a sedimentary sequence from Carboniferous to the Pliocene emerges. The basement in the northwestern part of the Southern Alps is of particular interest, as it exhibits an almost complete exposed cross-section through the lower and upper crust (e.g., Zingg et al., 1990).

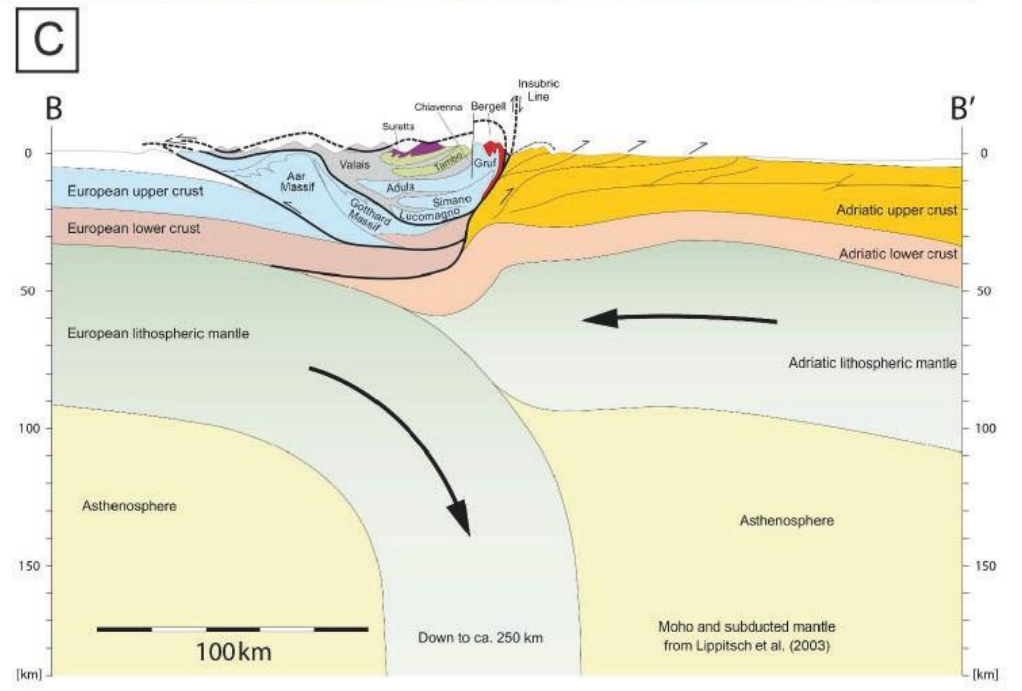
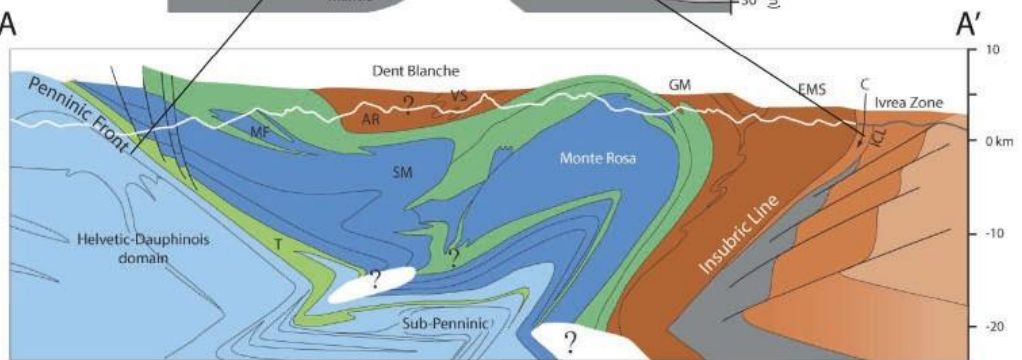
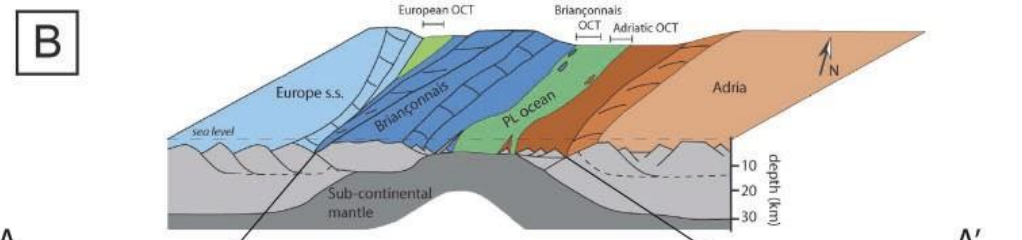
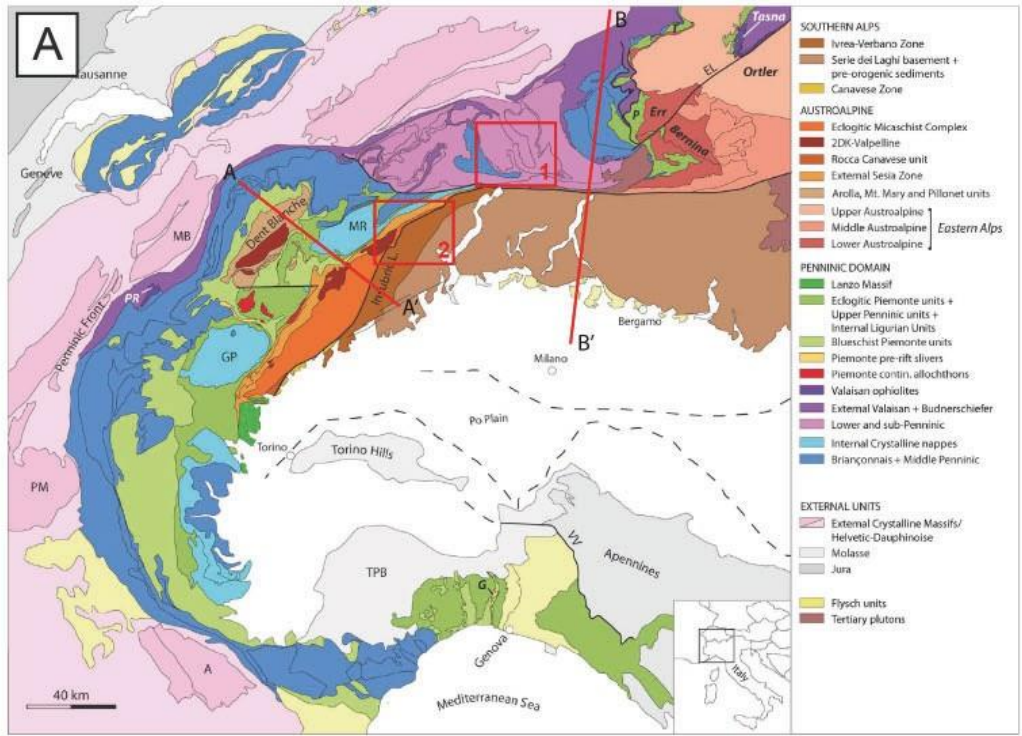
The two case studies investigated in this PhD research are located in the Alpine chain (Fig. 2.3A) and in particular, the case study 1 – Cima di Gagnone is located in the Penninic domain (European crust), whereas case study 2 – Anzola shear zone is located in the northwestern part of the Southern Alps (Adrian crust).

The crystalline basement in the internal portion of the Alps, which corresponds to the distal edge of the European continental margin, is even more strongly deformed internally (e.g., Pfiffner et al., 1997; Rutti, 2003). Indeed, south-dipping subduction of the European plate and subsequent continental collision with Adria produced the stack of the Penninic nappes in the Central Alps (Fig. 2.3C; Schmid et al., 2004). Even though the different crystalline basement blocks were thrust on top of each other, the tectonic contacts were later subjected to ductile folding, as for example is revealed in the largest crystalline block, the Gran Paradiso massif (GP in Fig. 2.3A), the domed surface of which

forms the contact to the Upper Penninic nappes. The Mesozoic sediments in the Lower and Middle Penninic nappes have been peeled off their crystalline substrate and form a separate nappe pile in the frontal region of the Penninic nappes (Fig. 2.3B, C). The Upper Penninic nappes overlie this and are located to the southeast of the Gran Paradiso massif: these are oceanic rocks that underwent high-pressure metamorphism during the Alpine orogeny. Based on geophysical data it can be assumed that the European lower crust was thickened by tectonic shortening beneath the Penninic nappes, as the boundary between the crust and the mantle, the Moho, is at a depth of over 50 kilometres below the Gran Paradiso massif (e.g., Pfiffner, 2014 and references therein).

The situation is completely different in the southeast, on the Adriatic side, although the upper crust has also been thickened by thrusting (Fig. 2.3B). The Mesozoic–Cenozoic sediments above it are also affected by thrusting, but without actually being sheared off, as was the case for the European crust. What is interesting, is the fact that the lower crust and the Adriatic mantle rise up towards the northwest. The lower crust thereby reaches the Earth surface and is now exposed in the Ivrea Zone, and the mantle below, also called the Ivrea Body or the Ivrea Mantle, also rises up and almost reaches the Earth surface (Fig. 2.3A, B; Handy et al., 1999). Tectonic contacts between the Penninic nappes and the Ivrea Body are steep and Upper Penninic oceanic rock units and continental crustal blocks from the Adriatic continental margin (e.g., the Sesia-Lanzo Zone) lie alongside each other. Two larger, steep, shearing zones indicate how the rocks were overthrust onto the Ivrea Body (Insubric Fault) and how the rocks of the Gran Paradiso massif were overthrust onto the steep zone. Simultaneously, the highly metamorphic rocks moved closer to the Earth surface due to erosion in the exhumation process (e.g., Pfiffner, 2014; Mohn et al., 2012; Beltrando et al., 2015 and reference therein).

Fig. 2.3 - Simplified tectonic map and geological sections (A-A'; B-B') of the Western and Central Alps showing the geographical locations of the two case studies (box in red). The Cima di Gagnone (case study 1) is in the Penninic domain in Central Alps; the Anzola shear zone (case study 2) is in the Ivrea-Verbano Zone, Italian Southern Alps (modified after Mohn et al., 2012; Beltrando et al., 2010). B) Palinspatic reconstruction of western Tethys during Jurassic rifting and exhumation of subcontinental mantle and relative sections (Beltrando et al., 2010a). C) Simplified section across the Central Alps (modified after Pfiffner, 2009; Burg et al., 2002).



2.2 Rheology of the crust

This PhD thesis deals with a rheological study at the outcrop scale, so introducing the concept of rheology is essential. The term ‘rheology’ derived from the Greek words rheo (flow) and logos (science) and denotes the study of deformation and flow of matter (e.g., Ranalli, 1995). Knowledge of rock rheology is fundamental to understanding the evolution and dynamics of the Earth. Rocks and minerals react differently to stress and depend on deformation mechanisms, crystallographic anisotropy, temperature, presence of fluids, strain rate and pressure. A simple model subdivides the crust into an upper part dominated by brittle deformation mechanisms and a lower part where plastic flow dominates (Fig. 2.4; Burov, 2011). The transition is referred to as the brittle–plastic transition (or brittle–ductile transition). For a theoretical uniform monolithologic crust with a gradual downward increase in temperature, we would expect a single brittle–plastic transitional zone at the depth where temperature-activated flow becomes important. Two different strength curves (brittle and plastic laws) can therefore be drawn, based on experimental data. For low temperatures (< ca. 500 °C) and confining pressures corresponding to shallow crustal levels, the maximum differential stress that rocks can sustain is defined by Byerlee’s law of frictional sliding (on oriented pre-existing fractures with no pore-fluid pressure) or alternatively by the Mohr-Coulomb or Griffith failure criteria (for intact rocks, e.g., Fossen, 2016). Under such conditions, deformation is in the brittle regime and is ruled by fracturing and frictional sliding, with final products being brittle fault rocks (e.g., gouges, cataclasites and pseudotachylites; Rutter et al., 2001). With increasing confining pressure, the differential stress required for failure increases until the brittle-ductile transition in the middle crust (Fig. 2.2; Bürgmann and Dresen, 2008). For higher temperatures, normally corresponding to middle and lower crust (ca. 500–600°C), deformation is described by a power-law equation derived from laboratory rock deformation experiments:

$$\dot{\epsilon} = A \sigma^n \exp(-Q/RT) \text{ (Eq. 2.1)}$$

where $\dot{\epsilon}$ is strain rate, σ is the differential stress raised to the stress exponent n , A is a constant, Q is the activation enthalpy, R is the gas constant and T is temperature (e.g., Karato, 2008). For the continental lithosphere, the crust’s power-law is typically modelled according to experimentally derived wet-quartz rheology whereas the lithospheric mantle is modelled according to olivine rheology (Kohlstedt et al., 1995). In such simplified lithospheric strength profile, these power-laws translate in

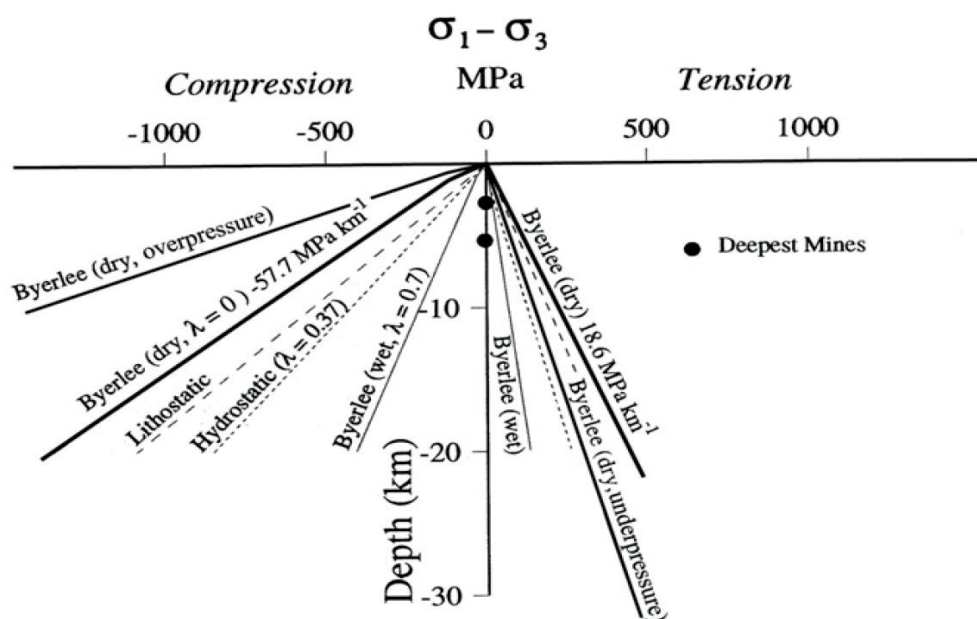


Fig. 2.4 - Dependence of brittle strength on depth/pressure: lithostatic pressure, fluid pressure and tectonically induced over- or underpressure. Note that rocks are weaker under extension than under compression, which explains frequent deep seismicity in overall weak rift zones. Tectonic extension or compression may change total pressure, and, consequently, brittle strength, by a factor of respectively 0.5–2. λ is pore pressure factor (Burov, 2011)

portions of the lithosphere deforming in the ductile manner (Fig. 2.5). Consequently, crustal levels deforming by power-law creep are generally weaker than levels deforming by cataclasis. This implies a weak lower crust and a strong middle crust corresponding to the transition between the brittle and ductile regimes, and an important strength contrast at the Moho, given by a large difference in plastic creep strength between quartz and olivine (e.g., Kohlstedt et al., 1995).

Lithospheric models have been improved ongoing to account for differences in tectonic regimes, geothermal profiles, water contents, melt contents, deformation mechanisms and different lithology (e.g., Bürgmann and Dresen, 2008). All these parameters influence the constitutive laws from which the strength profiles are constructed. The tectonic regime (i.e., the stress field) affects the slope of the Byerlee curve and therefore the position of the brittle-ductile transition: for example, in a compressive regime this is located at shallower depth and occurs at higher differential stresses than in extension (Rosenberg and Handy, 2005). These curves also depend on the changes in rock composition. The crust is layered and heterogeneous and varying mineralogical composition through the lithosphere can lead

to several layers of alternating brittle and plastic rheologies (Fig. 2.5). The brittle–plastic transition is generally gradual or recurring over a wide zone in the continental crust. The transition is also influenced by the presence of fluids, and the fact that “dry” rocks are more resistant to deformation (Fig. 2.5).

Overall, two end-member models can be used to describe the variation of rheological properties and strength in Earth (Fig. 2.5): 1) a model with a weak lower-crust sandwiched between a strong upper-crust and mantle (known as the “Jelly sandwich” model) and 2) a model with a strong crust overlying a weak mantle (known as the “Crème brûlée” model; Bürgmann and Dresen, 2008). The first model (the Jelly sandwich model) has been constructed assuming a wet lower crust (by using a wet-feldspar flow law), whereas the second model (the Crème brûlée model) has been constructed assuming a high geotherm in the mantle (which makes temperature at the Moho higher, thus modifying the dry olivine flow law) and a dry lower crust (using the dry-feldspar flow law; Fig. 2.5).

In the first model the lower crust is rheologically “weak”, whereas in the second model it is “strong”. The “Jelly sandwich” model is supported by geophysical observations, numerical and analogue

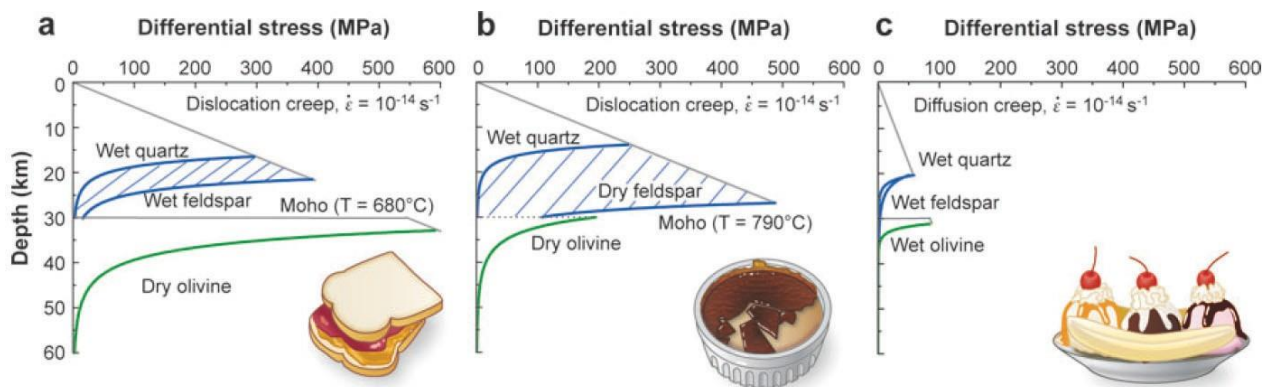


Fig. 2.5 - Schematic view of alternative first-order models of strength through continental lithosphere, from Bürgmann and Dresen (2008). The profile a, with a strong upper crust and mantle and a weak lower crust, is known as the “Jelly sandwich” model. The profile b, with a strong lower crust and a weak upper mantle, is known as the “Crème brûlée” model. The profile c, the “Banana split” model, considers the weakness of a major crustal fault zones through the thickness of the lithosphere, caused by various strain weakening and feedback processes. The three models clearly underline the importance of temperature, water content and lithology in determining the model’s outcome. For the flow law parameters used in the models, refer to Bürgmann and Dresen (2008).

models and by indications of decoupling at the Moho. Tectonic modelling shows that the lithosphere requires a relatively strong mantle and a relatively weak lower crust for plate tectonics to operate. The “Crème brûlée” model is supported by earthquake focal depths distributions and gravimetric anomalies, indicating that the lower crust is elastic and stronger compared to the underlying aseismic upper mantle. This model fits well with mechanically strong dry granulites residing in the lower crust (Bürgmann and Dresen, 2008). A strong lower crust has typically been explained with large parts of it being dry, thus incapable of deforming by crystal plastic flow (Austrheim, 2013). Finally, a third additional model, the “Banana split” model, considers that the strength of the lithosphere is greatly reduced along plate boundaries owing to various weakening processes involving thermal, fluid, and strain-rate effects. Relative weakness of major fault zones may exist at all depth levels. In the viscous regime, shear heating, grain-size reduction, dynamic recrystallization, chemical alterations and phase changes, and the development of rock fabrics can lead to the formation of weakened shear zones. It continues to be a question of much debate as to whether the overall style of continental deformation is governed by the properties and activity of discrete, weakened shear zones or by the bulk rheological properties of the viscously deforming lower lithosphere. Burov, (2011) has analysed the plausibility of each model and argued in favour of the “Jelly sandwich” model with a weak lower crust and a strong upper mantle. According to this author’s thermal and mechanical modelling of the lithosphere, “the mantle is strong and capable of supporting stresses and geological loads” for long time scales. From the above models, it is clear that the greatest controversies are related to the lower crust, and that the rheological behaviour of this layer is critical for understanding the overall strength of the continental lithosphere. Therefore, it is important to obtain as much information as possible about crust composition and evolution in order to predict its strength profile or rheological stratigraphy. Such information goes into the modelling of crustal-scale deformation, such as rifting and orogeny.

These models are valid at the crustal scale, but when we go into detail, it emerges that many factors can significantly change the rheological behaviour at similar crustal levels. Hence, there is a need to bring the study of rheology to the outcrop scale in order to obtain increasingly realistic models that take into account the complexity of natural cases.

2.3 Metamorphic Pressure-Temperature conditions

Furthering our understanding of the relationships between deformation and metamorphic processes are the major aim of this PhD thesis, therefore, it is important to present the basic concepts about how metamorphic conditions (P - T) are determined and discuss how deformation may influence these estimates. Metamorphic rocks show abundant evidence of complex histories of pressure, temperature and strain (Spear and Peacock, 1989). Features such as structural fabrics, reaction textures, mineral inclusions and chemical zoning in minerals all demonstrate the changing conditions that are recorded by metamorphic rocks. One of the most important efforts of the petrologist is to use the different information told by the rocks to decipher this complex history, which can then be related to thermal and tectonic processes that have happened in the crust. A fundamental concept necessary for the analysis of the metamorphic rocks is that of an equilibrium state, which will be referred to as the peak metamorphic condition (Spear and Peacock, 1989). The basis for this concept comes from an examination of the kinetics of metamorphic processes in the context of the metamorphic pressure-temperature path. Overall, most metamorphic recrystallization will occur near the peak metamorphic temperature and the mineralogy and mineral chemistry will reflect these conditions (Fig. 2.6). In many circumstances, it is possible to attribute an equilibrium state for a metamorphic rock that is the peak metamorphic temperature. One way in which metamorphic P - T conditions can be inferred is through the calculation of stable mineral equilibria that are possible in a particular system. Inferences about metamorphic conditions are then made through correlation of the computed phase equilibria with that observed in the sample (e.g., Bucher and Frey, 2002; Philpotts and Ague, 2009; Barker, 2014; Winter, 2014; Yardley and Warren, 2021). Calculation of phase equilibria involves solution of sets of equations that define the equilibrium condition of the system. Mineral assemblages and textures may provide qualitative information about the P - T conditions at which a rock equilibrated. These qualitative methods include the use of: i) the index minerals, characteristic minerals that provide an indication of the P - T conditions at which a rock formed (i.e., the aluminosilicates: kyanite, sillimanite, andalusite), ii) the metamorphic facies, assemblages of minerals, each characteristic for a particular bulk composition and indicating the range of P - T conditions at which the rock equilibrated; iii) petrogenetic grid, a phase diagram that show the relative stability of different mineral assemblages within a given chemical system of subsystem.

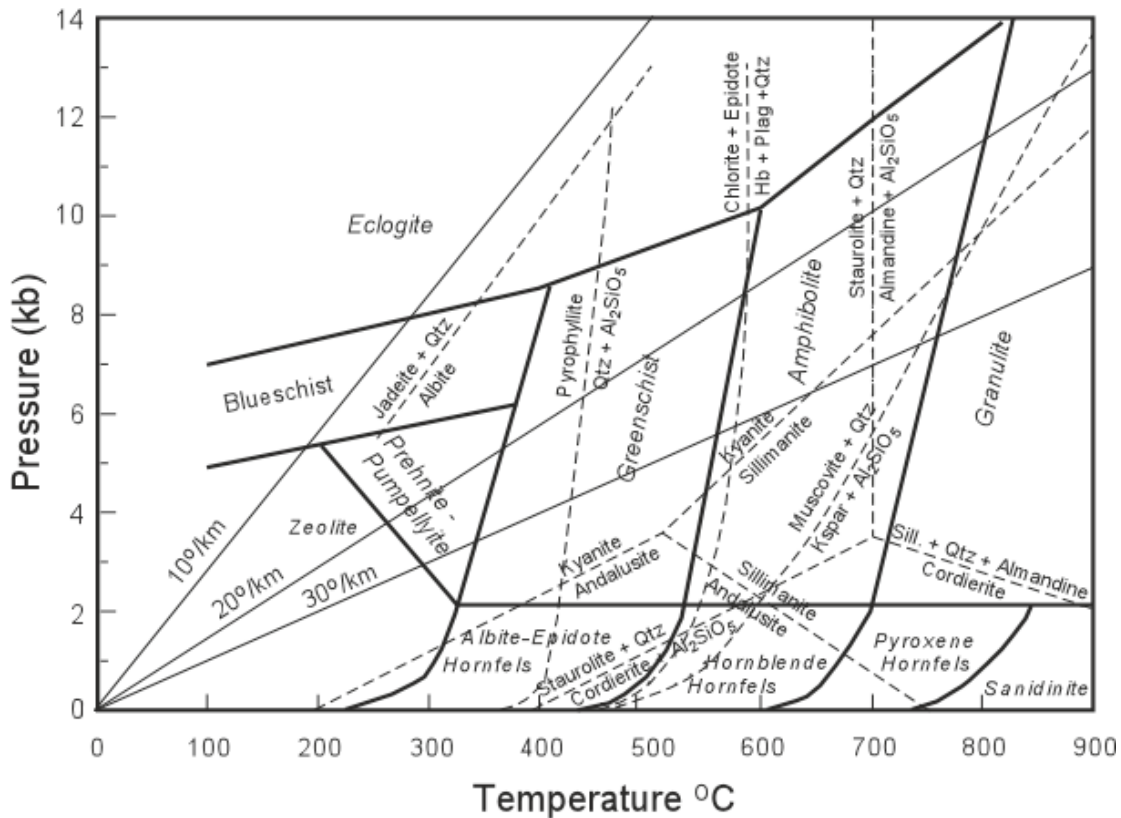


Fig. 2.6 - Simplified P - T diagram showing metamorphic reactions and stability field of diagnostic mineral assemblages in the KFMASH system (Spear, 1995). Metamorphic facies fields and geotherms for geothermal field gradients of 10, 20 and 30°C/km (at 15 km depth) are shown.

Conversely, the quantitative calculation of phase equilibria to reconstruct the P - T conditions of metamorphic rocks occur using two types of approaches: geothermobarometry and thermodynamic modelling (Spear and Peacock, 1989).

Geothermobarometry is the name given to applications whereby the pressure and temperature dependence of the equilibrium constant is used to infer metamorphic pressures and temperatures. The central notion of geothermobarometry is that the value of the equilibrium constant can be determined by measurement of the composition of coexisting minerals and application of appropriate activity models. A single equilibrium constant will define a line on a P - T diagram (e.g., Spear, 1995 and reference therein). As much as different equilibria have different P - T slopes, the intersection of two equilibria can be used to infer P - T point. By definition, geothermometers are those equilibria that are best suited to calculation of geologic temperatures and geobarometers are those equilibria that are best suited to calculation of geological pressures. In general, geothermometers are equilibria that have little pressure dependence so that an imprecise estimate of the pressure of equilibration will only produce

a small error in the estimate of temperature. Similarly, geobarometers are equilibria that are relatively insensitive to temperature. In this project research the coupling of several geothermobarometers were used to determine the P - T conditions in both case studies (see chapter 3.6 for details).

Thermodynamic modelling requires a thermodynamic database in order that the resulting calculation could directly related to the accuracy of the database (Palin et al., 2016). Several thermodynamic databases have been published in recent years, among these the most used is that from Holland and Powell (1985). Thanks to the advancement of technology in the recent decades, many are nowadays the software available for running these thermodynamic modelling on personal computer, such as Thermocalc (Powell and Holland, 2001), Gibbs (Spear et al., 2001), Perple_X (Connolly, 1990, 2005), Theriak-Domino (De Capitani and Petrakakis, 2010; Jowhar, 2012). The common final product is generally what is called P - T pseudosection, an equilibrium phase diagram which shows all the stable mineral assemblages of a rock at different P - T ranges for a single whole-rock chemical composition (bulk-rock composition). The stable mineral assemblages are marked as different areas in the P - T graph. Unlike geothermobarometry, which focuses only on single chemical equilibrium equations, pseudosections make use of multiple equilibrium equations to search for the P - T conditions. It is widely used in metamorphic rock analysis due to its consideration of multiple reactions, which resemble metamorphic processes of multiple minerals in reality (Spear and Peacock, 1989; Palin et al., 2016). Pseudosection is different from petrogenetic grid because pseudosection shows different mineral phases for a single rock chemical composition, while petrogenetic grid shows a set of reactions under different P - T conditions that would occur for a phase diagram for an idealized composition (e.g., Bucher and Frey, 1990). The results from a single pseudosection are not completely reliable, since in reality the rock specimen is not always in equilibrium. However, analysis can be done on fractions of the P - T - t path, e.g., at boundaries of mineral inclusions, or on local bulk composition analysis would improve precision and accuracy of the P - T - t path.

However, it is always important to bear in mind that during the determination of P - T conditions caution must be used applying these methods (geothermobarometry, pseudosection). Indeed, the use of these methods should always be interpreted on the basis of the studied context and must always be combined with the classical petrographic and geochemical observations (i.e., mineral assemblages, metamorphic facies, mineral chemistry, etc.).

Moreover, it is important to note that the interpretation of P - T paths with these methods is often made with the basic assumption that pressure is only caused by the weight of the overlying rock column (i.e., it is lithostatic) and that, therefore, pressure correlates directly with depth. This assumption implies that deviatoric stress does not play a role. Then, the pressure at certain depth corresponds to the vertical normal stress, which may be calculated by integrating the density over depth.

2.4 Differential stress, deviatoric stress and implications for phase equilibria

As a first approximation the depth-of-burial of metamorphic rocks is estimated from the Archimede's formula. This formula is derived from the stress balance of static fluids under the influence of gravity and relates pressure with depth via:

$$P = \rho gh \text{ (Eq. 2.2)}$$

where P is the lithostatic pressure, ρ is the density of the considered material, g is the acceleration of gravity and h is the height of the hydrostatic (lithostatic for rocks) column (depth). Tectonic stresses that develop during deformation can affect the value of pressure since the increase of differential and deviatoric stresses values (e.g., Fossen, 2016). The deviatoric stress is the difference between the mean stress and the total stress. The deviatoric stress tensor represents the anisotropic component of the total stress and it is generally considerably smaller than the isotropic mean stress, but of greater significance when it comes to the formation of geologic structures in most settings. While isotropic stress results in dilation (inflation or deflation), only the anisotropic component results in strain. The relationship between its principal stresses influences what type of structures are formed. The differential stress represents the difference between the maximum and minimum principal stresses that causes the rock to deform, i.e., the stress tensor is anisotropic. For lithostatic stress the principal stresses are all equal, and so the differential stress is zero. Therefore, the lithostatic model itself provides no differential stress to the lithosphere, regardless of depth of burial. This has an important implication because while the uniaxial-strain reference state of stress may be reasonably realistic in sedimentary basins, it may not be very realistic deep in the lithosphere. Regardless of the choice of reference state of stress, tectonic stress adds to the total differential stress in a rock. The amount of differential stress that can exist in the lithosphere is, however, limited by the strength of the rock itself. Moreover, the strength of rocks in

the crust is in practice controlled by anisotropic features, particularly weak fractures and shear zones. Any attempt to increase the differential/deviatoric stresses above the ultimate rock strength will lead to deformation (Fossen, 2016).

An interesting correlated issue in the metamorphic record typically result from High Pressure (and possibly High Temperature) lenses, enveloped within either rheologically weaker or stronger “host” rocks, which exhibit lower metamorphic conditions. Indeed, in such context it is not enough link the pressure record to lithostatic pressure value, because it would imply to build geologically models too complex to explain these large contrasts. Several studies have already argued that the pressure recorded by the metamorphic minerals could significantly differ from the lithostatic pressure (e.g., Mancktelow, 2008; Hobbs and Ord, 2016; Wheeler, 2018; Moulas et al., 2019; Schmalholz et al., 2020; Hess and Ague, 2021). This pressure deviation is directly related to the mechanical state of the deforming rocks (i.e., anisotropies, geometry and composition of the rocks). This long-existing concept has been repeatedly disputed. Considering the mechanical properties of rocks, several studies have suggested that the magnitude of pressure deviation from the lithostatic value is small, almost insignificant because rocks are weak and the differential stress that controls natural deformation is low (Burov et al., 2001; Jolivet et al., 2003). Recent experiments suggest that GPa-level of stresses can be supported by the weakest high-pressure phase (omphacitic pyroxene) when extrapolated to geological conditions (Moghadam et al., 2010). In addition, recent numerical models (Schmalholz and Podladchikov, 2013) suggest that low viscosity zones may develop significant over/under pressure despite their low effective shear stress. Recent studies demonstrated the occurrence of variable temperature, and pressure metamorphic records in correspondence of sharp interfaces between rocks with high viscosity contrast (Casini and Maino, 2018; Schmalholz et al., 2020). However, it is still widely debated and far to being proved if both tectonic overpressures could have a real impact on the metamorphic reactions or melt generation (e.g., Hobbs and Ord, 2016; Bauville and Yamato, 2021; Jiang, 2021). Moreover, an actual contribution of deviatorial stress to the metamorphic record has hardly ever been demonstrated until now. Most studies in this area are of theoretical nature (e.g., Hobbs and Ord, 2016; Wheeler, 2018; Casini and Maino, 2018; Hess and Ague, 2021). Consequently, there is an urgent need to test these concepts in natural laboratories. For example, further studies coupling numerical simulations with field and analytical evidence are needed to improve the knowledge of these fundamental questions.

2.5 Mechanisms of weakening and strain localization of the middle to lower crust

The case study 2 investigated in this thesis involves the study of a shear zone where there has been an evident strain localization leading to the development of a large crustal fault. This leads to the introduction of the concepts underlying strain localisation and thus the early stages of large fault, crustal to lithospheric scale faults/shear zone nucleation. Localization of deformation is ubiquitous in Earth materials and observed over a broad range of scales from mm-scale intracrystalline to lithospheric-scale. Deformation commonly localizes along structures determining the bulk strength of the lithosphere (e.g., Bürgmann and Dresen, 2008; Karato, 2008; Fossen and Cavalcante, 2017; Gardner et al., 2020; Piazzolo et al., 2020). In the brittle upper crust, localization is represented by fault zones transitioning into localized ductile shear zones in the middle-lower crust at the brittle-ductile transition hosting mylonites and ultramylonites (e.g., Döhmman et al., 2019). Several are the processes that have been considered responsible for strain localisation: fracturing, grain size reduction, syn-kinematic metamorphic reactions, presence of fluids, presence of melt and lithological heterogeneities (e.g., Burlini and Bruhn, 2005; Gardner et al., 2017 and references therein). These processes cause shear zone initiation at material heterogeneities and multiple defects commonly present in rocks that serve as nucleation points for shear zones on the microscale or macroscale. Comprehending which factor is most relevant is still a matter of debate. Certainly, it is a combination of these processes that significantly contribute to weakening and strain localization. Few of these are briefly discussed below.

2.5.1 Water presence

Water can promote weakening in several ways. It can cause metamorphic reactions and lead to partial melting by lowering the solidus conditions of minerals (e.g., Blenkinsop, 2000). The presence of water at grain boundary can promote metamorphic reactions through enhanced chemical diffusion (e.g., Brodie and Rutter, 1985). However, the low porosity of high-grade rocks of the lower crust do not allow large amounts of interstitial grain boundary water to freely circulate. That means that intracrystalline water in the lower crust is scarce and heterogeneously distributed (e.g., Yadley 1997). Shear zones usually represent the best way of increase the water flux at depth, since they enhanced interconnected porosity and permeability (e.g., Austrheim, 1987; Liu et al., 2010). The presence of syn-

kinematic amphibole, for example, in lower crustal shear zones (e.g., Tommasi et al., 2017) confirm that water preferentially localized along shear zones (Austrheim, 2013; Getsinger et al., 2013) and suggest the importance of fluids during shearing also at these depths. Even the fracturing is an efficient factor to facilitate fluid infiltration through the increasing of the permeability of rocks, thus mineral reactions and deformation even at lower crustal conditions (e.g., Austrheim, 1987, 2013). Intense fracturing under granulite facies conditions has been interpreted as indicative of high creep strength of the granulites that enable in situ stresses to reach magnitudes sufficient for fracture (Austrheim, 2013). The ingress of fluid in the lower crust occurs also after seismicity-induced fracturing of dry and strong granulites. Aqueous fluid infiltration can also trigger metamorphic reactions (typically hydration reactions; Bucher and Grapes, 2009; Schorn et al., 2017). The most important metamorphic reactions in the lower crust (i.e., the granulite - eclogite, the gabbro-eclogite and the eclogites-amphibolite transitions) are, indeed, all triggered by de-hydration, which produce fluids free to move in the rocks (Austrheim, 2013; Schorn, 2017). Heterogeneous distribution of fluids results in a rheological contrast between dry and wet mineralogical assemblages, producing highly differentiated rheological behaviour (anhydrous-strong vs hydrated-weaker) promoting localized shearing (Austrheim, 2013; Getsinger et al., 2013). The most important source of water in the lower crust is through dehydration reactions consuming biotite and/or amphibole. Water released during these reactions may contribute to strain localization at or near metamorphic facies boundaries (i.e., amphibolite to granulite facies) leading also to partial melting (e.g., Gardner et al., 2020).

2.5.1 Melt presence

Another fluid-related process that has a strong influence on the mechanical behaviour of rocks is partial melting. Rheological weakening was caused by localized melt-present deformation coupled with melt-induced reaction softening. This interpretation has been demonstrated in experimentally and naturally deformed rocks of different compositions representative of the crust (e.g., Piazzolo et al., 2020). The introduction of a phase with lower viscosity (the melt) to the system decrease, indeed, the strength of rocks (e.g., Rosenberg and Handy 2005). The greatest weakening effect of melt occur when it circulates along the grain boundaries forming an interconnected melt network causing a significant drop of the rock strength (Stuart et al., 2016; Lee et al., 2020; Gardner et al., 2020). In crustal systems, this typically happens for melt fractions $\geq 7\%$ (e.g., Rosenberg and Handy 2005). Weakening effect can

be explained by an increased contribution of melt assisted grain boundary sliding and deformation mechanism as the diffusion creep (e.g., Lee et al., 2020). For large fractions of melt (20%-50%; Rosenberg and Handy 2005), the strength of the rock is not determined any longer by the solid-bearing framework but by the melt portion. As melt has a significantly lower viscosity than the solid minerals, the bulk strength drops a few orders of magnitude (Rosenberg and Handy, 2005). The percentage of melt necessary for a switch from the solid-bearing to the melt-bearing framework is known as the critical melt fraction, or the rheological critical melt percentage, and is generally estimated above 30% melt (e.g., Burlini and Bruhn, 2005). This value essentially separates the fields of solid-state flow and magmatic flow. For small amounts of melt fraction (typically lower than 7% for crustal material: Rosenberg and Handy, 2005), melt affects rheology much like the hydrous fluids. The most important effect is enhancing grain boundary diffusivity (e.g., Karato, 2008). Moreover, melt can produce chemical disequilibrium with the rock, leading to the development of fine-grained reaction products able to deform by grain size sensitive creep (Gardner et al., 2020; Lee et al., 2021).

2.6 Relationships between deformation, metamorphism, and geochemistry

It has long been recognized that deformation and metamorphism are closely interlinked, but although many authors have touched upon various aspects of the subject, there has never been a completely satisfactory understanding of the interrelationships at the mechanistic level. Metamorphic reactions, for example, occur when one or more phases are in thermodynamic disequilibrium with respect the surroundings. Disequilibrium is normally achieved either through changes in P - T conditions or through chemical instabilities driven by deformation often under the presence of fluid (usually hydrous fluid) or melt (Etheridge et al., 1983; Karato, 2008). The literature is full of descriptions of mineralogical changes that mirror the intensity of strain in heterogeneously deformed rocks and with assessments of relative timing of deformation and metamorphism (e.g., Brodie and Rutter, 1985). Attention has recently been paid to the role of deformation in metamorphism and its effect on mineral and rock chemistry. In particular, the effect of localised shearing, which produces narrow mylonitic zones within initially homogeneous rocks, on the rock chemistry has been considered. These investigations have mainly considered changes in rock chemistry together with variations in mineral assemblage into the shear zones (e.g., Brodie and Rutter, 1985; Altenberger, 1995; Tursi et al., 2018). Most

examples have involved open systems where a fluid has been introduced leading to the formation of a hydrated, apparently retrograde, mineral assemblage. The main effect of the deformation has been to reduce grain size, increasing the grain boundary area available for reaction and diffusion and allowing the influx of a fluid phase. Ideally an isochemical shear zone in a homogeneous rock is required to gain any information about the effect of deformation on mineral chemistry.

It is largely accepted that geochemical investigations are nowadays fundamental to provide information about geological processes and relationships with the source or protoliths. However, in comparison with igneous rocks, only limited data are available on the distribution of rare earth elements (REE) in metamorphic rocks and particularly on the behaviour of these elements during progressive metamorphism and deformation (e.g., Brodie, 1981; Altenberger, 1995; Tursi et al., 2018; Corvò et al., 2020). Yet, mass transfer processes, governed by the channeling H₂O-rich fluids, profoundly modify the bulk rock chemistry of the deforming rocks. In addition, deformation triggers the mobilization of major elements and especially of trace element that consequently can control mineral reactions and the stability of mineral assemblages together with the P - T conditions (e.g., Tursi et al., 2018; Corvò et al., 2020). Despite the advantage in obtaining a lot of information about the evolution of rocks, the studies that investigate the role of deformation on rock geochemistry are still a few. The hope is that thanks to the increasing interest in the multidisciplinary approaches together with the technological advancements can spark interest in this kind of investigations.

2.7 Influence of local scale-rheology in the geodynamic models

In this PhD thesis, new data and interpretations are discussed in relation to the possible repercussions they may have on the geodynamic evolution of the case studies. For this reason, this paragraph briefly introduces numerical subduction-exhumation (related to case study 1) and rifting (case study 2) modelling proposed in literature.

2.7.1 Subduction-exhumation modelling in the orogens

Small- to medium-scale compositional and rheological changes have major consequences on plate-scale models, which describe geodynamics. The case study 1 (Cima di Gagnone, Central Alps) deal with rocks that were deformed and metamorphosed during a subduction-exhumation cycle, during the alpine orogeny. Models of subduction are typically driven by P - T estimates derived from the metamorphic record of different rock types. The occurrence of “anomalous” local variations in the metamorphic patterns could give heavy problems in converting P - T estimates into depths reached during subduction. In particular, this is the case of the relatively small blocks of rocks with very different P - T estimates (high-pressure or high-temperature) with respect their host that show middle metamorphic conditions. Mountain ranges, as for example Western Alps are usually made of tectonic nappes and have long been a testing ground for revolutionary ideas in tectonics, such as the nappe theory (e.g., Schmalholz et al., 2014). There is a general agreement that the overall tectonic structure of the Western Alps represents an imbricate nappe stack, and that the emplacement of the nappes happened in an ordered succession such that the stacked order from top to bottom reflects the paleogeographic position from internal to external, respectively. However, the discovery of high pressure and ultra-high pressure ((U)HP) metamorphism in the Western Alps (e.g., Chopin, 1984) invoked mantle depth tectonism that opened an extensive debate on the dynamics of tectonic nappes. Based on the nappe forming mechanism, the existing tectonic models of convergent orogens that can explain such differences in the metamorphic records have been mainly interpreted as: i) the result of late tectonic coupling within lithospheric mélanges (Model I - Fig. 2.7A; e.g., Trommsdorff, 1990), or ii) differential, compositionally-controlled re-equilibration of a coherent tectonic unit that experienced uniform (U)HP and HT conditions (Model II - Fig. 2.7B; e.g., Cavargna-Sani et al., 2014). In such models, metamorphic pressures recorded by ultrahigh- or high-pressure ((U)HP) crustal rocks were always

close to the lithostatic pressure. An alternative model considers the differences in the metamorphic record as generated by local deviations of P and T from lithostatic conditions and orogenic thermal gradient due to tectonic overpressure and shear heating, respectively (Model III - Fig. 2.7C; Schmalholz et al., 2014; Wheeler, 2014; Schenker et al., 2015; Casini and Maino, 2018; Moulas et al., 2019).

In the tectonic *mélange* (Model I; Fig. 2.7A), chaotically distributed blocks of rock preserving heterogeneous metamorphic conditions may result from tectonic mixing during the return flow inside a low-viscosity subduction channel (Butler et al., 2013, 2014). As consequence, different P - T - t paths and depths were recorded for different blocks in a tectonic *mélange*. The main advantage of this model is that channel flow may easily promote the exhumation of rocks subducted at depth of 60-100 km (e.g., Scambelluri et al., 2015). However, it requires the presence of important structures accommodating the tectonic coupling occurring at relatively low- T and low- P conditions.

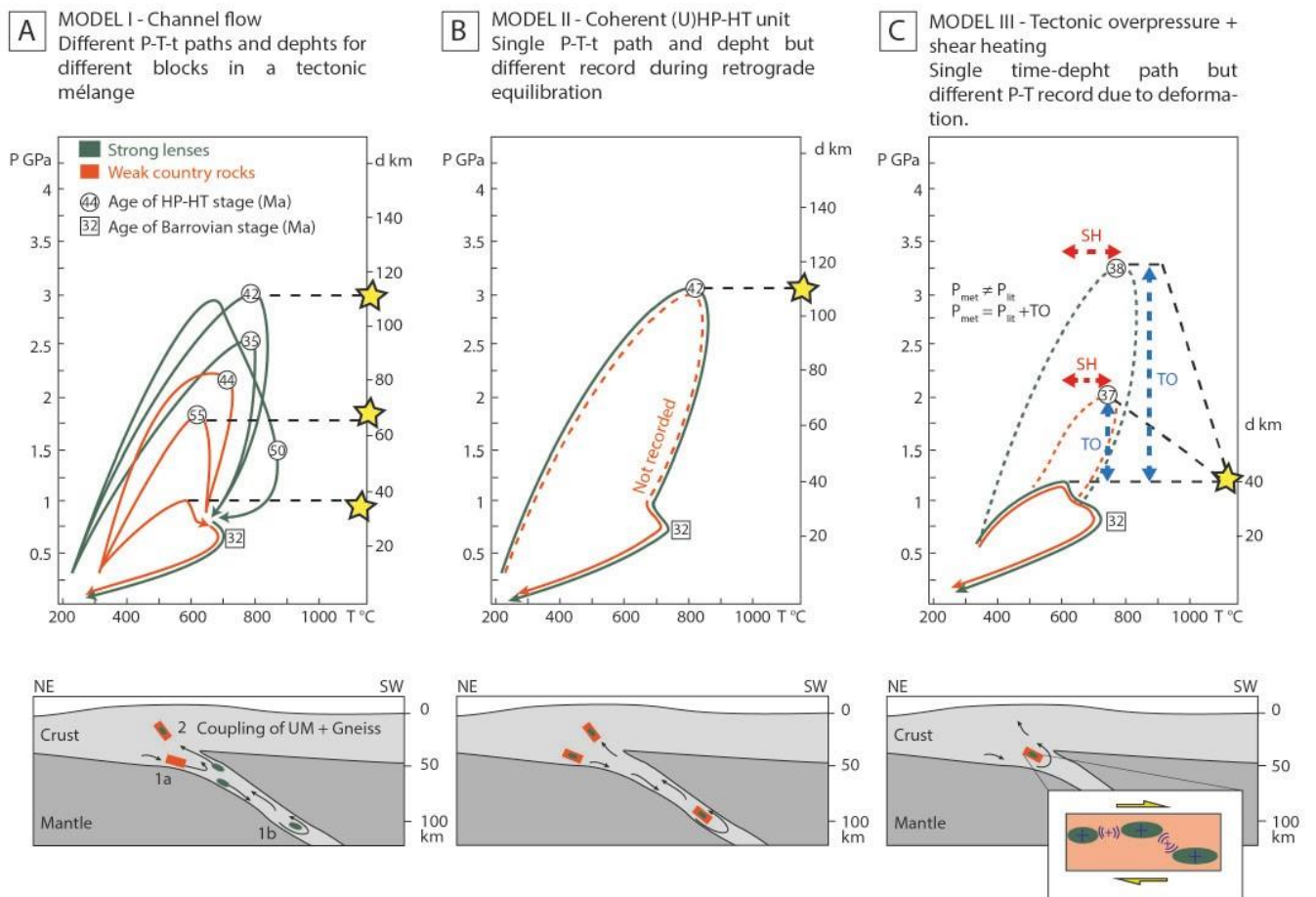


Fig. 2.7 - Sketch of subduction-exhumation models in the orogenic chains and related P - T - t paths resulted: A) Model I – Channel flow; B) Model II – Coherent (U)HP-HT unit; C) Model III – Tectonic overpressure (TO) + shear heating (SH). The yellow star represents the recorded metamorphic peak.

The exhumation of coherent (U)HP units (Model II; Fig. 2.7B) in a subduction channel is driven by Stokes flow supported by density differences between buoyant crustal material and denser surrounding rocks (Yamato et al., 2008). The structural coherence of the unit indicates that both weak and strong rocks experienced the same metamorphism and tectonic evolution. This conclusion contrasts with the heterogeneous metamorphism recorded by the different rheological rocks. This apparent discrepancy is commonly explained as resulting from differential preservation of the metamorphic assemblages and related isotopic systems, being the mafic rocks more retentive to peak conditions (e.g., Heinrich, 1982). This concept has the limitation that rocks must remain anhydrous or water-undersaturated at peak metamorphic conditions in order to limit partial melting and most of the UHP and HT record in metasediments must be lost due to re-hydration during a low-temperature exhumation.

The alternative model of tectonic overpressure and shear heating (Model III; Fig. 2.7C) try to link metamorphism to deformation in a coherent, physically based, chemical-mechanical model (Li et al., 2010; Schmalholz et al., 2014; Schenker et al., 2015). Therefore, here, deformation play a significant role in the determination of metamorphic P - T conditions. With this model, indeed, it is state that orogeny may have been driven by compressive tectonic forces that produced local stresses, deviating >50% from the actual lithostatic pressure. Consequently, P - T conditions are not simply converted into burial but deviatoric pressure and temperature have to be considered as additional factor that could influence the metamorphic equilibrium conditions. In this model, rocks experience a single deformation and time path with different P - T record controlled by rheology and geometry during deformation. Major problem of this model is the difficulty (or impossibility) to estimate the deviatoric component in the metamorphic pressure and thus to quantify the real contribute of the non-lithostatic component.

2.7.2 Rifting modelling of the fossil Adriatic margin

The case study 2 from this PhD thesis (Anzola shear zone of the Ivrea-Verbano Zone, Western Alps) investigates the factors that drove the nucleation of large shear zones accommodating the crust deformation during rifting. Rift-related shear zones can be usually found quite easily in the exhumed passive margins worldwide but understanding how they formed and under which conditions is challenging because of the long-lived geological history they commonly record. In the last decades, the combination of geophysical, structural, geochronological and sedimentological studies led to important advancement in understanding extensional tectonics, rift settings and related structures

(Manatschal et al., 2007; Mohn et al., 2010; 2012; Beltrando et al., 2014; 2015). Rift systems are generally subjected to shift in time and space within the evolving continental margins (Manatschal et al., 2007; Mohn et al., 2012; Beltrando et al., 2015). This is the case of the Mesozoic evolution of Southern Europe and North Africa where multiple rifting episodes characterize the Pangea breakup. Indeed, the Middle Triassic opening of the Mesozoic Ionian Basins was followed by the formation of the central Atlantic and the Alpine Tethys in the latest Triassic to Middle Jurassic times. Extension-related tectonics of the Adriatic margin began in the Late Triassic. During this epoch, extension of the upper crust was mainly controlled by major listric faults at the margins of Late Carboniferous-Early Permian basins. Subsequently, faulting around those centres gradually ceased and the site of extension shifted westwards towards the future site of crustal separation (Petri et al., 2019).

Manatschal et al. (2007), Mohn et al. (2012) and Beltrando et al. (2015) documented the rift-related evolution of the basement and the associated tectono-sedimentary record (Fig. 2.8). According to their studies, three modes can be recognized during Tethyan rift localization. An initial stretching mode (mode 1) characterized by a ductile and diffused deformation of the middle and deep crust is followed by a thinning mode (mode 2) linked to initial rift localization and lithospheric thinning and, finally, by an exhumation mode (mode 3) where the crustal extension leads to a complete exhumation of the subcontinental mantle. During the three modes of Tethyan rift, several generations and types of extensional structures are formed, namely high-angle and low-angle normal faults, anastomosing shear-zones and decoupling horizons (Petri et al., 2019). Such structures accommodate the lateral extraction of mechanically stronger levels derived from the middle and lower crust. The first extensional ductile shear zones in the lower crust nucleates during the thinning mode (Fig. 2.8, mode 2 of Manatschal et al. 2007) that is the less constrained stage among the three. Direct geological observations are not so common mainly because the fault systems and the sedimentary basins related to this mode are overprinted by subsequent, breakup-related deformation. However, the first step toward a complete understanding of the evolution of rift margin consists in detailed reconstruction and characterization of the development of rift-related structures, where preserves remnants or active rift margin can be directly investigated.

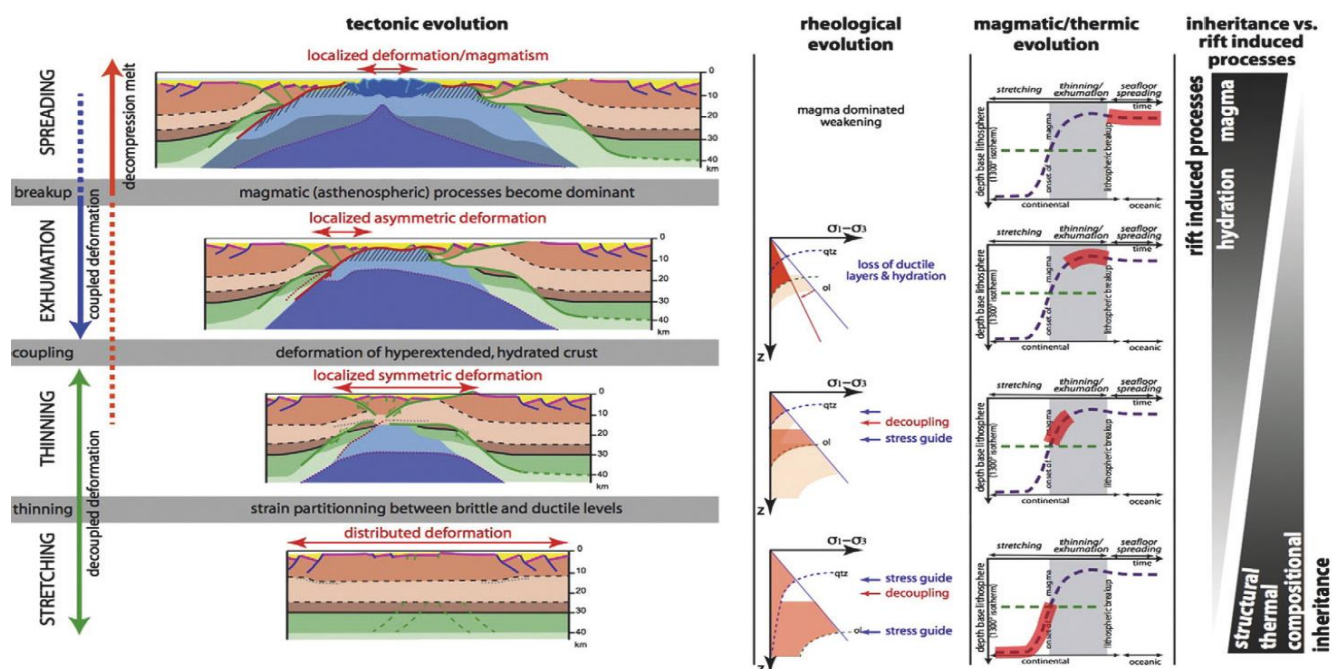


Fig. 2.8 - Conceptual model showing the tectonic, rheological, magmatic and thermal evolution of magma-poor rifted margins and their relation to inheritance and rift induced processes (from Manatschal et al., 2007).

2.8 References

- Altenberger, U., 1995. Long-term deformation and fluid-enhanced mass transport in a Variscan peridotite shear zone in the Ivrea Zone, northern Italy: a microtextural, petrological and geochemical study of a reactivated shear zone. *Geologische Rundschau*, 84(3), 591-606.
- Austrheim, H., 1987. Eclogitization of lower crustal granulites by fluid migration through shear zones. *Earth and Planetary Science Letters*, 81(2-3), 221-232.
- Austrheim, H., 2013. Fluid and deformation induced metamorphic processes around Moho beneath continent collision zones: Examples from the exposed root zone of the Caledonian mountain belt, W-Norway. *Tectonophysics*, 609, 620-635.
- Barker, A. J., 2014. A key for identification of rock-forming minerals in thin section. CRC Press.
- Bauville, A., & Yamato, P., 2021. Pressure-to-depth conversion models for metamorphic rocks: Derivation and applications. *Geochemistry, Geophysics, Geosystems*, 22, e2020GC009280.
- Beltrando, M., Rubatto, D., & Manatschal, G., 2010. From passive margins to orogens: The link between ocean-continent transition zones and (ultra) high-pressure metamorphism. *Geology*, 38(6), 559-562.
- Beltrando, M., Frasca, G., Compagnoni, R., & Vitale-Brovarone, A., 2012. The Valaisan controversy revisited: multi-stage folding of a Mesozoic hyper-extended margin in the Petit St. Bernard pass area (Western Alps). *Tectonophysics*, 579, 17-36.

- Beltrando, M., Manatschal G., Mohn G., Dal Piaz G.V., Vitale Brovarone A. and Masini E., 2014. Recognizing remnants of magma-poor rifted margins in high-pressure orogenic belts: The Alpine case study. *Earth. Sci. Rev.*, 131: 88-115.
- Beltrando, M., Stockli D.F., Decarlis A. and Manatschal G., 2015. A crustal-scale view at rift localization along the fossil Adriatic margin of the Alpine Tethys preserved in NW Italy. *Tectonics*, 34: 1927-1951.
- Blenkinsop, T., 2000. Magmatic and sub-magmatic deformation. *Deformation Microstructures and Mechanisms in Minerals and Rocks*, 59-64.
- Brodie, K. H., 1981. Variation in amphibole and plagioclase composition with deformation. *Tectonophysics*, 78(1-4), 385-402.
- Brodie, K. H., & Rutter, E. H., 1985. On the relationship between deformation and metamorphism, with special reference to the behaviour of basic rocks. In *Metamorphic reactions* (pp. 138-179). Springer, New York, NY.
- Bucher, K., & Frey, M., 2002. *Petrogenesis of metamorphic rocks*. Springer Science & Business Media.
- Bucher, K., & Grapes, R., 2009. The eclogite-facies Allalin Gabbro of the Zermatt–Saas ophiolite, Western Alps: a record of subduction zone hydration. *Journal of Petrology*, 50(8), 1405-1442.
- Burg, J.-P., Sokoutis, D., Bonini, M., 2002. Model-inspired interpretation of seismic structures in the Central Alps: Crustal wedging and buckling at mature stage of collision. *Geology*, 30, 643–646.
- Bürgmann, R., & Dresen, G., 2008. Rheology of the lower crust and upper mantle: Evidence from rock mechanics, geodesy, and field observations. *Annu. Rev. Earth Planet. Sci.*, 36, 531-567.
- Burov, E. B., 2011. Rheology and strength of the lithosphere. *Marine and Petroleum Geology*, 28(8), 1402-1443.
- Butler, J. P., Beaumont, C., & Jamieson, R. A., 2013. The Alps 1: A working geodynamic model for burial and exhumation of (ultra) high-pressure rocks in Alpine-type orogens. *Earth and Planetary Science Letters*, 377, 114-131.
- Butler, J. P., Beaumont, C., & Jamieson, R. A., 2014. The Alps 2: Controls on crustal subduction and (ultra) high-pressure rock exhumation in Alpine-type orogens. *Journal of Geophysical Research: Solid Earth*, 119(7), 5987-6022.
- Burlini, L., & Bruhn, D., 2005. High-strain zones: laboratory perspectives on strain softening during ductile deformation. *Geological Society, London, Special Publications*, 245(1), 1-24.
- Casini, L., Maino, M., 2018. 2D–thermo–mechanical modelling of spatial P–T variations in heterogeneous shear zones. *Ital. J. Geosci.* 137 (2), 272–282.
- Cavargna-Sani M., Epard J.L., Bussy F. & Ulianov A., 2014. Basement lithostratigraphy of the Adula nappe: implications for Palaeozoic evolution and Alpine kinematics. *International Journal of Earth Sciences*, 103(1), 61-82.
- Chopin C., 1984. Coesite and pure pyrope in high-grade blueschists of the Western Alps - a 1st record and some consequences. *Contrib. Mineral. Petrol.*, 86, 107-118.

- Connolly, J. A. D. 1990. Multivariable phase diagrams: An algorithm based on generalized thermodynamics. *American Journal of Science*, vol. 290, no. 6, 666-718.
- Connolly, J. A. D. 2005. Computation of phase equilibria by linear programming: a tool for geodynamic modeling and its application to subduction zone decarbonation. *Earth and Planetary Science Letters*, vol. 236, nos. 1-2, 524-541.
- Corvò, S., Langone, A., Padrón-Navarta, J. A., Tommasi, A., & Zanetti, A., 2020. Porphyroclasts: Source and Sink of Major and Trace Elements During Deformation-Induced Metasomatism (Finero, Ivrea-Verbano Zone, Italy). *Geosciences*, 10(5), 196.
- Dal Piaz, G. V., Bistacchi, A., & Massironi, M. (2003). Geological outline of the Alps. *Episodes*, 26(3), 175-180.
- De Capitani, C. and Petrakakis, K. 2010. The computation of equilibrium assemblage diagrams with Theriak/Domino software. *American Mineralogist*, vol. 95, no.7, 1006-1016.
- Deer, W. A., Howie, R. A., & Zussman, J. (Eds.). (1997). *Rock-forming minerals*. Geological Society of London.
- De Graciansky, P. C., Roberts, D. G., & Tricart, P. 2010. The Western Alps, from rift to passive margin to orogenic belt: an integrated geoscience overview. Elsevier.
- Döhmman, M. J., Brune, S., Nardini, L., Rybacki, E., & Dresen, G., 2019. Strain localization and weakening processes in viscously deforming rocks: Numerical modeling based on laboratory torsion experiments. *Journal of Geophysical Research: Solid Earth*, 124(1), 1120-1137.
- Etheridge, M. A., Wall, V. J., & Vernon, R. H., 1983. The role of the fluid phase during regional metamorphism and deformation. *Journal of metamorphic Geology*, 1(3), 205-226.
- Fossen, H. (2016). *Structural geology*. Cambridge university press.
- Fossen, H., & Cavalcante, G. C. G., 2017. Shear zones—A review. *Earth-Science Reviews*, 171, 434-455.
- Gardner, R., Piazzolo, S., Evans, L., & Daczko, N., 2017. Patterns of strain localization in heterogeneous, polycrystalline rocks—a numerical perspective. *Earth and Planetary Science Letters*, 463, 253-265.
- Gardner, R. L., Piazzolo, S., Daczko, N. R., & Trimby, P., 2020. Microstructures reveal multistage melt present strain localisation in mid-ocean gabbros. *Lithos*, 366, 105572.
- Getsinger, A. J., Hirth, G., Stünitz, H., & Goergen, E. T., 2013. Influence of water on rheology and strain localization in the lower continental crust. *Geochemistry, Geophysics, Geosystems*, 14(7), 2247-2264.
- Handy, M. R., Franz, L., Heller, F., Janott, B., & Zurrbriggen, R., 1999. Multistage accretion and exhumation of the continental crust (Ivrea crustal section, Italy and Switzerland). *Tectonics*, 18(6), 1154-1177.
- Heinrich, C.A., 1982. Kyanite-eclogite to amphibolite facies evolution of hydrous mafic and pelitic rocks, Adula nappe, Central Alps. *Contrib. Mineral. Petrol.* 81 (1), 30–38.
- Hess, B. L., & Ague, J. J., 2021. Quantifying the Effects of Non-hydrostatic Stress on Single-component Polymorphs. *Journal of Geophysical Research: Solid Earth*, 126(5), e2020JB021594.
- Hobbs B.E. & Ord A., 2016. Pressure and equilibrium in deforming rocks. *Journal of Metamorphic*

- Geology, 35, 967-982.
- Karato, S. I., 2008. Deformation of earth materials. An Introduction to the Rheology of Solid Earth, 463.
- Kohlstedt, D. L., Evans, B., & Mackwell, S. J. (1995). Strength of the lithosphere: Constraints imposed by laboratory experiments. *Journal of Geophysical Research: Solid Earth*, 100(B9), 17587-17602.
- Jiang, D., 2021. Comment on “Pressure-to-Depth Conversion Models for Metamorphic Rocks: Derivation and Applications” by Bauville and Yamato. *Geochemistry, Geophysics, Geosystems*, 22(7), e2021GC009737.
- Jowhar, T. N., 2012. Computer programs for PT history of metamorphic rocks using pseudosection approach. *International Journal of Computer Applications*, 41(8).
- Lee, A. L., Lloyd, G. E., Torvela, T., & Walker, A. M., 2020. Evolution of a shear zone before, during and after melting. *Journal of the Geological Society*, 177(4), 738-751.
- Lee, A. L., Stünitz, H., Soret, M., & Battisti, M. A., 2021. Dissolution precipitation creep as a process for the strain localisation in mafic rocks.
- Li, Z. H., Gerya, T. V., & Burg, J. P. 2010. Influence of tectonic overpressure on P–T paths of HP–UHP rocks in continental collision zones: thermomechanical modelling. *Journal of Metamorphic Geology*, 28(3), 227-247.
- Liu, J., Regenauer-Lieb, K., & Füsseis, F., 2010. Stochastic analysis of percolation and anisotropic permeability from micro-tomography and an application to mylonite. In *Advances in Geosciences: Volume 20: Solid Earth (SE)* (pp. 229-245).
- Manatschal, G., Müntener, O., Lavie, L. L., Minshull, T. A., & Péron-Pinvidic, G., 2007. Observations from the Alpine Tethys and Iberia–Newfoundland margins pertinent to the interpretation of continental breakup. *Geological Society, London, Special Publications*, 282(1), 291-324.
- Mohn, G., Manatschal, G., Beltrando, M., Masini, E. and Kuszniir, N., 2012. Necking of continental crust in magma-poor rifted margins: Evidence from the fossil Alpine Tethys margins: neck-ing of continental crust. *Tectonics*, 31 (1): TC1012.
- Mohn, G., Manatschal, G., Müntener, O., Beltrando, M., & Masini, E., 2010. Unravelling the interaction between tectonic and sedimentary processes during lithospheric thinning in the Alpine Tethys margins. *International Journal of Earth Sciences*, 99(1), 75-101.
- Moulas, E., Burg, J. P., & Podladchikov, Y., 2014. Stress field associated with elliptical inclusions in a deforming matrix: Mathematical model and implications for tectonic overpressure in the lithosphere. *Tectonophysics*, 631, 37-49.
- Moulas, E., Schmalholz, S. M., Podladchikov, Y., Tajčmanová, L., Kostopoulos, D., & Baumgartner, L., 2019. Relation between mean stress, thermodynamic, and lithostatic pressure. *Journal of metamorphic geology*, 37(1), 1-14.
- Palin, R. M., Weller, O. M., Waters, D. J., & Dyck, B., 2016. Quantifying geological uncertainty in metamorphic phase equilibria modelling; a Monte Carlo assessment and implications for tectonic

- interpretations. *Geoscience Frontiers*, 7(4), 591-607.
- Petri, B., Duretz, T., Mohn, G., Schmalholz, S. M., Karner, G. D., & Müntener, O., 2019. Thinning mechanisms of heterogeneous continental lithosphere. *Earth and Planetary Science Letters*, 512, 147-162.
- Pfiffner, A.O., 2009. *Geologie der Alpen*. Haupt UTB editions
- Pfiffner, O. A., 2014. *Geology of the Alps*. John Wiley & Sons.
- Philpotts, A, & Ague, J., 2009. *Principles of Igneous and Metamorphic Petrology*. Cambridge University Press.
- Piazolo, S., Daczko, N. R., Silva, D., & Raimondo, T., 2020. Melt-present shear zones enable intracontinental orogenesis. *Geology*, 48(7), 643-648.
- Powell, R., & Holland, T. J. B., 1985. An internally consistent thermodynamic dataset with uncertainties and correlations: 1. Methods and a worked example. *Journal of Metamorphic Geology*, 3(4), 327-342.
- Powell, R. and Holland, T. J. B. 2001. Course notes for THERMOCALC workshop 2001: Calculating Metamorphic Phase Equilibria (on CD-ROM).
- Ranalli, G., 1995. *Rheology of the Earth*. Springer Science & Business Media.
- Rosenberg, C. L., & Handy, M. R., 2005. Experimental deformation of partially melted granite revisited: implications for the continental crust. *Journal of metamorphic Geology*, 23(1), 19-28.
- Rutter, E. H., Holdsworth, R. E., & Knipe, R. J., 2001. The nature and tectonic significance of fault-zone weakening: an introduction. *Geological Society, London, Special Publications*, 186(1), 1-11.
- Rütti, R., 2003. *The tectono-metamorphic evolution of the northwestern Simano Nappe (Central Alps, Switzerland)* (Doctoral dissertation, ETH Zurich).
- Scambelluri, M., Pettke, T., Cannaò, E., 2015. Fluid-related inclusions in Alpine high-pressure peridotite reveal trace element recycling during subduction-zone dehydration of serpentized mantle (Cima di Gagnone, Swiss Alps). *Earth Planet. Sci. Lett.* 429, 45–59.
- Schenker, F.L., Schmalholz, S.M., Moulas, E., Pleuger, J., Baumgartner, L.P., Podladchikov, Y., Müntener, O., 2015. Current challenges for explaining (ultra)high-pressure tectonism in the Pennine domain of the Central and Western Alps. *J. Metamorph. Geol.* 33 (8), 869–886.
- Schmalholz, S. M., & Podladchikov, Y.Y., 2013. Tectonic overpressure in weak crustal-scale shear zones and implications for the exhumation of high-pressure rocks. *Geophysical Research Letters*, 40(10), 1984-1988.
- Schmalholz, S.M., Duretz, T., Schenker, F.L., Podladchikov, Y.Y., 2014. Kinematics and dynamics of tectonic nappes: 2-D numerical modelling and implications for high and ultra-high pressure tectonism in the Western Alps. *Tectonophysics* 631 (C), 160–175.
- Schmalholz, S. M., Moulas, E., Plümpner, O., Myasnikov, A. V., & Podladchikov, Y. Y., 2020. 2D Hydro-Mechanical-Chemical Modeling of (De) hydration Reactions in Deforming Heterogeneous Rock: The Periclase-Brucite Model Reaction. *Geochemistry, Geophysics, Geosystems*, 21(11), e2020GC009351.
- Schorn, S., 2018. Dehydration of metapelites during high-P metamorphism: the coupling between

- fluid sources and fluid sinks. *J. Metamorph. Geol.* 36 (3), 369–391.
- Spear, F. S., 1995. Metamorphic phase equilibria and pressure-temperature-time paths.
- Spear, F. S., & Peacock, S. M., 1989. Metamorphic pressure-temperature-time paths (Vol. 7). American Geophysical Union.
- Spear, F. S., Kohn, M. J., & Cheney, J. T., 1999. P-T paths from anatexitic pelites. *Contributions to mineralogy and petrology*, 134(1), 17-32.
- Spear, F. S., Pyle, J. M. and Storm, L. C. 2001. Short course: Thermodynamic modeling of mineral reactions: An introduction to Program Gibbs. Northeast Section, Geological Society of America, Vermont.
- Stuart, C. A., Piazzolo, S., & Daczko, N. R., 2016. Mass transfer in the lower crust: Evidence for incipient melt assisted flow along grain boundaries in the deep arc granulites of Fiordland, New Zealand. *Geochemistry, Geophysics, Geosystems*, 17(9), 3733-3753.
- Trommsdorff, V., 1990. Metamorphism and tectonics in the Central Alps: The Alpine lithospheric mélangé of Cima Lunga and Adula. *Memorie della Società Geologica Italiana*, 45, 39-49.
- Tommasi, A., Langone, A., Padrón-Navarta, J. A., Zanetti, A., & Vauchez, A., 2017. Hydrous melts weaken the mantle, crystallization of pargasite and phlogopite does not: Insights from a petrostructural study of the Finero peridotites, southern Alps. *Earth and Planetary Science Letters*, 477, 59-72.
- Tursi, F., Festa, V., Fornelli, A., Micheletti, F., & Spiess, R., 2018. Syn-shearing mobility of major elements in ductile shear zones: state of the art for felsic deformed protoliths. *Periodico di Mineralogia*, 87(3).
- Wheeler, J., 2014. Dramatic effects of stress on metamorphic reactions. *Geology* 42 (8), 647–650.
- Wheeler, J., 2018. The effects of stress on reactions in the Earth: sometimes rather mean, usually normal, always important. *Journal of Metamorphic Geology*, 36(4), 439-461.
- Winter, J. D., 2014. Principles of igneous and metamorphic petrology (Vol. 2). Harlow, UK: Pearson education.
- Yamato, P., Burov, E., Agard, P., Le Pourhiet, L., & Jolivet, L., 2008. HP-UHP exhumation during slow continental subduction: Self-consistent thermodynamically and thermomechanically coupled model with application to the Western Alps. *Earth and Planetary Science Letters*, 271(1-4), 63-74.
- Yardley, B. W., 1997. The evolution of fluids through the metamorphic cycle. In *Fluid flow and transport in rocks* (pp. 99-121). Springer, Dordrecht.
- Yardley, B., & Warren, C., 2021. *An introduction to metamorphic petrology*. Cambridge University Press.
- Zingg, A., Handy, M. R., Hunziker, J. C., & Schmid, S. M. (1990). Tectonometamorphic history of the Ivrea Zone and its relationship to the crustal evolution of the Southern Alps. *Tectonophysics*, 182(1-2), 169-192.

CHAPTER 3: Methods

3.1 Abstract

This chapter describes the analytical techniques and methods used in this PhD thesis. A multidisciplinary study was applied with the intention to investigate the relationships between metamorphic and deformation processes across the studied rheological boundaries. For that, the study started with detailed field work and targeted sampling followed by an appropriate selection and preparation of samples representative of observed lithologies/fabrics. A wide range of analytical techniques were used, including optical microscopy and Scanning Electron Microscopy (SEM) for microstructural characterization, Electron Backscatter Diffraction (EBSD) for characterization of crystallographic preferred orientations, X-ray fluorescence (XRF) for bulk rock chemistry, Electron Probe Microanalyzer (EPMA) and Laser Ablation Inductively Coupled Plasma Mass Spectrometry (LA-ICP-MS) for quantitative mineral chemistry and U-(Th)-Pb using LA-ICP-MS technique for dating geochronometers. The pressure- temperature conditions of deformation and of the metamorphic reactions are constrained through geothermobarometry and thermodynamic modelling (i.e., *Perple_X*). Since in both case studies, the deformation played an important role in modifying the chemical and structural pattern of the studied rocks, particular focus was given to considering the role of deformation on the rock's evolution. The result is the reconstruction of the Pressure-Temperature-time-Deformation-Composition (*P-T-t-D-X*) conditions of the studied rocks. The whole combined dataset was finally used to better place the case studies evolution in the frame of the regional geological setting.

3.2 Field work and sampling strategy

For each of the two case studies, several field works were done. For the case study 1, i.e., Cima di Gagnone, a detailed geological mapping and sampling was already done by my supervisor Matteo Maino during the geological survey of the sheet 1293 – Osogna for the Swiss Geological Atlas – Swisstopo, completed before that this PhD project started (before 2018). Since the huge amount of data and samples already available and the lack of time to perform further field works during three PhD years, only three days in June 2020 were spent on the Cima di Gagnone area, in order that the candidate could make a direct idea of the sample provenance and of the geological context (Fig. 3.1A). Conversely, for the case study 2, i.e., the Anzola shear zone area, since the lack of a detailed basic geological mapping, several field works were conducted during the PhD (at least few days for each year) not only along the valley hosting the shear zone (Fig. 3.1B; i.e., Val d'Ossola) but also for the adjacent valleys (i.e., Val Strona di Omegna and Val Cannobina). For both case studies, a chapter called “Field observations” reports the detailed description relative to the field work (chapter 4, 5.4; Figs. 4.3, 5.3). The sample strategy consisted in accurately collecting samples across the compositional and structural heterogeneous rocks boundary (e.g., close to mafic boudin or within the shear zone) and representative of different lithologies/fabrics.

3.2.1 Sample preparation

For case study 1, a suite of samples from the Cima di Gagnone area were already available. For case study 2, a few samples were already available and a suite of new samples was collected (around 50 specimens) from which around twenty are from the Anzola area.

Sample details, together with the GPS coordinates, can be found in chapter 4.5 and 5.5. In the laboratory, rock samples were firstly cut using a rotary diamond saw and successively grind on steel laps to make polished thin sections to allow petrographic observations and their used for other investigations (Grundmann and Scholz, 2015). The rocks chips obtained were cut and prepared by the candidate in the lab at the Dipartimento di Scienze della Terra e dell'Ambiente di Pavia (Fig. 3.2A) and then sent to external laboratories for thin sections preparation, namely, TS Lab & Geoservices at Cascina (Pisa, Italy) and Petrolab at Sant'Antioco (Sardegna, Italy). A preliminary petrological and microstructural study was performed on all the available thin sections and was fundamental before

further investigations. Petrographical analyses were conducted at the optical microscope; selected samples were further characterized at the SEM by acquiring both BSE images and qualitative chemical analyses.

Thin sections analysed with Electron Backscatter Diffraction (EBSD) technique were prepared at the School of Earth and Environment, University of Leeds, where the candidate spent two periods of about 2 months each. Here, thin sections were chemo-mechanically polished with a colloidal silica suspension to remove the damage induced by mechanical polishing, and to obtain a homogeneous flat surface (see section 3.4.2). Colloidal silica polishing is an essential step for quality EBSD results, as topography causes beam shadows when the sample surface is tilted at 70° from the horizontal position. Colloidal silica polishing was done with a Bühler Automet® vibratory polishing machine for a duration of ca. ten minutes per sample (Fig. 3.2B). Before the analyses, thin section was coated with a thin carbon film (ca. 5 nm).

For SEM- and EPMA based analysis, thin sections were coated with a thin carbon film (ca. 20 nm) to avoid electrical charging effects that may occur during the interaction of the electron beam with a non-conductive sample surface (Reed, 1975).

Thin sections used for LA-ICP-MS do not need to be coated. They also do not need to be polished, although this may facilitate sample inspection and point location. Petrographic thin sections can directly be analysed, e.g., after electron microprobe analyses of major elements; in this case the coating should be removed. Since the sampling depth by the laser generates is proportional (about 1:1) with the laser spot diameter (see sections 3.5.3), a thickness thicker than the classic 30 µm, e.g., 60-80 µm is needed for laser spots of about 50 µm. Several “thick” thin sections were prepared directly by the candidate (Fig. 3.3). Thin sections used for geochronological investigations usually are the same on which all the previous analytical techniques (obviously when possible) were done in order to maintain the textural control in-situ and allow to directly correlate petrological and microstructural information.

3.3 Petrography

Petrographic investigations were made using the typical optical microscope (e.g., Nikon APLHAPHOT-2 YS2) available at the University of Pavia and University of Leeds. Microphotographs were collected using specific devices (screen, computer, software, iPhone; Fig. 3.4A).

The optical microscope is an instrument consisting of two lens systems inserted into an optical tube, namely an eyepiece and an objective. The magnification power of the eyepiece and the objective may be different. An eyepiece with a magnification power of 10x and three objectives with a magnification power of 4x, 10x and 40x were usually used. Thin sections characterized by a thickness of 30-60 μm were observed for petrographic observations (Fig. 3.4B, C). For the description of the rocks and minerals present in the following doctoral thesis, the book as “Introduction to Optical Petrography” by Angelo Peccerillo and Diego Perugini (2005) and “Rock-forming minerals” of Deer, W. A., Howie, R. A., & Zussman, J. (1997) were consulted. Mineral abbreviations used in this PhD thesis follow Whitney and Evans, (2010).

3.4 Microstructural analysis

Microstructure and textural features of studied rocks were carried out on polished thin sections using SEM-BSE and EBSD analytical techniques.

3.4.1 Scanning electron microscope (SEM) – BSE - EDS

The Scanning Electron Microscope (SEM) was used for high-magnification imaging and semi-quantitative chemical analysis. SEM analyses were done using a Tescan Mira3 XMU-series FESEM equipped with an EDAX-EDX at the “Arvedi” laboratory at the University of Pavia (Fig. 3.5A) and using a Tescan VEGA3 XM at the Electron Microscopy Facility at University of Leeds (Fig. 3.5B).

In the SEM, electrons are produced in an electron gun either by thermo-emission from a tungsten filament or by emission from an electrostatic field gun (e.g., Reed, 2005; Fig. 3.5C). The electrons are accelerated by an electric potential difference (ΔV), resulting in a high energy monochromatic electron beam. This is focused perpendicular to the sample through a series of electromagnetic lenses and apertures that reduce the diameter of the beam. The sample is mounted horizontally on a sample-holder and placed on a movable stage that allows lateral analysis and beam focus. The whole system is kept under vacuum to avoid interaction of the beam with a medium such as air gas and water vapor. Typically, a beam generated by 15-20 kV accelerated voltage gives an interaction volume of about 1 μm diameter. The interaction of the electron beam with the sample results in both electron signals and electromagnetic radiations.

The electron signals are Back-Scattered electrons (BSE) and Secondary Electron (SE). When the

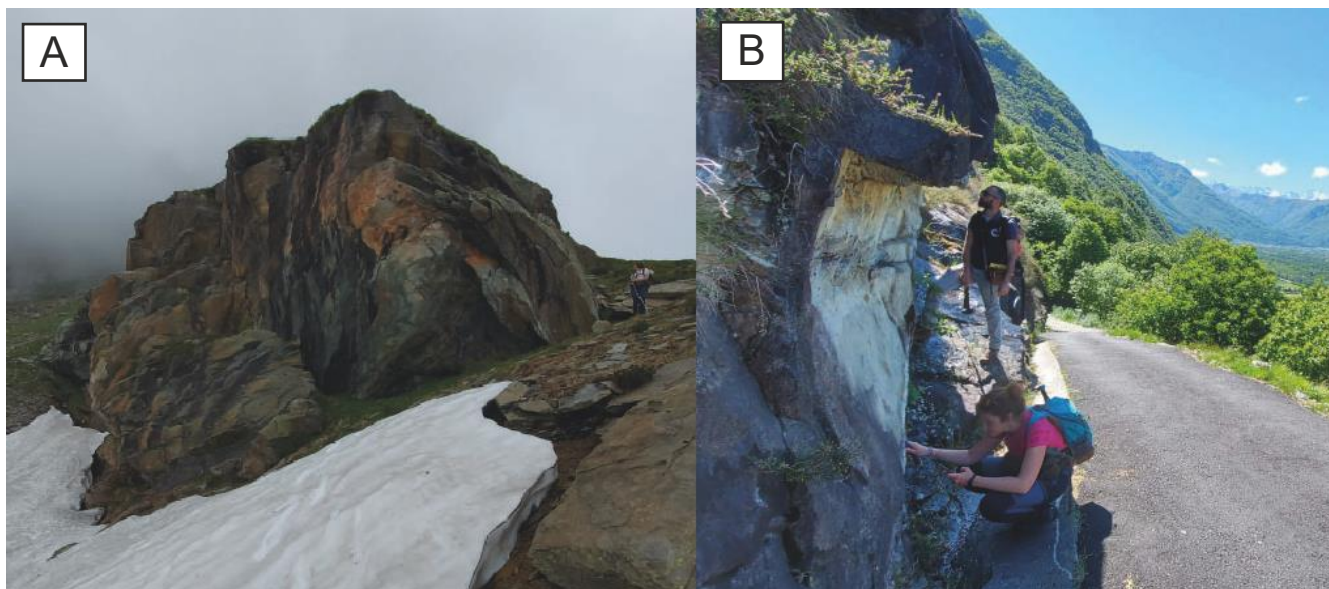


Fig. 3.1 – Pictures from the field work: A) Outcrop of ultramafic boudin at Cima di Gagnone; B) Outcrop of mafic body close to the Anzola village.

electron beam interacts with the sample's atoms it produces elastic and inelastic scattering of electrons. BSE consist in high energy backscattered electrons, whereas SE are low energy for scattered electrons (<50 eV). BSE are used for electron images, obtained by scanning the electron beam line by line over an area of the sample. BSE gives images based on the composition (i.e., based on the element's atomic number Z). The BSE are electrons scattered by atoms, so the more electrons an atom contains the higher the probability of elastic scatter. Therefore, the higher the atomic number the better the BSE signal. In a backscattered electron image, the average atomic number Z is imaged as shades of grey with the light shades having higher atomic numbers than the darker ones. This produces grey-scale electron images where differing compositions are identified by different grey tones (Fig. 3.5D). BSE imaging is a fundamental microstructural and textural investigation tool in this thesis.

In addition to the electronic signals, the sample also produces electromagnetic signals, such as for example Cathodoluminescence (CL), which are of most utility for chemical and textural analysis of zircon (Fig. 3.5E). In this project, CL images on zircon features of separated grains or on thin sections were obtained using two different instruments: i) a JEOL JXA-8200 electron microprobe (Dipartimento di Scienze della Terra, Università degli Studi di Milano, Italy) at 15-kV accelerating voltage and 15-nA beam current (see chapter 3.6.2); ii) a Philips 515 SEM equipped with a Centaurus CL detector system (300–650nm) and an EDAX EDS system at < 20 kV accelerating voltage, magnification ranges from 10× to 1000× and image size 512 × 512 at C.N.R., Istituto di Geoscienze e Georisorse of Pavia.

EDS (Energy Dispersive Spectroscopy) analysis is a semi-quantitative analysis that simultaneously identifies elements from the spectrum of measured X-rays. From the spectrum, EDS can detect major elements and their relative concentrations (Fig. 3.5F). Common rock-forming minerals are reconstructed based on the elements they contain and on the intensity of the signals (height of the spectrum peaks), which are then translated into relative element quantities. EDS is a semi-quantitative analysis because it is not sensitive enough to reveal minor and trace elements. In addition, if standards are lacking the instrument is not calibrated, which means that the intensity of the signal does not directly correlate with weight %. Nevertheless, due to the speed of acquisitions, EDS is a very practical semi-quantitative tool, used in this thesis for point analysis (for semiquantitative mineral composition) and compositional maps. At University of Pavia, data were processed with EDAX Genesis software using the ZAF algorithms the correction method, whereas at University of Leeds by using Aztec 3.3 software, also RGB filtered CL system.

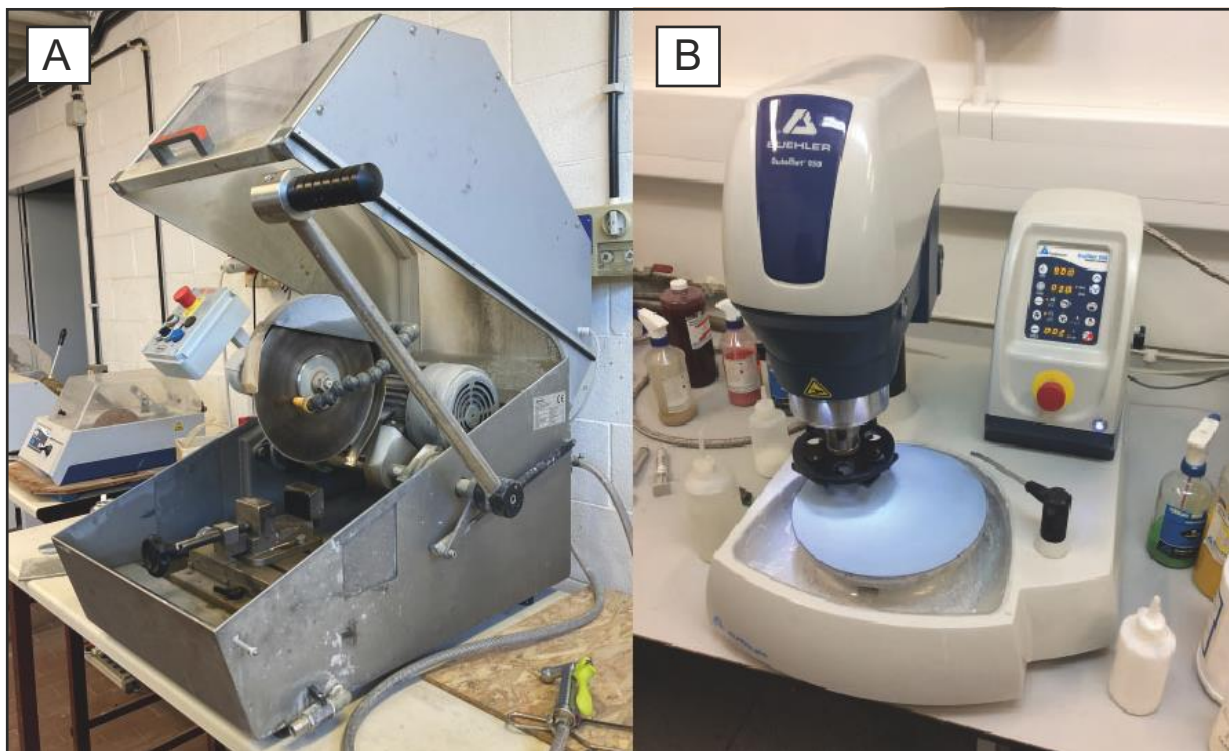


Fig. 3.2 – Thin sections preparation. A) Rotary diamond wire saw for cutting thin sections used at the Department of Earth and Environmental Sciences of University of Pavia. B) Colloidal silica polishing was done with a Böhler Automet® vibratory polishing machine at the School of Earth and Environment at the University of Leeds..

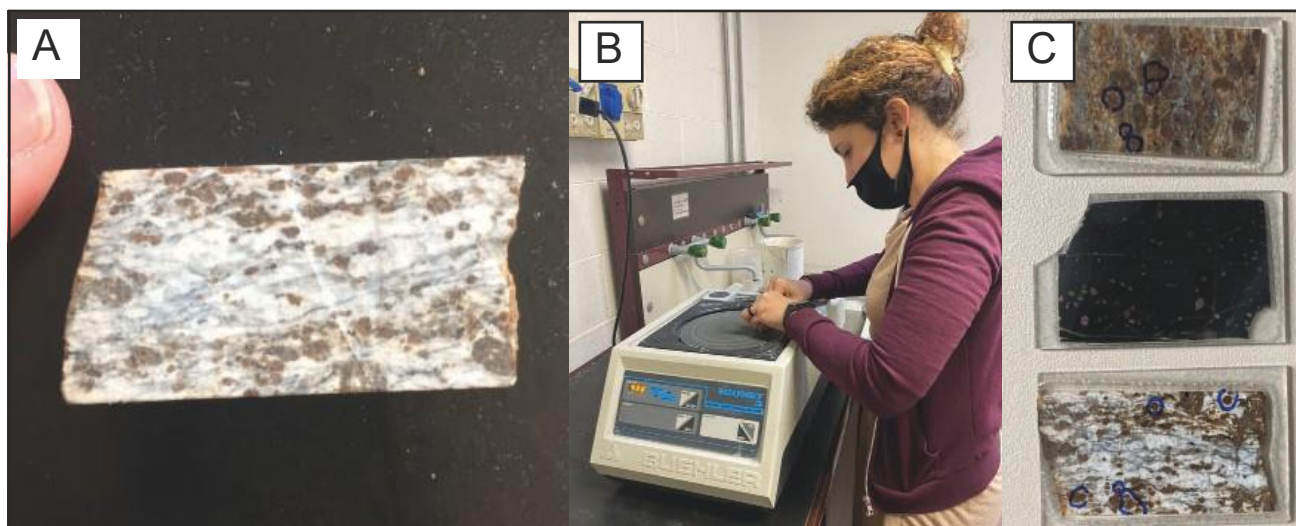


Fig. 3.3 - Preparation of LA-ICP-MS thin sections: A) chips to polish; B) polishing; C) resulted thin sections.

3.4.2 Electron Backscattered Diffraction (EBSD)

Electron Backscatter Diffraction (EBSD) is a SEM based analytical technique that measures crystallographic orientations of any crystalline material, providing textural and crystallographic information of polycrystalline samples (Engler and Randle, 2009; Schwarzer et al., 2009; Prior et al., 1999, 2009).

The technique exploits electrons probing with an electron beam and then backscattered from minerals. When the beam interacts with the atomic structures of the mineral, emitted electrons are diffracted according to Bragg's law: $n\lambda = 2d\sin\theta$; where λ is the wavelength of the incident beam, d is the distance between atomic planes, n is the order of reflection and θ is the Bragg's angle (Bragg and Bragg, 1913). Any diffraction that does not obey Bragg's law is destructive, namely it creates interfering waves cancel each other out. So, only specific angles of diffraction, characteristic of a specific set of lattice planes, get preserved. Diffracted electrons hit the EBSD detector (a phosphor screen), producing a pattern of lines, known as Kikuchi bands, that are specific of a crystallographic orientation (Nishikawa and Kikuchi, 1928; Fig. 3.6). The pattern is then recorded by a charge coupled device (CCD) camera. Given a known crystal structure, the pattern depends on the orientation in space of the crystal. The acquisition software recognizes the pattern (based on the angles and position of Kikuchi bands) and compares it with

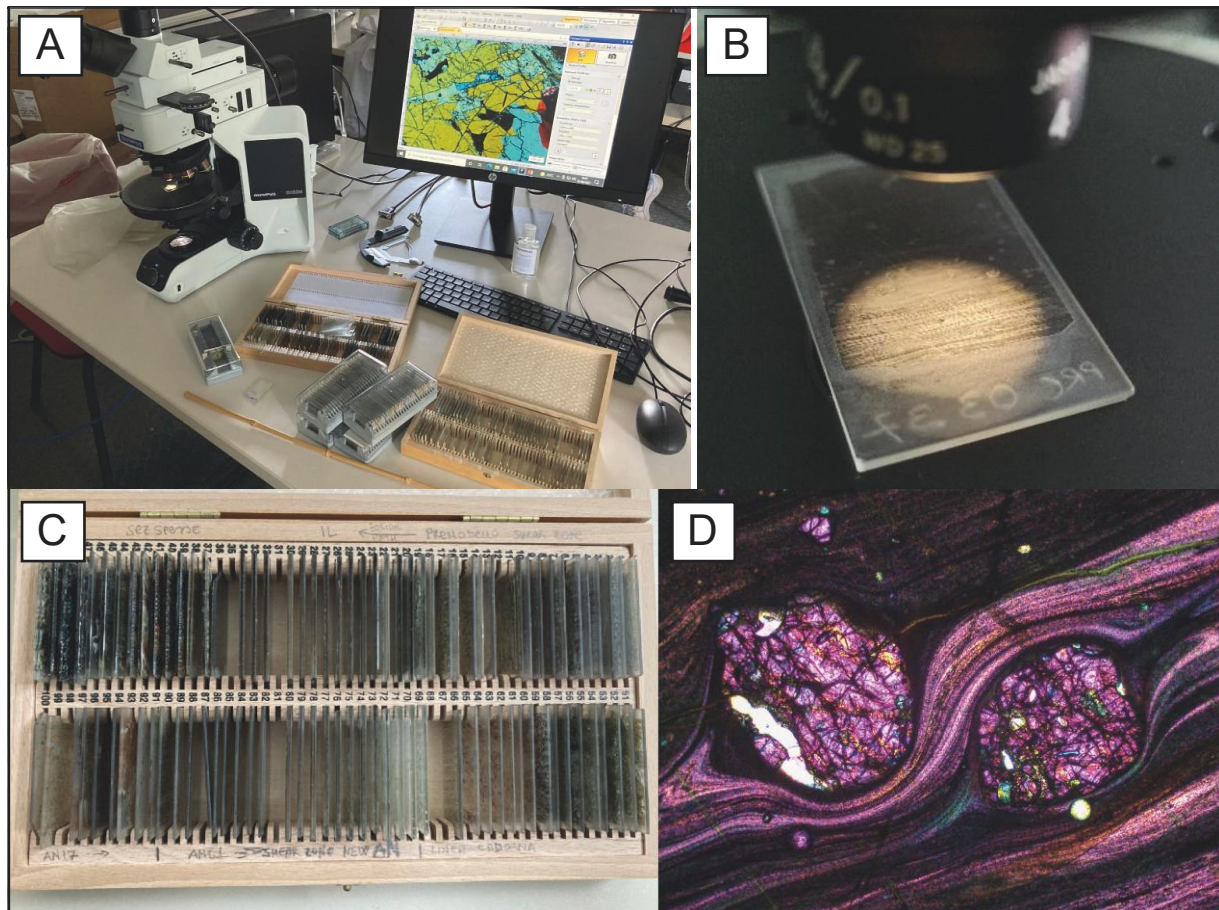


Fig. 3.4 - Example of: A) optical microscope used for microphotographs at DSTA; B) petrographic thin section (30 μ m); C) box with thin sections collection from the case study 2; D) example of microphotograph made by Iphone5S of ultramylonitic sample with lambda lens inserted.

theoretical match units of specific mineral phases derived from their lattice parameters. The process of attributing a specific crystallographic orientation to a mineral phase is referred to as “indexing”. Indexing translates the Kikuchi pattern into a set of three rotation angles, known as Euler angles, which together define the crystallographic orientation in a 3D space (Engler and Randle, 2009).

In this way, the orientation of each point is described by three rotations angles, required to bring the crystallographic orientation to coincide with the sample’s reference frame. Reliability of indexing is expressed by the Mean Angular Deviation (MAD), which corresponds to the angular deviation of the indexed pattern from the theoretical match unit. Accuracy of EBSD is generally on the order of 1-2°, and modern EBSD systems can get to < 0.5°. EBSD patterns are measured in raster mode using a predefined distance (step size). Scanning across an area produces maps where each pixel is a crystallographic orientation.

Therefore, EBSD data is essentially an orientation matrix (expressed as three rotation angles –

Euler angles) that relates the orientation of the crystal lattice to the sample's X-Y-Z reference frame. This orientation matrix can be visualized in different ways; the most common being EBSD maps where each pixel (positioned in the X-Y coordinates in the sample's reference frame; Z is the pole to the X-Y surface) represents an orientation of the crystals lattice. Moreover, crystallographic planes or directions can be plotted in stereographic projections, referred to as pole figures. EBSD data can also be processed to extract other quantitative information such as grain size, misorientation angles between two pixels or between set of pixels (i.e., within grains or at grain boundaries; Lloyd et al., 1997; Prior et al., 2009; Wheeler et al., 2001).

EBSD analysis is a key tool for providing information on deformation mechanisms and other metamorphic processes in polyphase rocks (Prior et al., 2009).

3.4.2.1 EBSD data acquisition and processing

Crystallographic orientation data presented in this PhD thesis were obtained from automatically indexed EBSD patterns collected using the FEI Quanta 650 FEG-ESEM (with Oxford X-max 80 SDD EDS, Oxford/HKL Nordleys EBSD system and Aztec software) at the Electron Optics Facility, University of Leeds, UK (Fig. 3.7). Thin sections for EBSD analyses were SYTON-polished and coated with 5 nm of carbon (see section 3.2.1). Analyses are performed with a working distance of 12 mm, an acceleration voltage of 20 kV and at a specimen tilt of 70°. EBSD maps were taken with average 10 µm step sizes determined by grain size and required resolution.

EBSD patterns were indexing and processed using AZtecCrystal software (HKL Technology, Oxford Instruments). The obtained electron backscatter diffraction patterns were automatically indexed by comparing obtained reflector intensities with those of theoretical reflectors. In addition, high-resolution orientation contrast (OC) images were taken (Prior et al., 1999), these depict qualitatively in different grayscale different crystallographic orientations. Noise reduction and removal of zero solutions are performed following the procedure of (Bestmann and Prior, 2003; Piazzolo et al., 2006; Prior et al., 2002). Data was passed once through a modified (3 × 3 filter with a 5° smoothing angle and a 1° artefact angle) Kuwahara filter (Kuwahara et al., 1976). To check for possible artefacts, we made sure that the low-angle boundary positions did not change with filtering.

The resulting data are presented in the form of colour-coded maps: crystallographic orientation and misorientation maps (i.e., Inverse Pole Figure and Texture Component). In an Inverse Pole Figure

(IPF) map each analysis point is colour coded according to the full crystallographic orientation; colour coding is defined according to the crystallographic orientation of the grain relative to one of the samples' coordinate system axes (either the X, Y or Z axis). The colour code is exemplified in the inset provided. In our case we use the colour coding relative to the sample Z direction (i.e., the pole to the sample foliation, Figs. 4.6, 4.8). The so-called Texture Component map each analysis point is

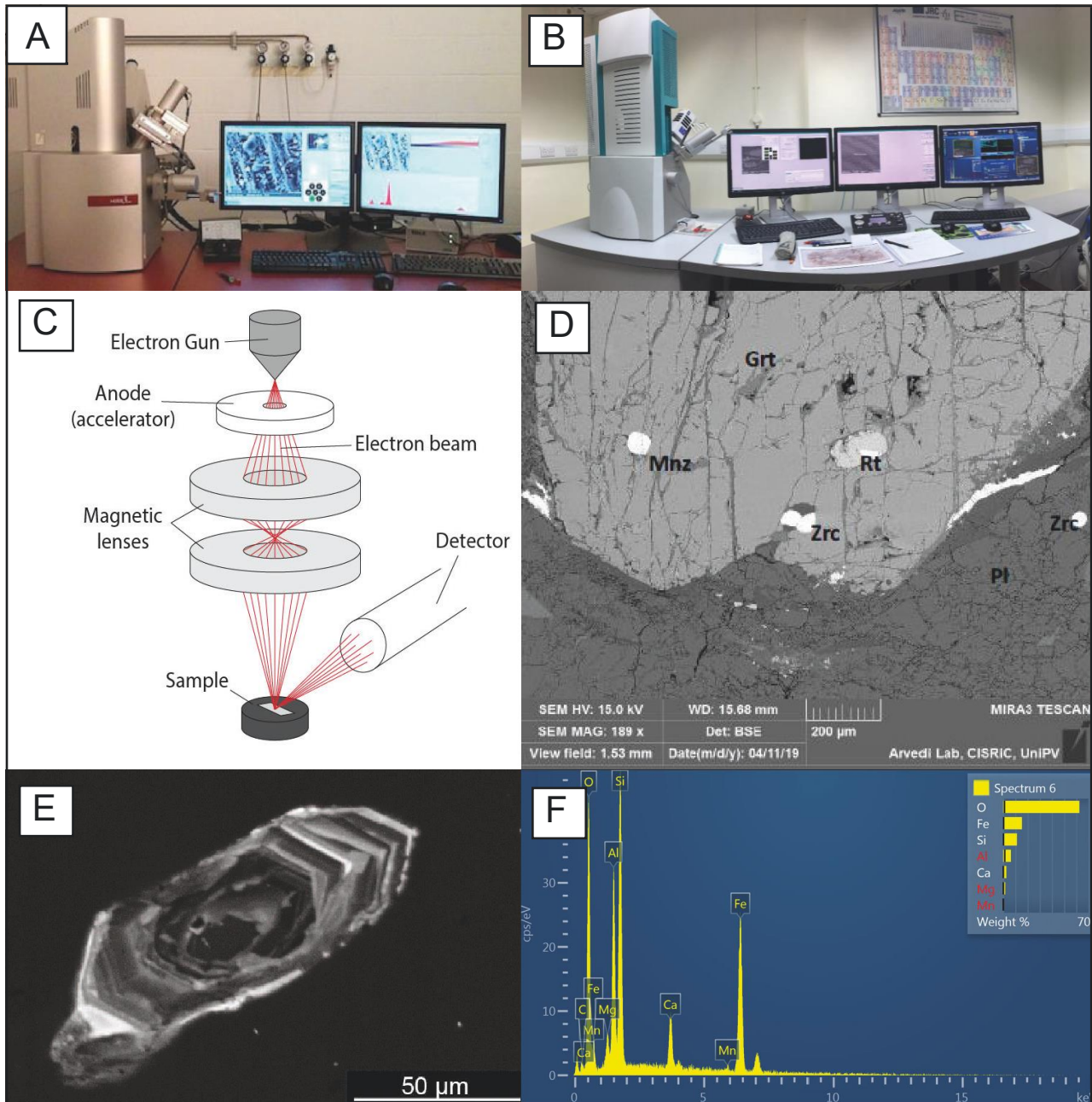


Fig. 3.5 – Scanning Electron Microscope: A) SEM-Tescan at the “Arvedi” laboratory at the University of Pavia; B) SEM-Vega3 at the University of Leeds. C) Scheme of the SEM functioning (ph. University of Cambridge). D) Example of BSE image and E) CL image on zircon separate crystal; F) EDS spectra for garnet crystal analysing by using Aztec 3.3 software at the University of Leeds.

colour coded according to the change in crystallographic orientation in degrees (i.e., misorientation angle) with respect to a chosen reference point (a reference orientation) within the map (Figs. 4.6, 4.8). The reference point is marked with a cross. The misorientation angle between two crystallographic orientations is defined as the smallest angular differences (considering crystal symmetry) between the chosen reference point and each other pixel (i.e., analyses point) of the same phase. The map is useful to spatially visualize the degree of orientation change from the chosen point and is here used as an aid to identify any intracrystalline lattice distortions and therefore associated deformation or replacement mechanisms. To assess if there are any crystallographic preferred orientations (CPO) within a population of grains of the same phase we utilize pole figure representations. Here, the crystallographic orientation of lattice directions and planes are plotted on the lower hemisphere of an equal area stereographic projection of crystallographic orientation plotting one representative orientation per grain. All pole figures presented in this work are referenced with the pole to the sample foliation (sample's Z direction) pointing upwards and the mineral lineation (sample's X direction) horizontal.

3.5 Chemical analysis

3.5.1 Bulk rock (XRF)

The X-Ray Fluorescence (XRF) technique was used to determine the bulk chemical composition of a selection of representative rock samples by giving the concentrations of each element in the form of wt% oxides or ppm. The XRF operates with an X-ray beam generated in a Rhodium X-ray tube. When X-rays hit the sample, some are absorbed by the sample giving fluorescence and some are scattered. Fluorescence is the result of the interaction between high-energy X-rays and the atoms of the substance. If the X-ray has sufficient energy to overcome the electron's binding energy, ionization occurs. The difference in energy resulting from ionization is emitted as X-rays fluorescence with characteristic energies, making it possible to distinguish between different elements. The intensity of the signal sent to the detector is a function of the number of photons emitted, thus to the quantity of the element in the sample. Light elements are very difficult to detect with XRF because most of the radiation is not absorbed and does not produce fluorescence. The XRF analysis is done at a constant temperature and in a vacuum chamber, reason for which gases and liquids cannot be measured easily. Analysis can be made either from glass-beads (pills) or from powder. The bead has the advantage of being chemically

more homogeneous than the corresponding powder.

A representative and homogeneous powder is usually the starting material for XRF analysis. This is obtained by crushing and grinding (milling) the rock sample until it becomes a fine powder. Bulk rock major and trace element composition for samples from this research were determined by standard X-ray fluorescence spectroscopy (XRF) spectroscopy and Laser Inductively Coupled Plasma Mass Spectrometry (LA-ICP-MS) at the Activation Laboratories Ltd., Ancaster, Canada (4E-Research + ICPMS method; <https://actlabs.com/geochemistry/litho-geochemistry-and-whole-rock-analysis/inaa-and-multi-methods/>). Appendices A.1.3 and A.2.3, tables S4.1 and S5.2, gives the major and trace element composition for samples for case study 1 and 2, respectively. The LOI was used as an indication of the volatile component of the rock. Bulk rock compositions were determined for pseudosection modelling (see section 3.6.2).

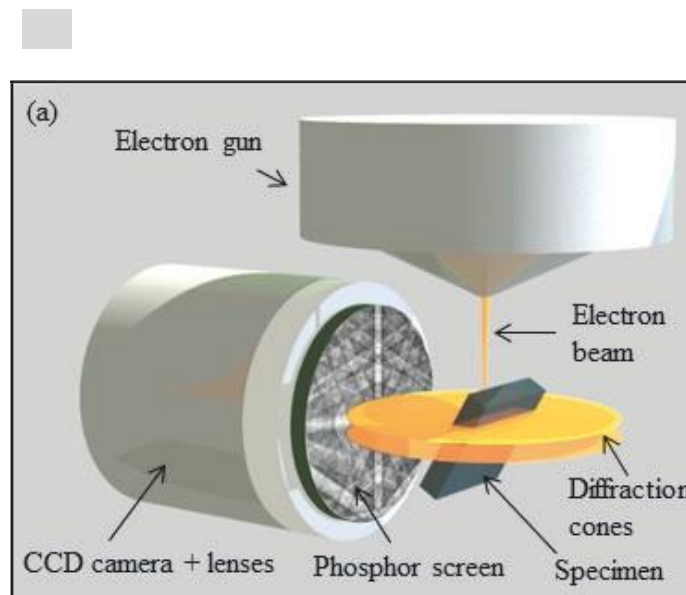


Fig. 3.6 - Sketch of the EBSD detection geometry and a conventional EBSD detector.

3.5.2 Major element (EPMA)

The Electron Probe Microanalyzers (EPMA) provides quantitative chemical analysis of major and trace elements (e.g., Reed, 1975, 2005). Like the SEM, it works on the principle that a focused electron beam interacting with a solid matter to emit electrons and X-rays of characteristic energies (see section 3.4.1). By measuring the intensities of the emitted X-rays, it is possible to quantify the elements in the substance analysed. The great advantage of the microprobe over the analytical SEM consists in the quality and number of X-ray detectors. SEMs are usually equipped with an EDS (Energy Dispersive Spectroscopy) detector: a Si-drift detector (SDD). This crystal absorbs all the incoming X-rays and gets ionized producing electrical

pulses, which are amplified and analysed by a multichannel analyser. Conversely, microprobes are equipped with 4+WDS (Wavelength Dispersive Spectroscopy) detectors. EDS measures X-rays intensities simultaneously whereas WDS measures X-rays wavelengths one at a time. The WDS uses different diffraction-crystals (LIF, PET, TAP, LDE) to transform the incoming multi-wave radiation in monochromatic radiation that is diffracted according to Bragg's law (see section 3.4.1).

WDS has a very high-spectral resolution where signal to background ratio is much better than for EDS, giving better detection limits and allowing for minor and trace elements quantification. Elements concentrations are calculated by comparing the signal's intensities with that of standards. The intensity of the signal is the number of counts per second measured by the WDS detectors. In first approximation (corrections have to be applied), the concentration C of an element (element wt%, e.g., Fe) is in function of the intensity (I) of the element in the substance X and in the standard std , and C is the concentration. Therefore, calibration of the machine by measurement of standards is required before each quantitative analysis.

Major element mineral chemistry was measured with the JEOL 8200 Super Probe Electron Microprobe Analyser (EMPA) at the Department of Earth Sciences, University of Milan (Italy), by the technician Andrea Risplendente. Thin sections were carbon coated. Working conditions were 15 kV accelerating voltage, 5 nA current, 1 μm beam diameter, 10 mm working distance, using wavelength dispersive spectrometry (WDS) and natural silicates as standards. A PhiRhoZ routine was used for matrix correction. Potassic feldspar was analysed with a defocussed beam to prevent K devolatilization during the analyses. Mineral analyses were always assisted by BSE images to inspect the microstructural site. The major elements measured were: Si, Ti, Al, Fe, Mn, Mg, Ca, Na, K, Cr and converted in the oxides SiO_2 , TiO_2 , Al_2O_3 , $\text{FeO}(\text{tot})$, MnO , MgO , CaO , Na_2O , K_2O , Cr_2O_3 , expressed as wt%. The microprobe was also used to acquire microprobe elemental maps (i.e., Garnet).

Microprobe results were given as oxide wt%. To obtain the mineral compositions, oxide wt% were converted into the corresponding moles of ions (by dividing by the molecular weight and multiplying by the number of atoms) that were then normalized based on the number of ions in the mineral formula unit. All minerals were normalised based on the number of cations unless stated otherwise (pyroxene 4, amphibole 13, plagioclase 5, garnet 8 and so on). The end-members compositions were computed as ratios of the cations.

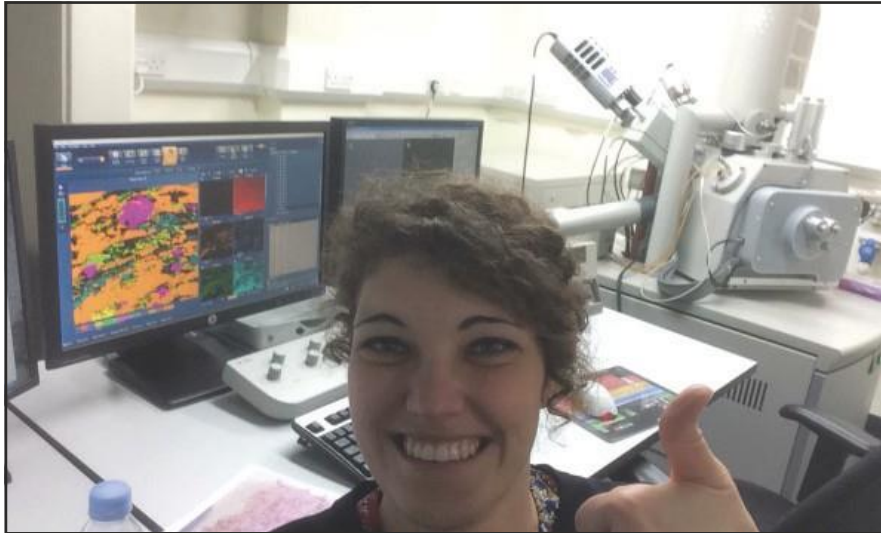


Fig. 3.7 – Me experiencing EBSD technique at the University of Leeds, Electron Microscopy Facility.

3.5.3 Trace element (LA-ICP-MS)

Laser ablation-inductively coupled plasma-mass spectrometry (LA-ICP-MS) is a long name for this analytical instrument and technique which is why the acronym LA-ICP-MS was created and is commonly used. LA-ICP-MS has an important potential of the technique for quantitative trace element determinations for geological samples (Košler, 2008). This technique combines a mass spectrometer (MS) with an inductively coupled plasma source (ICP) associated to a microprobe laser ablation (LA); the final aim is to determinate the geochemistry of samples (Sylvester and Jackson, 2016).

In LA-ICP-MS analysis, a (usually) flat surface of the sample is ablated with a pulsed (typically nanosecond) laser in a gas-tight chamber, producing a stream of tiny particles (aerosol) that is transported in a carrier gas (usually helium) to an inductively coupled argon plasma (ICP), which vaporizes and converts the particles to ions. The ions are separated based on their mass-to-charge ratios by the mass spectrometer and quantified by a detector. Ion signal intensities are converted to either element concentrations, by reference to an external calibration standard, or to isotopic ratios or ages after correction for any mass dependent measurement bias of the instrument. By moving the sample beneath the laser spot, or isotopic composition of millimetre-sized areas of the sample can be made (Fig. 3.8A; Abduriyim and Kitawaki, 2006; Sylvester and Jackson, 2016).

An ideal laser ablation system for LA-ICP-MS would have two key abilities: (1) to ablate a specified spot (with size varying between 10-55 μm ; Fig. 3.8B, C) in the target material by photo-chemical processes rather than physical disaggregation or melting; (2) to generate, and deliver to the ICP, a sample aerosol

with the same composition as the target material and one that comprises particles small enough to be completely vaporized and ionized in the ICP, thereby minimizing loss of analyte and avoiding volatility related element fractionation (Guillong and Günther, 2002) and isotopic fractionation (Jackson and Günther, 2003) in the inductively coupled plasma. Current systems are commonly based on deep-ultraviolet-light lasers with nanosecond pulse durations (frequency-quintupled Nd:YAG solid-state with $\lambda = 266$ nm or argon fluoride (ArF) gas excimer with $\lambda = 193$ nm; excimers are “excited dimers,” molecules of rare gas halides that are stable only in an excited electronic state). These ultraviolet nanosecond lasers come closer to the ideal than previous lasers, but still do not quite reach it.

To quantitate trace-element abundances via LA-ICP-MS techniques typically requires bracketing unknown samples with those of known compositions (external reference materials), in addition to knowing the abundance of one element (e.g., Si or Ca, determined independently by EPMA) in the unknown sample for internal calibration (Jackson, 2008). For external calibration of LA-ICP-MS analyses, only a few materials have sufficiently accurate reference values for >40 elements. The foremost of these are the series of synthetic glasses produced by the (US) National Institute of Standards and Technology Standard Reference Material (NIST SRM), which are doped with trace elements at varying concentrations (e.g., NIST SRM 610) and permit the accurate analysis of >60 elements using LA-ICP-MS techniques (Jenner and Arevalo, 2016). Hence, the NIST SRM glasses are currently the most reliable options with respect to calibrating LA-ICP-MS analyses for a broad range of elements. Instead, for major rock-forming elements, it is preferable to use well-characterized reference materials of natural compositions, such as the USGS fused glass from powdered basalt from Columbia River (BCR-2G), the Smithsonian National Museum of Natural History (NMNH) natural volcanic glass (VG-2, also referred to as NMNH 111240-52) from the Juan de Fuca Ridge or the MPI-DING glasses.

The LA-ICP-MS analyses are directly monitored on a screen that show spectra with Intensity (counts per second) vs. Number of readings for ^{42}Ca , ^{59}Co , ^{139}La and ^{232}Th of NIST612 glass (Fig. 3.8D, E). The dashed lines in the background and signal area demonstrate the selected time interval which was used for integration. Backgrounds were acquired for -30s (~60 readings) prior to the beginning of the ablation. Signals were acquired ~60 s (~120 readings) on the analyte signal. The first few ablation readings were rejected to avoid obtaining data from contamination on the sample surface (Longerich, 2008).

LA-ICP-MS results were treated by software GLITTER (Griffin, 2008) which is the first real-time interactive data reduction for this technique. It enables rapid selection of the best intervals for background and signal measurement. Time-resolved data for each analyte mass are displayed in a unique pixel-row display to allow quick recognition of inclusions and data spikes. Results in tables and plots change automatically when different integration intervals are selected. It provides calculation of the results for each analysis during the run. The first results are calculated as soon as one standard and one sample have been analysed. With each additional standard analysis, the data are instantaneously adjusted to take account of changes in the analytical conditions such as instrumental drift; no off-line reprocessing is required. Finally, it also provides a variety of plotting and diagnostic options allowing the user to evaluate the quality and significance of each analysis during the run.

Trace element concentrations have been determined by means of the LA-ICP-MS at the IGG-CNR, SS. of Pavia (Italy). A PerkinElmer SCIEX ELAN DCR-e quadrupole ICP-MS was coupled with a 266nm Nd:YAG laser (NewWave Research). Helium was used as carrier gas and mixed with Ar downstream of the ablation cell. Laser spot size was calibrated between 55 μm and laser beam fluency at 3.0 J/cm² and frequency of 10 Hz. Data reduction was performed with GLITTER software, using the reference synthetic glass NIST (SRM) 610 as external standards. ²⁹Si was used as internal standards for plagioclase; ⁴⁴Ca for clinopyroxene, and amphibole. Precision and accuracy were assessed via repeated analyses of basalt glass (BCR-2g) reference material, resulting better than 10% at ppm concentration level. The uncertainties related to the trace element data is of 1 σ . Detection limits were typically in the range of 100-500 ppb for Sc, 10-100 ppb for Sr, Zr, Ba, Gd and Pb, 1-10 ppb for Y, Nb, La, Ce, Nd, Sm, Eu, Dy, Er, Yb, Hf and Ta, and usually <1 ppb for Pr, Th, and U.

3.6 *P-T* estimates

The reconstruction of *P-T* conditions includes two types of approaches (Spear, 1989):

1. Backward approach: the method of inversely inferring the metamorphic events from rock samples via traditional petrological investigation methods (e.g., geothermobarometry).
2. Forward approach: using thermal modelling techniques to work on the geological evolutionary model of rocks, and is usually used to validate results obtained in the backward approach (e.g., *P-T* pseudosection).

In this research, we applied both methodologies to assure the best P - T - t - D - X reconstructions.

3.6.1 Geothermobarometry

The estimation of pressure (P) and temperature (T) conditions at which a geologic material formed is referred to as geobarometry and geothermometry, respectively, and collectively termed geothermobarometry (Spear, 1989). Geothermometers and geobarometers are commonly based on mineral assemblage and mineral composition information. The fundamental premise of geothermobarometry is that a rock's mineral assemblage and mineral compositions are sensitive to pressure and temperature conditions of formation and that events after mineral equilibration have not significantly modified these rock properties. The development of a geothermometer or geobarometer typically requires extensive experimental and theoretical calibration prior to use. Therefore, geothermobarometry utilizes the equilibrium constants of mineral assemblages in a rock to infer the metamorphic P - T conditions. The EPMA results are usually used in geothermobarometry to measure the distribution of components in the minerals and give precise determination of the chemical equilibrium within the specimen (Bucher and Frey, 2013). Reference data on the geothermometers and geobarometers is derived from both laboratory studies on artificial mineral assemblages, where minerals are grown at known temperatures and pressures and the chemical equilibrium measured directly, and from calibration using natural systems.

Geothermometers are usually represented by exchange reactions, which are sensitive to temperature but with little effect under changing pressure. For example, one of the best known and most widely applicable geothermometers is the garnet-biotite relationship where the relative proportions of Fe^{2+} and Mg^{2+} in garnet and biotite change with increasing temperature, so measurement of the compositions of these minerals to give the Fe-Mg distribution between them allows the temperature of crystallization to be calculated, given some assumptions. Some geothermometers techniques include: Ti saturation content of biotite; Fe-Mg exchange between garnet-biotite; Zr content in rutile; Zr content in titanite; Ti content in zircon crystallization.

Geobarometers are typically occurred as net-transfer reactions, which are sensitive to pressure but have little change with temperature, such as garnet-plagioclase-muscovite-biotite (GPMB) reaction that involves a significant volume reduction upon high pressure. Other geobarometers are: GASP; an acronym for the assemblage garnet-(Al_2SiO_5)-silica(quartz)-plagioclase. Despite the usefulness of

geothermobarometry, special attention should be paid to whether the mineral assemblages represent an equilibrium, any occurrence of retrograde equilibrium in the rock, and appropriateness of calibration of the results (Spear, 1989).

P-T conditions for case study 1 – Cima di Gagnone were determined by combining the following geo-thermometers and/or-barometers: i) the Garnet–Biotite (GB; Spear, 1993; Holdaway, 2000), ii) the Garnet–Alluminosilicate–Silica–Plagioclase (GASP; e.g., Holdaway, 2001), iii) the Garnet–Biotite–Muscovite–Plagioclase (GBMP; e.g., Holdaway, 2000, 2001; Wu, 2015), iv) the Garnet–Muscovite (GM; e.g., Wu, 2018), v) Garnet–Muscovite–Al₂SiO₅–Quartz (GMAQ; e.g., Wu, 2018) and vi) the Si–content in white mica (Si–Wm; i.e., Caddick and Thompson, 2008; Massonne and Schreyer, 1987).

P-T conditions for case study 2 – Anzola shear zone were determined by combining the following geo-thermometers and/or-barometers: i) the Garnet–Biotite (GB; Spear, 1993; Holdaway, 2000), ii) Ti in Amphibole (Liao et al., 2021), iii) Zr-in-Rutile (Kohn, 2020), v) the Garnet–Alluminosilicate–Silica–Plagioclase (GASP; e.g., Holdaway, 2001).

These methods were calibrated using: Bhattacharya et al. (1992), Holland and Powell (1985), Hodges and Crowley (1985), Hoisch (1990), Green and Hellman (1982), Krogh and Råheim (1978), Wu (2018) and Coggon and Holland (2002) for the GB, GASP, GPMB, GM, GMAQ and Si–Wm, respectively. Moreover, these methods were applied following textural criteria; the values referred to garnet rims were associated with the neighboring minerals (biotite, plagioclase, kyanite or muscovite) for which equilibrium texture are observable. Garnet cores were instead paired only with their inclusions. Data are listed in tables S4.4 and S5.5, in Appendices A.1.4 and A.2.3, respectively.

3.6.2 Thermodynamic modelling: *P-T-X* Pseudosection

Thermodynamic modelling is a powerful tool for calculating phase equilibria in the *P-T-X* space, given a starting bulk composition and a set of boundary constrains. This is done through modelling programs such as *Perple_X* (Connolly, 1990, 2005) that compute phase-equilibria based on thermodynamic principles. Typical outputs of thermodynamic modelling programs are pseudosections, i.e., diagrams showing stability fields of different phase assemblages in the *P-T-X* space. In 2D diagrams, one of the three variables is kept constant and the other two vary between the chosen boundaries. Pseudosections are particularly useful to predict: 1) the *P-T* conditions of

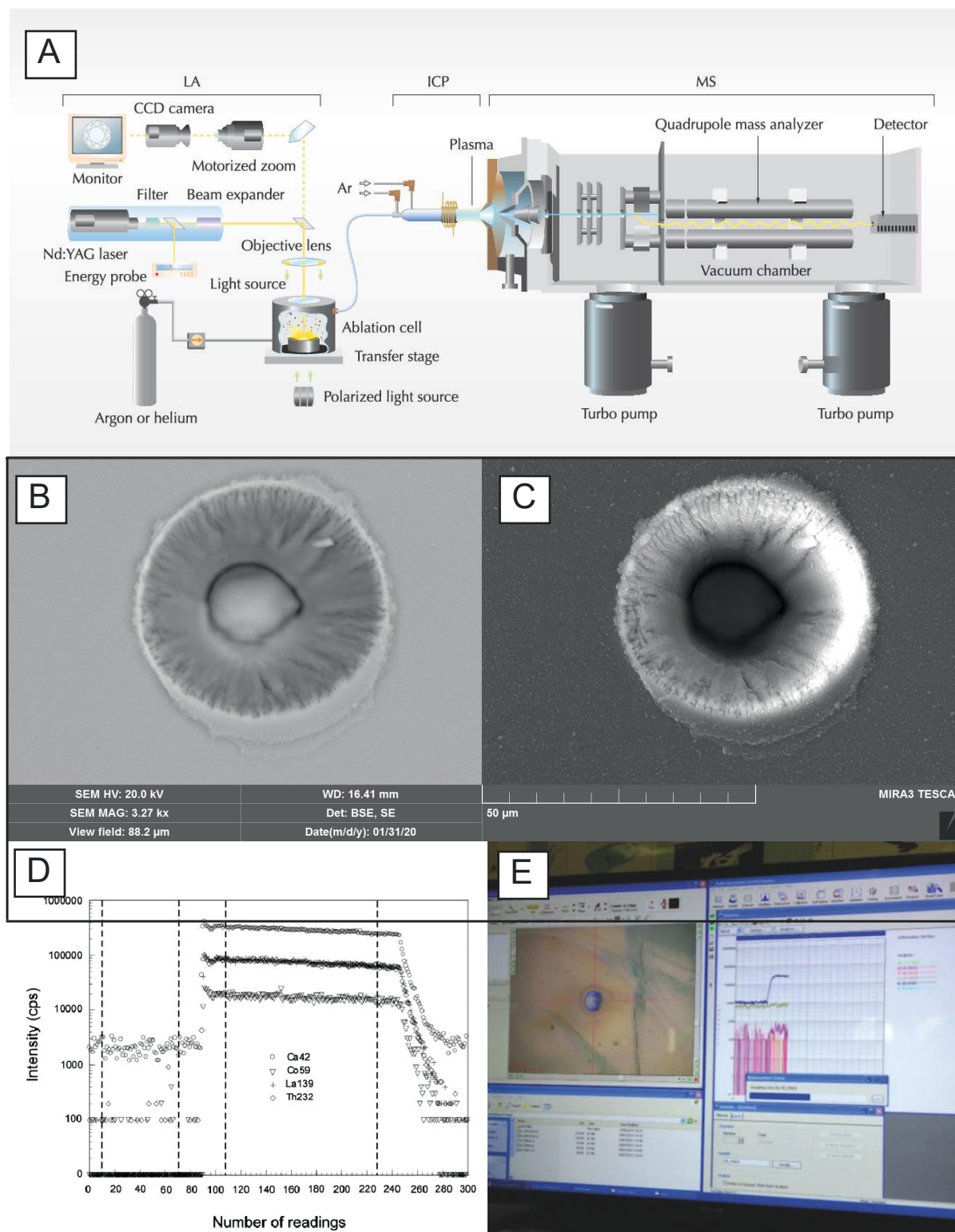


Fig. 3.8 – LA-ICP-MS analytical technique: A) Schematic diagram shows the components of a laser ablation system combined with a quadrupole ICP-MS instrument (Abduriyim and Kitawaki, 2006). SEM images of 193 nm excimer laser spot on tephra: B) BSE image and C) SE image (credit Antonio Langone). D) Laser ablation ICP-MS spectra showing intensity (counts per second) vs. Number of readings for ^{42}Ca , ^{59}Co , ^{139}La and ^{232}Th of NIST612 glass (Longerich, 2008). E) Real example of laser ablation procedure during the work analyses.

stability of a specific mineral assemblage in a rock with a given bulk composition, 2) changes in the mineral assemblage with changing metamorphic conditions (T - X or P - X diagrams), and 3) changes in chemical composition of minerals in the P - T space (mineral isopleths). In addition, pseudosections can be used to model melt-rock interactions (to find the stable mineral assemblage when mixing a melt composition with a rock composition), and to reconstruct the P - T path of a rock.

In this project, thermodynamic modelling is used especially with the objective of constraining the ambient conditions (P , T , X) for the studied area and combine the results with those from geothermobarometry methods.

For both case studies, pseudosections were obtained using Perple_X version 685 thermodynamic modelling package (Connolly, 2005), using the 10 components MnO-TiO₂-Na₂O-CaO-K₂O-FeO-MgO-Al₂O₃-SiO₂-H₂O (MnTiNCKFMASH) with H₂O in excess where migmatization do not occur, and considering the melt presence only where we have evidence of partial melting on the field. The bulk compositions were projected from the apatite pole onto the MnTiNCKFMASH subspace, removing minor component P2O₅ from the system (e.g., Thompson, 1957; Büttner, 2012).

The input bulk-rock compositions were obtained through XRF (see chapter 3.5.1, tables S4.1 and S5.2 in Appendices A.1.4 and A.2.3, respectively). The FeO content was kept as total iron. A T - X pseudosection was calculated for case study 1 to represent the changes in bulk composition as function of temperature. An additional calculation of the effective bulk composition was made for the samples that show core-rim re-equilibration (i.e., garnet), by quantifying the modal volumetric abundance of the cores, transform it into molar abundance, and thus subtracting the average core composition from the bulk rock composition. The previously approaches were chosen to determine as closely as possible the bulk composition effective at the scale of the thin section (Zuluaga et al., 2005; Buttner, 2012; Lanari and Engi, 2017). Compositional garnet isopleths of almandine [$\text{Fe}^{2+}/(\text{Fe}^{2+}+\text{Mg}+\text{Ca}+\text{Mn})$], pyrope [$\text{Mg}/(\text{Fe}^{2+}+\text{Mg}+\text{Ca}+\text{Mn})$], grossular [$\text{Ca}/(\text{Fe}^{2+}+\text{Mg}+\text{Ca}+\text{Mn})$] and rarely spessartine [$\text{Mn}/(\text{Fe}^{2+}+\text{Mg}+\text{Ca}+\text{Mn})$] were plotted. The position of these isopleths (with an error of $\pm 1\sigma$), calculated with the software Perplex, have been also indicated in the P - T pseudosections. As the effective bulk composition evolved between the four end-members could approximate the true metamorphic history and the P - T peak. Compositional isopleths for Si (a.p.f.u.) in muscovite, An% for plagioclase and Ti (a.p.f.u.) or Mg# [$100 \times \text{MgO}/(\text{FeO}_T + \text{MgO})$] for biotite were plotted.

3.7 Geochronology

As for the determination of trace element (see chapter 3.5.3), the analytical technique of LA-ICP-MS can be used, with several changes, for geochronological analyses (Fig. 3.9A-C).

Overall, U-(Th)-Pb multi-phase geochronometry of accessory minerals are performed on a routine basis for formation ages of magmatic and metamorphic rocks, structural and tectonic framework studies and detrital accessory minerals provenance analysis. Analyses can be performed directly on thin or thick sections and on mineral separates embedded in epoxy mounts. The laser spot size can vary from 5 to 120 μm (Fig. 3.9D) and the minimum laser spot size depends mainly on mineral internal structures (i.e., zoning, inclusions and fractures) and is mainly function of the geochronometer (e.g., the high Th content of monazite allows analyses with 5 μm laser spot size).

In order to completely apply the U–Th–Pb systematics with LA-ICP-MS, the signals of masses ^{202}Hg , $^{204}(\text{Pb}+\text{Hg})$, ^{206}Pb , ^{207}Pb , ^{208}Pb , ^{232}Th and ^{238}U masses were acquired (Tiepolo et al., 2003). The presence of common Pb is monitored by the net signal of ^{204}Pb (subtracted for the isobaric interference of ^{202}Hg and background). Remarkably, the signal of $^{204}(\text{Pb}+\text{Hg})$ is always undistinguishable from the background in the investigated samples. However, the relatively high Hg signal in the gas blank does not exclude the effective presence of common Pb in the analysed grains. The ^{235}U signal was calculated from ^{238}U based on the ratio $^{238}\text{U}/^{235}\text{U}=137.818$ (Hiess et al., 2012). U–Pb fractionation effects in geochronometers were simultaneously corrected for using a matrix matched external standard and considering the same integration intervals on the standard and the unknowns. Petrographic thin sections (27x45mm) and epoxy resin cylinder (1 or 2 inches in diameter and with a maximum thickness of 0.7 cm) of embedded minerals (e.g., zircon, monazite, titanite and rutile). The surface to be analysed must be polished and cleaned (without coatings). Generally, epoxy resin cylinder consists in mineral grains separated using conventional methods (Wilfley table, magnetic separation and heavy liquid), handpicked under a binocular microscope and then mounted in epoxy resin.

In the case study 1, U-(Th)-Pb geochronology was performed using LA-ICP-MS on zircon and monazite directly on the 30 μm -thick. Several epoxy resin cylinders with separated zircon grains were also prepared by the candidate and used for this technique (see chapter 3.10). Analytical methods for zircon and monazite geochronology are fully described in Tiepolo (2003) and Paquette and Tiepolo (2007). Dating was performed following the analytical procedure suggested by Langone et al. (2011,

2015) and Maino et al. (2012). Before the isotopic analyses, zircon grains were imaged by back-scattered electron imaging to locate, characterize (dimensions, microstructural position, and internal structures) and then select the most suitable crystals. Zircon features on thin section were observed obtaining CL images (see chapter 3.5.1). Monazite grains were also characterized by quantitative chemical analyses (Si, P, S, Ca, Y, La, Ce, Pr, Nd, Sm, Eu, Gd, Dy, Pb, Th, and U) and compositional maps (Y, Ce, Pr, Th, P, Ca, La, Nd, Sm, Gd) acquired using an electronic microprobe (JEOL JXA 8200 Super Probe, at the University of Milano; see chapter 3.5.2).

Analyses were carried out directly on polished thin sections and on epoxy resin cylinders using an ArF 193-nm excimer laser (GeolLas 102 from MicroLas) coupled with the 8900 Triple Quadrupole ICP-MS (Agilent) at C.N.R., Istituto di Geoscienze e Georisorse of Pavia (Fig. 3.9A, B). Analytical conditions vary from 10 μm diameter of 6 spot size, 8 J cm^{-2} of energy density, and 3 Hz of repetition rate for monazite, while for spot sizes of both 10 and 20 μm , a repetition rate of 5 Hz, and a laser fluence of 8 J cm^{-2} were used with zircons. Time-resolved signals were carefully inspected to verify the presence of perturbations related to inclusions, fractures or mixing of different age domains.

The instrumental and laser-induced U-Pb fractionations were standardized using matrix-matched reference zircon GJ-1 (Jackson et al., 2004; Piazzolo et al., 2016) adopted as external standard and the reference zircon Plesovice (Sláma et al., 2008) selected as validation standard. External standards and unknowns were integrated over the same time intervals to ensure the efficient correction of fractionation effects. Monazite analyses were instead corrected using the reference Moacir monazite as external standard (Cruz et al., 1996; Seydoux-Guillaume et al., 2002; Gasquet et al., 2010). The reproducibility of the standards was numerically propagated through all age determinations according to the equation of Horstwood et al. (2003). Only the analyses satisfying this procedure are considered accurate to within the quoted errors. The relative standard deviation of the analyses is mostly between 1-3%.

Data reduction was carried out with GLITTER TM software (Van Achterbergh et al., 2001). In order to better estimate the uncertainty affecting the $^{206}\text{Pb}/^{238}\text{U}$, $^{207}\text{Pb}/^{235}\text{U}$ and $^{208}\text{Pb}/^{232}\text{Th}$ isotope ratios, the external reproducibility of the standard was propagated relative to individual uncertainties for the isotope ratios. After this error propagation, each analysis is accurate within the quoted errors (i.e., $\pm 2\sigma$). Data processing and plotting was done by ISOPLOT-R software (Vermeesch, 2018) used for age

calculation and graphic representation. All errors on the final U–Pb ages for zircons and monazites reported in the main text are given at the 2σ level. Results and reference materials are reported in Appendix A.1.4 in Table S4.5.

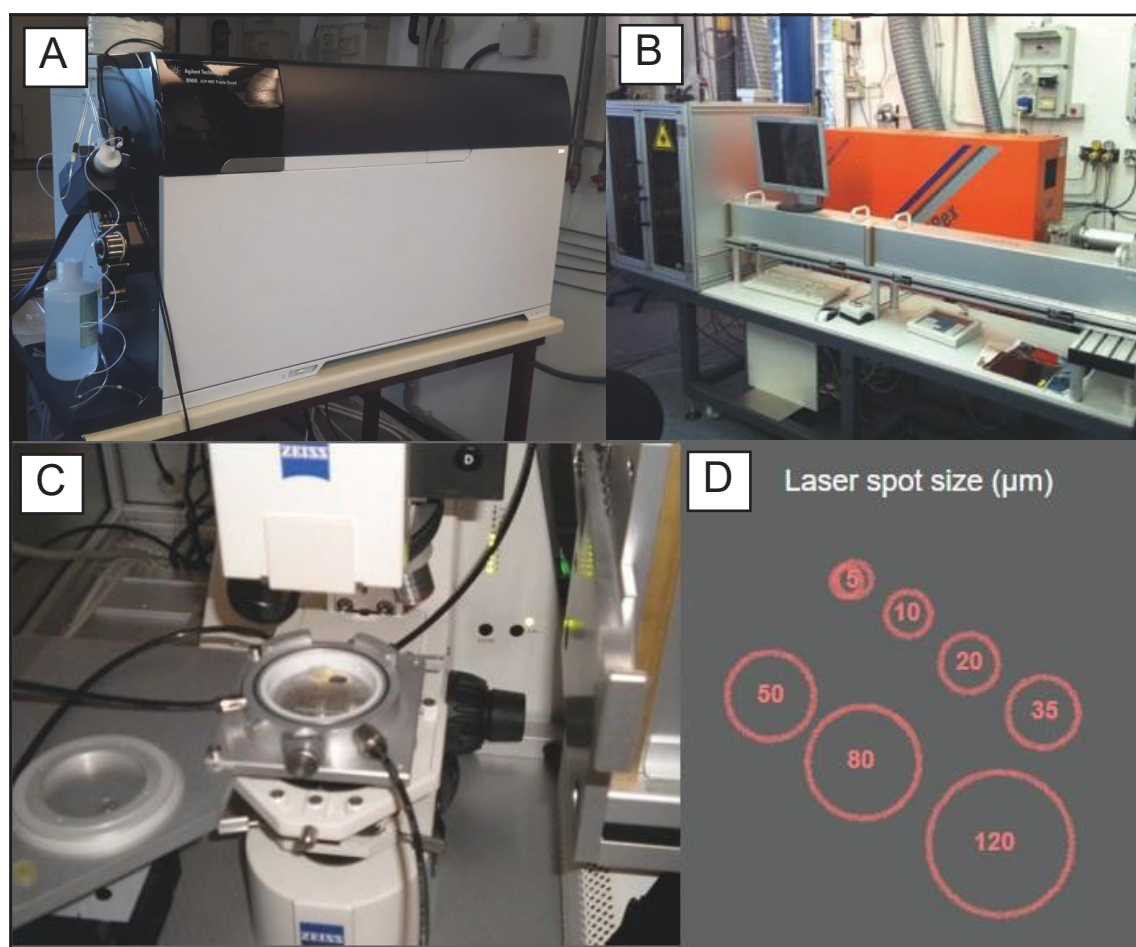


Fig. 3.9 – Geochronological analyses. A) 8900 Triple Quadrupole ICP–MS (Agilent) at C.N.R., Istituto di Geoscienze e Georisorse of Pavia. B) ArF 193–nm excimer laser (GeolLas 102 from MicroLas). C) Sample cell in the laser. D) Example of laser spot size.

3.8 References

- Aravadinou, E. and Xypolias P., 2017. Evolution of a passive crustal-scale detachment (Syros, Aegean region): Insights from structural and petrofabric analyses in the hanging-wall. *J. Struct. Geol.*, 103: 57-74.
- Abduriyim, A., & Kitawaki, H., 2006. Applications of laser ablation-inductively coupled plasma-mass spectrometry (LA-ICP-MS) to gemology. *Gems and Gemology*, 42(2), 98.
- Acquafredda, P., 2020. 2. XRF technique. In *Chemical Analysis in Cultural Heritage* (pp. 31-62). De Gruyter.
- Aleinikoff, J. N., Wintsch, R. P., Tollo, R. P., Unruh, D. M., Fanning, C. M., & Schmitz, M. D. (2007). Ages and origins of rocks of the Killingworth dome, south-central Connecticut: Implications for the tectonic evolution of southern New England. *American Journal of Science*, 307(1), 63-118.
- Bestmann, M., and Prior, D. J., 2003. Intragranular dynamic recrystallization in naturally deformed calcite marble: Diffusion accommodated grain boundary sliding as a result of subgrain rotation recrystallization. *Journal of Structural Geology*, 25(10), 1597–1613.
- Bhattacharya, A., Mohanty, L., Maji, A., Sen, S. K., and Raith, M., 1992. Non-ideal mixing in the phlogopite–annite binary: constraints from experimental data on Mg–Fe partitioning and a reformulation of the biotite–garnet geothermometer. *Contributions to Mineralogy and Petrology*, 111, 8–93.
- Bragg, W.H., Bragg, W.L., 1913. The Reflection of X-rays by Crystals. *Proc. R. Soc. Lond. Ser. Contain. Pap. Math. Phys. Character* 88, 428–438.
- Bucher, K., and Frey, M., 2013. *Petrogenesis of Metamorphic Rocks*. Springer Science & Business Media.
- Büttner, S. H., 2012. Rock Maker: an MS Excel™ spreadsheet for the calculation of rock compositions from proportional whole rock analyses, mineral compositions, and modal abundance. *Mineralogy and Petrology*, 104(1–2), 129–135.
- Coggon, R., and Holland, T. J. B., 2002. Mixing properties of phengitic micas and revised garnet phengite thermobarometers. *Journal of Metamorphic Geology*, 20(7), 683–696.
- Connolly, J. A. D., 2005. Computation of phase equilibria by linear programming: A tool for geodynamic modeling and its application to subduction zone decarbonation. *Earth and Planetary Science Letters*, 236(1–2), 524–541.
- Connolly, J.A.D., 1990. Multivariable phase-diagrams - an algorithm based on generalized thermodynamics. *Am. J. Sci.* 290, 666–718.
- Deer, W. A., Howie, R. A., & Zussman, J., 1997. *Rock-forming minerals*. Geological Society of London.
- Diener J.F.A., Powell R., White R.W., Holland T.J.B., 2007. A new thermodynamic model for clino- and orthoamphiboles in the system Na₂O-CaO-FeO-MgO-Al₂O₃-SiO₂-H₂O-O. *Journal of Metamorphic Geology*, 25, 631-56.
- Engler, O., Randle, V., 2009. *Introduction to Texture Analysis: Macrotexture, Microtexture, and Orientation*

- Mapping, Second Edition. CRC Press.
- Green, T. H., and Hellman, P. L. 1982. Fe–Mg partitioning between coexisting garnet and phengite at high pressure, and comments on a garnet–phengite geothermometer. *Lithos*, 15(4), 253–266.
- Griffin, W. L., 2008. GLITTER: data reduction software for laser ablation ICP-MS. *Laser Ablation ICP-MS in the Earth Sciences: Current practices and outstanding issues*, 308-311.
- Grundmann, G., and Scholz, H. 2015. Microscopic preparation for studies in mineralogy, Geology, conservation.
- Guillong M, Günther D, 2002. Effect of particle size distribution on ICP-induced elemental fractionation in laser-ablation-inductively coupled plasma-mass spectrometry. *Journal of Analytical Atomic Spectrometry* 17: 831-837.
- Herron, M. M., 1988. Geochemical classification of terrigenous sands and shales from core or log data. *Journal of Sedimentary Research*, 58(5), 820–829.
- Hiess, J., Condon, D. J., McLean, N., & Noble, S. R. (2012). $^{238}\text{U}/^{235}\text{U}$ systematics in terrestrial uranium-bearing minerals. *Science*, 335(6076), 1610-1614.
- Hodges, K. V., and Crowley, P. T., 1985. Error estimation and empirical geothermobarometry for pelitic systems. *American Mineralogist*, 70(7–8), 702–709.
- Hoisch, T. D., 1990. Empirical calibration of six geobarometers for the mineral assemblage quartz+ muscovite+ biotite+ plagioclase+ garnet. *Contributions to Mineralogy and Petrology*, 104(2), 225–234.
- Holdaway, M. J., 2000. Application of new experimental and garnet Margules data to the garnet–biotite geothermometer. *American Mineralogist*, 85(7–8), 881–892.
- Holdaway, M. J., 2001. Recalibration of the GASP geobarometer in light of recent garnet and plagioclase activity models and versions of the garnet–biotite geothermometer. *American Mineralogist*, 86(10), 1117–1129.
- Holland, T. J. B., and Powell, R., 1985. An internally consistent thermodynamic dataset with uncertainties and correlations: 2. Data and results. *Journal of Metamorphic Geology*, 3(4), 343–370.
- Jackson SE, Günther D, 2003. The nature and sources of laser induced isotopic fractionation in laser ablation-multicollector- inductively coupled plasma-mass spectrometry. *Journal of Analytical Atomic Spectrometry* 18: 205-212
- Jackson, S. E., Pearson, N. J., Griffin, W. L., and Belousova, E. A., 2004. The application of laser ablation–inductively coupled plasma–mass spectrometry to in situ U–Pb zircon geochronology. *Chemical Geology*, 211(1–2), 47–69.
- Jackson SE (2008) Calibration strategies for elemental analysis by LA–ICP–MS. In: Sylvester P (ed) *Laser Ablation ICP–MS in the Earth Sciences: Current Practices and Outstanding Issues*. Mineralogical Association of Canada Short Course Series 29, pp 169-188
- Jenner, F. E., & Arevalo Jr, R. D., 2016. Major and trace element analysis of natural and experimental igneous systems using LA–ICP–MS. *Elements*, 12(5), 311-316.

- Kylander-Clark, A. R., Hacker, B. R., & Cottle, J. M. (2013). Laser-ablation split-stream ICP petrochronology. *Chemical Geology*, 345, 99-112.
- Košler J. (2008). Chapter 6: laser ablation sampling strategies for concentration and isotope ratio analyses by ICP-MS. *Mineralogical Association of Canada Short Course*, Vol. 40, Vancouver, B.C. pp.79-92.
- Krogh, E. J., and Råheim, A., 1978. Temperature and pressure dependence of Fe–Mg partitioning between garnet and phengite, with particular reference to eclogites. *Contributions to Mineralogy and Petrology*, 66(1), 75–80.
- Kuwahara, M. K. S. M. K., Hachimura, K., Eiho, S., and Kinoshita, M., 1976. Processing of RI-angiocardigraphic images. In *Digital processing of biomedical images* (pp. 187-202). Springer, Boston, MA.
- Lanari, P., and Engi, M., 2017. Local bulk composition effects on metamorphic mineral assemblages. *Reviews in Mineralogy and Geochemistry*, 83(1), 55–102.
- Langone A. & Tiepolo M., 2015. U-Th-Pb multi-phase approach to the study of crystalline basement : application to the northernmost sector of the Ivrea-Verbanò Zone (Alps). *Periodico di Mineralogia*, 84, 3B, 633-655. <http://dx.doi.org/10.2451/2015pm435>
- Langone, A., Braga, R., Massonne, H-J., Tiepolo, M., 2011. Preservation of old (prograde metamorphic) U–Th–Pb ages in unshielded monazite from the high-pressure paragneisses of the Variscan Ulten Zone (Italy). *Lithos*, 127, 68-85. <http://dx.doi.org/10.1016/j.lithos.2011.08.007>
- Liao, Y., Wei, C., & Rehman, H. U., 2021. Titanium in calcium amphibole: Behaviour and thermometry. *American Mineralogist: Journal of Earth and Planetary Materials*, 106(2), 180-191.
- Lloyd, G.E., Farmer, A.B., Mainprice, D., 1997. Misorientation analysis and the formation and orientation of subgrain and grain boundaries. *Tectonophysics*, The Adolphe Nicolas Volume 279, 55–78.
- Maino, M., Dallagiovanna, G., Gaggero, L., Seno, S., & Tiepolo, M., 2012. U–Pb zircon geochronological and petrographic constraints on late to post-collisional Variscan magmatism and metamorphism in the Ligurian Alps, Italy. *Geological Journal*, 47(6), 632-652.
- Nishikawa, S., Kikuchi, S., 1928. Diffraction of Cathode Rays by Mica. *Nature* 121, 1019.
- Reed S.J., 1975. *Electron Microprobe Analysis*. Cambridge University Press.
- Reed, S.J.B., 2005. *Electron Microprobe Analysis and Scanning Electron Microscopy in Geology*. Cambridge University Press.
- Paquette J.L. & Tiepolo M., 2007. High resolution (5 µm) U–Th–Pb isotope dating of monazite with excimer laser ablation (ELA)-ICPMS. *Chemical Geology*, 240, 222-237. <http://dx.doi.org/10.1016/j.chemgeo.2007.02.014>
- Peccerillo A., and Perugini D., 2003. *Introduzione alla petrografia ottica*. Morlacchi.
- Piazolo, S., Bestmann, M., Prior, D. J., and Spiers, C. J., 2006. Temperature dependent grain boundary migration in deformed–then–annealed material: Observations from experimentally deformed

- synthetic rocksalt. *Tectonophysics*, 427(1–4), 55–71.
- Piazolo, S., Belousova, E., La Fontaine, A., Corcoran, C., and Cairney, J. M., 2017. Trace element homogeneity from micron-to atomic scale: Implication for the suitability of the zircon GJ-1 as a trace element reference material. *Chemical Geology*, 456, 10-18.
- Prior, D. J., Boyle, A. P., Brenker, F., Cheadle, M. C., Day, A., Lopez, G., Potts, G. J., Reddy, S., Spiess, R., Timms, N. E., Trimby, P., Wheeler, J. and Zetterstrom, L., 1999. The application of electron backscatter diffraction and orientation contrast imaging in the SEM to textural problems in rocks. *American Mineralogist*, 84(11-12), 1741-1759.
- Prior, D. J., Wheeler, J., Peruzzo, L., Spiess, R., and Storey, C., 2002. Some garnet microstructures: An illustration of the potential of orientation maps and misorientation analysis in microstructural studies. *Journal of Structural Geology*, 24(6–7), 999–1011.
- Prior, D.J., Mariani, E., Wheeler, J., 2009. EBSD in the Earth Sciences: Applications, Common Practice, and Challenges. In: Schwartz A., Kumar M., Adams B., Field D. (eds), in: *Electron Backscatter Diffraction in Materials Science*. Springer, Boston, MA.
- Schwarzer, R. A., Field, D. P., Adams, B. L., Kumar, M., and Schwartz, A. J., 2009. Present State of Electron Backscatter Diffraction and Prospective Developments. *Electron Backscatter Diffraction in Materials Science*, 2nd ed., Springer US, pp. 1-20.
- Sláma, J., Košler, J., Condon, D.J., Crowley, J.L., Gerdes, A., Hanchar, J. M., Horstwood, M. S.A., Morris, G. A., Nasdala, L., Norberg, N., Schaltegger, U., Schoene, B.R., Tubrett, M. N., and Whitehouse, M. J., 2008. Plešovice zircon – A new natural reference material for U–Pb and Hf isotopic microanalysis. *Chemical Geology*, 249(1–2), 1–35.
- Sylvester, P. J., & Jackson, S. E., 2016. A brief history of laser ablation inductively coupled plasma mass spectrometry (LA–ICP–MS). *Elements*, 12(5), 307-310.
- Spear, F. S., 1989. Petrologic determination of metamorphic pressure-temperature-time paths. *Metamorphic pressure-temperature-time paths*, 7, 1-55.
- Spear, F. S., 1993. *Metamorphic Phase Equilibria and Pressure–Temperature–Time–Paths*. Mineralogical Society of America, 799.
- Spencer, K.J., Hacker, B.R., Kylander-Clark, A.R.C., Andersen, T.B., Cottle, J.M., Stearns, M.A., Poletti, J.E., Seward, G.G.E., 2013. Campaign-style titanite U-Pb dating by laser-ablation ICP: Implications for crustal flow, phase transformations and titanite closure. *Chemical Geology* 341, 84e101.
- Taylor, S. R., and McLennan, S. M., 1985. *The continental crust: its composition and evolution*. Blackwell, Oxford, p. 312.
- Tiepolo M., 2003. In situ Pb geochronology of zircon with laser ablation–inductively coupled plasma–sector field mass spectrometry. *Chemical Geology*, 199, 1-2, 159-177. [http://dx.doi.org/10.1016/S0009-2541\(03\)00083-4](http://dx.doi.org/10.1016/S0009-2541(03)00083-4)
- Thompson, J. J. B., 1957. The graphical analysis of mineral assemblages in pelitic schists. *American*

Chapter 3

- Mineralogist: *Journal of Earth and Planetary Materials*, 42(11-12), 842-858.
- Van Achterberg, E., Ryan, C. G., and Griffin, W. L., 2001. GLITTER Version 4 user's manual on-line interactive data reduction for the LA-ICPMS microprobe; Macquarie Research Ltd. North Ryde, NSW, Australia, 71.
- Wheeler, J., (2014). Dramatic effects of stress on metamorphic reactions. *Geology*, 42(8), 647–650.
- Vermeesch, P., 2018. IsoplotR: a free and open toolbox for geochronology. *Geoscience Frontiers*, 9, 1479-1493.
- White, R. W., Powell, R., and Baldwin, J. A., 2008. Calculated phase equilibria involving chemical potentials to investigate the textural evolution of metamorphic rocks. *Journal of Metamorphic Geology*, 26(2), 181–198.
- Whitney, D. L., & Evans, B. W. (2010). Abbreviations for names of rock-forming minerals. *American mineralogist*, 95(1), 185-187.
- Wu, C. M., 2015. Revised empirical garnet–biotite–muscovite–plagioclase geobarometer in metapelites. *Journal of Metamorphic Geology*, 33(2), 167–176.
- Wu, C. M., 2018. Metapelitic Garnet–Muscovite–Al₂SiO₅–Quartz (GMAQ) Geothermobarometry. *Journal of Earth Science*, 29(5), 977–988.
- Zuluaga, C. A., Stowell, H. H., and Tinkham, D. K. (2005). The effect of zoned garnet on metapelite pseudosection topology and calculated metamorphic PT paths. *American Mineralogist*, 90(10), 1619–1628.

CHAPTER 4:
Case study 1 - Cima di Gagnone



4. Case study 1 - Cima di Gagnone

The content of this chapter was published as an original article *Lithos* as Corvò et al., (2021) with title: Local variations of metamorphic record from compositionally heterogeneous rocks (Cima di Gagnone, Central Alps): Inferences on exhumation processes of (U)HP–HT rocks. Elsevier Ltd. All rights reserved. Received 16 December 2020, accepted in revised form 15 March 2021, available online 20 March 2021 and published on 25 March 2021. This study was financed by Swisstopo, SUPSI (Swiss; project n°.12RAFGOSO and n°.12RA1CARTOTIGR) and IGG-C.N.R. (PRIN2017 “Micro to Macro—how to unravel the nature of the large magmatic events; 20178LPCPWLagoneAntonio”). The PhD tenure for this work involved in particular the further acquisition of new data, processing of previously obtained data, interpretation, writing of the manuscript. The published paper is formatted to fit the format of the PhD thesis. Following the manuscript of Piccoli et al., (2021-published in June), which proposes an alternative petrological and geodynamic interpretation of the Cima di Gagnone metapelites, a critical discussion of the integrated dataset is reported in Appendix A.1.6 to avoid modifying the Chapter 4, which coincides with Corvò et al., (2021-published before in March).

4.1 Abstract

The record of metamorphic conditions is commonly highly heterogeneous in spatially close rocks of different composition and rheology. The well-studied Cima di Gagnone area in the Central Alps represents such an example, as relatively small, 1- to 100s meter scale, ultrahigh–pressure and high–temperature ultramafic lenses are enveloped within amphibolite–facies metasediments. We present new field observations, microstructural and petrological analyses, and thermodynamic modelling results on these metasediments, showing that these rocks generally experienced medium pressure and medium temperature conditions of 1.0–1.2 GPa and 640–700°C, followed by a retrograde stage around 0.6–0.8 GPa and 600–675°C. However, a few samples from the immediate proximity of the ultramafic lenses record significantly higher P – T conditions of 1.3–1.7 GPa and 750–850°C, approaching the high pressure and high temperature conditions of the ultramafic bodies (1.5–3.1 GPa, 650–850°C). Mineral/bulk chemistry changes during growth of new mineral phases hint to local melt/fluid interaction (i.e., metasomatism) between metasediments and ultramafics during the high temperature deformation. Preliminary U–Pb LA–ICP–MS dating suggests that zircon grains from the metasomatic reaction zone have been fully re–equilibrated during the early stage of Alpine exhumation (~36 Ma), while the

large part of the metasediments records only pre-Alpine ages. We finally recast these new data into the regional P - T - t - D paths and discuss the consequences of these findings for understanding the exhumation processes of HP rocks. We found different local equilibria (ΔP up to 2 GPa; ΔT up to 160°C) that cannot be explained simply by retrograde metamorphism or by tectonic amalgamation. Rather, our work suggests a significant role of deformation in producing variable pressure and temperature record within the rocks.

4.2 Introduction

Metamorphic terranes often preserve relicts of variable metamorphic conditions associated with compositionally heterogeneous rocks. This variability commonly results in small lenses of one rock type characterized by significantly higher pressure (P) and/or temperature (T) conditions than its surrounding host rocks (Evans and Trommsdorff, 1978; Chopin, 1984; Smith, 1988; Liou et al., 2004). The reasons for the coexistence of such different metamorphic records may be related to the contribution of several mechanical and geochemical processes, including variation of stress and strain rate gradients, multiple metamorphic reactions, element diffusion and/or fluid-rock interaction (Etheridge et al., 1983; Passchier and Trouw, 2005; Philpotts and Ague, 2009).

It has long been accepted that deformation and metamorphism are closely interlinked (Brodie and Rutter, 1985), but the effect of tectonic deformation on the metamorphic reactions is still a matter of a lively scientific debate (Stüwe and Sandiford, 1994; Tommasi and Vauchez, 1997; Wheeler, 2014, 2020; Gerya, 2015; Hobbs and Ord, 2017; Moulas et al., 2019). An important aspect to consider is the possible role of deformation on metamorphic processes localized at the interface between rocks with different composition (e.g., Wheeler, 2014; Schmalholz et al., 2020).

These interfaces are sites of complex processes, such as multiple interactions with chemically heterogeneous fluids, deformation-driven mineral changes, or amplification of stress and/or strain rate in local domains (Scambelluri and Philippot, 2001; Schmid and Podladchikov, 2003; Moulas et al., 2014; Zheng and Hermann, 2014; Casini and Maino, 2018; Luisier et al., 2019). Local fluid-rock interaction is commonly testified by the growth of new mineral phases and from changes in mineral and bulk-rock compositions (Jamtveit and Austrheim, 2010). On the other hand, localization of melt flux can severely change the metamorphic record at different scale (Pognante, 1991; Sawyer et al., 2001). The presence of melt along grain boundaries, in turn, decrease the viscosity of rocks by 3–5

orders of magnitude, enhancing deformation and markedly changing the deformation regime (Arzi, 1978; Dell'Angelo and Tullis, 1988; Piazzolo et al., 2020). Furthermore, the mineral changes may exert an important influence on the rheological behaviour of rocks during deformation (White and Knipe, 1978; Brodie and Rutter, 1985; Smith et al., 2015). Thus, the structural and metamorphic patterns provide key information to constrain the geodynamic evolution of deforming rocks and must be carefully assessed in the study of collisional belts. However, linking such heterogeneous metamorphic records with tectonically coherent Pressure–Temperature–time–Deformation (P – T – t – D) paths is challenging.

A major limitation for reconstructing complete P – T – t – D paths in compositionally heterogeneous units is a direct consequence of the composition of silica-rich rocks. These are mainly gneisses or schists, which are more sensitive to dehydration/rehydration processes during decompression, commonly resulting in a loss of the prograde and peak metamorphic record (e.g., Heinrich, 1982). Moreover, the complete resetting of geochronometers in consequence of fluid/melt flux (e.g., Rubatto and Hermann, 2007) often masks the correct timing of metamorphic events. However, these obstacles may be overcome by coupling petrological and geochronological analyses on the most retentive minerals, such as garnet and zircon, which may provide information on the prograde segment of the P – T – t – D path (e.g., Liati and Gebauer., 1999; Williams et al., 2002; Caddick et al., 2010).

Strong heterogeneities in the metamorphic record typically result from HP (and possibly HT) lenses, enveloped within either rheologically weaker or stronger “host” rocks, which exhibit lower metamorphic conditions. Examples of such pairings are: mafic/ultramafic-metasediments, quartz-rich rocks-micaschist, orthogneiss-micaschist, metacarbonate-micaschists that occur in a range of field localities: in the European Alps - e.g., Adula-Cima Lunga, Monte Rosa, Dora-Maira, Zermatt-Saas, Ulten Zone (Evans et al., 1979; Chopin, 1984 ; Godard et al., 1996; Tumiati et al., 2018; Luisier et al., 2019; Frezzotti et al., 2011), Western Norway (e.g., Smith, 1984), Cycladic Archipelago (e.g., Gyomlai et al., 2020), Kokchetav massif of northern Kazakhstan (Sobolev and Shatsky, 1990), central western Korean Peninsula (e.g., Kwon et al., 2020) and central China (e.g., Wang et al., 1989).

In this contribution, we combine structural, microstructural, and petrological analyses, as well as a preliminary geochronological investigation, to improve the description of the P – T – t – D path experienced by the worldwide renowned Cima di Gagnone area (Central Alps, Switzerland; Fig. 4.1A, B). Here, (ultra)high pressure/high temperature, (U)HP/HT hereafter, ultramafic lenses are enveloped within amphibolite-facies metasediments (Fig. 4.2; e.g., Evans et al., 1979; Pfiffner and Trommsdorff,

1998), as the result of the Alpine subduction/collision deformation phases (Schmid et al., 1996). While the Ultra-Mafic rocks (UM, hereafter) have been intensively investigated (e.g., Evans and Trommsdorff, 1974; 1978; Ernst, 1978; Heinrich, 1982; Becker, 1993; Nimis and Trommsdorff, 2001; Skemer et al., 2006; Scambelluri et al., 2014, 2015), less attention has been devoted to their host rocks (Grond et al., 1995; Pfiffner, 1999). Following a recent paper on the deformation evolution (Maino et al., 2021), we performed coupled microstructural and petrological investigations on the host metasediments to investigate whether they hold Alpine HP-HT relicts that until now have been missed. If this were the case, it should be possible to elucidate their relationship with the metamorphic history experienced by the ultramafics.

The final goal is to provide key information to interpret the tectonic evolution of rocks with heterogeneous composition and metamorphic record. Our results indicate that metasediments enveloping the UM show variable metamorphic conditions in relation to: 1) deformation (micro) structures, and 2) distance from the UM lenses. Fluid-assisted metasomatism is furthermore documented as being strongly localized at the interface between ultramafic lenses and the metapelitic

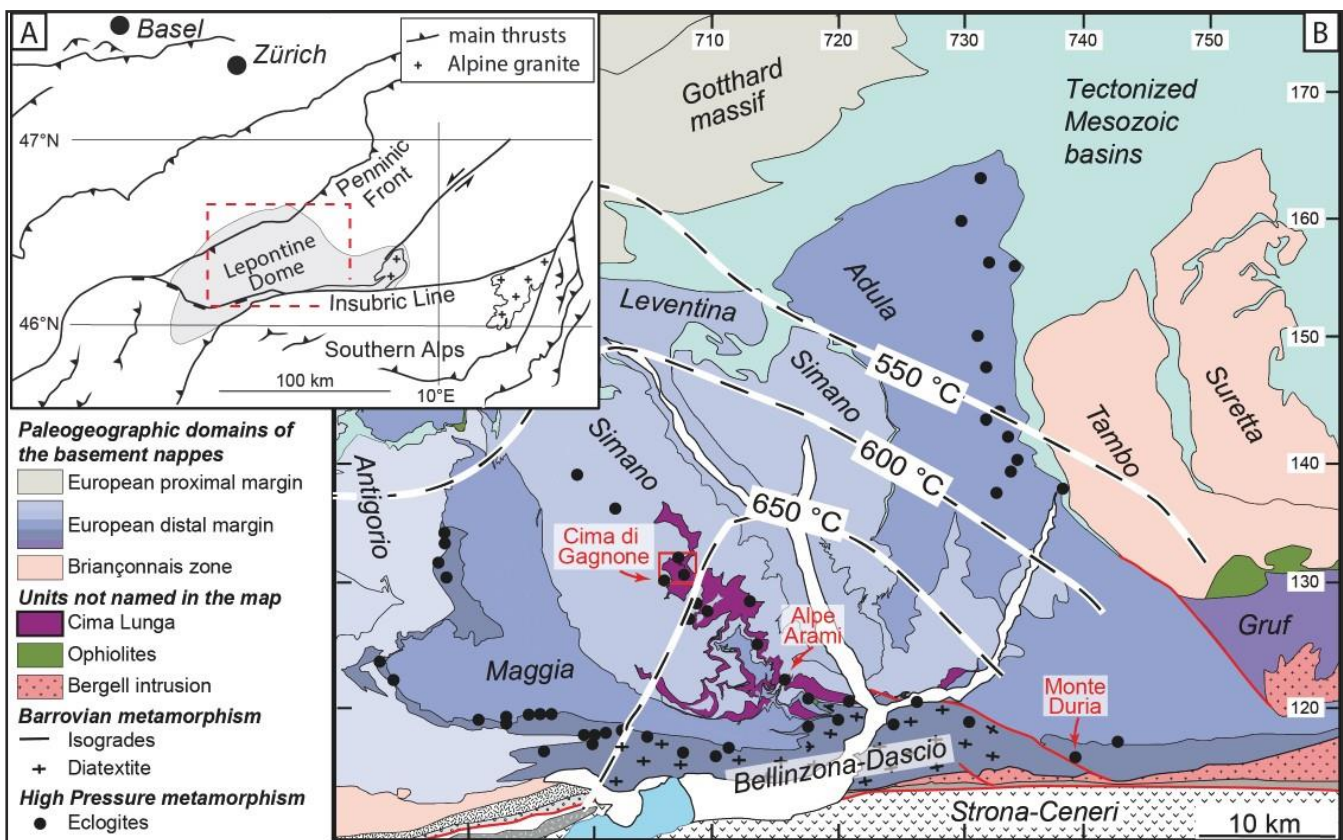


Fig. 4.1– Overview (A) and tectonic map (B) of the Cima Lunga unit within the Lepontine Dome (modified after Todd and Engi, 1997, Brouwer et al., 2005; Burg and Gerya 2005; Steck, 2013, 2019; Cavargna et al., 2014; Maino et al., 2021). Isotherms refer to the Barrovian metamorphism.

host throughout all part of the metamorphic evolution, including the HP–HT stage. We finally discuss these new data in relation to the exhumation models currently proposed for the Cima di Gagnone rocks

4.3 Geological setting

4.3.1 Location and metamorphic evolution

The Cima di Gagnone area belongs to the Cima Lunga unit, which is exposed in the central domain of the Lepontine dome of the Central Alps (Maxelon and Mancktelow, 2005; Steck et al., 2013, 2019; Fig. 4.1A–B). The unit, positioned above the Simano nappe and below the Maggia nappe, is part of a tectonic stack interpreted as the western continuation of the Adula Nappe (Dal Vesco, 1953). The Cima Lunga consists of micaschists, paragneisses and minor orthogneisses enveloping UM ellipsoidal lenses (metres to hectometres in size) of garnet–peridotite and enstatite–olivine–chlorite rocks (chlorite harzburgite), both partially talc-bearing (Figs. 4.1–4.3; Evans and Trommsdorff, 1974, 1978; Pfiffner and Trommsdorff, 1998). UM rocks host metabasaltic eclogites, metarodingites, plagioclase amphibolites, calcsilicate rocks and marbles, indicating that the Cima di Gagnone UM represent serpentinized mantle that experienced dehydration and (U)HP metamorphism during the Alpine subduction. Most authors consider serpentinization likely occurred during the formation of Tethys in the Mesozoic (Evans and Trommsdorff, 1978; Pfiffner and Trommsdorff, 1998).

All rock types show a dominant amphibolite–facies metamorphic assemblage, which is commonly attributed to the Barrovian phase of the Lepontine Dome (Niggli, 1960; Frey et al., 1974; Engi et al., 1995). However, UM rocks preserve in their cores relicts of (U)HP metamorphism pre-dating the amphibolite–facies stage (Gebauer, 1994, 1996, 1999). Peak pressure conditions in the eclogites, associated with the UM lenses, are constrained between 1.5 and 2.5 GPa at temperature between 600–700°C by Heinrich (1986), while Brouwer et al. (2005) report peak pressures of up to 2.8–3.1 GPa (625–675°C) and a decompressional stage at 0.8–1.1 GPa and 800–875°C. Garnet metaperidotite equilibrated at 800–850°C and 2.5–3.0 GPa (Evans et al., 1979; Heinrich, 1982, 1986; Pfiffner and Trommsdorff, 1997; Nimis and Trommsdorff, 2001; Scambelluri et al., 2014), while the chlorite harzburgites assemblage indicates lower temperature at similar pressure (650–800°C and 2.3 GPa; Scambelluri et al., 2014). The occurrence of eclogite–facies metarodingites and HP metacarbonates within the UM lenses suggests that HP conditions were attained during the Alpine cycle (Evans et al., 1979; Pfeifer et al., 1991; Pfiffner,

1996; Pfiffner and Trommsdorff, 1997; Scambelluri et al., 2014, 2015). UHP-HT conditions have been estimated also for the metaperidotite lenses from the southern part of Adula-Cima Lunga nappe, i.e., Alpe Arami and Monte Duria (Fig. 4.1B). At Alpe Arami, most of the studies determined peak conditions around 3.0 GPa and 800–850°C (e.g., Nimis and Trommsdorff, 2001), although controversial pressure estimations in excess of 10 GPa have been claimed (e.g., Dobrzhinetskaya et al., 1996). At Monte Duria, the eclogitic peak at $P = 2.6\text{--}3.0$ GPa and $T = 710\text{--}750^\circ\text{C}$, was followed by granulite-facies condition at $T = 850^\circ\text{C}$ and $P = 0.9$ GPa (Tumiati et al., 2018; Pellegrino et al., 2020).

Cores of UM lenses in Cima di Gagnone preserve a foliation (Fig. 4.3A–G) associated with the HT assemblage ($800 \pm 175^\circ\text{C}$; Skemer et al., 2006), while metasomatic metamorphism is more pronounced towards the rims, resulting in a shell-like structure highlighted by the presence of late veins containing talc, enstatite, magnesite, anthophyllite or chlorite (Pfeifer, 1981, 1987). Lens rim alteration and veining have been interpreted as evidence of rehydration of the UM rocks by fluid release from the nearby metasediments during decompression and exhumation (breakdown of muscovite to biotite; Heinrich, 1982; Pfeifer, 1987). Kyanite- and andalusite-bearing quartz veins in the metasediments suggest that the release of fluids triggering metasomatism occurred late in the decompression history ($P \leq 0.8$ GPa), but still at amphibolite-facies conditions with T of $\sim 650^\circ\text{C}$ (Fruh-Green, 1987; Pfeifer, 1987; Allaz et al., 2005).

In contrast to the UM, the Cima di Gagnone metasediments show exclusively amphibolite-facies signatures with a typical assemblage of plagioclase + quartz + biotite + muscovite + garnet + kyanite \pm staurolite (Fig. 4.3H), generally consistent with pressure of 0.6–0.8 GPa and temperature of 600–660°C (Grond et al., 1995; Pfiffner, 1999). However, rare metapelites in contact with UM lenses preserve corona and pseudomorphic textures interpreted as relicts of a poorly-preserved eclogite-facies assemblage composed of phengite + paragonite + garnet \pm quartz (Heinrich, 1982; Fruh-Green, 1987). However, these relicts are unsuitable for constraining P – T peak conditions, and hence interpretations vary. While Heinrich (1982, 1986) suggests that both ultramafic/mafic rocks and metasediments experienced the same metamorphic evolution (thus peak at $\sim 1.5\text{--}2.5$ GPa; $550\text{--}650^\circ\text{C}$), Grond et al. (1995) and Pfiffner and Trommsdorff (1998) propose different paths where the metasediments reached significantly lower peak conditions (~ 1 GPa; $550\text{--}650^\circ\text{C}$). Pressure-peak conditions of ~ 1 GPa and $\sim 500^\circ\text{C}$ followed by retrograde re-equilibration at 0.7–0.8 GPa and $\sim 650^\circ\text{C}$ is also recorded by the Simano and Maggia nappes, which comprise the Cima Lunga unit (Rutti et al., 2005).

4.3.2 Tectonic evolution

The Cima Lunga unit is characterized by complex structures developed within and around the viscous UM lenses embedded in the metapelitic/gneissic weaker matrix. The interior of the lenses preserves structural elements locally discordant to the matrix schistosity. These patterns are traditionally described as related to multiple, distinct Alpine deformation phases (D1–D4) and associated with four schistositities (S1–S4) developed at decreasing metamorphic conditions, from upper amphibolite to greenschist facies (Grond et al., 1995; Pfiffner and Trommsdorff, 1998). However, a recent detailed structural analysis showed that all rock types shared a continuous progressive deformation highlighted by a single schistosity and lineation (Maino et al., 2021). The Cima Lunga unit is described as a high-strain shear zone that accommodated complex heterogeneous deformation throughout all the Alpine evolution. Differences in the deformation patterns between UM lenses and the matrix are attributed to contrasting rheology, rather than superimposed tectonic phases (see Maino et al., 2021, for more details).

Garnet cores from the metapelites often preserve an inherited discordant foliation (S_{gar}), which is attributed to a prograde Alpine or, more likely, Variscan tectono-metamorphic stage (Grond et al., 1995; Pfiffner, 1999; Rutti, 2003). Lattice preferred orientation (LPO) of olivine is dominated by the transition between C-type to B-type indicating temperature of deformation between 650 and 800°C (Frese et al., 2003; Skemer et al., 2006), suggesting that the main schistosity in the UM developed under HT conditions.

4.3.3 Geochronological background

Incipient melting or subsolidus re-equilibration at prograde (U)HP conditions of the metaperidotites of Cima di Gagnone is dated at 43 ± 2.0 Ma, while the initiation of the decompressional stage, still at (U)HP conditions, is constrained at 35 ± 0.5 Ma (U–Pb SHRIMP on zircon; Gebauer, 1994, 1996, 1999). The HP peak in the eclogites is dated at 35 Ma, while the retrograde amphibolite stage is constrained at 30 ± 1.5 Ma (SHRIMP U–Pb–dating on zircon; Gebauer, 1994). Consistent garnet Sm–Nd ages of about 40 ± 4.0 Ma from garnet lherzolite and eclogites are interpreted to hallmark the residence time at eclogite-facies conditions (Becker, 1993). UM record also ages < 33 Ma, which have instead been related to subsequent decompression and Barrovian metamorphism (Hunziker et al., 1992; Gebauer,

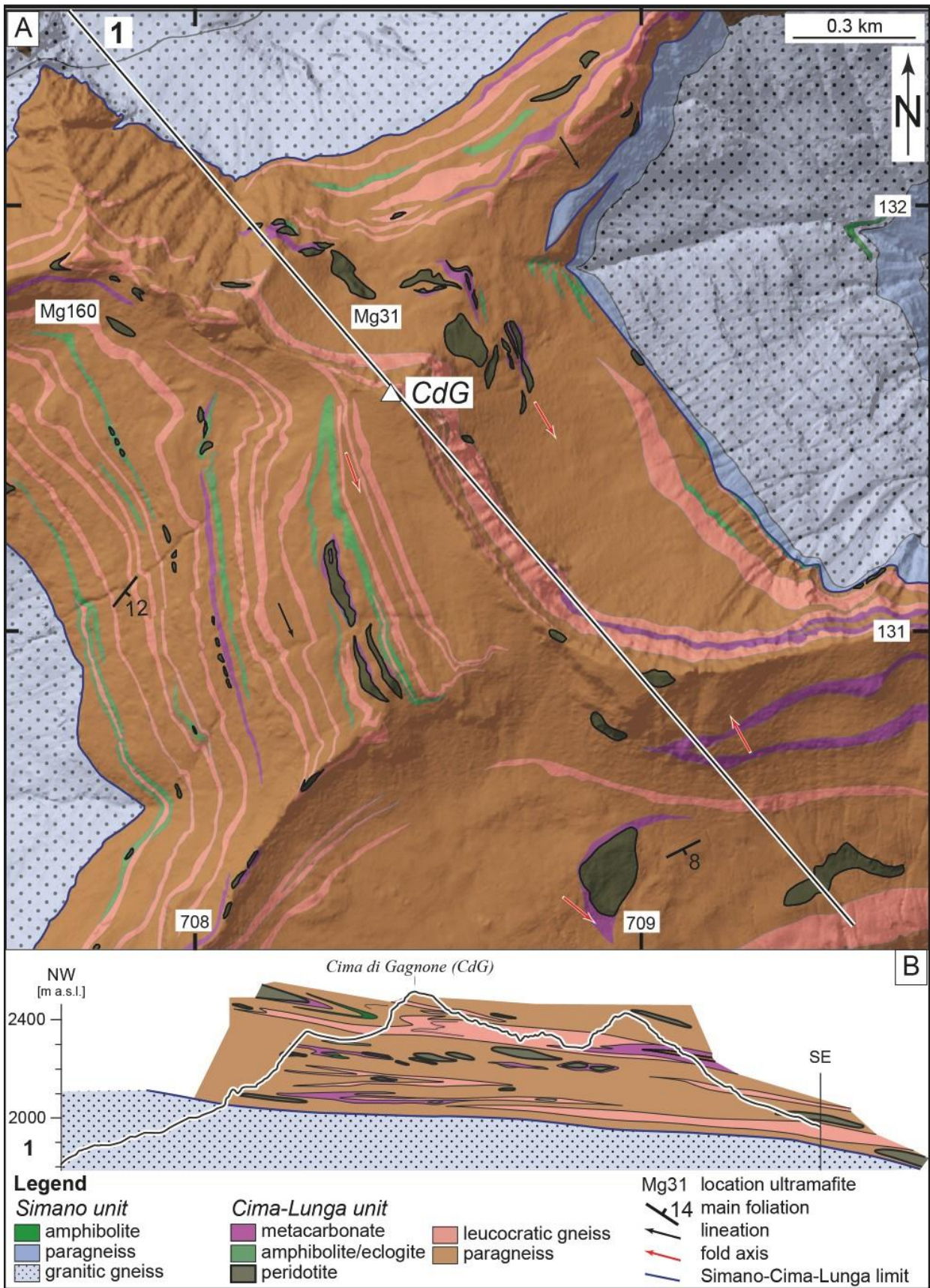


Fig. 4.2 – Cima di Gagnone area: A) geological map and (B) geological cross-section parallel to the fold axis and stretching lineation. Labels of the studied ultramafic lenses are reported following the nomenclature of Pfiffner and Trommsdorff (1998).

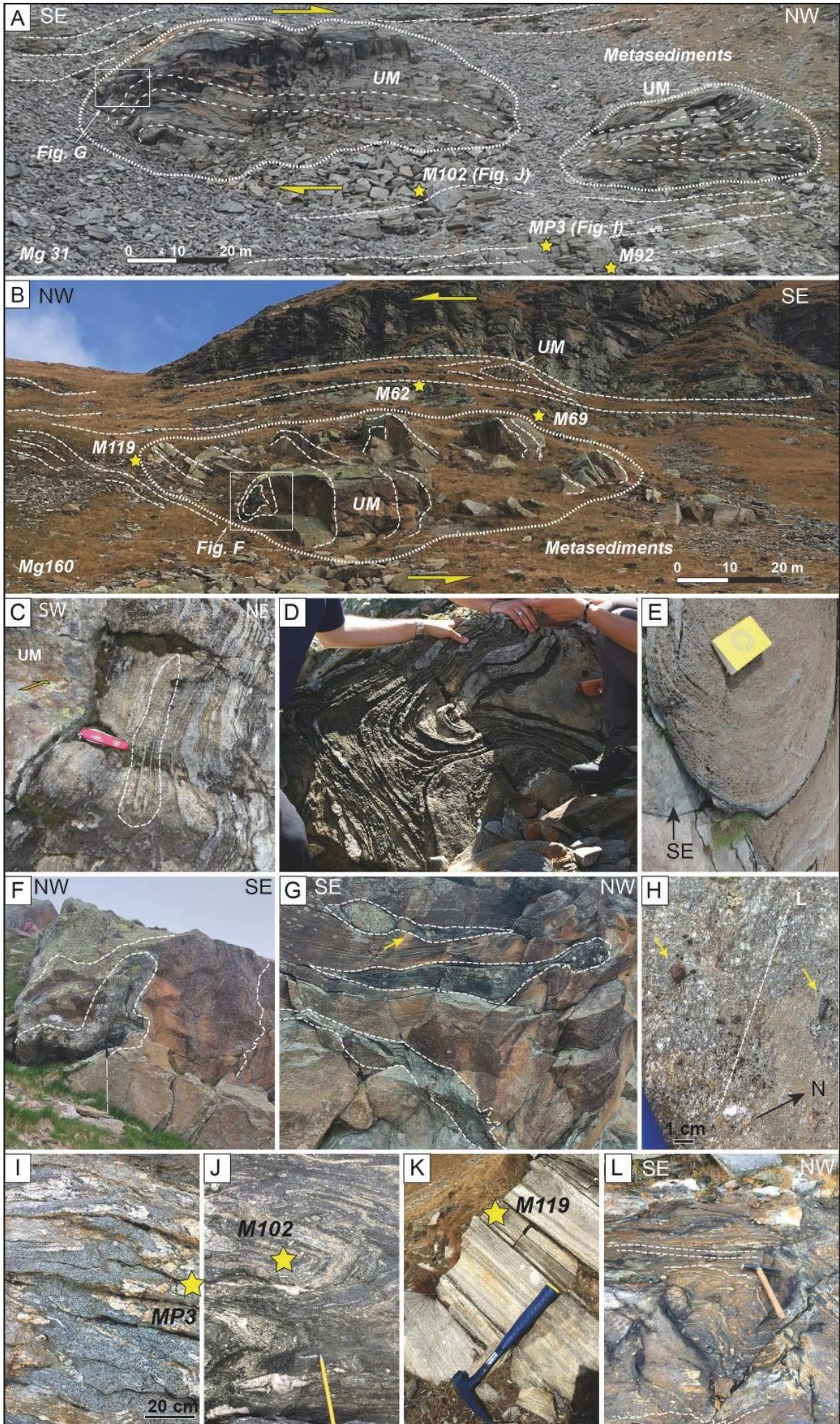
1994, 1996; Liati et al., 2009). Zircon grains from the Cima di Gagnone metasediments show instead mostly Palaeozoic ages, although a few grains from leucosomes provided an Alpine age of 33 ± 0.6 Ma, attributed to the Barrovian stage (Gebauer, 1996).

These ages agree with the data from the SW part of the Adula nappe, where eclogites and garnet peridotites yield consistent U–Pb, Lu–Hf and Sm–Nd ages between 42 and 34 Ma, which are interpreted to date the duration of (U)HP stage (Becker, 1993; Gebauer, 1994, 1996; Brouwer et al., 2005; Hermann et al., 2006). U–Pb SHRIMP zircon data from eclogites and their metasedimentary or gneissic country rocks from the central and northern sectors of the Adula yield mostly Palaeozoic ages (330–340 and 370 Ma), although a few ages around 32–33 Ma matching the Barrovian stage are also reported (Liati et al., 2009). In addition, garnet from eclogite of the northern sectors of the Adula nappe show two distinct Lu–Hf age populations of ~ 332 and 38 Ma, respectively (Herwartz et al., 2011).

Allanite and monazite U–Th–Pb dating from individual samples from the Adula, Maggia and Simano nappes of the Lepontine dome documents a general rejuvenation of Barrovian metamorphism from the southern margin of the orogen (Bellinzona–Dascio zone) toward north (Fig. 4.1B), with ages between 32 and 17 Ma (e.g., Janots et al., 2009; Rubatto et al., 2009; Berger et al., 2011; Boston et al., 2017). Zircon and magmatic allanite ages between 32 and 22 Ma from the southernmost migmatitic belt of the Lepontine dome further highlight a long-lasting thermal perturbation associated with magmatism close to the Insubric Line (Rubatto et al., 2009; Gregory et al., 2012).

4.4 Field relationships

The Cima di Gagnone area is dominated by tightly folded metasediments forming non-cylindrical folds with sub-horizontal axial planes (Fig. 4.2; see Maino et al., 2021, for a complete description of the structure of the Cima di Gagnone area). These rocks show a dominant SSE-dipping schistosity (S_2) and a nearly constant SE-dipping stretching lineation mostly parallel to the fold axes, apart in the fold hinges where axes become orthogonal to the shear direction. Meter- to centimetre-scale cat-eye structures confirm the presence, at all scale, of tubular-shaped sheath folds. Schistosity is marked by alternating mica- and quartz/feldspar-rich layers, wrapping around more rigid crystals such as garnet. Strongly asymmetric fabric elements such as shear band boudins, σ - and δ -shaped porphyroclasts or winged inclusions are abundant in the metasediments and consistently indicate high strain accommodated by



mainly top-to N simple shear (Passchier, 1988; Grasemann and Dabrowski, 2015).

Even though field evidence of partial melting is generally rare in the metasediments, there is an increase of partial melting features moving towards or in proximity of UM lenses. In the latter cases, migmatitic structures are abundant showing complex relationships with the main S₂ foliation. Stromatic leucosomes are either discordant (cut the foliation; Fig. 4.3I) or share fold axial planes with the surrounding rocks (Fig. 4.3J). Ultra-mylonites or cataclasites are rare in the host rocks and totally absent around the ultramafic lenses. Here, the foliation wraps around the lenses, which might appear as either isolated bodies or train of lenses (Figs. 4.2A–B, 4.3A–B).

The UM lenses are intensively deformed, as evidenced by superimposed stages of folding and boudinage of the internal layering (Fig. 4.3E–G). Their internal foliation is defined by bands of orthopyroxene, olivine, chlorite and, at places, garnet. The long axes of olivine, enstatite, Cr-diopside and elongated garnet, mark a mainly SE-dipping grain lineation (Piazolo and Passchier, 2002) lying on the foliation plane. Crystallization of these Alpine HP minerals was syn-kinematic with respect to the pervasive internal deformation, as testified by s-shaped inclusion trails and folds in garnet and enstatite porphyroblasts (Evans and Trommsdorff, 1974; Grond et al., 1995; Pfiffner and Trommsdorff, 1998).

Fig. 4.3 – Structural features and relationships between ultramafics (UM) and metasediments. A, B) Field pictures of the two studied UM outcrops (Mg31 and Mg160, respectively, after Pfiffner and Trommsdorff, 1998) deformed under dominant top-to-N simple shear (Maino et al., 2021). C, D) Eye-structures from sheath folds developed in carbonate rocks enveloping the UM (D is a fallen block). E) Map view of a sheath fold developed in the chlorite harzburgite. F) Complex folding and boudinage structures characterizing the internal layering of the UM lenses. G) Detail of the Mg160 outcrop (garnet metaperidotite) characterized by folded and boudinaged (yellow arrows) amphibolite layers (early eclogite). H) The common micaschist with biotite + muscovite + plagioclase + quartz assemblage with occurrence of garnet and staurolite porphyroblasts (yellow arrows). I, L) Evidence of partial melting highlighted by leucosomes discordant on the foliation (I) or folded and shared on the schistosity (J, L). Dotted line contours the UM lenses; dashed lines mark either the lineation (in G) or the main foliation (other pictures); yellow stars indicate the location of collected samples.

The rims of the UM lenses are injected by several metasomatic veins filled with talc, enstatite, magnesite, anthophyllite or chlorite, accompanied by localized ductile-to-brittle deformation discordant to the main foliation (Pfeifer, 1981, 1987). This late event generated during exhumation under amphibolite-facies conditions (Pfeifer, 1981,1987; Pfiffner and Trommsdorff, 1998; Pfiffner, 1999).

4.5 Sampling strategy and analytical methods

In order to characterize the possible variations of the metamorphic record and P - T conditions, we focused our study on paragneisses and micaschists (Appendix 1; Fig. S4.1, Table S4.1), as their mineral assemblages have a solid thermodynamic database that helps to determine P - T conditions of mineral equilibration (Holland and Powell, 1998). We are in particular interested in examining potential differences in their microstructures and petrologic evolution in relation to their proximity to UM lenses. Specifically, we collected six representative meta-sedimentary samples in two ways (Fig. 4.3A, B):

i) Series representing increasing distance, between 10 to 50 m, with respect to the UM lenses. As these samples would represent the conditions dominant within the Cima Lunga unit, we named this group as Country rocks: sample MP3 (Fig. 4.3A, I), M92 (Fig. 4.3A), M62 (Fig. 4.3B).

ii) Selection of samples originating from the contact of (< 2 m) UM lenses. These samples are taken to describe the possible metamorphic and geochemical influence provided by the mafic/ultramafic rocks to the nearby metapelites. We refer to this group of samples as Halos (sample M119, M102, M69; Fig. 4.3A, B, J, K). It is important to highlight that both metasedimentary sample groups are macroscopically very similar; however, they show significant microstructural and compositional differences as described in the next chapters.

A full description of the analytical methods and procedures are reported in chapter 3, whereas results and related tables are available in the supporting information (Appendix 1; Figs. S4.1–S4.8, Tables S4.1–S4.5). Mineral abbreviations are after Whitney and Evans (2010).

4.6 Petrography and microstructure

4.6.1 Country rocks

Country rocks (M92, MP3, M62; Fig. 4.4) are fine-grained (average grain size of 0.2 mm) and show a well-defined schistosity (regional S2 of Grond et al., 1995) consisting of alternating mica- and quartz/plagioclase-rich layers (Fig. 4.4). The dominant assemblage is Pl + Qz + Bt + Ms + Grt ± Ky ± St (Fig. 4.4A, C, D, F) with mineral modal abundances in the range of 15–22 vol.% for plagioclase, 15–35 vol.% for quartz, 15–22 vol.% for biotite, 10–15 vol.% for muscovite, 10–12 vol.% for garnet, and 5–10 vol.% for kyanite. Staurolite locally occurs within MP3 (5 vol.%) and M62 (rare).

Garnet shows two main grain size populations (Fig. 4.5A–D): i) Type I consists of small, inclusion-poor grains (0.1–0.5 mm in diameter), and ii) Type II is characterized by much larger grains (1–4 mm in diameter). This latter group generally consists of inclusion-rich (quartz, plagioclase, muscovite and biotite, rutile) cores surrounded by inclusion-poor rims (Fig. 4.5A). The inclusions show a preferred orientation forming an internal foliation at an angle with respect to the external foliation (Fig. 4.5A). Type II garnets have either rounded isometric shapes with occasionally resorbed textures or form incipient ribbons slightly elongated parallel to the schistosity and deformed by several fractures filled with chlorite, plagioclase and quartz (Fig. 4.5A–D).

Kyanite occurs within mica-rich layers following the foliation or it lies on quartz-plagioclase layers appearing mainly as anhedral, sometimes poikilitic grains; in some cases, it exhibits skeletal, highly irregular shape. All these textures may be present in the same sample (Fig. 4.4C, D). Staurolite occurs as poikiloblasts along the main foliation (Fig. 4.4C, D, F). Both kyanite and staurolite are rich in partially aligned inclusions of quartz, plagioclase, rutile, and ilmenite (Fig. 4.4C, D).

Plagioclase is more abundant than K-feldspar, which is rare and occurs as an interstitial phase (Fig. S4.2). Locally, samples collected from stromatic leucosomes (i.e., MP3) exhibits evidence of crystallization from a melt such as cusps and lobes grain boundaries (Fig. 4.4E; Sawyer, 2008).

In the matrix, biotite and white mica mark the schistosity showing typical elongated sub-rectangular grain shapes (Fig. 4.4).

Zircon and monazite are mainly present within the matrix as small subhedral crystals (ca. 50–100 µm long and 25–50 µm width). Other accessory phases include apatite, epidote and rutile, this latter

being predominantly dispersed throughout the schistosity associated with biotite and often showing thick black rims of ilmenite. In places, it is even found included in garnet and staurolite. Late retrograde products, such as sericitization of plagioclase and chloritization of biotite and garnet locally occur.

Microstructural features are shown through textural analyses and electron-backscatter-diffraction (EBSD) compositional maps (Figs. 4.4–4.6, S4.3). The two different types of garnet grains (Type I, small and inclusions-poor; Type II, large and inclusion-rich) reveal different microstructural features (Fig. 4.6). Type II garnet cores contain several inclusions of quartz and plagioclase depicting a folded internal foliation (S1), which is abruptly truncated by an inclusion-poor rim (Fig. 4.6C1–2). The crystallographic orientation of the garnet cores slightly changes with respect to the rim, which in turn is characterized by the presence of subgrains around 50–100 μm (Fig. 4.6C1–2). In contrast, the smaller, inclusions-poor garnets (Type I) show no change in crystallographic orientation within the grain (Fig. 4.6D). Plagioclase and quartz in the matrix usually form ribbons. The grains show evidence of crystal-plastic deformation such as undulose extinction recognized in EBSD by significant change in crystallographic orientation within a single grain, distinct subgrains, subgrains boundaries and locally deformation lamellae. However, both minerals exhibit a weak and diffuse crystallographic preferred orientation (CPO) pattern (Figs. 4.6B, S4.3B, C). Quartz CPO is, indeed, quite complex showing three main maxima in (0001) pole figure, while CPO of plagioclase shows one maximum for (001) (Figs. 4.6B, S4.3B, C). The relative fabric strength measure indexes (Skemer et al., 2005), namely the J- and M-index, are respectively equal to 1.98 and 0.03 for plagioclase and 1.13 and 0.007 for quartz. In contrast, biotite and muscovite are strongly aligned, showing undulose extinction (Fig. 4.4B, C) and a strong CPO consistent with the (001) plane parallel to the dominant S2 foliation (Fig. S4.3D, E). The J- and M-index are respectively 8.39 and 0.18 for biotite and 7.85 and 0.19 for muscovite.

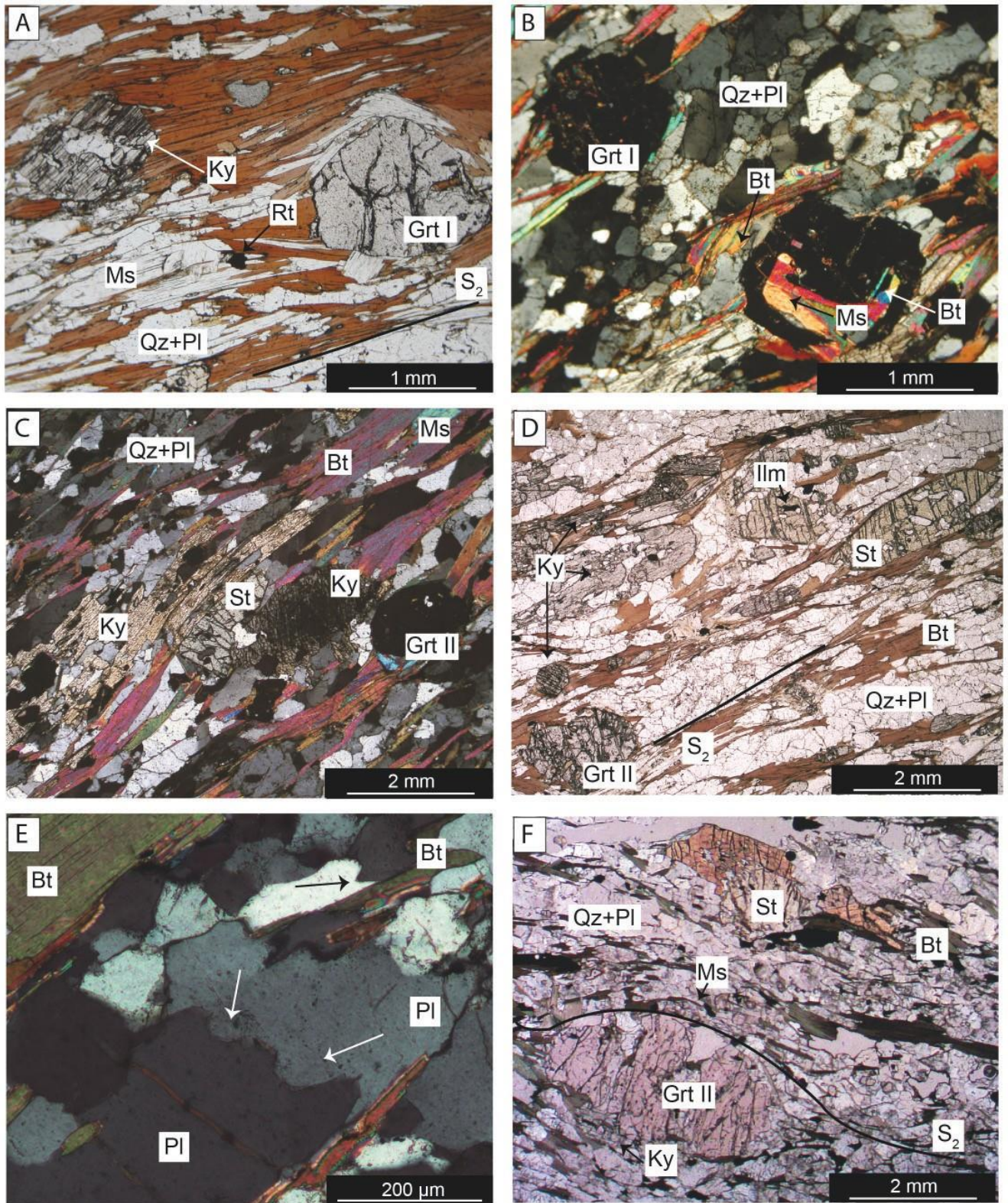


Fig. 4.4 – Major features of Country rocks samples, plane and crossed polarized light. S indicates the main schistosity. A) Paragenesis made of Pl + Qz + Bt + Ms + Grt(I) + Ky + Rt of sample M92. B) Rounded garnet porphyroclasts with muscovite and biotite inclusions. C, D) Paragenesis of MP3 made of Pl + Qz + Bt + Ms + Grt (I and II) + Ky + St + Rt, and the different textures of kyanite (mimetic and poikiloblastic) and staurolite. E) Entrapped melt features showing typical cusps and lobes of plagioclase indicated by arrows. F) M62 paragenesis made of Pl + Qz + Bt + Ms + Grt (II) + Ky + St + Rt.

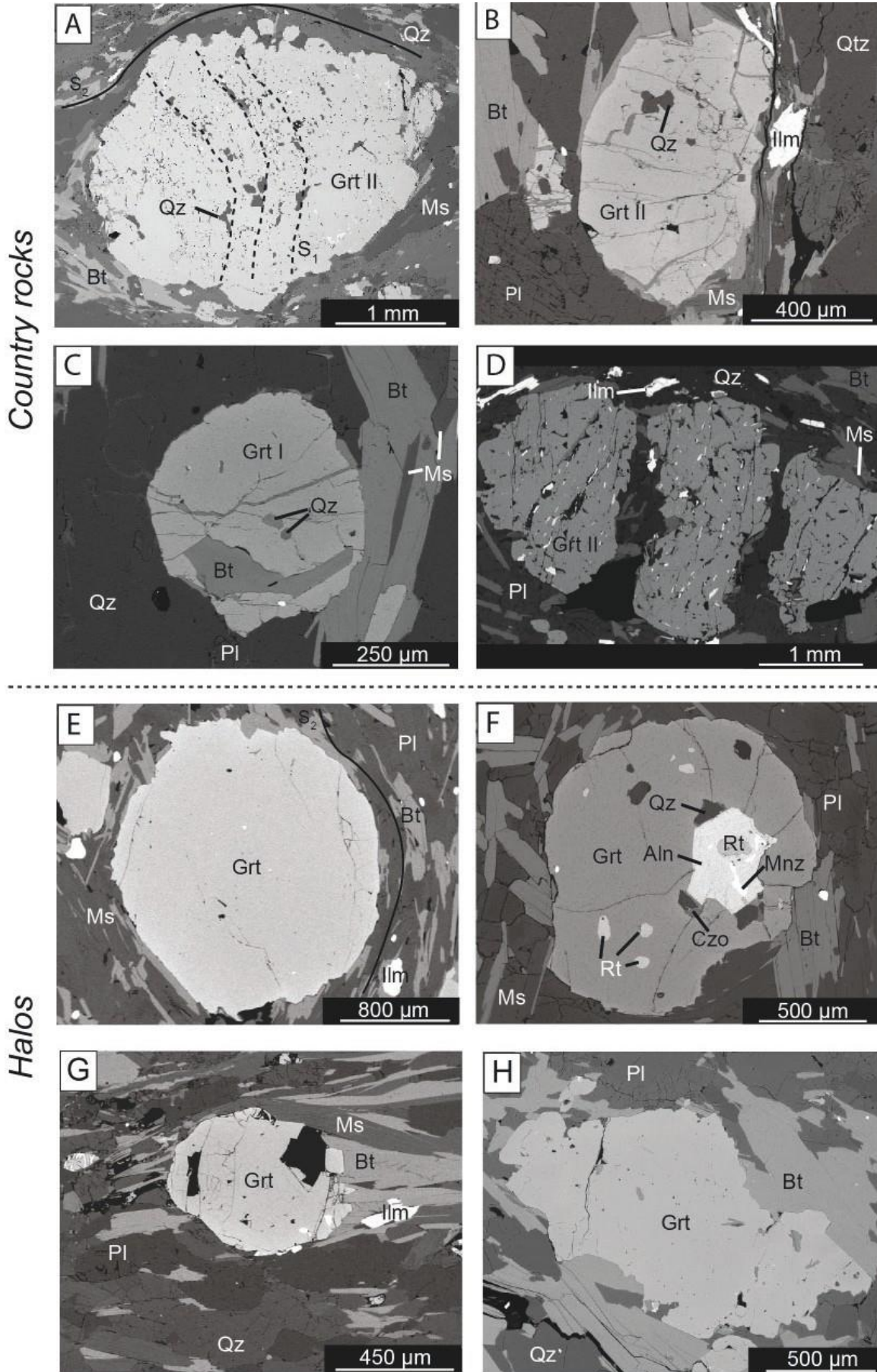
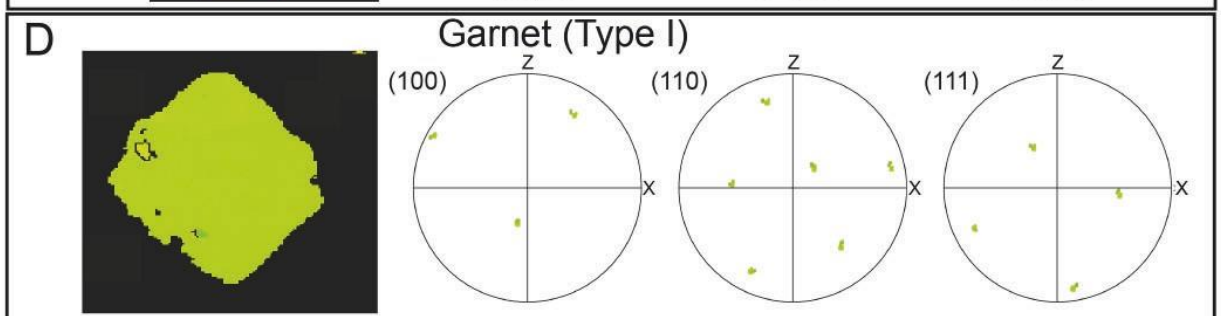
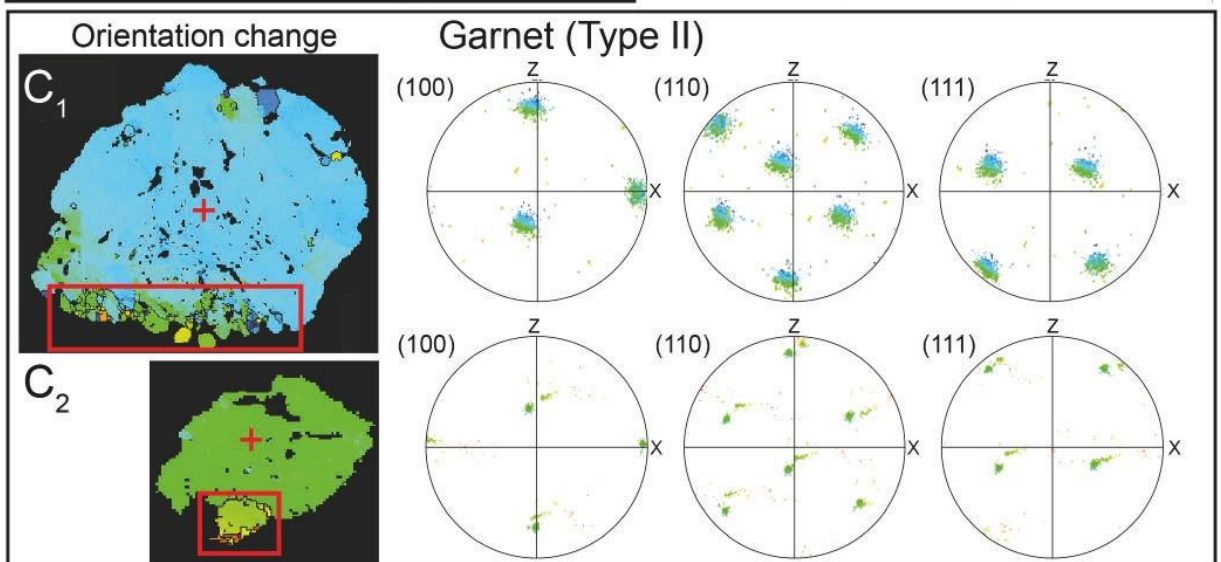
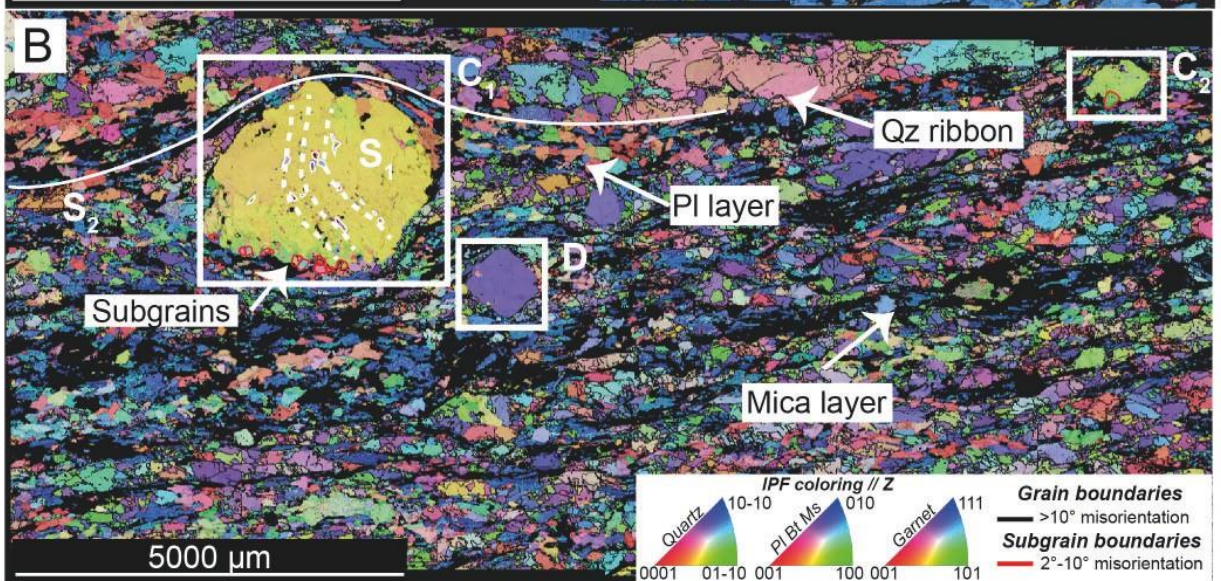
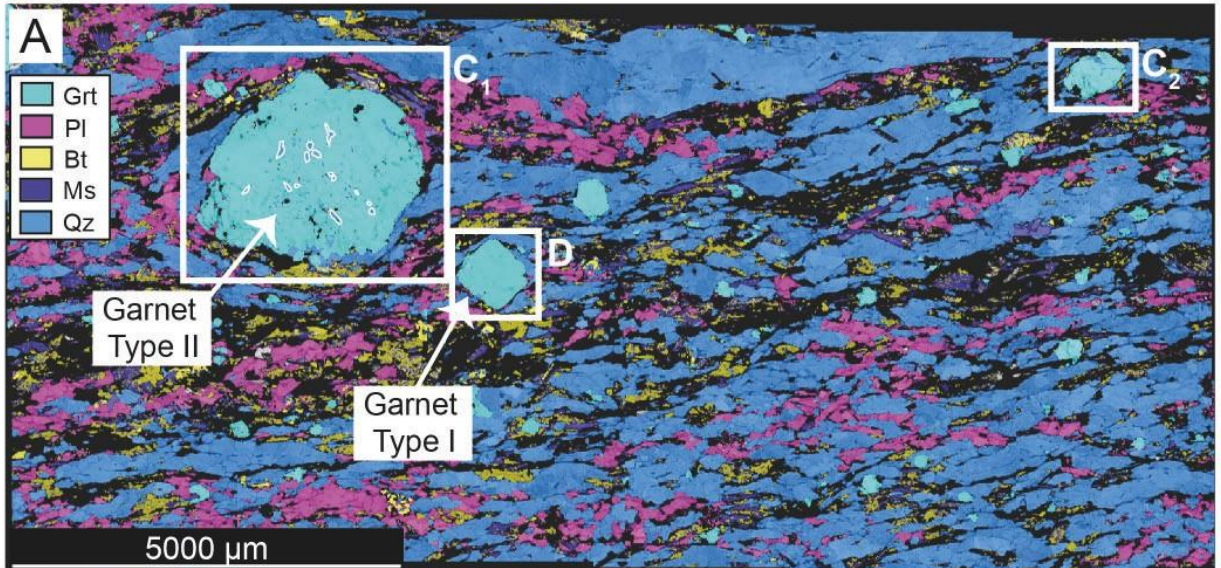


Fig. 4.5 – Petrological features of garnet shown in backscattered electron (BSE) images in Country rocks: A) M92 (Type II = Grt II). B) MP3 (Type II) C) MP3 (Type I = Grt I). D) M62 (Type II). Halos garnet. E, F) M119. G) M102. H) M69. S1 and S2 indicate the pre-peak foliation and the main foliation, respectively.



4.6.2 Halos

Metapelites surrounding the UM bodies are generally characterized by a mineral assemblage consisting of Pl + Bt + Ms + Grt \pm Qz \pm Ky, with variable textures and proportions between the minerals (Fig. 4.7). These metapelites are usually well foliated and consist of granoblastic layers composed of quartz + feldspar \pm garnet (e.g., M119; Fig. 4.7A–D), alternating with micaceous layers (e.g., M102, M69; Fig. 4.7). The mineral modal abundance is 18–30 vol.% for plagioclase, 15–30 vol.% for biotite, 10–17 vol.% for garnet, 8–15 vol.% for muscovite and 5–24 vol.% for quartz. An exception is sample M119 that shows a more peculiar assemblage, characterized by abundant micas, while quartz occurs only as inclusions within garnet. Kyanite locally occurs within samples M102 (10 vol.%) and M119 (rare). Staurolite was not observed in this group of samples.

Garnet crystals are up to 2 mm in diameter and show few small inclusions of quartz, plagioclase, biotite, muscovite, and epidote (Figs. 4.5E–H, 4.7A–C, F).

Plagioclase locally has a poikilitic texture including white mica and biotite (e.g., in sample M102) and shows cusp- and lobe-like shapes and string of beads (Fig. 4.7E; Sawyer, 2008). K-feldspar is present as an interstitial phase (e.g., M119, M102).

Fig. 4.6 – Microstructural features and EBSD map of representative Country rocks sample: M92. S1 and S2 indicate the pre-peak foliation and the main foliation, respectively. A) Mineral phases map, light blue = garnet, purple = plagioclase; yellow = biotite; dark blue = muscovite, blue = quartz. B) Inverse Pole Figure (IPF) map shows basic microstructure, crystal orientations and quartz grain boundary without spatial relationships. C1, C2) garnet (Type II) represented by detailed Texture Component (TC) map and relative pole figure (see Appendix A.1 for a detailed description). Colours correspond to the relative change (in degrees) in crystallographic orientation with respect the reference crystallographic orientation of mineral phases (red cross; max angle for the two textural components = 60°). Red boxes show subgrains. D) Uniform colour of garnet (Type I) indicates that all points show the same crystallographic orientation, as confirmed in the pole figure (lower hemisphere of the equal area stereographic projection). We present the resulting data in the form of colour-coded maps: mineral phase and misorientation maps (i.e., Inverse Pole Figure and Texture Component). The crystallographic orientation of lattice directions and planes are plotted on the lower hemisphere of the equal area stereographic projection of crystallographic orientation (CPO) with one point per grain analysis.

White mica and biotite are generally aligned defining the foliation, although several crystals are oriented at high angle with respect to the foliation plane (Fig. 4.7A–D).

Kyanite occurs rarely, either as sub-prismatic crystals parallel to the foliation or show anhedral/poikilitic texture along the quartz–feldspar layer (Fig. 4.7C, D).

Zircon grains appears in the matrix as subhedral crystals up to 200 μm long and 100 μm wide. Rutile is abundant and predominantly dispersed within the foliated matrix, showing its peculiar yellow–brown colour (Fig. 4.7A). It is also often found included in garnet or associated with biotite. Monazite grains are mostly subhedral to anhedral with a size between 50–150 μm ; rare apatite crystals are observed along the foliation plane (S2). Samples M119 and M69 hold a peculiar association of zoned anhedral monazite (250–500 μm), enveloped by allanite, in turn surrounded by clinozoisite. These composite porphyroblasts are abundant in M119 (up to 5 vol.%) and are generally elongated parallel to the foliation (Fig. 4.7A).

Microstructural and EBSD analyses were performed on sample M119, for which the petrographic observation evidenced a poorly oriented texture differing from the other samples (Fig. 4.8). Mineral phases show a poor shape preferred orientation (SPO), except for biotite and plagioclase that allows to recognize a weak foliation (parallel to S2) surrounding the garnet porphyroblasts (Fig. 4.8B). Garnet grains are homogenous, mostly inclusion–poor as the Type I described for Country rocks, and do not show any internal foliation, neither subgrains nor other pervasive intracrystalline deformation features (Fig. 4.8C1, C2). Plagioclase CPO is less diffuse than that from Country rocks; a maximum is well recognized in (001) plane perpendicular to Z axes (Fig. S4.4B). The J– and M–index for plagioclase are equal to 2.45 and 0.01, respectively. Biotite and muscovite show a main orientation in the (001) plane parallel to the dominant S2 foliation, even though their CPO is less marked than in the samples of the group Country rocks (Fig. S4.4C, D). The J– and M–index for biotite are 3.87 and 0.06 and for muscovite 6.43 and 0.06, respectively.

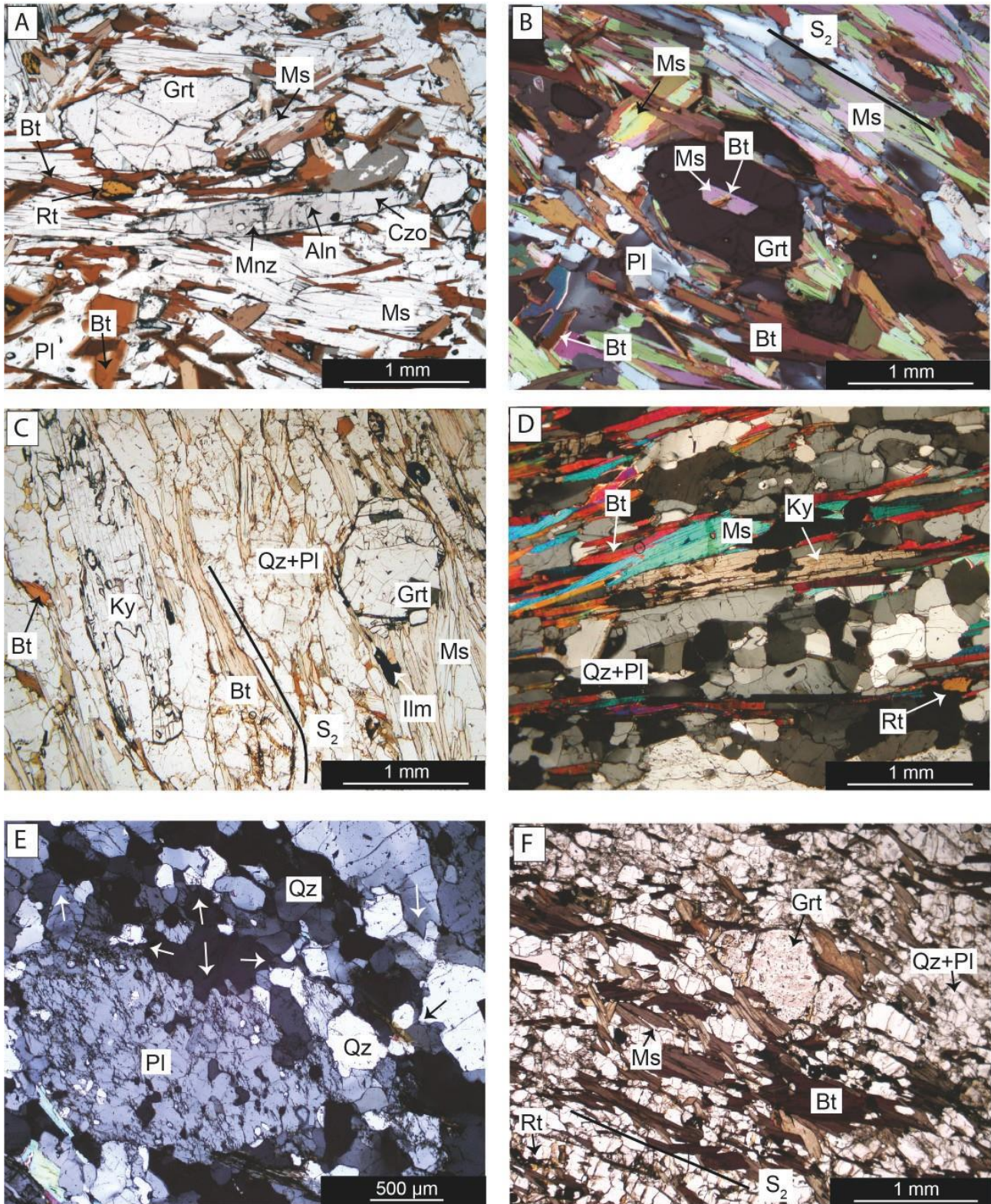
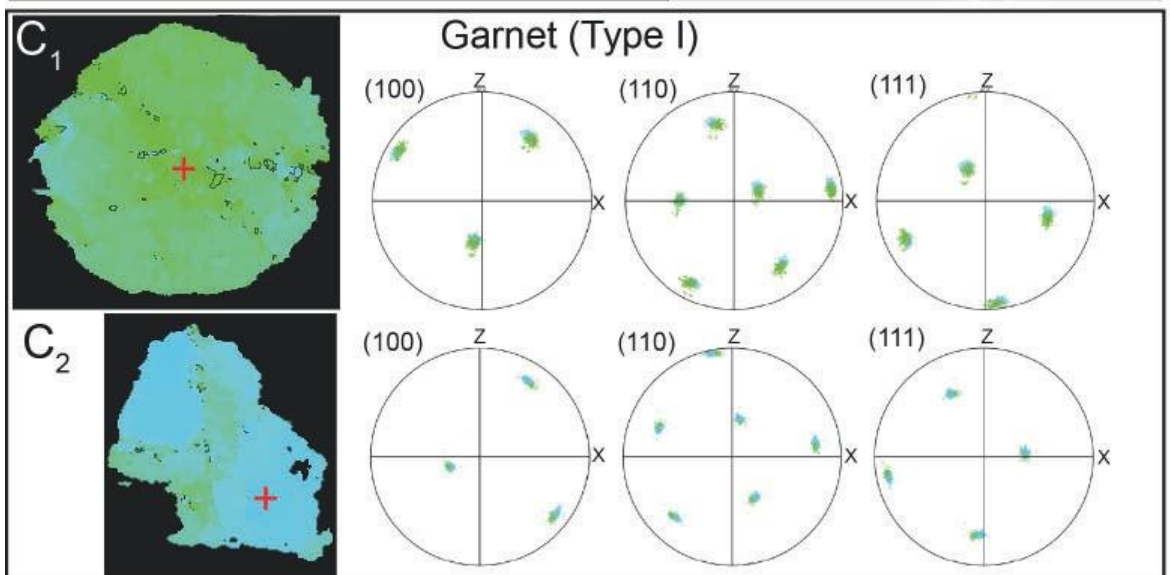
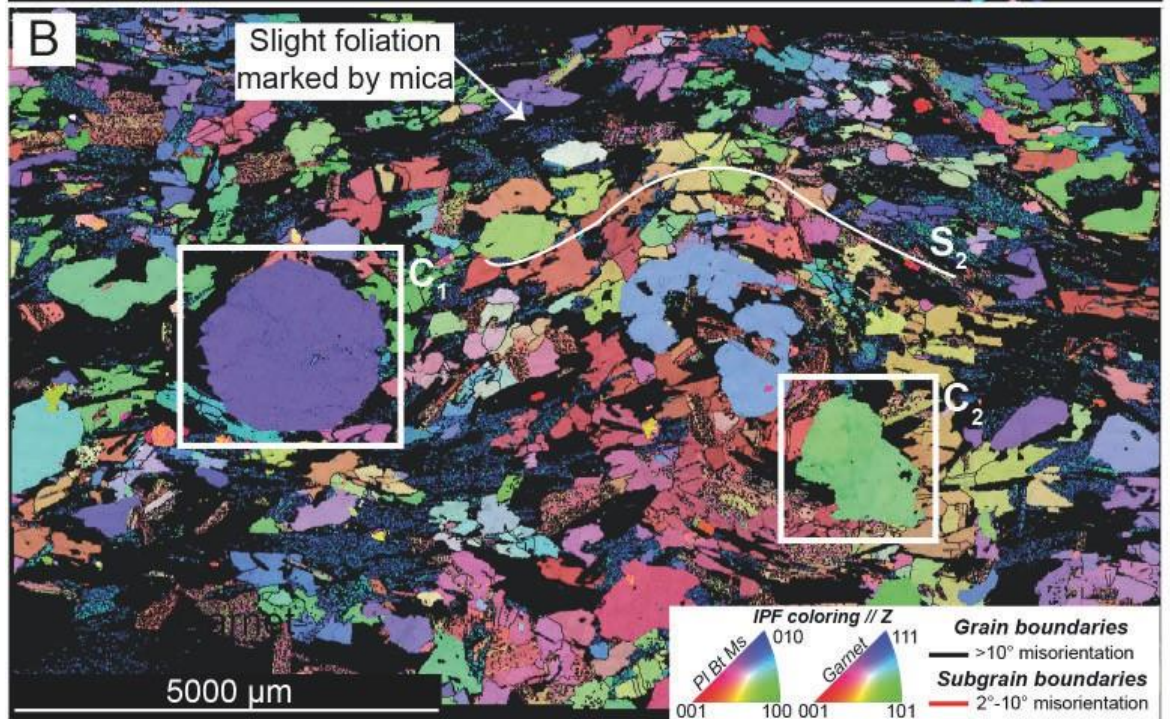
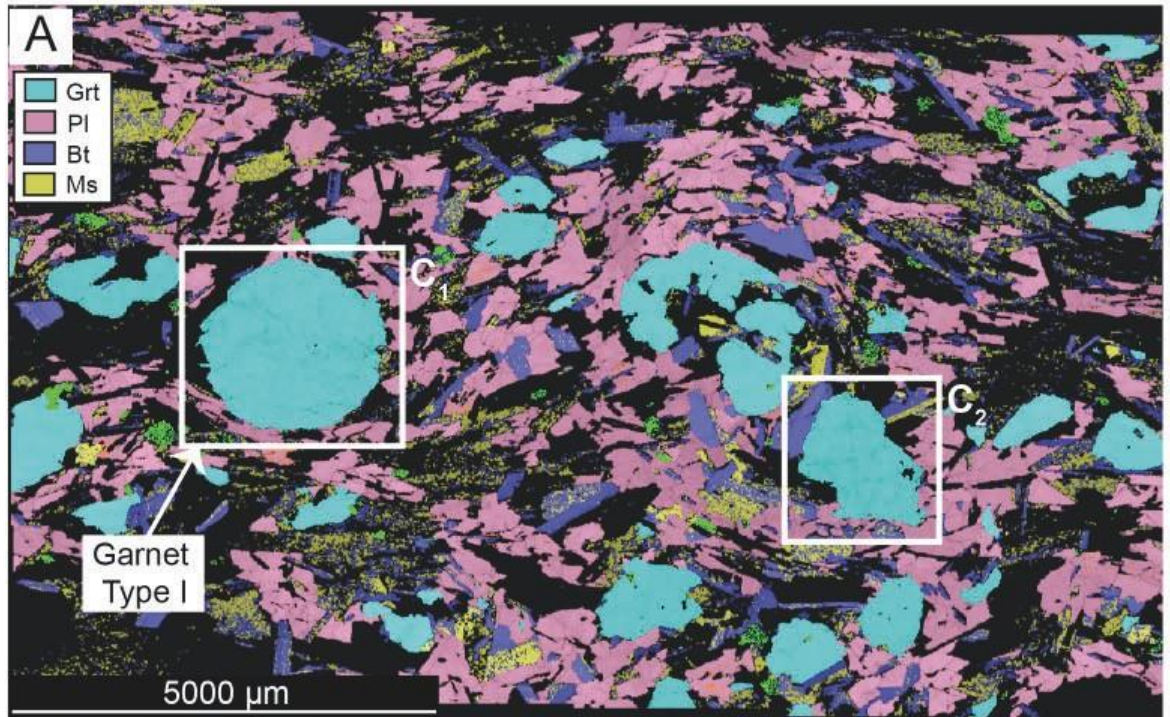


Fig. 4.7 – Major features of Halos samples, plane and crossed polarized light. A) Typical M119 assemblage made of Pl + Qz + Bt + Ms + Grt + Ky+ Rt and the Mnz + Aln + Czo association. B) Garnet porphyroblast with biotite and muscovite inclusions. C) M102 paragenesis made of Pl + Qz + Bt + Ms + Grt + Ky+ Rt. D) Mimetic kyanite, mica-rich and quartz-plagioclase-rich layers underline the foliation. E) Entrapped melt features showing typical cusps and lobes and string of beads of plagioclase, indicated by arrows. E) M69 assemblage made of Pl + Qz + Bt + Ms + Grt + Rt.



4.7 Mineral Chemistry

Major elements were determined for garnet, biotite, muscovite, plagioclase and staurolite. Average mineral analyses on the six representative samples are listed in Tables S4.2, S4.3 and shown in Figure 4.9. Chemical profiles and X-ray maps were collected only for garnet (Fig. 4.10).

4.7.1 Country rocks

Most garnets (Type I) show MgO content in the range of 2.5 to 6.5 wt.%, CaO, MnO and FeO vary from 2 to 9 wt.%, 0.5 to 4.0 wt.% and from 26.5 to 36.5 wt.%, respectively. Sample MP3 records the largest compositional ranges (Fig. 4.9A, Table S4.3). In this sample, garnet (Type I) is characterized by a pronounced core-to-rim decrease in pyrope and grossular, an increase in almandine and spessartine components ($\text{Alm}_{63 \rightarrow 69}$, $\text{Py}_{21 \rightarrow 15}$, $\text{Grs}_{14 \rightarrow 10}$, $\text{Sps}_{2 \rightarrow 5}$; Fig. 4.10A–D, Table S4.3). Garnet (Type I) in sample M62 show a core-to-rim increase in pyrope and spessartine, accompanied by a slight but systematic decrease in almandine and grossular content ($\text{Alm}_{69 \rightarrow 63}$, $\text{Py}_{14 \rightarrow 16}$, $\text{Grs}_{12 \rightarrow 9}$, $\text{Sps}_{5 \rightarrow 11}$; Table S4.3). Garnet (Type I) from sample M92 (up to 500 μm) show a gradual trend characterized by a core-to-rim decrease of grossular and an increase in almandine and pyrope, while spessartine is almost constant ($\text{Alm}_{69 \rightarrow 71}$, $\text{Py}_{14 \rightarrow 16}$, $\text{Grs}_{15 \rightarrow 11}$, $\text{Sps}_{3 \rightarrow 2}$; Table S4.3). Conversely, garnet Type II (up to 1–2 mm) show inhomogeneous distribution of elements, as highlighted by X-ray maps for Mn and Ca (Fig. 4.10F, G). Starting from the Ca-rich core, it is possible to recognize an asymmetric oscillatory zoning with Ca-rich alternating with Ca-poor rings (Fig. 4.10E–H). A similar Ca-garnet zoning was already observed by Rutti, (2003).

Plagioclase is mostly oligoclase in composition with anorthite ranging from 22.7 to 32.7 mol%, and from 24 to 29 mol%, for M92 and MP3 respectively, and between 25 and 40 mol% for M62 (Fig. 4.9B, Table S4.2).

Fig. 4.8 – Microstructural features and EBSD map of Halos sample M119. S2 indicate the main foliation. A) Mineral phases map, light blue = garnet, purple = plagioclase; dark blue = biotite; yellow = muscovite. B) Inverse Pole Figure (IPF) map shows basic microstructure and crystal orientations without spatial relationships. C1–2) garnet porphyroblasts represented by a detailed texture component (TC) map and relative pole figure (lower hemisphere of the equal area stereographic projection; see Appendix A.1.2 for a detailed description). Colours represent a relative rotation with respect to the specific reference crystallographic orientation of mineral phases (red cross; max angle = 60°). S2 indicate the main foliation.

White mica is almost pure muscovite with a $K/(K+Na+Ca)$ ratio of 0.90. Muscovite has an XFe average of 0.47, 0.49 for sample M92, MP3, respectively, whereas M62 records higher values up to 0.70. The Si content ranges from 3.10 to 3.18 atom per formula unit (a.p.f.u.) for M92, from 3.04 to 3.08 a.p.f.u. for MP3, from 3.10 to 3.12 a.p.f.u. for M62 (Fig. 4.9C, Table S4.2).

Biotite appears homogeneous with respect to XFe ($= Fe/(Fe+Mg)$), that ranges between 0.50 and 0.52 for samples M92 and MP3, respectively, and of 0.42 for M62. Al and Ti contents range between 2.4–2.7 a.p.f.u. and 0.08 to 0.11 a.p.f.u. on average, respectively (Fig. 4.9D, Table S4.2). Some biotite crystals show low K content, likely as consequence of partial chloritization.

Staurolite shows XFe between 0.80–0.85 in sample MP3, while it ranges from 0.75 to 0.78 in M62 (Table S4.2). Analogously, the ZnO content of staurolite from MP3 is higher, ranging from 1.06 to 1.68 wt.%, with respect to that measured in staurolite from M62 metapelite (0.52–0.74 wt.%, Table S4.2).

4.7.2 Halos

Garnets show MgO content in the range of 2–8 wt.%, CaO from 3 to 8 wt.% with the lowest values in sample M102. MnO and FeO vary from 0.5 to 10 wt.% and from 25 to 34 wt.%, respectively (Fig. 4.9B; Table S4.3). Garnet shows gradual core-to-rim decrease in grossular and pyrope, associated with an increase in almandine and spessartine ($Alm_{55 \rightarrow 65}$, $Py_{30 \rightarrow 15}$, $Grs_{22 \rightarrow 15}$, $Sps_{2 \rightarrow 5}$; Fig. 4.10N, R; Table S4.3). All garnets show typical outermost rims rich in manganese (Fig. 4.10I–R). Locally, garnet cores have high pyrope component reaching values up to 0.26 molar fraction, which is significantly higher with respect to the values obtained for garnets in the Country rocks.

Plagioclase in sample M119 has the highest anorthite content ($28 < An < 50$), ranging in composition from oligoclase to andesine. In samples M102 and M69, the anorthite (An) component of plagioclase is 29% and 20 mol%, respectively (Fig. 4.9B, Table S4.2).

White mica is mostly pure muscovite with a $K/(K+Na+Ca)$ ratio of 0.90, except for sample M119 that shows a composition richer in the celadonite component (Table S4.2). Muscovite has an average XFe = 0.30, 0.42 and 0.38 for samples M119, M102, M69, respectively. Si-content ranges from 3.08 to 3.19 a.p.f.u. for sample M102, while reach higher values of 3.16 to 3.35 a.p.f.u. in sample M119, and 3.18 to 3.29 a.p.f.u. in sample M69 (Fig. 4.9C, Table S4.2). The highest Si-values in M119 and M69 samples were obtained for muscovite included in garnet and less often from the cores of large muscovite flakes.

The composition of biotite is comparable to that from samples of the Country Rocks group. The XFe is generally between 0.44 and 0.51, whereas the Al and Ti contents are on average 2.4–2.8 a.p.f.u. and 0.11–0.14 a.p.f.u, respectively (Fig. 4.9D, Table S4.2).

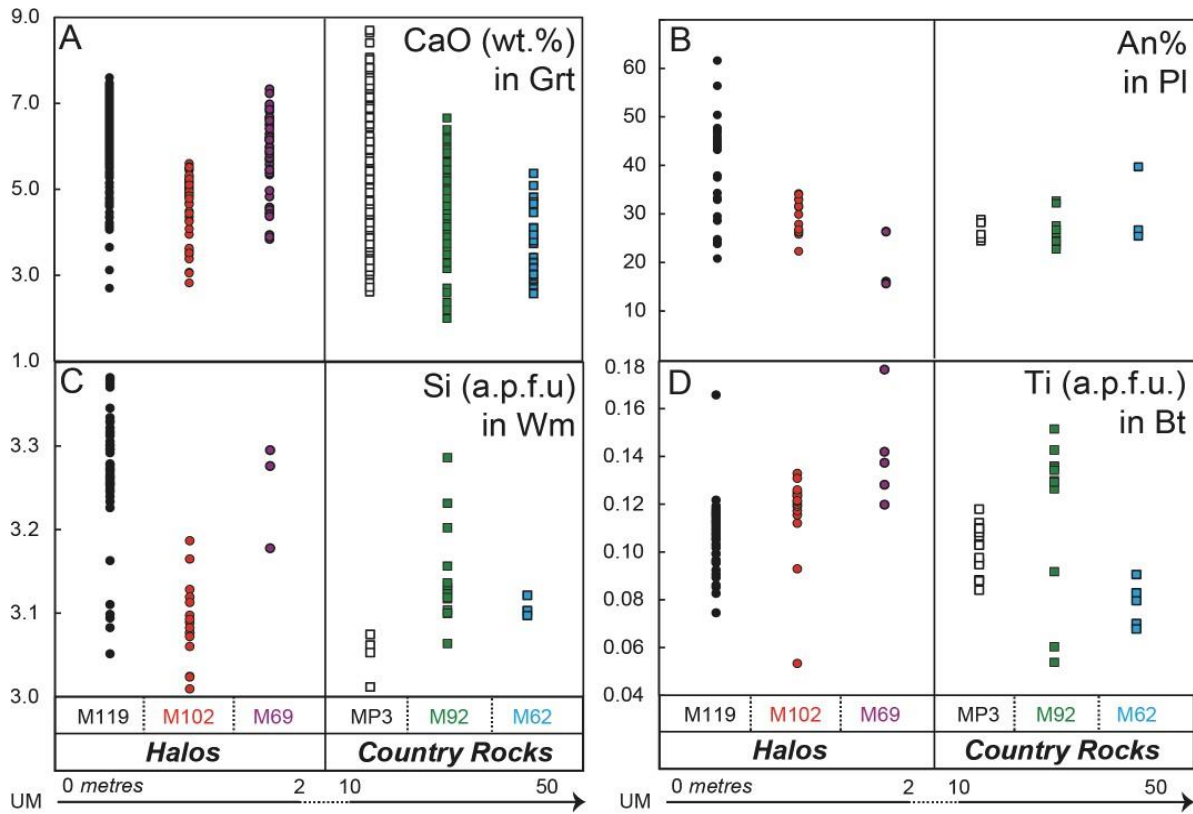


Fig. 4.9 – Major element composition. A) CaO (wt.%) in garnet. B) An% in plagioclase. C) Si (a.p.f.u.) in white mica. D) Ti (a.p.f.u.) in biotite. Arrow indicates the approximate distance in metre from the UM bodies.

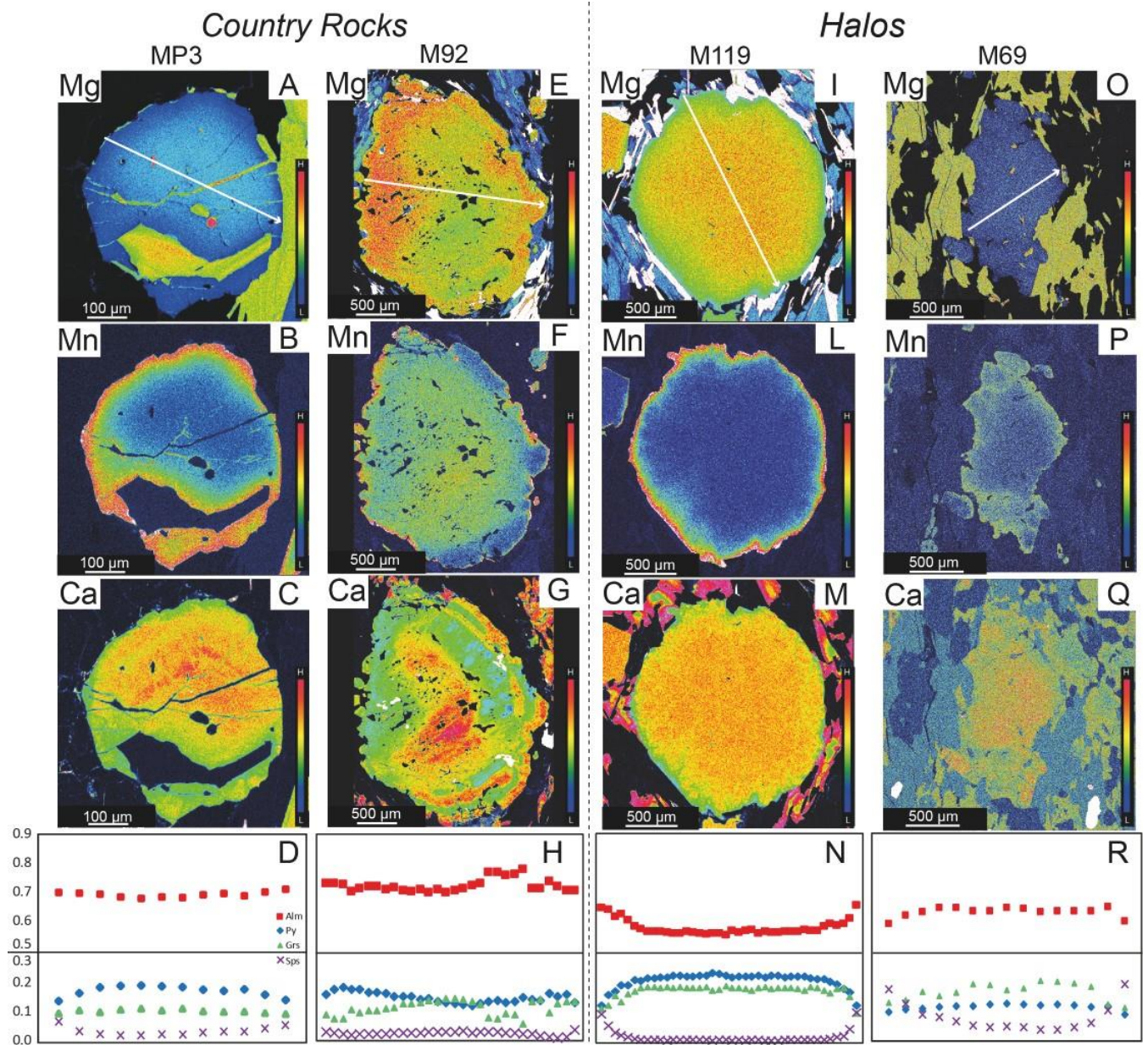


Fig. 4.10 – Representative garnet compositional maps and profiles. A–D) MP3, garnet Type I. E–H) M92, garnet Type II. I–N) M119. O–R) M69.

4.8 P – T estimates

4.8.1 Geothermobarometry

We estimated the P – T conditions of Country rocks and Halos combining several geothermometers and geobarometers (see Appendix 1.2.3). Two distinct mineral assemblages preserving different P – T stages are considered: i) garnet cores + mineral inclusions, and ii) garnet rims + matrix.

4.8.1.1 Country rocks

By pairing the garnet cores and their inclusions from Country rocks we obtained average geothermobarometric values in the range of 600–730°C, and 0.8–1.1 GPa (Fig. S4.5A; Table S4.4). The garnet rims/matrix pairs yield temperature between 550–640°C and pressure values between 0.7–0.8 GPa (Fig. S4.5A, B; Table S4.4). Considering the Si-content in the muscovite, we determined higher pressure values between 0.8–1.3 GPa for the rims and 1.2–1.5 GPa derived mainly from the core of large muscovite crystals or from muscovite included within garnet cores (Fig. S4.5C, D; Table S4.4; see Appendix 1.2.3 for details).

4.8.1.2 Halos

P – T conditions recorded by the Halos are generally higher with respect to those obtained from the Country rock samples. Samples M119 and M102 yield T and P in the range of 730–800°C and 1.1–1.6 GPa from pairs garnet cores/inclusions. Lower P – T values of 600–700°C and 0.7–1.1 GPa were obtained by pairing garnet rim compositions with matrix minerals (Fig. S4.5A, B; Table S4.4). Sample M69 shows lower P – T conditions around 600–640°C and 0.9–1.1 GPa for the garnet core–inclusions system, and around 500–600°C and 0.6–0.9 GPa for garnet rim/matrix-forming minerals, respectively (Fig. S4.5A, B; Table S4.4).

The estimation of pressure using the Si-content in the muscovite indicates variable values between 1.0–1.9 GPa and 1.6–2.5 GPa (assuming T of 650° and 800°C, respectively), being the higher values captured by the inclusions within garnets, or the cores of large muscovite crystals (Fig. S4.5C, D; Table S4.4).

4.8.2 *P–T* pseudosections

The *P–T* conditions of the representative samples have been deduced from the mineral assemblage stability fields (Figs. 4.11, 4.12). The obtained *P–T* pseudosection were contoured by the isopleths of garnet, Si (a.p.f.u.) in potassic white mica (Figs. 4.11, 4.12); even the isopleths for An% in feldspar and the Ti (a.p.f.u) or Mg# in biotite were considered and reported in the Supplementary Material (Figs. S4.6, S4.7). The reader is referred to Appendix 1.2.4 for methods including bulk rock chemistry, *P–T* pseudosection construction, activity models and databases used.

4.8.2.1 Country rocks

Petrographic and microstructural observations indicate that the common assemblage includes Pl + Ms + Bt + Grt + Qz + Rt ± Melt. Melt is considered only for sample MP3 based on the microstructural evidence of melt presence such as string of beads textures and cusped/lobated shapes (Fig. 4.11E, F). The main assemblage is overgrown by kyanite in sample M92 and M62 (Fig. 4.11A–D), whereas samples M62 and MP3 develop staurolite at lower *P–T* conditions (Fig. 4.11C–F). In all samples, a transition between rutile and ilmenite occurs (Fig. 4.11). Considering sample M92 and M62, the garnet isopleths overlap in the same fields, providing peak pressure and temperature conditions of 0.9–1.1 GPa and 630–700°C, followed by a retrograde stage around 0.6–0.8 GPa and 600–680°C (Fig. 4.11B, D; Table S4.3). Sample MP3, collected from the stromatic leucosome, gave similar peak pressure conditions (0.8–1.1 GPa) but higher temperature between 700–750°C, and the same retrograde path (Fig. 4.11E, F). Noticeably, the Si-isopleths calculated for muscovite in this sample indicate *P–T* conditions significantly higher than those constrained by the garnet isopleths, thus suggesting non equilibrium between Grt and Ms (Table S4.2; Fig. 4.11B, D, F).

4.8.2.2 Halos

Samples from the Halos group share a mineral assemblage consisting of Pl + Ms + Bt + Grt + Rt ± Melt (Fig. 4.12). Isopleths relative to the garnet cores of sample M119 have a composition of Alm₅₈->54, Py₂₅->20, Grs₁₇->21, falling in two different *P–T* fields (Fig. 4.12A, B). A first field indicates *P* around 1.7 GPa and *T* around 750°C; the second field is consistent with higher *T* of ~800°C and somewhat lower *P* around 1.5 GPa. The garnet core isopleths calculated for sample M102 (Alm₅₅->57, Py₃₀->28, Grs₁₅->13)

constrain a P - T field at 1.5 GPa and 750°C, while for sample M69 (Alm₆₂₋₆₆, Py₁₄₋₁₂, Grs₂₂₋₁₇) the P field is at slightly lower condition around 1.4 GPa while T is at 740°C.

The isopleths of the garnet rims indicate decompression to 0.8 GPa and cooling to 720–650°C. This retrograde path is consistent with the appearance of kyanite in samples M102 and M119 combined with decrease in muscovite content in sample M69 (Fig. 4.12).

The P - T conditions calculated for sample M102 from garnet isopleths and Si-values in zoned white mica and in muscovite flakes included in garnet are in good agreement, while samples M119 and M69 apparently capture significantly higher pressure up to 2.5 GPa (Table S4.2, S4.5; Fig. 4.12). In addition, the Si content of white mica inclusions or in the cores of large flake from sample M119 coincides with the highest pressure P - T field (1.7 GPa and 750°C; Fig. 4.12A, B), suggesting that these samples experienced even higher pressure assemblage reaching the jadeite stability field. However, no jadeite crystals have been found from the petrographic observations suggesting that the stability field occur at lower P - T conditions.

4.9 U–Pb Geochronology

In this work, we present preliminary results from U–Pb analyses on zircon (for methods see chapter 3.7; Appendix 1.2.5), collected from samples MP3 and M119 representative of the two groups recording HT metamorphic conditions (i.e., the Halos and the leucosomes of the Country rocks). These samples preserve signatures of melt presence, in particular cusps and lobes texture and string of beads (Figs. 4.4E, 4.7E), which may induce further disturbance of the geochronological signatures at high temperature (Rubatto and Hermann, 2007).

4.9.1 Zircon Zoning and Isotopic Results

4.9.1.1 Country rocks (representative sample MP3)

A total of thirty-one zircon grains separated from sample MP3 were analysed for U–Pb dating (Fig. 4.13A, B). The cathodoluminescence (CL) images revealed variable zoning features characterised by cores surrounded by rims (Fig. 4.13A, B). Cores show complex zoning, mainly convolute although domains with oscillatory zoning rarely occur. Rims show either oscillatory zoning or discontinuous highly luminescent patches, which truncate the other structures. U–Pb data were collected from all the three domains, although the thin patchy rims (< 20 μm) are difficult to detect.

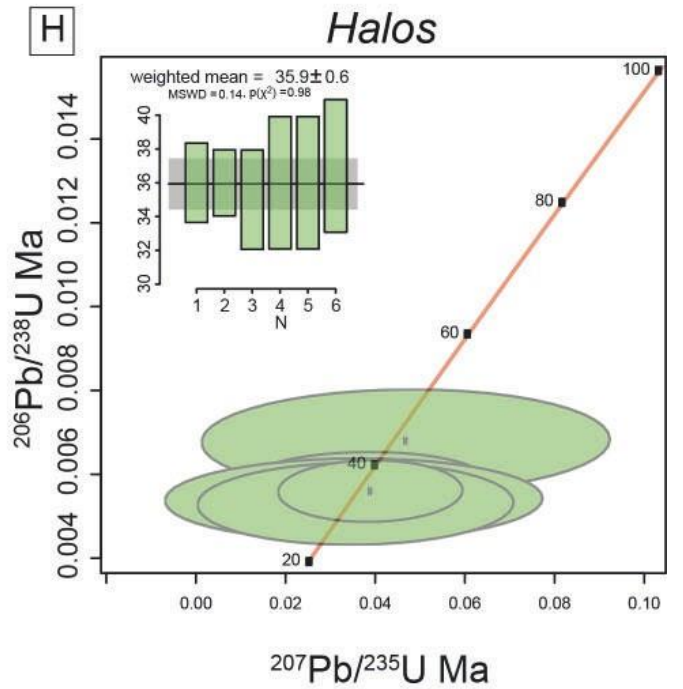
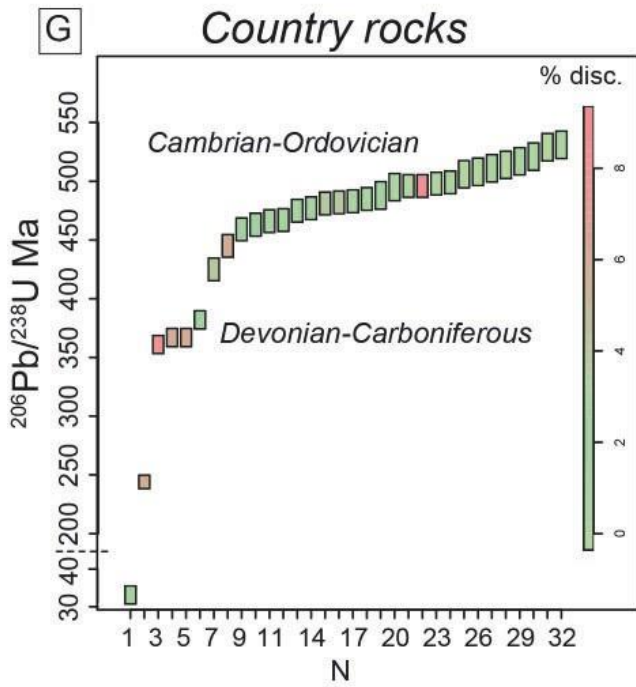
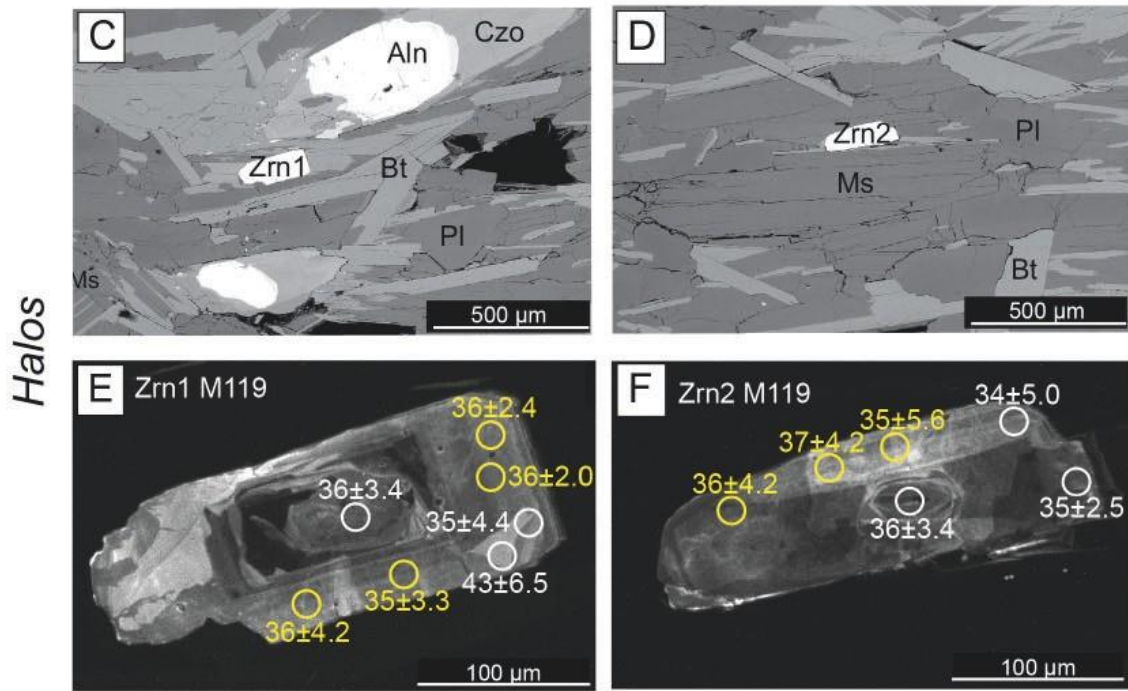
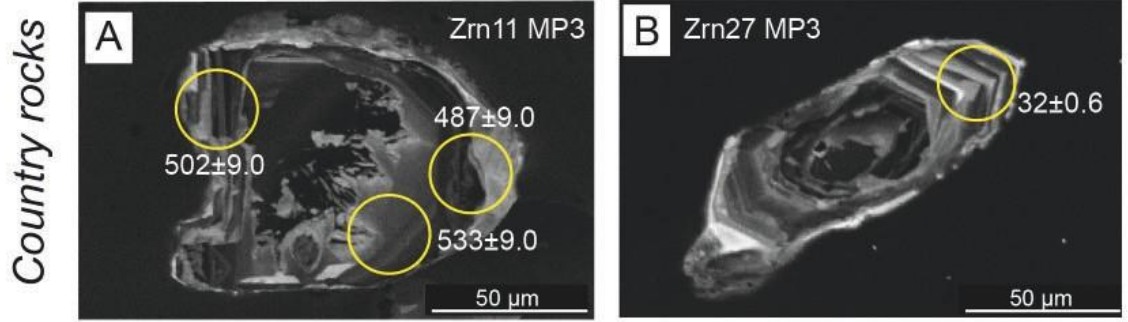
Among the thirty-seven spot analyses (25 μm), eighteen zircon U–Pb data yield concordant ages between 533 ± 9.0 and 384 ± 7.0 Ma (Fig. 4.13A, G; Table S4.5). Considering the U–Pb data with concordance better than 90%, the measured ages show a main population over the Cambrian–Ordovician, and minor cluster through the Devonian–Carboniferous (Fig. 4.13G). We did not find specific correlation between ages and zircon texture, as oscillatory zoning domains record the same age populations as the cores. It is interesting to note that only one relatively thick zircon rim yields an Alpine age of 32 ± 0.6 Ma (Fig. 4.13B; Table S4.5).

4.9.1.2 Halos (representative sample M119)

Zircon of sample M119 were analysed in situ directly on thin section. We selected two large zircon grains, Zrn1 and Zrn2 (250–300 μm in length), aligned along the muscovite and biotite foliation (Fig. 4.13C–F). These crystals exhibit complex zoning features with a core characterized by different CL signal with respect to the external domains. This appears as a thick rim (50–80 μm) with a faint oscillatory zoning (Fig. 4.13E, F; Corfu et al., 2003).

Thirteen laser spots (10- μm diameter) were performed on cores and rims of both Zrn1 and Zrn2, of which seven from the outer rims gave concordant ages between 34 ± 5.0 and 37 ± 4.2 Ma (Fig. 4.13H; Table S4.5). Concordant data result in a weighted average age of 36 ± 1.2 Ma (MSWD = 0.14; Fig. 4.13H, Table S4.5). Noticeably, also the discordant ages from both cores and rims show $^{206}\text{Pb}/^{238}\text{U}$ ages ranging between 34 ± 5.0 and 36 ± 3.4 Ma and only one older age at 43 ± 6.5 Ma (Fig. 4.13H, Table S4.5). Notwithstanding the large errors associated to the U–Pb data, due to the small dimensions of the used spot size, the zircon U–Pb data and the internal features suggest an Alpine overprint.

Fig. 4.13 – A, B) CL-images of dated separated zircon (e.g., Zrn11, Zrn27) from MP3, ablated area of 25 μm in diameter, the ages reported are concordant. C, D) Microstructural position, internal structures and E, F) CL-images of dated zircon grains (Zrn1, Zrn2) from sample M119, ablated area of 10 μm in diameter, concordant ages are reported in yellow, discordant ages in white colour, $\pm 1\sigma$ (which is a 2σ interval) is the error. G) Distribution of the $^{206}\text{Pb}/^{238}\text{U}$ ages relative to the thirty-one zircon from the Country rocks sample (i.e., MP3). The green-to-red bar indicates the % of discordance of data. N indicates the number of zircon crystals. H) U–Pb concordia diagram and $^{206}\text{Pb}/^{238}\text{U}$ weighted mean age diagram for two analysed zircon grains from the Halos sample (i.e., M119).



4.10 Discussion

4.10.1 *P-T-t-D* paths

Field observations show that metasediments have a regional and pervasive deformation fabric throughout all the Cima di Gagnone area and are characterised by non-cylindrical folding associated with a dominant sub-horizontal schistosity deflected around the mafic/ultramafic lenses (Fig. 4.3A, B). Outcrop-scale sheath-like folds are abundant in the weaker metasediments (e.g., micaschists and metacarbonates) around the UM, which, in turn show complex internal folding and boudinage (Fig. 4.3C–G). Integration of field data and numerical modelling demonstrated that sheath folds developed in the relatively weak rocks due to presence of more viscous lenses (Maino et al., 2021). The recognition within the inclusions of three consecutive stages of folding-boudinage-folding implies that herein the deformation switched from shortening to stretching to shortening again. Such rotating internal foliation is related to super-simple shear flow that accounts for the transition between stretching and shortening stages (Maino et al., 2021). However, this complexity is associated with a single penetrative schistosity and lineation, suggesting a coupled progressive deformation rather than multiple distinct phases. Overall, these structural features argue for a large bulk shear strain accommodated by the Cima Lunga unit during the Alpine deformation. Deformation is pervasive throughout the entire unit, although not uniform, as strain is characterized by sharp gradients at the boundaries between UM and host rocks. However, these boundaries do not show any mylonitic or cataclastic shear zones, precluding the existence of any structural discontinuities necessary for mixing tectonically different blocks (Maino et al., 2021). Even though metasediments and UM share the same structural evolution, the record of *P-T* conditions in the studied samples changes systematically as a function of the distance to the UM bodies, being maximum in the Halos i.e., at the interface between the country rocks and the mafic inclusions (Figs. 4.14, 4.15).

4.10.2 Country rocks

Thermodynamic modelling and thermo-barometry indicate that large part of the metasediments of the Cima di Gagnone experienced peak *P-T* conditions of 1.0–1.2 GPa and 650–720°C, followed by a retrograde stage around 0.6–0.8 GPa and 600–675°C (Figs. 4.11, 4.14). These estimations are in accordance with the dominant recrystallized amphibolite-facies mineral assemblage of the Country

rocks made of Pl + Qz + Bt + Ms + Grt, the core-to-rim zoning of garnet crystals, and the growth of retrograde kyanite, staurolite, and ilmenite bordering rutile rims (Figs. 4.4–4.6, 4.9, 4.10; Tables S4.2–S4.4).

Deformation temperature between 600 and 700°C and syn-kinematic recrystallization are confirmed by microstructural features, such as straight grain boundaries between quartz and plagioclase, quartz ribbons, subgrains formation along rims of inclusion-rich garnet and well pronounced schistosity defined by subparallel mica flakes, quartz, plagioclase and, when present, staurolite and kyanite porphyroblasts (Figs. 4.4, 4.6). These results are supported by published estimates for the metasediments of Cima Lunga unit (Grond et al., 1995; Pfiffner, 1999; Rutti, 2003). In addition, the neighbouring units (Maggia and Simano) experienced the same amphibolite-facies re-equilibration (~0.8 GPa and 650°C), which has been shown to follow peak conditions with similar P values (~1 GPa), but significantly lower temperature (~500°C; Rutti et al., 2005).

Moreover, garnet from the Cima Lunga unit is characterized by the widespread occurrence of inclusion-rich cores (Type II) indicating an early stage of growth at 0.8–1.2 GPa and 600–700°C (Fig. 4.5A, B; 4.11). These cores developed during a tectono-metamorphic event predating the main Alpine phase recorded by the inclusion-poor rims (Grond et al., 1995; Rutti, 2003). Whether this stage was early Alpine or even pre-Alpine is hard to determine. Eclogitic rocks in the Adula nappe contain, in fact, coexisting Alpine and Variscan garnet populations with HP signature dated at 324 ± 7.0 Ma and 38.8 ± 4.0 Ma, respectively (Herwartz et al., 2011; Sandmann et al., 2014). In any case, however, the preservation of intermediate *P–T* conditions suggest that Country rocks never recorded Alpine HP–HT metamorphism.

A slightly different path is instead recorded by the stromatic leucosomes locally intruding the amphibolite-facies fabric (e.g., sample MP3; Figs. 4.3E, 4.4E). Here, intermediate P values (0.8 GPa) are associated with T conditions (700–750°C) higher than those recorded in the Country rocks (Figs. 4.11, 4.14). This is followed by a cooling path matching that recorded by the Country rocks (Fig. 4.11C, D). Although a precise dating of the HT event requires more detailed geochronological investigation (which is beyond the scope of this contribution), the available U–Pb data may be used to discriminate whether HT conditions occurred either during the Alpine or pre-Alpine cycles. Zircon dating from this sample provided Pre-Variscan ages (530–380 Ma – sample MP3) with only one age from a relatively

thick rim at around 32 Ma (Fig. 4.13A, B, G). These data agree with ages for similar leucosomes from the Cima di Gagnone orthogneisses, as well as for the Adula gneisses that show dominant protolith and/or metamorphic Palaeozoic ages (Gebauer, 1994, 1996, 1999; Liati et al., 2009; Cavargna–Sani et al., 2014). These studies also detected a few Alpine ages < 33 Ma, which are usually related to thermal influence of the late thrusting and final exhumation of the units, marking the beginning of the doming of the Lepontine dome (e.g., Janots et al., 2009; Rubatto et al., 2009; Berger et al., 2011; Gregory et al., 2012; Boston et al., 2017). Our data, together with literature, indicate therefore that the Alpine crystallization/recrystallization of zircon was very limited in the Cima di Gagnone metasediments, coherently with relatively low peak temperatures reached by these rocks.

Overall, the Cima di Gagnone metasediments are generally characterised by intermediate pressure and temperature conditions throughout all the Alpine cycle, with a most pronounced thermal signal produced during the final exhumation phase.

4.10.3 Halos

The metamorphic evolution depicted for the largest part of the Cima di Gagnone metasediments contrasts with that of the metapelites close to the UM (Figs. 4.12, 4.14). Although all metasediments still preserve a dominant fabric developed at amphibolite–facies conditions, some Halos occurrences suggest distinctive, though variable, peak pressure, and temperature records (e.g., samples M102, M69, M119; Figs. 4.12, 4.14). These samples exhibit peak temperature (720–770°C and 800–850°C) and pressure (1.3–1.7 GPa; Fig. 4.14) significantly higher with respect those recorded by the Country rocks.

In addition, the high Si–content (i.e., up to 3.38 a.p.f.u.) preserved within phengitic inclusions in garnet cores (i.e., sample M119; Fig. 4.9C; Table S4.2) points to significantly higher pressure, up to 2.5 GPa, in the immediate proximity of the UM bodies (Table S4.4). These high–Si muscovite inclusions could represent the relicts of a largely re–equilibrated (U)HP mineral assemblage represented by the generalized reaction $\text{Phengite} + \text{Garnet1} + \text{Paragonite} = \text{Muscovite} + \text{Biotite} + \text{Plagioclase} + \text{Garnet2} + \text{H}_2\text{O}$, as already reported by previous authors (Heinrich, 1982; Früh–Green, 1987). The phengitic inclusions may have avoided Si–exchange as they are protected by the garnet host; however, their Si–content and garnet cores isopleths do not fit, indicating contradicting P – T records of these two minerals (Figs. 4.12A, B, S4.5; Table S4.4). Finally, we must emphasize that both the inferred P – T conditions and

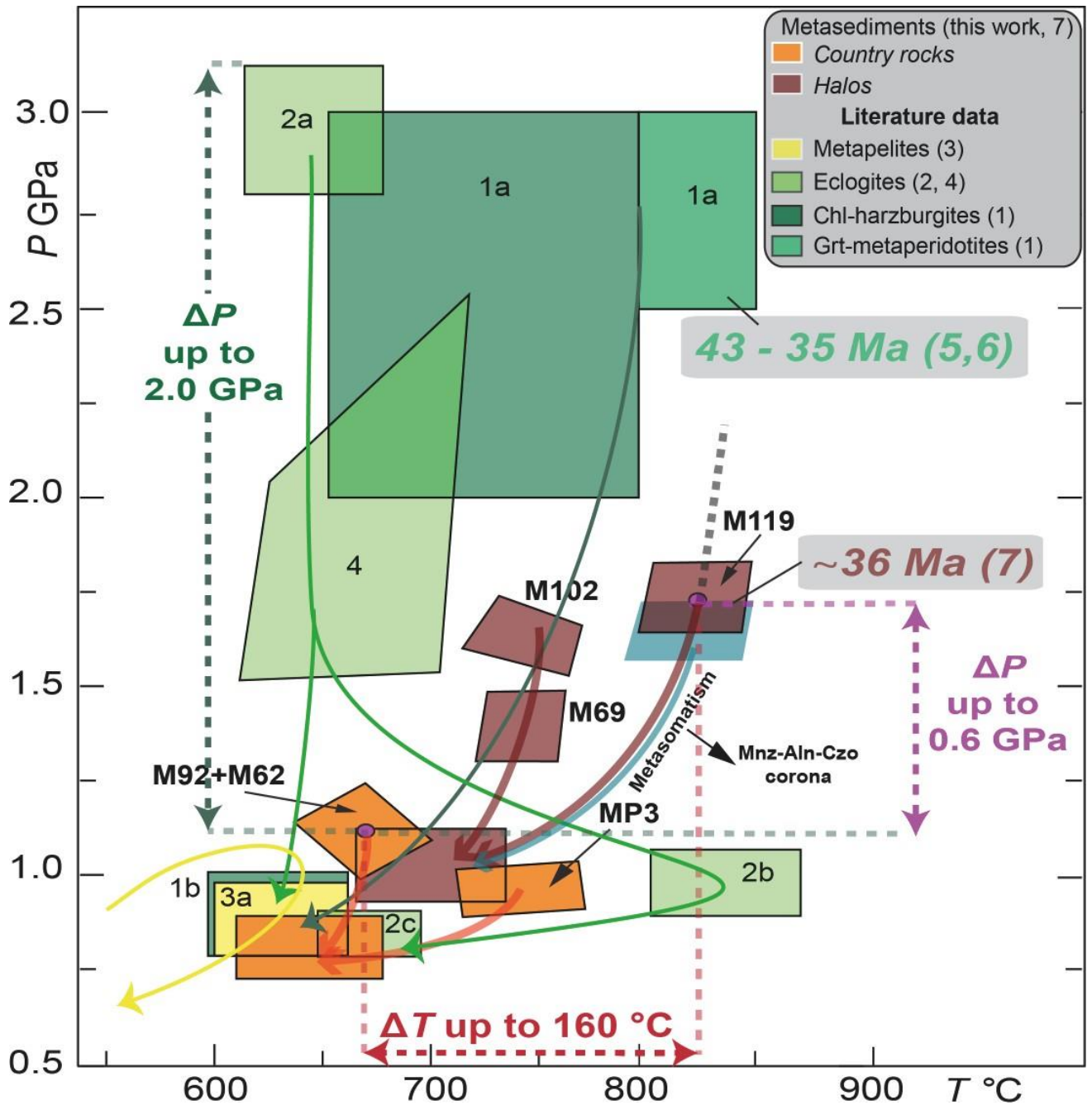


Fig. 4.14 – Compilation of P – T – t paths from the present study and the literature. Inferred P – T paths and fields of the samples analysed in this study are based on pseudosection modelling and petrographic assemblages (orange squares, Country rocks; brown squares, Halos). Fields from literature data are indicated with numbers: 1 – Nimis and Trommsdorff (2001) and Scambelluri et al. (2014); 2 – Brower et al. (2005); 3 – Grond et al. (1995); 4 – Heinrich (1986). Geochronological data are from: 5 – Gebauer (1996, 1999); 6 – Becker et al. (1993). Differential pressure and temperature depicted in the diagram are calculated from the average values between the Country rocks (samples M92 and M62) and the Halos (sample M119) or the pressure peak estimation from eclogites.

the mineral assemblage do not match the range of applicability set for the barometer (calibrated for a T range from 250°C to 650°C at a P up to 2.8 GPa; Massonne and Schreyer 1987), preventing to derive reliable information on the metamorphic evolution from this geobarometer.

Furthermore, the sample recording the highest P – T conditions (i.e., M119) is characterized by a peculiar microstructure characterized by coarse grain size for all minerals, significantly lower CPO of plagioclase, biotite and white mica, weak intracrystalline deformation of garnet (i.e., rare subgrains; Fig. 4.8). This weak fabric is accompanied by melt microstructures indicating that deformation occurred in presence of melt; hence, this sample was not significantly overprinted by the regional, otherwise pervasive, amphibolite-faces deformation (Fig. 4.7E).

Finally, these HT conditions are further confirmed by the almost complete resetting of the U–Pb isotopic system in both rim and core domains of zircon grains (Fig. 4.13C–F). Concordant ages from the thick rims indicate an age of ~36 Ma, which predates the Barrovian stage (Fig. 4.13H). On the other hand, this age is synchronous with the timing of the HP phases constrained in both the Cima Lunga and Adula nappes (Becker, 1993; Gebauer, 1996; 1999; Brouwer et al., 2005; Hermann et al., 2006; Herwartz et al., 2011; Sandmann et al., 2014).

4.10.4 Petrological and geochemical interferences between UM and metasediments

Our results show that HT conditions were associated with the presence of melt dominantly localised in the neighbourhood of the UM lenses (Fig. 4.3A, B), arguing for a significant but highly localized effect of melt/fluid–rock interaction. It should be noted that the sample equilibrated at the highest P – T conditions (i.e., M119), shows a strongly different bulk composition with respect to the other metasediments (Appendix 1.2.6; Fig. S4.1; Table S4.1). It is in fact characterised by anomalously low SiO_2 content coherently with the absence of quartz in the matrix, although this mineral is present as inclusions within garnet. M119 contains very high CaO, Al_2O_3 , FeO and MgO concentrations, up to about two times than in the other samples. At the same time, M119 resulted enriched in incompatible elements such as Th, Nb, La, Ce, Nd, Zr, Hf, Y with respect to other samples (Fig. S4.8).

To evaluate the dependence of the mineral assemblage on both temperature and chemical variations, we calculated a T–X pseudosection considering the bulk composition of two representative

samples (Fig. 4.15A, B; see Appendix 1.2.4). This diagram shows how the mineral assemblages evolve as a function of the bulk chemical composition (Δ Bulk in mol%) from a reference metapelitic composition (e.g., MP3: bulk composition reported in Fig. 4.11) to the CaO- and Al₂O₃-rich composition of the HT sample M119 (bulk composition reported in Fig. 4.12). The results of the T-X pseudosection clearly indicate that the assemblage of sample M119 is stable only if very high contents of CaO, Al₂O₃, FeO and MgO meet with depletion of SiO₂ at the minimum temperature of ~700°C for a pressure fixed at 1.125 GPa.

Such apparent variations of SiO₂, CaO, Al₂O₃, FeO and MgO cannot be attributed only to local partial melting with consumption of quartz and extraction of melt/hot fluids. Indeed, the exotic chemical composition of M119 is more likely the consequence of the interaction with rocks enriched in CaO, Al₂O₃, FeO, MgO, but undersaturated in SiO₂. A possible source of CaO, Al₂O₃, FeO and MgO are the amphibole- and chlorite-rich layers enveloping the ultramafic lenses. These hydrated mafic rocks were also the possible source of fluids required to trigger fluid-fluxed melting in the surrounding metapelites. Amphibole and chlorite formed during the retrogressive alteration of the chlorite-harzburgites lenses due to the infiltration of fluids produced by dehydration of the neighbouring metapelites (Pfeifer, 1981, 1987). We therefore suggest that localised exchange of fluids from the metapelites to the ultramafic bodies and back, occurred during the early decompressional evolution, still at HP-HT conditions.

Significant fluid circulation at the interface between metapelites and UM is further documented by the local occurrence of the corona microstructure around Mnz, made by Aln in turn enveloped by Czo. While monazite is present as relict, thus likely stable in association with the garnet (cores), allanite and clinozoisite show equilibrium texture with the late, amphibolite-facies assemblage. The CaO, Al₂O₃, FeO-rich composition likely promoted the formation of the coronae of allanite and clinozoisite at the expense of the monazite. Recent works on similar phosphate-epidote association and textures acknowledge the evolution from monazite to allanite and finally to clinozoisite as due the interaction with a fluid containing mainly Si, Ca, Al, Fe and F at decreasing *P-T* conditions (Regis et al., 2012; Hentschel et al., 2020). In our case, the possible origin of the fluid can be: i) an exotic reservoir located outside the unit, or ii) dehydration-rehydration processes at the ultramafics-metasediments interface. The chemical composition of the halo, the localisation around the UM lenses of the metasomatic front, as well as the lack of any clear evidence for an external supply of fluids support the second process as

the most likely.

Evidence for fluids/melts percolation within mafic/ultramafics and metasediments at Cima di Gagnone unit was already documented by previous authors at different metamorphic stages (e.g., Pfeifer, 1981, 1987; Heinrich, 1982; Fruh-Green, 1987; Pfiffner, 1999; Scambelluri et al., 2014, 2015). Mobility of Ca, Al, Si, Fe and Mg is described in the metaperidotites, which display decreasing Al_2O_3 and CaO with increasing MgO concentrations and light-REE depletion (Scambelluri et al., 2014, 2015). The authors interpreted this reaction as predating the Alpine subduction, being thus acquired during fluid-rock interactions in the oceanic lithosphere. However, they reported an enrichment in fluid-related elements (i.e., B, Be, As, Sb, Pb) in the peridotite, suggesting interactions with sedimentary reservoirs and fluids during subduction burial (Scambelluri et al., 2014); this transfer process pre-dates peak metamorphism and dehydration of the ultramafic rocks at sub-arc depths.

Heinrich, (1982, 1986) and Pfeifer, (1981, 1987) focused instead on the fluid-rock interactions occurred at amphibolite-facies conditions ($P < 0.8$ GPa and $T = 650^\circ\text{C}$). These authors describe a concentric zonation in the mafic and ultramafic lenses resulting from a mechanism in which dehydrating metapelites provide H_2O required for hydration reactions within the mafic/ultramafic lenses. In particular, Pfeifer, (1981, 1987) distinguished five different zones in the UM: 1) original harzburgite (mainly olivine-enstatite-chlorite-Cr-Fe spinel), 2) hydrated zone (olivine-talc-chlorite-Cr-Fe-spinel \pm amphibole), 3) hydrated and carbonatized zone (talc-magnesite-chlorite-amphibole-Fe-spinel), 4) zone strongly enriched in Ca, Al and Si (amphibole-chlorite-Fe-spinel \pm magnesite, pentlandite), 5) complex marginal zonation (mono- and bi-mineralic zones of phlogopite, amphibole and plagioclase). This zoning is dissected by several generations of veins that promoted such diffusion-dominated mass transfer mechanism justifying these changes of the mineral assemblage. The occurrence of retrograde veins confirms that the mobility of the Si, Al, Ca, Fe, and Mg occurred even across the metasediments during decompression (Pfeifer, 1981, 1987).

All these data indicate that the Cima di Gagnone rocks experienced multiple cycles of interactions with fluids (dehydration/rehydration) at the interface between metasediments and UM. As we do not know the crystallization/re-equilibration ages from monazite and allanite, we cannot fix the precise timing of fluid-rock interaction documented in this work. However, we may use petrological and geochronological arguments to constrain this event in terms of its position within the metamorphic

evolution. In general, the Aln–Czo coronae were stable during the development of the amphibolite–facies fabric, post–dating the HT–HP assemblage (780–840°C; 1.3–1.7 GPa) within the Halos. The occurrence of quartz only as inclusions within garnet core supports that during the prograde Alpine phase quartz was stable but became unstable during the T–peak conditions. Finally, the preliminary geochronological analysis suggests an almost complete reset of zircon coevally with the decompression stage of the (U)HP rocks of the Cima Lunga and Adula nappes (< 40Ma). All these features suggest that metasediments experienced an HT–HP metasomatic process during the early stage of the exhumation driven by fluid mobility and wet melting at the interface with ultramafic lenses.

A fluid assisted HT stage ($T > 800^{\circ}\text{C}$) at pressure of ~ 0.9 GPa has been also reported in the garnet metaperidotite of the Monte Duria in the southern Adula (Tumiati et al., 2018; Pellegrino et al., 2020). Multiple cycles of fluid–rock interactions, at the boundary between rocks with different chemistry and rheology, have been described in other geological settings, such as the Ulten Zone and Saualpe–Koralpe of the Eastern Alps, where metasomatic bands at the boundary between ultramafic/mafic rocks and metasediments have been observed (Godard et al., 1996; Tumiati et al., 2003, 2007; Marocchi et al., 2009; Langone et al., 2011; Schorn, 2018). The apparent differences in bulk chemistry of paired lithologies and HT conditions are also the driving forces for metasomatic processes leading to the formation of skarns and/or listwaenites (e.g., Buckman and Ashley, 2010; Pirajno, 2013; Gahlan et al., 2018). In the latter case, ultramafic lenses, enclosed in HT metapelites and/or metagranites, are characterized by extensive replacement of silicates by carbonates, or may develop an outer reaction band rich of hydrous minerals such as tremolite, chlorite, phlogopite and talc. In literature (e.g., Buckman and Ashley, 2010; Pirajno, 2013; Gahlan et al., 2018), these rocks are, indeed, generally considered as resulting from metasomatism at a metric scale, between two very different compositions (e.g., pelitic and ultramafic), at temperatures high enough to allow significant diffusion.

In summary, cycles of dehydration/rehydration of UM and metasediments are interpreted to trigger metamorphic reactions and metasomatism which is documented by the crystallisation of new hydrous minerals and veins and the release of a trondhjemitic residual melt from ultramafic (Del Moro et al., 1999). Therefore, in the Cima di Gagnone type–locality, the interplay between metapelites and ultramafic exerts a crucial first–order control to allow assemblage equilibrium during HT metamorphism and amphibolite–facies retrogression.

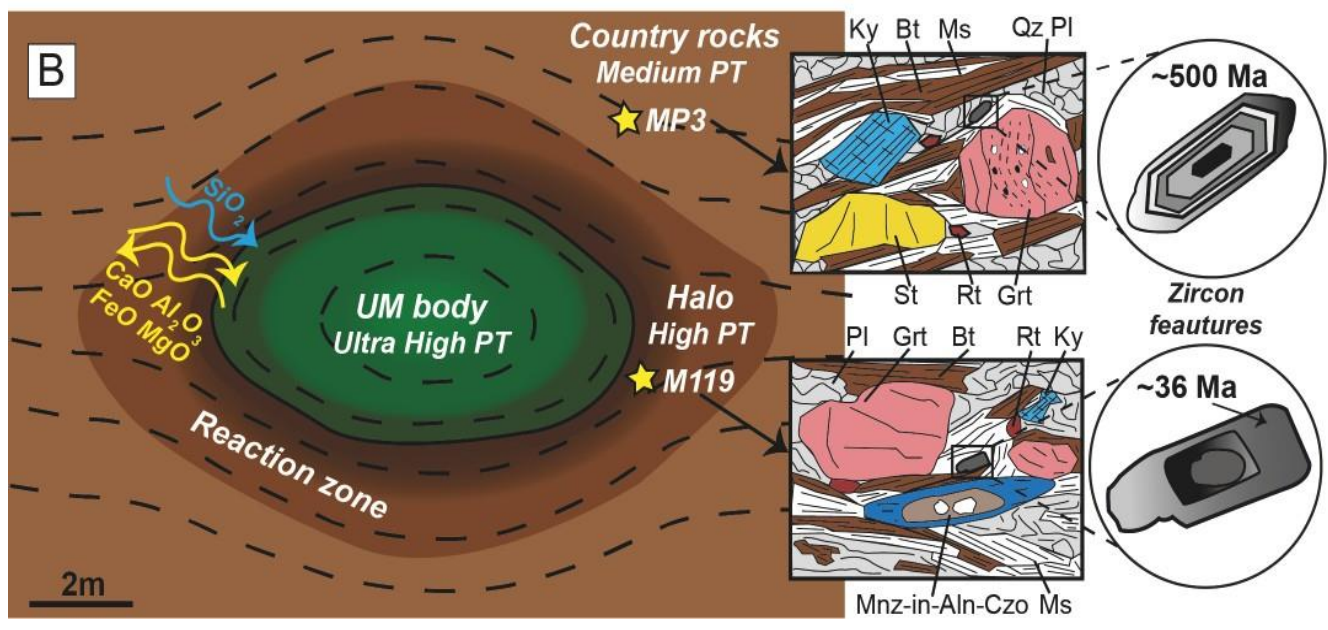
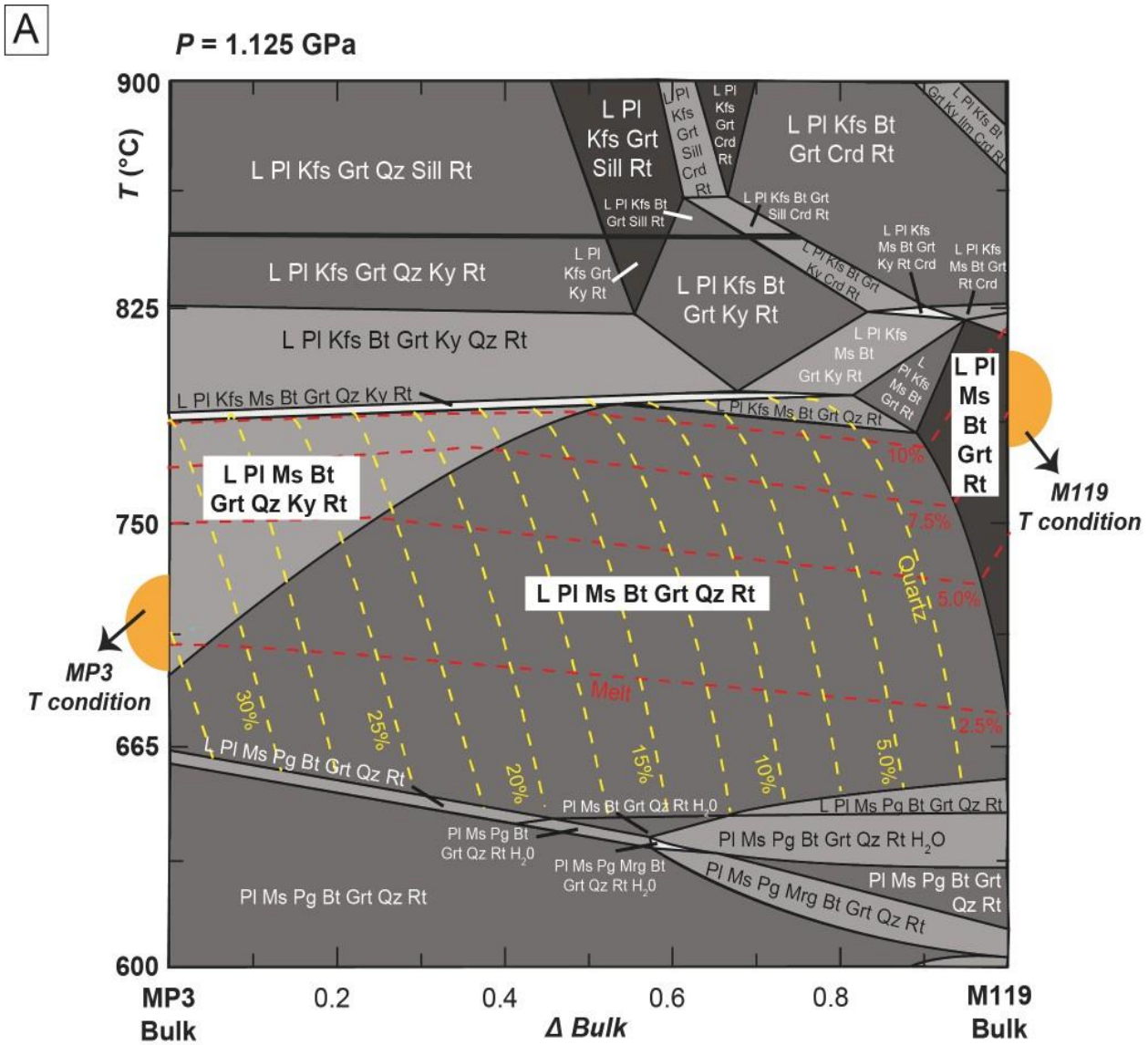


Fig. 4.15 – A) T-X pseudosection obtained varying the bulk composition (Δ Bulk) from Country rocks (i.e., MP3 sample) to the Halos (i.e., M119). The diagram is calculated in the system $\text{MnO-TiO}_2\text{-Na}_2\text{O-CaO-K}_2\text{O-FeO-MgO-Al}_2\text{O}_3\text{-SiO}_2\text{-H}_2\text{O}$. Diagram fields with bold characters and white background indicate the interesting mineral assemblages of the studied samples; orange circles indicate the P-T conditions recorded by the samples and already shown in the P-T pseudosection (Figs. 11, 12); dash lines indicate the relative isomodes (vol.%) for quartz (yellow dashed lines) and melt (red dashed lines). B) Schematic sketch of the reaction zone (brown zoned band) characterized by the interaction between UM and Halos. Dashed lines represent the outcrop foliation. Arrows indicate the direction of chemical component mobility (SiO_2 , CaO, Al_2O_3 , FeO, MgO). Stars indicate the representative samples location (i.e., MP3, M119); in the sketches on the right the relative mineral assemblages and zircon textures are reported.

4.10.5 Inferences on the exhumation of Cima Lunga–Adula nappe

Let us discuss the implications of our findings on the geodynamic history of the tectonic nappes including (U)HP rocks. The heterogeneous metamorphism of the Cima di Gagnone rocks is, in fact, a paradigm of how large temperature and pressure differentials (up to ~2 GPa and ~150°C) coexist in a single tectonic unit. Such differences in the metamorphic records have been mainly interpreted as: i) the result of late tectonic coupling within lithospheric mélanges (e.g., Trommsdorff, 1990; Engi et al., 2001; Berger et al., 2008; Scambelluri et al., 2015), or ii) differential, compositionally–controlled re–equilibration of a coherent tectonic unit that experienced uniform (U)HP and HT conditions (e.g., Schmidt et al., 1996; Herwartz et al., 2011; Cavargna–Sani et al., 2014).

An alternative model considers the differences in the metamorphic record as generated by local deviations of P and T from lithostatic conditions and orogenic thermal gradient due to tectonic overpressure and shear heating, respectively (Pleuger and Podladchikov, 2014; Schmalholz et al., 2014; Wheeler, 2014; Schenker et al., 2015; Casini and Maino, 2018; Moulas et al., 2019).

The distinct P – T paths observed within the Cima di Gagnone rocks (Fig. 4.14) apparently fits the predicted heterogeneity of a tectonic channel. However, the absence of any structures driving the late coupling between UM and metasediments (e.g., ultramylonite or cataclasite) excludes the physical validity of this process. On the contrary, the deformation features of UM and metasediments indicate that Cima di Gagnone rocks experienced intense shear strain as a coherent tectonic unit (Maino et al., 2021). Besides, the spatial distribution of HP–HT relicts found in this work is not random, as expected in a tectonic channel. Metasediments show, instead, a systematic metamorphic gradient with higher P – T conditions close to the UM lenses. The consistency of the internal structure of the Cima Lunga–Adula nappe complex is further supported by several studies on its structural record (e.g., Nagel, 2008; Herwartz et al., 2011; Cavargna–Sani et al., 2014; Pleuger and Podladchikov, 2014; Sandmann et al., 2014; Maino et al., 2021).

Another explanation would be that both metasediments and mafic/ultramafic rocks experienced the same metamorphic conditions, though the degree of preservation of the HP/HT assemblage changes in relation with the reactivity of rocks with different composition. It is, in fact, well described in literature that the ultramafic/mafic rocks are more retentive to peak conditions (Heinrich, 1982; Griffin, 1987; Rubie, 1990), while metasediments are generally rheologically weaker at mid crustal

conditions and record the retrogressive path more readily (Gardner et al., 2017). Thus, a heterogeneous metamorphic record is commonly interpreted as either a lack of equilibrium during the prograde path or the result of different rheological response to the metasomatic events during the exhumation. However, several lines of evidence argue against this model:

(i) Our results demonstrate that the retentive minerals, such as garnet and zircon, well preserve at least the HT phase, if any. The chemical signals of HT conditions strongly affect the mineral assemblage. Very different peak temperatures are recorded among, but also within, mafic, ultramafic rocks and metasediments (Fig. 4.14). Retrogressive paths cannot justify these different records. Our preliminary geochronological results confirm that some metasediments experienced HT conditions, which cannot be temporally associated with a late Barrovian stage.

(ii) On the other hand, the mica-rich composition of the metasediments does not account for slow reaction kinetics preventing a broad equilibration of the mineral assemblage during the burial. Furthermore, large part of the metasediments (Country rocks) preserves two garnet generations related to two different tectono-metamorphic stages, the first of which predates the metamorphic peak. Since both textures developed at medium pressure/temperature conditions, we argue that the HP-HT conditions were developed only in the Halos, rather than only here preserved.

(iii) Retrogressive metasomatism as a mechanism deleting the HP-HT record does not explain why the highest conditions are preserved only close to the UM lenses. It may be obviously supposed that the lenses acted as a physical protection from post-peak strain and chemical re-equilibration. However, studied samples were collected close to metasomatized rims. Therefore, the highest P - T record are preserved right where important fluid-rock interaction occurred during all the tectono-metamorphic history. Fluids are powerful vehicles for the metasomatic processes and the lenses did not provide any protection from these processes.

(iv) It is shown that local fluid-rock interaction resulted in localized partial melting of metasediments. However, the greater part of the unit avoids massive migmatization excluding extensive melting of mica-rich rocks, as would be expected during isothermal decompression at HT conditions (e.g., Henrich, 1982).

(v) Finally, rocks of a coherent (U)HP-HT unit should be dehydrated during the prograde path to avoid extensive melting. This assumption is at odds with the evidence of fluid-rock interactions at HP-

HT since are the metasediments that provided the fluids (the ultramafics are volumetrically too small for this).

Overall, petrological and geochronological data demonstrate that different rocks attained very different P - T conditions during a common tectonic evolution. These P - T differences largely exceed the analytical uncertainties and are marked by unmistakable evidences such as the distribution of migmatites and the zircon resetting that overcome any possible overinterpretation of thermobarometric estimations or thermodynamic modelling. Differential mineral assemblage equilibria linked to either slow kinetics or efficient retrogression fail to explain such P - T variations. We show that this heterogeneity cannot be explained with the current tectonic models proposed for this geodynamic context, including the tectonic *mélange* or a heterogeneous re-equilibration of a coherent tectonic unit that experienced uniform (U)HP and HT conditions. We highlight that heterogeneous metamorphism is locally developed, rather than locally preserved. On the other hand, the rocks that did not record HP-HT conditions did not even experience them. Different local equilibria are related to the proximity to the UM, suggesting that the rheological and chemical contrasts between UM and surrounding rocks had a significant role in modifying the local metamorphic gradients.

A possible solution of this paradox may be found if the heterogeneous metamorphism is linked with local pressure and temperature deviations associated with rheological heterogeneities (Mancktelow 1993; Pleuger and Podladchikov, 2014; Schmalholz et al., 2014; Gerya, 2015; Schenker et al., 2015; Casini and Maino, 2018; Luisier et al., 2019). A complete dissertation on the possible link between deformation and metamorphism is beyond the aim of this work. We highlight here that our study shows that variable temperature, and pressure metamorphic records might occur in correspondence of sharp interfaces between rocks with high viscosity contrast. Our findings agree with the predictions of theoretical models showing that significant pressure deviations may be concentrated in strong inclusions, as well as at the interface between strong and weak domains (Schmid, 2002; Schmid and Podladchikov, 2003; Mancktelow, 1993; 2008; Moulas et al., 2014; Casini and Maino 2018). Accordingly, the related P - T paths should indicate higher pressure conditions within the stronger lenses, as well as in the metasediments at the contact or trapped between groups of UM inclusions (Halos). In such a scenario, the pressure recorded in the matrix – Country rocks – should be most representative of the ambient pressure, i.e., depth at the time of metamorphism.

As regards the temperature record, our study shows that all the Cima di Gagnone rocks experienced higher temperature with respect to the neighbouring Maggia and Simano nappes ($\Delta T \sim 50\text{--}100^\circ\text{C}$). Halos around the UM record further higher temperature with an increase up to 100°C . Such a big differential temperature requires the summation of several processes. Advection of exotic hot fluids or fast exhumation may contribute to increase the temperature, as well as shear heating. However, dissipation of viscous heat during deformation requires high strain rate and/or high stress to generate a recordable signal. Moreover, shear heating may be effective only if it is extremely localized (e.g., Platt, 2015; Maino et al., 2015; Maino et al., 2020). We note that the absence of significant ultra-mylonites or cataclasites structures precludes a clear localisation of heat within well recognizable structures. It seems thus unlikely that shear heating alone may account for the anomalous signal recorded by the Cima di Gagnone rocks. Overall, although the overpressure + shear heating mechanism is more adequate to account at least part of the recorded P - T variations, also this model fails to convincingly explain the whole metamorphic record.

Additional explanations for the HT-HP records may be found from unconventional models that consider large effects of differential stress on mineral phase equilibria, causing the offset up or down of phase transformation (e.g., Wheeler, 2014, 2018, 2020). Overall, information from the relationships between thermal budget and deformation are still lacking and further investigations are needed to present a complete model.

4.11 Conclusions

New data from the (U)HP-HT site of Cima di Gagnone of the Central Alps are presented. We discuss the interference between ultramafic lenses and the enveloping siliciclastic metasediments based on structural observations, petrological and microstructural analyses, and thermodynamic modelling. We documented that, even though metasediments share the same structural evolution with UM, large differences in the P - T paths are recorded: while the large part of the unit (Country rocks) experienced $P < 1.2$ and $T < 700^\circ\text{C}$, a few occurrences (Halos) preserve higher conditions of $1.3\text{--}1.7$ GPa and $750\text{--}850^\circ\text{C}$. These estimates approach the P - T peak conditions experienced by the mafic/ultramafics ($1.5\text{--}3.2$ GPa, $740\text{--}850^\circ\text{C}$). These pressure and temperature deviations are not randomly distributed in the unit but occur at the sharp interfaces between rocks with high viscosity contrast.

Petrological and geochemical evidences further shown that fluids migrated throughout the interface between metasediments and ultramafic lenses during this HT stage, resulting in wet melting and a discontinuous metasomatic zone at the rim of the ultramafic lenses and adjacent to the lenses within the metasedimentary country rocks. Preliminary U–Pb zircon data confirm that, while the large part of the metasediments generally records a pre–Alpine signal, zircon grains from these metasomatic Halos have been full re–equilibrated during the early stage of the Alpine exhumation (~36 Ma), synchronously with the (U)HP–HT conditions recorded by the UM. The significant cycles of dehydration/re–hydration which occurred between metapelites and UM exerted a crucial first–order control to allow locally assemblage equilibrium during HT metamorphism in the Cima di Gagnone type–locality.

The large range of P – T estimates among and within the UM and metasediments vary in pressure by up to 2 GPa and temperature by up to ~160°C, although different P – T paths converge to the common amphibolite–facies re–equilibration. This heterogeneity cannot be explained with the current tectonic models proposed for this geodynamic context, which consider tectonic mixing, non-homogeneous retrogression or lack of equilibration of mineral assemblages. We highlight that heterogeneous metamorphism is locally developed, rather than locally preserved. Different local equilibria are related to the proximity to the UM, suggesting that the rheological and chemical contrasts between UM and surrounding rocks had a significant role in modifying the local metamorphic gradients. Such deviations may be theoretically explained as produced by the deformation, via tectonic overpressure and/or shear heating. However, these mechanisms alone provide an insufficient description of the recorded pressure and, particularly, temperature excursions, unless extreme unlikely conditions are assumed.

Even a complete explanation of these findings is far from our present knowledge, what is clear is that the chemical gradient between compositionally different lithologies combined with fluids circulations result in coexisting heterogeneous metamorphic equilibria, which are not representative of the ambient conditions. In these cases, caution should be used in converting estimations of metamorphic pressure into burial depth. We finally note that finding the relative contribution of the multiple mechanisms controlling the thermal budget of deforming rocks represents the currently most significant challenge for such heterogeneous (U)HP–HT occurrences.

4.12 References

- Aravadinou, E. and Xypolias P., (2017). Evolution of a passive crustal-scale detachment (Syros, Aegean region): Insights from structural and petrofabric analyses in the hanging-wall. *J. Struct. Geol.*, 103: 57-74.
- Allaz, J., Maeder, X., Vannay, J.-C., and Steck, A. (2005). Formation of aluminosilicate-bearing quartz veins in the Simano nappe (Central Alps): Structural, thermobarometric and oxygen iso-tope constraints. *Schweizerische Mineralogische und Petrographische Mitteilungen*, 85, 191-214.
- Arzi, A.A. (1978). Critical phenomena in the rheology of partially melted rocks. *Tectonophysics*, 44, 173-184.
- Becker, H. (1993). Garnet peridotite and eclogite Sm-Nd mineral ages from the Lepontine dome (Swiss Alps): New evidence for Eocene high-pressure metamorphism in the central Alps. *Geology*, 21(7), 599-602.
- Berger, A., and Bousquet, R. (2008). Subduction-related metamorphism in the Alps: review of iso-topic ages based on petrology and their geodynamic consequences. Geological Society, London, Special Publications, 298(1), 117-144.
- Berger, A., Schmid, S. M., Engi, M., Bousquet, R., and Wiederkehr, M. (2011). Mechanisms of mass and heat transport during Barrovian metamorphism: A discussion based on field evidence from the Central Alps (Switzerland/Northern Italy). *Tectonics*, 30(1).
- Bestmann, M., and Prior, D. J. (2003). Intragranular dynamic recrystallization in naturally deformed calcite marble: Diffusion accommodated grain boundary sliding as a result of subgrain rotation recrystallization. *Journal of Structural Geology*, 25(10), 1597-1613.
- Bhattacharya, A., Mohanty, L., Maji, A., Sen, S. K., and Raith, M. (1992). Non-ideal mixing in the phlogopite-annite binary: constraints from experimental data on Mg-Fe partitioning and a reformulation of the biotite-garnet geothermometer. *Contributions to Mineralogy and Petrology*, 111, 8-93.
- Boston, K. R., Rubatto, D., Hermann, J., Engi, M., and Amelin, Y. (2017). Geochronology of accessory allanite and monazite in the Barrovian metamorphic sequence of the Central Alps, Switzerland. *Lithos*, 286, 502-518.
- Brodie, K. H., and Rutter, E. H. (1985). On the relationship between deformation and metamorphism, with special reference to the behaviour of basic rocks. In *Metamorphic reactions*, 138-179. Springer, New York, NY.
- Brouwer, F. M., Burri, T., Engi, M., and Berger, A. (2005). Eclogite relics in the Central Alps: PT evolution, Lu-Hf ages and implications for formation of tectonic mélange zones. *Schweizerische Mineralogische und Petrographische Mitteilungen*, 85, 147-174.
- Buckman, S., and Ashley, P. (2010). Silica-carbonate (listwanites) related gold mineralisation associated with epithermal alteration of serpentinite bodies. Conference Paper, NEO 2010.

- Burg, J. P., and Gerya, T. V. (2005). The role of viscous heating in Barrovian metamorphism of collisional orogens: thermomechanical models and application to the Lepontine Dome in the Central Alps. *Journal of Metamorphic Geology*, 23(2), 75–95.
- Büttner, S. H. (2012). Rock Maker: an MS Excel™ spreadsheet for the calculation of rock compositions from proportional whole rock analyses, mineral compositions, and modal abundance. *Mineralogy and Petrology*, 104(1–2), 129–135.
- Caddick, M. J., Konopásek, J., and Thompson, A. B. (2010). Preservation of Garnet Growth Zoning and the Duration of Prograde Metamorphism. *Journal of Petrology*, 51(11), 2327–2347.
- Casini, L., and Maino, M. (2018). 2D–thermo–mechanical modelling of spatial P–T variations in heterogeneous shear zones. *Italian Journal of Geosciences*, 137(2), 272–282.
- Cavargna–Sani, M., Epard, J. L., and Steck, A. (2014). Structure, geometry and kinematics of the northern Adula nappe (Central Alps). *Swiss Journal of Geosciences*, 107(2–3), 135–156.
- Chopin, C. (1984). Coesite and pure pyrope in high–grade blueschists of the Western Alps: a first record and some consequences. *Contributions to Mineralogy and Petrology*, 86(2), 107–118.
- Coggon, R., and Holland, T. J. B. (2002). Mixing properties of phengitic micas and revised garnet phengite thermobarometers. *Journal of Metamorphic Geology*, 20(7), 683–696.
- Connolly, J. A. D. (2005). Computation of phase equilibria by linear programming: A tool for geodynamic modeling and its application to subduction zone decarbonation. *Earth and Planetary Science Letters*, 236(1–2), 524–541.
- Corfu, F., Hanchar, J. M., Hoskin, P. W., and Kinny, P. (2003). Atlas of zircon textures. *Reviews in Mineralogy and Geochemistry*, 53(1), 469–500.
- Dobrzhinetskaya, L., Green, H. W., and Wang, S. (1996). Alpe Arami: a peridotite massif from depths of more than 300 kilometers. *Science*, 271(5257), 1841–1845.
- Dal Vesco, E. (1953). Genesi e metamorfosi delle rocce basiche e ultrabasiche nell’ambiente mesozonale dell’orogene pennidico. *Schweizerische Mineralogische und Petrographische Mitteilungen*, 33, 173–480.
- Dell’Angelo, L. N. and Tullis, J. (1988). Experimental deformation of partially melted granitic aggregates. *Journal of Metamorphic Geology*, 6, 495–515.
- Del Moro, A., Martin, S., Prosser, G., 1999. Migmatites of the Ulten zone (NE Italy), record of melt transfer in deep crust. *Journal of Petrology* 40 (12), 1803–1826.
- Diener J.F.A., Powell R., White R.W., Holland T.J.B. (2007). A new thermodynamic model for clino- and orthoamphiboles in the system $\text{Na}_2\text{O}-\text{CaO}-\text{FeO}-\text{MgO}-\text{Al}_2\text{O}_3-\text{SiO}_2-\text{H}_2\text{O}-\text{O}$. *Journal of Metamorphic Geology*, 25, 631–56.
- Engi, M., Todd, C. S., and Schmatz, D. R. (1995). Tertiary metamorphic conditions in the eastern Lepontine Alps. *Schweizerische Mineralogische und Petrographische Mitteilungen*, 75, 347–369.
- Engi, M., Berger, A., and Roselle, G. T. (2001). Role of the tectonic accretion channel in collisional orogeny. *Geology*, 29(12), 1146.

- Ernst, W. G. (1978). Petrochemical study of lherzolitic rocks from the western alps. *Journal of Petrology*, 19(3), 341–392.
- Etheridge, M. A., Wall, V. J., and Vernon, R. H. (1983). The role of the fluid phase during regional metamorphism and deformation. *Journal of Metamorphic Geology*, 1(3), 205–226.
- Evans, B. W., and Trommsdorff, V. (1974). Stability of Enstatite + Talk, and CO₂–Metasomatism of Metaperidotite, Val d’Efra, Lepontine Alps. *American Journal of Sciences*, 274, 274–296.
- Evans, B. W., and Trommsdorff, V. (1978). Petrogenesis of garnet lherzolite, Cima di Gagnone, Lepontine Alps. *Earth and Planetary Science Letters*, 40(3), 333–348.
- Evans, B. W., Trommsdorff, V., and Richter, W. (1979). Petrology of an eclogite–metarodingite suite at Cima di Gagnone, Ticino, Switzerland. *American Mineralogist*, 64(1–2), 15–31.
- Frese, K., Trommsdorff, V., and Kuze, K. (2003). Olivine [100] normal to foliation: lattice preferred orientation in prograde garnet peridotite formed at high H₂O activity, Cima di Gagnone (Central Alps). *Contributions to Mineralogy and Petrology*, 145, 75–86.
- Frey, M., Hunziker, J. C., Frank, W., Bocquet, J., Dal Piaz, G., Jager, E., and Niggli E. (1974). Alpine Metamorphism of the Alps. A Review, 54.
- Frezzotti, M. L., Selverstone, J., Sharp, Z. D., and Compagnoni, R. (2011). Carbonate dissolution during subduction revealed by diamond-bearing rocks from the Alps. *Nature Geoscience*, 4(10), 703–706.
- Früh–Green, G. L. (1987). Stable isotope investigations of fluid rock of eclogite–facies rocks: case studies from the Swiss and Italian Alps. PhD Thesis, ETH Zurich.
- Gahlan, H. A., Azer, M. K., and Asimow, P. D. (2018). On the relative timing of listwaenite formation and chromian spinel equilibration in serpentinites. *American Mineralogist: Journal of Earth and Planetary Materials*, 103(7), 1087–1102.
- Gardner, R., Piazzolo, S., Evans, L., and Daczko, N. (2017). Patterns of strain localization in heterogeneous, polycrystalline rocks—a numerical perspective. *Earth and Planetary Science Letters*, 463, 253–265.
- Gebauer, D. (1994). A P–T–t path for some high–pressure ultramafic/ mafic rock associations and their felsic country rocks based on SHRIMP–dating of magmatic and metamorphic zircon domains. In Example: Central Swiss Alps. Extended abstract version for 16th general meeting of IMA, Pisa, Italy (pp. 4–9).
- Gebauer, D. (1996). A P–T–t path for a (ultra?) high–pressure ultramafic/ mafic rock associations and their felsic country rocks based on SHRIMP–dating of magmatic and metamorphic zircon domains. Example: Alpe Arami (Central Swiss Alps). In S. Basu, A. and Hart (Ed.), *Earth Processes: Reading the Isotopic Code*, 301–330.
- Gebauer, D. (1999). Alpine geochronology of the Central Alps and Western Alps: new constraints for a complex geodynamic evolution. *Schweizerische Mineralogische und Petrographische Mitteilungen*, 79, 191–208.
- Gerya, T. (2015). Tectonic overpressure and underpressure in lithospheric tectonics and metamorphism.

- Journal of Metamorphic Geology, 33(8), 785–800.
- Gyomlai, T., Agard, P., Marschall, H. R., Jolivet, L., and Gerdes, A. (2021). Metasomatism and deformation of block-in-matrix structures in Syros: The role of inheritance and fluid-rock inter-actions along the subduction interface. *Lithos*, 105996.
- Godard, G., Martin, S., Prosser, G., Kienast, J. R., and Morten, L. (1996). Variscan migmatites, eclogites and garnet-peridotites of the Ulten zone, Eastern Austroalpine system. *Tectonophysics*, 259(4), 313-341.
- Grasemann, B., and Dabrowski, M. (2015). Winged inclusions: Pinch-and-swell objects during high-strain simple shear. *Journal of Structural Geology*, 70, 78–94.
- Green, T. H., and Hellman, P. L. (1982). Fe–Mg partitioning between coexisting garnet and phengite at high pressure, and comments on a garnet–phengite geothermometer. *Lithos*, 15(4), 253–266.
- Gregory, C. J., Rubatto, D., Hermann, J., Berger, A., and Engi, M. (2012). Allanite behaviour during incipient melting in the southern Central Alps. *Geochimica et Cosmochimica Acta*, 84, 433–458.
- Griffin, W. L., and O'Reilly, S. Y. (1987). Is the continental Moho the crust–mantle boundary? *Geology*, 15(3), 241–244.
- Grond, R., Wahl, F., and Pfiffner, M. (1995). Mehrphasige alpine Deformation und Metamorphose in der Nördlichen Cima–Lunga–Einheit, Zentralalpen (Schweiz) = Polyphase Alpine deformation and metamorphism in the northern Cima Lunga unit, Central Alps (Switzerland). *Schweizerische Mineralogische und Petrographische Mitteilungen*, 75, 371–386.
- Heinrich, C. A. (1982). Kyanite-eclogite to amphibolite facies evolution of hydrous mafic and pelitic rocks, Adula nappe, Central Alps. *Contributions to Mineralogy and Petrology*, 81(1), 30-38.
- Heinrich, C. A. (1986). Eclogite facies regional metamorphism of hydrous mafic rocks in the Central Alpine Adula Nappe. *Journal of Petrology*, 27(1), 123-154.
- Hentschel, F., Janots, E., Trepmann, C. A., Magnin, V., and Lanari, P. (2020). Corona formation around monazite and xenotime during greenschist–facies metamorphism and deformation. *European Journal of Mineralogy*, 32(5), 521–544.
- Hermann, J., Rubatto, D., and Trommsdorff, V. (2006). Sub–solidus Oligocene zircon formation in garnet peridotite during fast decompression and fluid infiltration (Duria, Central Alps). *Mineralogy and Petrology*, 88, 181–206.
- Herron, M. M. (1988). Geochemical classification of terrigenous sands and shales from core or log data. *Journal of Sedimentary Research*, 58(5), 820–829.
- Herwartz, D., Nagel, T. J., Münker, C., Scherer, E. E., and Froitzheim, N. (2011). Tracing two orogenic cycles in one eclogite sample by Lu–Hf garnet chronometry. *Nature Geoscience*, 4(3), 178–183.
- Hobbs, B. E., and Ord, A. (2017). Pressure and equilibrium in deforming rocks. *Journal of Metamorphic Geology*, 35(9), 967–982.
- Hodges, K. V., and Crowley, P. T. (1985). Error estimation and empirical geothermobarometry for pelitic

systems. *American Mineralogist*, 70(7–8), 702–709.

Hoisch, T. D. (1990). Empirical calibration of six geobarometers for the mineral assemblage quartz+ muscovite+ biotite+ plagioclase+ garnet. *Contributions to Mineralogy and Petrology*, 104(2), 225–234.

Holdaway, M. J. (2000). Application of new experimental and garnet Margules data to the garnet–biotite geothermometer. *American Mineralogist*, 85(7–8), 881–892.

Holdaway, M. J. (2001). Recalibration of the GASP geobarometer in light of recent garnet and plagioclase activity models and versions of the garnet–biotite geothermometer. *American Mineralogist*, 86(10), 1117–1129.

Holland, T. J. B., and Powell, R. (1985). An internally consistent thermodynamic dataset with uncertainties and correlations: 2. Data and results. *Journal of Metamorphic Geology*, 3(4), 343–370.

Holland, T. J. B., and Powell, R. (1998). An internally consistent thermodynamic data set for phases of petrological interest. *Journal of Metamorphic Geology*, 16(3), 309–343.

Hunziker, J. C., Desmons, J., and Hurford A.J. (1992). Thirty–two years of geochronological work in the Central and Western Alps: a review on seven maps. *Mémoires de Géologie*, (13). Lausanne.

Jackson, S. E., Pearson, N. J., Griffin, W. L., and Belousova, E. A. (2004). The application of laser ablation–inductively coupled plasma–mass spectrometry to in situ U–Pb zircon geochronology. *Chemical Geology*, 211(1–2), 47–69.

Jamtveit, B., and Austrheim, H. (2010). Metamorphism: the role of fluids. *Elements*, 6(3), 153–158.

Janots, E., Engi, M., Rubatto, D., Berger, A., Gregory, C., Rahn, M., (2009). Metamorphic rates in collisional orogeny from in situ allanite and monazite dating. *Geology*, 37(1), 11–14.

Krogh, E. J., and Råheim, A. (1978). Temperature and pressure dependence of Fe–Mg partitioning between garnet and phengite, with particular reference to eclogites. *Contributions to Mineralogy and Petrology*, 66(1), 75–80.

Kuwahara, M. K. S. M. K., Hachimura, K., Eiho, S., and Kinoshita, M. (1976). Processing of Riangiocardigraphic images. In *Digital processing of biomedical images* (pp. 187–202). Springer, Boston, MA.

Kwon, S., Samuel, V. O., Song, Y., Kim, S. W., Park, S. I., Jang, Y., and Santosh, M. (2020). Eclogite resembling metamorphic disequilibrium assemblage formed through fluid-induced metasomatic reactions. *Scientific reports*, 10(1), 1–10.

Lanari, P., and Engi, M. (2017). Local bulk composition effects on metamorphic mineral assemblages. *Reviews in Mineralogy and Geochemistry*, 83(1), 55–102.

Langone, A., Braga, R., Massonne, H. J., and Tiepolo, M. (2011). Preservation of old (prograde metamorphic) U–Th–Pb ages in unshielded monazite from the high-pressure paragneisses of the Variscan Ulten Zone (Italy). *Lithos*, 127(1–2), 68–85.

Liati, A. and Gebauer, D. (1999). Constraining the prograde and retrograde P–T–t path of Eocene HP rocks by SHRIMP dating of different zircon domains: inferred rates of heating, burial, cooling and exhumation for central Rhodope, northern Greece. *Contributions to Mineralogy and Petrology*, 135,

340–354.

- Liati, A., Gebauer, D., and Fanning, C. M. (2009). Geochronological evolution of HP metamorphic rocks of the Adula nappe, Central Alps, in pre–Alpine and Alpine subduction cycles. *Journal of the Geological Society*, 166, 797–810.
- Liou, J. G., Tsujimori, T., Zhang, R. Y., Katayama, I., and Maruyama, S. (2004). Global UHP met-amorphism and continental subduction/collision: the Himalayan model. *International Geology Review*, 46(1), 1–27.
- Luisier, C., Baumgartner, L., Schmalholz, S. M., Siron, G., and Vennemann, T. (2019). Metamorphic pressure variation in a coherent Alpine nappe challenges lithostatic pressure paradigm. *Nature communications*, 10(1), 1–11.
- Maino, M., Casini, L., Ceriani, A., Decarlis, A., Di Giulio, A., Seno, S., Setti, M., and Stuart, F. M. (2015). Dating shallow thrusts with zircon (U–Th)/He thermochronometry—The shear heating connection. *Geology*, 43(6), 495–498.
- Maino, M., Casini, L., Boschi, C., Di Giulio, A., Setti, M., and Seno, S. (2020). Time–dependent heat budget of a thrust from geological records and numerical experiments. *Journal of Geo-physical Research: Solid Earth*, 125(3), e2019JB018940.
- Maino, M., Adamuszek, M., Schenker, F. L., Seno, S., and Dabrowski, M. (2021). Sheath fold development around deformable inclusions: Integration of field-analysis (Cima Lunga unit, Central Alps) and 3D numerical models. *Journal of Structural Geology*, 144, 104255.
- Mancktelow, N. S. (1993). Tectonic overpressure in competent mafic layers and the development of isolated eclogites. *Journal of Metamorphic Geology*, 11 (6), 801–812.
- Mancktelow, N. S. (2008). Tectonic pressure: Theoretical concepts and modelled examples. *Lithos*, 103(1–2), 149–177.
- Marocchi, M., Mair, V., Tropper, P., and Bargossi, G. M. (2009). Metasomatic reaction bands at the Mt. Hochwart gneiss–peridotite contact (Ulten Zone, Italy): insights into fluid–rock interaction in subduction zones. *Mineralogy and Petrology*, 95(3–4), 251.
- Massonne, H.–J., and Schreyer, W. (1987). Phengite geobarometry based on the limiting assemblage with K–feldspar, phlogopite, and quartz. *Contributions to Mineralogy and Petrology*, 96, 212–224.
- Maxelon, M., and Mancktelow, N. S. (2005). Three–dimensional geometry and tectonostratigraphy of the Pennine zone, Central Alps, Switzerland and Northern Italy. *Earth–Science Reviews*, 71(3–4), 171–227.
- McDonough, W. F., and Sun, S. S. (1995). The composition of the Earth. *Chemical Geology*, 120(3–4), 223–253.
- Moulas, E., Burg, J. P., and Podladchikov, Y. (2014). Stress field associated with elliptical inclusions in a deforming matrix: Mathematical model and implications for tectonic overpressure in the lithosphere. *Tectonophysics*, 631, 37–49.
- Moulas, E., Schmalholz, S. M., Podladchikov, Y., Tajčmanová, L., Kostopoulos, D., and Baumgartner,

- L. (2019). Relation between mean stress, thermodynamic, and lithostatic pressure. *Journal of Metamorphic Geology*, 37(1), 1–14.
- Nagel, T. J. (2008). Tertiary subduction, collision and exhumation recorded in the Adula nappe, central Alps. *Geological Society Special Publication*, 298(1), 365–392.
- Niggli, A., and Wondratschek, H. (1960). Eine Verallgemeinerung der Punktgruppen I. Die einfachen Kryptosymmetrien. *Zeitschrift für Kristallographie – New Crystal Structures*, 114(1–6), 215–231.
- Nimis, P., and Trommsdorff, V. (2001). Revised thermobarometry of Alpe Arami and other garnet peridotites from the Central Alps. *Journal of Petrology*, 42(1), 103–115.
- Passchier, C. W. (1988). Analysis of deformation paths in shear zones. *Geologische Rundschau*, 77(1), 309–318.
- Passchier, C. W., and Trouw, R. A. (2005). *Microtectonics*. Springer Science and Business Media.
- Pellegrino, L., Malaspina, N., Zanchetta, S., Langone, A., and Tumiatì, S. (2020). High pressure melting of eclogites and metasomatism of garnet peridotites from Monte Duria Area (Central Alps, N Italy): A proxy for melt-rock reaction during subduction. *Lithos*, 358, 105391.
- Petrini, K. and Podladchikov, Y. (2000). Lithospheric pressure–depth relationship in compressive regions of thickened crust. *Journal of Metamorphic Geology*, 18(1), 67–77.
- Pfeifer, H. R. (1981). A model for fluids in metamorphosed ultramafic rocks III. Mass transfer under amphibolite facies conditions in olivine-enstatite rocks of the Central Alps, Switzerland. *Bulletin de Minéralogie*, 104(6), 834–847.
- Pfeifer, H. R. (1987). A Model for Fluids in Metamorphosed Ultramafic Rocks: IV. Metasomatic Veins in Metaharzburgites of Cima di Gagnone, Valle Verzasca, Switzerland. In *Chemical Transport in Metasomatic Processes* (pp. 591–632). Springer Netherlands.
- Pfeifer, H. R., Colombi, A., Ganguin, J., Hunziker, J. C., Oberhänsli, R., and Santini, L. (1991). Relics of high–pressure metamorphism in different lithologies of the Central Alps, an updated inventory. *Schweizerische Mineralogische Und Petrographische Mitteilungen*, 71, 441–451.
- Pfiffner, M. (1999). *Genese der hochdruckmetamorphen ozeanischen Abfolge der Cima Lunga–Einheit (Zentralalpen)*. PhD Thesis, ETH Zurich.
- Pfiffner, M., and Trommsdorff, V. (1997). Evidence for high–pressure metamorphosed ophiocarbonate rocks, Cima di Gagnone, Central Alps. *Terra Nova*, 9(1), 26.
- Pfiffner, M., and Trommsdorff, V. (1998). The high–pressure ultramafic–mafic–carbonate suite of Cima Lunga–Adula, central Alps: excursions to Cima di Gagnone and Alpe Arami. *Schweizerische Mineralogische Und Petrographische Mitteilungen*, 78(2), 337–354.
- Philpotts, A., and Ague, J. (2009). *Principles of igneous and metamorphic petrology*. Cambridge University Press.
- Piazolo, S., and Passchier, C. W. (2002). Controls on lineation development in low to medium grade shear zones: a study from the Cap de Creus peninsula, NE Spain. *Journal of structural Geology*, 24(1), 25–44.

- Piazolo, S., Bestmann, M., Prior, D. J., and Spiers, C. J. (2006). Temperature dependent grain boundary migration in deformed–then–annealed material: Observations from experimentally deformed synthetic rocksalt. *Tectonophysics*, 427(1–4), 55–71.
- Piazolo, S., Belousova, E., La Fontaine, A., Corcoran, C., and Cairney, J. M. (2017). Trace element homogeneity from micron-to atomic scale: Implication for the suitability of the zircon GJ-1 as a trace element reference material. *Chemical Geology*, 456, 10–18.
- Piazolo, S., Daczko, N. R., Silva, D., and Raimondo, T. (2020). Melt–present shear zones enable intracontinental orogenesis. *Geology*, 48(7), 643–648.
- Pirajno, F. (2013). Effects of metasomatism on mineral systems and their host rocks: alkali metasomatism, skarns, greisens, tourmalinites, rodingites, black-wall alteration and listvenites. In *Metasomatism and the chemical transformation of rock* (pp. 203–251). Springer, Berlin, Heidelberg.
- Platt, J. P. (2015). Influence of shear heating on microstructurally defined plate boundary shear zones. *Journal of Structural Geology*, 79, 80–89.
- Pleuger, J., and Podladchikov, Y. Y. (2014). A purely structural restoration of the NFP20–East cross section and potential tectonic overpressure in the Adula nappe (Central Alps). *Tectonics*, 33, 656–685.
- Pognante, U. (1991). Petrological constraints on the eclogite– and blueschist facies metamorphism and P–T–t paths in the western Alps. *Journal of Metamorphic Geology*, 9(1), 5–17.
- Prior, D. J., Boyle, A. P., Brenker, F., Cheadle, M. C., Day, A., Lopez, G., Potts, G. J., Reddy, S., Spiess, R., Timms, N. E., Trimby, P., Wheeler, J. and Zetterstrom, L. (1999). The application of electron backscatter diffraction and orientation contrast imaging in the SEM to textural problems in rocks. *American Mineralogist*, 84(11–12), 1741–1759.
- Prior, D. J., Wheeler, J., Peruzzo, L., Spiess, R., and Storey, C. (2002). Some garnet microstructures: An illustration of the potential of orientation maps and misorientation analysis in microstructural studies. *Journal of Structural Geology*, 24(6–7), 999–1011.
- Regis, D., Cenko–Tok, B., Darling, J., and Engi, M. (2012). Redistribution of REE, Y, Th, and U at high pressure: Allanite–forming reactions in impure meta–quartzites (Sesia Zone, Western Italian Alps). *American Mineralogist*, 97(2–3), 315–328.
- Rubatto, D., and Hermann, J. (2007). Zircon behaviour in deeply subducted rocks. *Elements*, 3(1), 31–35.
- Rubatto, D., Hermann, J., Berger, A., Engi, M. (2009). Protracted fluid–induced melting during Barrovian metamorphism in the Central Alps. *Contributions to Mineralogy and Petrology*, 158, 703–722.
- Rubie, D. C. (1990). Role of kinetics in the formation and preservation of eclogites. Carswell, D. A., eds., *Eclogite Facies Rocks*, Glasgow, Scotland, Blackie, 111–140.
- Rütti, R. (2003). The tectono–metamorphic evolution of the northwestern Simano Nappe (Central Alps, Switzerland). PhD Thesis, ETH Zurich.
- Rutti, R., Maxelon, M., and Mancktelow, N. S. (2005). Structure and kinematics of the northern Simano nappe, Central Alps, Switzerland. *Eclogae Geologicae Helvetiae*, 98(1), 63–81.
- Sandmann, S., Nagel, T. J., Herwartz, D., Fonseca, R. O., Kurzwaski, R. M., Münker, C., and Froitzheim, N.

- (2014). Lu–Hf garnet systematics of a polymetamorphic basement unit: new evidence for coherent exhumation of the Adula Nappe (Central Alps) from eclogite-facies conditions. *Contributions to Mineralogy and Petrology*, 168(5), 1075.
- Sawyer, E. W. (2001). Melt segregation in the continental crust: Distribution and movement of melt in anatectic rocks. *Journal of Metamorphic Geology*, 19(3), 291–309.
- Sawyer, E. W. (2008). *Atlas of migmatites* (Vol. 9). NRC Research press.
- Scambelluri, M., and Philippot, P. (2001). Deep fluids in subduction zones. *Lithos*, 55(1–4), 213–227.
- Scambelluri, M., Pettke, T., Rampone, E., Godard, M., and Reusser, E. (2014). Petrology and trace element budgets of high-pressure peridotites indicate subduction dehydration of serpentized mantle (Cima di Gagnone, Central Alps, Switzerland). *Journal of Petrology*, 55(3), 459–498.
- Scambelluri, M., Pettke, T., and Cannaò, E. (2015). Fluid-related inclusions in Alpine high-pressure peridotite reveal trace element recycling during subduction-zone dehydration of serpentized mantle (Cima di Gagnone, Swiss Alps). *Earth and Planetary Science Letters*, 429, 45–59.
- Schenker, F. L., Schmalholz, S. M., Moulas, E., Pleuger, J., Baumgartner, L. P., Podladchikov, Y., Müntener, O. (2015). Current challenges for explaining (ultra)high-pressure tectonism in the Pennine domain of the Central and Western Alps. *Journal of Metamorphic Geology*, 33(8), 869–886.
- Schmalholz, S. M., Duretz, T., Schenker, F. L., and Podladchikov, Y. Y. (2014). Kinematics and dynamics of tectonic nappes: 2–D numerical modelling and implications for high and ultra-high pressure tectonism in the Western Alps. *Tectonophysics*, 631(C), 160–175.
- Schmalholz, S. M., Moulas, E., Plümpner, O., Myasnikov, A. V., and Podladchikov, Y. Y. (2020). 2D Hydro-Mechanical–Chemical modelling of (de)–hydration reactions in deforming heterogeneous rock: The periclase–brucite model reaction. *Geochemistry, Geophysics, Geosystems*, e2020GC009351.
- Schmid, D. W. (2002). *Finite and infinite heterogeneities under pure and simple shear*. ETH, Zurich.
- Schmid, D. W. and Podladchikov, Y. Y. (2003). Analytical solutions for deformable elliptical inclusions in general shear. *Geophysical Journal International*, 155(1), 269–288.
- Schmid, S. M., Pfiffner, O. A., Froitzheim, N., Schönborn, G., and Kissling, E. (1996). Geophysical–geological transect and tectonic evolution of the Swiss–Italian Alps. *Tectonics*, 15(5), 1036–1064.
- Schorn, S., (2018). Dehydration of metapelites during high–P metamorphism: The coupling between fluid sources and fluid sinks. *Journal of Metamorphic Geology*, 36(3), 369–391.
- Skemer, P., Katayama, I., Jiang, Z., and Karato, S. I. (2005). The misorientation index: Development of a new method for calculating the strength of lattice-preferred orientation. *Tectono-physics*, 411(1–4), 157–167.
- Skemer, P., and Katayama, I. (2006). Deformation fabrics of the Cima di Gagnone peridotite massif, Central Alps, Switzerland: evidence of deformation at low temperatures in the presence of water, 43–51.
- Sláma, J., Košler, J., Condon, D. J., Crowley, J. L., Gerdes, A., Hanchar, J. M., Horstwood, M. S.A., Morris, G. A., Nasdala, L., Norberg, N., Schaltegger, U., Schoene, B.R., Tubrett, M. N., and Whitehouse, M. J.

- (2008). Plešovice zircon – A new natural reference material for U–Pb and Hf isotopic microanalysis. *Chemical Geology*, 249(1–2), 1–35.
- Smith, D. C. (1984). Coesite in clinopyroxene in the Caledonides and its implications for geodynamics. *Nature*, 310(5979), 641–644.
- Smith, D. C. (1988). A review of the peculiar mineralogy of the Norwegian coesite-eclogite province, with crystal-chemical, petrological, geochemical and geodynamical notes and an extensive bibliography. In *Eclogites and eclogites-facies rocks* (pp. 1–206).
- Smith, J. R., Piazzolo, S., Daczko, N. R., and Evans, L. (2015). The effect of pre-tectonic reaction and annealing extent on behaviour during subsequent deformation: Insights from paired shear zones in the lower crust of Fiordland, New Zealand. *Journal of Metamorphic Geology*, 33(6), 557–577.
- Sobolev, N. V., and Shatsky, V. S. (1990). Diamond inclusions in garnets from metamorphic rocks: a new environment for diamond formation. *Nature*, 343(6260), 742–746.
- Spear, F. S. (1993). *Metamorphic Phase Equilibria and Pressure–Temperature–Time–Paths*. Mineralogical Society of America, 799.
- Steck, A., Della Torre, F., Keller, F., Pfeifer, H. R., Hunziker, J., and Masson, H. (2013). Tectonics of the Lepontine Alps: Ductile thrusting and folding in the deepest tectonic levels of the Central Alps. *Swiss Journal of Geosciences*, 106(3), 427–450.
- Steck, A., Epard, J. L., & Masson, H. (2019). The Maggia nappe: an extruding sheath fold basement nappe in the Lepontine gneiss dome of the Central Alps. *International Journal of Earth Sciences*, 108(8), 2429–2442.
- Taylor, S. R., and McLennan, S. M. (1985). *The continental crust: its composition and evolution*. Blackwell, Oxford (1985), p. 312
- Thompson, J. J. B. (1957). The graphical analysis of mineral assemblages in pelitic schists. *American Mineralogist: Journal of Earth and Planetary Materials*, 42(11–12), 842–858.
- Todd, C. S., and Engi, M. (1997). Metamorphic field gradients in the Central Alps. *Journal of Metamorphic Geology*, 15(4), 513–530.
- Tommasi, A., and Vauchez, A. (1997). Continental-scale rheological heterogeneities and complex intraplate tectono-metamorphic patterns: insights from a case-study and numerical models. *Tectonophysics*, 279(1–4), 327–350.
- Trommsdorff, V. (1990). Metamorphism and tectonics in the Central Alps: The Alpine lithospheric mélange of Cima Lunga and Adula – Search results – Pascal and Francis Bibliographic Databases. *Memorie della Società Geologica Italiana*, 45, 39–49.
- Tumiati, S., Thöni, M., Nimis, P., Martin, S., and Mair, V. (2003). Mantle–crust interactions during Variscan subduction in the Eastern Alps (Nonsberg–Ulten zone): geochronology and new petrological constraints. *Earth and Planetary Science Letters*, 210(3–4), 509–526.
- Tumiati, S., Godard, G., Martin, S., Klötzli, U., and Monticelli, D. (2007). Fluid-controlled crustal metasomatism within a high-pressure subducted mélange (Mt. Hochwart, Eastern Italian Alps).

- Lithos, 94(1–4), 148–167.
- Tumiati, S., Zanchetta, S., Pellegrino, L., Ferrario, C., Casartelli, S., and Malaspina, N. (2018). Granulite-facies overprint in garnet peridotites and kyanite eclogites of Monte Duria (Central Alps, Italy): clues from srilankite-and sapphirine-bearing symplectites. *Journal of Petrology*, 59(1), 115–151.
- Van Achterberg, E., Ryan, C. G., and Griffin, W. L. (2001). GLITTER Version 4 user's manual online interactive data reduction for the LA-ICPMS microprobe; Macquarie Research Ltd. North Ryde, NSW, Australia, 71.
- Wheeler, J., (2014). Dramatic effects of stress on metamorphic reactions. *Geology*, 42(8), 647–650.
- Vermeesch, P. (2018). IsoplotR: a free and open toolbox for geochronology. *Geoscience Frontiers*, 9, 1479–1493.
- Wang, X., Liou, J. G., and Mao, H. K. (1989). Coesite-bearing eclogite from the Dabie Mountains in central China. *Geology*, 17(12), 1085–1088.
- Wheeler, J. (2018). The effects of stress on reactions in the Earth: sometimes rather mean, usually normal, always important. *Journal of Metamorphic Geology*, 36(4), 439–461.
- Wheeler, J. (2020). A unifying basis for the interplay of stress and chemical processes in the Earth: support from diverse experiments. *Contributions to Mineralogy and Petrology*, 175(12), 1–27.
- White, S. T., and Knipe, R. J. (1978). Transformation–and reaction–enhanced ductility in rocks. *Journal of the Geological Society*, 135(5), 513–516.
- White, R. W., Powell, R., and Baldwin, J. A. (2008). Calculated phase equilibria involving chemical potentials to investigate the textural evolution of metamorphic rocks. *Journal of Metamorphic Geology*, 26(2), 181–198.
- Whitney, D. L., and Evans, B. W. (2010). Abbreviations for names of rock-forming minerals. *American mineralogist*, 95(1), 185–187.
- Williams, M. L., and Jercinovic, M. J. (2002). Microprobe monazite geochronology: Putting absolute time into microstructural analysis. *Journal of Structural Geology*, 24(6–7), 1013–1028.
- Wu, C. M. (2015). Revised empirical garnet–biotite–muscovite–plagioclase geobarometer in metapelites. *Journal of Metamorphic Geology*, 33(2), 167–176.
- Wu, C. M. (2018). Metapelitic Garnet–Muscovite–Al₂SiO₅–Quartz (GMAQ) Geothermobarometry. *Journal of Earth Science*, 29(5), 977–988.
- Zheng, Y. F., and Hermann, J. (2014). Geochemistry of continental subduction–zone fluids. *Earth, Planets and Space*, 66(1), 93.
- Zuluaga, C. A., Stowell, H. H., and Tinkham, D. K. (2005). The effect of zoned garnet on metapelite pseudosection topology and calculated metamorphic PT paths. *American Mineralogist*, 90(10), 1619–1628.

CHAPTER 5: Case study 2 - The Anzola Shear Zone



5. Case study 2 - The Anzola Shear Zone

The content of this chapter was recently submitted as original paper on Lithos with title: Role of inherited compositional and structural heterogeneity in shear zone development at mid-low levels of the continental crust (the Anzola shear zone; Ivrea-Verbano Zone, Western Alps). Elsevier Ltd. All rights reserved. Received 3 January 2022. The PhD candidate is the first author of this work. This study was financed by studentship at the University of Pavia and by IGG-C.N.R. (PRIN2017 “Micro to Macro—how to unravel the nature of the large magmatic events; 20178LPCPWLangoneAntonio”). For this work, the role of PhD candidate consisted in fieldwork, data acquisition and processing, interpretation, conceptualization and manuscript writing.

5.1 Abstract

The formation of shear zones is crucial to understand the deformation of the crust and the evolution of rifted margins. However, despite their intrinsic importance, a detailed characterization of the compositional and structural patterns of shear zones is often lacking, resulting in poorly constrained models of shear initiation. In this contribution, we reconstruct the pre-shearing lithological, structural and metamorphic properties of rocks forming a major, rift-related shear zone with the aim to assess the conditions promoting the strain localization. We focus on the Anzola shear zone, a major extensional structure from one of the best-preserved cross-sections through the middle to lower continental crust of a passive margin, the Ivrea-Verbano Zone (Western Alps, Italy). Until now, the Anzola shear zone is believed to have developed within a rheologically hard and isotropic gabbro rather than in the surrounding weaker and anisotropic volcano-sedimentary metamorphic sequence. New geological mapping shows that significant pre-existing heterogeneities related to the composition and deformation structures, characterize the Anzola shear zone. Field relationships and geochemistry reveal that the (ultra-)mylonitic rocks overprinted a multi-lithological sequence that have already experienced Variscan folding and late Variscan High-Temperature metamorphism, at the boundary between amphibolite and granulite facies. Our in-depth trace elements study is shown to be a powerful tool in reconstructing the pre-shearing relationships between wall rocks and mylonites and determining the protoliths of tectonites. Estimated P-T conditions indicate that mylonitic deformation started at high temperature (~820°C) with presence of melt and continued as solid-state deformation down to amphibolite facies (~650°C), following a retrograde path. We argue that

strain localisation was promoted by the rheological boundaries derived from pre-existing conditions, including: i) compositional and structural anisotropies of the volcano-sedimentary metamorphic sequence contrasted by ii) the close intrusion of a nearly isotropic gabbro and iii) the occurrence of rocks showing transitional metamorphic conditions between granulites (dominated by anhydrous minerals) to amphibolite facies (rich of hydrous minerals). Our findings finally suggest that pre-existing significant heterogeneities relate to rock composition, deformation and metamorphism represent the preferential loci for strain localization controlling the initiation and development of rift-related structures in the mid to lower crust of passive margins.

5.2 Introduction

Shear zones accommodate deformation during rifting evolution from the central ridges toward the passive margins. How strain is distributed within the lithosphere at different scale and where it localizes to initiate the development of shear zones, are key questions in geodynamic studies (Royden, 1996; Mouthereau et al., 2012; Gessner et al., 2013; Whitney et al., 2013)

Strain is localized in spatially restricted but continuous bands of reduced viscosity. The process of strain localization has been attributed to a number of microscale factors: brittle fracturing, grain size reduction with and without deformation mechanism changes, reaction softening, phase mixing, thermal softening and the presence of melt/fluid (e.g., Brodie, 1980; Brodie and Rutter, 1987; Rutter, 1999; Rybacki and Dresen, 2004, Passchier and Trouw, 2005; Walter et al., 2005; Svahnberg & Piazzolo 2010; Lee et al 2018, 2020; Gardner et al., 2020; Casini et al., 2021; Kaatz et al., 2021). These microscale processes may be accentuated by pre-existing heterogeneities such as mechanically weak layers (Passchier, 1982; Austrheim and Boundy 1994; Pennacchioni and Cesare 1997; Burg et al., 2011; Osagiede et al., 2021), stress concentrations around hard layers including compositionally contrasted rock pairs (e.g., Pennacchioni and Mancktelow 2007), inherited fault zone where fluid flow within damage zone will further enhance strain localization (e.g., Austrheim, 2013). Among these, lithological heterogeneities likely represent the most common factor in controlling strain localization at all scales (Fossen and Cavalcante, 2017, 2019), since compositional boundaries may often coincide with significant viscosity contrast (Treagus & Sokoutis, 1992; Arbaret & Burg, 2003; Smith et al. 2015; Maino et al., 2021).

In summary, pre-existing and/or inherited structural and compositional heterogeneities are commonly loci of shear zones development. In such zone of strain localization fluid flow is common resulting in micro to macro-scale rheological effects based on metamorphic reactions involving hydration and metasomatism (e.g., Beach, 1980; Austrheim, 1987). In turn, metamorphism triggering a change from a hydrous to anhydrous assemblage (e.g., reactions defining the amphibolite to granulite facies) is commonly accompanied by the release of free fluids and/or partial melting depending on the prevailing PT conditions (i.e., migmatites) that may further contribute to strain localization at or near metamorphic facies boundaries (e.g., Piazzolo et al. 2002; Giuntoli et al., 2018).

At the regional scale, pre-existing compositional/mechanical heterogeneities and their position (in depth) in the continental lithosphere have a first-order control on the development of shear zones

driving the evolution of rifted margins (Michibayashi and Mainprice, 2003; Lavier and Manatschal, 2006; Mohn et al., 2010, 2012; Manatschal et al., 2015; Aravadinou and Xypolias, 2017; Langone et al., 2018; Real et al., 2018; Petri et al., 2019). Mechanically weak boundaries were, indeed, documented to produce detachment faults and decoupling horizons, especially at mid-crustal depth in magma-poor rifted margin during major lithospheric thinning (Prosser et al., 2003; Mohn et al., 2012). Nevertheless, detailed reconstruction of their compositional and geometrical pattern is often poorly constrained due to lack of correlations between field relationships, microstructure and geochemical characterization. The Ivrea-Verbano Zone (IVZ; Fig. 5.1), in the Italian Southern Alps, preserves remnants of the former Alpine Tethys rifted margin (e.g., Rutter et al., 1993; Petri et al., 2019) where localisation of detachment faults has been related to inherited structures (Manatschal et al., 2015; Beltrando et al., 2014, 2015). However, the role of geometrical and compositional heterogeneities of these structures at the outcrop scale has been poorly investigated. Therefore, new detailed petrological, structural and geochemical investigations are required for a robust interpretation of the mechanisms leading to the initiation of deformation.

In this paper, we investigate a rift-related shear zone developed in the middle-lower crust with the aim to determine compositional, structural and/or metamorphic gradients or breaks from wall rock to shear zone centre. We selected the Anzola shear zone (Val d'Ossola, Northern Italy) as a well-exposed high-temperature extensional fault (Rutter et al., 2007; Simonetti et al., 2021) where can explore the relationships between strain localisation and compositional/structural heterogeneities. Until now, the Anzola shear zone has been described as a fault zone affecting gabbroic rocks bounded by amphibolite facies metapelite and felsic granulite (e.g., Brodie, 1981). Previous works assumed that the compositional homogeneity of the gabbro minimizes the role of initial chemical/structural heterogeneity in the shear zone localization. This leads to consider the strain localization as driven by processes involving dynamic recrystallization and metamorphic reactions (Brodie, 1981; Altenberger, 1997; Stünitz, 1998). Moreover, the role of the amphibole in both mechanical and metamorphic processes has been stressed to explain the paradox of shear zone localization in the mechanically stronger layer (i.e., gabbros). This contrasts the fact that, strain localization is theoretically expected in the surrounding weaker quartz-feldspar-rich layers (Williams and Burr 1994; Rybacki and Dresen, 2000). On the base of microstructural and chemical changes of amphiboles, shear zone development

was initially defined under prograde P - T conditions (Brodie, 1981), however, other observations led to attribute strain localization during retrograde P - T path (Altenberger, 1997; Stünitz, 1998).

In this work, we perform new detailed geological mapping of the Anzola shear zone with the aim to investigate the underlying reasons for strain localization. We combine the analysis of field relationships with petrological and geochemical characterization of samples collected across the shear zone. For the first time we integrate bulk and mineral analyses of major elements with the trace elements geochemical data. We found that the trace elements study is the most powerful tool in order to proof or disprove links between wall rock and shear zone and thus determine the protoliths of mylonites. The coupling of different geothermobarometers was used to determine the pre- and syn-deformation conditions of the studied area. Our results highlight that the Anzola shear zone is characterized by a complex pattern of lithotypes, which experienced multiple tectono-metamorphic stages before shear zone development. We argue that pre-existing lithological and metamorphic meso- to micro-scale variations associated with likely fluid circulation promoted strain localisation resulting in the Anzola shear zone. We finally discuss these new data in the framework of the regional rifting evolution.

5.3 Geological setting

5.3.1 The Ivrea-Verbano Zone

The IVZ in north-western Italy represents a cross-section through the middle to lower continental crust of the Southern Alpine basement (Fig. 5.1). During the Alpine collision, the IVZ underwent vertical exhumation and open folding, but it escaped the metamorphic overprint (Henk et al., 1997; Rutter et al., 2007; Wolff et al., 2012). Northward, the IVZ is separated from the Alpine metamorphic rocks (i.e., Sesia Zone) by the Insubric Line, while south-eastward, it is divided from Serie dei Laghi Unit by the by the Late-Variscan Cossato–Mergozzo–Brissago Line, which is in turn crosscut by the Pogallo Line (Fig. 5.1; Boriani et al., 1990).

Three main units are described in the IVZ (Fig. 5.1), from NW-SE: i) the mantle peridotites; ii) the Mafic Complex, and iii) the Kinzigite Formation.

The main peridotitic bodies – e.g., Finero and Balmuccia - crop out close to the Insubric Line (Hartmann and Wedepohl, 1993). These peridotitic lenses lie in different stratigraphic levels of the continental sequence. The crustal emplacement of these rocks is considered a consequence of the

tectonic evolution of the Kinzigite Formation that occurs in the end of the Variscan orogenesis and before the intrusion of the Mafic Complex (Quick et al., 2003).

The Mafic Complex consists of deformed and metamorphosed gabbros and diorites intruded into the metasedimentary sequences (i.e., schists and gneisses) of the Kinzigite Formation (Quick et al., 2003). In the south-western part of the IVZ, the transition between the upper and lower Mafic Complex corresponds to a zone, identified as the “paragneiss-bearing belt”, where paragneiss septa (i.e., depleted granulite) are interlayered with igneous rocks (Fig. 5.1; Sinigoi et al., 1996). The Mafic Complex mainly intruded during Permian (290-270 Ma; Peressini et al., 2007) with underplating dynamics and coeval with the acid magmatism and volcanism recognised in the upper crust (Karakas et al., 2019). Mantle-derived mafic magmatism probably started before the Permian, as indicated by the presence of mafic sills intruded during Carboniferous (e.g., ~314; Klötzli et al., 2014), and locally occurred even during Triassic and Jurassic (e.g., Zanetti et al., 2013; Denyszyn et al., 2018).

The Kinzigite Formation is considered as the originally upper part of the tilted crustal section made up of a heterogeneous group of metasediments, belonging to a volcano-sedimentary sequence, comprising mainly metapelites with intercalated metabasic rocks (i.e., volcanic sediments and MORB-like lavas) and minor marbles/calc-silicates and quartzites (Fig. 5.2; Zingg, 1990; Schmid, 1993; Quick et al., 2003; Kunz et al., 2014). At a regional scale, peak metamorphic grade preserved decreases from granulite (~900 °C and 900 MPa) to amphibolite facies (~600 °C and ~400 MPa) from NW to SE (Schmid & Wood, 1976; Brodie and Rutter, 1987; Zingg, 1990; Schmid, 1993; Redler et al., 2012; Kunz et al., 2014). Long-lasting high-grade metamorphism developed between the Late Carboniferous (~316 Ma; Ewing et al., 2013) to the Early Permian, coevally with the Mafic Complex intrusion (~290 Ma; Ewing et al., 2013).

The progressive switch at the mid to lower crustal levels from granulite to amphibolite facies is marked by a transition zone of ~1-5 kilometres that experienced extensive migmatization processes (Fig. 5.2A; e.g., Redler et al., 2012; Kunz et al., 2014; Carvalho et al., 2019). In the north-eastern part of the IVZ, this transition zone hosts two mylonitic shear zones, namely the Anzola (Brodie and Rutter, 1987) and the Forno-Rosarolo shear zones (Siegesmund et al., 2008; Fig. 5.1). Although described as separate shear zones and often named in different way (see Simonetti et al., 2021), these structures have been interpreted as a single fault system with vertical foliation and NNE-SSW strike (e.g., Rutter et al., 2007).

5.3.2 Tectonic evolution

The structure of the IVZ is the result of a complex tectonic evolution that developed between the Variscan and the Alpine orogenesis. During the late stages of Variscan convergence (320-290 Ma), the IVZ went through a lithospheric delamination that triggered magmatic underplating and led to polyphase deformation under amphibolite to granulite facies conditions (Handy et al., 1999). Variscan large-scale folding phases are described in the Kinzigite Formation of the IVZ (Brodie and Rutter, 1987; Rutter et al., 2007). Polyphasic folding is well preserved in the main upright fold of the Massone antiform that extends within the Kinzigitic Formation around 40 km NE-SW with a hinge line strongly curved through an angle of 115° within the axial plane. The Massone axial planar crenulation cleavage deforms pre-existing schistosity and lineations associated with an earlier folding phase, finally resulting in a Type 2 interference geometry with perpendicular fold hinges and axial planes (Fig. 5.2A; Ramsay, 1967; Rutter et al., 2007).

Since the Permian (290-270 Ma), the IVZ experienced post-orogenic extension associated with mafic underplating of calc-alkaline magmatism occurred along fault systems in all crustal levels (Boriani et al., 1990; Handy et al., 1999; Rutter et al., 2007; Siegesmund et al., 2008). Stretching led to crustal thinning and incipient exhumation of the lower crust supported by mylonitic shearing, as testified by the Cossato-Brissago-Mergozzo Line (CMBL; Fig. 5.2A; Brodie & Rutter, 1987; Henk et al., 1997).

In the Triassic-Jurassic time interval (230-180 Ma), the IVZ was involved in complex and polyphase rift tectonics (Beltrando et al., 2015; Petri et al., 2019 and reference therein). Crustal thinning (<10 km thick) was accommodated by several shear zones active during different phases of rifting (Manatschal et al., 2007; Mohn et al., 2012) at different crustal levels (e.g., Beltrando et al., 2015). The most prominent rifting-related structure in the southern portion of the IVZ is the Pogallo Line, which is interpreted as a low-angle normal fault that accommodated thinning (Hodges and Fountain, 1984) between Triassic and Jurassic age (ca. 210 and 170 Ma; Zingg, 1990; Wolff et al., 2012) under decreasing temperatures from amphibolite- to greenschist-facies conditions. In the northern sector of the IVZ, Late Triassic to Early Jurassic ductile shear zones developed within (ultra)mafic rocks (e.g., Langone et al., 2018; Corvò et al., 2020; Boriani and Villa, 1997) at granulite- to greenschist-facies conditions (Brodie, 1981; Kenkmann, 2000; Kenkmann and Dresen, 2002; Degli Alessandrini, 2018; Langone et al., 2018). Important rift-related structures have been described also in the central part of the IVZ, i.e., the

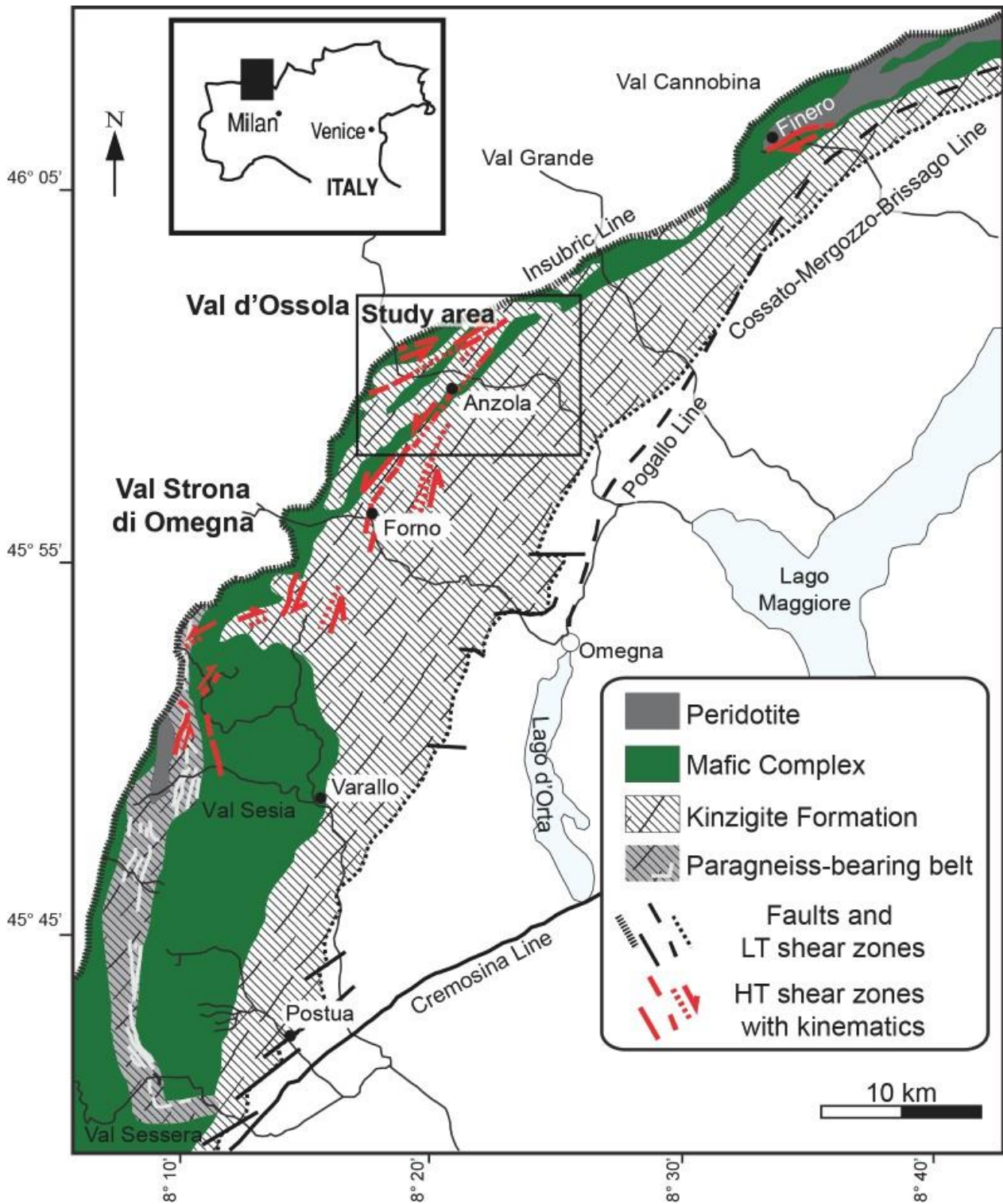


Fig. 5.1 – Geological sketch map of the Ivrea-Verbano Zone, modified after Ewing et al. (2015) and Simonetti et al. (2021). The locations of high-temperature shear zones are after Rutter et al. (1993). The studied area is reported in the black square.

Forno-Rosarolo and the Anzola shear zones (Figs. 5.1, 5.2A; Siegesmund et al., 2008; Simonetti et al., 2021). Onset of extension occurred since the upper Triassic as suggested by the emplacement of felsic dykes in lower crust lithologies (e.g., Stähle et al., 2001; Schaltegger et al., 2015; Bonazzi et al., 2020). Exhumation of the lower crust occurred along a large, noncoaxial mylonitic shear zone, i.e., Pogallo shear zone, which was linked to asymmetrical rift basins in the upper crust (Handy et al., 1999).

As last stage, during Alpine orogenesis (50-20 Ma), the IVZ accomplished the present-day sub-vertical attitude through a rotation of ca. 60° around a horizontal axis striking parallel to the Insubric Line in a clockwise sense viewed to the north (Henk et al., 1997; Rutter et al., 2007; Wolff et al., 2012). Consequently, the entire sequence experienced large-scale open folding (i.e., Proman antiform, Fig. 5.2A) and brittle faulting (Rutter et al., 2007).

5.3.3 The Anzola shear zone

The Anzola shear zone crops out in a quarry, 500 m east from the Anzola village in Val d'Ossola (Fig. 5.2B; Brodie, 1981; Brodie et al., 1989, Stünitz, 1998). Here, mylonitic amphibolites were the objects of several structural, microstructural and geochemical studies (Brodie, 1981; Brodie and Rutter, 1987; Brodie et al., 1989; Rutter and Brodie, 1990; Rutter et al., 1993; Altenberger, 1997; Stünitz, 1998; Rutter et al., 2007). The Anzola shear zone has always been described as an extensional amphibolite-facies mylonitic belt overprinting mainly gabbroic rocks.

Brodie (1981) was the first to study one mylonitic band of the Anzola shear zone, focusing on the role of deformation on mineral and rock chemistry. The author showed that the plagioclase and amphibole composition, varies in relation with the intensity of shearing, i.e., $Fe\#$ ($Fe^{2+}/(Fe^{2+}+Mg)$) and Ca increase within amphibole and plagioclase, respectively. These changes in mineral chemistry together with preliminary microstructural investigations suggested that shear zone developed with increasing temperature during prograde regional metamorphic conditions from low- to high-grade amphibolite facies.

Altenberger, (1997), in agreement with Brodie (1981), highlighted an increase in modal abundance of amphibole and grain size contrast within mylonitic layers with respect to the wall rocks. Moreover, amphibole is more extensively recrystallized with respect to plagioclase. According to the author, the pre-existing heterogeneity (i.e., general sample layering and grain-size variations) was the locus of

concentrated shear deformation.

The structural and geochemical features of the shear zone were further investigated by Stünitz (1998) who described a 10 metres wide N-S striking mylonitic belt showing a vertical foliation, discordant on the Variscan metamorphic schistosity (i.e., fold axial plane cleavage), with sharp boundaries with the surrounding host rocks. According to the Author two types of shear zones were recognisable on the base of their microstructure, grain size and mineral abundance. He confirmed that syn-tectonic recrystallization of plagioclase, clinopyroxene and amphibole produces compositional differences between porphyroclasts, and recrystallized grains as previously recognised by Brodie (1981). Relative to the porphyroclasts, recrystallized clinopyroxene, hornblende and plagioclase grains are characterized by higher Mg# values (Mg/Mg+Fe) and Al contents, lower Ti and higher Mg# values and lower anorthite and orthoclase components, respectively. Stünitz (1998) concluded that the Anzola shear zone recorded P - T conditions indicative of the transition from amphibolite to granulite facies, likely with a prograde initiation as suggested by Brodie (1981). However, the main activity of the shear zone was attributed to a retrograde P - T path, under amphibolite facies conditions (from about 550 to 650 °C) at pressures minor than 0.8 GPa.

Brodie et al. (1989) provided an attempt to date shear zone activity. Ar-Ar radiometric dating of hornblende were carried out from the undeformed gabbro and mylonitic amphibolites obtaining a minimum ^{40}Ar - ^{39}Ar age of about 247 Ma for unsheared gabbroic rocks and about 210-215 Ma for syn-kinematic amphibole grains. The authors suggested that crustal extension started around 280 Ma, after the emplacement of the gabbro, and was the beginning of a long-lasting period of crustal thinning and cooling of more than 100 Myr. According to the authors, the considerably younger dates (215 and 210 Ma) obtained from sheared metabasic rocks suggest that cooling and mylonitic shearing may be related. Despite the several studies on the microstructural and geochemical evolution of the shear zone, the PT conditions of deformation, i.e., prograde for Brodie (1981) and retrograde for Stünitz (1998), as well as the timing, are still poorly constrained. Furthermore, a detailed geological fieldwork, including the description of all the lithologies and their structural relationships, is lacking. In order to fill this gap, we carried out a geological mapping at 1:2.000 scale and we collected several samples across the shear zone including footwall and hanging wall rocks (Figs. 5.2, 5.3). Sampling localities are reported in Fig. 5.2B and Table S5.1.

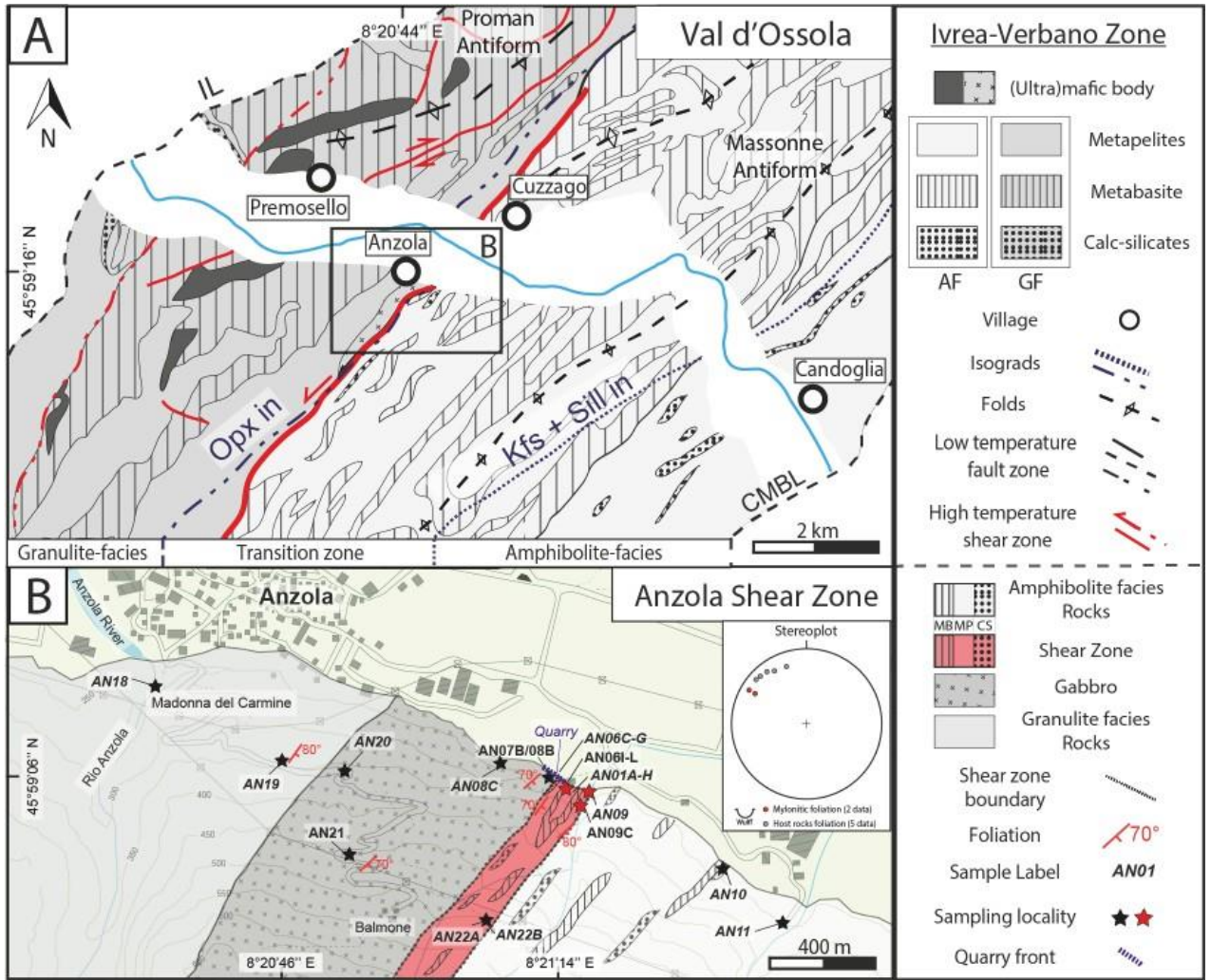


Fig. 5.2 – Schematic geological maps showing the main lithologies, tectonic structures and isograds through the Ivrea-Verbano Zone for A) the Val d’Ossola (modified after Rutter et al., 2007). Isograds (Kfs + Sill in and Opx in) are from Zingg (1980) and mark the transition between amphibolite to granulite facies. IL = Insubric Line; CMBL= Cossato-Mergozzo-Brissago Line. In the legend on the right: AF = Amphibolite facies; GF = Granulite facies. B) Detailed geological map and structural data of the study area. Sampling across the Anzola shear zone (red coloured), from footwall (NW) to hanging wall (SE), is marked with stars. Samples analysed for geochemical analyses are labelled in italic characters. In the legend on the right, the patterns labelled as MB, MP, CS refer to the different rock types: metabasite, metapelite, calc-silicate, respectively.

5.4 Field observations

Field relationships and macroscopic features are described moving from SE (hanging wall) to NW (footwall) across the shear zone (Figs. 5.2, 5.3). Studied outcrops comprise hanging wall and footwall rocks up to a distance of about 0.8 and 2.0 km, respectively, from the shear zone and following increasing metamorphic conditions from amphibolite- to granulite facies (Figs. 5.2, 5.3).

The hanging wall (SE) is characterised by upper amphibolite facies rocks with different composition: paragneisses (sample AN11) and minor mafic gneisses (AN10; Figs. 5.2B, 5.3A), both showing evidences for partial melting. Migmatitic paragneisses are metatexites with thin (up to ~1 cm) leucosomes occurring as patches or along the folded foliation (Fig. 5.3B; Sawyer, 2008). Melanosome mainly consists of fine-grained biotite, garnet, sillimanite, quartz, and feldspars. Mafic gneisses consist of plagioclase, clinopyroxene and amphibole, and appear as centimetres-meters thick intercalations within the paragneisses (Fig. 5.3A).

The overall thickness of the Anzola shear zone is around 100 m (Fig. 5.3A) and is characterized by a well-developed mylonitic fabric steeply dipping (~70°) towards SE (Fig. 5.2B) and a left-lateral south-westward shear-sense (Rutter et al., 2007). The shear zone is dominated by paragneisses and amphibolites (Fig. 5.3A). Paragneisses prevail in the SE portion, whereas amphibolites are abundant towards the NW boundary (Fig. 5.3A). All rock types show compositional layering on a centimetre to decimetre scale (Fig. 5.3B-G, S5.1A). Paragneisses are characterized by alternating coarse-grained levels of plagioclase, garnet, biotite and fine-grained layers with more abundant biotite and sillimanite (Fig. 5.3C-E). Mylonitic fabric is easily recognizable in hand specimen by a well-developed foliation defined by biotite and lineation defined by the alignment of sillimanite prisms along the foliation planes (e.g., AN09, AN09C, AN22A; Fig. 5.3C-E). Garnet porphyroblasts are distinctly rounded (Fig. 4.3C-E) in contrast to garnet-bearing rocks outside the shear zone (Fig. 5.3B). Strain partitioning is limited as compositional bands and foliation are subparallel to each other. Locally, boudinaged leucocratic rocks characterized by feldspar and greyish porphyroclasts up to 2 cm occur within paragneisses (e.g., AN22B, Fig. 5.3F; S5.1C). Amphibolites involved in the shear zone consist of predominant amphibole, clinopyroxene and plagioclase with rare occurrence of garnet (AN01, AN06I-L; Fig. 5.3G). At the outcrop scale, strain partitioning defines an anastomosing pattern (Fig. 5.3A). Closer the SE boundary, a low-strain zone occurs passing from protomylonitic (AN22A; Fig. 5.3C) to a high-strain

zone of (ultra)mylonitic paragneisses (AN09, AN09C; Fig. 5.3D, E). Towards the NW boundary, the shear zone is dominated by high-strain zone mainly made of alternating mylonitic (AN01, Fig. 5.3G) and ultramylonitic layers (AN06I, L; Fig. 5.3A), suggesting higher strain conditions with respect to the SE boundary. Here, ultramylonitic layers are defined by very small grain sizes (<0.125 mm) and straight compositional boundaries between plagioclase- and amphibole-rich layers.

Towards NW, a lithologically heterogeneous domain separates the shear zone from a up to 800 m thick gabbroic body (Fig. 5.2B). Here, centimetre thick mafic gneisses, paragneisses and calc-silicates define folded layers (AN06C-G; Figs. 5.2B, 5.3H, I) with axial planes steeply dipping towards SE and axes towards around E (Figs. 5.2, 5.3H), coherent with the main Variscan folding phase (D2; see Rutter et al., 2007 for further details). Mafic gneisses and paragneisses have the same mineral assemblages as in the shear zone, i.e., mafic gneisses consist of clinopyroxene, plagioclase amphibole and minor garnet, while paragneisses are made of garnet, feldspars, sillimanite, quartz and minor biotite. Calc-silicates consist mainly of clinopyroxene, plagioclase, calcite and green amphibole. Large crystals (up to 1-2 cm) of titanite are clearly observable in hand specimen (AN06G; Fig. S5.1E). These rocks are here documented for the first time (AN06G; Figs. 5.2B, 5.3H, I). The contact between the folded gneisses and the gabbroic rocks is marked by lenses of calc-silicates (AN06C) and pockets of coarse-grained garnet, amphibole and plagioclase (Fig. 5.3I, L).

Proceeding to NW within the footwall of the shear zone, mafic rocks belonging to a gabbroic body occur (Gabbro of Anzola as defined by Cavallo et al. 2004; samples AN07B, AN08B, AN08C, AN20, AN21; Figs. 5.2, 5.3A). The gabbroic rocks are generally coarse grained made of plagioclase and clinopyroxene and minor amphibole (sample AN07B/08B). Locally thin discontinuous layers or lenses richer in amphibole or plagioclase are recognisable (Fig. 5.3L). The gabbro within 5 m of the folded sequence shows a weak sub-vertical foliation dipping towards SE (Fig. 5.2B; 5.3L) which becomes indistinct towards the gabbro *sensu stricto* (Fig. 5.3A). The latter is defined by its isotropic texture characteristic for the main gabbro body. Locally, pegmatites and leucocratic dikes of plagioclase and pyroxene crosscut the gabbro (Fig. 5.3M).

Further to the NW, the gabbro is in contact with the felsic granulites (sample AN18, AN19; Fig.

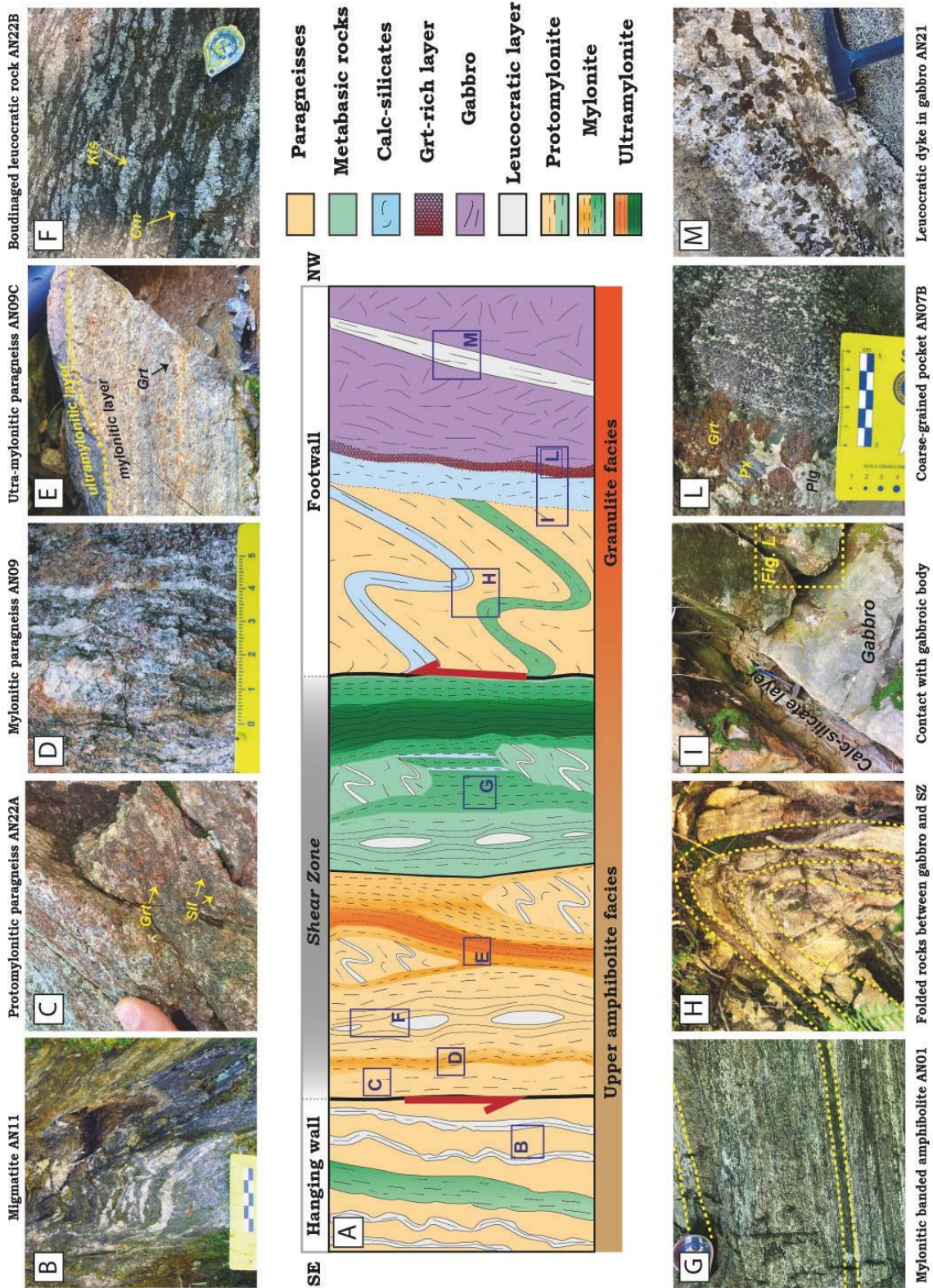


Fig. 5.3 – Sketch of the Anzola shear zone transect (not at scale; approximate thickness of the shear zone ~100m) and representative outcrop pictures. Shear zone edges are defined on the base of foliation orientation (see Figure 5.2B for geological mapping and measurements). A) Schematic cross section; B) Migmatitic paragneiss (AN11). C) Protomylonitic paragneiss (AN22A). D) Mylonitic paragneiss outcrop (i.e., AN09). E) Ultra-mylonitic paragneiss (sample AN09C). F) Boudinaged leucocratic rock (AN22B). G) Mylonitic banded amphibolites (AN01). H) Folded domain made by calc-silicates and gneisses. I) Contact between calc-silicates and gabbroic body. L) Coarse-grained pocket (AN07) at the contact with gabbro (AN07). M) Leucocratic dyke cutting the gabbro.

5.2B), which become the dominant rock type showing the typical high-grade paragenesis consisting of abundant garnet, quartz, feldspars, sillimanite and rare or absent biotite. The contact between felsic granulites and gabbro is not well-exposed, however, a weak foliation is locally recognisable (Fig. 5.2B).

Felsic granulites are characterized by brownish needles of rutile easily recognisable on the fresh surfaces of the samples. The texture is prevalently isotropic, with a weak foliation steeply dipping towards SE (Fig. 5.2B) still concordant with the regional attitude.

5.5 Sampling strategy and analytical methods

To characterize the lithological, microstructural, petrological and geochemical variations across the shear zone, we collected samples across the wall rocks and the mylonitic/ultramylonitic shear zone (Figs. 5.2, 5.3, S5.1). A detailed list of samples is reported in Supplementary material (Table S5.1). Samples (around 40 and initial label AN = Anzola) were subdivided in (Figs. 5.2, 5.3): i) proto- and ultramylonitic rocks from the shear zone (sample labelled AN01A-I, AN06I-L, AN09, AN09C, AN22A, AN22B; Figs. 5.2, 5.3) and metamorphic rocks representative of the wall rocks at the footwall and hanging wall, i.e., paragneisses, mafic gneisses and felsic granulites (samples labelled AN10, AN11, AN06C-H, AN18, AN19; Figs. 5.2B, S5.1). Samples from the gabbro of Anzola are considered as a subcategory of the wall rocks and are identified as gabbroic rocks (samples labelled AN07, AN08B, AN08C; AN20, AN21). Mineral abbreviations are after Whitney and Evans (2010).

5.6 Petrography and microstructure

5.6.1 Wall rocks

5.6.1.1 Hanging wall rocks

Migmatitic paragneisses (sample AN11) are characterized by a layered texture consisting of alternating thin (up to 5 cm-sized) leucosomes and thicker (up to 10 cm) biotite-rich mesosomes (Fig. 5.4A) defining them as stromatic migmatites (following Sawyer, 2008 for migmatite terminology). The boundaries between stromatic leucosomes and melanosomes are generally marked by a local increase of biotite towards the mesosomes. Leucosomes consists of large garnet grains including clusters of quartz, abundant rutile, and graphite (<1 cm; Fig. 5.4A). The mesosome is medium- to coarse-grained, composed of biotite, garnet, prismatic, aligned sillimanite, K-feldspar, plagioclase, and quartz (Fig.

5.4A; Table S5.1). Clear evidence for partial melting is especially in the form of resorbed biotite and sillimanite associated with films of K-feldspar and quartz. Accessory phases are rutile, ilmenite, graphite, apatite, zircon, and monazite. Rutile is abundant and associated with ilmenite.

Rocks characterized by a grano-nematoblastic texture and dominant mineral assemblage of Amph + Cpx + Pl + Scp (Table S5.1) are intercalated with the migmatitic paragneisses (sample AN10; Fig. 5.4B). The average grain size is around 0.5 mm. These samples are strongly banded alternating dark layers of subhedral amphibole and plagioclase and whitish layers of anhedral plagioclase, subhedral clinopyroxene and subhedral scapolite (Fig. 5.4B; Table S5.1). From these observations, hereafter, we identified these samples as scapolite-bearing gneisses. Accessory minerals are ilmenite, apatite, zircon and titanite. The latter is the most abundant and it is present in subhedral or rounded crystals with grain size up to 250 μm . Rare and altered epidote is present as evidence of retrograde metamorphic reactions.

5.6.1.2 Footwall rocks

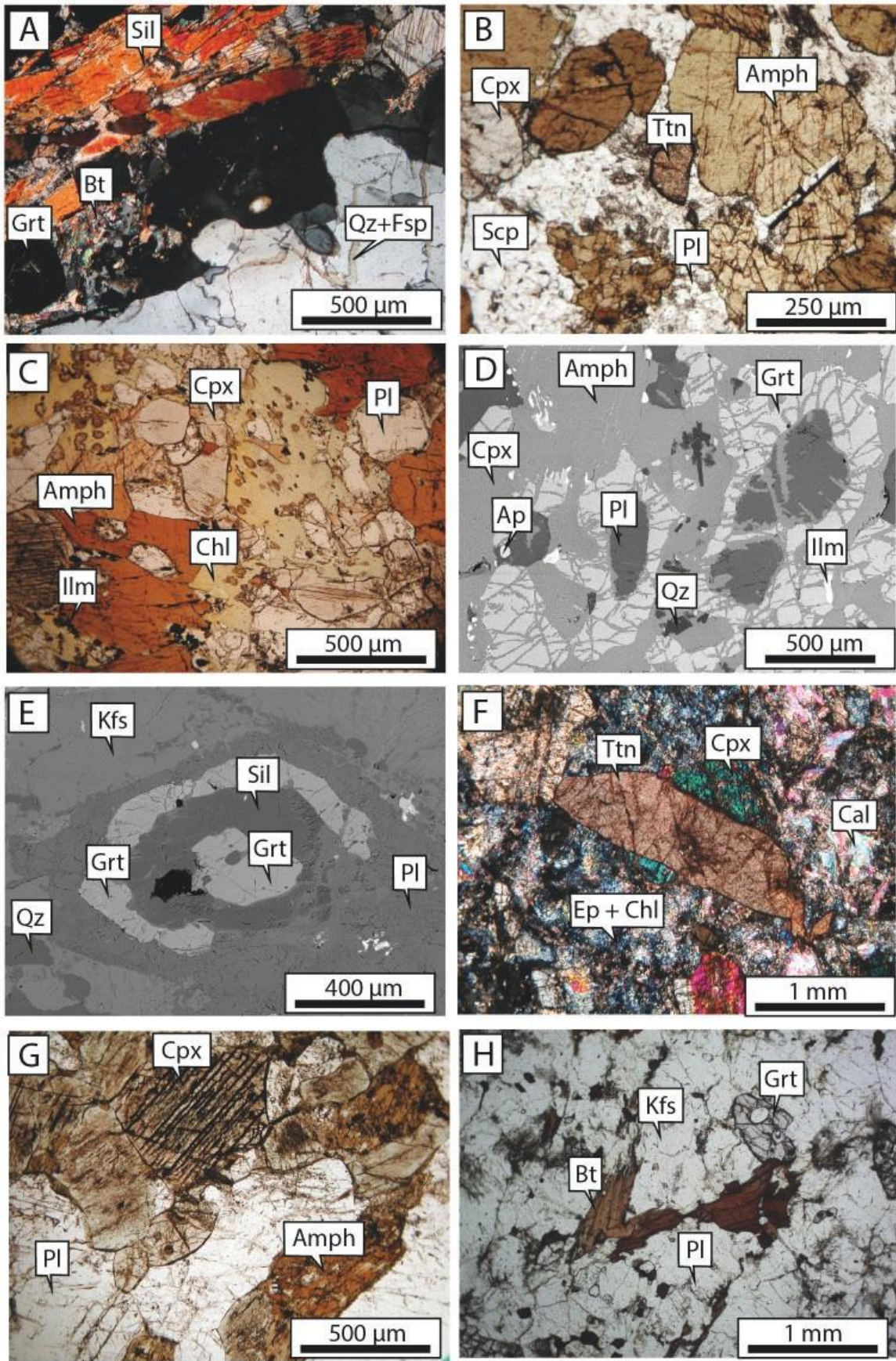
Mafic gneisses (sample AN06F) show a grano-nematoblastic texture and consists of two levels made of Cpx + Pl \pm Grt \pm Amph and of Amph + Cpx + Pl + Grt, respectively (Fig. 5.4C). In the first layer, amphibole occurs only as interstitial grains, whereas garnet is rare. Conversely, the amphibole-rich portion is characterized by major modal abundance of garnet occurring as both poikiloblasts enclosing plagioclase, clinopyroxene and amphibole, or as coronitic texture surrounding plagioclase (Fig. 5.4D) or in fine-grained mineral aggregates. Abundant amphibole (up to 40 vol.%) occurs as both interstitial mineral phases and as large grains including plagioclase and clinopyroxene. The fine-grained alteration shows a pale yellowish colour and composition comparable to chlorite (Fig. 5.4C). Relicts of brown amphibole are visible suggesting that the fine-grained aggregates represent an alteration product of amphibole. A thin layer of chlorite has been observed also between garnet and plagioclase in the coronitic texture. Amphibole contains several tiny oxide exsolutions along the cleavages. Ilmenite is the most abundant accessory mineral and locally is partially replaced by rutile and titanite. As other accessory minerals, apatite occurs in both layers, whereas titanite is present only in the Amph-poor portion.

Paragneisses (sample AN06D) show a weak foliated texture characterized by large garnet porphyroclasts surrounded by a matrix mainly composed of quartz, plagioclase and K-feldspar. The

mineral assemblage consists of Pl + Kfs + Qz + Grt + Sil + Bt (Fig. 5.4E; Table S5.1). Garnet occurs mainly as large, fractured (up to 2 mm) grains with a high density of inclusions of quartz, sillimanite, biotite, plagioclase, and accessory minerals such as rutile and zircon. Prismatic subhedral grains of sillimanite are present as both isolated grains along the foliation or aggregates surrounded by tiny film or atollar garnet, plagioclase, and K-feldspar (Fig. 5.4E). Biotite is rare, commonly chloritized and associated with garnet. White mica locally replaces the sillimanite. Rutile, ilmenite, graphite, apatite, zircon, and monazite (up to 100 μm) are accessory phases. Rutile-reach grain size up to 500 μm and it is the most abundant among the accessory mineral especially observable as inclusion in garnet or along the matrix.

Calc-silicates are coarse-grained (mm-cm sized) and consists of plagioclase, epidote and titanite (sample AN06C, AN06G; Fig. 5.4F). Sigmoidal/lozenge shaped crystals of titanite of about 1x2 mm preferentially are dispersed in the matrix or found associated with the clinopyroxene, as well as radial aggregates of epidote up to 2 mm in size (AN06G; Table S5.1). Apatite is abundant and form aggregates. At the contact with gabbroic rocks, calc-silicate (AN06C) are characterized by granoblastic texture and consist mainly of Cpx + Cal + Pl \pm Scp and minor quartz and K-feldspar (Fig. 5.4F; Table S5.1). Titanite, apatite, zircon and sulphides are common accessory minerals. Both samples show evidence for retrograde replacement reactions that have promoted the formation of chlorite, white mica, epidote and albite at the expense of the primary assemblages. In the sample AN06G, especially, the primary mineral assemblage is almost completely overprinted.

Fig. 5.4 – Microphotograph reporting the main petrographic features of the wall rocks. A) Migmatitic paragneiss (AN11) made of melanosome mainly constitutes by garnet rutile and prismatic sillimanite and leucosome made by Qz and Fsp; B) Scapolite-bearing gneiss (AN10) with mineral assemblage made by Cpx + Amph + Pl + Ttn; C) Mafic gneiss (AN06F) from the folded layers at the footwall made by Amph + Pl + Cpx + Chl + Ilm; D) Backscattered electron image (BSE) of sample (AN06F) showing garnet corona around plagioclase and surrounded by Amph + Cpx + Qz + Ap + Ilm; E) BSE image of paragneiss (AN06D) from folded layer at the footwall showing the garnet relict surrounded by a film of Sil + Grt + Pl + Kfs. F) Calc-silicate (AN06C) with very big crystals of titanite and mainly constitute by epidote and chlorite and calcite; G) Gabbros (AN07/AN08) sample with typical mineral assemblage composed by Cpx + Pl + Amph; H) Felsic granulite (AN18) mainly constitute by feldspar, biotite and garnet.



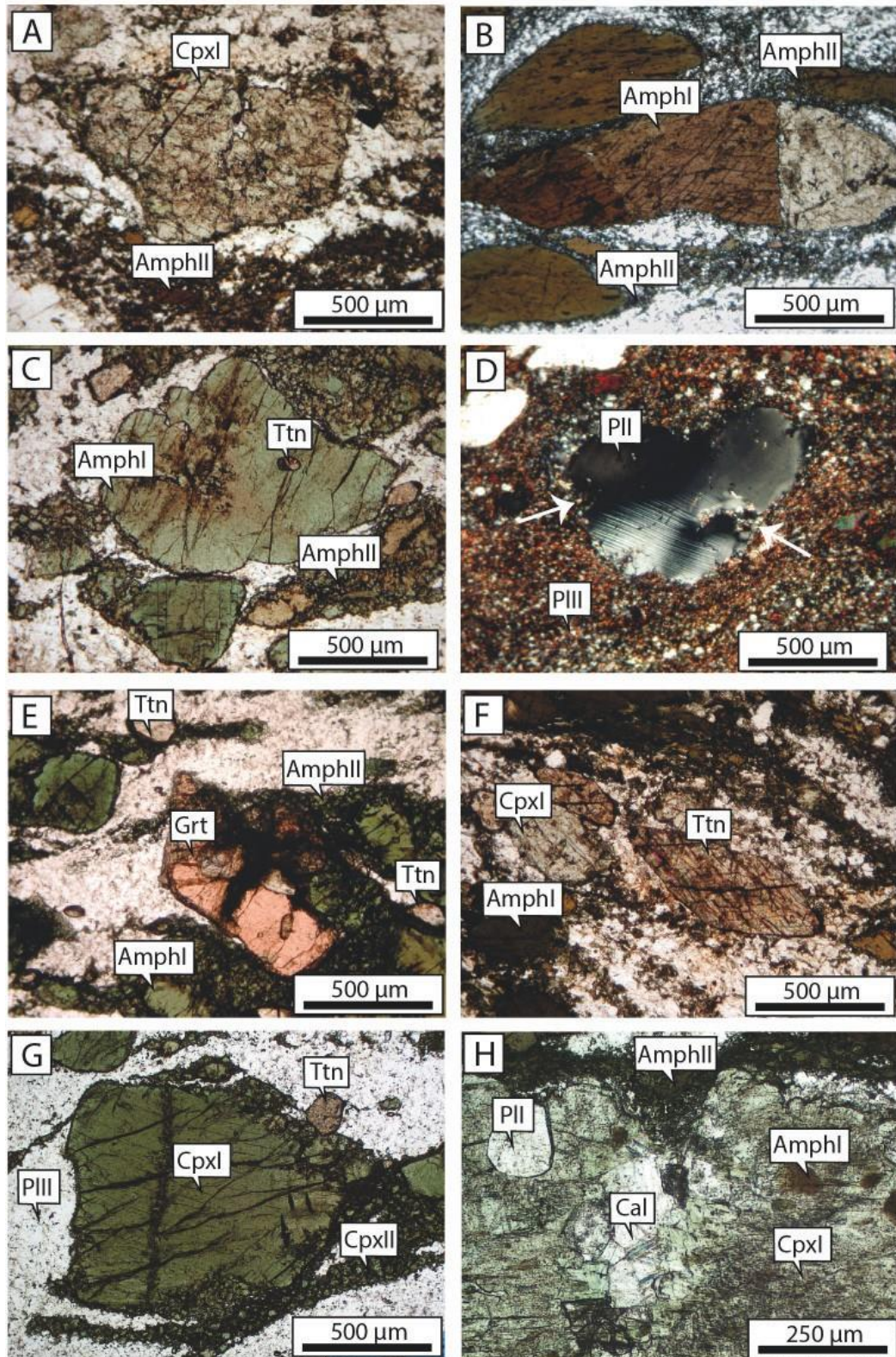


Fig. 5.5 – Microphotograph of the main petrographic and microstructural features of the mylonitic amphibolites (AN01). A) Cpx porphyroclast and recrystallized amphibole (Amphll); B) Amphibole porphyroclasts (Amphl); C) Amphibole porphyroclasts in Pl/Cpx-rich mylonite and titanite grains; D) Plagioclase porphyroclasts (Pll) and matrix rich in amphibole and plagioclase; E) Garnet relict surrounded by Amph, Pl and Ttn; F) Big crystals of titanite; G) Clinopyroxene in Cpx/Pl-rich layer (AN01D), with recrystallized Cpxll and Plll; H) Calcite in Cpx porphyroclasts and surrounded and included amphibole.

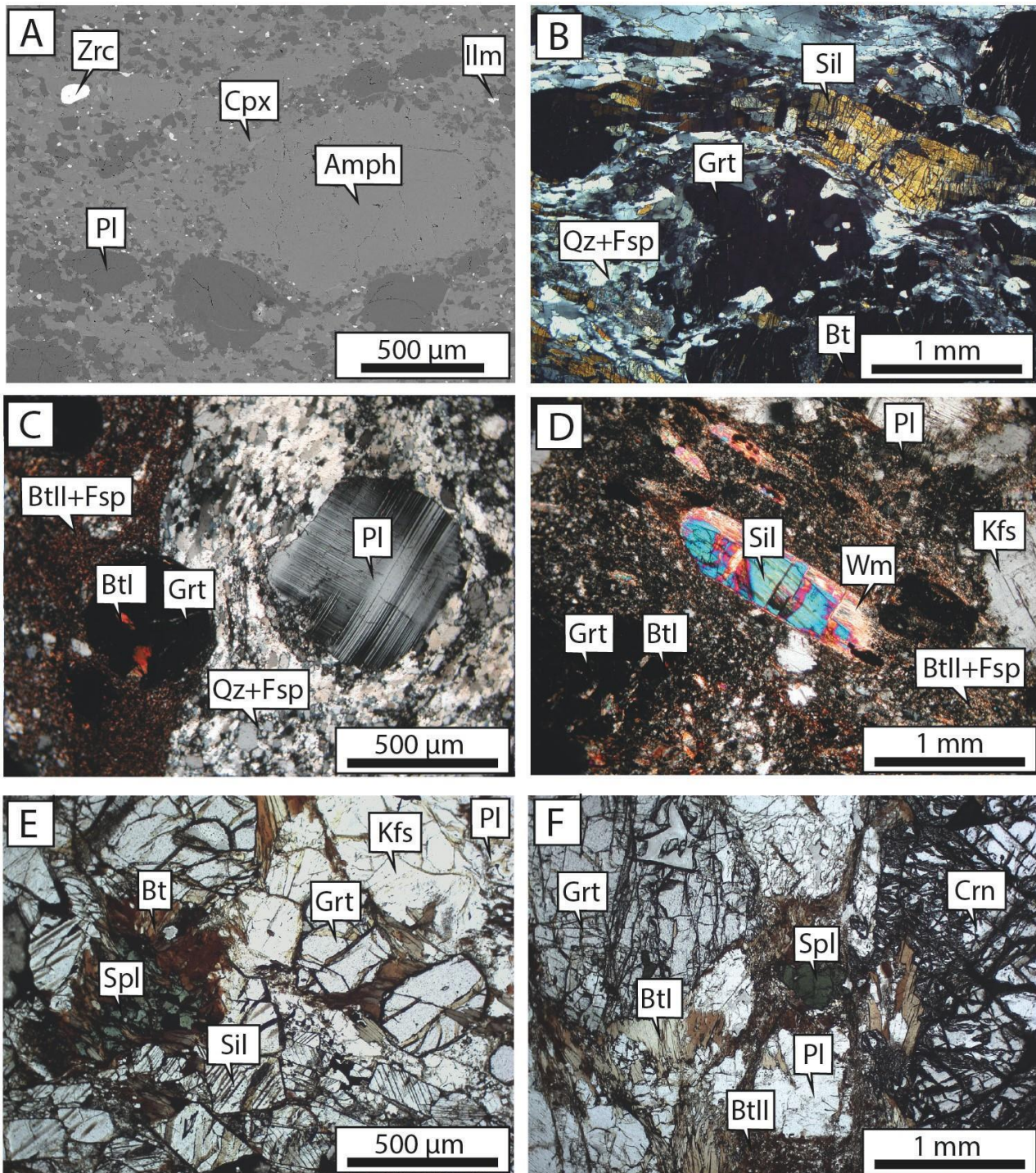


Fig. 5.6 – Microphotograph reporting the main petrographic and microstructural features of the mylonitic paragneisses. A) Back-Scattered Electron (BSE) image of mafic ultramylonite (AN06L) with amphibole and plagioclase porphyroclasts and matrix mainly made of Amph + Pl + Cpx; B) Mylonitic felsic granulite (AN09) with evident foliation marked by quartz + feldspatic and/or garnet + sillimanite layers; C) Ultra-mylonitic felsic granulite (AN09C) with layer enriched in Grt + Bt + Fsp and layer constitutes by Pl + Qz; D) Ultra-mylonitic felsic granulite (AN09C) with layer enriched in porphyroblast of prismatic sillimanite with an alteration rim of muscovite surrounded by fine matrix made of Bt + Fsp. E) Felsic mylonitic gneiss (AN22A) with mineral assemblage made of Grt + Kfs + Pl + Sil + Spl + Bt; F) Corundum-bearing leucocratic rock (AN22B) made of Grt + Kfs + Pl + Bt + Spl + Crn.

5.6.1.2.1 Gabbroic rocks

Gabbroic rocks (samples AN07B, AN08B, AN08C, AN20, AN21A) show a mainly coarse-grained granoblastic and nearly isotropic texture (Fig. 5.4G; Table S5.1, Fig. S5.1B). It consists of mm- to cm-sized euhedral-subhedral grains of plagioclase with polysynthetic gemination, euhedral-subhedral clinopyroxene and subhedral amphibole (Fig. 5.4G). Predominantly accessory phases are ilmenite and apatite, mainly included in pyroxene. The inner portion of the body (i.e., AN08C, AN20) displays an isotropic texture with equigranular crystals (in the order of mm- μ m size). Toward the shear zone, the gabbro (AN21, AN08C) shows well-defined foliation marked by amphibole aligned almost parallel to the schistosity of the shear zone rocks (Fig. 5.3A), differently to what is stated by Stünitz, (1998; see figure 3 of the cited work). Closer to the shear zone, the gabbro contains big garnet grains (up to 2 cm in size; AN07B/AN08B; Fig. S5.1E) and the rock is coarse grained (cm-sized) clearly shown by clinopyroxene grains (i.e., AN07B; Fig. S5.1E). The gabbroic body is locally crosscut by leucocratic dykes showing coarse-grained granoblastic texture of plagioclase and clinopyroxene (AN21B; Fig. 5.3L).

5.6.1.2.2 Felsic Granulite

Felsic granulites (AN18, AN19) consist of coarse-grained garnet (0.5–2 mm), plagioclase, sillimanite, K-feldspar, quartz, and subordinated biotite (Fig. 5.4H; Table S5.1). The texture is mainly granoblastic and no evidence of deformation were observed. Garnet occurs as elongate porphyroblasts with variable concentrations of inclusions of plagioclase, quartz, rutile and zircon (Fig. 5.4H). Sillimanite shows a variable modal abundance among the samples (more abundant in granulite AN18) occurring mainly in prismatic subhedral grains and locally as inclusions in garnet. Plagioclase is the dominant feldspar; K-feldspar locally occurs in association with garnet and biotite (Fig. 5.4H). Biotite is rare and is mostly chloritized at the rim. Retrograde white mica is observable around garnet grains. Accessory minerals are apatite, zircon, monazite, rutile and graphite, which is less abundant than in samples from the upper amphibolite and transition zones (i.e., AN11, AN09). Rutile is the most abundant among the accessory minerals occurring in rounded shape and often in association with ilmenite.

5.6.2 Shear zone rocks

5.6.2.1 Amphibolites

A detailed petrographic characterization of mylonitic amphibolites was carried out on several thin sections, representative of the main grain size, mineral abundance and textural variations (AN01A-I; Fig. 5.5). This sample group corresponds to the mylonitic rocks described in the previous studies (Brodie., 1981; Brodie et al., 1989; Altenberger, 1997; Stünitz, 1998) who interpreted these as derived from the adjacent gabbroic body.

Mylonitic amphibolites consist of alternating bands of plagioclase- and amphibole/clinopyroxene-rich layers (Fig. S5.1A). Mylonitic texture is characterized by core and mantle structure where porphyroclasts (diameter of 0.5-1.0 mm) of plagioclase, amphibole or clinopyroxene and, rarely, garnet, are surrounded by a fine-grained recrystallized matrix composed of alternations of monophasic layers (either plagioclase, amphibole or clinopyroxene) with mixtures of plagioclase + clinopyroxene (\pm garnet and titanite) or plagioclase + amphibole (Fig. 5.5A-E). Modal abundances of amphibole (28-42%), plagioclase (28-36%) and clinopyroxene (15-25%), strongly varies along layers (Fig. S5.1; Table S5.1).

In Cpx/Pl-rich layers of the amphibolites (i.e., AN01D, Fig. S5.1A, D), clinopyroxene is preserved mainly as porphyroclasts (CpxI; Fig. 5.5G) showing tails of recrystallized clinopyroxene (CpxII; Fig. 5.5G) and/or amphibole (AmplI; Fig. 5.5C). Porphyroclasts are locally replaced by a greenish amphibole, which also occurs in fractures within the porphyroclasts or as equant grains adjacent to clinopyroxene grains (e.g., thin section AN01D, Fig. 5.5C, G). Clinopyroxene porphyroclasts can include inclusions of plagioclase, amphibole, calcite and ilmenite.

Amphibole porphyroclasts show intracrystalline deformation as evidenced by strong undulose extinction and deformation bands. Their long axes are orientated parallel to the foliation and are characterized by tails of recrystallized amphibole grains, which usually are beard-like overgrowths on the porphyroclasts (Fig. 5.5B). Brown-amphibole occurs as porphyroclasts, whereas green-amphibole (AmphI) predominates in the fine-grained recrystallized matrix (AmphII) (Fig. 5.5C, E). Amphibole porphyroclasts can include apatite, plagioclase, clinopyroxene and zircon.

Rarely, large porphyroclasts of sub-rounded pinkish garnet were observed along the clinopyroxene/

plagioclase-rich layers. These garnet grains locally show a poikilitic texture with clinopyroxene and plagioclase (e.g., thin sections AN01, D, H, I; Fig. 5.5E).

Most of the plagioclase is completely recrystallized as fine-grained matrix (PII) but it locally occurs as porphyroclasts or ribbon (PII) (Fig. 5.5A-G). Rounded or ellipsoidal plagioclase porphyroclasts show undulose extinction, bent twin planes and small grains at their margins by subgrain rotation and by “bulging recrystallization” (Fig. 5.5D; Drury et al. 1985).

Locally, calcite is present in the strain shadows as termination of the porphyroclasts or between amphibole porphyroclasts (e.g., AN01B; Fig. 5.5H). Titanite, ilmenite, apatite and zircon are common as accessories minerals (Fig. 5.5C, F). Ilmenite is quite abundant in mylonitic samples occurring in recrystallized interstitial grain along the foliation. Elongated or sigmoidal shaped crystals of titanite preferentially occur within the Cpx/Pl-rich layers but also as inclusions in amphibole porphyroclasts (e.g., AN01A, B, D; Fig. 5.5C). In some cases, titanite occurs in big crystals with up to 500 μm wide x 1 mm long showing the typical lozenge shape and double set of twinning (Fig. 5.5F). Usually, when zircon is very common, titanite is less abundant (e.g., AN01C). Late alteration product such as calcite, chlorite, epidote, and mica are concentrated in fractures and cross-cutting veins.

Ultramytonitic amphibolites (i.e., AN06L; clasts <10% and matrix grain size <0.125 mm) have a mineral assemblage mainly constituted by porphyroclasts of amphibole and plagioclase (up to 1 mm large), surrounded by a finer matrix (average of 100 μm) made by recrystallized amphibole, plagioclase and clinopyroxene (Fig. 5.6A; Table S5.1). Biotite porphyroclasts are mainly aligned along the main foliation. Clinopyroxene is mainly preserved as recrystallized grains (~150 μm) in the matrix (Fig. 5.6A). The rare garnet occurs in poikilitic texture with plagioclase and ilmenite and has a size of 250 to 500 μm . Quartz was locally observed as cluster surrounded by biotite and matrix forming minerals. Rounded apatite and anhedral ilmenite are abundant as accessory minerals (size up to 250 μm), several grains of zircon with size up to 100 μm occur. Chlorite, epidote and rare crystals of white mica are present as alteration products in late fractures and/or veins.

5.6.2.2 Paragneisses

Sheared paragneisses (i.e., AN09, AN09C, AN22A; Fig. S5.1) have a mineral assemblage of Grt + Sil + Kfs + Qz + Pl ± Bt (Fig. 5.6; Table S5.1). Mylonitic domains are characterized by large garnet porphyroclasts up to 5 mm in size wrapped by a matrix of sillimanite, feldspar, and recrystallized quartz (Fig. 5.6B, C). Randomly oriented quartz, plagioclase, biotite, and rutile are observed as inclusions in garnet porphyroclasts (Fig. 5.6B-E). Syn-kinematic biotite (BtII) occurs along the main foliation, in strain shadows around garnet and feldspar porphyroclasts (Fig. 5.6C, D). Locally, relicts of biotite (BtI) are present in low strain domains with anhedral shape and included in garnet porphyroclasts (Fig. 5.6C, D). Sillimanite is observable both as big porphyroclasts (up to 1-2 mm long) and along the mylonitic foliation with a smaller grain size (up to 250 µm; Fig. 5.6B). Feldspars occur as porphyroclasts up to 500 µm in size and syn-kinematic mineral along the main foliation showing evidence of ductile deformation such as undulose extinction and deformation lamellae (Fig. 5.6B-F). Quartz is mostly present along the matrix showing the typical fabric of dynamic recrystallization formed by irregular grain boundaries and deformation lamellae (Fig. 5.6B, C; Passchier and Trouw, 2005). Rutile (with average grain size of 150 µm), ilmenite, monazite (grain size up to 500 µm) and zircon are abundant as accessory minerals and occur in the fine-grained matrix (Table S5.1). Ultramylonitic paragneisses occur as thin, mm-cm sized layers (sample AN09C) among the mylonitic domains. The mineral assemblage consists of rounded garnet, sillimanite porphyroclasts embedded in a recrystallized matrix of plagioclase and biotite (Fig. 5.6C-D). In this domain, sillimanite porphyroclasts are surrounded by secondary white mica (Fig. 5.6D).

Locally, paragneisses contain boudinaged leucocratic layers (AN22B) showing a mylonitic fabric characterized by K-feldspar, corundum and minor Bt + Grt + Pl + Spl (Fig. 5.6F; Table S5.1). K-feldspar porphyroclasts are the main constituent of the leucocratic layer and are characterized by plagioclase exsolution. The greyish corundum porphyroclasts are up to 2 cm in size. Garnet occurs as porphyroclast (grain size up to 5 mm) including biotite, plagioclase, and zircon. Green spinel occurs as a minor constituent of the corundum-bearing leucocratic sample (AN22B), it is mostly associated with garnet, corundum and biotite (Fig. 5.6E). Locally a greenish spinel surrounded by biotite is recognisable also within the mylonitic paragneiss (AN22A; Fig. 5.6F). Biotite showing kinking occurs along the foliation as well as are included within garnet and spinel. Plagioclase is mainly hosted within strain shadows around garnet. Several grains of monazite up to 500 µm in size is observable as accessory mineral.

5.7 Bulk and Mineral chemistry across the shear zone

5.7.1 Bulk Rock

Bulk rock composition was determined for representative samples across the Anzola shear zone rocks. A full description of the analytical methods is presented in chapter 3.5.1, whereas results and related tables are available in Figure 5.7 and in the Supplementary material (Table S5.2; Figure S5.2).

Both major and trace elements bulk rocks composition highlight a strong lithological variability across the Anzola transect.

SiO₂ contents range between 46 to 49 wt.% for mafic rocks of the hanging wall, shear zone and footwall (Scp-bearing gneiss, mylonitic amphibolites, gabbros, respectively), whereas is between 48-65 wt.% for calc-silicates from the footwall and paragneisses from hanging wall, shear zone and footwall (migmatitic paragneiss, mylonitic paragneisses, felsic granulites, respectively; Fig. 5.7A).

Paragneisses and felsic granulites are characterised by Al₂O₃ in the range of 21.5 and 25.0 wt. %, except for one felsic granulite (AN19) that contain lower Al₂O₃ content around 16.4 wt.%, probably due to the scarce abundance of sillimanite. Mafic rocks and calc-silicates show even lower values in Al₂O₃ ranging from 11.0 to 16.4 wt.% (Fig. 5.7A).

TiO₂ contents span mainly between 1.0 to 1.2 wt.% and reach the highest values within mylonitic amphibolites and rutile-rich granulite, maybe due to the abundance of titanium-rich accessory minerals such as titanite, ilmenite and rutile (Fig. S5.2A).

The MgO versus CaO diagram was plotted to emphasise the lithological heterogeneity along the Anzola profile (Fig. 5.7B). Paragneisses and felsic granulites, both undeformed and mylonitic samples, show low MgO and CaO values ranging between 2.0-4.0 wt.% and 0.5-5.0 wt.%, respectively. Conversely, mafic rocks have MgO and CaO values that don't exceed 4 wt.% and 10 wt.% in that order. Specifically, mylonitic amphibolites display values of MgO ~6.0 wt.% and CaO ~12.5 wt.%, lower respect with the Scp-bearing gneisses from the hanging wall (MgO = 6.0 wt.% and CaO = 16 wt.%) and gabbroic rocks (MgO ~8.5 wt.% and CaO ~15.75 wt.%). Calc-silicate from the footwall stands out respect with the other lithologies having the higher CaO content of ~20 wt.% and lower MgO of ~3.0 wt.%.

Bulk trace elements that allow to distinguish the different rock types (i.e., mafic from the metasedimentary rocks) are in particular the REE elements and Cr versus Co (Fig. 5.7C, D; S5.2B; Table S5.2).

The concentrations in High-REE (HREE) have a similar flat trend for all the studied samples, but generally metasedimentary rocks have REE concentration higher than 40 times C1 chondrite, whereas mafic rocks show lower concentration below C1 chondrite (Fig. 5.7C, D). The highest values are reached for felsic granulite (AN18), whereas the lowest for Scp-bearing gneiss (AN10). Light-REE (LREE) show more significant differences among lithologies (Fig. 5.7C, D). Overall, the mafic rocks have LREE concentrations lower than metasedimentary rocks (Light-REE > 100CI). Among the mafic protoliths, the highest values come from the inner portion of the gabbroic body (AN20), whereas the hanging wall Scp-bearing gneiss is the lithology that show a significant depletion in LREE.

Paragneisses, felsic granulite and calc-silicate show negative anomaly in Eu (except that for felsic granulite AN18), with lower REE values for calc-silicate (AN06D) and felsic granulite (AN18; Fig. 5.7C). The Eu concentration is maybe due to the different abundance of feldspar: negative anomaly means the predominance of K-feldspar, whereas positive anomaly means dominance of plagioclase as it is effectively observed for felsic granulite (AN18) and usually for mafic rocks (Dostal & Capedri, 1979). Calc-silicate reproduce the general paragneisses and felsic granulites with lower concentration in LREE. HREE concentrations have a flat pattern comparable with those of the mafic rocks (Fig. 5.7C, D).

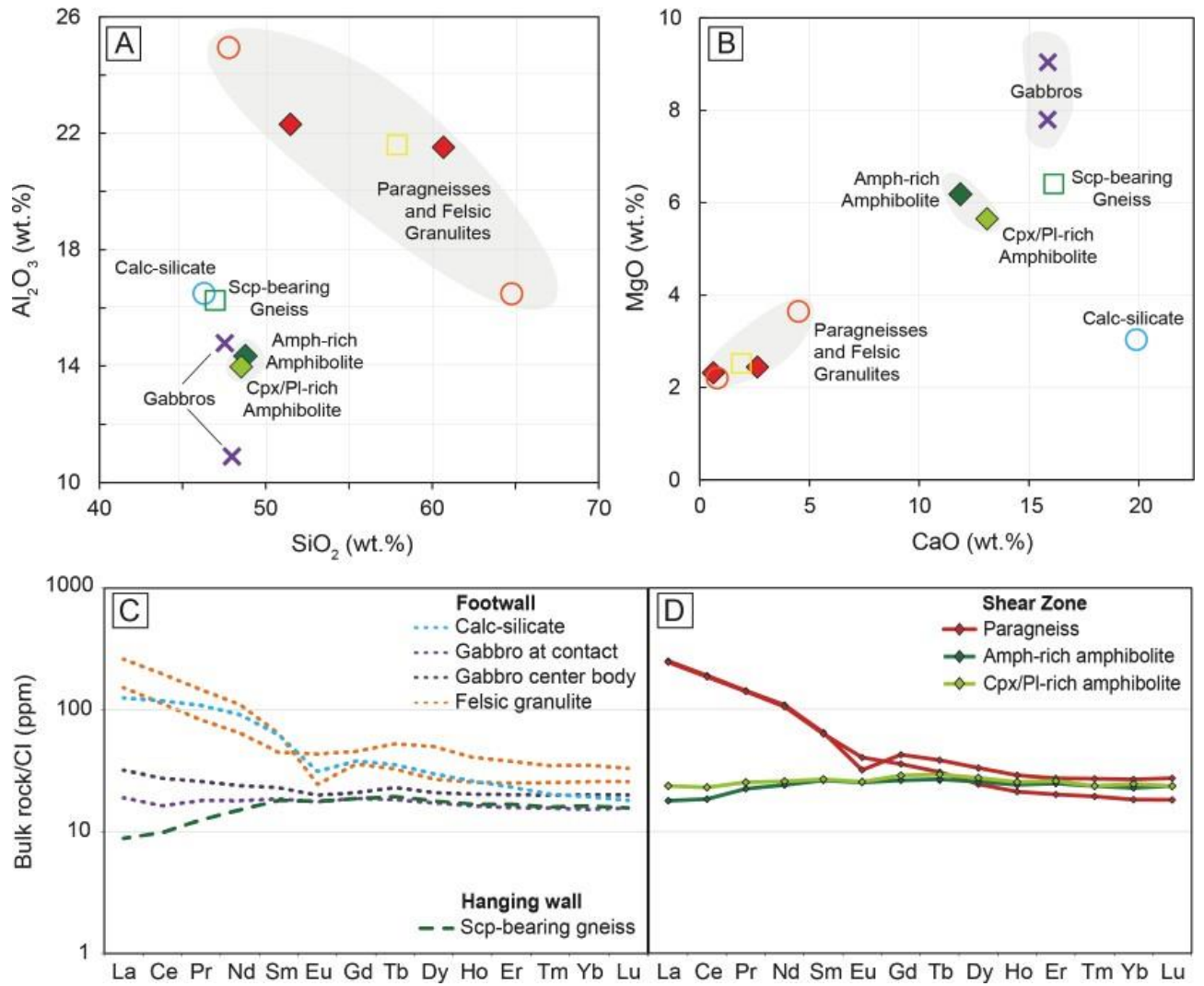


Fig. 5.7 – Bulk rock diagrams: A) Al_2O_3 (wt.%) versus SiO_2 (wt.%). B) MgO (wt.%) versus CaO (wt.%). C) REE patterns for footwall and hanging wall rocks; D) REE patterns for shear zone rocks. All data are normalised to chondrites values according to McDonough and Sun, (1995).

5.7.2 Mineral chemistry: Major elements

In this section, we reported the results of mineral composition from mafic rocks (i.e., amphibole, clinopyroxene, feldspar, garnet), calc-silicates (i.e., clinopyroxene, feldspar), paragneisses and felsic granulite (i.e., feldspar, garnet, biotite, spinel). Details on the methods are reported in chapter 3.5.2; results are reported in Appendix 2 (Table S5.3) and Figure 5.8, 5.9. Links to the petrographic relationships are highlighted through reference to figures 5.4-5.6.

5.7.2.1 Amphibole

According to the classification of Hawthorne et al. (2012), amphibole is mostly pargasite ($\text{Na} + \text{K} > 0.50$ a.p.f.u. and $\text{Si} < 6.5$ a.p.f.u.), with a few edenite and hornblende grains analysed within mylonitic amphibolites (Fig. 5.8A; cf. Fig. 5.5B). In the Amph-rich mylonites (i.e., AN01A, AN01C), the amphibole composition tendentially changes from pargasite in the brown porphyroclasts (AmphI) to green edenite in the syn-kinematics grains (AmphII; Fig. 5.8A; cf. Fig. 5.5H).

5.7.2.2 Clinopyroxene

In the studied samples, clinopyroxene is prevalently diopside ($\text{Fe} < 50$ mol%; Fig. 5.8B). Exceptions are the gabbroic rocks (AN08B, C, AN07) where clinopyroxene has an augitic composition ($20 \text{ mol}\% < \text{Ca} < 45 \text{ mol}\%$; Fig. 5.8B; cf. 5G) and in the Cpx/Pl-rich mylonitic amphibolites (AN01D; cf. 5G) where has hedenbergitic composition ($\text{Fe} > 50 \text{ mol}\%$), as well as clinopyroxene from the calc-silicates (i.e., AN06C; Fig. 5.8B, cf. Fig. 5.4F).

5.7.2.3 Plagioclase

Plagioclase from the mafic rocks, ranges in composition mainly from andesine to labradorite (Fig. 5.8C). Anorthite content up to 90-100 mol% were obtained from the calc-silicate sample (AN06C; Fig. 5.8C). Plagioclase in the gabbro (AN08B, C, AN07) has labradorite composition with anorthite content between 50-60 mol%. Plagioclase from mylonitic amphibolites shows lower anorthite contents ($< 50 \text{ mol}\%$), particularly in the Amph-rich mylonites (30-40 mol%) and, generally for all syn-kinematic grains (PlII). Few plagioclase grains found as inclusion in amphibole (i.e., AN01D) are oligoclase, with an anorthite content around 25-35 mol%.

Paragneisses and felsic granulite contain both plagioclase and K-feldspar, except for the felsic

granulite which present only plagioclase (AN18; Fig. 5.9A; Table S5.3). The latter ranges in composition from labradorite to andesine: the highest anorthite contents were obtained for the low deformed migmatite (AN11, average An = 64 mol%). Mylonitic paragneisses are characterized by anorthite contents ranging from 40 to 55 mol%, with the highest values related to plagioclase included in garnet (55 mol%), whereas felsic rocks from the footwall (AN06D, AN18, AN19) show mainly andesine composition (30 mol% < An < 40 mol%). K-feldspar has orthoclase content mainly in the range of 80-95 mol% (Fig. 5.9A). The mylonitic paragneiss (AN09) is characterised by lower orthoclase contents (75 mol%).

5.7.2.4 Garnet

As shown in the ternary diagram (Fig. 5.9B), garnet is significant variable among sample types. All samples fall close to the almandine + spessartine vertex (> 50%). The grossular content of garnet allows to distinct three main groups associated with different lithotypes: i) garnet from Cpx/Pl-rich mylonitic layers from amphibolites shows the highest grossular content (~35-40%); ii) intermediate values (~20-25%) characterize garnet from the Amph-rich mylonitic amphibolites and gabbroic rocks; iii) paragneisses host garnet with the lowest grossular content (~5%). On the other hand, starting from the Alm + Sps vertex, the increase in the pyrope component (15% → 40%) is observed from corundum-bearing leucocratic rocks (AN22B) across mylonitic paragneisses (AN22A, AN09C3, AN09) and from hanging wall paragneiss, migmatite (AN11), to the footwall paragneiss (AN06D) and felsic granulite (AN18, AN19). Moreover, pyrope content minor or greater than 35% (dashed grey line in Fig. 5.9B) marks samples from either the footwall or hanging wall, respectively. The increase in pyrope content over 35% also correlates with the switch from amphibolite to granulite-facies (Fig. 5.9B). Interestingly, this change of metamorphic facies is also marked by a slightly decreases of the grossular content within granulitic samples.

5.7.2.5 Biotite

Overall, biotite from paragneisses and felsic granulite has Fe# (Fe/Fe+Mg) that ranges between 0.25 and 0.60, with any specific distinction on the base of the metamorphic grade or deformation (i.e., BtI, BtII; Fig. 5.9C, S5.2C; Table S5.3). High Fe# values are recorded by corundum-bearing leucocratic rock (AN22B) and chloritized felsic granulite (AN19), whereas low Fe# values are shown by mylonitic paragneiss (AN09) and felsic granulite (AN18). Overlapping of Fe# values are present only by two

mylonitic paragneisses (AN09C, AN22A; Fig. 5.9C). Al contents range mainly between 1.2-1.6 a.p.f.u. for all rock types except for biotite from corundum-bearing rock where Al is higher (from about 1.7 to 1.9 a.p.f.u.). Ti contents range between 0.15 to 0.45 a.p.f.u. with an average value of 0.3 a.p.f.u, low values for felsic granulite (AN18), corundum-bearing rock (AN22B) and scattered biotite from ultramylonitic paragneiss (AN09C3; Fig. S5.2C).

5.7.2.6 Spinel

Spinel occurs as minor component in mylonitic paragneiss (AN22A) and corundum-bearing leucocratic rock (AN22B; Table S5.1). Spinel grains occurring in the two samples show the same petrographically features. Nevertheless, the spinel crystals in mylonitic paragneiss are hercynite/gahnite in composition with ZnO content around 12 wt.%, whereas in corundum-bearing sample spinel is hercynite with ZnO content around 0.9 wt.% (Table S5.3).

5.7.3 Mineral chemistry: Trace Elements

Trace elements concentrations were determined for main mineral phases, i.e., clinopyroxene and amphibole, for representative mafic rocks and calc-silicates: Scp-bearing gneiss (AN10) from the hanging wall, mylonitic amphibolites (AN01A, AN01D), calc-silicate (AN06C) and gabbros (AN07B, AN08B, AN08C) from the footwall (Fig. 5.3-5.6; Table S5.1). The reason why we focused only on these samples is that the Anzola shear zone has been always described as developed at the expense of the gabbroic body (e.g., Brodie, 1981; Altenberger, 1997; Stünitz, 1998; Rutter et al., 2007). In particular, we focused on the Rare Earth Element (REE) concentrations with the aim to diagnose the protoliths of mylonitic amphibolites. Results are reported in Supplementary material (Table S5.4). In Figure 5.10 we plotted clinopyroxenes and amphiboles REE patterns for the studied samples normalised to chondrites values according to McDonough and Sun, (1995).

Clinopyroxene REE patterns show concentrations between 1- and 10-times CI for all samples except for gabbroic rocks that have higher concentration (>10 times CI; Fig. 5.10A). Mylonitic amphibolites have similar clinopyroxene REE behaviour despite the different compositional layering (Amph-rich, Cpx-Pl rich). Scp-bearing gneiss from the hanging wall is strongly depleted in LREE (around 1 time CI). Mylonitic amphibolites and calc-silicates share a similar quite homogeneous REE patterns with a slight increasing in the HREE concentrations. Clinopyroxene REE patterns for gabbroic samples were

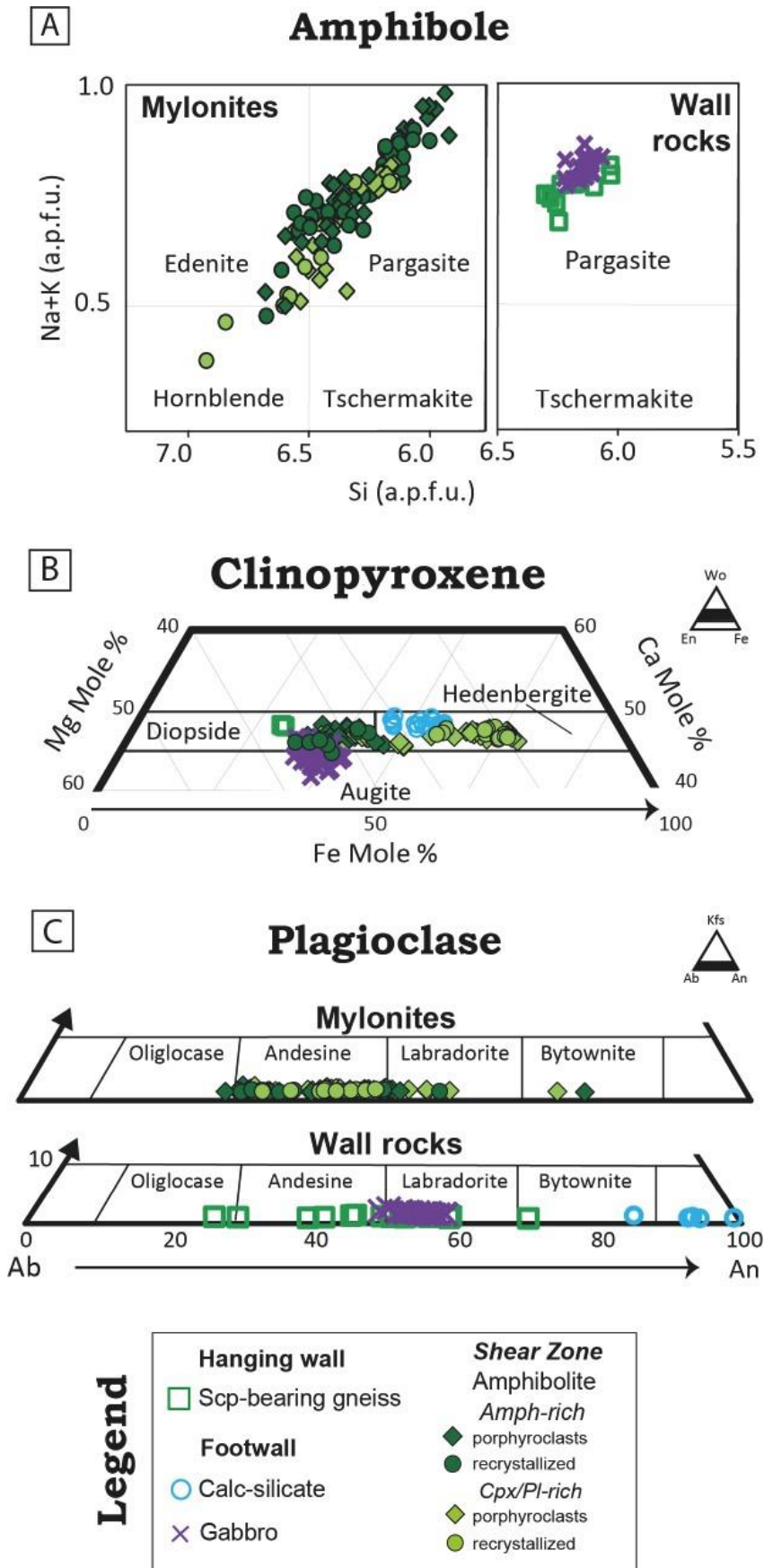


Fig. 5.8 –Classification and geochemical diagrams for main mineral phases for the mafic rocks and calc-silicates. Mineral composition diagrams for: A) Amphibole; B) Clinopyroxene; C) Plagioclase. Legend of the symbols is reported; in particular, “porphyroclasts” referred to AmphI, CpxI and PlI whereas “recrystallized” referred to AmphII, CpxII, PlII in figure 5.5 of petrography.

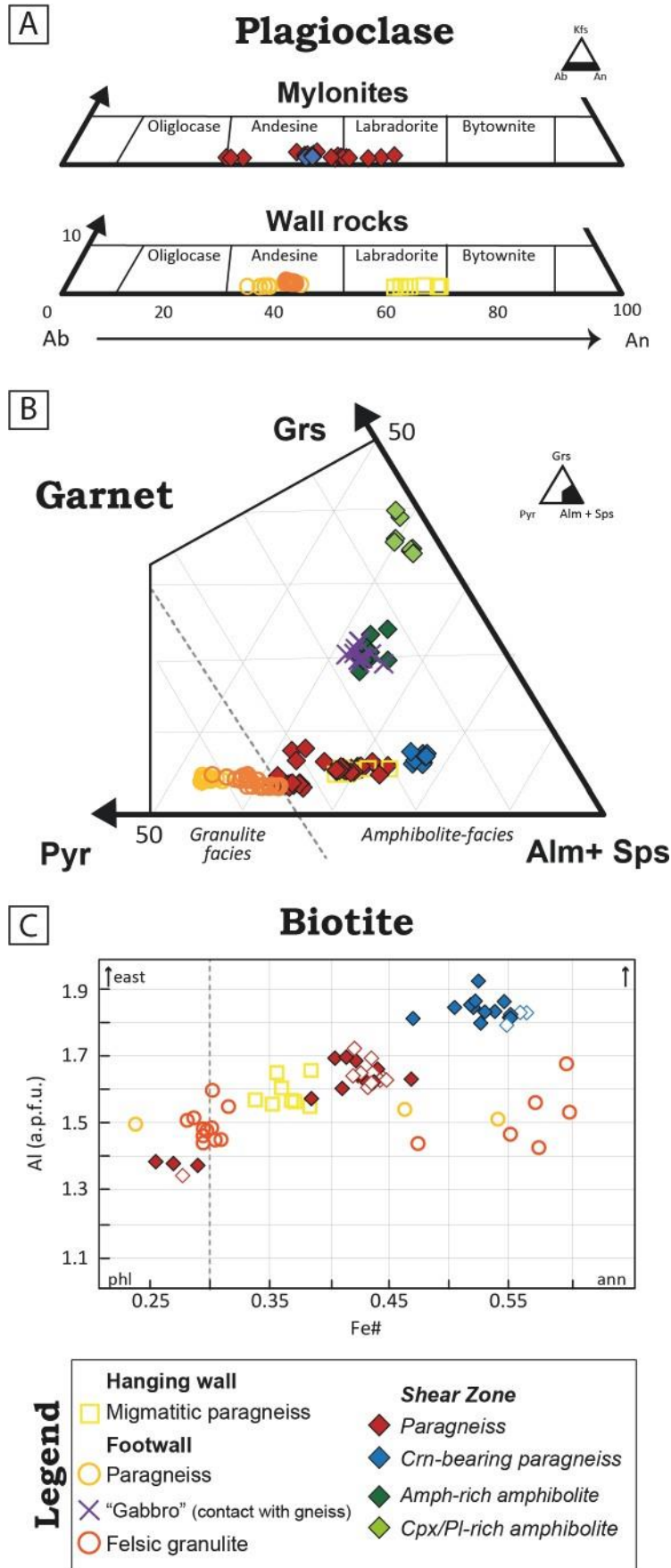


Fig. 5.9 – Classification and geochemical diagrams for main mineral phases for paragneisses and felsic granulites. Mineral composition diagrams for: A) Plagioclase; B) Garnet. C) Aluminium (a.p.f.u.) versus Fe# (Fe/Fe+Mg) diagram for Biotite; Btl and BtlI from Fig. 5.7 were distinguished in filled and open diamond, respectively. Legend of the symbols is reported.

distinguished on the base of the grain size (e.g., Fig. S5.1E – Gabbroic rocks AN07B): coarse-grained (CpxI) and fine-grained (CpxII). Coarse grained parts share a similar pattern to the fine-grained one and negative anomaly in Eu, whereas fine-grained part show a more flattened trend.

Amphibole REE patterns show comparable behaviour between 10- and 100-times CI for all samples, except for the REE pattern of porphyroclast (AmphI) in Amph-rich mylonitic amphibolites and the Scp-bearing gneiss from the hanging wall that show strong depletion in LREE (Fig. 5.10B). Amphibole from Amph-rich mylonites shows similar REE patterns but with significantly different concentrations where porphyroclasts (AmphI) are overall richer in REE up to about 3 times the normalized REE values from syn-kinematic grains (AmphII; Fig. 5.10B; c.f., Fig. 5.5B). A negative Eu anomaly is apparent for the amphibole from the Amph-rich mylonites, whereas it is only slightly evident for the other samples. Amphibole REE patterns for gabbroic samples were distinguished, as clinopyroxenes, on the base of the sample grain size (e.g., Fig. S5.1E – Gabbroic rocks AN07B): coarse-grained (AmphI) and fine-grained (AmphII).

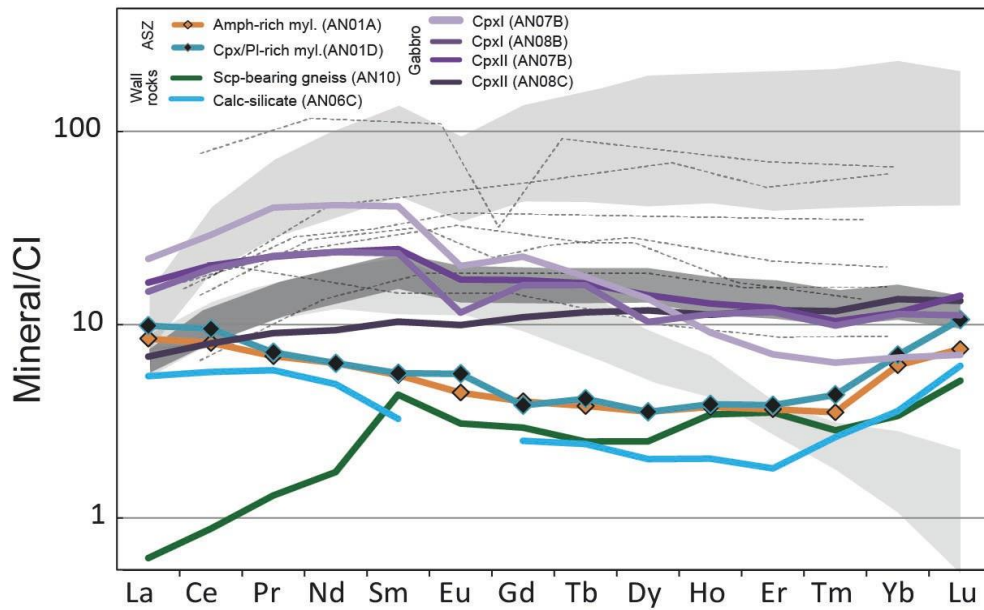
5.8 Geothermobarometry

Pressure (P) estimates in the range between 0.7-0.8 GPa were determined for the aluminosilicate bearing mylonitic rocks, namely paragneisses and felsic granulites, using the Garnet-Aluminosilicate-Plagioclase geobarometer (GASP; Holdaway, 2001) considering sillimanite as the stable aluminosilicate. P conditions of the IVZ have been presented by several authors (e.g., Zingg, 1980; Henk et al., 1997; Barboza and Bergantz, 2000; Luvizotto and Zack, 2009; Redler et al., 2013; Kunz et al., 2014; Kunz and White, 2019) giving an average value of 0.7 GPa for granulite to amphibolite facies boundary. The mineral assemblages of mafic rocks are not suitable for pressure estimates by conventional geobarometers.

Temperature conditions were determined by combining the following geothermometers: Zr-in-Rutile, Ti-in-Amphibole and Garnet-Biotite (Grt-Bt) exchange. Results are reported in Figure 5.11 and Supplementary material (Table S5.5, S5.6). Since the Zr-in-Rutile and Ti-in-Amphibole geothermometers are pressure dependent, we set the pressure at 0.7 GPa in accordance with our and literature estimates. The applied geothermometers allow to assess both pre-shear and syn-shear conditions. The pre-shear conditions have been estimated from samples avoiding mylonitic deformation through the Zr-in-Rutile geothermometer (Kohn, 2020) and the Grt-Bt (Holdaway, 2000)

A

Clinopyroxene - REE



B

Amphibole - REE

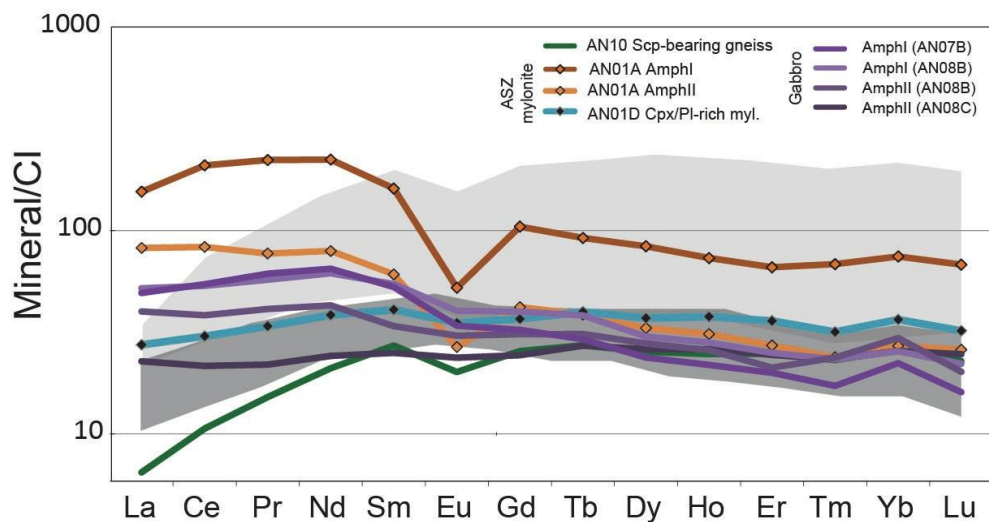


Fig. 5.10 – REE diagrams for A) Clinopyroxene. In colours our samples, in thick dark-grey line data for mafic intrusion from Val Strona di Omegna (Berno et al., 2020), in light grey band data for Finero mafic complex from Zanetti et al. (2013), in dashed lines data for Mafic Complex from Mazzucchelli et al. (1992). Gabbro data are distinguished on the base of the grain size (coarse grained-CpxI; small grained-CpxII) B) Amphibole. In colours our samples, in dark-grey band data from Berno et al. (2020), in light grey band data from Zanetti et al. (2013). Data for Amph-rich mylonites and gabbro are distinguished on the base of textural features (i.e., porphyroclasts, recrystallized, coarse and small grained).

in several lithologies ranging from upper amphibolite to granulite facies conditions, while the Ti-in-Amphibole geothermometer (Liao et al., 2021) was used only in a Scp-bearing gneiss from the hanging wall (Fig. 5.11). Syn-shear temperature conditions were constrained on mylonitic amphibolites (Ti-in-Amphibole; Liao et al., 2021) and paragneisses (Grt-Bt; Holdaway, 2000). The Ti-in-Amphibole was used for the different generations of amphiboles, i.e., the porphyroclasts (AmphI) and the syn-kinematic recrystallised grains (AmphII). For the Grt-Bt geothermometer we paired the chemical analyses of syn-kinematic biotite (BtII) with garnet rims (Fig. 5.6C, F). Constraints on the pre-shear conditions from the Zr-in Rutile geothermometer define a slightly decreasing trend from granulite facies (816 ± 27 °C) to upper amphibolite facies rocks (716 ± 65 °C, Fig. 5.11). Our estimates agree with data from similar rocks in the studied area (Luvizotto & Zack, 2009). The Grt-Bt geothermometer yielded higher temperatures in the footwall (up to 900 ± 20 °C for the felsic granulites) with respect to the migmatites in the hanging wall (600 ± 40 °C), partially overlapping estimates from the Zr-in-Rutile (Fig. 5.11). The Ti-in-Amphibole geothermometer provided temperature of 828 ± 28 °C in agreement with other geothermometers.

Syn-kinematic conditions from mylonitic samples were defined by Grt-Bt and Ti-in-Amphibole geothermometers providing temperatures between ~ 550 and ~ 700 °C and ~ 750 and ~ 950 °C, respectively. As regard the Ti-in-Amphibole, the T values gradually decrease as function of the textural positions, i.e., from amphibole included in clinopyroxene and porphyroclasts to recrystallized grains (Fig. 5.11; c.f., Fig. 5.5).

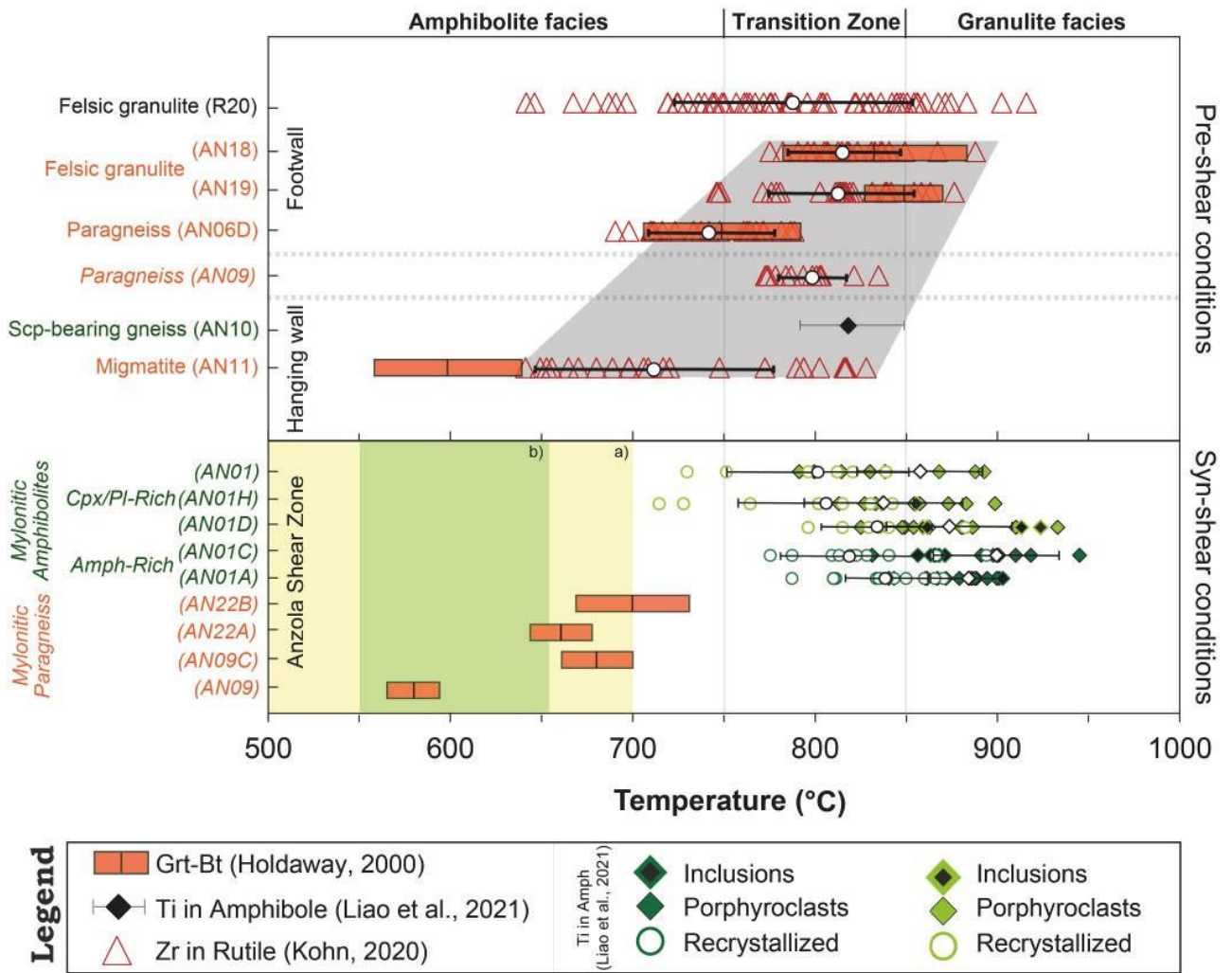


Fig. 5.11 –Pre-shear and syn-kinematic temperature estimates for the studied samples across the Anzola transect. Zr-in-Rutile temperature conditions for felsic granulite (R20) are from the studied area from Luvizotto & Zack, (2009) recalculated with the new calibration of Kohn, (2020). The grey box encloses the Zr-in-Rutile data and broadly defines the temperature gradient from granulitic to upper amphibolitic facies conditions. The temperature conditions for mylonitic amphibolites determined by Brodie (1981) and Stünitz (1998) are also shown as boxes a) and b), respectively. Ti-in-Amphibole estimates for Scp-bearing gneiss (AN10) and Grt-Bt data are reported as median values and relative standard deviations. For Zr-in-Rutile and Ti-in-Amphibole mylonites single crystals data median with standard deviations is defined by white circles/diamond and black lines.

5.9 Discussion

5.9.1 Pre- and syn-deformational PT conditions

Mineral assemblages from the footwall rocks (Grt + Sill + Pl + Kfs + Qz ± Bt; Fig. 11) indicate granulite facies conditions at T of ca. 800-900 °C comparable to our temperature estimates (Zr-in-Rutile and Grt-Bt geothermometers) and to the literature data determined by Zr-in-Rutile from felsic granulites (Luvizotto & Zack, 2009; Fig. 5.11). The lower Zr-in-Rutile and Grt-Bt thermometric results (Fig. 5.11) for the hanging wall (~550-800 °C) are consistent with the mineral assemblages and the decreasing metamorphic field gradient towards SE. Hanging wall rocks are characterized by: i) the stability of amphibole and the lack of orthopyroxene in mafic rocks (Fig. 5.4, 5.5); ii) the occurrence of sillimanite and minor biotite in paragneisses (Fig. 5.6); iii) the lack of muscovite (except for retrograde white mica; Fig. 5.6D). These observations indicate conditions below the Opx-in isograd and above the Kfs + Sill-in isograd suggesting that the pre-shear conditions of the studied samples resulted between upper amphibolite to granulite facies conditions, in agreement with previous estimates and metamorphic field gradient studies (e.g., Zingg, 1980; Fig. 5.2A).

Temperature estimates from mylonitic rocks revealed interesting features. The Ti-in-Amphibole geothermometer applied for mylonitic amphibolites provided systematically higher T for porphyroclasts with respect to those of surrounding recrystallized grains (Fig. 5.11). This suggests that deformation started at high temperature conditions (i.e., temperature estimates from amphibole porphyroclasts) not significantly different from pre-shear conditions as recorded in the footwall. We further observed some textural features suggesting high temperature conditions during deformation, such as the occurrence of interstitial ilmenite within mylonitic amphibolites (i.e., AN01D, AN01E) could suggest the presence of a melt component during the first deformation phases (e.g., Ghatak, 2020). The T obtained from mylonitic paragneisses are systematically lower with respect to T estimated by Ti-in-Amphibole geothermometer including recrystallized grains (Fig. 5.11). This difference would indicate that the two geothermometers recorded different stages of the deformation, in agreement with the observations of local occurrence of retrograde minerals within the matrix of mylonitic paragneisses. Here, we observed sillimanite porphyroclasts always surrounded by white mica, especially within the ultramylonitic portions (Fig. 5.6D).

T estimates for mylonitic amphibolites were determined in previous studies on the base of

microstructural and chemical changes in amphiboles (from porphyroclasts to recrystallized grains) within and outside the mylonitic bands (Brodie, 1981; Stünitz, 1998). Brodie (1981) reported increasing T in mylonitic amphibolites during prograde regional metamorphism from low- to high-grade amphibolite facies (between 500-700 °C). Conversely, Stünitz (1998) stated that the deformation of amphibolites occurred during a retrograde P - T path under amphibolite facies conditions at approximately 550 to 650 °C and confining pressures of probably less than 0.8 GPa. Literature data are in perfect agreement with our T estimates based on Grt-Bt geothermometry, resulting lower than T determined with the Ti-in-Amphibole geothermometry (up to ca. 200 °C). Based on our data, we suggest that the shear zone was active from granulite to amphibolite facies conditions (Fig. 5.11). Lithologies recorded different stages of deformation started at higher T conditions, in presence of melt and in a diffuse mode, as still recognisable within mylonitic amphibolites, and continued under lower T conditions with a progressive strain localization as documented by the (ultra-)mylonitic paragneisses (Fig. 5.6D). Summing up, our approach based on the coupling of different geothermometers allow to reconstruct the T evolution of the shear zone. It set at the pre-existing rheological boundary between granulite to upper amphibolite facies as testify by geothermobarometers on wall rocks. Then, the deformation started at high T as documented by the amphibole-based geothermometer, and continued down to amphibolite facies, as documented by Grt-Bt geothermometer and literature data.

5.9.2 Protoliths within the Anzola shear zone are compositionally heterogeneous

Up to now, the Anzola shear zone has been interpreted to have formed by localized deformation of the footwall gabbroic rocks (e.g., Brodie, 1981; Altenberger, 1997; Stünitz, 1998) suggesting compositional homogeneity between the localized shear zone and wall rocks. However, our new geological and structural mapping, petrographic and geochemical analyses reported in this work document that the Anzola Shear zone is characterized by significant lithological heterogeneity.

Our field study shows that mylonitic zone and anastomosing ultramylonitic bands developed within two main lithologies, namely the paragneisses and amphibolites (Fig. 5.3A). Minor lithologies such as corundum-bearing felsic rocks and calc-silicates are interlayered within paragneisses and amphibolites, respectively (Fig. 5.3). Such lithological variations and the relative abundances among rock types also characterize the wall rocks. The hanging wall is characterised by upper amphibolite

facies rocks with different composition: paragneisses and minor mafic gneisses, both showing evidence for partial melting (Fig. 5.3A, B). The footwall is characterized by centimetre thick folded layers made of mafic gneisses, paragneisses and calc-silicates (Fig. 5.3A, G).

Petrographical observations, bulk rock (Fig. 5.7) and mineral chemistry (Figs. 5.8, 5.9) indicate that the mylonitic and ultramylonitic paragneisses are derived from protoliths with high affinity to the adjacent wall rock (hanging wall; Fig. 5.3, 5.7, 5.9). Little variations occur in term of mineral assemblage and abundance (Table S5.1), such as the presence of Crn-bearing paragneiss (AN22B; Fig. 5.6F, 5.9C) or the absence of K-feldspar and abundance of sillimanite and rutile in felsic granulite (AN18; Fig. 5.4H, 7B). Furthermore, the increase of pyrope content in garnet show variations in relation of the switch of the metamorphic conditions in upper amphibolite to granulite facies (Fig. 5.9B). The protoliths of the mylonitic amphibolites cannot be associated with the adjacent gabbroic rocks as sustained by previous references (e.g., Brodie, 1981; Altenberger, 1997; Stünitz, 1998). Firstly, the gabbro is compositionally homogeneous, and it does not show apparent anisotropies except for a weak foliation at the contact with host rocks (Fig. 5.3I). The granoblastic and isotropic texture of the gabbroic samples is incompatible with the apparent compositional banding, i.e., Amph-rich and Cpx/Pl-rich layers, characterizing the mylonitic amphibolites (Fig. 5.3G, S5.1A, B). Moreover, these latter are generally richer in amphibole, which occurs only as thin layers or lenses within the gabbroic rocks (Fig. 5.3G, I). Further evidence for a different origin of mylonitic amphibolites is that they contain also abundant zircon and titanite grains, locally up to hundred microns in size that were never observed within the mafic body (Figs. 5.4G, 5.5).

Furthermore, mineral compositions, and in particular trace elements, provide fundamental information in order to shed light on different rock types involved by shearing (Figs. 5.7, 5.8). Plagioclase from gabbroic rocks have higher anorthitic contents (i.e., labradorite) with respect to plagioclase porphyroclasts analysed within the mylonitic amphibolites (i.e., andesine; Fig. 5.8C). Analogously, clinopyroxene from gabbroic samples are typical augite, whereas Amph-rich mylonites and Scp-bearing gneiss from the hanging wall contain diopside (Fig. 5.8B). Besides that, clinopyroxene porphyroclasts within the Cpx/Pl-rich mylonitic layers (e.g., AN01D) are hedenbergite as well as the composition of clinopyroxenes occurring in the calc-silicates at the contact with the shear zone (e.g., AN06C; Fig. 5.8B). Amphiboles are mainly pargasite in composition with minor hornblende as recrystallized grains within Cpx/Pl-rich mylonites (Fig. 5.8A). These results suggest that the amphibole composition alone is not

diagnostic to discriminate between domains that experienced different strain, as previously suggested by other authors (e.g., Brodie, 1981). Therefore, the observations at the microscale of alternating amphibole- and hedenbergite-bearing mylonitic layers, lead us to suggest that mylonites developed from the metamorphic volcano-sedimentary sequence of the Kinzigite Formation instead of gabbroic rocks. This observation is further supported by the occurrence at the outcrop scale of alternating layers of mafic gneisses and calc-silicates at the footwall of the shear zone (Fig. 5.3A, H).

As major element compositions, even the clinopyroxene REE patterns mark differences among mylonitic amphibolites and gabbroic rocks (Fig. 5.10A). Clinopyroxene from mylonitic amphibolites, indeed, have general lower REE concentration with respect to those within the gabbro; on the contrary, they partially mimic the composition of Cpx within the Scp-bearing gneiss from the hanging wall (Fig. 5.10A). Similarities were observed also between clinopyroxene from Cpx/Pl-rich mylonitic layers and the clinopyroxene within calc-silicates from the footwall (Fig. 5.10A). The REE patterns of clinopyroxene from gabbroic rocks share many similarities with clinopyroxene from other mafic bodies of the IVZ (Mazzucchelli et al., 1992, Zanetti et al., 2013 and Berno et al. 2020). In particular, the comparison of the REE patterns highlights a strong affinity of the Anzola gabbro with the mafic intrusion of the adjacent Val Strona di Omegna (Berno et al., 2020; Fig. 5.10A). The REE patterns of amphibole from mylonitic samples are extremely variable (Fig. 5.10B). Such variations can be attributed to control by variations in: i) the rock types/bulk chemistry, i.e., Amph-rich (amphibolite) vs Cpx/Pl-rich (calc-silicate) layers and ii) the textural features, e.g., porphyroclasts (AmphI) vs syn-kinematic grains (AmphII). Analogously to clinopyroxene also the REE patterns of amphibole from mylonites do not show strong affinity with REE patterns of amphibole from gabbroic rocks (Fig. 5.10B). Only the REE patterns of AmphII partially overlap those obtained from gabbroic rocks but differ for a more pronounced LREE fractionation over HREE and a more apparent Eu anomaly. As for clinopyroxene, the amphibole compositions of Anzola gabbro share many similarities with amphibole REE patterns of other mafic intrusions of the adjacent Val Strona di Omegna (Berno et al., 2020; Fig. 5.10B). It is worth to note that the REE patterns of AmphI share many similarities with those obtained from amphiboles within hornblendites fractionated from dioritic magmas and intruded in metamorphic roof (Liou and Guo, 2019). Even in our case, we cannot exclude that the REE patterns of AmphI are inherited from a magmatic protolith such as amphibole-rich dikes or sills intruded within metamorphic roof of the gabbroic intrusion. Moreover, similar mafic

dykes and sills have been documented within the migmatitic roof of the Mafic Complex exposed in other localities of the IVZ (Quick et al., 1993).

Summing up, both major and trace element compositions of clinopyroxene and amphibole do not indicate a total magmatic origin (i.e., gabbroic rocks) for the mylonitic amphibolites. Consequently, the hypothesis of gabbroic rocks as the main protolith for mylonitic amphibolites is inconsistent with the new data presented here. In contrast, the Anzola shear zone developed from a heterogeneous protolith consisting of alternating calc-silicates, paragneisses and mafic gneisses of the Kinzigite Formation (i.e., a metamorphic volcano-sedimentary sequence). Beside the dominant siliciclastic protolith (now metamorphosed to paragneisses), Amphl-rich layers may represent either dykes/sills related to the gabbroic rocks that intruded in the metamorphic roof or supracrustal mafic volcanics before shearing.

5.9.3 Formation of a major crustal shear zone along pre-existing rheological boundaries

The previous assumption that the Anzola shear zone developed within the gabbroic body (Brodie, 1981; Altenberger, 1997; Stünitz, 1998, Rutter et al., 2007) raises the question of why strain localization occurred in the presumably rheologically hardest lithology of the area. In the previous literature, attention has been focused on the role of amphibole to promote weakening during either prograde or retrograde geodynamic paths.

In this work, we show that the Anzola shear zone developed in a complex compositional, structural and metamorphic setting dominated by alternated paragneisses and supracrustal mafic rocks (Fig. 5.12). High strain deformation overprinted metamorphic rocks that already experienced both Variscan and late Variscan tectono-metamorphic and magmatic stages (Fig. 5.12A). In particular, the shear zone took advantage from the pre-existing boundary between upper amphibolite and granulite facies rocks, which is characterized by abundant migmatites (Fig. 5.12B). Beside the intrinsic heterogeneity of migmatites, all the gneissic rocks involved by shearing were characterized by abrupt changes in composition and structural features (Fig. 5.12A). The boundaries between compositionally contrasted rock pairs, indeed, coincide with significant viscosity variations and mechanically weaker layers (e.g., Prosser et al., 2003; Pennacchioni and Mancktelow 2007; Smith et al. 2015, Gardner et al. 2016, 2017).

Another factor favouring the development of mylonites is likely related to inherited Variscan structures, such as folds and associated shear planes (Fig. 5.12A). The attitude of fold limbs results indeed almost parallel to the shear planes suggesting that they promote preferential shear along them (e.g., Hughes et al., 2014). Folding of compositionally contrasted lithologies has dramatic effects on their rheological behaviour and distribution of metasomatic reactions (Corvò et al., 2021; Maino et al., 2021) and represent important pathways favouring strain localization at all scales (e.g., Austrheim, 1987; Piazzolo et al. 2002; Fossen et al., 2017, 2019; Schmalholz et al., 2020). We thus suggest that the lithological and structural inherited heterogeneities had first-order control driving the development of mylonites (Fig. 5.12B). On the other hand, lithological variability alone does not explained why deformation localised both in the stronger mafic rocks and weaker paragneisses and calc-silicates. We highlight the role of fluids channelized into the shear zone to further promote weakening once deformation started as testified by our observations of abundant presence of syn-kinematic amphibole and titanite grains in mylonitic amphibolites (e.g., Vauchez et al., 2012; Getsinger et al., 2013; Kohn, 2017).

Moreover, it remains still enigmatic why deformation does not affect the rocks at the contact with gabbro. These rocks show the same lithological and structural features as those characterizing the protoliths of mylonitic rocks. However, here, we observed local evidence for de-hydration reactions due to contact metamorphic effects. The static growth of coronitic garnet replacing amphibole is documented in the mafic gneisses from the footwall (Fig. 5.4D). In this zone we observed also larger sizes of mineral phases and metasomatic effects leading to the formation of reaction boundaries between gabbros and their host rocks (marbles/calcsilicates). These features have never been documented in other mafic rocks of the entire crustal section exposed in the Ivrea-Verbano zone. On the other hand, a similar feature of intrusion related rheological hardening has been observed and described at a small scale in granulite-facies metamorphic rocks from the Fiordland, New Zealand (Smith et al. 2015). Therefore, a possible reason why this meter-thick region escaped deformation could be the local (meter scale) contact metamorphic effect due to the intrusion of gabbroic rocks promoted dehydration reaction that changed the rheological behaviour of these gneisses (Fig. 5.12A; e.g., Harlov, 2012). Alternatively, it could be that the original magmatic contact between the gneiss and the gabbroic rocks is curvilinear whereas deformation occurred mainly along planar planes saving up some gneisses in bights of the contact.

5.9.4 The role of the Anzola shear zone during the Triassic-Jurassic rifting phases

In the following section, we discuss the implications of our findings in the framework of the geodynamic evolution of IVZ, with particular focus on Val d'Ossola section (Fig. 5.12).

After the Variscan orogeny, the IVZ experienced post-orogenic extension (Handy et al., 1999). From the Early to Middle Permian (290–260 Ma), the lithospheric extension was associated to intense magmatic activity (e.g., Petri et al., 2017 and references therein). Consequently, heat advected by hydrous melts combined with lithospheric extension was responsible for widespread regional high temperature metamorphism (e.g., Ewing et al., 2015).

In the meantime, mafic magmas intruded at mid crustal levels (ca. 280 Ma; Peressini et al., 2007; Brodie et al., 1989) within metamorphic rocks showing evidence for partial melting and intense folding. The rocks at the contact with mafic intrusion reached high temperature conditions developing locally features comparable to those due to contact metamorphism (e.g., Barboza & Bergantz, 2000; Fig. 5.12A, C). All these features promoted the formation of crustal boundary characterized by significant rheological and compositional heterogeneities (Fig. 5.12A). From the Early Mesozoic, multiple episodes of rifting affected the IVZ. During these events, deformation was mainly accommodated by several shear zones active at different crustal levels (Manatschal et al., 2007; Beltrando et al., 2015; Petri et al., 2019). Although precise geochronological estimates are still lacking, the Anzola shear zone has been interpreted as a main extensional structure accommodating the Triassic-Jurassic rift-related deformation (Fig. 5.12D; Simonetti et al. 2021 and references therein). In this tectonic setting, localization of strain was influenced by crustal scale rheological boundaries originating from lithological contrasts and/or the transition from rheologically relatively soft amphibolite facies rocks to rheological hard granulite facies rocks (Fig. 5.12A, B; e.g., Piazzolo et al. 2002). Once strain is localized at these boundaries, positive feedback between deformation and external fluid (water rich fluid or melt) influx will accentuate strain localization (Austrheim, 1987, 2013; Getsinger et al., 2013; Lee et al., 2020; Casini et al., 2021; Piazzolo et al. 2020). Triassic-Jurassic mantle derived magmatic rocks and fluids that have been extensively documented within middle-lower crustal lithologies of the IVZ (Schaltegger et al., 2015; Galli et al., 2019; Denyszyn et al., 2018; Bonazzi et al., 2020; Corvò et al., 2020) are likely the sources for melt/fluid components. The occurrence of local magmatism, the large availability of hot

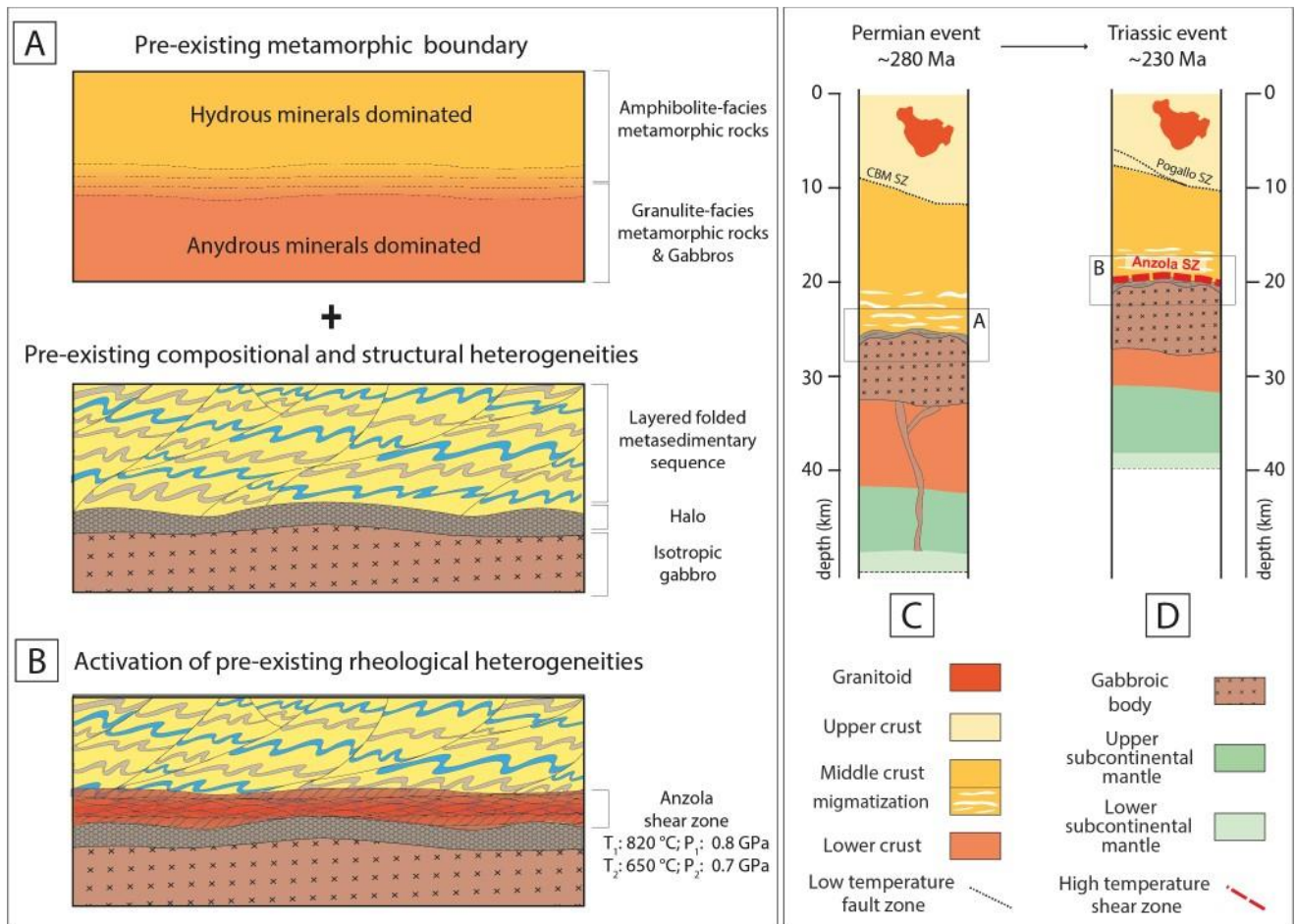


Fig. 5.12 – Interpretation of the geological conditions that promoted the nucleation of the Anzola shear zone at the transition between middle to lower crust at the meso-scale (A, B) and regional scale (C, D), (modified after Gardner et al., 2017). A) Before the Anzola shearing, the transition between middle to lower crust is characterized by the juxtaposition of: i) a gradual transition from anhydrous conditions (granulite facies) to hydrated assemblages (amphibolite facies rocks) and, ii) pre-existing compositional and deformational heterogeneities (late Variscan undeformed isotropic gabbro and its contact aureole vs folded Variscan metamorphic volcano-sedimentary sequence). B) The combinations of these factors resulted in the formation of strong rheological contrasts that promoted the initiation of the Anzola shearing during Triassic, when the Tethyan rifting stage triggered renewed extensional tectonics. P-T conditions for deformation are reported as T_1 , T_2 , P_1 , P_2 to indicate that deformation started at high temperature (T_1 : ~820°C; P_1 : 0.8 GPa) and continued down to amphibolite facies (T_2 : ~650°C P_2 : 0.7 GPa) following a retrograde path. Interpretative, paleo-cross section of the Val d’Ossola lithosphere: C) during Permian (pre-Anzola shearing) and D) during Triassic (during Anzola shearing). Note the migmatization at the middle-lower crust transition and the metamorphic halos developed due to the emplacement of the gabbroic body during Permian age. During Triassic, this layer is overprinted by the nucleation of the shear zone. Modified after Petri et al., (2017).

fluids and the intrinsic heterogeneity of metamorphic rocks in specific crustal/rheological boundaries allowed the development of several crustal-scale shear zones during Triassic-Jurassic rifting.

5.10 Conclusions

In this work, we present new field observations, petrological and geochemical data from a major extensional shear zone – the Anzola shear zone – of the middle/lower crust of the Ivrea-Verbano Zone (Western Alps) with the aim to define the nature of pre-shear heterogeneities and reconstruct the factors that promoted strain localisation. While the shear zone has been previously described as developed within an isotropic gabbroic body, our new geological mapping revealed instead significant pre-existing lithological and structural heterogeneities. Mylonitic rocks derive from a metamorphic volcano-sedimentary sequence, in which the gabbro was intruded before the shear zone development. In particular, petrographical and geochemical data indicate that the protoliths of (ultra-)mylonitic rocks coincide with the folded paragneisses, mafic gneisses and calc-silicates rocks rather than the nearly isotropic gabbro. Noticeably, trace elements characterization resulted as the most powerful tool to constrain the geochemical links between minerals from the wall rock and shear zone. The coupling of different geothermobarometers (Zr-in-Rutile, Grt-Bt, Ti-in-Amphibole geothermometers and GASP barometer) show that the deformation started at high temperature (T: ~820°C; P: 0.8 GPa) and continued down to amphibolite facies (T: ~650°C P: 0.7 GPa) following a retrograde path. Overall, the Anzola shear zone is characterized by a complex pattern of lithotypes that experienced, before shearing, multiphase Variscan folding followed by high-temperature metamorphism at the upper amphibolite to granulite facies transition. The rheological contrast between i) hard (isotropic gabbro) and relatively weak (folded metavolcanites and metasediments) lithologies summed to the ii) layering of anhydrous- and hydrous-dominated metamorphic assemblages (transition between amphibolite to granulite facies), promoted the strain localisation. We thus confirm that the pre-existing rheological boundaries and the inherited compositional and structural rock heterogeneities had first-order control driving the nucleation of shear zones.

We finally considered that the Anzola shear zone developed in a complex setting at middle/lower crustal levels during multiple episodes of rifting affecting the IVZ at Triassic-Jurassic time. In this frame, the Anzola shear zone played a significant role in accommodating the deformation during crustal thinning and exhumation phases.

5.11 References

- Altenberger, U., 1997. Strain localization mechanisms in deep-seated layered rocks. *Geol. Rundsch.*, 86(1): 56-68.
- Aravadinou, E. and Xypolias P., 2017. Evolution of a passive crustal-scale detachment (Syros, Aegean region): Insights from structural and petrofabric analyses in the hanging-wall. *J. Struct. Geol.*, 103: 57-74.
- Arbaret, L., & Burg, J.P. 2003. Complex flow in lowest crustal, anastomosing mylonites: Strain gradients in a Kohistan gabbro, northern Pakistan. *Journal of Geophysical Research*, 108, 2467.
- Austrheim, H., 1987. Eclogitization of lower crustal granulites by fluid migration through shear zones. *Earth and Planetary Science Letters*, 81(2-3), 221-232.
- Austrheim, H., 2013. Fluid and deformation induced metamorphic processes around Moho beneath continent collision zones: Examples from the exposed root zone of the Caledonian mountain belt, W-Norway. *Tectonophysics*, 609, 620-635.
- Austrheim, H. and Boundy, T.M. 1994. Pseudotachylytes generated during seismic faulting and eclogitization of the deep crust. *Science*, 265, 82–83.
- Barboza, S. A., & Bergantz, G. W., 2000. Metamorphism and anatexis in the mafic complex contact aureole, Ivrea Zone, Northern Italy. *Journal of Petrology*, 41(8), 1307-1327.
- Beach, A., 1980. Retrogressive metamorphic processes in shear zones with special reference to the Lewisian complex. *Journal of Structural Geology*, 2(1-2), 257-263.
- Beltrando, M., Manatschal G., Mohn G., Dal Piaz G.V., Vitale Brovarone A. and Masini E., 2014. Recognizing remnants of magma-poor rifted margins in high-pressure orogenic belts: The Alpine case study. *Earth. Sci. Rev.*, 131: 88-115.
- Beltrando, M., Stockli D.F., Decarlis A. and Manatschal G., 2015. A crustal-scale view at rift localization along the fossil Adriatic margin of the Alpine Tethys preserved in NW Italy. *Tectonics*, 34: 1927-1951.
- Berno, D., Tribuzio, R., Zanetti, A., & Hémond, C., 2020. Evolution of mantle melts intruding the lowermost continental crust: constraints from the Monte Capio–Alpe Cevia mafic–ultramafic sequences (Ivrea–Verbano Zone, northern Italy). *Contributions to Mineralogy and Petrology*, 175(1), 1-28.
- Bonazzi, M., Langone, A., Tumiatì, S., Dellarole, E., Mazzucchelli, M., Giovanardi, T., & Zanetti, A., 2020. Mantle-Derived Corundum-Bearing Felsic Dykes May Survive Only within the Lower (Refractory/Inert) Crust: Evidence from Zircon Geochemistry and Geochronology (Ivrea–Verbano Zone, Southern Alps, Italy). *Geosciences*, 10(8), 281.
- Boriani, A. and Villa I.M., 1997. Geochronology of regional meta-morphism in the Ivrea-Verbano Zone and Serio dei Laghi, Italian Alps. *Schweiz. Miner. Petrogr.*, 77: 381-402. <https://doi.org/10.5169/SEALS-58492>.
- Boriani, A., Burlini L. and Sacchi R., 1990. The Cossato-Mergozzo-Brissago Line and the Pogallo Line (Southern Alps, Northern Italy) and their relationships with the late-Hercynian magmatic and

- metamorphic events. *Tectonophysics*, 182: 91-102.
- Brodie, K.H., 1980. Variations in mineral chemistry across a phlogopite shear zone. *J. Struct. Geol.*, 2, 265–272.
- Brodie, K.H., 1981. Variation in amphibole and plagioclase composition with deformation. *Tectonophysics* 78, 385–402.
- Brodie, K.H. and Rutter E.H., 1987. Deep crustal extensional faulting in the Ivrea Zone of Northern Italy. *Tectonophysics*, 140: 193-212.
- Brodie, K.H., Rutter E.H. and Rex D., 1989. On the age of deep crustal extensional faulting in the Ivrea zone, Northern Italy. *Geol. Soc. London Spec. Publ.*, 45: 203-210..
- Burg, J. P., 2011. The Asia–Kohistan–India collision: review and discussion. *Arc-continent collision*, 279-309.
- Carvalho, B.B., Bartoli, O., Ferri, F., Cesare, B., Ferrero, S., Remusat, L., Capizzi, L., and Poli, S., 2019. Anatexis and fluid regime of the deep continental crust: New clues from melt and fluid inclusions in metapelitic migmatites from Ivrea Zone (NW Italy). *Journal of Metamorphic Geology*, 37(7), 951-975.
- Casini, L., Maino, M., Sanfilippo, A., Ildefonse, B., & Dick, H. J., 2021. High-Temperature Strain Localization and the Nucleation of Oceanic Core Complexes (16.5° N, Mid-Atlantic Ridge). *Journal of Geophysical Research: Solid Earth*, 126(9), e2021JB022215.
- Cavallo, A., Bigioggero, B., Colombo, A., & Tunesi, A., 2004. The Verbano Cusio Ossola province: a land of quarries in northern Italy (Piedmont). *Periodico di Mineralogia*, 73(3), 197-210.
- Corvò, S., Langone, A., Padrón-Navarta, J.A., Tommasi, A. and Zanetti, A., 2020. Porphyroclasts: Source and sink of major and Trace Elements during deformation-induced metasomatism (Finero, Ivrea-Verbano Zone, Italy). *Geosciences*, 10: 196. <https://doi.org/10.3390/geosciences10050196>.
- Corvò, S., Maino, M., Langone, A., Schenker, F. L., Piazzolo, S., Casini, L., & Seno, S., 2021. Local variations of metamorphic record from compositionally heterogeneous rocks (Cima di Gagnone, Central Alps): Inferences on exhumation processes of (U) HP–HT rocks. *Lithos*, 390, 106126.
- Degli Alessandrini, G., 2018. Deformation mechanisms and strain localization in the mafic continental lower crust. PhD thesis, School Geogr. Earth Environ. Sci. Univ. Plymouth, 366 pp.
- Denyszyn, S. W., Fiorentini, M. L., Maas, R., & Dering, G., 2018. A bigger tent for CAMP. *Geology*, 46(9), 823-826.
- Dostal, J., & Capedri, S., 1979. Rare earth elements in high-grade metamorphic rocks from the western Alps. *Lithos*, 12(1), 41-49.
- Drury, M.R., Humphreys, F.J., White, S., 1985. Large strain deformation studies using polycrystalline magnesium as a rock analogue. II. Dynamic recrystallisation mechanism at high temperatures. *Phys Earth Planet Inter* 40: 208-222.
- Drury, M. R., Vissers, R. L., Van der Wal, D., & Strating, E. H. H., 1991. Shear localisation in upper mantle peridotites. *Pure and Applied Geophysics*, 137(4), 439-460.

- Ewing, T.A., Hermann, J. and Rubatto, D., 2013. The robustness of the Zr-in-rutile and Ti-in-zircon thermometers during high-temperature metamorphism (Ivrea-Verbano Zone, Northern Italy). *Contrib. Miner. Petrol.*, 165: 757-779.
- Ewing, T. A., Rubatto, D., Beltrando, M., & Hermann, J., 2015. Constraints on the thermal evolution of the Adriatic margin during Jurassic continental break-up: U–Pb dating of rutile from the Ivrea-Verbano Zone, Italy. *Contributions to mineralogy and petrology*, 169(4), 44.
- Fossen, H. and Cavalcante, G.C.G., 2017. Shear zones - A review. *Earth Sci. Rev.*, 171: 434-455. <https://doi.org/10.1016/j.earsci-rev.2017.05.002>
- Fossen, H., Cavalcante, G.C.G., Pinheiro, R.V.L., Archanjo, C.J., 2019. Deformation–progressive or multiphase? *J. Struct. Geol.* 125, 82–99
- Galli, A., Grassi, D., Sartori, G., Gianola, O., Burg, J. P., & Schmidt, M. W., 2019. Jurassic carbonatite and alkaline magmatism in the Ivrea zone (European Alps) related to the breakup of Pangea. *Geology*, 47(3), 199-202
- Gardner, R. L., Piazzolo, S., & Daczko, N. R., 2016. Shape of pinch and swell structures as a viscosity indicator: application to lower crustal polyphase rocks. *Journal of Structural Geology*, 88, 32-45.
- Gardner, R. L., Piazzolo, S., & Daczko, N. R., 2017. Determining relative bulk viscosity of kilometre-scale crustal units using field observations and numerical modelling. *Tectonophysics*, 721, 275-291.
- Gardner, R. L., Piazzolo, S., Daczko, N. R., & Trimby, P., 2020. Microstructures reveal multistage melt present strain localisation in mid-ocean gabbros. *Lithos*, 366, 105572.
- Gessner, K., Gallardo, L. A., Markwitz, V., Ring, U., & Thomson, S. N., 2013. What caused the denudation of the Menderes Massif: Review of crustal evolution, lithosphere structure, and dynamic topography in southwest Turkey. *Gondwana research*, 24(1), 243-274.
- Getsinger, A.J., Hirth, G., Stünitz, H., Goergen, E.T., 2013. Influence of water on rheology and strain localization in the lower continental crust: Water, Rheology, and Strain Localization. *Geochem. Geophys. Geosystems* 14, 2247–2264.
- Ghatak, H., 2020. Deformation-assisted melt migration and melt-rock interaction during the intracontinental Alice Springs orogeny, Central Australia. PhD Thesis, Macquarie University.
- Giuntoli, F., Menegon, L., & Warren, C. J., 2018. Replacement reactions and deformation by dissolution and precipitation processes in amphibolites. *Journal of Metamorphic Geology*, 36(9), 1263-1286.
- Handy, M. R., Franz, L., Heller, F., Janott, B., & Zurrbriggen, R., 1999. Multistage accretion and exhumation of the continental crust (Ivrea crustal section, Italy and Switzerland). *Tectonics*, 18(6), 1154-1177.
- Harlov, D. E., 2012. The potential role of fluids during regional granulite-facies dehydration in the lower crust. *Geoscience Frontiers*, 3(6), 813-827.
- Hartmann, G. and Hans Wedepohl, K., 1993. The composition of peridotite tectonites from the Ivrea Complex, Northern Italy: Residues from melt extraction. *Geochim. Cosmochim. Acta*, 57: 1761-1782. .
- Hawthorne, F. C., Oberti, R., Harlow, G. E., Maresch, W. V., Martin, R. F., Schumacher, J. C., & Welch, M.

- D., 2012. Nomenclature of the amphibole supergroup. *American Mineralogist*, 97(11-12), 2031-2048.
- Henk, A., Franz, L., Teufel, S. and Oncken, O., 1997. Magmatic underplating, extension, and crustal reequilibration: Insights from a cross-section through the Ivrea Zone and Strona-Ceñneri Zone, Northern Italy. *J. Geol.*, 105: 367-378.
- Hodges, K.V. and Fountain, D.M., 1984. Pogallo Line, South Alps, Northern Italy: An intermediate crustal level, low-angle normal fault? *Geology*, 12 (3): 151-155.
- Holdaway, M. J., 2000. Application of new experimental and garnet Margules data to the garnet-biotite geothermometer. *American mineralogist*, 85(7-8), 881-892.
- Holdaway, M. J., 2001. Recalibration of the GASP geobarometer in light of recent garnet and plagioclase activity models and versions of the garnet-biotite geothermometer. *American Mineralogist*, 86(10), 1117-1129.
- Hughes, A. N., Benesh, N. P., & Shaw, J. H., 2014. Factors that control the development of fault-bend versus fault-propagation folds: Insights from mechanical models based on the discrete element method (DEM). *Journal of Structural Geology*, 68, 121-141.
- Karakas, O., Wotzlaw, J.F., Guillong, M., Ulmer, P., Brack, P., Econoñmos, R., Bergantz, G.W., Sinigoi, S. and Bachmann, O., 2019. The pace of crustal-scale magma accretion and differentiation beneath silicic caldera volcanoes: *Geology*, 47: 719-723.
- Kaatz, L., Zertani, S., Moulas, E., John, T., Labrousse, L., Schmalholz, S. M., & Andersen, T. B., 2021. Widening of hydrous shear zones during incipient eclogitization of metastable dry and rigid lower crust—Holsnøy, western Norway. *Tectonics*, 40.
- Kenkmann, T., 2000. Processes controlling the shrinkage of porphyñroclasts in gabbroic shear zones. *J. Struct. Geol.*, 22: 471-487.
- Kenkmann, T. and Dresen, G., 2002. Dislocation microstructure and phase distribution in a lower crustal shear zone - an example from the Ivrea-Zone, Italy. *Int. J. Earth Sci.*, 91 (3): 445-458.
- Klötzli, U.S., Sinigoi, S., Quick, J.E., Demarchi, G., Tassinari, C.C.G., Sato, K. And Günes, Z., 2014. Duration of igneous activity in the Sesia Magmatic System and implications for high-temperature metamorphism in the Ivrea-Verbano deep crust. *Lithos*, 206–207: 19-33.
- Kohn, M. J., 2017. Titanite petrochronology. *Reviews in Mineralogy and Geochemistry*, 83(1), 419-441.
- Kohn, M. J., 2020. A refined zirconium-in-rutile thermometer. *American Mineralogist: Journal of Earth and Planetary Materials*, 105(6), 963-971.
- Kunz, B.E., Johnson, T.E., White, R.W. and Redler, C., 2014. Partial melting of metabasic rocks in Val Strona di Omegna, Ivrea Zone, Northern Italy. *Lithos*, 190-191, 1-12.
- Kunz, B.E., Regis, D. and Engi, M., 2019. Zircon ages in granulite facies rocks: decoupling from geochemistry above 850°C? *Contrib. Miner. Petrol.*, 137: 26. .
- Langone A., Zanetti A., Daczko N.R., Piazzolo S., Tiepolo M. and Mazzucchelli M., 2018. Zircon U-Pb dating of a lower crustal shear zone: A case study from the northern sector of the Ivrea-Verbano Zone (Val

- Cannobina, Italy). *Tectonics*, 37: 322-342. <https://doi.org/10.1002/2017TC004638>
- Lavier, L. L., & Manatschal, G., 2006. A mechanism to thin the continental lithosphere at magma-poor margins. *Nature*, 440(7082), 324-328.
- Lee, A.L., Torvela, T., Lloyd, G.E. and Walker, A.M. 2018. Melt organisation and strain partitioning in the lower crust. *Journal of Structural Geology*, 113, 188–199, <https://doi.org/10.1016/j.jsg.2018.05.016>
- Lee, A. L., Lloyd, G. E., Torvela, T., & Walker, A. M., 2020. Evolution of a shear zone before, during and after melting. *Journal of the Geological Society*, 177(4), 738-751.
- Liao, Y., Wei, C., & Rehman, H. U., 2021. Titanium in calcium amphibole: Behaviour and thermometry. *American Mineralogist: Journal of Earth and Planetary Materials*, 106(2), 180-191.
- Liou, P., and Guo, J., 2019. Generation of Archaean TTG gneisses through amphibole-dominated fractionation. *Journal of Geophysical Research: Solid Earth*, 124(4), 3605-3619.
- Luvizotto, G.L., Zack T., Meyer H.P., Ludwig T., Triebol S., Kronz A., Münker C., Stockli D.F., Prowatke S., Klemme S., Jacob D.E. and von Eynatten H., 2009. Rutile crystals as potential trace element and isotope mineral standards for microanalysis. *Chem. Geol.*, 261 (3-4): 346-369.
- Maino, M., Adamuszek, M., Schenker, F. L., Seno, S., & Dabrowski, M., 2021. Sheath fold development around deformable inclusions: Integration of field-analysis (Cima Lunga unit, Central Alps) and 3D numerical models. *Journal of Structural Geology*, 144, 104255.
- Manatschal, G., Müntener, O., Lavier, L. L., Minshull, T. A., & Péron-Pinvidic, G., 2007. Observations from the Alpine Tethys and Iberia–Newfoundland margins pertinent to the interpretation of continental breakup. *Geological Society, London, Special Publications*, 282(1), 291-324.
- Manatschal, G., Lavier, L., & Chenin, P., 2015. The role of inheritance in structuring hyperextended rift systems: Some considerations based on observations and numerical modeling. *Gondwana Research*, 27(1), 140-164.
- Mazzucchelli, M., Rivalenti, G., Vannucci, R., Bottazzi, P., Ottolini, L., Hofmann, A. W., ... & Demarchin, G., 1992. Trace element distribution between clinopyroxene and garnet in gabbroic rocks of the deep crust: An ion microprobe study. *Geochimica et Cosmochimica Acta*, 56(6), 2371-2385.
- McDonough, W. F., & Sun, S. S., 1995. The composition of the Earth. *Chemical geology*, 120(3-4), 223-253.
- Michibayashi, K., & Mainprice, D., 2004. The role of pre-existing mechanical anisotropy on shear zone development within oceanic mantle lithosphere: an example from the Oman ophiolite. *Journal of Petrology*, 45(2), 405-414.
- Mohn, G., Manatschal, G., Beltrando, M., Masini, E. and Kuszniir, N., 2012. Necking of continental crust in magma-poor rifted margins: Evidence from the fossil Alpine Tethys margins: necking of continental crust. *Tectonics*, 31 (1): TC1012. .
- Mohn, G., Manatschal, G., Müntener, O., Beltrando, M., & Masini, E., 2010. Unravelling the interaction between tectonic and sedimentary processes during lithospheric thinning in the Alpine Tethys margins. *International Journal of Earth Sciences*, 99(1), 75-101.

- Mouthereau, F., Lacombe, O., & Vergés, J., 2012. Building the Zagros collisional orogen: timing, strain distribution and the dynamics of Arabia/Eurasia plate convergence. *Tectonophysics*, 532, 27-60.
- Osagiede, O., Haehn, D. A., Spaulding, A. C., Otto, N., Cochuyt, J. J., Lemini, R., ... & Colibaseanu, D. T., 2021. Influence of surgeon specialty and volume on the utilization of minimally invasive surgery and outcomes for colorectal cancer: a retrospective review. *Surgical endoscopy*, 35(10), 5480-5488.
- Passchier, C.W., 1982. Pseudotachylyte and the development of ultramylonite bands in the Saint-Barthelemy Massif, French Pyrenees. *Journal of Structural Geology*, 4.
- Passchier, C.W. and Trouw, R.A.J., 2005. *Microtectonics*. Springer, Berlin.
- Pennacchioni, G. and Cesare, B., 1997. Ductile–brittle transition in pre-Alpine amphibolite facies mylonites during evolution from water-present to water deficient conditions (Mont Mary nappe, Italian Western Alps). *Journal of Metamorphic Geology*, 15, 777–791, . 1997.00055.x
- Pennacchioni, G. and Mancktelow, N.S., 2007. Nucleation and initial growth of a shear zone network within compositionally and structurally heterogeneous granitoids under amphibolite facies conditions. *Journal of Structural Geology*, 29, 1757–1780,
- Pennacchioni, G. and Mancktelow, N.S., 2018. Small-scale ductile shear zones: neither extending, nor thickening, nor narrowing. *Earth-Science Reviews*, 184, 1–12, <https://doi.org/10.1016/j.earscirev.2018.06.004>
- Peressini, G., Quick J.E., Sinigoi S., Hofmann A.W. and Fanning M., 2007. Duration of a large mafic intrusion and heat transfer in the lower crust: a SHRIMP U-Pb Zircon study in the Ivrea-Verbano Zone (Western Alps, Italy). *J. Petrol.*, 48: 1185-1218. .
- Petri, B., Duretz, T., Mohn, G., Schmalholz, S. M., Karner, G. D., & Müntener, O., 2019. Thinning mechanisms of heterogeneous continental lithosphere. *Earth and Planetary Science Letters*, 512, 147-162.
- Piazolo, S., Bons, P. D., Jessell, M. W., Evans, L., & Passchier, C. W., 2002. Dominance of microstructural processes and their effect on microstructural development: insights from numerical modelling of dynamic recrystallization. *Geological Society, London, Special Publications*, 200(1), 149-170.
- Piazolo, S., Daczko, N. R., Silva, D., & Raimondo, T., 2020. Melt-present shear zones enable intracontinental orogenesis. *Geology*, 48(7), 643-648.
- Prosser, G., Caggianelli, A., Rottura A., Del Moro, A., 2003. Strain localisation driven by marble layers: the Palmi shear zone (Calabria-Peloritani terrane, Southern Italy). *GeoActs*, 2, 155-166.
- Quick, J. E., Sinigoi, S., Snoke, A. W., Kalakay, T. J., Mayer, A., Peressini, G., 2003. Geological map of the southern Ivrea-Verbano Zone, northwestern Italy. US Geological Survey.
- Ramsay, J. G., 1967. *Folding and fracturing of rocks*. Mc Graw Hill Book Company, 568.
- Real, C., Froitzheim N., Carosi R., and Ferrando S., 2018. Evidence of large-scale Mesozoic detachments preserved in the basement of the Southern Alps (northern Lago di Como area). *Italy. J. Geosci.*, 137: 283-293. <https://doi.org/10.3301/IJG.2018.15>.
- Redler, C., Johnson T.E., White R.W. and Kunz B.E., 2012. Phase equilibrium constraints on a deep crustal

- metamorphic field gradient: metapelitic rocks from the Ivrea Zone (NW Italy): Ivrea Zone metamorphic field gradient. *J. Metam. Geol.*, 30: 235-254. <https://doi.org/10.1111/j.1525-1314.2011.00965.x>.
- Royden, L., 1996. Coupling and decoupling of crust and mantle in convergent orogens: Implications for strain partitioning in the crust. *Journal of Geophysical Research: Solid Earth*, 101(B8), 17679-17705.
- Rutter, E. H., 1999. On the relationship between the formation of shear zones and the form of the flow law for rocks undergoing dynamic recrystallization. *Tectonophysics*, 303(1-4), 147-158.
- Rutter, E.H. and Brodie K.H., 1990. Some geophysical implications of the deformation and metamorphism of the Ivrea zone, Northern Italy. *Tectonophysics*, 182 (1-2): 147-160.
- Rutter, E.H., Brodie K.H. and Evans P.J., 1993. Structural geometry, lower crustal magmatic underplating and lithospheric stretching in the Ivrea-Verbanò zone, northern Italy. *J. Struct. Geol.*, 15: 647-662.
- Rutter, E.H., Brodie K.H., James T. and Burlini L., 2007. Large-scale folding in the upper part of the Ivrea-Verbanò Zone, NW Italy. *J. Struct. Geol.*, 29: 1-17.
- Rybacki, E., & Dresen, G., 2004. Deformation mechanism maps for feldspar rocks. *Tectonophysics*, 382(3-4), 173-187.
- Sawyer, E.W., 2008. *Atlas of Migmatites*. vol. 9. NRC Research Press.
- Schaltegger, U., Ulianov, A., Müntener, O., Ovtcharova, M., Peytcheva, I., Vonlanthen, P., ... & Girlanda, F., 2015. Megacrystic zircon with planar fractures in miaskite-type nepheline pegmatites formed at high pressures in the lower crust (Ivrea Zone, southern Alps, Switzerland). *American Mineralogist*, 100(1), 83-94.
- Schmalholz, S. M., Moulas, E., Plümpner, O., Myasnikov, A. V., & Podladchikov, Y. Y., 2020. 2D Hydro-Mechanical-Chemical Modeling of (De) hydration Reactions in Deforming Heterogeneous Rock: The Periclase-Brucite Model Reaction. *Geochemistry, Geophysics, Geosystems*, 21(11), e2020GC009351.
- Schmid, S.M., 1993. Ivrea zone and adjacent southern Alpine basement. In: J.F. Raumer and F. Neubauer (Eds.). *Pre-Mesozoic geology in the Alps*, Springer, Berlin, Heidelberg, p. 567-583.
- Schmid, R., and Wood, B.J., 1976. Phase relationships in granulitic metapelites from the Ivrea-Verbanò zone (Northern Italy). *Contrib. Miner. Petrol.*, 54: 255-279.
- Siegesmund, S., Layer P., Dunkl I., Vollbrecht A., Steenken A., Wemmer K. and Ahrendt H., 2008. Exhumation and deformation history of the lower crustal section of the Valstrona di Omegna in the Ivrea Zone, southern Alps. *Geol. Soc. London Spec. Publ.*, 298: 45-68. <https://doi.org/10.1144/SP298.3>.
- Simonetti, M., Langone, A., Corvò, S., Bonazzi, M., 2021. Triassic-Jurassic rift-related deformation and temperature-time evolution of the fossil Adriatic margin: A review from Ossola and Strona di Omegna valleys (Ivrea-Verbanò Zone). *Ofioliti*, 46(2), 147-161.
- Sinigoi, S., Quick, J. E., Mayer, A., & Budahn, J., 1996. Influence of stretching and density contrasts on the chemical evolution of continental magmas: an example from the Ivrea-Verbanò Zone. *Contributions to Mineralogy and Petrology*, 123(3), 238-250.

- Smith, J. R., Piazzolo, S., Daczko, N. R., & Evans, L., 2015. The effect of pre-tectonic reaction and annealing extent on behaviour during subsequent deformation: Insights from paired shear zones in the lower crust of Fiordland, New Zealand. *Journal of Metamorphic Geology*, 33(6), 557-577.
- Stähle, V., Frenzel, G., Hess, J. C., Saupé, F., Schmidt, S. T., & Schneider, W., 2001. Permian metabasalt and Triassic alkaline dykes in the northern Ivrea zone: clues to the post-Variscan geodynamic evolution of the Southern Alps. *Schweizerische Mineralogische und Petrographische Mitteilungen*, 81(1), 1-21.
- Stünitz H., 1998. Syndeformational recrystallization - dynamic or compositionally induced? *Contrib. Mineral. Petrol.*, 131: 219–236.
- Svahnberg, H., & Piazzolo, S., 2010. The initiation of strain localisation in plagioclase-rich rocks: Insights from detailed microstructural analyses. *Journal of Structural Geology*, 32(10), 1404-1416.
- Treagus, S. H., & Sokoutis, D., 1992. Laboratory modelling of strain variation across rheological boundaries. *Journal of Structural Geology*, 14(4), 405-424.
- Vauchez, A., Tommasi, A., Mainprice, D., 2012. Faults (shear zones) in the Earth's mantle. *Tectonophysics* 558–559, 1–27. <https://doi.org/10.1016/j.tecto.2012.06.006>
- Walter, T. R., Troll, V. R., Cailleau, B., Belousov, A., Schmincke, H. U., Amelung, F., & Vd Bogaard, P., 2005. Rift zone reorganization through flank instability in ocean island volcanoes: an example from Tenerife, Canary Islands. *Bulletin of Volcanology*, 67(4), 281-291.
- Whitney, D. L., & Evans, B. W., 2010. Abbreviations for names of rock-forming minerals. *American mineralogist*, 95(1), 185-187.
- Whitney, D. L., Teyssier, C., Rey, P., & Buck, W. R., 2013. Continental and oceanic core complexes. *Bulletin*, 125(3-4), 273-298.
- Williams, M. L., & Burr, J. L., 1994. Preservation and evolution of quartz phenocrysts in deformed rhyolites from the Proterozoic of southwestern North America. *Journal of structural geology*, 16(2), 203-221.
- Wolff R., Dunkl I., Kiesselbach G., Wemmer K. and Siegesmund S., 2012. Thermochronological constraints on the multiphase exhumation history of the Ivrea-Verbano Zone of the Southern Alps. *Tectonophysics*, 579: 104-117. <https://doi.org/10.1016/j.tecto.2012.03.019>.
- Zanetti, A., Mazzucchelli, M., Sinigoi, S., Giovanardi, T., Peressini, G., & Fanning, M., 2013. SHRIMP U–Pb zircon Triassic intrusion age of the Finero mafic complex (Ivrea–Verbano Zone, Western Alps) and its geodynamic implications. *Journal of Petrology*, 54(11), 2235-2265.
- Zingg, A., 1980. Regional metamorphism in the Ivrea Zone (Southern Alps, N-Italy): field and microscopic investigations. *Schweizerische Mineralogische und Petrographische Mitteilungen* 60, 153–179.
- Zingg A., 1990. The Ivrea crustal cross-section (Northern Italy and Southern Switzerland). In: M.H. Salisbury and D.M. Fountain (Eds.), *Exposed cross-sections of the continental crust*. Springer Netherlands, Dordrecht, p. 1-19. <https://doi.org/10.1007/978-94-009-0675-41>.

CHAPTER 6: Thesis Conclusions

6.1 Overall conclusions

PhD thesis explored the interplay between metamorphism and deformation at rheological boundaries generated by inherited differences. In particular, the research focused on the role of pre-existing compositional, structural and metamorphic heterogeneities on how: 1) different paired rock types may record contrasting metamorphic conditions (HP vs MP, HT vs MT); and 2) they drive localization of strain during the shear zone nucleation.

The two case studies highly debated topics for the geological community, as they are representative of fundamental processes occurring in the middle to lower crust during opposite regional tectonic regime (compressive and extensional). In both case studies, pre-existing rock compositional and structural features influenced their evolution in time and space, triggering complex interaction between deformation and metamorphic processes.

In the case study 1 (Cima di Gagnone, Central Alps), the interface between ultramafic lenses and metasediments was the locus for fluid-rock interaction processes (metasomatism, hydration-dehydration). Even though metasediments share the same structural evolution with ultramafic boudins, large differences in the P–T paths are recorded. Large part of the unit experienced $P < 1.2$ and $T < 700^{\circ}\text{C}$, whereas a few occurrences preserve higher metamorphic conditions of 1.3–1.7 GPa and 750–850°C. These estimates approach the P–T peak conditions experienced by the ultramafic rocks (1.5–3.2 GPa, 740–850°C). It is important to highlight that the temperatures exceeding 800 °C were not only related to the maximum pressure peak conditions recorded by the Gagnone metaperidotites (3.0 GPa). Rather, micaschists record the same HT conditions at the significantly lower P of 1.3–1.7 GPa, in the stability field of hydrated minerals (biotite and amphibole). These pressure and temperature deviations are not randomly distributed in the unit but changes systematically as a function of the distance from the strong lithology (i.e., ultramafic rocks), being maximum at the interface between the two rock pairs. Moreover, the high temperature conditions, the geochemical gradient and the presence of fluids promoted (wet) melting and metasomatism at the boundary between micaschists and ultramafic rocks. The results for this case study suggest that heterogeneous metamorphism conditions are locally developed, rather than locally preserved. Different local equilibria are related to the proximity to the strong lithology, suggesting that the rheological and chemical contrasts between strong and surrounding weak rocks had a significant role in modifying the local metamorphic gradients.

Chapter 6

Moreover, what it is clear is that the chemical gradient between compositionally different lithologies combined with fluids circulations result in coexisting heterogeneous metamorphic equilibria, which are not representative of the ambient conditions. In these cases, caution should be used in converting estimations of metamorphic pressure into burial depth.

The case study 2 (Anzola Shear Zone, Western Alps) finds that inherited compositional and structural rock heterogeneities are crucial for weakening and strain localization at middle to lower crustal layers. While the Anzola shear zone has been previously described as developed within an isotropic mafic body, our new geological mapping revealed instead significant pre-existing lithological and structural heterogeneities. The Anzola shear zone developed within a multi-lithological metamorphic volcanic-sedimentary sequence that before shearing, experienced multiphase Variscan folding and late Variscan High-Temperature metamorphism, at the boundary between amphibolite and granulite facies conditions. Besides the rheological contrasts due to the compositional and structural anisotropies, strain localisation was further promoted by i) the close intrusion of the nearly isotropic mafic body and ii) the occurrence of rocks showing transitional metamorphic conditions between granulites (dominated by anhydrous minerals) to amphibolite facies (rich of hydrous minerals). The results for this case study suggest that detailed petrological, structural and geochemical investigations allow a better comprehension at the outcrop scale of the role of structural and compositional heterogeneities that lead to the initiation of strain localization. Moreover, the trace elements study resulted as the most powerful tool to reconstruct the pre-shearing relationships between wall rocks and mylonites and thus determine the protoliths of the shear zone rocks. What it is evident is that the boundaries characterized by alternated different lithologies and by pre-existing structural features combined with the regional tectono-metamorphic conditions, become the preferential loci for the nucleation of large-scale deformation structure. In these contexts, accuracy should be used in the characterization of compositional and structural features at the meso to micro-scale.

Summing up, despite the differences, the two case studies highlight how context characterized by different compositional rock types produced divergent rheological behaviour in the rock assemblages at local scale. In Cima di Gagnone area, heterogeneous deviatoric stress likely produced contrasted metamorphic assemblage at same lithostatic pressure conditions, while in the Anzola area strain is localized where contrasting compositional + structural + metamorphic layering occur, generating the

initiation of a major crustal shear zone.

In conclusion, this PhD thesis provide new information from natural occurrences with the aim to improve the comprehension of the mechanisms of deformation and metamorphism. As a final remark, it is highlighted the crucial role of careful investigations on: i) all the lithologies involved in the study area; ii) the rheological behaviour of the studied rocks; iii) the relationships between deformation and metamorphic processes at the boundary of different paired rock types.

6.2 Current and future work

This PhD research is far from being complete, as the complexity of natural systems mean that lots of aspects remain open to further analysis and discussion. A huge amount of data was collected during this thesis, unfortunately there was not time to write in an appropriate and complete chapter on all collected data. Anyway, even if these data are still being processing, most of them have been presented (poster or oral presentation) at conferences already. For that reason, short descriptive paragraphs are reported in Appendices as individual sections.

For case study 1, in chapter 4, only preliminary geochronological data on zircon were presented. However, a more complete geochronology is planned in order to better constrain the time evolution of Cima di Gagnone area. Therefore, further zircon (in-situ and in separate grains) and monazite dating (partial data) are presented in Appendix A.1.5.

For case study 2, a huge amount of data was collected. At the PhD beginning, the idea was to focus on the petrochronological and microstructural characterization of one among the shear zones outcropping in Val d'Ossola (e.g., Premosello and Anzola shear zones). Then, since a series of unexpected events, Covid times and on the base of the analysis developments, this case study focused on the Anzola shear zone. To note that while for case study 1 most of field data were already ready at the beginning of PhD project, for case study 2 field work and sampling started almost from the beginning. Consequently, this part of the project was more “experimental” and evolved from the results of data. Planned works to extend case study 2 are listed here identifying potential papers to write and submit:

1 – Appendix 3: U-Pb titanite dating on case study 2 samples

2 – Appendix 4: Microstructural characterization (SEM-EBSD) of mylonitic amphibolites from the Anzola shear zone.

APPENDICES

**APPENDIX 1:
Supplementary data
for case study 1**

A.1.1 Thin sections scans of the representative studied samples

Country rocks

M92



M62



MP3



Halos

M69



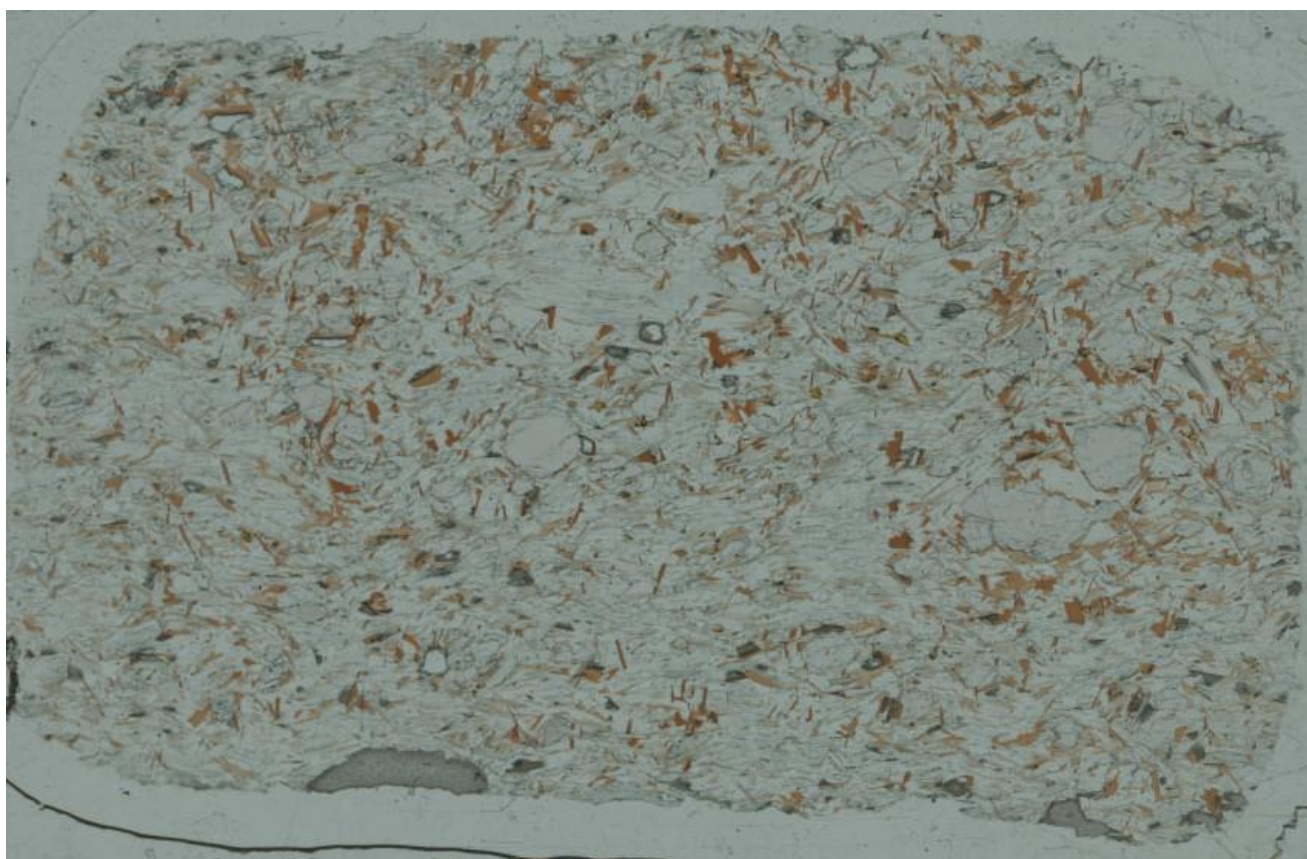
M102



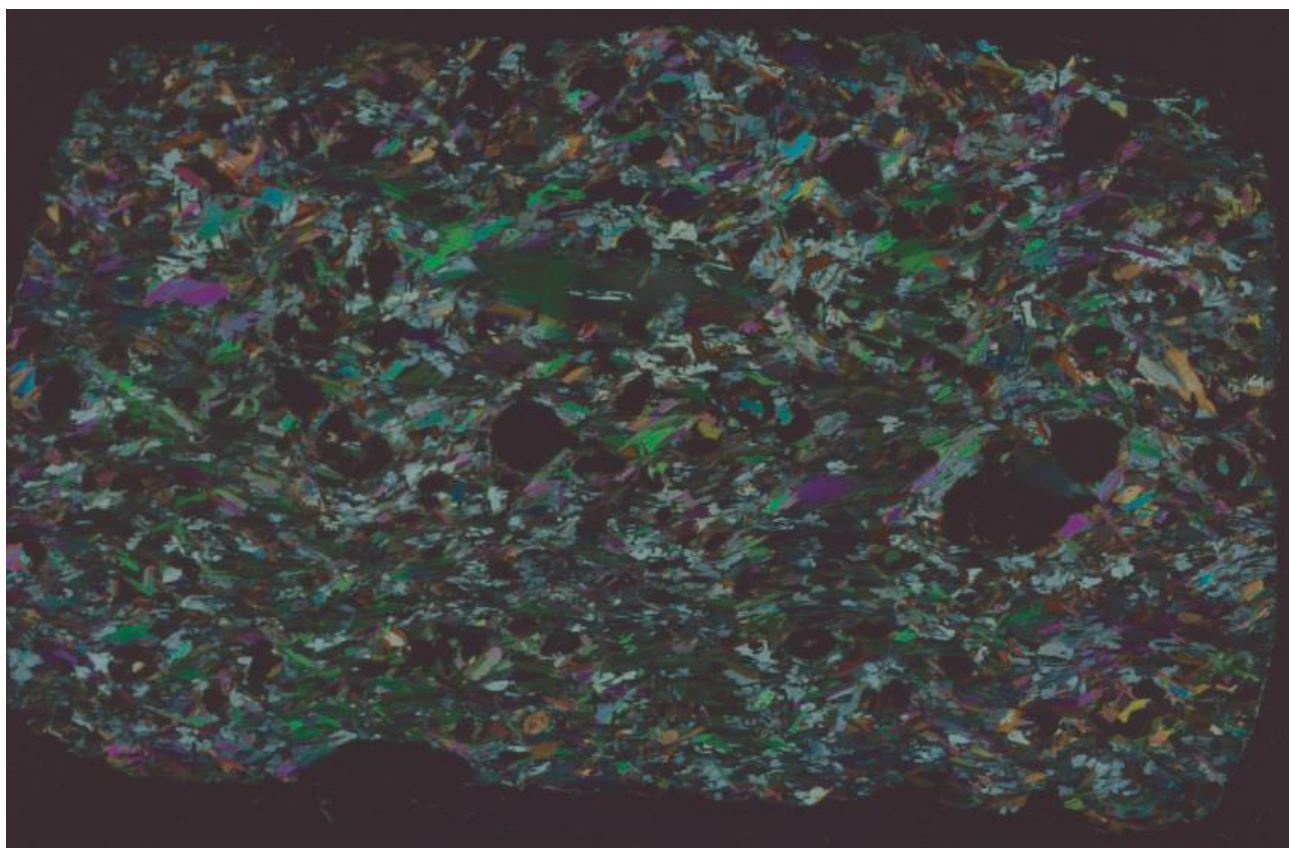
M119



M119 - Nicols //



M119 - Nicols X



A.1.2 Supplementary information on methods

This Appendix presents additional data for case study 1. No in-depth analysis or interpretation is provided. A detailed description of the methods used is reported in chapter 3.

A.1.2.1 Quantitative Orientation Analysis and Phase Percentage estimation (EBSD)

Crystallographic orientation data on two samples (i.e., M92, M119) were obtained from automatically indexed EBSD patterns collected using the FEI Quanta 650 FEG–ESEM (with Oxford X-max 80 SDD EDS, Oxford/HKL Nordleys EBSD system and Aztec software) at the Electron Optics Facility, University of Leeds, UK. In our case we use the colour coding relative to the sample Z direction (i.e., the pole to the sample foliation, Figs. 4.6, 4.8). The so-called Texture Component map each analysis point is colour coded according to the change in crystallographic orientation in degrees (i.e., misorientation angle) with respect to a chosen reference point (a reference orientation) within the map (Figs. 4.6, 4.8). The reference point is marked with a cross. The misorientation angle between two crystallographic orientations is defined as the smallest angular differences (considering crystal symmetry) between the chosen reference point and each other pixel (i.e., analyses point) of the same phase. The map is useful to spatially visualize the degree of orientation change from the chosen point and is here used as an aid to identify any intracrystalline lattice distortions and therefore associated deformation or replacement mechanisms. To assess if there are any crystallographic preferred orientations (CPO) within a population of grains of the same phase we utilize pole figure representations. Here, the crystallographic orientation of lattice directions and planes are plotted on the lower hemisphere of an equal area stereographic projection of crystallographic orientation plotting one representative orientation per grain. All pole figures presented in this work are referenced with the pole to the sample foliation (sample's Z direction) pointing upwards and the mineral lineation (sample's X direction) horizontal.

A.1.2.2 Mineral chemistry (EPMA)

Major element mineral compositions of six representative samples (i.e., M92, MP3, M62, M119, M102, M69) were obtained using a scanning electron microprobe (JEOL JXA–8200; Dipartimento di Scienze della Terra, Università degli Studi di Milano, Italy) at 15–kV accelerating voltage and 15–nA beam current. Counting time was 30 s on the peak and 10 s on the backgrounds. Natural silicates were

utilized as standards, and data reduction was carried out using the CITZAF package. Representative average data are listed in Table S4.2, S4.3. Grain locations, internal features (inclusions, fractures, etc.), Backscattered–Electron (BSE) images and detailed X–ray compositional maps of the main mineral phases (i.e., garnet, plagioclase, biotite, muscovite) were obtained with the aid of the same electron microprobe instrument in scanning mode.

A.1.2.3 Geothermobarometry

P–T conditions of six samples were determined by combining the following geo–thermometers and/or–barometers: i) the Garnet–Biotite (GB) (Spear, 1993; Holdaway, 2000), ii) the Garnet–Aluminosilicate–Silica–Plagioclase (GASP; e.g., Holdaway, 2001), iii) the Garnet–Biotite–Muscovite–Plagioclase (GBMP; e.g., Holdaway, 2000, 2001; Wu, 2015), iv) the Garnet–Muscovite (GM; e.g., Wu, 2018), v) Garnet–Muscovite–Al₂SiO₅–Quartz (GMAQ; e.g., Wu, 2018) and vi) the Si– content in white mica (Si–Wm; i.e., Caddick and Thompson, 2008; Massonne and Schreyer, 1987). The thermobarometers were calibrated using the method of Bhattacharya et al. (1992), Holland and Powell (1985), Hodges and Crowley (1985), Hoisch (1990), Green and Hellman (1982), Krogh and Råheim (1978), Wu (2018) and Coggon and Holland (2002) for the GB, GASP, GPMB, GM, GMAQ and Si–Wm, respectively. Geothermobarometry was applied following textural criteria; the values referred to garnet rims were associated with the neighbouring minerals (biotite, plagioclase, kyanite or muscovite) for which equilibrium texture are observable. Garnet cores were instead paired only with their inclusions. Data are listed in Table S4.4.

A.1.2.4 P–T, T–X pseudosection modelling

In order to characterize the P–T path evolution of the individual zones, P–T pseudosections were calculated for six samples representative of the two groups of samples: (M92, MP3A, M62 and M119, M102, M69 for the Country rocks and Halos, respectively; Figs.4.11, 4.12). A T–X pseudosection (Fig. 4.15A) was calculated to represent the changes in bulk composition from Country rocks (sample, MP3) going towards the Halos (sample M119) as function of temperature. For the T–X diagram, we fixed the pressure at 1.125 GPa simulating the conditions where both the samples mineral assemblages were stable at peak conditions. We considered MP3 and M119 samples because are the most representative of Country rocks and Halos, respectively, and because they easily model the melt presence. Bulk–rock composition used for the pseudosection calculations has been obtained by standard X–ray fluorescence (XRF) spectroscopy and inductively coupled plasma–mass spectrometry (ICP–MS) made

by the Activation Laboratories Ltd., Ancaster, Canada (4E-Research + ICPMS method; Table S4.1). Pseudosections were calculated in the system $\text{MnO-TiO}_2\text{-Na}_2\text{O-CaO-K}_2\text{O-FeO-MgO-Al}_2\text{O}_3\text{-SiO}_2\text{-H}_2\text{O}$ (MnTiNCKFMASH) with H_2O in excess where migmatization do not occur (e.g., sample M92, M62, M69), and considering the melt presence only where we have evidence of partial melting (e.g., samples M119, M102, MP3). The bulk compositions were projected from the apatite pole onto the MnTiNCKFMASH subspace, removing minor component P_2O_5 from the system (e.g., Thompson, 1957; Büttner, 2012). Only for three sample (M92, MP3A, M62, Country rocks), an additional calculation of the effective bulk composition was made by quantifying the modal volumetric abundance of the garnet cores, transform it into molar abundance, and thus subtracting the average core composition from the bulk rock composition. The previously approaches were chosen to determine as closely as possible the bulk composition effective at the scale of the thin section (Zuluaga et al., 2005; Buttner, 2012; Lanari and Engi, 2017). The calculations were constructed using the Perple_X (Connolly, 2005) version 6.8.5, combined to the thermodynamic dataset 5.5 of Holland and Powell (1998). The mixing models used are: Gt(WPPH) = garnet, feldspar = feldspars, Pl(h) = plagioclase, Bio(HP) = biotite, Mica(CHA1) = muscovite, St(HP) = staurolite, Chl(HP) = chlorite, Ctd(HP) = chloritoid, Opx (HP) = orthopyroxene, Omph (GHP) = omphacite, IlGkPy = ilmenite, Sp(HP) = spinel, GlTrTsPg = amphibole, hCrd = cordierite, Sapp(HP) = sapphirine, T = talc, and melt(HP) = melt only for samples that show evidences of partial melting (Holland and Powell, 1998; Coggon and Holland, 2002; Diener et al., 2007; White et al., 2008; for further details please refer to: http://www.perplex.ethz.ch/PerpleX_solution_model_glossary.html).

Compositional garnet isopleths of pyrope ($\text{Mg}/(\text{Fe}^{2+}+\text{Mg}+\text{Ca}+\text{Mn})$), almandine ($\text{Fe}^{2+}/(\text{Fe}^{2+}+\text{Mg}+\text{Ca}+\text{Mn})$), grossular ($\text{Ca}/(\text{Fe}^{2+}+\text{Mg}+\text{Ca}+\text{Mn})$) and rarely spessartine ($\text{Mn}/(\text{Fe}^{2+}+\text{Mg}+\text{Ca}+\text{Mn})$) were plotted. The position of these isopleths (with an error of $\pm 1\sigma$), calculated with the software Perplex, have been also indicated in the P-T pseudosections. As the effective bulk composition evolved between the four end-members could approximate the true metamorphic history and the P-T peak. Compositional isopleths for Si (a.p.f.u.) in muscovite, An% for plagioclase and Ti (a.p.f.u.) or Mg# ($100 \times \text{MgO}/(\text{FeO} + \text{MgO})$) for biotite were plotted and reported in Figs. 4.11B, D, F; 4.12 B, D, F; S4.6; S4.7.

A.1.2.5 U-Pb Geochronology

We performed U-Pb geochronology on zircon grains either separated from one sample (MP3, Country rock) showing evidence of migmatitization or directly on the 30 μm -thick, thin section of

sample M119 (Halos). Before the isotopic analyses, zircon grains were imaged by back-scattered electron imaging to locate, characterize (dimensions, microstructural position, and internal structures) and then select the most suitable crystals. Zircon features on thin section of sample M119 were observed obtaining CL images using a JEOL JXA-8200 electron microprobe (Dipartimento di Scienze della Terra, Università degli Studi di Milano, Italy) at 15-kV accelerating voltage and 15-nA beam current. CL images of thirty-one separated zircon from sample MP3 were obtained using Philips 515 SEM equipped with a Centaurus CL detector system (300–650nm) and an EDAX EDS system at < 20 kV accelerating voltage, magnification ranges from 10× to 1000× and image size 512 × 512 at C.N.R., Istituto di Geoscienze e Georisorse of Pavia. Analyses were carried out directly on polished thin sections using an ArF 193-nm excimer laser (GeolLas 102 from MicroLas) coupled with the 8900 Triple Quadrupole ICP-MS (Agilent) at C.N.R., Istituto di Geoscienze e Georisorse of Pavia. Analytical details and results are reported in Table S4.5.

A.1.2.6 Whole rock

According to the classification scheme for the siliciclastic sediments proposed by Herron (1988), sample compositions lie mainly within the compositional field of shale ($0.2 < \log (\text{SiO}_2/\text{Al}_2\text{O}_3) < 0.6$,

$0.2 < \log (\text{FeO}_T/\text{K}_2\text{O}) < 0.6$), except for M92 that falls within the wacke field ($\log (\text{SiO}_2/\text{Al}_2\text{O}_3) = 0.6$; $\log (\text{FeO}_T/\text{K}_2\text{O}) = 0.1$). M119 differs significantly from the other samples for its higher Al_2O_3 (up to 25 wt.%) and lower SiO_2 (up to 45 wt.%) contents. M92 and M102 present a similar bulk composition with higher SiO_2 (ca. 67 wt.%) and lower in Al_2O_3 (ca. 16 wt.%). MP3, M62 and M69 have similar bulk compositions except for the CaO and Na_2O contents that are higher in the last two samples (Fig. S1 and Table 4.1). The M119 sample stands out among others for the higher trace elements concentrations, especially in Zr, Hf, Y, La, Nd, Ce, Th, Pb, which are the main components of accessory minerals such as zircon, monazite, allanite, epidote, effectively more abundant and bigger in size in this sample. Only Rb, Sr (concentrated in mica), Zn, and Cu (occurring in oxides and sulphides) are findable in quite similar amount in all samples, except for Zn, which is abundant in staurolite and in sample MP3.

A.1.2.7 References

- Bhattacharya, A., Mohanty, L., Maji, A., Sen, S. K., and Raith, M., 1992. Non-ideal mixing in the phlogopite-annite binary: constraints from experimental data on Mg-Fe partitioning and a reformulation of the biotite-garnet geothermometer. *Contributions to Mineralogy and Petrology*, 111, 8-93.
- Büttner, S. H., 2012. Rock Maker: an MS Excel™ spreadsheet for the calculation of rock compositions from proportional whole rock analyses, mineral compositions, and modal abundance. *Mineralogy and Petrology*, 104(1-2), 129-135.
- Caddick, M.J., Konopásek, J., Thompson, A.B., 2010. Preservation of Garnet Growth Zoning and the Duration of Prograde Metamorphism. *J. Petrol.* 51 (11), 2327-2347.
- Coggon, R., and Holland, T. J. B., 2002. Mixing properties of phengitic micas and revised garnet phengite thermobarometers. *Journal of Metamorphic Geology*, 20(7), 683-696.
- Connolly, J. A. D., 2005. Computation of phase equilibria by linear programming: A tool for geodynamic modeling and its application to subduction zone decarbonation. *Earth and Planetary Science Letters*, 236(1-2), 524-541.
- Diener J.F.A., Powell R., White R.W., Holland T.J.B., 2007. A new thermodynamic model for clino- and orthoamphiboles in the system $\text{Na}_2\text{O}-\text{CaO}-\text{FeO}-\text{MgO}-\text{Al}_2\text{O}_3-\text{SiO}_2-\text{H}_2\text{O}-\text{O}$. *Journal of Metamorphic Geology*, 25, 631-56.
- Green, T. H., and Hellman, P. L., 1982. Fe-Mg partitioning between coexisting garnet and phengite at high pressure, and comments on a garnet-phengite geothermometer. *Lithos*, 15(4), 253- 266.
- Herron, M. M., 1988. Geochemical classification of terrigenous sands and shales from core or log data. *Journal of Sedimentary Research*, 58(5), 820-829.
- Hodges, K. V., and Crowley, P. T., 1985. Error estimation and empirical geothermobarometry for pelitic systems. *American Mineralogist*, 70(7-8), 702-709.
- Hoisch, T. D., 1990. Empirical calibration of six geobarometers for the mineral assemblage quartz+ muscovite+ biotite+ plagioclase+ garnet. *Contributions to Mineralogy and Petrology*, 104(2), 225-234.
- Holdaway, M. J., 2000. Application of new experimental and garnet Margules data to the garnet- biotite geothermometer. *American Mineralogist*, 85(7-8), 881-892.
- Holdaway, M. J., 2001. Recalibration of the GASP geobarometer in light of recent garnet and plagioclase activity models and versions of the garnet-biotite geothermometer. *American Mineralogist*, 86(10), 1117-1129.
- Holland, T.J.B., and Powell, R., 1985. An internally consistent thermodynamic dataset with uncertainties and correlations: 2. Data and results. *Journal of Metamorphic Geology*, 3(4), 343-370.
- Holland, T.J.B., Powell, R., 1998. An internally consistent thermodynamic data set for phases of petrological interest. *J. Metamorph. Geol.* 16 (3), 309-343.
- Krogh, E. J., and Råheim, A., 1978. Temperature and pressure dependence of Fe-Mg partitioning between garnet and phengite, with particular reference to eclogites. *Contributions to Mineralogy and Petrology*, 66(1), 75-80.
- Lanari, P., and Engi, M., 2017. Local bulk composition effects on metamorphic mineral assemblages. *Reviews in Mineralogy and Geochemistry*, 83(1), 55-102.
- Massonne, H.-J., Schreyer, W., 1987. Phengite geobarometry based on the limiting assemblage with K-feldspar, phlogopite, and quartz. *Contrib. Mineral. Petrol.* 96, 212-224.
- Spear, F. S., 1993. *Metamorphic Phase Equilibria and Pressure-Temperature-Time-Paths*. Mineralogical Society of America, 799.
- Taylor, S. R., and McLennan, S. M., 1985. *The continental crust: its composition and evolution*. Blackwell, Oxford (1985), p. 312
- Thompson, J. J. B., 1957. The graphical analysis of mineral assemblages in pelitic schists. *American Mineralogist: Journal of Earth and Planetary Materials*, 42(11-12), 842-858.
- White, R. W., Powell, R., and Baldwin, J. A., 2008. Calculated phase equilibria involving chemical

- potentials to investigate the textural evolution of metamorphic rocks. *Journal of Metamorphic Geology*, 26(2), 181–198.
- Wu, C. M., 2015. Revised empirical garnet–biotite–muscovite–plagioclase geobarometer in metapelites. *Journal of Metamorphic Geology*, 33(2), 167–176.
- Wu, C. M., 2018. Metapelitic Garnet–Muscovite–Al₂SiO₅–Quartz (GMAQ) Geothermobarometry. *Journal of Earth Science*, 29(5), 977–988.
- Zuluaga, C. A., Stowell, H. H., and Tinkham, D. K., 2005. The effect of zoned garnet on metapelite pseudosection topology and calculated metamorphic PT paths. *American Mineralogist*, 90(10), 1619–1628.
- and *Petrology*, 66(1), 75–80.
- Lanari, P., and Engi, M., 2017. Local bulk composition effects on metamorphic mineral assemblages. *Reviews in Mineralogy and Geochemistry*, 83(1), 55–102.
- Massonne, H.-J., Schreyer, W., 1987. Phengite geobarometry based on the limiting assemblage with K-feldspar, phlogopite, and quartz. *Contrib. Mineral. Petrol.* 96, 212–224. Spear, F. S., 1993. *Metamorphic Phase Equilibria and Pressure–Temperature–Time–Paths*. Mineralogical Society of America, 799.
- Taylor, S. R., and McLennan, S. M., 1985. *The continental crust: its composition and evolution*. Blackwell, Oxford (1985), p. 312
- Thompson, J. J. B., 1957. The graphical analysis of mineral assemblages in pelitic schists. *American Mineralogist: Journal of Earth and Planetary Materials*, 42(11-12), 842-858.
- White, R. W., Powell, R., and Baldwin, J. A., 2008. Calculated phase equilibria involving chemical potentials to investigate the textural evolution of metamorphic rocks. *Journal of Metamorphic Geology*, 26(2), 181–198.
- Wu, C. M., 2015. Revised empirical garnet–biotite–muscovite–plagioclase geobarometer in metapelites. *Journal of Metamorphic Geology*, 33(2), 167–176.
- Wu, C. M., 2018. Metapelitic Garnet–Muscovite–Al₂SiO₅–Quartz (GMAQ) Geothermobarometry. *Journal of Earth Science*, 29(5), 977–988.
- Zuluaga, C. A., Stowell, H. H., and Tinkham, D. K., 2005. The effect of zoned garnet on metapelite pseudosection topology and calculated metamorphic PT paths. *American Mineralogist*, 90(10), 1619–1628.

A.1.3 Figures

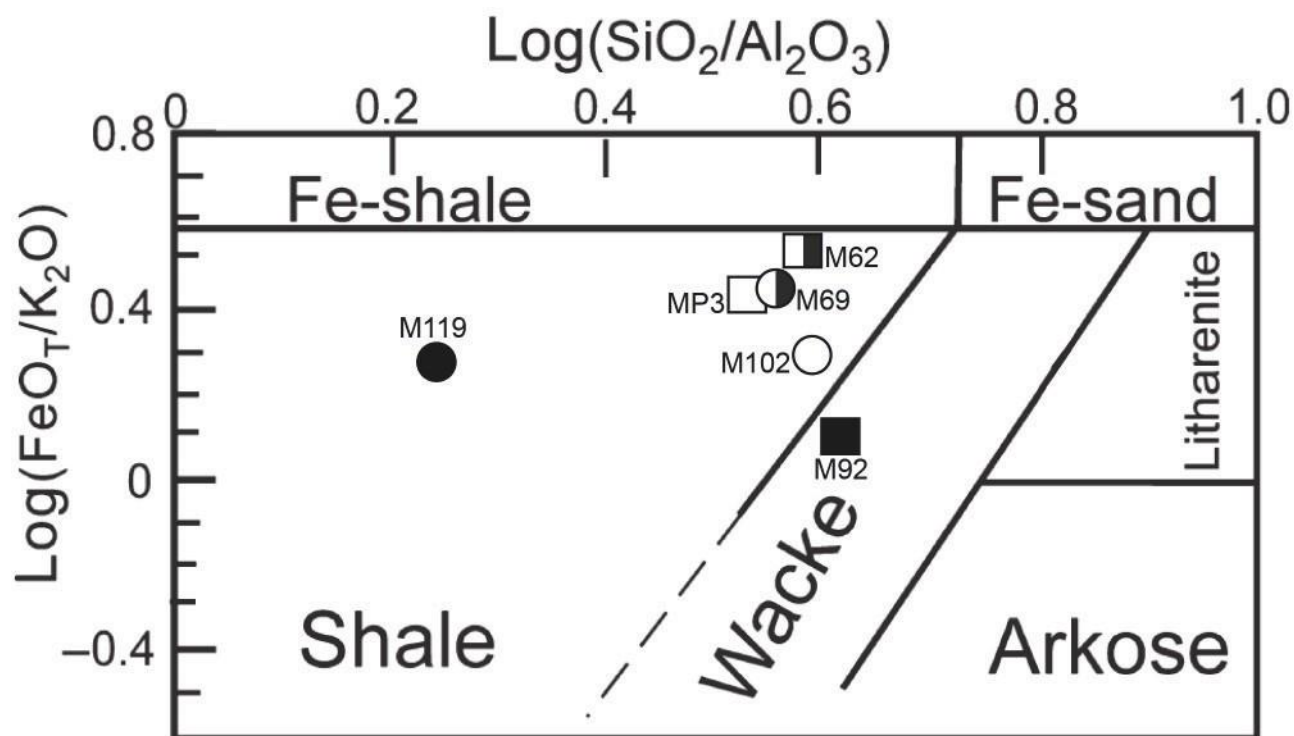


Figure S4.1 – Chemical classification of representative samples from this work, modified after Herron (1988).

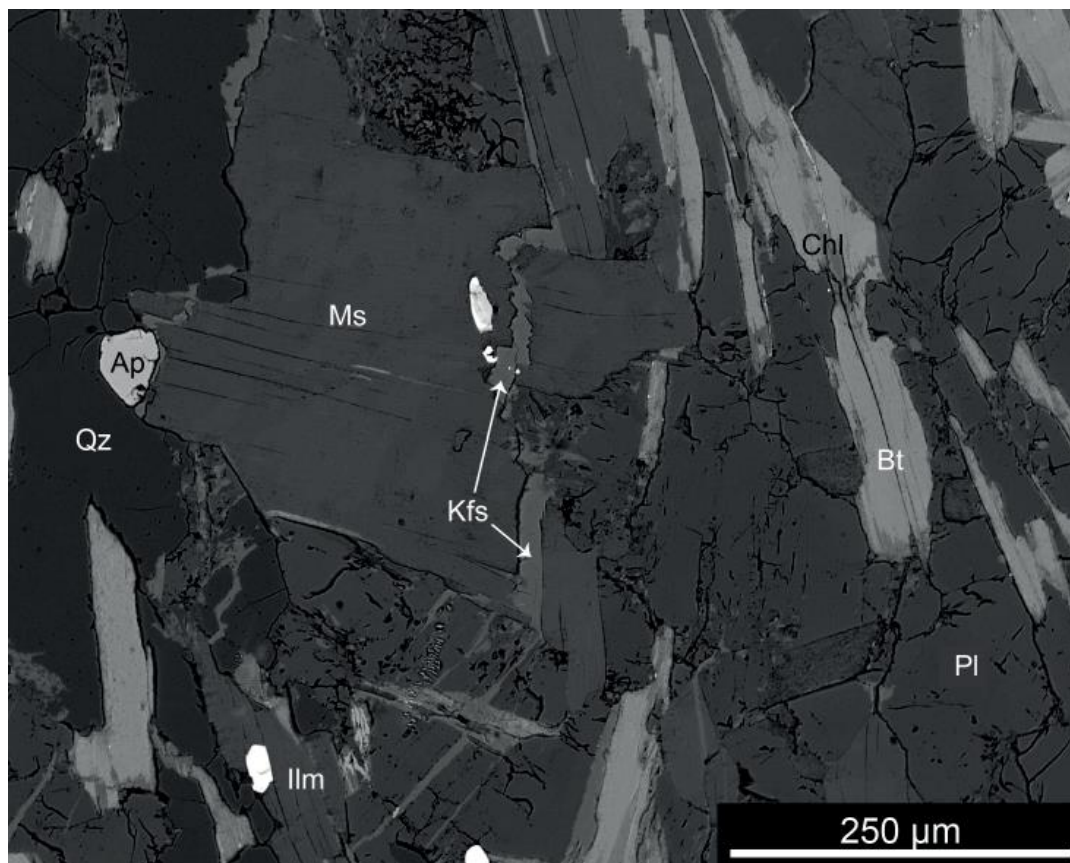


Figure S4.2 – BSE image showing films of K-feldspar located along the grain boundary (e.g., sample M92).

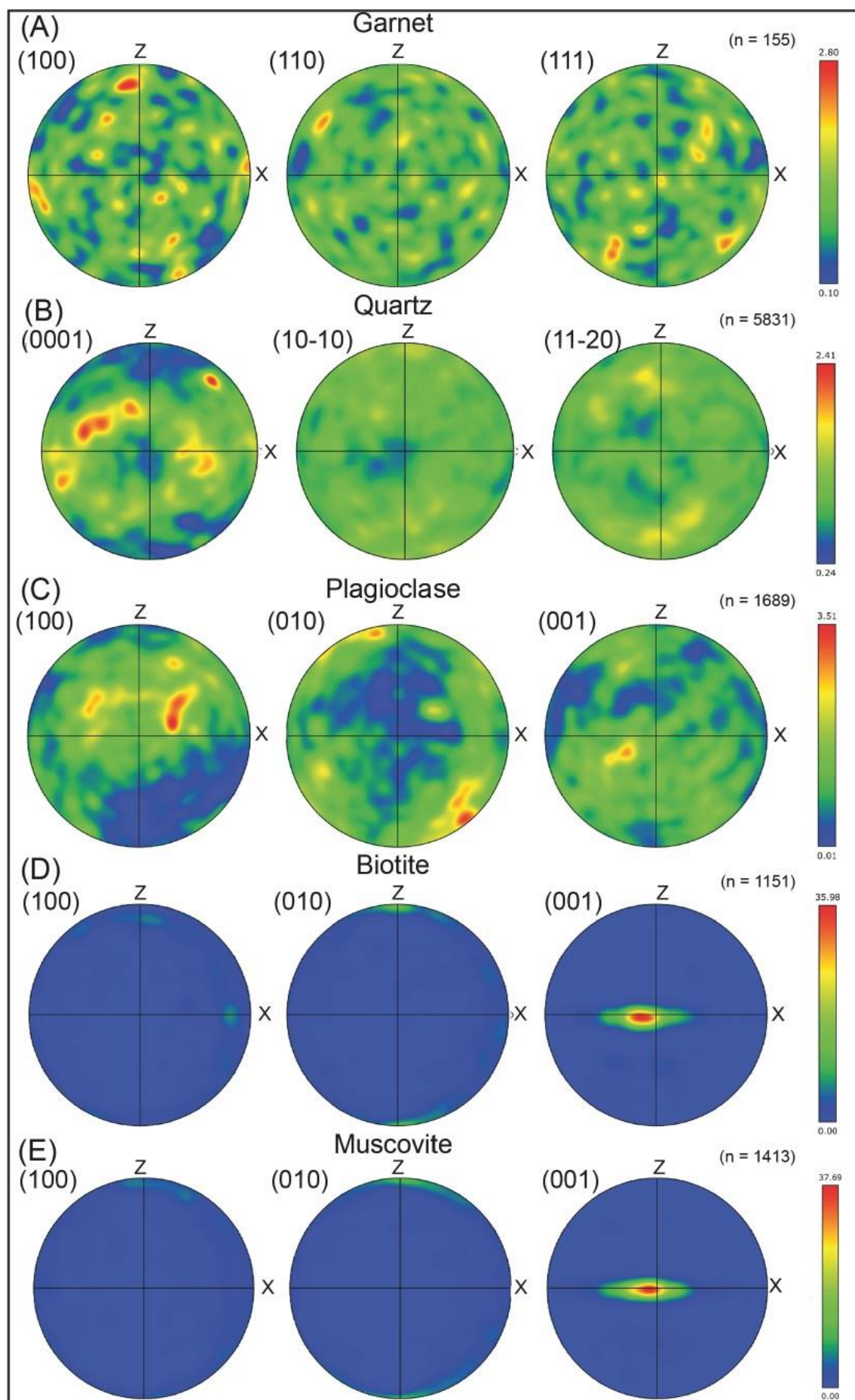


Figure S4.3 – EBSD pole figures of main Country rocks mineral phases: A) Garnet. B) Quartz. C) Plagioclase. D) Biotite. E) Muscovite. The number of grains (n) is reported in brackets. Pole figures are plotted in the lower hemisphere of the equal area stereographic projection.

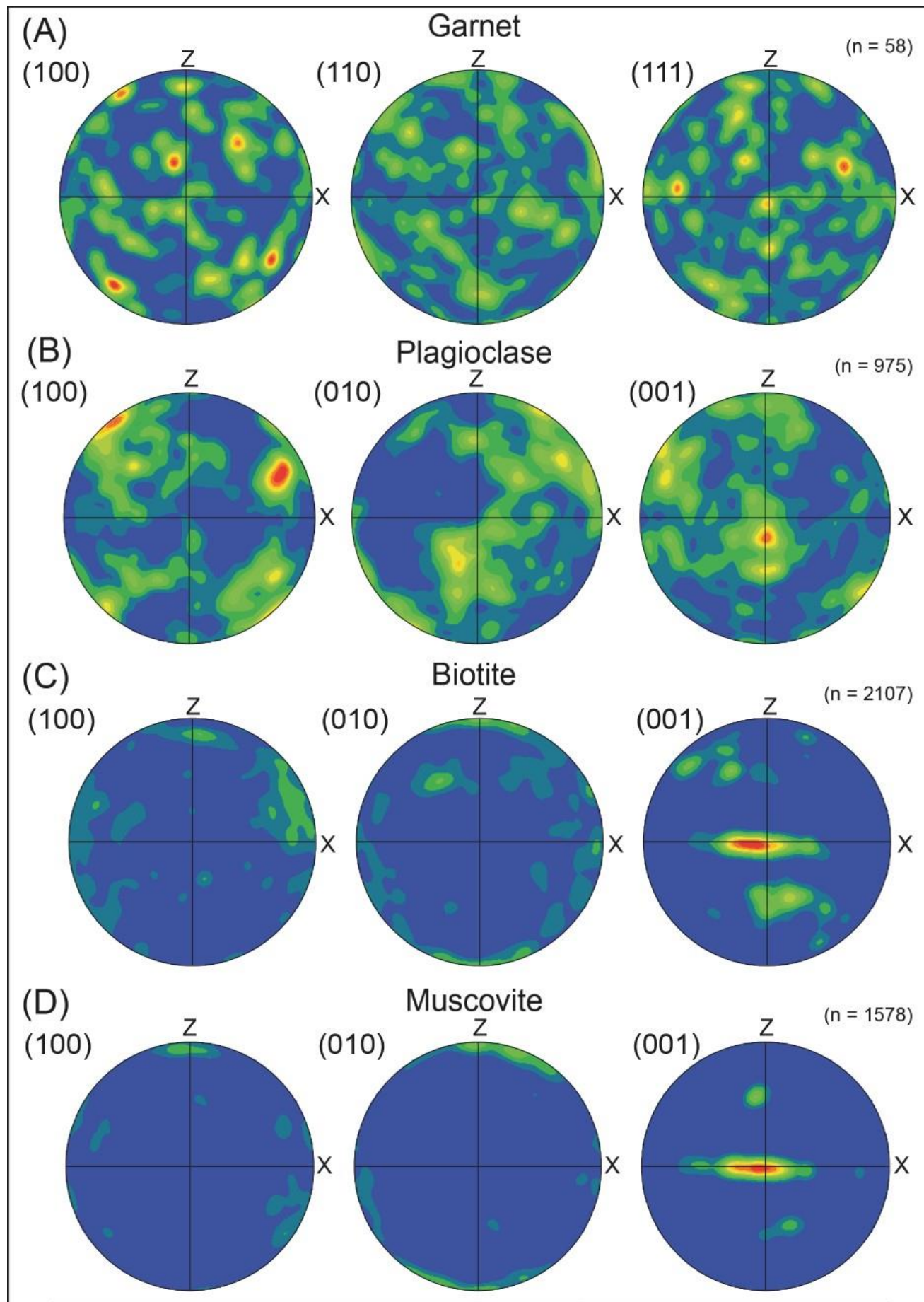


Figure S4.4 – EBSD pole figures of main Halos mineral phases: A) Garnet. B) Plagioclase. D) Biotite. E) Muscovite. The number of grains (n) is reported in brackets. Pole figures are plotted in the lower hemisphere of the equal area stereographic projection.

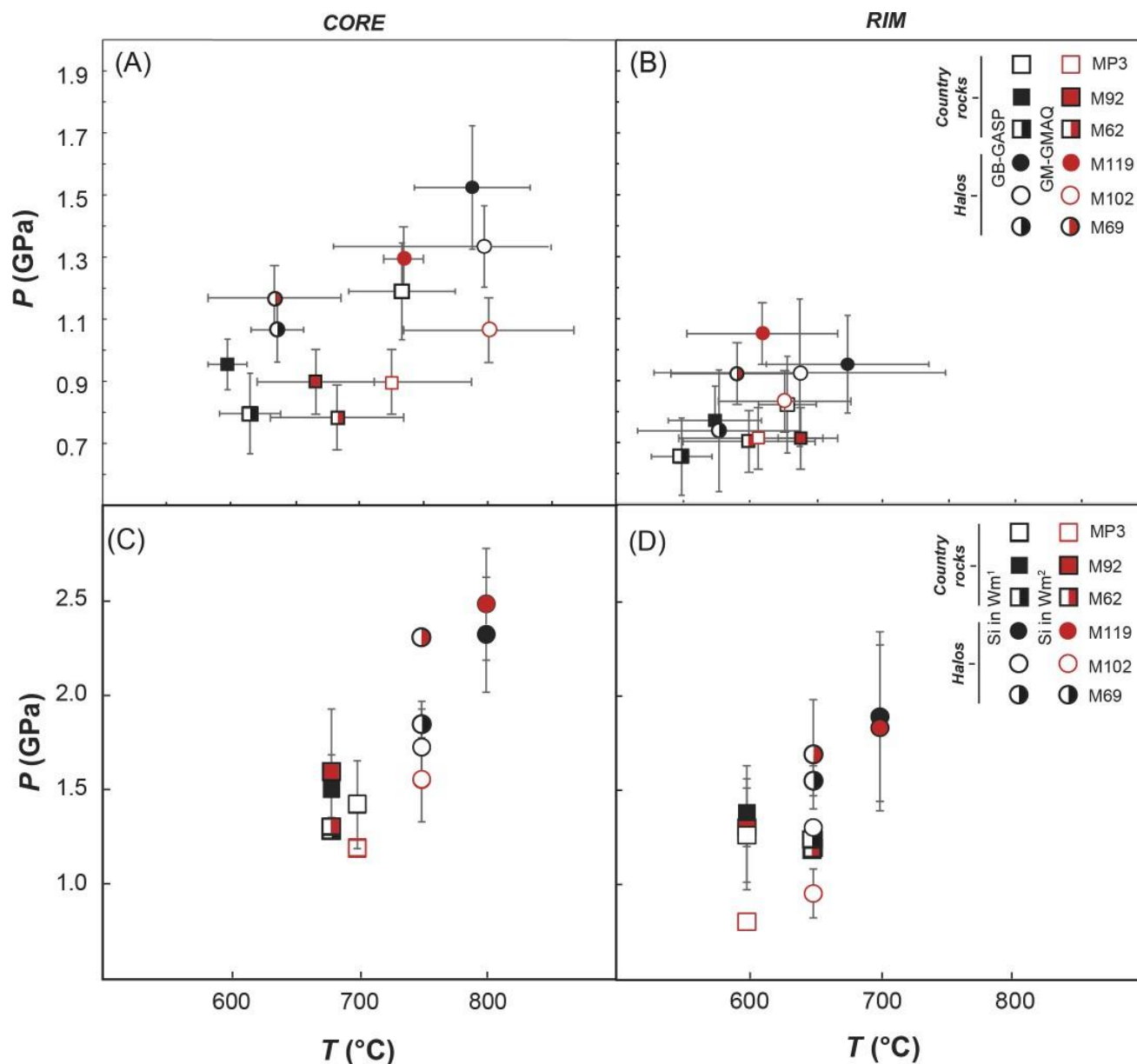


Figure S4.5 – Average P–T estimates by: Garnet–Biotite (GB) and Garnet–Muscovite (GM) thermometry combined with the Garnet–Aluminosilicate–Silica–Plagioclase (GASP) and Garnet–Muscovite–Al₂SiO₅– Quartz (GMAQ) geobarometry determined for A) garnet core paired with their inclusions and B) garnet rims associated with the neighbouring minerals (biotite, plagioclase, kyanite or muscovite). C, D) Si-in-white mica geobarometer estimates (Si-in-Wm1 refers to Caddick and Thompson, 2008; Si-in-Wm2 refers to Massonne and Schreyer, 1987). Bars indicate the standard deviation ($\pm 1\sigma$), they are calculated as standard deviation on the average number (N) of analyses indicated in Table S5.4.

Country rocks

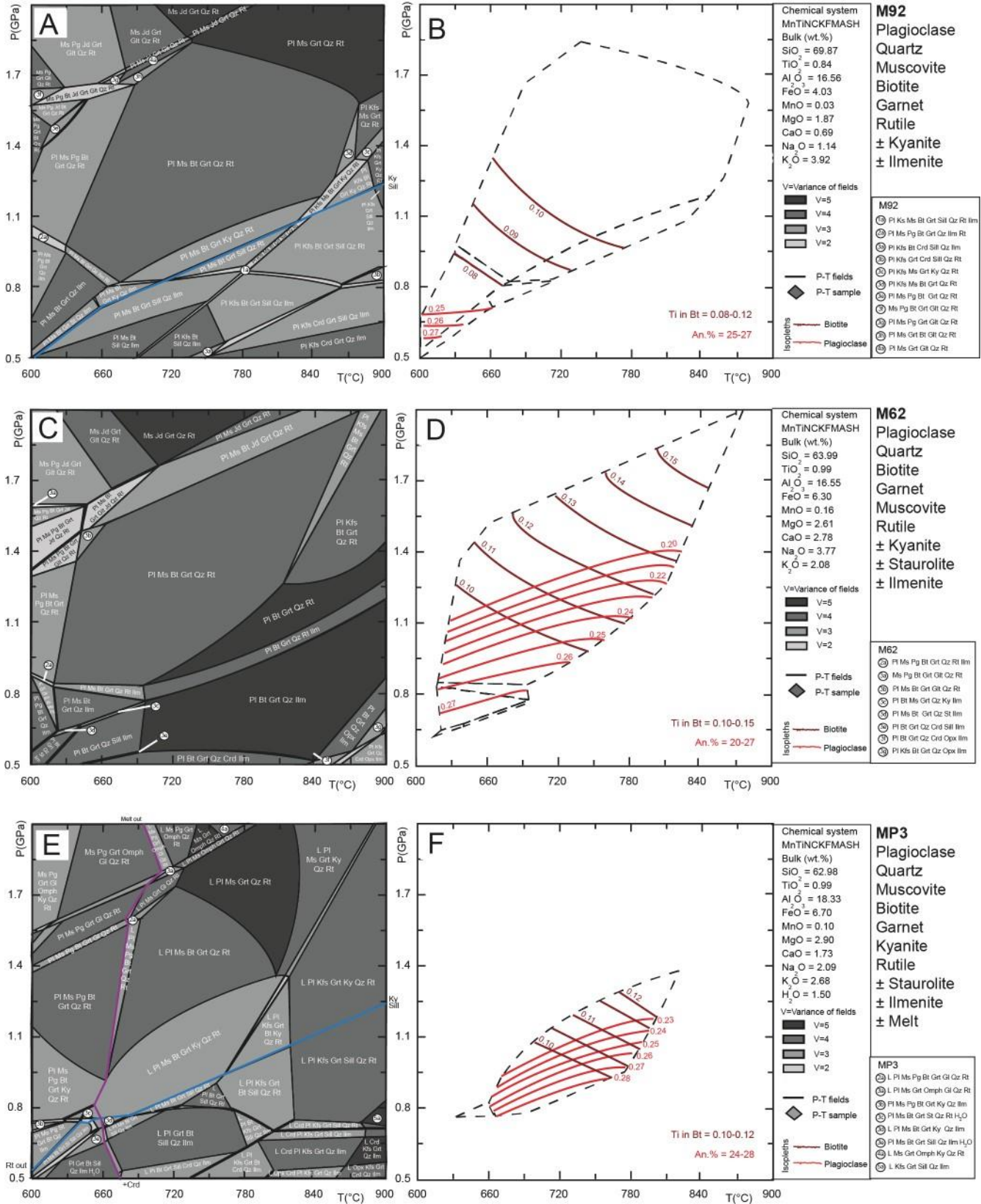


Figure S4.6 – P–T pseudosections for Country rocks. A, B) M92. C, D) M62. E, F) MP3. P–T conditions, P–T paths and fields inferred from the mineral assemblage are shown; isopleths for An% in plagioclase and Ti (a.p.f.u.) or Mg# for biotite are reported.

Halos

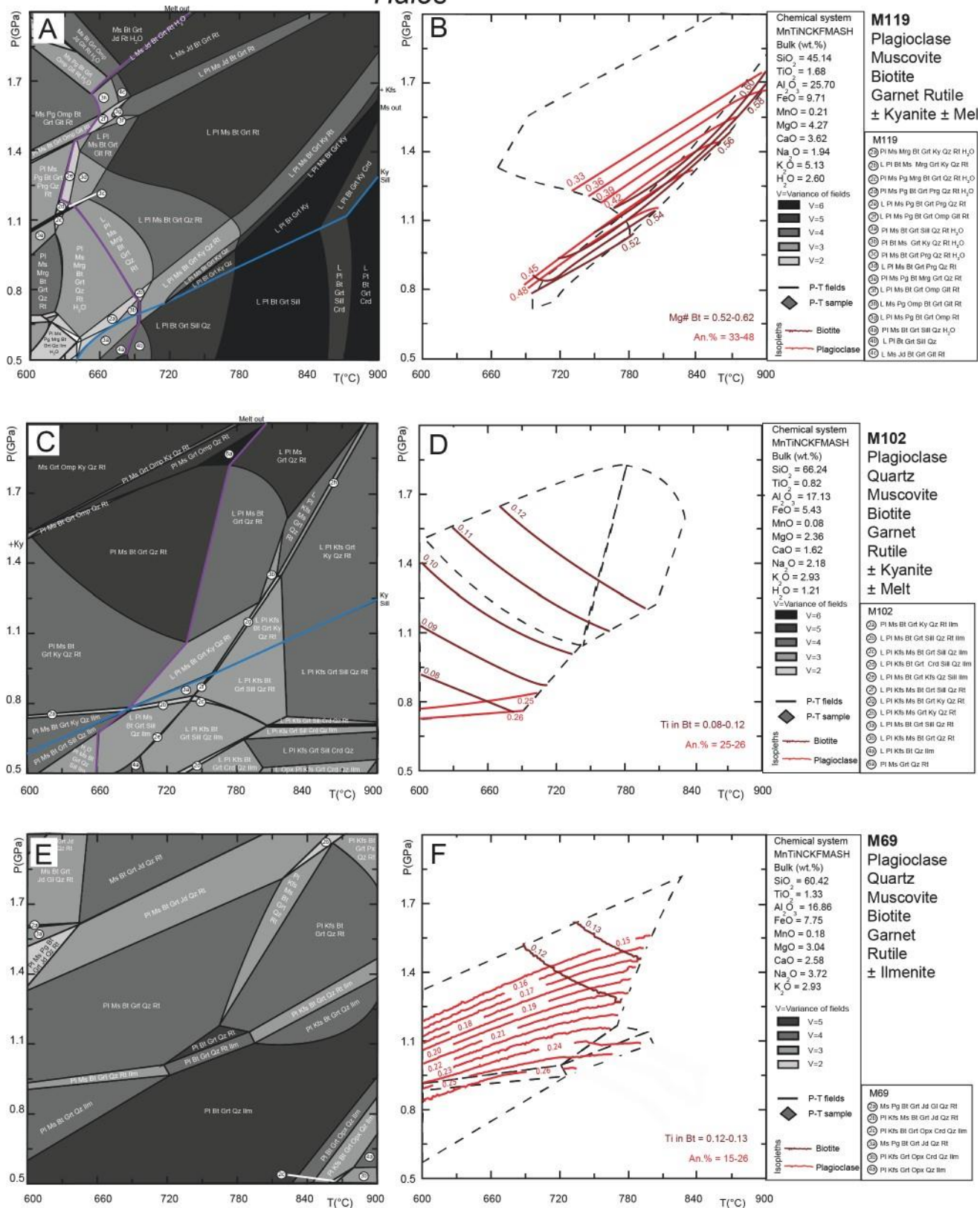


Figure S4.7 – P–T pseudosections for Halos. A, B) M119. C, D) M102. E, F) M69. P–T conditions, P–T paths and fields inferred from the mineral assemblage are shown; isopleths for An% in plagioclase and Ti (a.p.f.u.) or Mg# for biotite are reported.

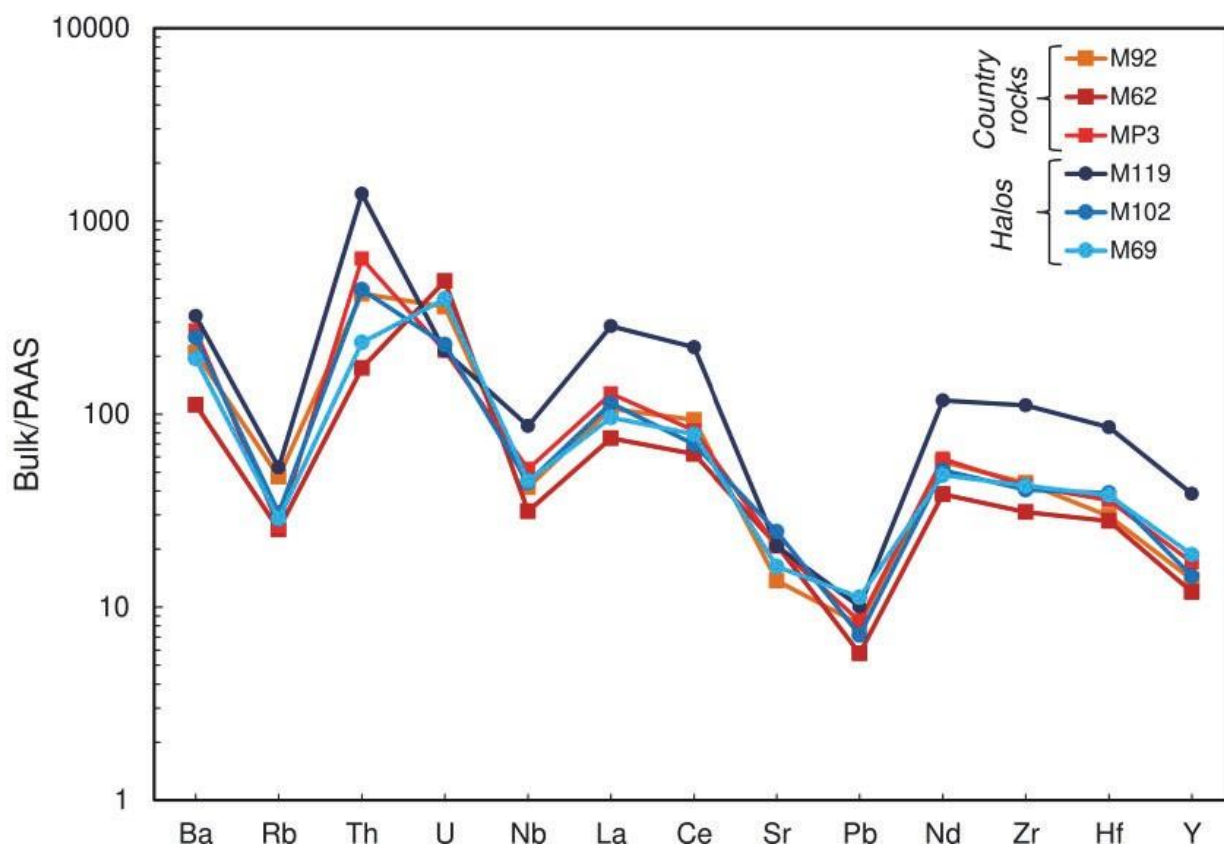


Figure S4.8 – Bulk trace element of this work samples normalized to Post-Archean Australian Shales (PAAS) after Taylor and McLennan (1985).

A.1.4 Tables

Table S4.1. Major and trace element bulk rock analyses of this work samples

Sample	<i>Country rocks</i>			<i>Halos</i>		
	MP3	M92	M62	M119	M102	M69
(wt.%)						
SiO ₂	59,22	68,37	61,97	44,76	66,00	58,70
TiO ₂	0,92	0,82	0,95	1,68	0,82	1,29
Al ₂ O ₃	17,45	16,57	16,30	25,47	17,07	16,38
FeO _t	7,53	5,34	7,53	10,72	6,02	8,37
MnO	0,11	0,07	0,21	0,24	0,08	0,18
MgO	2,79	1,90	2,58	4,23	2,35	2,95
CaO	1,94	0,96	2,92	3,60	1,85	2,72
Na ₂ O	1,94	1,10	3,60	1,93	2,17	3,61
K ₂ O	2,49	3,78	1,99	5,07	2,92	2,85
P ₂ O ₅	0,18	0,12	0,14	0,02	0,18	0,17
L.O.I	1,40	1,71	0,73	1,74	1,71	1,16
Total	95,98	100,71	98,92	99,45	101,16	98,38
µg/g (i.e., ppm)						
Rb	91,2	163,2	87,0	182,5	106,3	99,0
Ba	924,6	710,7	381,0	1101,9	851,9	661,0
Sr	245,8	163,1	250,0	246,1	293,4	193,0
Nb	19,5	15,7	11,8	32,6	16,6	16,9
Zr	235,7	244,2	172,0	616,5	224,9	236,0
Hf	6,4	5,3	5,0	15,3	7,0	6,8
Y	38,4	31,3	27,0	86,9	32,5	42,0
Ga	25,4	21,3	21,0	29,8	21,2	22,0
Zn	225,2	87,8	54,0	61,3	94,0	104,0
Cu	26,4	14,8	58,0	31,4	41,0	19,0
Ni	23,9	18,1	35,0	72,4	17,6	16,0
Co	12,9	10,7	20,0	20,2	11,6	9,1
Cr	92,0	63,4	80,2	121,3	67,4	81,2
V	140,5	89,9	129,0	163,2	100,7	165,0
Sc	17,5	16,1	15,4	28,8	16,1	18,4
La	47,0	39,3	27,5	104,9	41,8	35,3
Ce	78,7	89,5	59,5	212,7	66,9	75,6
Nd	41,7	40,4	27,4	83,9	36,5	34,3
Pb	31,0	29,8	21,0	36,8	26,2	41,0
Th	27,1	17,9	7,4	58,8	18,8	10,0
U	2,6	4,4	6,0	2,6	2,8	4,8
W	0,9	3,3	2,0	6,5	0,8	1,0
XMg	0,27	0,26	0,28	0,28	0,28	0,26
log(SiO ₂ /Al ₂ O ₃)	0,53	0,62	0,58	0,24	0,59	0,55
log(FeOT/K ₂ O)	0,43	0,10	0,53	0,28	0,27	0,42

FeOT, total Fe as FeO; L.O.I., loss on ignition; XMg = [MgO/(FeOT + MgO)].

Table S4.2. Representative average analyses of plagioclase, muscovite, biotite and staurolite for Country rocks.4.

Sample position	MP3								Country rock M92						M62							
	pl	σ	ms	σ	bt	σ	st	σ	pl	σ	ms	σ	bt	σ	pl	σ	ms	σ	bt	σ	st	σ
N	6		4		8		9		9		15		5		3		3		8		4	
(wt.%)																						
SiO ₂	61,14	0,49	45,39	0,23	35,74	0,39	28,28	0,28	62,29	1,39	48,10	1,37	36,32	0,48	61,42	2,32	48,03	0,53	37,06	0,43	28,45	0,20
TiO ₂	0,02	0,03	0,50	0,12	1,78	0,18	0,61	0,04	0,01	0,01	0,67	0,20	2,31	0,07	0,00	0,00	0,77	0,08	1,44	0,15	0,73	0,06
Al ₂ O ₃	23,28	0,55	35,82	0,46	19,45	0,33	54,53	0,75	23,84	0,99	34,97	1,34	18,50	0,58	25,70	1,43	35,24	0,16	19,68	0,66	54,87	0,46
Cr ₂ O ₃	0,01	0,02	0,02	0,05	0,03	0,03	0,05	0,03	0,01	0,01	0,03	0,03	0,04	0,02	0,03	0,03	0,05	0,01	0,03	0,02	0,07	0,03
FeO	0,04	0,04	0,88	0,06	18,14	0,75	12,42	0,40	0,22	0,29	1,50	0,29	19,31	0,46	0,34	0,50	3,20	0,33	16,05	0,80	12,45	0,52
MnO	0,02	0,02	0,01	0,01	0,12	0,04	0,31	0,05	0,02	0,02	0,01	0,02	0,13	0,02	0,02	0,03	0,05	0,07	0,18	0,05	0,80	0,09
MgO	0,00	0,01	0,51	0,08	10,01	0,54	0,03	0,03	0,01	0,01	0,98	0,29	9,64	0,16	0,00	0,00	0,75	0,09	12,58	0,89	0,02	0,02
CaO	5,55	0,42	0,02	0,01	0,04	0,03	1,38	0,20	5,50	0,77	0,01	0,01	0,02	0,03	6,50	1,66	0,03	0,02	0,02	0,01	2,11	0,19
Na ₂ O	8,31	0,22	1,16	0,03	0,14	0,08	0,02	0,01	7,95	1,10	0,70	0,09	0,23	0,09	8,08	0,96	0,79	0,16	0,24	0,03	0,00	0,01
K ₂ O	0,08	0,01	8,78	0,06	9,00	0,33	0,01	0,01	0,58	1,39	9,26	0,33	8,90	0,12	0,12	0,00	9,13	0,11	9,32	0,21	0,00	0,01
ZnO							1,24	0,21													0,62	0,10
Total	98,46	0,40	93,09	0,50	97,81	1,22	98,87	2,00	100,44	1,58	96,24	1,50	96,48	1,28	102,21	0,41	98,03	0,82	96,46	1,10	100,12	1,68
Cat./O	5/8		7/11		8/11		15/23		5/8		7/11		8/11		5/8		7/11		8/11		15/23	
Si	2,75	0,02	3,06	0,01	2,72	0,02	3,88	0,05	2,75	0,04	3,14	0,06	2,75	0,03	2,68	0,09	3,11	0,01	2,73	0,02	3,85	0,03
Ti	0,00	0,00	0,03	0,01	0,10	0,01	0,06	0,00	0,00	0,00	0,03	0,01	0,13	0,00	0,00	0,00	0,04	0,00	0,08	0,01	0,07	0,01
Al	1,24	0,03	2,85	0,02	1,74	0,03	8,82	0,07	1,24	0,04	2,69	0,09	1,65	0,05	1,32	0,08	2,69	0,01	1,71	0,03	8,76	0,06
Fe	0,00	0,00	0,05	0,00	1,15	0,05	1,43	0,05	0,01	0,01	0,08	0,02	1,22	0,03	0,00	0,00	0,17	0,02	0,99	0,07	1,41	0,06
Mn	0,00	0,00	0,00	0,00	0,01	0,00	0,04	0,01	0,00	0,00	0,00	0,00	0,01	0,00	0,01	0,02	0,00	0,00	0,01	0,00	0,09	0,01
Mg	0,00	0,00	0,05	0,01	1,13	0,06	0,00	0,00	0,00	0,00	0,10	0,03	1,09	0,02	0,00	0,00	0,07	0,01	1,38	0,08	0,00	0,00
Ca	0,27	0,02	0,00	0,00	0,00	0,00	0,28	0,04	0,26	0,04	0,00	0,00	0,00	0,00	0,30	0,08	0,00	0,00	0,00	0,00	0,43	0,04
Na	0,73	0,02	0,15	0,00	0,02	0,01	0,00	0,00	0,68	0,09	0,09	0,01	0,03	0,01	0,68	0,08	0,10	0,02	0,01	0,02	0,00	0,00
K	0,00	0,00	0,75	0,01	0,87	0,03	0,00	0,00	0,03	0,08	0,77	0,04	0,86	0,01	0,01	0,00	0,75	0,01	0,88	0,03	0,00	0,00
Zn							0,13	0,02													0,06	0,01
Total	4,99	0,01	6,94	0,01	7,75	0,21	14,64	0,02	4,98	0,02	6,91	0,25	7,74	0,16	5,01	0,01	6,93	0,00	7,78	0,01	14,69	0,02
X _{Fe}			0,49	0,03	0,50	0,02	0,84	0,02			0,47	0,05	0,53	0,01			0,70	0,03	0,42	0,03	0,77	0,02
an	26,80	1,96							26,74	3,58					30,60	7,91						
ab	72,72	1,94							69,69	7,97					68,73	7,94						
or	0,48	0,08							3,58	8,78					0,63	0,06						

X_{Fe} = Fe/(Fe + Mg), an = Ca/(Na + Ca + K), ab = Na/(Na + Ca + K), or = K/(Na + Ca + K). N is the number of analyses.

Table S4.2. Representative average analyses of plagioclase, muscovite, biotite and staurolite for Halos.

<i>Halos</i>																	
M119						M102						M69					
pl	σ	ms	σ	bt	σ	pl	σ	ms	σ	bt	σ	pl	σ	ms	σ	bt	σ
31		44		45		15		16		16		5		3		5	
58,37	3,00	49,65	1,53	36,46	0,83	61,24	0,78	46,85	0,97	36,72	0,67	64,46	1,47	50,72	1,80	37,39	0,68
0,02	0,02	0,86	0,31	1,93	0,26	0,01	0,02	0,73	0,14	2,09	0,35	0,02	0,02	0,65	0,21	2,54	0,37
25,87	1,99	31,57	1,84	20,60	0,61	24,67	1,37	35,48	1,41	19,69	0,55	23,36	1,17	33,35	0,76	19,06	0,59
0,01	0,02	0,02	0,03	0,03	0,03	0,01	0,02	0,03	0,02	0,04	0,03	0,02	0,03	0,06	0,03	0,04	0,04
0,12	0,11	1,45	0,27	16,27	1,08	0,07	0,05	1,22	0,13	18,13	1,51	0,04	0,02	1,65	0,24	18,55	0,92
0,02	0,02	0,02	0,02	0,08	0,03	0,02	0,03	0,01	0,01	0,09	0,03	0,02	0,02	0,02	0,01	0,23	0,12
0,01	0,01	2,03	0,54	11,45	0,73	0,00	0,00	1,00	0,29	10,78	1,11	0,01	0,01	1,56	0,33	10,20	0,51
7,99	2,16	0,01	0,01	0,03	0,03	6,18	0,76	0,00	0,01	0,02	0,02	4,22	1,15	0,01	0,00	0,04	0,05
7,11	1,27	0,69	0,15	0,41	0,05	8,16	0,44	0,89	0,11	0,25	0,06	9,21	0,77	0,31	0,10	0,22	0,10
0,10	0,03	9,25	0,35	8,76	0,21	0,10	0,02	9,31	0,14	8,70	0,22	0,22	0,08	9,65	0,41	9,20	0,32
99,61	0,83	95,55	1,32	96,01	0,63	100,48	1,37	95,53	1,84	96,50	1,22	101,58	0,84	98,00	1,34	97,46	0,78
5/8		7/11		8/11		5/8		7/11		8/11		5/8		7/11		8/11	
2,62	0,11	3,26	0,08	2,69	0,05	2,71	0,05	3,09	0,05	2,72	0,02	2,80	0,06	3,25	0,06	2,75	0,03
0,00	0,00	0,04	0,02	0,11	0,01	0,00	0,00	0,04	0,01	0,12	0,02	0,00	0,00	0,03	0,01	0,14	0,02
1,37	0,11	2,45	0,14	1,79	0,06	1,29	0,06	2,76	0,08	1,72	0,03	1,20	0,06	2,52	0,10	1,65	0,05
0,00	0,00	0,08	0,02	1,01	0,07	0,00	0,00	0,07	0,01	1,12	0,10	0,00	0,00	0,09	0,01	1,14	0,06
0,00	0,00	0,00	0,00	0,00	0,00	0,00	0,00	0,00	0,00	0,01	0,00	0,00	0,00	0,00	0,00	0,01	0,01
0,00	0,00	0,20	0,05	1,26	0,08	0,00	0,00	0,10	0,03	1,19	0,12	0,00	0,00	0,15	0,03	1,12	0,05
0,39	0,11	0,00	0,00	0,00	0,00	0,29	0,03	0,00	0,00	0,00	0,00	0,20	0,05	0,00	0,00	0,00	0,00
0,62	0,11	0,09	0,02	0,06	0,01	0,70	0,04	0,11	0,02	0,04	0,01	0,78	0,06	0,04	0,01	0,03	0,01
0,01	0,00	0,78	0,03	0,82	0,02	0,01	0,00	0,78	0,01	0,82	0,02	0,01	0,00	0,79	0,04	0,86	0,03
5,01	0,01	6,90	0,35	7,75	0,30	5,00	0,01	6,94	0,20	7,73	0,32	4,99	0,01	6,87	0,04	7,72	0,02
		0,30	0,07	0,44	0,03			0,42	0,06	0,49	0,04			0,38	0,08	0,51	0,02
38,17	10,55					29,37	3,61					20,04	5,76				
61,27	10,46					70,07	3,55					78,72	5,41				
0,55	0,19					0,57	0,12					1,24	0,40				

Table S4.3. Representative average analyses of garnet

Sample position	Country rock												Halos											
	MP3				M92				M62				M119				M102				M69			
core	σ	rim	σ	core	σ	rim	σ	core	σ	rim	σ	core	σ	rim	σ	core	σ	rim	σ	core	σ	rim	σ	
(wt.%)																								
SiO ₂	38,43	0,31	37,77	0,37	38,52	0,19	38,55	0,21	38,20	0,51	38,71	0,23	38,86	0,23	38,09	0,61	38,91	0,20	38,02	0,34	38,11	0,19	37,81	0,31
TiO ₂	0,05	0,04	0,02	0,02	0,04	0,03	0,04	0,04	0,06	0,02	0,04	0,04	0,03	0,03	0,02	0,03	0,04	0,03	0,07	0,05	0,03	0,02	0,04	0,03
Al ₂ O ₃	22,39	0,24	22,27	0,30	22,29	0,11	22,32	0,20	22,18	0,17	22,25	0,23	22,60	0,13	22,32	0,17	23,02	0,17	22,39	0,22	21,51	0,08	21,29	0,36
Cr ₂ O ₃	0,00	0,01	0,03	0,03	0,02	0,02	0,01	0,01	0,01	0,02	0,02	0,02	0,02	0,02	0,04	0,02	0,03	0,04	0,02	0,02	0,03	0,02	0,02	0,03
FeO _t	29,77	2,07	32,30	0,84	32,51	0,89	33,45	0,73	32,69	0,57	29,70	1,33	28,25	0,95	30,45	0,79	27,93	0,51	31,13	0,81	30,39	0,52	28,70	1,12
MnO	0,85	0,27	2,17	0,96	1,14	0,18	1,01	0,46	2,44	0,43	5,18	2,15	0,78	0,33	3,21	1,25	0,55	0,07	2,03	1,30	2,19	0,16	6,62	2,39
MgO	5,41	0,68	3,84	0,69	3,52	0,29	4,06	0,35	3,54	0,57	4,25	0,54	5,57	0,58	3,87	0,46	6,93	0,12	4,20	1,03	3,28	0,10	2,54	0,36
CaO	5,15	1,24	3,68	0,53	5,28	0,53	4,04	0,80	4,22	0,66	3,28	0,36	6,54	0,47	4,64	1,25	5,30	0,25	4,54	0,54	6,16	0,35	4,80	1,06
Na ₂ O	0,01	0,01	0,02	0,01	0,01	0,01	0,01	0,02	0,00	0,01	0,01	0,02	0,02	0,02	0,02	0,01	0,04	0,01	0,03	0,03	0,00	0,01	0,02	0,02
K ₂ O	0,00	0,00	0,01	0,01	0,00	0,00	0,00	0,01	0,07	0,07	0,09	0,07	0,00	0,01	0,01	0,01	0,00	0,00	0,01	0,01	0,00	0,00	0,00	0,01
Total	102,07	0,26	102,12	0,34	103,35	0,46	103,51	0,50	103,42	0,61	103,56	0,25	102,68	0,60	102,67	0,30	102,75	0,29	102,48	0,44	101,71	0,39	101,85	0,50
Si	2,95	0,02	2,94	0,02	2,96	0,01	2,96	0,01	2,95	0,03	2,97	0,02	2,96	0,01	2,95	0,03	2,94	0,02	2,94	0,02	2,98	0,01	2,98	0,02
Ti	0,00	0,00	0,00	0,00	0,00	0,00	0,00	0,00	0,00	0,00	0,00	0,00	0,00	0,00	0,00	0,00	0,00	0,00	0,00	0,00	0,00	0,00	0,00	0,00
Al	2,03	0,01	2,05	0,02	2,02	0,01	2,02	0,02	2,02	0,02	2,01	0,02	2,03	0,01	2,04	0,02	2,05	0,01	2,04	0,02	1,98	0,01	1,98	0,02
Cr	0,00	0,00	0,00	0,00	0,00	0,00	0,00	0,00	0,00	0,00	0,00	0,00	0,00	0,00	0,00	0,00	0,00	0,00	0,00	0,00	0,00	0,00	0,00	0,00
Fe ₂₊	1,86	0,16	2,04	0,06	2,05	0,07	2,09	0,04	2,02	0,06	1,86	0,09	1,74	0,07	1,90	0,05	1,68	0,02	1,94	0,08	1,94	0,02	1,83	0,08
Fe ₃₊	0,06	0,02	0,07	0,03	0,04	0,03	0,05	0,02	0,09	0,04	0,05	0,03	0,06	0,02	0,07	0,05	0,08	0,03	0,08	0,04	0,05	0,02	0,06	0,03
Mn	0,06	0,02	0,14	0,06	0,07	0,01	0,07	0,03	0,16	0,03	0,34	0,14	0,05	0,02	0,21	0,08	0,03	0,00	0,13	0,09	0,15	0,01	0,44	0,16
Mg	0,62	0,07	0,45	0,08	0,40	0,03	0,46	0,04	0,41	0,07	0,49	0,06	0,63	0,06	0,45	0,05	0,78	0,01	0,48	0,11	0,38	0,01	0,30	0,04
Ca	0,42	0,10	0,31	0,04	0,44	0,04	0,33	0,07	0,35	0,05	0,27	0,03	0,53	0,04	0,38	0,10	0,43	0,02	0,38	0,04	0,52	0,03	0,40	0,09
Na	0,00	0,00	0,00	0,00	0,00	0,00	0,00	0,00	0,00	0,00	0,00	0,00	0,00	0,00	0,00	0,00	0,01	0,00	0,00	0,00	0,00	0,00	0,00	0,00
K	0,00	0,00	0,00	0,00	0,00	0,00	0,00	0,00	0,01	0,01	0,01	0,01	0,00	0,00	0,00	0,00	0,00	0,00	0,00	0,00	0,00	0,00	0,00	0,00
H	0,00	0,00	0,00	0,00	0,00	0,00	0,00	0,00	0,00	0,00	0,00	0,00	0,00	0,00	0,00	0,00	0,00	0,00	0,00	0,00	0,00	0,00	0,00	0,00
Total	8,00	0,00	8,00	0,00	8,00	0,00	8,00	0,00	8,00	0,00	8,00	0,00	8,00	0,00	8,00	0,00	8,00	0,00	8,00	0,00	8,00	0,00	8,00	0,00
X _{Fe}	0,75	0,04	0,83	0,03	0,84	0,01	0,82	0,01	0,84	0,02	0,80	0,02	0,74	0,03	0,82	0,02	0,69	0,01	0,81	0,04	0,84	0,00	0,86	0,01
py	0,21	0,03	0,15	0,03	0,14	0,01	0,16	0,01	0,14	0,02	0,16	0,02	0,22	0,02	0,15	0,02	0,27	0,00	0,17	0,04	0,13	0,00	0,10	0,01
alm	0,63	0,05	0,69	0,02	0,69	0,02	0,71	0,01	0,69	0,02	0,63	0,03	0,59	0,02	0,65	0,02	0,58	0,01	0,66	0,02	0,65	0,01	0,61	0,03
grs	0,14	0,03	0,10	0,01	0,15	0,02	0,11	0,02	0,12	0,02	0,09	0,01	0,18	0,01	0,13	0,03	0,15	0,01	0,13	0,01	0,17	0,01	0,14	0,03
sps	0,02	0,01	0,05	0,02	0,03	0,00	0,02	0,01	0,05	0,01	0,11	0,05	0,02	0,01	0,07	0,03	0,01	0,00	0,05	0,03	0,05	0,00	0,15	0,05

FeOT, total Fe as FeO; Alm = Fe/(Ca + Fe + Mg + Mn), py = Mg/(Ca + Fe + Mg + Mn), grs = Ca/(Ca + Fe + Mg + Mn), sps = Mn/(Ca + Fe + Mg + Mn), X_{Fe} = Fe/(Fe + Mg)

The calculation has been performed on the basis of Cat./O = 8/12

Table S4.4. Geothermobarometry

	Sample	N	Sample position	GB		GASP		GBMP		GM		GMAQ		N	Si in Wm ¹			Si in Wm ²		
				T(°C)	σ	P (GPa)	σ	P (GPa)	σ	T(°C)	σ	P (GPa)	σ		T(°C)	P (GPa)	σ	T(°C)	P (GPa)	σ
<i>Country rock</i>	MP3	2	core	730	40	1,1	0,15	1,3	0,19	721	60	0,9	0,10	3	700	1,4	0,23	700	1,2	0,06
		2	rim	629	22	0,8	0,16	1,0	0,14	607	58	0,7	0,10	3	600	1,3	0,25	600	0,8	0,03
	M92	5	core	600	15	0,9	0,08	1,1	0,05	664	44	0,9	0,10	8	680	1,5	0,18	680	1,6	0,33
		5	rim	575	35	0,8	0,10	0,9	0,11	639	17	0,7	0,10	5	600	1,4	0,18	600	1,3	0,33
	M62	2	core	616	13	0,8	0,04	0,9	0,18	680	50	0,8	0,10	3	680	1,3	0,05	680	1,3	0,05
		2	rim	550	30	0,7	0,98	0,8	0,07	600	50	0,7	0,10	3	650	1,2	0,05	650	1,2	0,05
<i>Halos</i>	M119	8	core	783	43	1,5	0,19	1,5	0,10	730	15	1,3	0,10	25	800	2,3	0,30	800	2,5	0,29
		10	rim	675	61	1,0	0,16	1,1	0,14	610	57	1,1	0,10	12	700	1,9	0,45	700	1,8	0,44
	M102	6	core	792	151	1,3	0,13	1,4	0,35	794	64	1,1	0,10	9	750	1,7	0,20	750	1,6	0,22
		6	rim	639	110	0,9	0,24	1,0	0,28	627	50	0,8	0,10	4	650	1,3	0,01	650	1,0	0,13
	M69	2	core	622	20	1,0	0,10	1,1	0,05	633	50	1,2	0,10	2	750	1,8	0,12	750	2,3	0,06
		2	rim	578	61	0,7	0,20	0,8	0,19	591	50	0,9	0,10	2	650	1,6	0,08	650	1,7	0,29

GB = Garnet-Biotite (Spear F. S., et al. 1993; Holdaway, 2000; calibration of Bhattacharya et al., 1992)

GASP = Garnet-Al₂SiO₅-Silica-Plagioclase (Holdaway, 2001; calibration of Holland & Powell, 1995)

GBMP = Garnet-Biotite-Muscovite-Plagioclase (Holdaway, 2000, 2001; Wu, 2015; calibration of Hodges & Crowley, 1985; Hoisch, 1990)

GM = Garnet-Muscovite (Wu, 2018; calibration of Green and Hellman, 1982; Krogh and Råheim, 1978)

GMAQ = Garnet-Muscovite-Al₂SiO₅-Quartz (Wu, 2018)

Si in Wm¹ = Si-in-white mica (Caddick and Thompson, 2008; Coggon and Holland, 2002), T values are arbitrarily fixed;

Si in Wm² = Si-in-white mica (Massonne & Schreyer, 1987), T values are arbitrarily fixed;

N is the number of EMPA analyses selected for the P-T estimates.

Table S4.5. U-Pb analyses of zircon from this work samples (e.g., M119, MP3)

Country rocks			Data for Wetherill plot ³							Ages ³						U-Pb Concordant Ages (Ma)	
MP3	Identifier	Zrn# Zoning	²⁰⁷ Pb/ ²⁰⁶ Pb	1σ abs	²⁰⁷ Pb/ ²³⁵ U	1σ abs	²⁰⁶ Pb/ ²³⁸ U	1σ abs	Rho	²⁰⁷ Pb/ ²⁰⁶ Pb	1σ abs	²⁰⁷ Pb/ ²³⁵ U	1σ abs	²⁰⁶ Pb/ ²³⁸ U	1σ abs	% U-Pb disc ⁴	2σ abs
	006SMPL	1 Core	0,0587	0,0010	0,6074	0,0108	0,0750	0,0008	0,08	557,47	9,49	481,94	8,55	465,97	5,24	3	
	007SMPL	2 Rim	0,0579	0,0010	0,5948	0,0105	0,0745	0,0008	0,08	524,84	8,93	473,95	8,34	463,21	5,09	2	
	008SMPL	3 Rim	0,0568	0,0010	0,2021	0,0036	0,0258	0,0003	0,08	483,00	8,33	186,88	3,33	164,15	1,81	12	
	009SMPL	4 Rim	0,0581	0,0010	0,4697	0,0083	0,0586	0,0006	0,08	532,03	9,04	390,95	6,90	367,17	4,05	6	
	010SMPL	5 Rim	0,0570	0,0010	0,6321	0,0111	0,0803	0,0009	0,08	492,31	8,37	497,38	8,77	498,09	5,47	0	498
	011SMPL	6 Rim	0,0590	0,0010	0,6247	0,0112	0,0768	0,0009	0,08	565,62	9,68	492,78	8,80	476,81	5,38	3	
	012SMPL	8 Rim	0,0581	0,0010	0,6398	0,0113	0,0798	0,0009	0,08	534,67	9,08	502,15	8,87	494,69	5,51	1	497
	013SMPL	8 Core	0,0577	0,0010	0,6496	0,0117	0,0816	0,0009	0,08	518,39	8,83	508,23	9,15	505,79	5,84	0	507
	014SMPL	9 Rim	0,0582	0,0010	0,6630	0,0117	0,0825	0,0009	0,08	538,05	9,14	516,44	9,11	511,09	5,62	1	513
	015SMPL	10 Rim	0,0583	0,0010	0,6717	0,0118	0,0835	0,0009	0,08	541,80	9,25	521,73	9,15	516,68	5,60	1	518
	016SMPL	11 Rim	0,0576	0,0010	0,6211	0,0110	0,0782	0,0009	0,08	513,44	8,75	490,54	8,68	485,37	5,37	1	487
	017SMPL	11 Core	0,0585	0,0010	0,6932	0,0123	0,0859	0,0010	0,08	547,04	9,33	534,73	9,49	531,42	5,90	1	533
	018SMPL	11 Rim	0,0582	0,0010	0,6465	0,0114	0,0806	0,0009	0,08	535,79	9,10	506,33	8,92	499,40	5,48	1	502
	019SMPL	12 Rim	0,0586	0,0010	0,6177	0,0108	0,0764	0,0008	0,08	552,27	9,41	488,39	8,55	474,60	5,13	3	
	020SMPL	12 Core	0,0584	0,0010	0,6338	0,0113	0,0787	0,0009	0,08	543,68	9,22	498,45	8,90	488,48	5,58	2	492
	021SMPL	13 Rim	0,0578	0,0010	0,4677	0,0083	0,0586	0,0006	0,08	522,19	8,94	389,59	6,93	367,17	4,05	6	
	022SMPL	14 Rim	0,0577	0,0010	0,6201	0,0110	0,0779	0,0009	0,08	519,15	8,84	489,91	8,69	483,34	5,36	1	486
	023SMPL	15 Rim	0,0573	0,0010	0,5832	0,0103	0,0737	0,0008	0,08	503,87	8,55	466,52	8,23	458,65	5,12	2	461
	024SMPL	16 Rim	0,0580	0,0010	0,5455	0,0097	0,0682	0,0008	0,08	528,63	8,99	442,04	7,85	425,48	4,78	4	
	025SMPL	17 Rim	0,0559	0,0010	0,1823	0,0033	0,0236	0,0003	0,08	448,40	7,73	170,00	3,05	150,56	1,70	11	
	029SMPL	18 Rim	0,0548	0,0009	0,2919	0,0051	0,0386	0,0004	0,08	405,30	6,95	260,03	4,56	244,15	2,60	6	
	030SMPL	19 Rim	0,0580	0,0010	0,6848	0,0120	0,0855	0,0009	0,08	530,89	9,08	529,66	9,26	529,11	5,65	0	529
	031SMPL	20 Rim	0,0585	0,0010	0,6791	0,0119	0,0841	0,0009	0,08	549,28	9,31	526,22	9,23	520,79	5,66	1	523
	032SMPL	21 Rim	0,0568	0,0010	0,6271	0,0111	0,0800	0,0009	0,08	485,33	8,31	494,28	8,77	496,00	5,46	0	495
	033SMPL	22 Rim	0,0682	0,0012	0,6736	0,0123	0,0716	0,0008	0,07	874,03	15,47	522,90	9,57	445,97	5,01	15	
	034SMPL	23 Rim	0,0725	0,0012	0,7142	0,0126	0,0715	0,0008	0,06	998,61	17,00	547,24	9,65	445,07	4,91	19	
	035SMPL	24 Rim	0,0576	0,0010	0,6507	0,0114	0,0819	0,0009	0,08	514,58	8,77	508,92	8,93	507,63	5,51	0	508
	036SMPL	25 Core	0,0566	0,0012	0,0385	0,0009	0,0049	0,0001	0,06	477,15	10,51	38,35	0,85	31,70	0,34	17	
	037SMPL	25 Rim	0,0647	0,0011	0,7141	0,0127	0,0800	0,0009	0,07	765,90	13,25	547,20	9,71	495,94	5,42	9	
	038SMPL	26 Rim	0,0601	0,0010	0,5916	0,0105	0,0714	0,0008	0,08	607,90	10,39	471,91	8,39	444,58	4,96	6	
	039SMPL	27 Rim	0,0471	0,0009	0,0317	0,0006	0,0049	0,0001	0,09	55,31	1,02	31,71	0,60	31,38	0,34	1	32
	040SMPL	28 Rim	0,0596	0,0010	0,6365	0,0113	0,0775	0,0009	0,08	587,99	10,08	500,11	8,90	481,36	5,35	4	
	041SMPL	28 Core	0,0596	0,0010	0,6375	0,0114	0,0776	0,0009	0,08	589,81	10,11	500,75	8,95	481,54	5,40	4	
	042SMPL	29 Rim	0,0587	0,0010	0,6078	0,0107	0,0751	0,0008	0,08	557,10	9,49	482,17	8,47	466,69	5,10	3	
	043SMPL	30 Rim	0,0576	0,0010	0,6591	0,0116	0,0830	0,0009	0,08	514,96	8,78	514,06	9,02	514,06	5,59	0	514
	044SMPL	31 Rim	0,0553	0,0010	0,4650	0,0085	0,0610	0,0007	0,08	424,78	7,45	387,74	7,08	381,89	4,31	2	384
	045SMPL	32 Rim	0,0597	0,0010	0,4732	0,0084	0,0575	0,0006	0,08	593,44	10,22	393,42	7,01	360,53	4,02	8	

Halos																	2σ abs	
M119																		
006SMPL	1	Rim	0,0469	0,0082	0,0359	0,0062	0,0055	0,0002	0,03	46,18	8,11	35,78	6,20	36	1,19	0	36	2,4
007SMPL	1	Rim	0,0477	0,0061	0,0371	0,0046	0,0056	0,0002	0,03	85,41	10,84	36,96	4,62	36	1,01	2	36	2,0
008SMPL	1	Rim	0,0535	0,0190	0,0399	0,0139	0,0054	0,0003	0,02	351,75	124,81	39,69	13,87	35	2,20	13	35	
009SMPL	1	Rim	0,0503	0,0203	0,0468	0,0186	0,0068	0,0005	0,03	207,04	83,71	46,48	18,50	43	3,23	7	43	
010SMPL	1	Rim	0,0475	0,0104	0,0357	0,0076	0,0055	0,0003	0,03	71,93	15,70	35,62	7,63	35	1,63	1	35	3,3
011SMPL	1	Rim	0,0476	0,0136	0,0366	0,0103	0,0056	0,0003	0,03	77,94	22,31	36,49	10,26	36	2,08	2	36	4,2
013SMPL	1	Core	0,0602	0,0127	0,0462	0,0095	0,0056	0,0003	0,03	611,13	128,41	45,89	9,42	36	1,70	22	36	
016SMPL	2	Rim	0,0465	0,0143	0,0360	0,0109	0,0056	0,0003	0,03	21,04	6,49	35,95	10,91	36	2,08	-1	36	4,2
017SMPL	2	Rim	0,0475	0,0141	0,0380	0,0111	0,0058	0,0003	0,03	73,94	22,00	37,82	11,08	37	2,08	2	37	4,2
018SMPL	2	Rim	0,0473	0,0234	0,0352	0,0172	0,0054	0,0004	0,03	61,88	30,65	35,14	17,18	35	2,78	1	35	5,6
020SMPL	2	Rim	0,0488	0,0200	0,0356	0,0144	0,0053	0,0004	0,03	135,82	55,81	35,50	14,36	34	2,52	4	34	
021SMPL	2	Rim	0,0524	0,0091	0,0390	0,0066	0,0054	0,0002	0,03	304,21	52,71	38,88	6,60	35	1,26	11	35	
022SMPL	2	Core	0,0502	0,0111	0,0389	0,0084	0,0056	0,0003	0,03	201,95	44,58	38,74	8,38	36	1,70	7	36	

A.1.5 U-(Th)-Pb geochronology: Monazite

Monazite grains from metapelitic samples in the vicinity of UM bodies (i.e., M119) were selected for geochronological analysis. Before that, geochemical analyses were performed.

Monazite chemistry is critical to age interpretation (Kohn et al. 2005); thus, prior to U–Th–Pb isotopic analysis, it was first characterized via the electron microprobe (at University of Milan; see section A.1.1.2) by acquiring chemical compositional maps (e.g., Y, Th, Ce, Pr, La, Nd, Sm, P, Ca) on the whole grain and punctual analyses to characterize the major elements content. The punctual analyses were carried out considering the internal texture and the different compositional zoning.

In monazite, Y and Th are good tracers because they are strongly and systematically zoned, and because their variations can be linked to silicate reactions and trace-element mass balance (Kohn et al. 2005). In the majority of the studied sample, Y_2O_3 content has similar values ranging from 1.32 to 2.32 wt.%, except for monazite included in allanite from two samples close to UM (i.e. M119 and M69) whose Y_2O_3 content is extremely low with an average value of 0.03 wt.%. Where Y_2O_3 content recorded the lowest values (i.e. sample M119 and M69), ThO_2 content reaches the highest amount up to 8 wt.%. In the other samples ThO_2 content ranges from 1.80-6.67 wt.%. Yttrium content shows an opposite trend if we consider the Yttrium value in the bulk rock of the same samples, that reaches the highest values up to 86.9 ppm for sample M119, and 42.0 ppm for sample M69 which contain the association monazite-allanite-clinozoisite. In the other samples the Yttrium content is on average lower, around 32.0 ppm.

In this sample monazite is always included in allanite, which in turn is surrounded by clinozoisite in a corona texture (Fig. 7.1.1.1). Here, the REE composition of monazite, allanite, clinozoisite and garnet, obtained by LA-ICP-MS were normalized to chondrite following McDonough and Sun, (1995) (Fig. 7.1.1.1).

Monazite has high LREE concentration (up to 100000 ppm) and low HREE content (down to 10 ppm); the Y content ranges between 400 to 700 ppm and a negative anomaly in Eu is present. Allanite shows the same REE pattern as monazite, but with one order of magnitude less for LREE concentration, a slight enrichment in HREE (between 10-100 ppm) and negative Eu anomaly. Clinozoisite shows a less scattered pattern in LREE (concentration down to 100000 ppm), absence of negative anomaly in Eu and a scattered pattern in HREE. The only rock-forming mineral that have significant concentrations

(≥ 1 ppm) of HREE is garnet (100-1000 ppm). Generally, monazite grains are nearly homogeneous in composition except for Th, which have mottled zoning with values ranging from 40000 to 70000 ppm. The monazite grains analysed in this study exhibit no systematic zoning of Y, which is mostly between 100 to 200 ppm, around 300-500 ppm in garnet associated with mnz-aln-czo association. Generally, garnet in the matrix shows a HREE pattern quite steady. In the textural sites where garnet is in contact or contains the monazite-allanite-clinozoisite association, it is characterised by lower concentration in Sm, Eu and an enrichment in HREE, while monazite shows a slight enrichment in LREE and depletion in HREE, the latter being less pronounced for allanite and clinozoisite.

Eighteen laser spots were collected on five monazite grains included in the typical allanite-clinozoisite association from sample M119 (Fig. A.1.1.2a,b; for methods see chapter 3.8 and section A.1.1.5). The monazite grains do not show systematic zoning as observed from the X-ray maps, except for the Th map that present a patchy zonation and was considered as reference for U–Th–Pb isotopic analysis (Fig. A.1.1.2c). Three laser spots were made on grain Mnz1, the $^{206}\text{Pb}/^{238}\text{U}$ and the $^{208}\text{Pb}/^{232}\text{Th}$ ages are concordant ranging between 39 ± 1.0 and 38 ± 1.0 Ma and at 36 ± 1.0 Ma, respectively (Fig. A.1.1.2b). For the Mnz2 grain four analyses were collected, the $^{206}\text{Pb}/^{238}\text{U}$ ages ranges between 38 ± 1.0 and 36 ± 1.0 Ma and the $^{208}\text{Pb}/^{232}\text{Th}$ among 38 ± 1.0 and 35 ± 1.0 Ma (Fig. A.1.1.2b). Three laser spots were made on grain Mnz3, the $^{206}\text{Pb}/^{238}\text{U}$ and the $^{208}\text{Pb}/^{232}\text{Th}$ ages are concordant ranging between 42 ± 1.0 and 37 ± 1.0 Ma and between 38 ± 1.0 and 37 ± 1.0 Ma, respectively (Fig. A.1.1.2b). Five analyses were collected for the Mnz4 grain, the $^{206}\text{Pb}/^{238}\text{U}$ ranges between 40 ± 1.0 and 38 ± 1.0 Ma and the $^{208}\text{Pb}/^{232}\text{Th}$ among 41 ± 1.0 and 38 ± 1.0 Ma (Fig. A.1.1.2b). Three laser spots were made on grain Mnz5, the $^{206}\text{Pb}/^{238}\text{U}$ and the $^{208}\text{Pb}/^{232}\text{Th}$ ages are concordant ranging between 40 ± 1.0 and 38 ± 1.0 and between 37 ± 1.0 and 34 ± 1.0 Ma, respectively (Fig. A.1.1.2b). The younger ages were mainly obtained from the darker BSE domains, which have higher concentration of Th respect to the bright domains (Fig. A.1.1.2b,c). U-Th-Pb analyses are all mainly concordant forming a single population which yields an average $^{206}\text{Pb}/^{238}\text{U}$ age of 38 ± 0.6 Ma (MSWD = 0.44) and $^{208}\text{Pb}/^{232}\text{Th}$ age of 37 ± 0.6 Ma (MSWD = 0.93) (Fig. A.1.1.3).

As the preliminary geochronological analysis on zircon from the Halos samples closer the UM (i.e., M119), even the monazite from the same sample give ages (ca 37 Ma) coeval with the decompression stage of the (U)HP rocks of the Cima Lunga and Adula nappes (< 40 Ma).

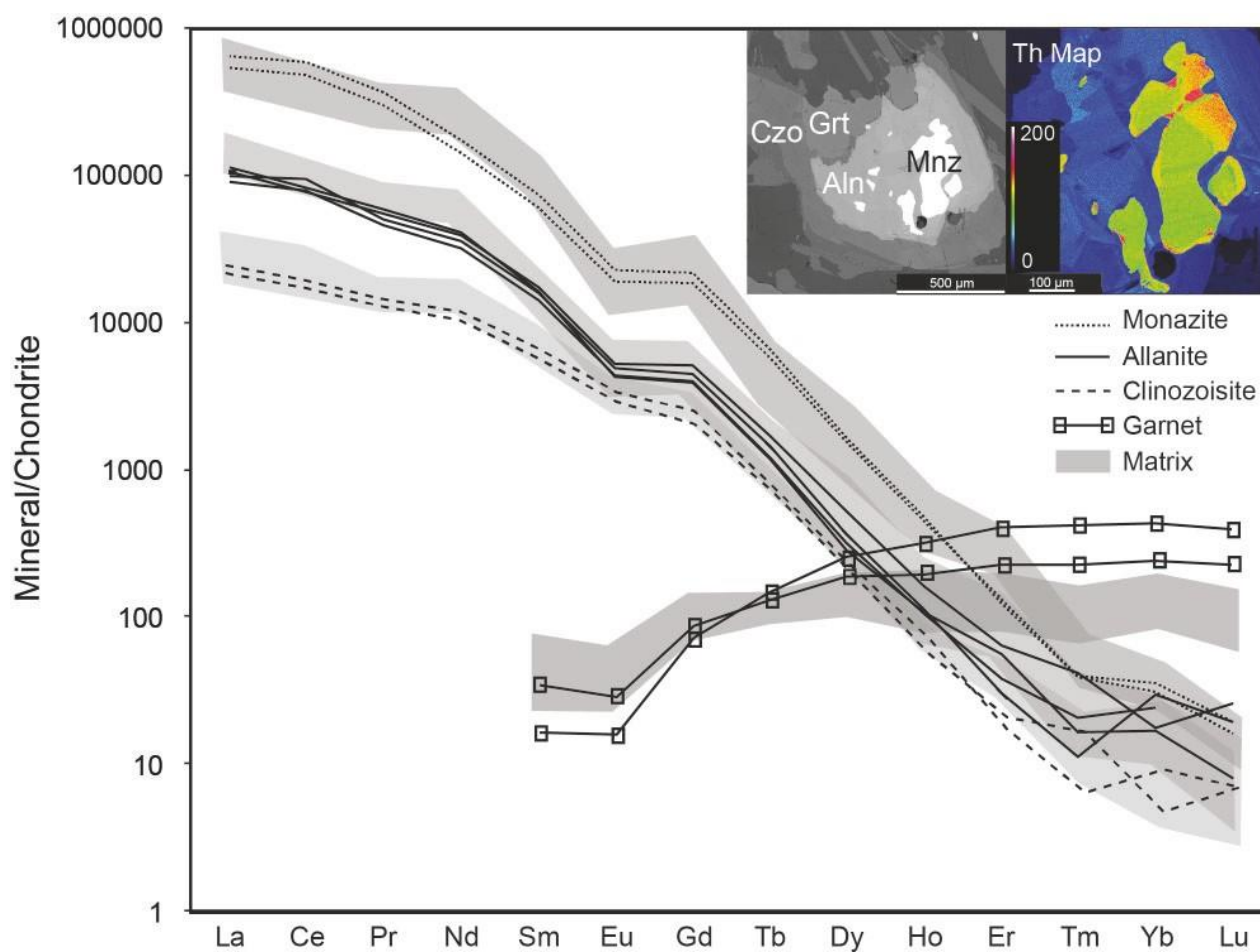


Fig. A.1.4.1 – Chondrite-normalised REE composition following McDonough and Sun, (1995) for monazite, allanite, clinozoisite and garnet associated in the figure on the top right corner. In grey shadow the related pattern for monazite, allanite, clinozoisite without garnet relationship and single garnet in the matrix.

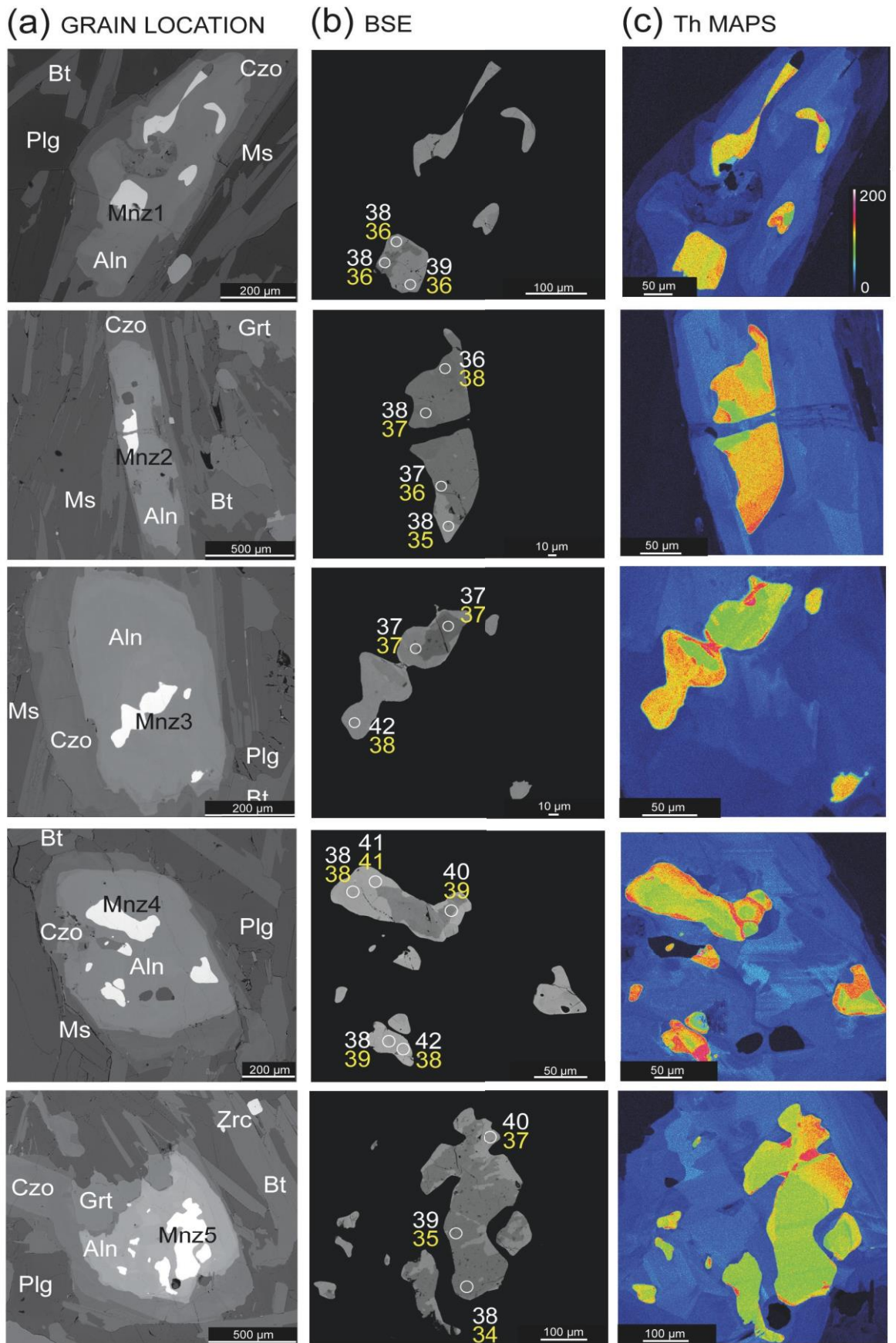


Fig.A.1.4.2 – Microstructural position, internal structure and compositional maps of dated monazite grains from sample M119. (a) Grain location; (b) Back-scattered electron (BSE) images; (c) Th compositional maps. Ablated areas (circles with a diameter of 10 μm in diameter) and corresponding $^{206}\text{Pb}/^{238}\text{U}$ concordant data (white) and $^{208}\text{Pb}/^{232}\text{Th}$ ages (yellow) are shown.

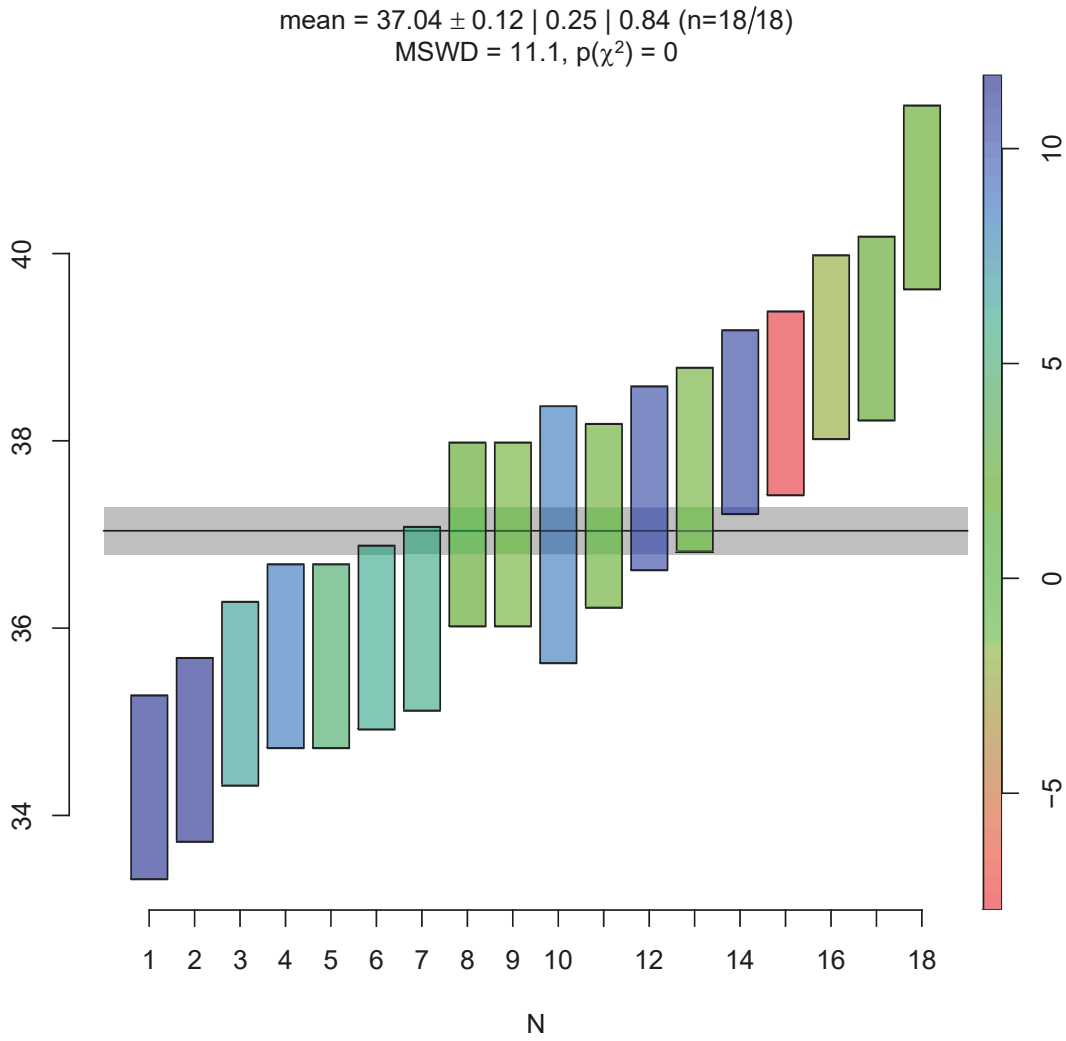


Fig.A.1.4.3 – Monazite Th-Pb ages with discordance expressed by the red-to-blu bar. N indicates the number of monazite analyses,

A.1.6 Integration to the discussion of Chapter 4

Comment on “Deep subduction, melting, and fast cooling of metapelites from the Cima Lunga Unit, Central Alps” by Piccoli, F., Lanari, P., Hermann, J., & Pettke, T. (2021). *Journal of metamorphic geology*, 40(1), 121-143.

Following the recent paper of Piccoli et al., (2021), which proposes an alternative petrological and geodynamic interpretation of the Cima di Gagnone metapelites, a new critical discussion of the integrated dataset is hereafter reported. This integration was added in appendix to avoid modifying the Chapter 4, which coincides with Corvò et al., (2021-March) and that was published before the Piccoli et al., (2021-June). On the other hand, since this PhD thesis postdates the Piccoli et al (2021) manuscript, the new integrated discussion offers the opportunity to improve the comprehension of the Cima di Gagnone evolution.

Piccoli et al., (2021) show new petrological and geochemical data obtained from a metapelitic sample collected at the boundary with the garnet peridotite (outcrop Mg160; Pfiffner and Trommsdorff, 1998), the same of one of the two Halos samples described in Corvò et al., (2021; see Fig.4.3B). On the base of textural analysis, petrological-geochemical data (i.e., Ti content in phengite, increasing P, Zr, and HREE contents in pyrope-rich garnet, growth zones in phengite and garnet) and thermodynamic simulations, the Authors state that the studied metapelite underwent high-P and high-T (HP–HT) metamorphism involving fluid-fluxed partial melting. In particular, they show that the mineral record preserves an evolution from prograde to HP–HT peak conditions (2.7 ± 0.1 GPa and 800°C) followed by near isobaric cooling (~ 2.5 GPa and $700\text{--}750^{\circ}\text{C}$) prior to decompression (1.0 GPa and $\sim 620^{\circ}\text{C}$; yellow arrow in Fig. A.1.6.1). The Authors concluded that the reconstructed P–T path suggests that the studied metapelites - coherently with the entire Cima Lunga nappe - were subducted to depths (ca. 90 km) where the slab gets heated by proximity to asthenospheric mantle related to slab break-off. This heating resulted in the dehydration of chlorite-to garnet peridotite and the liberated fluids triggered partial melting in the associated metapelites, which might have favoured the fast exhumation of the entire Cima Lunga unit.

Corvò et al., (2021) describes two groups of metasediments, distinguished as a function of the distance from the ultramafic rocks (Halos and Country rocks). Here, thanks to the adoption of a multidisciplinary approach, it was observed that even though metasediments share the same structural evolution with ultramafic boudins, large differences in the P–T conditions are recorded (Fig. A.1.6.1). Country rocks

experienced $P < 1.2$ and $T < 700^{\circ}\text{C}$, whereas a few occurrences (Halos) preserve higher metamorphic conditions of 1.3–1.7 GPa and 750–850°C. These estimates approach, although significantly lower, the P–T peak conditions experienced by the ultramafic rocks (1.5–3.2 GPa, 740–850°C). One of the most interesting results of Corvò et al., (2021) is that these pressure and temperature estimates are not randomly distributed in the unit but changes systematically as a function of the distance from the strong lithology (i.e., ultramafic rocks), being maximum at the interface between the two rock pairs. These different metamorphic records are re-interpreted by Piccoli et al (2021) as simply the result of the retrograde re-equilibration processes. Nevertheless, many evidences argue against this interpretation and they are hereafter summarized.

I) It is important to highlight that those temperatures, exceeding the wet melt curve, were not related to a quick thermal event occurred close to the maximum pressure peak conditions (2.7 – 3.0 GPa at ca. 35 Myr) as indicated in Piccoli et al., (2021; see Fig 4.13). On the contrary, temperature largely exceeding 700°C are recorded by several samples equilibrated at different pressure conditions (Fig. A 1.6.1). In particular, micaschists record HT conditions in the stability field of hydrated minerals (biotite and amphibole). A mineral assemblage consisting of Pl + Bt + Ms + Grt ± Qz ± Ky is largely documented in the garnet inclusions and both geothermobarometry and thermodynamic modelling indicate temperature between 700° and 850°C. The retrograde path depicted in Piccoli et al., (2021) simply does not consider all these data and cannot be considered representative of the entire unit.

II) Phengites with high Si-content values (i.e., up to 3.38 a.p.f.u.) were found and described also in Corvò et al. (2021) as preserved within garnet cores of Halos samples. These high-Si muscovite inclusions could represent the relicts of a largely re-equilibrated (U)HP mineral assemblage represented by the generalized reaction $\text{Phengite} + \text{Garnet}_1 + \text{Paragonite} = \text{Muscovite} + \text{Biotite} + \text{Plagioclase} + \text{Garnet}_2 + \text{H}_2\text{O}$, as already reported by previous authors (Heinrich, 1982; Früh-Green, 1987) and emphasized by Piccoli et al., (2021). Corvò et al (2021) did not consider the Si-content of phengite as robust indicator of high pressure (HT conditions, in fact do not fit the range of applicability set for the barometer, which is calibrated for a T range from 250 °C to 650 °C at a P up to 2.8 GPa; Massonne and Schreyer 1987). Nevertheless, pressure conditions as high as 2.7 GPa in the metapelites from Halos perfectly fit the Corvò et al.'s data and interpretation.

iii) Corvò et al. (2021) describes the sample recording the highest P–T conditions (i.e., M119) as

characterized by a peculiar microstructure consisted by coarse grain size for all minerals, significantly lower CPO of plagioclase, biotite and white mica, weak intracrystalline deformation of garnet (i.e., rare subgrains). This weak fabric is accompanied by melt microstructures indicating that deformation occurred in presence of melt. This implies that this sample was not significantly overprinted by the regional amphibolite-facies deformation. Differently, the rest of the metapelites (i.e. the Country rocks far from the ultramafic lenses) are widely recrystallized at amphibolite-facies mineral assemblage. However, the Country rocks record well preserved core-to-rim zoning of garnet crystals that refer to a previous (Variscan) tectono-metamorphic event (Grond et al., 1995; Rutti, 2003). This implies that large part of the unit did not experience alpine HT conditions, whereas these are recorded only in the close vicinity of the ultramafics.

iv) Contrasting features and geochronological results for zircon from the two groups of rocks confirm the heterogeneous geochronological records. Zircon from Halos provide concordant ages from thick rims indicating an age of ~36 Ma, which predates the Barrovian stage, but it is identical to the HP stage of eclogites and ultramafics. The age of ~ 36 Ma confirms the resetting of the U-Pb isotopic system of zircon grain at temperature over 800°C. Differently, zircon from Country rocks provided pre-Variscan ages with only one age from a relatively thick rim at around 32 Ma, associated with the Barrovian stage. This age record confirms that these rocks never experienced Alpine HT conditions, even though structural features confirmed that they were already coupled before or at early stage of the Alpine event.

All these arguments highlight that the Piccoli et al. (2021) interpretative model is robust only for the sample described in the article but does not represent the metamorphic history of the entire Cima Lunga unit. It does not fit the paths of several samples recording highly different P and T conditions, as represented in Fig. A.1.6.1. On the other hand, Corvò et al., (2021) try to give an explanation of the heterogeneous metamorphic records between Halos and Country rocks, arguing that it cannot be explained simply by retrograde metamorphism. It should be stressed that Corvò et al. (2021) provides a detailed discussion of all the models proposed to describe the Cima di Gagnone rocks, displaying pros and cons of each model. This analysis highlights that a fully comprehensive model of such complex context is far from the present knowledge but a significant impact of deformation on the metamorphic record is argued. Nor a model based on tectonic pressure plus shear heating is indicated as the best

solution, as they are not able to fully describe the observation.

However, it is interesting to note that even if the two papers - Corvò et al., (2021), and Piccoli et al. (2021) - provide contrasting interpretations of the P-T paths, many similarities may be found.

- Both state that the interface between ultramafic lenses and metasediments was the locus for fluid-rock interaction processes (metasomatism, hydration-dehydration), showing similar petrographic and geochemical evidences (i.e., garnet resorption texture, Si-depleted bulk composition of Halos, localized evidence of partial melting);

- Both speculate on the fact that metapelite and ultramafic rocks were coupled before Alpine event or at least in its early stage. While in Piccoli et al., (2021), melting evidence of aqueous fluid infiltration was supported by growth of metamorphic zircon rims and the occurrence of abundant post-kinematic biotite around and within garnet; in Corvò et al., (2021) significant localized of fluid circulation at the interface between metapelites and UM is documented by the local occurrence of the corona microstructure around Mnz, made by Aln in turn enveloped by Czo. While monazite is present as relict, thus likely stable in association with the garnet (cores), allanite and clinozoisite show equilibrium texture with the late, amphibolite-facies assemblage.

Therefore, both papers highlight the key role played by fluid-assisted and interaction processes occurred between Halos and ultramafic rocks and these rocks were already coupled before the Alpine metamorphism. Finally, both works findings open new scenarios for the geodynamic interpretation of the Cima Lunga unit underlining that more detailed geochronological study is needed to find out more these rocks evolution. In conclusion, the integration of the all the data confirms the interpretations that heterogeneous metamorphism was locally developed, rather than locally preserved. In this view, the interpretation of the geodynamic modelling explaining the rock evolution of the Cima di Gagnone area remains open.

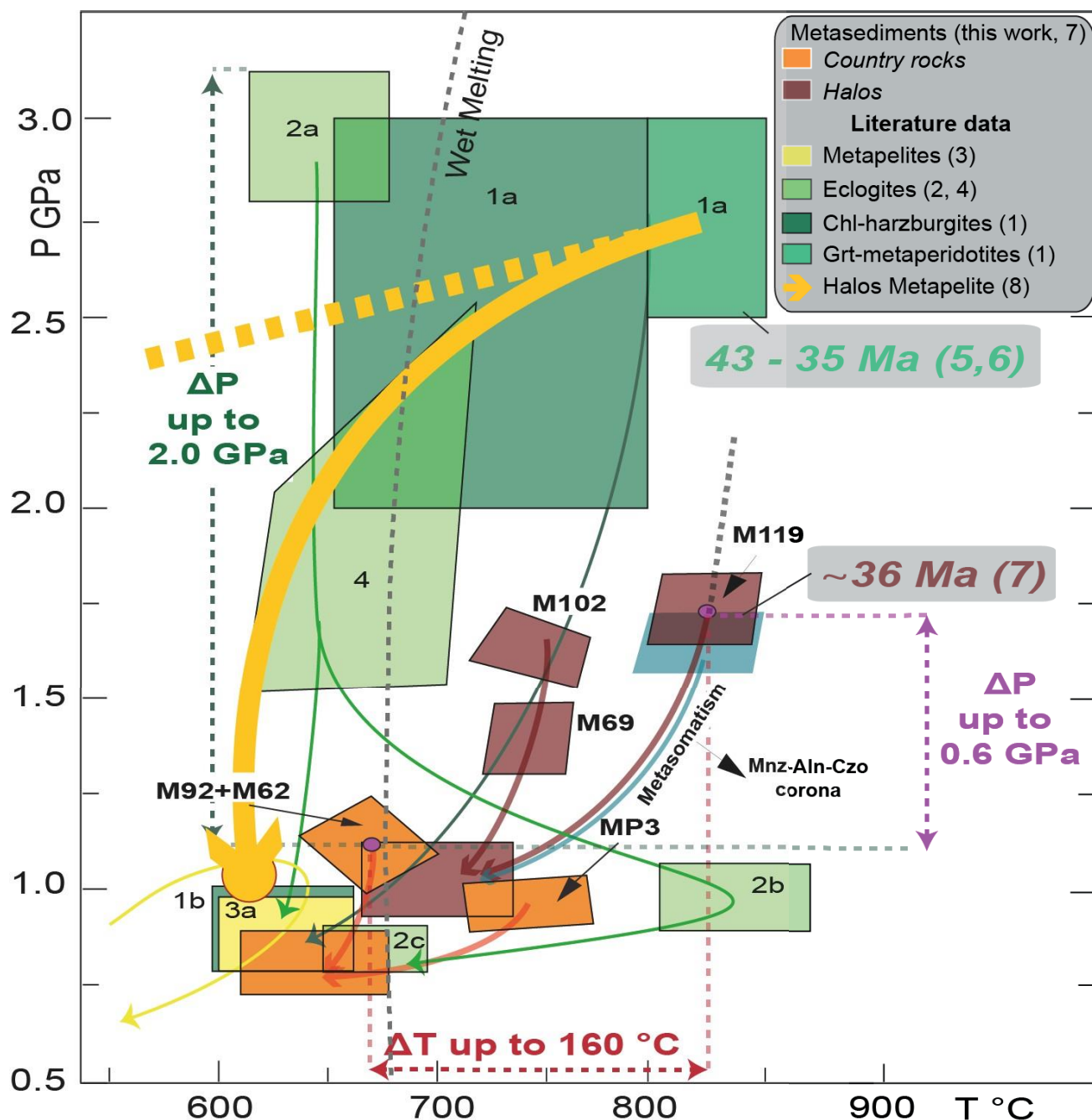


Fig. A.1.6.1 - Compilation of P-T-t paths from the present study and the literature. Inferred P-T paths and fields of the samples analysed in this study are based on pseudosection modelling and petrographic assemblages (orange squares, Country rocks; brown squares, Halos). Fields from literature data are indicated with numbers: 1 – Nimis and Trommsdorff (2001) and Scambelluri et al. (2014); 2 – Brower et al. (2005); 3 – Grond et al. (1995); 4 – Heinrich (1986). Geochronological data are from: 5 – Gebauer (1996, 1999); 6 – Becker et al. (1993). 8 – P-T paths for metapelite studied in Piccoli et al., (2021). Differential pressure and temperature depicted in the diagram are calculated from the average values between the Country rocks (samples M92 and M62) and the Halos (sample M119) or the pressure peak estimation from eclogites.

**APPENDIX 2:
Supplementary data
for case study 2**

A.2.1 Supplementary information on methods

This Appendix presents additional data for case study 2. No in depth analysis or interpretation is provided. A detailed description of the methods used is reported in chapter 3.

A.2.1.5 Zr-in-Rutile thermometer

Rutile trace element analyses were carried out at the IGG-CNR of Pavia by using a 193nm Excimer Laser (Geolas) combined with an Agilent 8900 ICP quadrupole mass spectrometer. The samples were ablated in spots of 35/50 μm at a laser energy of 4 Jcm^{-2} and a repetition rate of 10 Hz. Signals were recorded for 50 s per spot after measuring a gas blank of 40 s for background subtraction before each spot. Plasma conditions and gas flow rates were adjusted by optimising He and Ar flow, monitoring $^{232}\text{Th}^{16}\text{O}^+ / ^{232}\text{Th}^+$ ratios (always $\leq 0.2\%$) and $^{238}\text{U}^+ / ^{232}\text{Th}^+$ ratios (always between 0.95 and 1.05) while ablating NIST SRM 612 in no-gas mode (no reaction gas in the reaction cell). Individual mineral grains were ablated in a He atmosphere (flow rate 0.44 L/min) and the resulting aerosol was mixed with Ar carrier gas (flow rate 0.91 L/min) to be transported to the ICP-MS via signal smoothing device. Titanium, measured as ^{49}Ti , was used as the internal standard element for each analysis. TiO_2 was assumed to be 100 wt.%. Analyses were calibrated against the NIST SRM 610 glass (GeoReM preferred values: <http://georem.mpch-mainz.gwdg.de/>). Accuracy of the results was confirmed by analyses of the well-known USGS reference glass BCR-2G (Jochum et al., 2005) using newly compiled values (GeoReM preferred values: <http://georem.mpch-mainz.gwdg.de/>) and NIST SRM 612 glass. Analyses were collected in MS/MS mode. The following masses were measured and the dwell times for each mass is given in brackets (in ms): ^{29}Si (20), ^{45}Sc (20), ^{49}Ti (10), ^{51}V (20), ^{52}Cr (20), ^{53}Cr (20), ^{57}Fe (20), ^{88}Sr (20), ^{89}Y (20), ^{90}Zr (20), ^{93}Nb (20), ^{95}Mo (20), ^{98}Mo (20), ^{118}Sn (20), ^{178}Hf (20), ^{181}Ta (20), ^{182}W (20), ^{208}Pb (20), ^{232}Th (20), ^{238}U (20). The software GLITTER[®] was used to data reduction (Van Achterbergh et al., 2001). ^{29}Si was measured in order to detect possible silicate inclusions while ^{57}Fe was used as a good indicator in order to detect ilmenite.

References

- Jochum, K. P., Weis, U., Stoll, B., Kuzmin, D., Yang, Q., Raczek, I., ... & Enzweiler, J., 2011. Determination of reference values for NIST SRM 610–617 glasses following ISO guidelines. *Geostandards and Geoanalytical Research*, 35(4), 397–429.
- Van Achterbergh, E., Griffin, W. L., & Stiefenhofer, J., 2001. Metasomatism in mantle xenoliths from the Letlhakane kimberlites: estimation of element fluxes. *Contributions to Mineralogy and Petrology*, 141(4), 397–414.

A.2.2 Figures

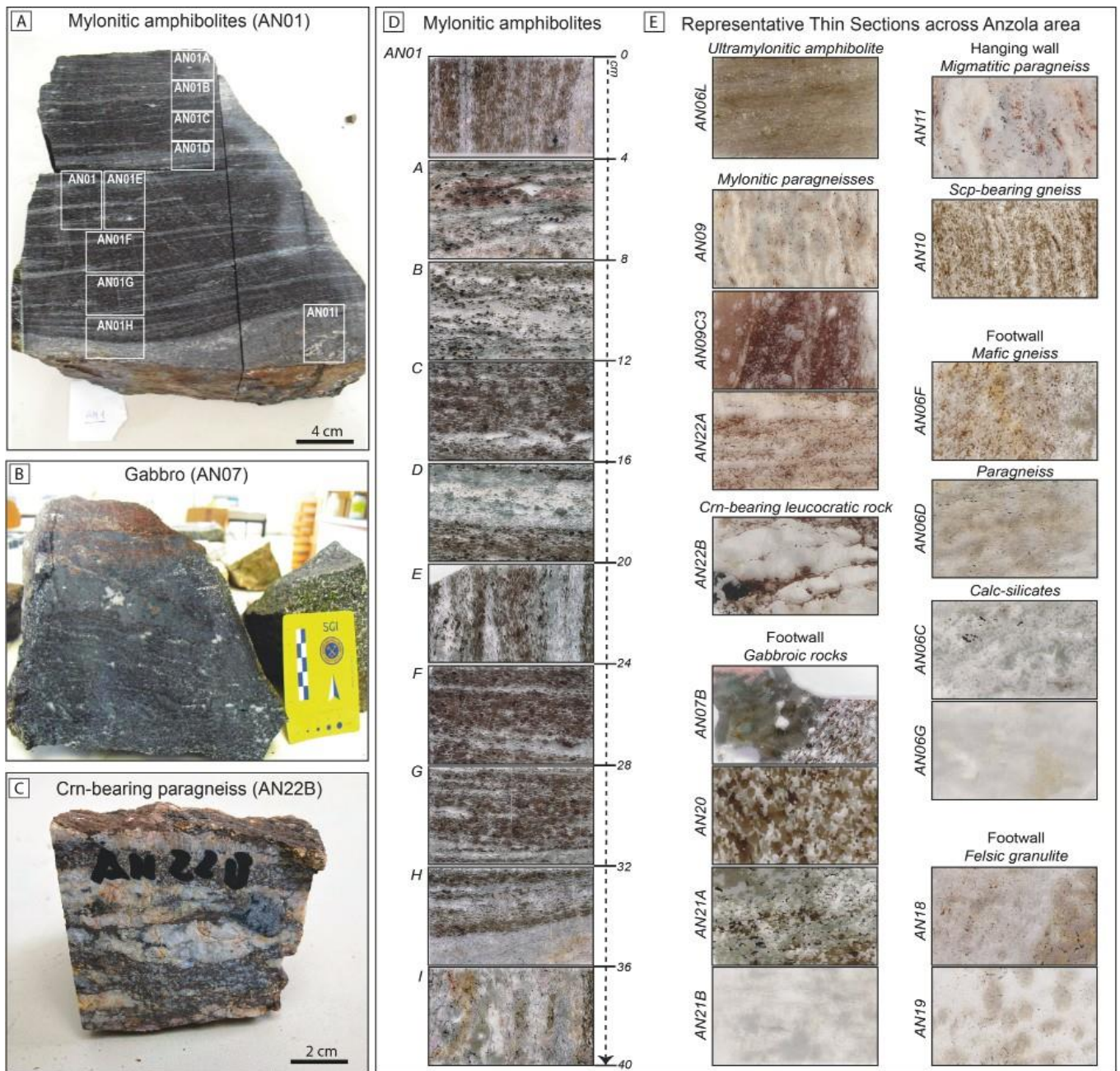


Fig. S5.1 – Representative hand specimens and thin sections of the studied samples. A) Block of mylonitic banded amphibolites (sample AN01). B) Gabbro sample from the contact with garnet layer (AN07). C) Protomylonitic paragneiss (sample AN22B), blue rounded corundum porphyroclasts and leucocratic layer are well visible at the mesoscale. D) Representative thin sections obtained from sample in A) with evidence of textural, grain size and modal abundance differences distinguishable at the thin section scale. E) Representative thin sections of the Anzola shear zone transect from hanging wall to footwall rocks across the shear zone.

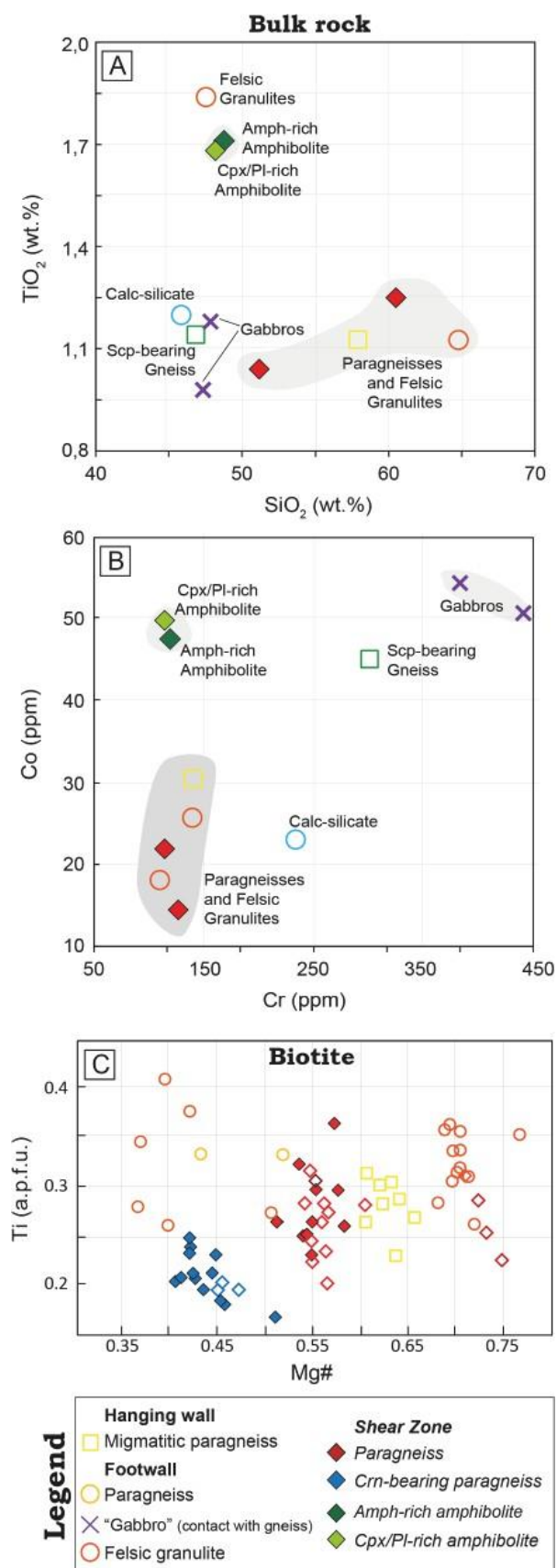


Fig. S5.2 – Bulk rock diagrams. A) TiO_2 (wt.%) versus SiO_2 (wt.%). B) Co (ppm) versus Cr (ppm). All data are normalised to chondrites values according to McDonough and Sun, (1995). C) Ti (a.p.f.u.) versus $\text{Mg}\# = (\text{Mg}/\text{Mg}+\text{Fe})$ diagram for Biotite; Btl and BtlI from Fig. 7 were distinguished in filled and open diamond, respectively.

Table S5.2 - Bulk rock major element composition of representative studied rocks across the Anzola transect. Iron contents are expressed as all ferric.

Locality Lithology Sample	Hanging wall		Shear Zone				Footwall				
	Migmatitic paragneiss AN11	Scp-bearing gneiss AN10	Paragneisses AN09	AN22A	Amph-rich amphibolites AN01A	Cpx/Pl-rich Amphibolites AN01D	Calc-silicate AN06C	Gabbro at contact with SZ AN08	Gabbro body AN20	Felsic granulite AN19	AN18
Major elements (wt.%)											
SiO ₂	57,91	46,93	60,47	51,4	48,91	48,39	45,97	47,48	47,98	64,78	47,68
TiO ₂	1,12	1,13	1,246	1,034	1,70	1,67	1,191	0,98	1,176	1,119	1,834
Al ₂ O ₃	21,52	16,20	21,58	22,16	14,49	14,10	16,44	14,76	10,9	16,4	24,92
FeO(T)	9,50	8,86	8,76	8,53	11,24	11,31	7,87	9,26	11,71	8,49	12,08
MnO	0,24	0,16	0,144	0,17	0,21	0,21	0,272	0,26	0,226	0,105	0,211
MgO	2,51	6,38	2,29	2,43	6,21	5,62	2,99	7,76	9,02	2,25	3,67
CaO	1,80	15,98	0,54	2,57	11,78	13,01	19,87	15,80	15,73	0,63	4,4
Na ₂ O	0,66	2,34	0,5	1,88	3,04	2,89	0,84	2,29	1,88	0,69	2,91
K ₂ O	3,15	0,51	2,53	6,85	0,48	0,49	0,99	0,45	0,39	2,16	0,39
P ₂ O ₅	0,15	0,09	0,1	0,11	0,16	0,15	0,15	0,08	0,02	0,04	0,15
Sum	100,50	100,80	100,3	98,46	100,10	99,84	100,6	100,40	100,7	98,7	99,97
LOI	0,91	1,26	1,13	0,37	0,57	0,73	3,09	0,26	0,34	1,12	0,36

Table S5.2 - Bulk rock trace element composition of representative studied rocks across the Anzola transect. Iron contents are expressed as all ferric.

Trace elements (ppm)												
Au	1	< 1	6	< 1	< 1	< 1	< 1	1	2	< 1	< 1	< 1
Ag	< 0.5	< 0.5	< 0.5	< 0.5	< 0.5	< 0.5	< 0.5	< 0.5	< 0.5	< 0.5	< 0.5	< 0.5
As	1	< 1	2	< 1	< 1	< 1	< 1	< 1	< 1	< 1	< 1	< 1
Ba	757	49	612	1114	44	34	229	31	19	601	134	
Be	1	< 1	< 1	2	< 1	1	2	< 1	< 1	< 1	1	
Bi	< 2	< 0.1	< 0.1	< 0.1	< 0.1	< 0.1	0.1	< 0.1	< 0.1	< 0.1	< 0.1	< 0.1
Br	< 0.5	< 0.5	< 0.5	< 0.5	< 0.5	< 0.5	< 0.5	< 0.5	< 0.5	< 0.5	< 0.5	< 0.5
Cd	< 0.5	< 0.5	< 0.5	< 0.5	< 0.5	< 0.5	< 0.5	< 0.5	< 0.5	< 0.5	< 0.5	< 0.5
Co	30.5	45	14.6	22.1	47.6	49.7	23.2	50.4	54.4	18.1	25.6	
Cr	139	303	124	113	118	113	232	447	384	109	137	
Cs	< 0.2	0.1	0.3	6	0.1	0.1	0.3	< 0.1	< 0.1	0.2	< 0.1	
Cu	85	96	28	24	3	32	121	15	88	10	39	
Ga		15	26	21	17	17	30	15	15	19	27	
Ge		1.2	2.3	1	1.4	1.5	1.8	1.3	1.9	2.1	2.8	
Hf	4.6	1.8	8.2	5.2	2.8	2.7	5	1.4	2.3	7.5	19.6	
Hg	< 1	< 1			< 1	< 1		< 1				
In		0.1	0.1	0.1	0.1	0.1	0.1	0.1	0.1	0.1	0.1	
Ir	< 1	< 1	< 1	< 1	< 1	< 1	< 1	< 1	< 1	< 1	< 1	
Mo	< 2	< 2	< 2	< 2	< 2	< 2	2	< 2	2	< 2	3	
Nb		1.4	22.3	15.9	2.4	2.9	16	3.3	5.5	17.7	41.8	
Ni	76	93	33	38	55	63	68	144	134	23	56	
Pb	27	< 5	13	26	< 5	< 5	10	< 5	< 5	5	6	
Rb	110	10	76	261	8	9	28	2	3	52	5	
S	0.073	0.005	0.006	0.005	0.003	0.002	0.127	0.003	0.007	0.007	0.019	
Sb	< 0.1	0.1	0.7	< 0.1	0.1	< 0.1	0.1	< 0.1	< 0.1	< 0.1	< 0.1	
Sc	26.2	34.7	20.3	20.1	43	42.3	30.4	39.4	46.2	20.3	28.3	
Se	< 0.5	< 0.5	< 0.5	< 0.5	< 0.5	< 0.5	< 0.5	< 0.5	< 0.5	< 0.5	< 0.5	
Sn		1	1	2	1	1	4	1	1	< 1	< 1	
Sr	145	138	133	254	157	178	334	191	70	101	567	
Ta	< 0.3	0.11	1.77	1.51	0.07	0.16	1.6	0.32	0.98	1.52	12	
Th	17.4	0.14	18.4	16.5	0.23	0.53	15.9	0.36	0.49	19.1	7.37	
U	1.5	0.17	2.06	2.51	0.23	0.37	7.42	0.13	0.2	1.91	1.34	
V	215	248	178	157	359	352	270	335	141	167		
W	< 1	< 1	< 1	< 1	< 1	< 1	< 1	< 1	< 1	< 1	< 1	
Y	38	24	42	28	35	34	38	22	28	41	56	
Zn	125	71	80	120	95	113	71	92	87	78	129	
Zr	200	68	309	179	104	90	174	44	73	311	765	
REE												
La	58.1	2.09	59.5	58.2	4.24	5.61	29.7	4.49	7.58	61.8	36	
Ce	111	6.03	117	114	11.3	14.1	72.7	10	16.8	121	68.9	
Pr	48	1.16	13.3	13.1	2.08	2.35	10.1	1.67	2.4	13.6	7.67	
Nd	8.69	6.89	50	48.4	11	11.8	41.8	8.21	10.9	50.5	29.6	
Sm	1.9	2.67	9.61	9.36	3.89	3.97	9.25	2.75	3.4	9.46	6.62	
Eu	< 0.1	1	1.8	2.28	1.42	1.44	1.76	0.99	1.12	1.38	2.45	
Gd		3.72	8.5	7.12	5.23	5.74	7.58	3.73	4.16	7.15	9.08	
Tb	4.29	0.7	1.39	1.11	0.97	1.06	1.28	0.66	0.83	1.18	1.9	
Dy		4.4	8.18	6.01	6.29	6.78	7.35	4.24	5.15	6.64	12.3	
Ho		0.92	1.58	1.16	1.32	1.39	1.42	0.89	1.11	1.39	2.23	
Er		2.68	4.37	3.22	3.96	4.16	3.72	2.52	3.22	4.01	6.05	
Tl		0.07	0.27	1.17	0.14	0.1	< 0.05	0.06	< 0.05	0.13	0.05	
Tm		0.393	0.67	0.479	0.582	0.584	0.502	0.385	0.491	0.625	0.86	
Yb	0.61	2.62	4.31	2.94	3.67	3.96	3.11	2.45	3.23	4.14	5.66	
Lu	2.032	0.385	0.673	0.447	0.581	0.58	0.445	0.385	0.493	0.632	0.815	

Table S5.3a – Average major elements composition (wt.%) for feldspar from the mafic samples.

Plagioclase Sample	Scp-bearing gneiss AN10						Mylonitic amphibolite										
	Texture position	core	interstitial	rim	inclusion	porphyr	AN01A	rix	inclusion	porphyr	AN01C	rix					
N of analysis	8	σ	2	σ	4	σ	1	7	σ	13	σ	3	σ	8	σ	9	σ
SiO ₂	53,82	1,71	58,16	0,16	55,70	0,56	56,66	55,09	1,13	54,89	1,28	63,72	4,43	60,91	0,64	60,39	0,52
TiO ₂	0,02	0,02	0,05	0,02	0,02	0,01	0,00	0,03	0,04	0,01	0,01	0,04	0,01	0,02	0,03	0,02	0,02
Al ₂ O ₃	28,38	1,33	25,55	0,33	27,16	0,73	25,59	25,59	1,63	24,66	1,69	22,38	2,62	23,74	0,32	23,96	0,42
Cr ₂ O ₃	0,02	0,02	0,01	0,01	0,02	0,04	0,03	0,02	0,02	0,01	0,02	0,03	0,00	0,02	0,02	0,02	0,02
FeOT	0,06	0,03	0,32	0,03	0,08	0,04	0,15	0,10	0,04	0,10	0,08	0,14	0,04	0,13	0,16	0,14	0,09
MnO	0,01	0,01	0,03	0,03	0,02	0,04	0,00	0,00	0,01	0,01	0,01	0,03	0,02	0,01	0,01	0,01	0,01
NiO	0,02	0,03	0,00	0,00	0,00	0,01	0,00	0,00	0,01	0,03	0,03	0,00	0,00	0,01	0,02	0,02	0,02
MgO	0,01	0,01	0,02	0,01	0,01	0,01	0,00	0,01	0,01	0,01	0,01	0,00	0,00	0,01	0,01	0,01	0,01
CaO	11,56	1,39	8,21	0,17	10,11	0,62	9,41	9,84	0,64	9,49	0,94	4,66	3,00	6,50	0,29	6,83	0,29
Na ₂ O	4,82	0,80	6,70	0,29	5,61	0,33	6,30	5,88	0,45	6,18	0,56	9,29	1,91	8,09	0,20	7,82	0,24
K ₂ O	0,08	0,04	0,04	0,02	0,08	0,02	0,08	0,14	0,04	0,10	0,02	0,15	0,10	0,12	0,04	0,08	0,02
Total	98,80	0,33	99,07	0,71	98,80	0,56	98,23	96,71	2,84	95,49	2,60	100,44	0,65	99,55	0,92	99,30	0,70
Cat./O	5/8																
Si	2,46	0,07	2,63	0,01	2,53	0,03	2,59	2,56	0,03	2,59	0,05	2,81	0,15	2,72	0,01	2,71	0,02
Ti	0,00	0,00	0,00	0,00	0,00	0,00	0,00	0,00	0,00	0,00	0,00	0,00	0,00	0,00	0,00	0,00	0,00
Al	1,53	0,07	1,36	0,01	1,46	0,03	1,38	1,40	0,05	1,37	0,06	1,17	0,15	1,25	0,01	1,27	0,02
Cr	0,00	0,00	0,00	0,00	0,00	0,00	0,00	0,00	0,00	0,00	0,00	0,00	0,00	0,00	0,00	0,00	0,00
FeT	0,00	0,00	0,01	0,00	0,00	0,00	0,01	0,00	0,00	0,00	0,00	0,01	0,00	0,00	0,01	0,01	0,00
Mn	0,00	0,00	0,00	0,00	0,00	0,00	0,00	0,00	0,00	0,00	0,00	0,00	0,00	0,00	0,00	0,00	0,00
Ni	0,00	0,00	0,00	0,00	0,00	0,00	0,00	0,00	0,00	0,00	0,00	0,00	0,00	0,00	0,00	0,00	0,00
Mg	0,00	0,00	0,00	0,00	0,00	0,00	0,00	0,00	0,00	0,00	0,00	0,00	0,00	0,00	0,00	0,00	0,00
Ca	0,57	0,07	0,40	0,01	0,49	0,03	0,46	0,49	0,02	0,48	0,04	0,22	0,14	0,31	0,01	0,33	0,01
Na	0,43	0,07	0,59	0,02	0,49	0,03	0,56	0,53	0,06	0,57	0,06	0,79	0,15	0,70	0,02	0,68	0,02
K	0,00	0,00	0,00	0,00	0,00	0,00	0,00	0,01	0,00	0,01	0,00	0,01	0,01	0,01	0,00	0,00	0,00
Tot cations	4,99	0,01	4,99	0,01	4,99	0,01	5,00	5,00	0,02	5,01	0,02	5,01	0,00	5,00	0,01	5,00	0,01
An	56,76	7,03	40,30	1,56	49,68	2,96	45,00	47,67	3,35	45,66	4,60	21,70	14,12	30,54	1,30	32,42	1,50
Ab	42,79	6,86	59,45	1,63	49,83	2,80	54,50	51,54	3,49	53,78	4,58	77,47	14,41	68,81	1,51	67,12	1,48
Or	0,44	0,20	0,25	0,07	0,48	0,17	0,50	0,83	0,20	0,56	0,12	0,83	0,49	0,68	0,23	0,47	0,15

Table S5.3b – Average major elements composition (wt.%) for feldspar from the mafic samples.

Mylonitic amphibolite															
AN01D				AN01H								AN01			
porphyr core	porphyr rim			rix	inclusion		porphyr		rix	porphyr		rix	porphyr		
10	4	10	σ	4	σ	5	σ	5	σ	3	σ	9	σ		
58,51	1,28	58,26	0,76	58,40	1,27	57,39	1,03	53,77	2,21	56,86	0,55	56,13	1,13	55,71	2,74
0,01	0,01	0,02	0,02	0,02	0,02	0,02	0,02	0,01	0,01	0,03	0,03	0,01	0,02	0,04	0,05
25,59	0,60	24,91	0,27	26,10	0,63	26,46	0,29	28,87	1,40	26,90	0,32	27,40	0,66	27,18	1,51
0,01	0,02	0,01	0,03	0,02	0,02	0,02	0,02	0,01	0,02	0,01	0,01	0,00	0,00	0,01	0,01
0,08	0,04	0,08	0,05	0,08	0,04	0,15	0,05	0,05	0,04	0,08	0,03	0,14	0,02	0,20	0,17
0,01	0,02	0,02	0,03	0,01	0,01	0,01	0,01	0,01	0,01	0,02	0,02	0,01	0,02	0,01	0,01
0,01	0,01	0,06	0,04	0,01	0,02	0,01	0,01	0,01	0,01	0,02	0,02	0,00	0,01	0,02	0,03
0,00	0,01	0,01	0,01	0,00	0,01	0,00	0,00	0,01	0,01	0,00	0,00	0,01	0,01	0,03	0,04
8,23	0,72	8,00	0,72	8,58	0,81	9,37	0,48	12,25	1,61	9,77	0,40	9,85	1,15	10,12	2,16
6,78	0,58	6,74	0,44	6,71	0,50	6,42	0,31	4,67	0,95	6,09	0,29	5,99	0,65	5,72	1,25
0,12	0,04	0,15	0,05	0,11	0,03	0,16	0,03	0,10	0,03	0,10	0,02	0,08	0,01	0,08	0,02
99,35	1,38	98,26	0,23	100,03	1,03	99,99	1,00	99,76	0,38	99,89	0,36	99,63	0,16	99,13	0,70
2,63	0,03	2,65	0,02	2,61	0,04	2,58	0,02	2,44	0,08	2,56	0,02	2,53	0,04	2,53	0,10
0,00	0,00	0,00	0,00	0,00	0,00	0,00	0,00	0,00	0,00	0,00	0,00	0,00	0,00	0,00	0,00
1,36	0,03	1,33	0,02	1,38	0,04	1,40	0,02	1,54	0,09	1,43	0,02	1,46	0,04	1,46	0,10
0,00	0,00	0,00	0,00	0,00	0,00	0,00	0,00	0,00	0,00	0,00	0,00	0,00	0,00	0,00	0,00
0,00	0,00	0,00	0,00	0,00	0,00	0,01	0,00	0,00	0,00	0,00	0,00	0,01	0,00	0,01	0,01
0,00	0,00	0,00	0,00	0,00	0,00	0,00	0,00	0,00	0,00	0,00	0,00	0,00	0,00	0,00	0,00
0,00	0,00	0,00	0,00	0,00	0,00	0,00	0,00	0,00	0,00	0,00	0,00	0,00	0,00	0,00	0,00
0,00	0,00	0,00	0,00	0,00	0,00	0,00	0,00	0,00	0,00	0,00	0,00	0,00	0,00	0,00	0,00

Table S5.3c – Average major elements composition (wt.%) for feldspar from the mafic samples.

Calc-silicate AN06C		AN08C		Gabbro AN08B		AN07B	
5	σ	9	σ	6	σ	10	σ
44,52	2,01	53,54	0,36	54,17	0,46	55,21	0,61
0,02	0,04	0,01	0,02	0,00	0,00	0,02	0,02
32,65	4,66	28,81	0,37	28,28	0,27	29,05	0,50
0,03	0,03	0,01	0,01	0,00	0,01	0,01	0,02
0,13	0,02	0,08	0,04	0,10	0,08	0,11	0,04
0,03	0,03	0,00	0,01	0,01	0,01	0,00	0,01
0,02	0,02	0,03	0,02	0,01	0,01	0,02	0,02
0,00	0,01	0,01	0,01	0,00	0,01	0,01	0,01
20,86	3,85	11,67	0,22	11,08	0,39	10,95	0,41
0,75	0,56	4,80	0,17	5,10	0,25	5,24	0,27
0,05	0,03	0,15	0,01	0,19	0,02	0,22	0,05
99,07	2,21	99,10	0,18	98,94	0,40	100,83	0,29
2,09	0,08	2,44	0,02	2,47	0,01	2,47	0,02
0,00	0,00	0,00	0,00	0,00	0,00	0,00	0,00
1,80	0,20	1,55	0,02	1,52	0,01	1,53	0,03
0,00	0,00	0,00	0,00	0,00	0,00	0,00	0,00
0,00	0,00	0,00	0,00	0,00	0,00	0,00	0,00
0,00	0,00	0,00	0,00	0,00	0,00	0,00	0,00
0,00	0,00	0,00	0,00	0,00	0,00	0,00	0,00
0,00	0,00	0,00	0,00	0,00	0,00	0,00	0,00
1,06	0,24	0,57	0,01	0,54	0,02	0,52	0,02
0,07	0,05	0,42	0,02	0,45	0,02	0,45	0,02
0,00	0,00	0,01	0,00	0,01	0,00	0,01	0,00
5,04	0,05	5,00	0,01	5,00	0,01	5,00	0,01
93,16	5,19	56,83	1,29	53,97	2,07	52,93	2,27
6,54	5,03	42,30	1,27	44,95	1,97	45,80	2,05
0,30	0,20	0,88	0,07	1,08	0,13	1,25	0,27

Table S5.3d – Average major elements composition (wt.%) for clinopyroxene from the studied samples.

Clinopyroxene Sample	Scp-bearing gneiss AN10		AN1A				Mylonitic amphibolites				AN01C			
	core 1	rim 1	core 3	σ	rim	σ	rix 13	σ	core 9	σ	rim 4	σ	rix 5	σ
Texture position N of analysis														
SiO ₂	52,55	52,38	50,97	0,17	50,05	1,43	50,34	1,18	52,71	0,58	52,52	0,55	52,90	0,58
TiO ₂	0,23	0,20	0,29	0,08	0,25	0,11	0,18	0,10	0,12	0,05	0,15	0,05	0,14	0,08
Al ₂ O ₃	1,57	1,63	1,98	0,31	1,69	0,67	1,41	0,44	1,17	0,32	1,12	0,18	1,25	0,61
Cr ₂ O ₃	0,00	0,00	0,04	0,03	0,01	0,02	0,02	0,02	0,03	0,03	0,01	0,02	0,02	0,02
FeOT	9,27	9,45	13,60	0,45	13,28	0,55	13,84	0,60	11,78	0,20	11,74	0,15	11,64	0,50
MnO	0,22	0,27	0,67	0,01	0,69	0,06	0,67	0,04	0,43	0,05	0,47	0,03	0,43	0,04
NiO	0,01	0,00	0,02	0,02	0,03	0,02	0,02	0,02	0,02	0,03	0,02	0,02	0,02	0,02
MgO	12,49	12,39	9,61	0,34	9,77	0,09	9,68	0,40	11,74	0,43	11,67	0,64	11,80	0,55
CaO	23,67	23,54	22,68	0,13	22,91	0,26	22,85	0,18	22,54	0,30	22,65	0,47	22,66	0,52
Na ₂ O	0,46	0,42	0,48	0,04	0,37	0,17	0,36	0,07	0,49	0,10	0,47	0,06	0,44	0,11
K ₂ O	0,00	0,00	0,00	0,00	0,01	0,00	0,00	0,01	0,00	0,00	0,00	0,00	0,03	0,05
Total	100,47	100,29	100,33	0,63	99,05	0,82	99,38	1,12	101,05	0,66	100,80	1,03	101,34	0,57
Si	1,95	1,96	1,94	0,01	1,93	0,05	1,94	0,03	1,97	0,01	1,97	0,01	1,97	0,01
Ti	0,01	0,01	0,01	0,00	0,01	0,00	0,01	0,00	0,00	0,00	0,00	0,00	0,00	0,00
Al	0,07	0,07	0,09	0,01	0,08	0,03	0,06	0,02	0,05	0,01	0,05	0,01	0,06	0,03
Cr	0,00	0,00	0,00	0,00	0,00	0,00	0,00	0,00	0,00	0,00	0,00	0,00	0,00	0,00
Fe ²⁺	0,21	0,26	0,38	0,02	0,35	0,07	0,37	0,06	0,33	0,01	0,33	0,02	0,33	0,02
Fe ³⁺	0,07	0,03	0,06	0,03	0,08	0,07	0,08	0,05	0,04	0,01	0,04	0,01	0,03	0,01
Mn	0,01	0,01	0,02	0,00	0,02	0,00	0,02	0,00	0,01	0,00	0,01	0,00	0,01	0,00
Ni	0,00	0,00	0,00	0,00	0,00	0,00	0,00	0,00	0,00	0,00	0,00	0,00	0,00	0,00
Mg	0,69	0,69	0,54	0,02	0,56	0,00	0,56	0,03	0,65	0,02	0,65	0,03	0,65	0,03
Ca	0,94	0,94	0,92	0,00	0,95	0,01	0,94	0,01	0,90	0,01	0,91	0,03	0,90	0,02
Na	0,03	0,03	0,04	0,00	0,03	0,01	0,03	0,01	0,04	0,01	0,03	0,00	0,03	0,01
K	0,00	0,00	0,00	0,00	0,00	0,00	0,00	0,00	0,00	0,00	0,00	0,00	0,00	0,00
H	0,02	0,00	0,00	0,01	0,00	0,00	0,00	0,00	0,00	0,00	0,00	0,00	0,00	0,00
cations	4,00	4,00	4,00	0,00	4,00	0,00	4,00	0,00	4,00	0,00	4,00	0,00	4,00	0,00
wollastonite	48,85	48,66	48,06	0,36	48,33	0,23	47,94	0,24	46,56	0,38	46,80	1,39	46,72	0,41
enstatite	35,86	35,64	28,33	0,79	28,68	0,39	28,27	1,03	33,73	0,83	33,51	1,48	33,83	1,04
ferrosilite	15,29	15,70	23,61	0,65	23,00	0,55	23,79	1,04	19,71	0,60	19,69	0,25	19,45	1,07
mg#	70,60	70,03	55,75	1,38	56,75	0,99	55,49	2,00	63,97	1,20	63,89	1,20	64,35	1,94

Table S5.3d – Average major elements composition (wt.%) for clinopyroxene from the studied samples.

Mylonitic amphibolites																		
AN01D						AN01H						AN01						
core		rim		rix		core		rim		rix		core		rim		rix		
18	σ	8	σ	19	σ	11	σ	5	σ	5	σ	7	σ	5	σ	2	σ	
50,12	1,61	50,62	1,50	49,95	1,37	52,17	0,43	52,23	0,64	51,02	2,89	51,26	1,12	51,76	0,43	52,22	0,13	
0,31	0,18	0,29	0,15	0,30	0,18	0,24	0,09	0,20	0,12	0,41	0,53	0,23	0,13	0,19	0,10	0,09	0,00	
2,02	0,79	1,97	0,52	1,90	0,88	1,73	0,39	1,46	0,63	2,90	3,63	1,62	0,77	1,64	0,39	1,04	0,40	
0,03	0,03	0,03	0,04	0,02	0,02	0,04	0,03	0,01	0,01	0,11	0,17	0,01	0,02	0,02	0,03	0,05	0,00	
19,48	4,15	18,31	4,09	20,43	3,78	13,68	1,50	14,68	2,84	15,19	2,60	14,17	1,50	12,87	0,31	12,50	0,08	
0,35	0,06	0,36	0,05	0,36	0,05	0,32	0,09	0,30	0,09	0,35	0,08	0,37	0,08	0,34	0,09	0,40	0,06	
0,04	0,03	0,03	0,03	0,03	0,03	0,01	0,01	0,02	0,01	0,03	0,03	0,01	0,02	0,01	0,02	0,00	0,00	
6,35	2,82	7,17	2,72	5,84	2,58	10,86	0,96	10,36	1,94	10,34	1,47	10,25	1,01	10,89	0,47	11,28	0,28	
21,92	0,53	22,11	0,49	21,90	0,80	21,97	0,31	22,20	0,39	20,08	4,62	22,22	0,58	22,50	0,29	22,61	0,35	
0,45	0,12	0,44	0,06	0,41	0,10	0,31	0,08	0,24	0,04	0,36	0,32	0,34	0,11	0,36	0,05	0,37	0,06	
0,00	0,00	0,00	0,00	0,03	0,09	0,00	0,01	0,01	0,00	0,16	0,35	0,01	0,01	0,01	0,00	0,01	0,01	
101,07	0,74	101,32	0,70	101,17	0,82	101,33	0,36	101,70	0,27	100,96	1,17	100,50	0,73	100,59	0,38	100,55	0,11	
1,94	0,03	1,94	0,02	1,94	0,03	1,96	0,01	1,96	0,01	1,93	0,09	1,95	0,02	1,95	0,01	1,97	0,01	
0,01	0,01	0,01	0,00	0,01	0,01	0,01	0,00	0,01	0,00	0,01	0,02	0,01	0,00	0,01	0,00	0,00	0,00	
0,09	0,04	0,09	0,03	0,09	0,04	0,08	0,02	0,06	0,03	0,13	0,17	0,07	0,04	0,07	0,02	0,05	0,02	
0,00	0,00	0,00	0,00	0,00	0,00	0,00	0,00	0,00	0,00	0,00	0,01	0,00	0,00	0,00	0,00	0,00	0,00	
0,58	0,13	0,55	0,13	0,62	0,13	0,41	0,05	0,44	0,11	0,46	0,08	0,40	0,04	0,37	0,02	0,35	0,03	
0,06	0,04	0,04	0,01	0,05	0,02	0,02	0,01	0,02	0,02	0,02	0,01	0,05	0,01	0,04	0,02	0,05	0,03	
0,01	0,00	0,01	0,00	0,01	0,00	0,01	0,00	0,01	0,00	0,01	0,00	0,01	0,00	0,01	0,00	0,01	0,00	
0,00	0,00	0,00	0,00	0,00	0,00	0,00	0,00	0,00	0,00	0,00	0,00	0,00	0,00	0,00	0,00	0,00	0,00	
0,36	0,15	0,41	0,15	0,34	0,14	0,61	0,05	0,58	0,10	0,58	0,08	0,58	0,05	0,61	0,02	0,63	0,02	
0,91	0,02	0,91	0,01	0,91	0,04	0,88	0,01	0,89	0,01	0,81	0,18	0,90	0,02	0,91	0,01	0,91	0,01	
0,03	0,01	0,03	0,00	0,03	0,01	0,02	0,01	0,02	0,00	0,03	0,02	0,02	0,01	0,03	0,00	0,03	0,00	
0,00	0,00	0,00	0,00	0,00	0,00	0,00	0,00	0,00	0,00	0,01	0,02	0,00	0,00	0,00	0,00	0,00	0,00	
0,01	0,01	0,00	0,00	0,00	0,01	0,00	0,00	0,00	0,00	0,00	0,00	0,00	0,00	0,00	0,00	0,00	0,01	
4,00	0,00	4,00	0,00	4,00	0,00	4,00	0,00	4,00	0,00	4,00	0,00	4,00	0,00	4,00	0,00	4,00	0,00	
47,41	0,63	47,39	0,37	47,34	1,38	45,76	0,56	45,96	0,35	42,62	7,17	46,44	0,40	46,91	0,67	46,74	0,11	
18,95	7,88	21,25	7,73	17,48	7,38	31,45	2,60	29,77	5,18	30,92	3,88	29,80	2,55	31,57	1,01	32,44	0,38	
33,64	7,58	31,37	7,55	35,18	6,76	22,79	2,67	24,27	5,06	26,46	6,69	23,76	2,65	21,52	0,66	20,82	0,49	
36,37	14,84	40,81	14,74	33,43	13,46	58,57	4,86	55,56	9,47	54,81	7,57	56,28	4,98	60,10	1,52	61,66	0,73	

Table S5.3e – Average major elements composition (wt.%) for clinopyroxene from the studied samples.

Calc-silicate AN06C		AN08C				Gabbro AN08B		AN07B			
25	σ	core 13	σ	rim 2	σ	10	σ	core 20	σ	rim 7	σ
49,90	0,49	50,59	0,32	50,64	0,42	50,26	0,48	51,30	0,62	51,70	0,85
0,30	0,09	0,37	0,05	0,39	0,02	0,40	0,15	0,38	0,11	0,33	0,16
2,81	0,68	3,79	0,16	3,50	0,44	3,59	0,55	3,58	0,58	2,95	1,08
0,08	0,07	0,06	0,03	0,08	0,04	0,05	0,02	0,08	0,04	0,05	0,04
17,73	1,21	10,65	0,19	10,51	0,01	11,63	0,49	12,17	0,74	12,15	1,01
0,66	0,07	0,43	0,09	0,41	0,03	0,72	0,13	0,93	0,10	0,90	0,12
0,02	0,03	0,03	0,02	0,03	0,01	0,02	0,02	0,04	0,03	0,04	0,03
6,71	0,66	11,67	0,12	11,94	0,11	11,05	0,35	11,42	0,61	11,67	0,79
22,63	0,27	21,66	0,23	21,91	0,13	21,40	0,23	20,64	0,43	20,82	0,49
0,22	0,03	0,58	0,04	0,60	0,06	0,60	0,04	0,59	0,06	0,54	0,08
0,01	0,01	0,00	0,00	0,01	0,01	0,01	0,01	0,00	0,01	0,00	0,00
101,07	0,37	99,84	0,31	100,01	0,15	99,73	0,35	101,12	0,33	101,17	0,36
1,93	0,02	1,90	0,01	1,90	0,01	1,90	0,02	1,91	0,02	1,93	0,03
0,01	0,00	0,01	0,00	0,01	0,00	0,01	0,00	0,01	0,00	0,01	0,00
0,13	0,03	0,17	0,01	0,15	0,02	0,16	0,02	0,16	0,03	0,13	0,05
0,00	0,00	0,00	0,00	0,00	0,00	0,00	0,00	0,00	0,00	0,00	0,00
0,55	0,04	0,28	0,01	0,26	0,01	0,31	0,01	0,34	0,02	0,34	0,03
0,02	0,01	0,05	0,01	0,07	0,01	0,06	0,01	0,04	0,02	0,03	0,02
0,02	0,00	0,01	0,00	0,01	0,00	0,02	0,00	0,03	0,00	0,03	0,00
0,00	0,00	0,00	0,00	0,00	0,00	0,00	0,00	0,00	0,00	0,00	0,00
0,39	0,04	0,65	0,01	0,67	0,01	0,62	0,02	0,64	0,03	0,65	0,04
0,94	0,01	0,87	0,01	0,88	0,00	0,87	0,01	0,82	0,02	0,83	0,02
0,02	0,00	0,04	0,00	0,04	0,00	0,04	0,00	0,04	0,00	0,04	0,01
0,00	0,00	0,00	0,00	0,00	0,00	0,00	0,00	0,00	0,00	0,00	0,00
0,00	0,00	0,00	0,00	0,00	0,00	0,00	0,00	0,00	0,00	0,00	0,00
4,00	0,00	4,00	0,00	4,00	0,00	4,00	0,00	4,00	0,00	4,00	0,00
48,85	0,61	46,52	0,41	46,57	0,04	46,10	0,46	44,14	0,91	44,07	0,72
20,14	1,88	34,88	0,32	35,31	0,10	33,11	0,95	33,98	1,56	34,33	1,88
31,01	2,18	18,60	0,41	18,12	0,06	20,79	0,99	21,89	1,50	21,60	2,07
40,28	3,91	66,14	0,51	66,95	0,19	62,86	1,61	62,57	2,52	63,09	3,38

Table S5.3f – Average major elements composition (wt.%) for amphibole from the studied samples.

Amphibole Sample	Scp-bearing gneiss AN10								Mylonitic amphibolite										
	core		rim		inclusion		AN01A		rix		inclusion		core		AN01C		rix		
Texture position N of analysis	7	σ	3	σ	1	9	σ	5	σ	14	σ	4	σ	8	σ	3	σ	10	σ
SiO ₂	40,73	0,74	41,63	0,17	39,38	38,38	1,22	37,90	0,96	39,07	1,03	42,66	0,64	42,30	0,42	41,97	0,66	42,97	0,33
TiO ₂	1,96	0,27	1,87	0,22	2,58	2,31	0,18	2,19	0,17	1,93	0,19	2,27	0,06	2,49	0,35	2,69	0,11	1,93	0,32
Al ₂ O ₃	13,91	0,63	13,22	0,41	12,81	12,66	0,70	11,98	0,40	12,04	0,44	10,63	0,76	11,44	0,29	11,60	0,26	10,89	0,57
Cr ₂ O ₃	0,10	0,05	0,07	0,03	0,00	0,04	0,04	0,07	0,04	0,03	0,04	0,04	0,03	0,07	0,04	0,01	0,01	0,04	0,03
FeOT	16,29	0,36	15,74	0,74	20,75	20,39	0,75	20,49	0,82	20,69	0,80	18,07	0,54	18,12	0,39	18,29	0,73	18,17	0,46
MnO	0,23	0,03	0,20	0,03	0,45	0,47	0,03	0,45	0,03	0,45	0,07	0,28	0,04	0,33	0,03	0,28	0,02	0,29	0,03
NiO	0,02	0,03	0,04	0,02	0,07	0,02	0,02	0,04	0,05	0,03	0,03	0,03	0,03	0,02	0,03	0,05	0,05	0,01	0,01
MgO	9,30	0,29	9,77	0,22	6,37	6,62	0,47	6,98	0,51	7,11	0,43	9,52	0,25	9,22	0,32	9,00	0,40	9,58	0,38
CaO	11,79	0,07	11,85	0,11	11,44	11,55	0,09	11,57	0,14	11,66	0,10	11,61	0,14	11,44	0,14	11,38	0,11	11,68	0,12
Na ₂ O	2,02	0,10	1,92	0,05	1,81	1,59	0,14	1,63	0,10	1,60	0,10	1,84	0,13	2,03	0,07	2,03	0,08	1,77	0,11
K ₂ O	1,16	0,08	1,10	0,05	2,03	2,17	0,09	1,98	0,04	1,77	0,13	1,20	0,08	1,25	0,05	1,30	0,07	1,16	0,09
Total	97,50	0,51	97,40	0,17	97,69	96,20	1,95	95,27	1,35	96,38	1,52	98,14	0,60	98,71	0,52	98,61	0,21	98,48	0,59
Si	6,16	0,09	6,27	0,03	6,13	6,07	0,07	6,07	0,09	6,16	0,07	6,45	0,09	6,37	0,04	6,33	0,07	6,47	0,06
Ti	0,22	0,03	0,21	0,02	0,30	0,28	0,02	0,26	0,02	0,23	0,02	0,26	0,01	0,28	0,04	0,31	0,01	0,22	0,04
Al	2,48	0,12	2,35	0,07	2,35	2,36	0,08	2,26	0,06	2,24	0,06	1,89	0,13	2,03	0,05	2,06	0,05	1,93	0,10
Cr	0,01	0,01	0,01	0,00	0,00	0,00	0,00	0,01	0,01	0,00	0,00	0,00	0,00	0,01	0,01	0,00	0,00	0,00	0,00
Fe ²⁺	2,06	0,04	1,98	0,10	2,70	2,66	0,14	2,70	0,12	2,71	0,10	2,29	0,08	2,28	0,05	2,31	0,10	2,29	0,06
Fe ³⁺	0,00	0,00	0,00	0,00	0,00	0,04	0,08	0,05	0,05	0,01	0,05	0,00	0,00	0,00	0,00	0,00	0,00	0,00	0,00
Mn	0,03	0,00	0,03	0,00	0,06	0,06	0,00	0,06	0,00	0,06	0,01	0,04	0,01	0,04	0,00	0,04	0,00	0,04	0,00
Ni	0,00	0,00	0,00	0,00	0,01	0,00	0,00	0,01	0,01	0,00	0,00	0,00	0,00	0,00	0,00	0,01	0,01	0,00	0,00
Mg	2,09	0,06	2,19	0,05	1,48	1,56	0,13	1,66	0,14	1,67	0,12	2,14	0,05	2,07	0,07	2,02	0,08	2,15	0,09
Ca	1,91	0,02	1,91	0,01	1,91	1,96	0,04	1,98	0,04	1,97	0,04	1,88	0,01	1,84	0,02	1,84	0,02	1,88	0,03
Na	0,59	0,03	0,56	0,02	0,55	0,49	0,05	0,50	0,03	0,49	0,04	0,54	0,04	0,59	0,02	0,59	0,02	0,52	0,03
K	0,22	0,02	0,21	0,01	0,40	0,44	0,02	0,40	0,01	0,36	0,03	0,23	0,02	0,24	0,01	0,25	0,01	0,22	0,02
cations	15,78	0,02	15,73	0,03	15,87	15,92	0,09	15,97	0,05	15,91	0,07	15,73	0,05	15,75	0,03	15,75	0,04	15,72	0,02
Mg#	50,40	0,70	52,53	1,51	35,35	37,00	3,05	38,17	3,04	38,09	2,39	48,40	1,33	47,53	1,31	46,71	2,09	48,41	1,36
Na+K	0,78	0,02	0,73	0,03	0,87	0,91	0,08	0,91	0,04	0,84	0,05	0,73	0,05	0,75	0,03	0,75	0,04	0,71	0,02
Al + Fe ³⁺ + 2Ti (apfu)	1,08	0,09	1,04	0,09	1,08	1,02	0,08	0,90	0,05	0,87	0,08	0,86	0,04	0,96	0,06	1,00	0,03	0,83	0,10
Na+K+2Ca (apfu)	0,78	0,02	0,73	0,03	0,87	0,93	0,10	1,02	0,08	0,97	0,11	0,73	0,05	0,75	0,03	0,75	0,04	0,72	0,02

Table S5.3g – Average major elements composition (wt.%) for amphibole from the studied samples.

Mylonitic amphibolite																					
AN01D								AN01				AN01H									
inclusion	σ	core	σ	rim	σ	rix	σ	core	σ	rim	σ	rix	σ	inclusion	σ	core	σ	rim	σ	rix	σ
4		6		4		6		4		5		6		2		5		3		7	
40,31	0,60	41,25	0,75	41,95	0,57	42,06	1,17	42,95	1,21	42,89	1,05	42,75	1,00	43,30	0,36	43,31	1,28	43,62	0,25	44,39	1,26
2,49	20,22	2,50	0,31	2,14	0,23	1,99	0,26	1,96	0,44	2,01	0,40	1,64	0,32	2,10	0,13	2,26	0,33	2,14	0,12	1,62	0,39
12,64	5,43	12,63	0,56	12,10	0,41	12,42	0,91	11,77	0,65	11,70	0,57	11,77	1,20	11,08	0,78	11,63	0,57	11,60	0,55	10,82	1,00
0,09	6,71	0,04	0,03	0,04	0,02	0,07	0,04	0,02	0,02	0,02	0,03	0,05	0,03	0,10	0,03	0,04	0,04	0,04	0,03	0,02	0,03
21,86	11,64	19,55	1,24	18,99	0,38	19,45	1,33	18,30	0,87	18,34	0,39	18,57	0,92	19,13	0,01	18,17	0,39	18,05	0,55	18,68	0,79
0,22	11,57	0,26	0,02	0,25	0,04	0,24	0,04	0,24	0,04	0,27	0,07	0,25	0,05	0,24	0,02	0,19	0,08	0,19	0,04	0,19	0,06
0,04	0,10	0,02	0,02	0,03	0,03	0,02	0,02	0,01	0,02	0,02	0,02	0,02	0,03	0,00	0,00	0,02	0,02	0,02	0,02	0,02	0,02
6,34	3,37	7,84	0,80	8,58	0,29	8,45	1,18	9,11	0,66	9,04	0,43	8,78	0,58	8,74	0,54	9,37	0,62	9,20	0,31	9,27	0,50
11,41	2,71	11,40	0,07	11,56	0,07	11,56	0,15	11,60	0,27	11,58	0,23	11,74	0,14	11,22	0,18	11,30	0,10	11,43	0,14	11,61	0,16
2,21	4,92	2,10	0,20	1,84	0,15	1,82	0,09	1,76	0,38	1,72	0,34	1,60	0,23	1,54	0,17	1,71	0,16	1,43	0,14	1,22	0,23
1,07	0,62	1,27	0,11	1,27	0,04	1,29	0,12	0,84	0,13	0,87	0,13	0,90	0,12	0,95	0,20	1,12	0,18	1,18	0,03	1,01	0,16
98,65	1,20	98,83	0,89	98,73	1,13	99,36	0,57	98,56	0,51	98,47	0,38	98,07	0,52	98,38	0,09	99,10	0,45	98,91	0,52	98,84	0,65
6,19	0,03	6,24	0,09	6,33	0,04	6,31	0,13	6,44	0,15	6,44	0,12	6,45	0,15	6,52	0,04	6,45	0,13	6,50	0,05	6,62	0,16
0,29	3,16	0,29	0,03	0,24	0,02	0,23	0,03	0,22	0,05	0,23	0,05	0,19	0,04	0,24	0,01	0,25	0,04	0,24	0,01	0,18	0,04
2,29	1,07	2,25	0,10	2,15	0,07	2,20	0,18	2,08	0,13	2,07	0,12	2,09	0,21	1,97	0,14	2,04	0,12	2,04	0,08	1,90	0,18
0,01	1,22	0,00	0,00	0,00	0,00	0,01	0,00	0,00	0,00	0,00	0,00	0,01	0,00	0,01	0,00	0,00	0,00	0,00	0,00	0,00	0,00
2,81	1,49	2,48	0,16	2,40	0,04	2,44	0,18	2,29	0,12	2,30	0,06	2,34	0,12	2,41	0,00	2,26	0,07	2,25	0,08	2,33	0,11
0,00	1,50	0,00	0,00	0,00	0,00	0,00	0,00	0,00	0,00	0,00	0,00	0,00	0,00	0,00	0,00	0,00	0,00	0,00	0,00	0,00	0,00
0,03	0,02	0,03	0,00	0,03	0,01	0,03	0,01	0,03	0,01	0,03	0,01	0,03	0,01	0,03	0,00	0,02	0,01	0,02	0,00	0,02	0,01
0,00	0,01	0,00	0,00	0,00	0,00	0,00	0,00	0,00	0,00	0,00	0,00	0,00	0,00	0,00	0,00	0,00	0,00	0,00	0,00	0,00	0,00
1,45	0,77	1,77	0,18	1,93	0,06	1,89	0,25	2,03	0,14	2,02	0,08	1,97	0,13	1,96	0,12	2,08	0,12	2,04	0,05	2,06	0,10
1,88	0,23	1,85	0,02	1,87	0,03	1,86	0,02	1,86	0,04	1,86	0,03	1,90	0,02	1,81	0,03	1,80	0,03	1,83	0,04	1,86	0,03
0,66	0,65	0,62	0,06	0,54	0,04	0,53	0,03	0,51	0,11	0,50	0,10	0,47	0,07	0,45	0,05	0,49	0,05	0,41	0,04	0,35	0,07
0,21	0,24	0,24	0,02	0,24	0,01	0,25	0,02	0,16	0,03	0,17	0,03	0,17	0,02	0,18	0,04	0,21	0,04	0,22	0,00	0,19	0,03
15,81	8,34	15,77	0,07	15,74	0,04	15,75	0,05	15,64	0,09	15,63	0,08	15,63	0,08	15,57	0,02	15,63	0,07	15,56	0,03	15,52	0,08
34,05	18,03	41,63	4,01	44,57	1,19	43,52	5,11	46,96	2,95	46,73	1,51	45,69	2,59	44,83	1,55	47,85	2,16	47,59	1,47	46,91	2,16
0,81	17,78	0,77	0,07	0,74	0,04	0,75	0,04	0,64	0,09	0,63	0,08	0,62	0,08	0,57	0,02	0,63	0,07	0,56	0,03	0,51	0,08
1,05	0,05	1,07	0,03	0,97	0,03	0,96	0,10	0,96	0,08	0,96	0,08	0,92	0,12	0,96	0,07	1,00	0,06	1,02	0,04	0,89	0,10
0,81	0,14	0,77	0,07	0,74	0,04	0,75	0,05	0,64	0,09	0,63	0,08	0,64	0,09	0,57	0,02	0,63	0,07	0,56	0,03	0,52	0,08

Table S5.3h – Average major elements composition (wt.%) for amphibole from the studied samples.

Calc-silicate AN06C	AN08C		Gabbro AN08B				AN07B	
	10,00	σ	core 8	σ	rim 3	σ	5	σ
44,28	40,98	0,13	40,55	0,30	40,66	0,17	41,25	0,21
0,01	2,28	0,13	2,47	0,24	2,41	0,38	2,34	0,27
25,93	13,47	0,32	13,24	0,50	13,18	0,16	13,59	0,37
0,01	0,12	0,04	0,12	0,05	0,09	0,08	0,14	0,04
0,24	15,35	0,23	16,62	0,60	16,58	0,42	16,98	0,51
0,06	0,28	0,07	0,45	0,03	0,48	0,03	0,53	0,06
0,02	0,04	0,03	0,04	0,04	0,05	0,03	0,04	0,03
0,08	10,26	0,15	9,56	0,42	9,53	0,33	9,70	0,55
23,51	11,37	0,10	11,34	0,07	11,30	0,04	11,08	0,08
0,04	2,08	0,08	2,09	0,08	2,16	0,05	2,00	0,06
1,28	1,33	0,06	1,35	0,09	1,36	0,04	1,48	0,10
95,47	97,56	0,45	97,83	0,19	97,80	0,35	99,15	0,33
6,33	6,17	0,03	6,14	0,04	6,16	0,02	6,16	0,03
0,00	0,26	0,01	0,28	0,03	0,27	0,04	0,26	0,03
4,37	2,39	0,05	2,36	0,08	2,35	0,03	2,39	0,06
0,00	0,01	0,00	0,01	0,01	0,01	0,01	0,02	0,00
0,03	1,93	0,03	2,10	0,08	2,10	0,05	2,12	0,07
0,00	0,00	0,00	0,00	0,00	0,00	0,00	0,00	0,00
0,01	0,04	0,01	0,06	0,00	0,06	0,00	0,07	0,01
0,00	0,00	0,00	0,00	0,01	0,01	0,00	0,01	0,00
0,02	2,30	0,04	2,15	0,09	2,15	0,08	2,16	0,12
3,60	1,83	0,02	1,84	0,01	1,83	0,01	1,77	0,01
0,01	0,61	0,02	0,61	0,02	0,63	0,01	0,58	0,02
0,23	0,25	0,01	0,26	0,02	0,26	0,01	0,28	0,02
14,61	15,80	0,02	15,83	0,01	15,84	0,03	15,81	0,02
38,47	54,33	0,71	50,59	1,91	50,59	1,44	50,40	2,14
0,24	0,80	0,02	0,83	0,01	0,84	0,03	0,81	0,02
2,70	1,08	0,03	1,06	0,05	1,06	0,06	1,07	0,06
3,45	0,80	0,02	0,83	0,01	0,84	0,03	0,81	0,02

Tab. S5.3i – Average major elements composition (wt.%) for feldspars from the felsic samples.

Feldspar Sample	Migmatitic paragneiss								Mylonitic paragneisses							
	AN11				AN09				AN09C				AN22A			
	Texture position	Kfs	Pl	σ	Kfs	Pl	σ	Kfs	Pl	σ	Kfs	Pl	σ	Kfs	Pl	σ
N of analysis	7	σ	9	σ	9	σ	5	σ	2	σ	8	σ	8	σ	7	σ
SiO2	64,26	0,40	51,53	0,97	66,11	0,74	58,90	3,76	62,82	0,22	54,45	3,66	64,99	0,53	55,93	0,27
TiO2	0,01	0,02	0,03	0,03	0,02	0,02	0,02	0,01	0,01	0,01	0,01	0,01	0,02	0,03	0,02	0,02
Al2O3	18,94	0,21	30,65	0,43	18,50	0,25	25,80	2,17	18,70	0,12	28,08	2,40	19,26	0,17	28,90	0,26
Cr2O3	0,00	0,01	0,00	0,02	0,01	0,01	0,01	0,01	0,07	0,03	0,11	0,03	0,02	0,02	0,01	0,02
FeOT	0,05	0,02	0,04	0,05	0,09	0,20	0,07	0,08	0,36	0,03	0,50	0,13	0,04	0,04	0,06	0,07
MnO	0,00	0,01	0,00	0,01	0,00	0,00	0,00	0,00	0,25	0,01	0,32	0,05	0,01	0,02	0,01	0,01
MgO	-0,01	0,02	-0,01	0,01	0,00	0,00	0,01	0,01	0,00	0,00	0,01	0,01	0,01	0,01	0,01	0,01
CaO	0,10	0,03	12,98	0,62	0,21	0,16	8,27	2,82	0,02	0,01	10,54	2,96	0,14	0,15	10,63	0,19
Na2O	1,32	0,48	4,12	0,41	2,03	1,00	6,68	1,59	0,75	0,04	5,63	1,60	1,15	0,35	5,94	0,19
K2O	14,16	0,55	0,09	0,02	13,55	1,52	0,09	0,02	14,91	0,13	0,21	0,07	14,95	0,56	0,11	0,03
Total	98,84	0,53	99,43	0,61	100,55	0,69	99,87	0,62	97,96	0,06	99,91	0,37	100,60	0,37	101,66	0,34
Cat./O	5/8															
Si	2,98	0,01	2,35	0,03	3,01	0,01	2,63	0,14	2,96	0,01	2,47	0,15	2,97	0,01	2,48	0,01
Ti	0,00	0,00	0,00	0,00	0,00	0,00	0,00	0,00	0,00	0,00	0,00	0,00	0,00	0,00	0,00	0,00
Al	1,04	0,01	1,65	0,03	0,99	0,01	1,36	0,13	1,04	0,01	1,50	0,14	1,04	0,01	1,51	0,01
Cr	0,00	0,00	0,00	0,00	0,00	0,00	0,00	0,00	0,00	0,00	0,00	0,00	0,00	0,00	0,00	0,00
FeT	0,00	0,00	0,00	0,00	0,00	0,01	0,00	0,00	0,01	0,00	0,02	0,01	0,00	0,00	0,00	0,00
Mn	0,00	0,00	0,00	0,00	0,00	0,00	0,00	0,00	0,01	0,00	0,01	0,00	0,00	0,00	0,00	0,00
Ni	0,00	0,00	0,00	0,00	0,00	0,00	0,00	0,00	0,00	0,00	0,00	0,00	0,00	0,00	0,00	0,00
Mg	0,00	0,00	0,00	0,00	0,00	0,00	0,00	0,00	0,01	0,00	0,00	0,00	0,00	0,00	0,00	0,00
Ca	0,00	0,00	0,63	0,03	0,01	0,01	0,40	0,14	0,00	0,00	0,51	0,15	0,01	0,01	0,51	0,01
Na	0,12	0,04	0,36	0,04	0,18	0,09	0,58	0,13	0,07	0,00	0,49	0,14	0,10	0,03	0,51	0,02
K	0,84	0,03	0,01	0,00	0,79	0,09	0,01	0,00	0,90	0,01	0,01	0,00	0,87	0,04	0,01	0,00
Tot cations	4,98	0,01	5,01	0,01	4,98	0,01	4,98	0,01	5,00	0,00	5,03	0,01	5,00	0,01	5,02	0,01
An	0,49	0,13	63,19	3,34	1,02	0,79	40,44	13,91	0,15	0,07	50,23	14,09	0,70	0,77	49,43	1,14
Ab	12,29	4,29	36,29	3,38	18,31	8,91	59,04	13,89	7,10	0,42	48,59	13,83	10,39	3,20	49,93	1,13
Or	87,23	4,33	0,52	0,10	80,64	9,43	0,52	0,08	92,80	0,42	1,19	0,41	88,91	3,26	0,61	0,16

Tab. S5.3l – Average major elements composition (wt.%) for feldspars from the felsic samples.

Crn-bearing leucocratic rock AN22B				Paragneiss AN06D				Felsic granulite AN19				AN18	
Kfs		Pl		Kfs		Pl		Kfs		Pl		Pl	
6	σ	5	σ	10	σ	10	σ	3	σ	8	σ	16	σ
65,00	0,46	57,05	0,18	64,88	1,09	57,51	3,59	65,20	0,71	60,81	2,87	58,28	0,25
0,02	0,03	0,01	0,01	0,02	0,02	0,02	0,02	0,02	0,02	0,01	0,01	0,02	0,02
19,32	0,18	27,98	0,14	19,60	1,68	27,97	2,72	19,28	0,19	25,75	2,19	26,99	0,17
0,02	0,03	0,00	0,00	0,01	0,02	0,02	0,03	0,03	0,03	0,01	0,02	0,01	0,01
0,01	0,03	0,04	0,04	0,05	0,03	0,41	0,78	0,08	0,08	0,29	0,73	0,03	0,02
0,01	0,02	0,02	0,01	0,01	0,02	0,01	0,02	0,01	0,01	0,01	0,02	0,01	0,01
0,01	0,01	0,01	0,01	0,01	0,01	0,41	0,85	0,00	0,00	0,08	0,20	0,00	0,01
0,13	0,05	9,47	0,11	0,63	1,74	6,44	3,18	0,12	0,09	5,41	1,65	8,48	0,12
1,43	0,61	6,62	0,12	1,30	1,72	6,00	3,08	1,05	0,31	7,72	1,90	6,81	0,10
14,47	0,86	0,14	0,03	14,25	3,66	1,86	3,63	14,93	0,55	1,05	2,67	0,26	0,03
100,43	0,55	101,34	0,21	100,78	0,55	100,64	1,77	100,73	0,96	101,17	0,82	100,89	0,41
2,97	0,00	2,53	0,01	2,96	0,08	2,57	0,08	2,98	0,01	2,68	0,08	2,59	0,01
0,00	0,00	0,00	0,00	0,00	0,00	0,00	0,00	0,00	0,00	0,00	0,00	0,00	0,00
1,04	0,01	1,46	0,01	1,05	0,08	1,48	0,20	1,04	0,01	1,34	0,14	1,41	0,01
0,00	0,00	0,00	0,00	0,00	0,00	0,00	0,00	0,00	0,00	0,00	0,00	0,00	0,00
0,00	0,00	0,00	0,00	0,00	0,00	0,02	0,03	0,00	0,00	0,01	0,03	0,00	0,00
0,00	0,00	0,00	0,00	0,00	0,00	0,00	0,00	0,00	0,00	0,00	0,00	0,00	0,00
0,00	0,00	0,00	0,00	0,00	0,00	0,00	0,00	0,00	0,00	0,00	0,00	0,00	0,00
0,01	0,00	0,45	0,00	0,03	0,08	0,30	0,15	0,01	0,00	0,25	0,08	0,40	0,01
0,13	0,05	0,57	0,01	0,11	0,15	0,51	0,26	0,09	0,03	0,66	0,16	0,59	0,01
0,84	0,05	0,01	0,00	0,83	0,22	0,11	0,22	0,87	0,03	0,06	0,16	0,01	0,00
4,99	0,01	5,03	0,00	4,99	0,01	5,00	0,04	4,99	0,00	5,01	0,01	5,01	0,01
0,63	0,22	43,84	0,64	2,98	8,16	30,26	13,95	0,57	0,46	25,68	7,00	40,20	0,61
12,95	5,40	55,36	0,73	11,44	14,43	50,62	25,19	9,57	2,84	66,68	13,08	58,36	0,49
86,40	5,50	0,78	0,16	85,57	22,57	19,13	38,75	89,83	3,08	7,66	19,98	1,43	0,20

Table S5.3m – Average major elements composition (wt.%) for garnet from the studied samples.

Garnet Sample	Migmatitic paragneiss								Mylonitic paragneisses						Crn-bearing leucocratic rock					
	AN11				AN09				AN09C3			AN22A			AN22B					
	core		rim		core		rim		core		rim	core		rim	core		rim			
Texture position																				
N of analysis	4	σ	4	σ	6	σ	6	σ	8	σ	7	σ	8	σ	3	σ	6	σ	3	σ
SiO2	38,25	0,28	38,24	0,42	38,07	0,12	38,08	0,16	37,93	0,23	37,81	0,35	32,85	12,32	37,03	0,14	36,60	0,16	36,59	0,23
TiO2	0,12	0,20	0,03	0,02	0,03	0,03	0,03	0,02	0,01	0,01	0,02	0,02	0,04	0,03	0,03	0,01	0,04	0,03	0,02	0,02
Al2O3	22,00	0,09	22,28	0,15	22,71	0,17	22,61	0,20	22,09	0,11	21,84	0,37	20,02	7,51	22,40	0,16	22,27	0,18	22,38	0,16
Cr2O3	0,02	0,01	0,03	0,01	0,03	0,03	0,01	0,01	0,10	0,04	0,11	0,05	0,02	0,02	0,03	0,04	0,02	0,03	0,01	0,01
FeOT	31,46	0,24	32,05	0,90	30,68	0,52	30,78	0,46	31,40	1,12	31,57	1,43	29,00	10,88	33,06	0,79	32,80	0,47	33,07	0,59
MnO	1,02	0,03	1,06	0,08	0,54	0,05	0,55	0,04	1,57	0,05	1,64	0,12	0,82	0,32	0,95	0,17	3,18	0,25	3,18	0,17
MgO	6,56	0,26	6,05	0,64	8,37	0,24	8,15	0,16	5,98	0,59	5,80	0,88	5,63	2,11	6,04	0,53	3,97	0,17	4,04	0,30
CaO	2,08	0,08	2,23	0,07	1,54	0,18	1,48	0,07	2,28	0,30	2,31	0,38	1,89	0,71	2,02	0,10	2,70	0,18	2,53	0,27
Na2O	0,00	0,00	0,00	0,00	0,01	0,01	0,01	0,01	0,13	0,07	0,17	0,04	0,02	0,03	0,01	0,02	0,01	0,03	0,01	0,01
K2O	0,00	0,00	0,01	0,01	0,00	0,01	0,00	0,01	0,11	0,02	0,12	0,03	0,00	0,00	0,00	0,00	0,00	0,00	0,00	0,01
Total	101,52	0,38	101,98	0,34	101,98	0,35	101,72	0,48	101,67	0,31	101,43	0,68	90,28	33,86	101,57	0,62	101,60	0,44	101,84	0,32
Cat./O	2/3																			
Si	2,96	0,01	2,95	0,03	2,90	0,01	2,91	0,01	2,91	0,01	2,91	0,02	2,54	0,95	2,87	0,02	2,87	0,01	2,87	0,02
Ti	0,01	0,01	0,00	0,00	0,00	0,00	0,00	0,00	0,00	0,00	0,00	0,00	0,00	0,00	0,00	0,00	0,00	0,00	0,00	0,00
Al	2,00	0,00	2,03	0,02	2,04	0,01	2,04	0,02	2,00	0,01	1,98	0,03	1,82	0,68	2,05	0,00	2,06	0,01	2,07	0,01
Cr	0,00	0,00	0,00	0,00	0,00	0,00	0,00	0,00	0,01	0,00	0,01	0,00	0,00	0,00	0,00	0,00	0,00	0,00	0,00	0,00
Fe2+	1,97	0,02	2,00	0,07	1,79	0,04	1,82	0,02	1,76	0,09	1,75	0,11	1,67	0,63	1,94	0,08	1,95	0,04	1,97	0,03
Fe3+	0,07	0,00	0,07	0,04	0,17	0,02	0,15	0,01	0,26	0,02	0,28	0,06	0,21	0,08	0,21	0,03	0,20	0,03	0,20	0,04
Mn	0,07	0,00	0,07	0,01	0,03	0,00	0,04	0,00	0,10	0,00	0,11	0,01	0,05	0,02	0,06	0,01	0,21	0,02	0,21	0,01
Ni	0,00	0,00	0,00	0,00	0,00	0,00	0,00	0,00	0,01	0,00	0,00	0,00	0,00	0,00	0,00	0,00	0,00	0,00	0,00	0,00
Mg	0,76	0,03	0,70	0,07	0,95	0,03	0,93	0,02	0,68	0,07	0,67	0,10	0,65	0,24	0,70	0,06	0,46	0,02	0,47	0,03
Ca	0,17	0,01	0,18	0,01	0,13	0,01	0,12	0,01	0,19	0,02	0,19	0,03	0,16	0,06	0,17	0,01	0,23	0,02	0,21	0,02
Na	0,00	0,00	0,00	0,00	0,00	0,00	0,00	0,00	0,02	0,01	0,03	0,01	0,00	0,00	0,00	0,00	0,00	0,00	0,00	0,00
K	0,00	0,00	0,00	0,00	0,00	0,00	0,00	0,00	0,01	0,00	0,01	0,00	0,00	0,00	0,00	0,00	0,00	0,00	0,00	0,00
Tot cations	8,00	0,00	8,00	0,00	8,00	0,00	8,00	0,00	8,00	0,00	8,00	0,00	7,11	2,67	8,00	0,00	8,00	0,00	8,00	0,00
XFe	0,73	0,01	0,75	0,02	0,67	0,01	0,68	0,01	0,75	0,03	0,75	0,04	0,66	0,25	0,75	0,02	0,82	0,01	0,82	0,01
py	25,52	0,93	23,59	2,42	32,77	0,99	31,96	0,69	25,06	2,35	24,49	3,62	22,84	8,58	24,36	2,25	16,25	0,67	16,49	1,15
alm	66,40	0,66	67,81	2,19	61,70	1,26	62,64	0,76	64,36	3,20	64,56	4,15	58,65	22,00	67,61	2,21	68,40	1,31	68,70	0,80
sps	2,26	0,06	2,34	0,18	1,19	0,12	1,23	0,09	3,73	0,13	3,94	0,34	1,89	0,73	2,18	0,38	7,41	0,56	7,38	0,35
grs	5,82	0,26	6,25	0,22	4,34	0,52	4,16	0,20	6,86	0,86	7,02	1,08	5,50	2,08	5,85	0,32	7,95	0,55	7,44	0,84

Table S5.3n – Average major elements composition (wt.%) for garnet from the studied samples.

Mylonitic amphibolites				Paragneiss AN06D				Gabbro		Felsic granulite														
AN01H		AN01D		AN06D		AN08B		AN07B		AN19		AN18												
core	rim	core	rim	core	rim	core	rim	core	rim	core	rim	core	rim											
g	σ	2	σ	6	σ	2	σ	12	σ	7	σ	3	σ	9	σ	15	σ	5	rim	σ	6	σ	9	σ
38,49	0,44	38,23	0,49	38,33	0,48	38,16	0,17	38,01	0,22	37,72	1,00	38,33	0,05	37,17	0,21	37,61	0,23	37,71	0,09	37,73	0,14	37,80	0,27	
0,06	0,03	0,08	0,05	0,07	0,02	0,04	0,02	0,04	0,04	0,03	0,02	0,08	0,02	0,09	0,03	0,03	0,03	0,03	0,04	0,01	0,02	0,01	0,02	
21,80	0,31	21,92	0,06	20,94	0,26	20,93	0,18	23,07	0,20	22,81	0,57	21,60	0,27	21,60	0,20	23,04	0,16	23,05	0,14	22,93	0,17	23,05	0,15	
0,03	0,05	0,02	0,02	0,01	0,02	0,00	0,00	0,05	0,03	0,04	0,03	0,10	0,05	0,15	0,04	0,03	0,03	0,03	0,03	0,02	0,03	0,02	0,03	
28,74	0,39	28,89	0,63	26,04	0,24	26,76	0,04	27,42	0,37	27,31	0,43	25,79	0,20	25,39	0,47	30,38	0,36	30,21	0,33	28,90	0,37	29,10	0,41	
1,60	0,23	1,90	0,30	1,88	0,18	2,00	0,13	0,48	0,04	0,50	0,02	3,84	0,16	5,27	0,14	0,43	0,04	0,43	0,04	0,49	0,02	0,43	0,04	
3,95	0,28	3,12	0,42	0,80	0,25	0,75	0,05	10,48	0,25	10,36	0,29	4,00	0,22	3,95	0,27	8,85	0,26	8,80	0,10	9,37	0,30	9,45	0,35	
7,84	0,48	8,32	0,98	13,74	0,73	12,93	0,24	1,70	0,07	1,75	0,05	8,18	0,59	7,55	0,22	1,38	0,02	1,38	0,02	1,75	0,08	1,77	0,13	
0,01	0,01	0,03	0,01	0,02	0,02	0,00	0,00	0,01	0,02	0,01	0,03	0,01	0,01	0,02	0,02	0,01	0,01	0,01	0,01	0,03	0,03	0,02	0,02	
0,00	0,00	0,01	0,01	0,00	0,00	0,00	0,00	0,01	0,02	0,01	0,01	0,00	0,00	0,00	0,01	0,00	0,00	0,00	0,00	0,00	0,01	0,00	0,00	
102,55	0,52	102,51	0,17	101,84	0,70	101,57	0,39	101,28	0,30	100,57	1,86	101,93	0,03	101,20	0,30	101,76	0,50	101,67	0,28	101,23	0,24	101,67	0,59	
2,96	0,03	2,95	0,03	2,99	0,02	3,00	0,00	2,86	0,01	2,86	0,02	2,96	0,00	2,90	0,01	2,86	0,01	2,87	0,01	2,87	0,01	2,86	0,01	
0,00	0,00	0,00	0,00	0,00	0,00	0,00	0,00	0,00	0,00	0,00	0,00	0,00	0,00	0,01	0,00	0,00	0,00	0,00	0,00	0,00	0,00	0,00	0,00	
1,98	0,03	2,00	0,01	1,93	0,01	1,94	0,01	2,05	0,01	2,04	0,01	1,97	0,02	1,99	0,01	2,06	0,01	2,07	0,01	2,05	0,01	2,05	0,01	
0,00	0,00	0,00	0,00	0,00	0,00	0,00	0,00	0,00	0,00	0,00	0,00	0,01	0,00	0,01	0,00	0,00	0,00	0,00	0,00	0,00	0,00	0,00	0,00	
1,76	0,03	1,78	0,08	1,62	0,05	1,69	0,00	1,51	0,03	1,50	0,03	1,57	0,04	1,46	0,04	1,70	0,03	1,73	0,02	1,62	0,05	1,61	0,04	
0,09	0,04	0,09	0,05	0,08	0,05	0,07	0,01	0,22	0,03	0,24	0,06	0,09	0,02	0,20	0,02	0,23	0,03	0,19	0,03	0,22	0,02	0,23	0,02	
0,10	0,01	0,12	0,02	0,12	0,01	0,13	0,01	0,03	0,03	0,03	0,00	0,25	0,01	0,35	0,01	0,03	0,00	0,03	0,00	0,03	0,00	0,03	0,00	
0,00	0,00	0,00	0,00	0,00	0,00	0,00	0,00	0,00	0,00	0,00	0,00	0,00	0,00	0,00	0,00	0,00	0,00	0,00	0,00	0,00	0,00	0,00	0,00	
0,45	0,03	0,36	0,05	0,09	0,03	0,09	0,01	1,18	0,03	1,17	0,02	0,46	0,02	0,46	0,03	1,00	0,03	1,00	0,01	1,06	0,03	1,07	0,04	
0,65	0,04	0,69	0,08	1,15	0,06	1,09	0,02	0,14	0,01	0,14	0,01	0,68	0,05	0,63	0,02	0,11	0,00	0,11	0,00	0,14	0,01	0,14	0,01	
0,00	0,00	0,00	0,00	0,00	0,00	0,00	0,00	0,00	0,00	0,00	0,00	0,00	0,00	0,00	0,00	0,00	0,00	0,00	0,00	0,00	0,00	0,00	0,00	
0,00	0,00	0,00	0,00	0,00	0,00	0,00	0,00	0,00	0,00	0,00	0,00	0,00	0,00	0,00	0,00	0,00	0,00	0,00	0,00	0,00	0,00	0,00	0,00	
8,00	0,00	8,00	0,00	8,00	0,00	8,00	0,00	8,00	0,00	8,00	0,00	8,00	0,00	8,00	0,00	8,00	0,00	8,00	0,00	8,00	0,00	8,00	0,00	
0,80	0,01	0,84	0,02	0,95	0,02	0,95	0,00	0,59	0,01	0,60	0,01	0,78	0,01	0,78	0,01	0,66	0,01	0,66	0,00	0,63	0,01	0,63	0,01	
15,31	1,07	12,16	1,49	3,11	0,97	2,95	0,21	41,29	0,94	41,21	0,54	15,55	0,82	15,86	1,04	35,25	1,03	34,83	0,50	37,21	1,27	37,46	1,23	
59,31	0,83	60,24	2,24	54,21	1,44	56,36	0,03	52,81	0,87	52,64	0,63	53,12	1,17	50,35	1,14	59,83	1,08	60,27	0,51	56,70	1,42	56,51	1,34	
3,53	0,49	4,21	0,72	4,17	0,39	4,43	0,32	1,08	0,08	1,13	0,07	8,48	0,35	12,02	0,36	0,97	0,09	0,98	0,09	1,11	0,06	0,98	0,08	
21,85	1,40	23,38	3,01	38,51	2,34	36,27	0,50	4,82	0,20	5,02	0,22	22,85	1,68	21,77	0,61	3,95	0,07	3,93	0,05	4,98	0,23	5,05	0,35	

Table S5.3o – Average major elements composition (wt.%) for biotite from the studied samples.

Biotite Sample	Migmatitic paragneiss				Mylonitic paragneisses				Crn-bearing leucocratic rock				Paragneiss		Felsic granulite			
	AN11		AN09		AN09C3		AN22A		AN22B		AN06D		AN19		AN18			
N of analysis	8	σ	4	σ	9	σ	14	σ	16	σ	3	σ	6	σ	6	σ		
SiO ₂	36,17	0,52	38,52	0,19	35,42	0,51	36,15	0,35	34,54	0,26	36,74	1,60	35,87	0,78	37,42	0,30		
TiO ₂	5,05	0,50	4,98	0,70	3,93	1,50	5,06	0,84	3,69	0,40	6,14	0,39	5,75	1,13	6,02	0,58		
Al ₂ O ₃	17,15	0,41	15,09	0,21	17,64	0,57	18,14	0,51	19,90	0,39	16,41	0,36	16,10	1,18	16,42	0,48		
FeO ^T	13,83	0,68	11,15	0,46	16,80	1,39	16,80	0,59	20,60	0,97	15,85	6,65	21,69	1,69	11,66	0,39		
MnO	0,02	0,01	0,02	0,02	0,34	0,06	0,02	0,02	0,08	0,03	0,12	0,10	0,07	0,04	0,02	0,01		
MgO	12,99	0,53	16,79	0,70	11,58	0,81	11,68	0,39	8,97	0,64	11,72	3,44	8,32	1,50	15,40	0,56		
CaO	0,01	0,01	0,01	0,01	0,09	0,12	0,02	0,02	0,02	0,02	0,10	0,05	0,02	0,02	0,09	0,06		
Na ₂ O	0,10	0,02	0,11	0,01	0,26	0,07	0,13	0,07	0,14	0,05	0,09	0,04	0,07	0,03	0,08	0,03		
K ₂ O	9,38	0,55	9,95	0,13	7,47	3,23	9,73	0,11	9,46	0,34	8,66	1,07	9,05	0,59	8,88	0,81		
Total	94,70	0,83	96,60	0,29	93,52	3,61	97,72	0,80	97,38	0,79	2,72	0,04	96,93	0,74	95,98	1,15		
Cat./O	8/11																	
Si	2,70	0,02	2,79	0,01	2,69	0,05	2,40	0,07	2,09	0,06	1,44	0,02	2,71	0,02	2,69	0,05		
Ti	0,28	0,03	0,27	0,04	0,22	0,08	0,25	0,04	0,17	0,02	0,34	0,01	0,33	0,06	0,33	0,03		
Al	1,51	0,04	1,29	0,02	1,58	0,08	1,42	0,07	1,42	0,06	0,99	0,44	1,44	0,10	1,39	0,06		
Fe ^T	0,86	0,05	0,67	0,03	1,07	0,09	0,93	0,05	1,04	0,05	0,01	0,01	1,37	0,12	0,70	0,02		
Mn	0,00	0,00	0,00	0,00	0,02	0,00	0,00	0,00	0,00	0,00	1,29	0,34	0,00	0,00	0,00	0,00		
Mg	1,45	0,05	1,81	0,07	1,31	0,10	1,16	0,06	0,81	0,06	0,00	0,00	0,94	0,17	1,65	0,06		
Ca	0,00	0,00	0,00	0,00	0,01	0,01	0,00	0,00	0,00	0,00	0,01	0,00	0,00	0,00	0,01	0,00		
Na	0,02	0,00	0,01	0,00	0,04	0,01	0,02	0,01	0,02	0,01	0,01	0,01	0,01	0,00	0,01	0,00		
K	0,89	0,05	0,92	0,01	0,72	0,31	0,82	0,03	0,73	0,04	0,82	0,08	0,87	0,05	0,81	0,07		
Tot cations	7,71	0,03	7,76	0,03	7,67	0,16	7,71	0,04	7,70	0,02	7,63	0,03	7,68	0,07	7,66	0,05		
XMg	0,63	0,02	0,73	0,02	0,55	0,03	0,55	0,01	0,44	0,03	0,57	0,18	0,40	0,05	0,70	0,01		

Table S5.3p – Average major elements composition (wt.%) for other phases from the studied samples

Sample Mineral	Ultramylonitic paragneiss			Promylonitic paragneiss		Crn-bearing leucocratic rock	
	AN09C3 Ms altered	AN09C3 Ms	AN09C3 Chl	AN22A1 Spinel	AN22A1 Hercynite	AN22B1 Spinel	AN22B1 Hercynite Corundum
SiO ₂	49,40	47,64	39,04	0,01		0,00	0,00
TiO ₂	0,03	0,02	0,00	0,00		0,00	0,02
Al ₂ O ₃	29,9	34,55	32,87	61,87		61,66	103,27
Cr ₂ O ₃	0,15	0,03	0,15	0,42		0,36	0,00
FeO	2,98	2,13	1,17	24,75		37,15	0,26
MnO	0,27	0,30	0,23	0,05		0,27	0,00
NiO	0,03	0,04	0,01	0,11		0,03	0,04
MgO	2,68	0,39	0,00	4,45		3,70	0,00
CaO	0,17	0,01	25,24	0,02		0,00	0,00
Na ₂ O	0,23	0,14	0,13	0,77		0,05	0,00
K ₂ O	9,75	10,28	0,10	0,01		0,00	0,00
ZnO				11,84		1,34	0,00
Total	95,70	95,63	99,02	104,30		104,57	103,61

Table S5.4a – Average trace elements concentration (ppm) in clinopyroxene from the studied ~~fire~~ rocks.

Amphibole Sample Texture N of analysis	Scp-bearing gneiss AN10		Mylonitic amphibolite				AN01D (Cpx/Pl-rich)		AN08C		Gabbro				AN07B	
	11	σ	AN01A (Amph-rich)		Amphll		25	σ	12	σ	AN08B		AN07B			
			Amphl	σ	6	σ					coarse grained	σ	4	σ		
Li7	12,57	8,64	10,46	5,90	11,61	4,01	4,21	1,31	10,39	5,18	16,62			8,77	3,41	
Be9			12,14	5,86	13,94	7,15	11,27	3,57	16,56	10,60	11,49			12,75	6,42	
B11	17,70	3,19	14,16	4,55	18,12	7,29	13,97	5,19	14,34			35,52				
Mg25	54877,35	1607,08	40834,56	1247,17	36281,58	896,07	51126,02	2589,37	62235,05	1466,85	60314,00	3100,02	57982,98	1124,37	64850,33	4353,93
Si29	187219,12	4170,37	187072,30	4569,98	185932,03	5675,06	188348,80	7995,09	195112,87	4958,45	184345,03	2774,67	182997,85	4042,39	197053,00	4058,66
Ca43	85717,82	2658,07	84239,47	2038,72	83944,23	2262,90	81938,52	1868,99	80181,66	1324,77	83403,82	3668,36	82773,34	5057,00	80203,53	2868,35
Ca44	84334,71	0,00	82905,32	0,00	82905,33	0,01	82190,61	0,01	81475,89	0,02	81475,92	0,01	81475,92	0,01	81475,91	0,00
Sc45	48,73	2,78	80,44	3,71	57,91	3,77	55,83	4,58	53,28	2,73	52,07	2,14	52,24	1,50	54,24	1,96
Ti49	12247,31	580,95	13455,50	772,23	13421,85	1172,24	14847,92	1055,85	12725,98	791,43	12913,30	1017,35	13871,36	532,75	13536,45	1287,64
V51	414,94	22,06	605,32	52,22	588,92	65,05	507,81	50,37	458,15	44,10	486,50	50,83	530,09	65,03	469,65	19,34
Cr53	589,34	40,87	232,38	11,18	223,85	68,85	164,21	21,50	890,44	89,21	841,23	32,69	907,71	23,95	860,57	30,95
Co59	75,45	2,15	57,74	1,75	61,11	2,08	73,42	3,67	80,11	2,62	86,52	5,13	89,23	5,36	90,13	2,82
Ni60	184,41	6,74	101,39	6,71	106,83	7,50	105,92	17,51	292,35	17,89	375,05	49,68	401,84	46,98	416,98	23,30
Zn66	127,27	7,13	233,86	11,74	240,01	12,77	182,56	12,90	168,46	8,23	202,17	14,00	215,89	21,64	215,92	6,51
Rb85	23,00	1,68	24,23	5,36	35,03	8,01	16,08	1,95	6,03	0,49	6,38	0,79	6,64	0,39	6,86	0,27
Sr88	38,53	4,64	29,60	3,88	37,51	5,22	32,94	8,91	68,51	8,50	77,46	9,64	82,11	5,24	82,84	1,44
Y89	35,34	3,65	102,62	3,64	32,35	6,50	51,54	2,63	37,38	1,37	37,56	1,12	41,02	1,65	31,56	1,25
Zr90	56,21	7,96	48,79	11,67	42,06	4,90	63,03	15,85	65,32	2,71	66,20	3,76	63,69	3,72	69,97	4,45
Nb93	2,62	0,53	23,53	1,04	13,79	2,96	4,34	0,48	6,16	0,39	11,28	3,25	14,83	0,74	9,92	1,61
Cs133	0,27	0,05	0,08	0,03	0,10	0,03	0,20	0,13	0,05	0,01	0,07		0,06	0,00	0,04	
Ba138	87,26	6,21	105,96	34,80	311,67	61,91	20,12	4,74	48,69	6,04	61,71	6,04	69,76	4,32	58,90	2,83
La139	1,56	0,38	31,48	15,21	21,85	5,48	6,55	0,74	5,39	0,69	10,61	1,68	12,19	1,21	11,69	0,99
Ce140	6,70	1,33	112,11	43,55	54,01	15,14	18,66	1,28	13,23	1,40	27,14	5,31	32,40	3,22	33,41	1,69
Pr141	1,44	0,25	18,35	5,74	7,16	2,35	3,16	0,21	2,03	0,18	4,49	1,04	5,09	0,53	5,69	0,62
Nd146	9,83	0,98	93,32	22,98	33,92	12,23	17,54	0,83	11,06	0,95	22,64	4,72	28,40	3,36	28,55	2,96
Sm149	4,08	0,60	22,67	3,12	7,68	2,99	6,06	0,86	3,70	0,37	6,14	1,68	8,12	0,17	7,81	2,37
Eu151	1,15	0,33	2,92	0,19	1,29	0,28	1,99	0,18	1,34	0,17	1,94	0,47	2,24	0,22	1,92	0,18
Gd157	5,19	0,70	20,02	2,28	7,06	2,52	7,31	0,86	4,85	0,47	6,75	1,49	8,07	1,55	6,47	0,86
Tb159	0,99	0,18	3,33	0,10	1,06	0,41	1,44	0,13	0,98	0,11	1,22	0,17	1,37	0,19	1,05	0,14
Dy163	6,35	0,78	20,59	0,75	6,07	1,41	9,14	0,79	6,42	0,53	7,14	0,55	7,22	0,99	5,84	1,03
Ho165	1,37	0,23	4,02	0,12	1,29	0,27	2,05	0,14	1,43	0,07	1,42	0,18	1,62	0,16	1,19	0,17
Er167	4,01	0,76	10,60	0,74	3,27	0,54	5,73	0,51	3,92	0,34	3,54	0,64	4,15	0,36	3,19	0,56
Tm169	0,58	0,12	1,66	0,16	0,43	0,05	0,78	0,09	0,58	0,05	0,57	0,11	0,59	0,17	0,43	0,11
Yb173	4,20	0,88	11,77	1,08	3,32	0,46	5,83	0,81	4,12	0,45	4,57	1,04	4,00	0,38	3,59	0,43
Lu175	0,55	0,12	1,62	0,16	0,51	0,08	0,79	0,09	0,61	0,07	0,54	0,10	0,50	0,10	0,40	0,03
Hf177	2,14	0,50	3,59	0,96	2,83	0,67	2,93	0,60	1,80	0,38	2,06	0,38	2,00	0,38	2,33	0,23
Ta181	0,14	0,04	1,59	0,13	0,87	0,47	0,60	0,17	0,34	0,05	0,72	0,35	1,19	0,15	0,39	0,08
Pb208	0,18	0,05	8,81	0,70	8,71	0,82	4,73	0,55	1,64	0,18	1,66	0,32	1,91	0,37	1,69	0,26
Th232	0,06	0,02	0,46	0,44	0,15	0,02	0,09	0,05	0,48	0,06	0,46	0,10	0,58	0,12	0,43	0,12
U238	0,05		0,05	0,02			0,05	0,02	0,13	0,04	0,17	0,06	0,13	0,06	0,13	0,08

Table S5.4b – Average trace elements concentration (ppm) in amphibole from the studied mafic rocks.

Clinopyroxene Sample N of analysis	Scp-bearing gneiss AN10		Mylonitic amphibolite				Calc-silicate AN06C		AN07B (coarse-grained)		AN07B (fine-grained)		Gabbro AN08B		AN08C	
	8	σ	AN01A (Amph-rich)		AN01D (Cpx/Pl-rich)		6	σ	4	σ	5	σ	10	σ	13	σ
			10	σ	21	σ										
Li7	42,77	12,24	38,86	9,63	32,23	8,03	10,93	4,53	14,86	5,73	29,83	8,19	25,06	8,48	22,22	7,88
Be9	18,28		16,43		9,32		1,49				18,78	5,39	15,99	3,64		
B11	13,47	2,05	18,47	6,04	15,38	4,48	15,72	5,26			23,54	9,53	15,69	2,80		
Mg25	78825,14	4341,70	55545,52	1615,26	23541,00	2391,31	36744,37	1397,64	65751,06	536,48	77411,88	2221,52	69944,54	3813,42	73860,01	903,74
Si29	247719,65	13105,66	246006,00	6119,42	225883,96	9461,51	230543,45	14116,15	245482,36	4736,91	245961,36	5025,95	231514,43	8070,67	242984,59	1894,66
Ca43	168499,26	4472,43	161517,49	2519,24	155958,46	3311,79	160132,13	1893,36	155064,92	1372,40	151395,49	3856,09	154361,38	4234,85	154136,46	2964,26
Ca44	168669,42	0,00	162237,15	0,01	155804,82	0,01	22,60	0,00	154375,43	0,01	154375,42	0,01	154375,42	0,00	154595,28	343,36
Sc45	47,06	3,01	55,50	4,32	53,29	7,08	66,06	18,00	61,85	4,58	62,68	4,76	56,70	3,41	54,83	4,85
Ti49	887,48	249,52	1133,99	379,41	2963,69	442,35	1196,79	163,23	2979,75	183,69	2061,06	261,34	2519,10	476,55	2148,85	159,34
V51	179,06	30,64	288,35	36,02	654,18	151,97	373,18	117,99	506,74	26,59	266,14	15,84	310,94	30,09	261,14	32,23
Cr53	243,64	53,87	118,16	13,12	138,55	27,47	618,08	442,36	326,93	102,13	420,21	26,90	525,97	171,48	361,53	112,46
Co59	46,02	2,42	46,36	2,43	80,50	2,73	40,67	2,83	75,31	4,57	64,39	4,16	61,64	5,16	51,75	1,22
Ni60	88,66	5,36	66,22	2,82	167,95	9,59	76,42	10,07	382,40	53,73	260,25	19,64	231,36	47,31	146,27	8,18
Zn66	73,61	6,79	164,25	7,15	177,60	10,47	150,62	17,14	163,11	7,83	147,38	13,03	140,93	13,31	109,76	7,69
Rb85	0,33	0,10	0,10	0,04	0,15	0,06	0,09	0,10	0,09	0,10	0,19	0,17	0,17	0,04	0,13	0,01
Sr88	9,26	0,97	11,32	1,19	25,70	2,00	25,80	3,12	21,29	5,34	15,88	1,28	16,45	1,61	14,10	0,94
Y89	3,52	0,88	4,99	1,90	4,75	2,24	2,72	0,72	13,23	1,30	14,81	2,04	17,35	3,60	16,23	0,79
Zr90	15,32	6,69	28,88	21,47	117,54	16,55	74,08	12,22	62,97	1,96	56,18	3,64	50,24	2,85	51,37	3,30
Nb93	0,10	0,01	0,06	0,02	0,07	0,04	0,01	0,00	0,10	0,04	0,09		0,16	0,06	0,08	0,01
Cs133			0,03	0,02	0,03	0,01	0,02	0,01	0,04		0,05		0,05	0,02	0,04	0,01
Ba138	0,22	0,13	1,68	2,12	0,48	0,92	0,29	0,29	0,16	0,06	0,35	0,27	0,32	0,40	0,14	0,09
La139	0,15	0,05	2,01	0,46	2,34	0,63	1,48	0,59	5,19	0,34	3,52	0,29	3,92	0,57	1,62	0,18
Ce140	0,54	0,14	4,94	1,21	5,83	1,78	4,17	1,58	17,89	1,56	11,93	1,30	12,43	2,39	4,92	0,36
Pr141	0,12	0,04	0,64	0,24	0,67	0,19	0,61	0,24	3,75	0,24	2,10	0,29	2,09	0,53	0,84	0,11
Nd146	0,79	0,25	2,90	1,04	2,99	0,98	2,58	0,87	18,99	2,18	10,86	2,60	10,86	3,40	4,28	0,70
Sm149	0,64	0,25	0,81	0,33	0,87	0,40	0,63	0,19	6,07	0,31	3,47	0,49	3,64	1,42	1,53	0,36
Eu151	0,17	0,09	0,25	0,07	0,32	0,11	0,15	0,03	1,13	0,12	0,65	0,15	0,96	0,33	0,56	0,10
Gd157	0,58	0,14	0,80	0,39	0,79	0,35	0,53	0,18	4,47	1,10	3,19	0,60	3,38	1,32	2,18	0,39
Tb159	0,09	0,04	0,14	0,08	0,15	0,06	0,10	0,03	0,64	0,06	0,58	0,13	0,59	0,21	0,42	0,07
Dy163	0,61	0,25	0,87	0,46	0,91	0,35	0,51	0,11	3,35	0,33	2,55	0,62	3,49	0,79	2,92	0,31
Ho165	0,19	0,06	0,21	0,10	0,21	0,10	0,12	0,06	0,50	0,04	0,62	0,05	0,70	0,20	0,61	0,06
Er167	0,56	0,25	0,58	0,22	0,60	0,27	0,28	0,06	1,12	0,37	1,86	0,60	1,95	0,70	1,90	0,20
Tm169	0,07	0,03	0,09	0,04	0,11	0,05	0,06	0,02	0,16	0,02	0,24	0,04	0,26	0,09	0,29	0,04
Yb173	0,54	0,16	0,99	0,38	1,10	0,51	0,60	0,11	1,09	0,25	1,83	0,36	1,86	0,55	2,18	0,34
Lu175	0,13	0,06	0,18	0,05	0,27	0,11	0,16	0,04	0,27	0,09	0,28	0,05	0,35	0,17	0,33	0,07
Hf177	0,85	0,27	1,64	1,00	3,29	0,67	2,27	0,51	2,14	0,36	1,46	0,31	1,69	0,40	1,41	0,20
Ta181	0,02		0,04		0,90	1,81	0,01	0,00	0,04	0,00	0,04	0,01	0,08	0,05	0,05	0,03
Pb208	0,12	0,01	1,65	0,16	1,19	0,18	1,22	0,26	0,21	0,03	0,26	0,08	0,29	0,09	0,22	0,07
Th232	0,04		0,05	0,01	0,06	0,04	0,03	0,03	0,19	0,08	0,11	0,04	0,18	0,06	0,16	0,05
U238			0,02	0,01	0,04	0,02	0,02	0,00	0,06	0,03	0,05	0,03	0,13	0,05	0,07	0,02

Table S5.5 – Geothermobarometry results of the studied samples across the Anzola shear zone. Results are reported as median values and relative standard deviations.

Method			Ti-in-Amphibole (0,7 GPa) Liao et al., 2021			Zr-in-Rutile (0,7 GPa) Kohn, 2020		Grt-Bt Holdaway, 2000	GASP Holdaway, 2001	
Location	Sample	Texture position	Ti (a.p.f.u.)	Si (a.p.f.u.)	T (°C)	Zr (ppm)	T (°C)	T (°C)	P (GPa)	
Hanging wall	Migmatitic paragneiss	AN11				1105±603	716±65	600±40	0,8	
	Scp-bearing gneiss	AN10	0,22	6,19	818±28					
Shear Zone	<i>Paragneiss</i>	AN09				1654±250	796±20	580±10	0,7	
		AN09C						680±20	0,8	
		AN22A						660±10	0,7	
		AN22B						700±20	0,8	
	<i>Crn-bearing leucocratic rock</i>	AN01A	includi	0,3	6,13	903				
			big	0,27	6,1	883±20				
			rix	0,23	6,16	839±22				
		AN01C	includi	0,26	6,45	866±7				
			big	0,29	6,36	898±31				
			rix	0,22	6,47	821±35				
		AN01D	includi	0,28	6,19	888±34				
			big	0,27	6,28	872±32				
			rix	0,23	6,31	833±29				
		<i>Amphibolite</i>	AN01	big	0,22	6,44	831±48			
rix	0,19			6,45	805±42					
AN01H	includi		0,24	6,5	846±13					
	big		0,25	6,47	856±29					
	rix	0,18	6,62	802±50						
Footwall	Paragneiss	AN06D				1100±288	745±30	750±100	0,8	
	Felsic granulite	AN19				1942±505	816±30	900±20	0,7	
		AN18				2028±440	815±35	830±50	0,8	

APPENDIX 3:
U-Pb titanite dating on
case study 2 samples

A.3 U-Pb titanite dating on case study 2 samples

This section concerns a petro-chronological and microstructural study of titanite from mylonitic amphibolites forming the Anzola shear zone (see chapter 5, 5.6.2.1). The work is completed and in preparation for a future publication. The results of this work were object of an oral presentation entitled “Titanite as powerful petrochronometer for unravelling the evolution of a major extensional shear zone in the middle crust (Val d’Ossola, Ivrea-Verbano Zone)” at European Mineralogical Conference (EMC 2021) in the session “T8-S1. Geochronology: new trends and applications” and of a poster presentation entitled “Unravelling the evolution of a major extensional lower crust shear zone from Val d’Ossola (Ivrea-Verbano Zone, Western Alps, Italy)”, (which also was awarded as the best poster presentation) at the Metamorphic Studies Group Meeting 2021. This appendix is written as a draft for a manuscript to be submitted in the near future.

Titanite microstructural and petrochronological characterization of a major rift-related shear zone in the middle continental crust

Corvò, S.^{1,2*}, Maino, M.^{1,2}, Piazzolo, S.³, Kylander-Clark A. R.C.⁴, Langone, A.²

¹Dipartimento di Scienze della Terra e dell’Ambiente, Università degli Studi di Pavia, Pavia, Italy

²Institute of Geosciences and Earth Resources of Pavia, C.N.R., Pavia, Italy

³School of Earth and Environment, University of Leeds, Leeds, United Kingdom

⁴Department of Earth Science, University of California, Santa Barbara, United States

*Corresponding author: stefania.corvo@unipv.it

Keywords: titanite, amphibolites, shear zone, microstructures, U-Pb geochronology, petrochronology

Abstract

Unravel a shear zone evolution requires detailed reconstruction and correlation between petrochronology and microstructural analyses. Titanite is considered a useful accessory mineral for understanding crustal processes because its properties make it a powerful petrochronometer that allow to determine both age (U-Pb isotopes), as well as the deformation (microstructural features) and pressure-temperature conditions (trace-element composition) of the host rocks. In this contribution, we combine microstructural and petrochronological data of titanite with the attempt to constrain the activity of a shear zone (i.e., Anzola shear zone) outcropping in an exhumed section of the pre-Alpine middle to lower continental crust, i.e., Ivrea-Verbano Zone (Italian Southern Alps). Following

the Variscan orogeny, the Ivrea-Verbanò Zone experienced a complex thermal history characterized by post-orogenic extension and subsequently, in the Triassic-Jurassic time interval, by a complex and polyphasic rifting stage, which resulted in shear zones developed at different continental crustal levels. Although these events are largely accepted, there are currently only a few constraints on the activity of the rifting-related structures, limiting a clear understanding of their role during the rifting processes. To address these questions, titanite-bearing samples were collected directly from mylonitic amphibolites of the Anzola shear zone area. Microstructural analysis of titanite have been combined with trace element analyses and U–Pb age dating to correlate their internal deformation features to the rock petrochronological record. Mylonites are characterized by abundant titanite grains along the foliation showing contrasting microstructural features: i) diffuse intracrystalline deformation or iii) localized incipient recrystallization, with an average orientation change within an individual grain around 15–25°. Geochronological results for mylonitic amphibolites suggest that deformation took place in a time interval ranging from about 240 to 185 Ma (Triassic-Jurassic). Thanks to the modern approach adopted, we found out that titanite isotopic data not always show correlation with the spot position and textural features within the grain. Moreover, the relationships between titanite chemistry and isotopic data change from one sample to another at the thin section scale (few centimetres) in dependence of the mineral assemblage, the bulk chemistry and mineral rheological reply to deformation. However, the adopted microstructural and petrochronological approach allowed to make interesting constrains on the role of the Anzola shear zone during Triassic-Jurassic extension and exhumation.

1. Introduction

Geodynamic models aim to quantify rates of tectonic and metamorphic processes but often run into the difficulty to constrain the timing of deformation stages. The time scales over which deformation localizes into shear zones is a key information to correlate the relative steps of crustal processes. Several analytical techniques applied on accessory minerals - such as zircon, monazite, titanite and rutile - link ages with temperature, mineral reactions and petrologic evolution based on textural and chemical correlation (e.g., Cherniak et al., 2010; Kohn et al., 2017; McGregor et al., 2021). In addition to the link between chemistry and geochronology, resetting ages correlated with increased element mobility due to crystal-plastic deformation has been documented within zircon, monazite and rutile (Piazolo et al., 2016; Erickson et al., 2018; Moore et al., 2020). The increasing knowledge on the influence of

deformation on the element redistribution potentially affecting the geochronological results induces to evaluate the use of other deformed minerals and their microstructure for geological research.

In the last decades, titanite (formerly sphene: CaTiSiO_5) has gained a great interest in the petrological community thanks to its advantageous compositional and textural properties that make it a powerful tracer in the Earth's continental crust (e.g., Oberti et al., 1981; Brooks, 2019). Titanite is a widespread accessory mineral that crystallizes over a wide range of crustal pressures and temperatures in many rock types, especially metamorphosed mafic, calc-silicates and igneous rocks (e.g., Frost et al., 2001; Hayden et al., 2008; Kohn, 2017). U-Pb isotopic systematic on titanite is considered as a powerful petrochronometer because it has a high closure temperature (660-700°C; Scott and St-Onge, 1995) and easily incorporate a wide range of minor and trace elements, including significant concentrations of Uranium, rare earth elements (REE) and high field strength elements (HFSE) (e.g., Frost et al., 2001; Kohn, 2017; Garber et al., 2017; Scibiorski et al., 2019; Scibiorski and Cawood, 2022). However, titanite is a reactive mineral, whose abundance and composition in a rock strongly depend on the bulk-rock chemistry especially in high-grade metamorphic rocks (e.g., Scott and St. Onge, 1995; Kohn, 2017; Scibiorski et al., 2019; Scibiorski and Cawood, 2022). Titanite U-Pb ages are traditionally interpreted as susceptible to diffusive resetting (Cherniak 1993), although Pb is considered to diffuse too slowly at $T \leq 800$ °C to reset ages over 1 μm length scales (Kohn and Corrie 2011). In particular, recent work have focused on the relationships between titanite U-Pb and high-spatial resolution geochemical signatures revealing the potential extent of decoupling between the U-Pb isotopic system and the behaviour of trace elements (e.g., Y, Zr, REE) as pressure-temperature conditions change through time (Garber et al., 2017). Moreover, titanite is prone to recrystallizes dynamically and statically (e.g., Spencer et al., 2013; Stearn et al., 2015; Kirkland et al., 2016) experiencing significant Pb diffusion, compositional zoning, variations in trace element content and preservation of microstructural features (e.g., Cherniak, 1993; Gordon et al., 2021), such that titanite U-Pb ages may provide important information about deformation, growth cooling, and/or fluid alteration (e.g., Bestmann et al., 2005; Kohn and Corrie, 2011; Kirkland et al., 2016; Garber et al., 2017; Walters and Kohn, 2017; Scibiorski et al., 2019; Cavosie et al., 2022).

Therefore, a robust interpretation of titanite U-Pb ages requires a careful evaluation of both the chemical and microstructural patterns related to the isotopic variations within deformed grains. In particular, titanite that experienced multistage thermal history may contain multiple generations of

grains likely showing complex chemical/deformation and U–Pb patterns (e.g., Frost et al., 2001; Stearn et al., 2015; Scibiorski and Cawood, 2022). In order to exploit the dependence of titanite U–Pb ages from deformation and metamorphic processes, the combination of microstructural and geochemical investigation with in-situ geochronology is fundamental.

In this work, we study deformed titanite grains collected from a mylonitic shear zone with the aim to test whether U–Pb titanite dating can be used to determine the activity of a major shear zone. We address this approach to the Anzola shear zone from the pre-Alpine middle to lower continental crust of the Ivrea-Verbano Zone (IVZ; Italian Southern Alps). The structure of the IVZ is the result of a complex tectono-metamorphic evolution between the Variscan and the Alpine orogenesis. In particular, in the Triassic–Jurassic time interval, the IVZ was characterized by a complex and polyphasic rifting stage that was accommodated by shear zones at different crustal levels, the age of which is poorly constrained (Fig. A.3.1; e.g., Mulch et al., 2002; Beltrando et al., 2015; Petri et al., 2019; Simonetti et al., 2021). Laser Ablation Split-Stream coupled to Inductively Coupled Plasma–Multi-Collector–Mass Spectrometer (LASS-ICP–(MC) MS) analyses are addressed to structural domains documented through EBSD imaging. Our findings highlight the importance of deformation on trace element redistribution and age resetting in titanite, whereas the chemical correlation between REE patterns and U–Pb ages is generally weak.

2. Geological setting

2.1 The Ivrea-Verbano Zone

The Ivrea-Verbano Zone (IVZ) in north-western Italy represents a cross-section through the middle to lower continental crust of the Southern Alpine basement (Fig. A.3.1). The IVZ escaped significant Alpine deformation and metamorphism and consists of three main tectono-stratigraphic units, from NW–SE: i) the Kinzigite Formation; ii) the mantle peridotites and iii) the Mafic Complex. The Kinzigite Formation is considered the originally upper part of the crustal section made up of a volcano-sedimentary sequence, comprising mainly metapelites with intercalated metabasic rocks and minor marbles/calc-silicates and quartzites (e.g., Zingg, 1990; Kunz et al., 2014). Peridotitic bodies tectonically emplaced within the Kinzigite Formation at the end of the Variscan orogenesis (Late Carboniferous) and before the intrusion of the Mafic Complex (Quick et al., 2003; Zanetti et al., 2013). The Mafic Complex consists of deformed and metamorphosed gabbros and diorites, which intruded metasediments of the Kinzigite Formation during the Permian (290–270 Ma; Peressini et al., 2007) coevally with the acid magmatism

and volcanism in the upper crust (Karakas et al., 2019). However, mantle-derived mafic magmatism started before the Permian (e.g., ~314; Klötzli et al., 2014) and locally occurred up to the Jurassic (e.g., Zanetti et al., 2013; Denyszyn et al., 2018). At a regional scale, peak metamorphic grade decreases from granulite (~900 °C and 900 MPa) to amphibolite facies (~600 °C and ~400 MPa) from NW to SE (Schmid & Wood, 1976; Brodie and Rutter, 1987; Zingg, 1990; Schmid, 1993; Redler et al., 2012; Kunz et al., 2014). Long-lasting high-grade metamorphism developed between the Late Carboniferous (~316 Ma; Ewing et al., 2013) to the Early Permian, coevally with the Mafic Complex intrusion (~290 Ma; Ewing et al., 2013). The progressive switch from granulite to amphibolite facies is marked by a transition zone hosting major system of shear zones, including the Anzola and Premosello shear zones (Fig. A.3.1A, B, e.g., Brodie and Rutter, 1987; Rutter et al., 2007; Redler et al., 2012; Kunz et al., 2014; Carvalho et al., 2019). These structures are thought to have accommodated, since the Triassic, crustal thinning associated with the early Tethyan rifting in the middle to lower crust, while the Pogallo normal fault was active at shallower crustal levels (e.g., Manatschal et al., 2007; Mohn et al., 2012; Beltrando et al., 2015). While the Pogallo shear zone has been constrained between Triassic and Jurassic times through Ar-Ar/K-Ar dating on micas (Hodges and Fountain, 1984; Zingg, 1990; Mulch et al., 2002; Wolff et al., 2012), the Anzola and Premosello shear zones lack modern direct geochronological investigations (Brodie et al., 1989; Pittarello et al., 2012; Kusiak et al., 2019). In this work, we focus on the Anzola shear zone, which consists of ultramylonites and mylonites developed at the expense of previous amphibolites, paragneisses and minor calcsilicates, belonging to the volcano sedimentary Kinzigite Formation (Chapter 5). Despite the Anzola shear zone attracted many structural, microstructural, and geochemical studies (Brodie, 1981; Brodie et al., 1989; Brodie and Rutter, 1987; Altenberger, 1997; Stünitz, 1998; Rutter and Brodie, 1990; Rutter et al., 1993; 2007), the age of deformation is still poorly constrained.

2.2 Timing of Triassic rift-related deformation

Although there is a general agreement that ductile shear zones drove the exhumation of the lower-middle continental crust of the IVZ between Late Triassic and Early Jurassic, there are currently only a few timing constraints concerning their evolution (see Simonetti et al., 2021 for a complete review and references therein). Until now, the only direct attempt to date the Anzola shear zone activity was provided by Brodie et al. (1989). The authors performed Ar-Ar radiometric dating of hornblende obtaining a minimum age of about 247 Ma for unsheared mafic rocks and about 210-215 Ma for syn-

kinematic amphibole grains. On the base of these results, the authors suggested that crustal extension started around 280 Ma, after the emplacement of the mafic intrusion, and was the beginning of a long-lasting period of crustal thinning and cooling of more than 100 Myr. The only Triassic geochronological data obtained for the Premosello shear zone (NW of the Ossola valley) derives from zircon from high-grade felsic mylonitic metapelites (Kusiak et al., 2019), even if authors did not consider this data in the age calculations due to high common Pb. However, Kusiak et al. (2019) highlighted the presence of one strongly deformed detrital core zircon yielding an apparent Jurassic U-Pb age (185 Ma) that they tentatively attributed to deformation. This interpretation has been recently reinforced by the dating of high temperature deformation in metagabbros from the northernmost sector of the IVZ (Finero area; Langone et al., 2018). Here, according to U-Pb zircon dating and Ar-Ar ages (Borioni and Villa, 1997) from deformed hornblende grains from the shear zone, Langone et al. (2018) proposed that the high temperature shearing occurred during Late Triassic and ended during Early Jurassic (about 183 Ma) under amphibolite-facies conditions. A recent indirect dating of high temperature deformation during Early Jurassic (U-Pb zircon: 187 Ma) has been also provided by Corvò et al. (2020) for mylonites and ultramylonites developed within the mantle rocks of the Finero area. The most recent ages were presented for the Pogallo Line, which was broadly investigated by Mulch et al. (2002) and Wolff et al., (2012). Mulch et al., (2002) used the Ar-Ar method to date separates of undeformed muscovite porphyroclasts, which give an age of ~182 Ma, and in-situ deformed muscovite and fine-grained muscovite, which provided the same average age (148 ± 5 and 147 ± 7 Ma, respectively). Conversely, Wolff et al. (2012) performed K-Ar dating for biotite in granulites and in amphibolite-facies obtained an age of 163 ± 3 Ma and of 184 ± 13 Ma, respectively. According to the authors, these ages should represent the activity of the Pogallo Line (PL) during Jurassic crustal thinning. In more recent studied, these considerably younger dates (from 215 to 170 Ma) were reinterpreted as possible evidence for a Late Triassic to Early activity of the shear zones (e.g., Ewing et al., 2015; Beltrando et al., 2015; Petri et al., 2019).

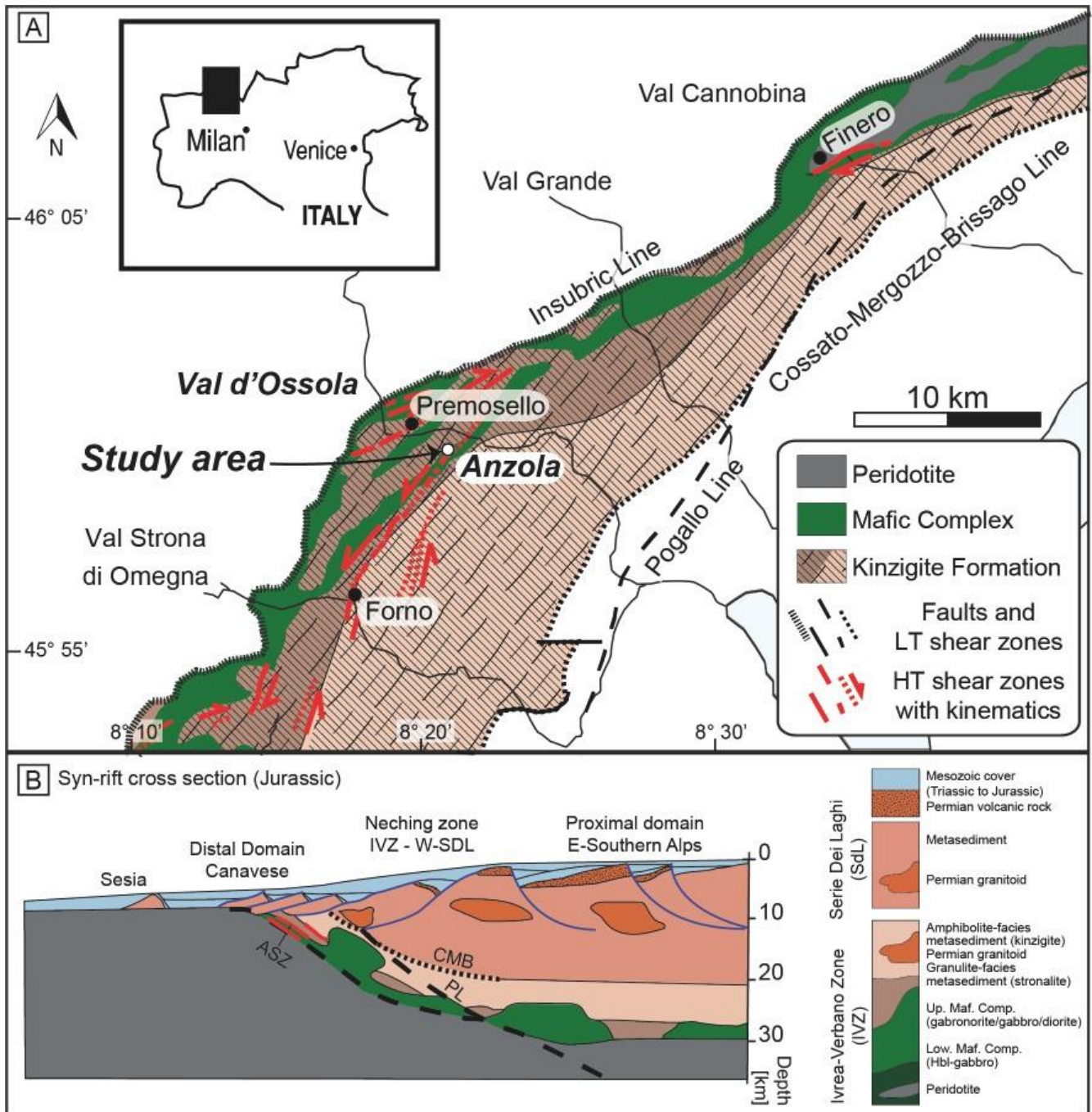


Fig. A.3.1 - Geological sketch map of: A) the Ivrea-Verbano Zone, modified after Ewing et al. (2015) and Simonetti et al. (2021). The locations of high-temperature shear zones are after Rutter et al. (1993). B) Reconstructed post-rift cross-section and relative lithotectonic map modified after Beltrando et al., (2015b); Petri et al., (2019).

3. Methods

Two representative titanite-bearing thin sections (i.e., AN01A, AN01D) from mylonitic amphibolite sample (AN01; Fig. A.3.2A) of the Anzola shear zone were selected for in-situ analyses on titanite grains. The crystals were mapped with a scanning electron microscope (SEM) and with Electron Backscatter diffraction (EBSD) to determine textural and microstructural features. This was followed by Laser Ablation Split-Stream coupled to Inductively Coupled Plasma-Multi-Collector-Mass Spectrometer (LASS-ICP-(MC)MS) analyses to determine the isotopic date and trace-element concentrations. Mineral abbreviations are after Whitney and Evans, (2010).

3.1 Microstructural analysis

Titanite grains from selected samples were imaged in thin section using Back-Scattered Electron (BSE) with a Scanning Electron Microscope (SEM), Tescan Mira3 XMU-series FESEM equipped with an EDAX-EDX at the “Arvedi” laboratory at the University of Pavia. Electron backscatter diffraction maps were collected using the FEI Quanta 650 FEG-ESEM (with Oxford X-max 80 SDD EDS, Oxford/HKL Nordleys EBSD system and Aztec software) at the Electron Optics Facility, University of Leeds, UK. A working distance of 20 mm, a 70° stage tilt, a 20 kV accelerating voltage, 4 x 4 binning, and a pixel/step size of 0,5-1 µm were used during the analyses. For the entire map area, post processing included correcting for wild spikes and a 5 nearest neighbour zero solutions correction. Quantitative orientation analyses are presented in maps and pole figures elaborated with the new upgraded software of the Oxford instruments, AztecCrystal 2.2 (AztecFlexStudentLicense2022). The change in orientation is shown relative to a specific spot within the titanite grain by Grain Reference Orientation Deviation (GROD) and Weighted Burgers Vector (WBV) maps, Pole Figures (PF) and Inverse Pole Figure (IPF) for titanite crystallographic system (monoclinic; (100), (010), (001)) and Misorientation profile tendentially from core to rim of the grains. Results for representative titanite from the studied samples are shown in Figures A.3.3, A.3.4. For further details about EBSD instrument and data acquisition and processing, the reader is referred to the official website <https://nano.oxinst.com/products/ebsd/>.

3.2 U-Pb LASS-ICP-(MC)MS analysis

U-Pb isotopic concentrations and trace-element compositions in titanite grains were collected simultaneously from the same spot using Laser ablation split-stream (LASS) technique at the University of California Santa Barbara following methods of Kylander-Clark et al. (2013) and Spencer et al. (2013). Titanite U-Pb petrochronology results are summarized in Figures A.3.5, A.3.6., (for the complete dataset table write to stefania.corvo@unipv.it). Spot location was guided with the aid of BSE images and EBSD maps. Instrumentation consists of a Photon Machines 193 nm ArF Excimer laser and ‘HelEx’ ablation cell coupled to a Nu Instruments HR Plasma high-resolution multi-collector MC-ICPMS (U, Th, and Pb isotopes)

Appendix

and an Agilent 7700X Quadrupole ICP-MS (major and trace elements). Typical excimer laser (193 nm wavelength) settings were 30–100% of 3 mJ, 4 Hz repetition rate, and a 25–40 μm diameter laser spot. The resulting laser ablation pits are ~ 10 μm deep Bear Lake Road titanite (Aleinikoff et al., 2007) was used as the primary reference material, and Y1710C5 (Spencer et al., 2013) was used as the secondary reference material to assess in-run accuracy. The dates reported in this paper have a minimum uncertainty of 2%. On the Plasma HR, masses $^{204}\text{Pb}+\text{Hg}$, ^{206}Pb , ^{207}Pb , and ^{208}Pb were measured on secondary electron multipliers, and masses ^{232}Th and ^{238}U were measured on Faraday cups. ^{43}Ca (assuming 19_25 wt % Ca in titanite) was used as an internal standard to reduce elemental data collected on the 7700X. Measured peaks were ^{27}Al , ^{28}Si , ^{31}P , ^{43}Ca , ^{49}Ti , ^{51}V , ^{52}Cr , ^{56}Fe , ^{88}Sr , ^{89}Y , ^{90}Zr , ^{93}Nb , ^{139}La , ^{140}Ce , ^{141}Pr , ^{146}Nd , ^{140}Sm , ^{153}Eu , ^{157}Gd , ^{159}Tb , ^{163}Dy , ^{165}Ho , ^{166}Er , ^{169}Tm , ^{172}Yb , ^{175}Lu , ^{178}Hf , ^{181}Ta , and ^{182}W . We measured ^{91}Zr and ^{93}Zr for a small subset of samples and obtained Zr concentrations within uncertainty of those obtained using ^{90}Zr . The $^{238}\text{U}/^{206}\text{Pb}$ and $^{207}\text{Pb}/^{206}\text{Pb}$ isotopic ratios for each analysis were plotted on Tera–Wasserburg concordia diagrams using Isoplot (Ludwig, 2003). All date uncertainties are reported at the 95% confidence interval, assuming a Gaussian distribution of measurement errors. Because the samples in this study exhibit a broad spread of U/Pb ratios—and thus, well-constrained common $^{207}\text{Pb}/^{206}\text{Pb}$ ratios—we report the ^{207}Pb -corrected $^{206}\text{Pb}/^{238}\text{U}$ date obtained by regressing $^{238}\text{U}/^{206}\text{Pb}$ vs $^{207}\text{Pb}/^{206}\text{Pb}$. Stated 2 σ date uncertainties are internal; that is, they include in-run errors and decay constant errors only.

4. Results

4.1 Petrography and microstructures of mylonitic amphibolites

Titanite-bearing samples from the Anzola shear zone consist in mylonitic amphibolites. Two thin sections from a hand specimen of mylonitic banded amphibolites were selected for this study, i.e., AN01A and AN01D, as representative of the compositional layering, i.e., amphibole- and clinopyroxene rich layers, respectively (Fig. A.3.2A). Mylonitic amphibolites show alternating greenish darker and lighter bands (Fig. A.3.2A): the darker bands are dominated by amphibole, whereas the lighter ones are mainly composed of clinopyroxene and plagioclase (Fig. A.3.2B, C). The mylonitic fabric is characterized by porphyroclasts (diameter of 0.5–1.0 mm) of plagioclase, amphibole or clinopyroxene and, rarely, garnet (Fig. A.3.2B, C). Porphyroclasts are surrounded by a fine-grained recrystallized matrix consisting of plagioclase \pm amphibole \pm clinopyroxene \pm garnet \pm titanite. The microstructure of mylonitic amphibolites shows evidence of dynamic recrystallisation and plastic deformation as suggested in particular by the fabric of the main mineral phases, i.e., plagioclase, clinopyroxene and amphibole, characterized by relicts of large porphyroclasts with tails of small, new recrystallized grains

(Fig. A.3.2B-E; e.g., Passchier and Trouw, 2005). Garnet is observed as large sub-rounded fragmented pinkish porphyroclasts along the clinopyroxene/plagioclase-rich layers (Fig. A.3. 2C). Titanite form part of the equilibrium mineral assemblage of the studied samples preferentially occurring in elongated sigmoidal shaped crystals within the lighter Cpx/Pl-rich layers or randomly distributed in the Amph-rich domain (e.g., AN01A, D; Fig. A.3.2B-E). Locally, titanite occurs in big crystals (up to 0.5mm wide x 0.5mm long) showing the typical wedge-shape and double set of twinning (Fig. A.3.2D, E). Beside titanite, ilmenite, apatite and zircon are common accessories minerals, whereas rutile is absent. Ilmenite is quite abundant in the studied thin sections. It mainly occurs in recrystallized interstitial grains along the foliation and in association with titanite rims (Fig. A.3.2F-G), whereas zircon is rare along titanite-rich layers. Late alteration product such as calcite, chlorite, epidote, and mica are concentrated in fractures and cross-cutting veins. According to mineral and bulk geochemistry the lighter bands of the mylonitic amphibolites are former calcsilicate layers, whereas the darker amphibole rich layers derived from amphibolites (Chapter 5). For that reason, we will present results on the base of the layering and textural distinction in order to highlight potential differences even for titanite features.

4.2 Titanite textural and microstructural features (SEM-EBSD)

4.2.1 Amphibolite-rich mylonitic amphibolite (AN01A)

In Amph-rich domain, titanite crystals are randomly distributed even if a preferential concentration is observed at contact with clinopyroxene porphyroclasts and along the recrystallized plagioclase-amphibole rich matrix (Fig. A.3.2B, C). Less frequently, it is observed in association with amphibole. In this domain, titanite grains occurs prevalently as elongated and sigmoidal shapes and more rarely in subhedral wedge shape, with average grain size ranges from $\sim 100 \times 300 \mu\text{m}$ and $\sim 250 \times 500 \mu\text{m}$. All titanite display strong core-rim zoning in BSE images; rims are typically $< 50 \mu\text{m}$ in width, and in some grain the boundary between core and rims is gradational (Fig. A.3.2F, G). Locally ilmenite occurs along titanite rims (Fig. A.3.2F; A.3.3A-Eii). As for the other main mineral phases, even titanite show evidence of partial recrystallized microstructures displayed by irregular grain boundaries with cusps and lobes (Fig. A.3.2D, F, G; e.g., Passchier and Trouw, 2005). Strong correlations between core-rim zoning in BSE images and microstructural evidence of recrystallization are observed (Fig. A.3.3). Twenty-one titanite grains from Amph-rich domains were analysed by EBSD technique. Representative results for Amph-rich domain (AN01A) are shown in Fig. A.3.3. They mostly record strong variable progressive degrees

of intragrain misorientation and distortion up to $\sim 25^\circ$, as shown by grain reference orientation maps (GROD), misorientation profiles and pole figures (Fig. A.3.3A-Eiii-v). Overall, this group of titanite shows syn-kinematic overgrowths along the foliation and two main microstructural features: 1) intracrystalline deformation (Fig. A.3.3Biii, Diii); and 2) incipient recrystallization of neoblastic grains emphasized towards the rims reflecting the growth zoning observed in BSE images (Fig. A.3.3Biii, Ciii- Ttn7B1). In particular, intracrystalline deformation is generally pronounced towards the outermost rims of titanite grains, locally displaying an abrupt change in orientation from the undeformed core towards the rims (Fig. A.3.3Aiii), or locally showing a progressive increase of the misorientation values from the core to rim (Fig. A.3.3Diii). Only one grain revealed at EBSD results peculiar microstructural features showing that the apparently coherent 'grain' is an aggregate of multiple individual and different in size grains, each with straight boundaries (Fig. A.3.3Cii-iii, Ttn7B2). The biggest grains of the aggregate show a progressive change in orientation from core to rim, whereas smaller grains present apparently chaotic different orientations that is well illustrated from the pole figures (Fig. A.3.3Civ, Ttn7B2). A set of slight twins, dominantly in $\{111\}$ orientation (Timms et al., 2019), are often observed in few of the analysed titanite grains (Fig. A.3.3E). The sets of twins are disoriented from host grain by $\sim 74^\circ / \langle -10-2 \rangle$, according to the indexing reported in Timms et al., (2019) and Papapavlou et al., (2018). Planar deformation bands (PDBs; McGregor et al. 2021) are recognisable in the analysed titanite grains (Fig. A.3.3Biii, Diii) and are defined by systematic crystallographic disorientation corresponding to a slip plane of (111) and slip direction of $\langle 110 \rangle$ (and equivalent $(-11-1)$, $\langle -110 \rangle$). These geometric configurations can be explained by dislocation glide with Weighted Burgers Vector analysis (WBV; $b = (001)$); according to definition of Wheeler et al., 2009), which shows WBV average magnitude up to $1 \times 10^{14} \text{m}^{-2}$ (Fig. A.3.3iv).

4.2.2 Clinopyroxene/Plagioclase-rich mylonitic amphibolite (AN01D)

In Cpx/Pl-rich domain, titanite crystals are distributed only along Cpx/Pl-rich domain and especially along the rims of clinopyroxene porphyroclasts (Fig. A.3.2C, E). Here, titanite grains occurs in two textural features: as small ($\sim 100 \times 250 \mu\text{m}$) elongated and sigmoidal grains, and as large ($\sim 250 \times 500 \mu\text{m}$) subhedral wedge-shape grains. Most titanites are unzoned in BSE images, although some grains display narrow ($< 10 \mu\text{m}$) rims and a patchy core-rim zoning (Fig. A.3.2H, I). Locally, ilmenite occurs along titanite rims (Fig. 2F; 4Aii, Cii). Even in this textural domain, titanite show evidence of partial recrystallized microstructures displayed by irregular grain boundaries and lobated rims (Fig. A.3.2E, H,

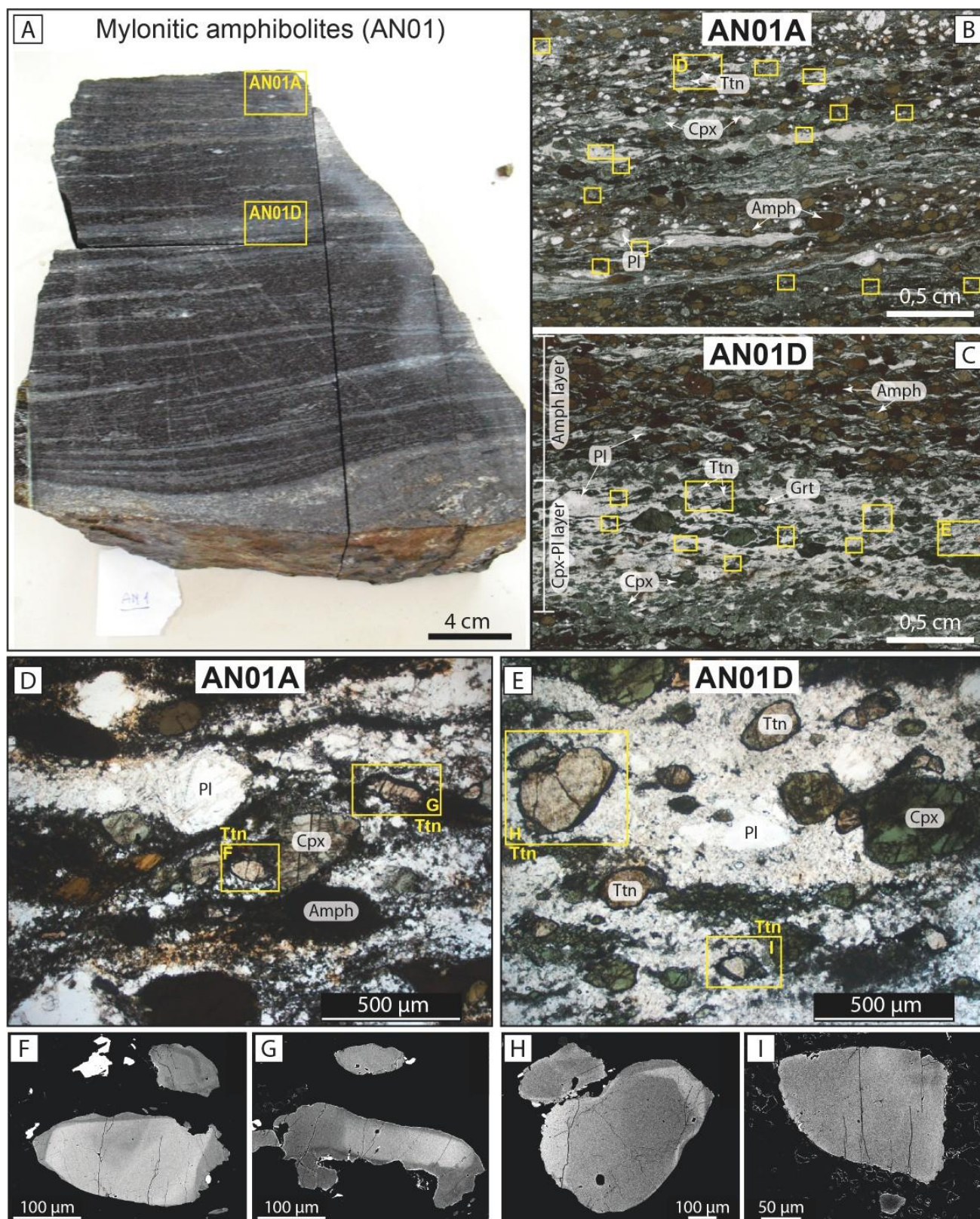


Fig. A.3.2 - Titanite and host rock textural features. A) Hand specimen of mylonitic banded amphibolites (sample AN01). In yellow boxes are reported the studied thin sections (AN01A; AN01D) selected for titanite in-situ analyses and representative of the main textural host rock features. B, C) Plane polarized (PPL) photomicrographs of the studied mylonitic amphibolites thin sections for: B) Amph-rich layer (AN01A) and C) Cpx/Pl-rich layers (AN01D). Small yellow boxes show locations of titanite grains (light brown) outlining their textural distribution in the thin section. D, E) Representative PPL photomicrographs showing the sample mineral assemblages and textures of main mineral phases and titanite grains for Amph-rich layer (AN01A) and Cpx/Pl-rich layer (AN01D), respectively. F, G) Back-Scattered Electron (BSE) images highlighting the zoning from core to rim in titanite grains from the Amph-rich domain (AN01A). H, I). BSE images of zoning within titanite grains from the Cpx/Pl-rich domain (AN01D).

l; 4Aii; e.g., Passchier and Trouw, 2005). In the Cpx/Pl-rich domain, the lack of internal titanite zoning and homogeneity of intragrain structures is well correlated by microstructural features. Of the thirty grains analysed, mostly appear undeformed, whereas pronounced crystal-plastic deformation is present in other grains. Representative EBSD results for Cpx/Pl-rich domain (AN01D) are shown in Fig. A.3.4, by grain reference orientation maps (GROD), misorientation profiles and pole figures (Fig. A.3.4A-Diii-v). In such nice deformed titanite grains, deformation is well preserved up to $\sim 15\text{-}50^\circ$ of crystallographic misorientation accommodated by low-angle grain boundaries and incipient recrystallization shown in the form of local development of subgrains (Fig. A.3.4A, B). Some crystals often display one sets of polysynthetic twin lamellae typically few micrometers wide, mostly straight to locally slightly kinked or/and tapered (Fig. A.3.4Diii). Planar deformation bands (PDBs) are recognisable in the analysed titanite grains and are defined by systematic crystallographic disorientation corresponding to a slip plane of (111) and slip direction of $\langle 110 \rangle$ (and equivalent $(-11-1)$, $\langle -110 \rangle$; Fig. A.3.4A; McGregor et al., 2021). Also for this group of titanites, the geometric configurations can be explained by dislocation glide with Weighted Burgers Vector analysis (WBV; $b = (001)$; Wheeler et al., 2009), which shows a WBV average magnitude up to $2 \times 10^{14} \text{m}^{-2}$ (Fig. A.3.4iv).

4.3 U-Pb LASS-ICP-(MC)MS Petrochronology

4.3.1 Amphibole-rich mylonitic amphibolite (AN01A)

A total of 108 analyses were performed on 13 grains whose petrochronology results are summarized in Fig. A.3.5A-E. On the Tera-Wasserburg diagrams the U-Pb data shows good alignments defining Triassic-Jurassic lower intercepts (Fig. A.3.5A). The obtained alignment of the U-Pb data is strongly correlated with the textural position of spot analyses: the U-Pb data from titanite undeformed cores define the oldest lower intercept at about $240.5 \pm 6.6 \text{ Ma}$ (M.S.W.D = 3.4), whereas the isotopic data from the recrystallized rims result in the youngest lower intercept at about $185.1 \text{ Ma} \pm 2.6 \text{ Ma}$ (M.S.W.D = 5.4; Fig. A.3.5A). On the base of the textural and microstructural features, U-Pb titanite data are divided in 4 different groups: group 1) in black colour (29 analyses) identifies old ages from undeformed core of titanite grains; g2) in light brown (20 analyses) refers to U-Pb data between the old and young intercepts referring to slightly deformed intermediate textural position within titanite grain not corresponding to core neither to rim; g3) in green (26 analyses) and g4) in red (33 analyses) correspond to young ages from recrystallized rims of titanite grains or relative to titanite characterized by incipient recrystallization of neoblastic grains. The two different colours (red and green) were conferred to split U-Pb data

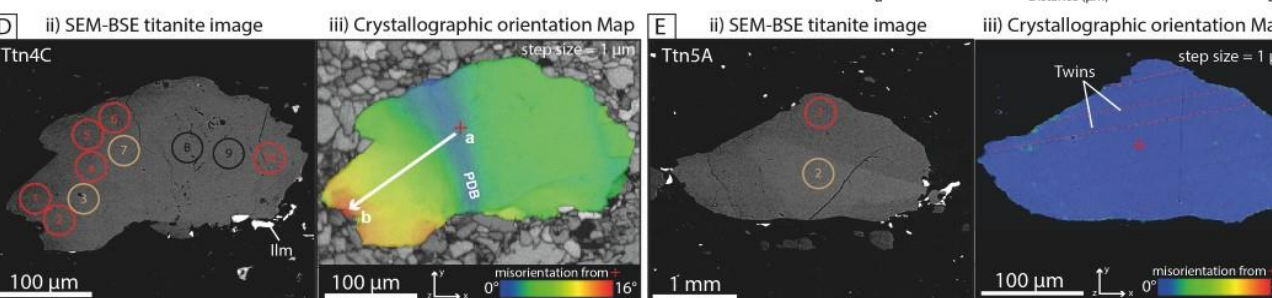
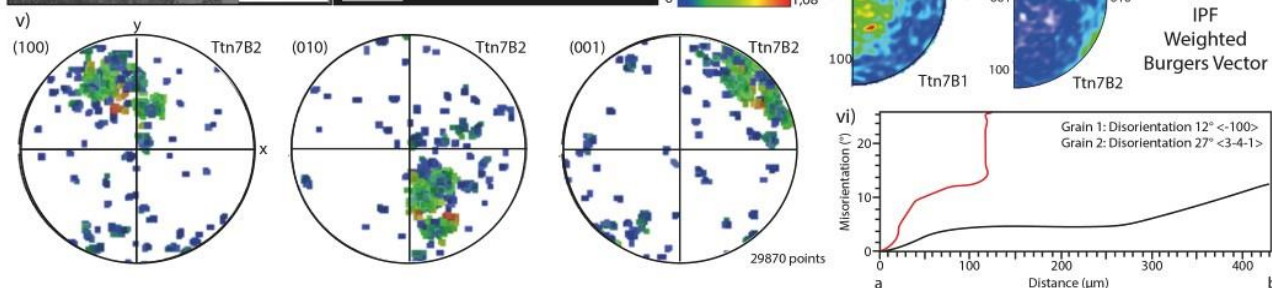
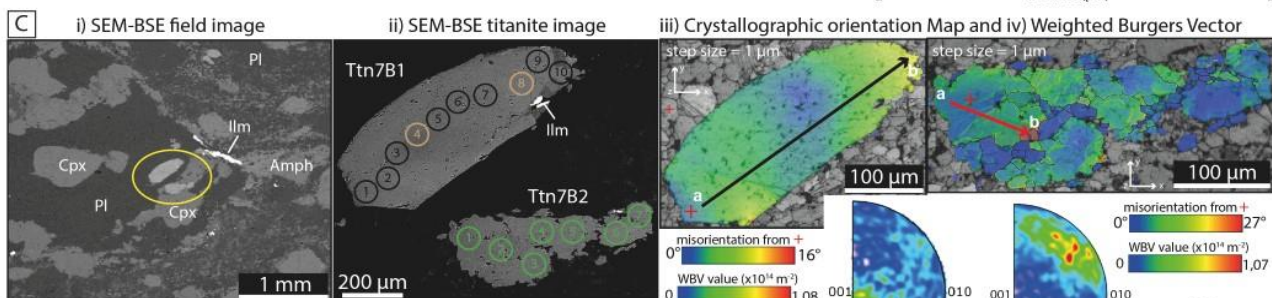
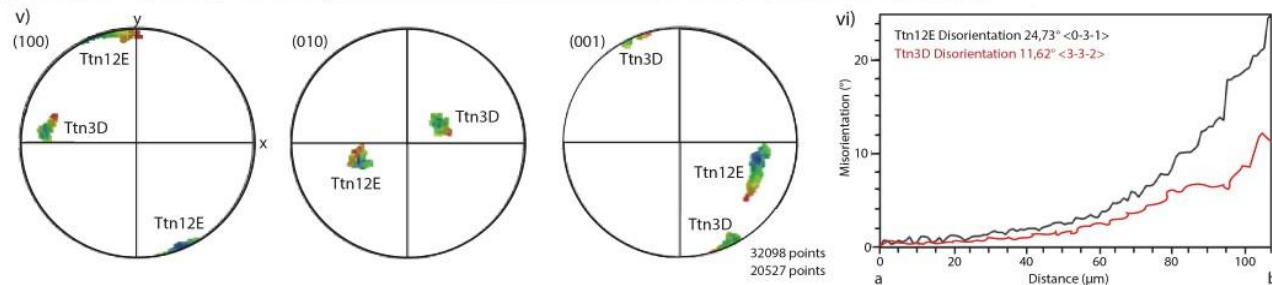
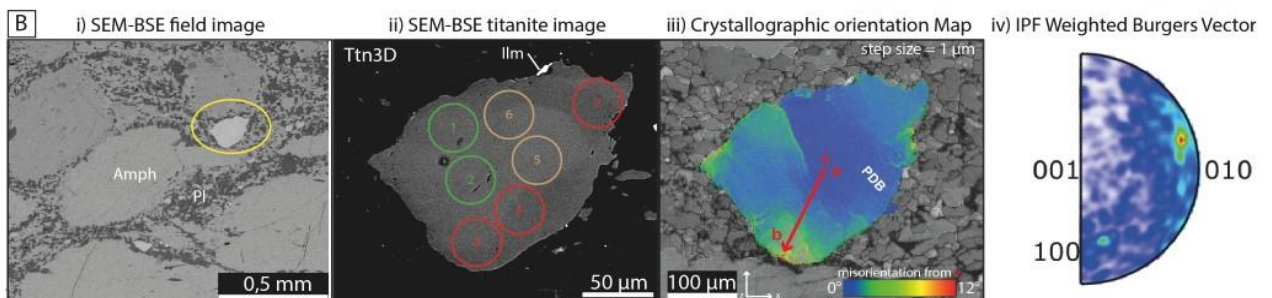
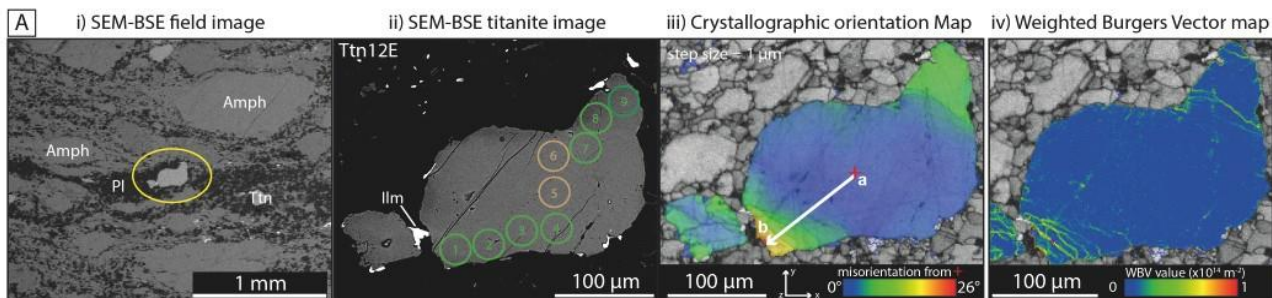
characterized by different content in common Pb and so, concentration in $^{206}\text{Pb}/^{207}\text{Pb}$. Finally, it is interesting to note that no strong correlations exist between chemistry and U-Pb ages, except for the common Pb (Pb_c), which is inversely correlated with respect to the trace elements concentration (ppm) of La, Zr, Y and Nb (Fig. A.3.5B-E). The REE patterns of the analysed titanite normalised to chondrite for the different U-Pb groups is shown in Fig. A.3.6A. They show concentrations between 1000-10000CI, with overlapping concentrations for group 1, 2 and 3, characterized by decreasing concentration from LREE to HREE, with negative anomaly in Eu. Conversely, group 4 shows a partial overlapping respect with the patterns of the other groups, being characterized by wider range in LREE concentrations, lower concentration in HREE down to 1000CI and absence of negative anomaly in Eu (Fig. A.3.6A).

4.3.2 Clinopyroxene/Plagioclase-rich mylonitic amphibolite (AN01D)

A total of 91 analyses were performed on 12 grains; the petrochronology results are summarized in Fig. A.3.5F, G. The U-Pb data define a cloud delimited by lower intercepts at about 256.8 ± 3.8 Ma (M.S.W.D=1.4) and 176.2 ± 3.9 Ma (M.S.W.D=1.4; Fig. A.3.5F). For that reason, U-Pb data are distinguished by different colours, each reporting the U-Pb analyses made on the same titanite grain (Fig. A.3.5F). Respect to the Amph-rich domain, no significant correlation between U-Pb data and textural position (i.e., core and/or rims) were observed in the Cpx/Pl-rich domain. Consequently, a single group of U-Pb is individuated. Conversely, the isotopic data are more correlated with chemistry. Indeed, the U-Pb data defining younger lower intercepts show low Sr concentrations (15 ppm), whereas higher concentrations were observed for U-Pb data defining older higher intercept (60 ppm; Fig. A.3.5G). The REE patterns of the analysed titanite were normalised to chondrite and shown in Fig. A.3.6B. A distinction of patterns between data of young and old intercepts were made. However, no different patterns were observed since they show overlapping concentration around 1000CI, decreasing trend from LREE to HREE and negative anomaly in Eu (Fig. A.3.6B).

Fig. A.3.3 - Representative textural and microstructural features of titanite from the mylonitic amphibolites Amph-rich domain AN01A. i-ii) BSE panoramic images of analysed titanite grain location, textural zoning and features. The numbered circles in ii) represent the LASS spot analyses performed on titanite grains coloured according to the colour used to distinguish the different group of U-Pb data reported in Fig. 5 and tables 2. iii) Crystallographic orientation map showing degrees of misorientation across the grain and when present sets of twins. iv) Detailed Weighted Burgers Vector (WBV) analyses (map or pole figures) of region or grain shown in iii). v) Pole figures for (100), (010), (001). Lower hemisphere, equal area projections in the sample x-y-z reference frame. The colours of point in pole figures reflect the colours of the misorientation map for titanite in iii). vi) Misorientation profile (a-b) across the grain shown in iii-iv).

Amph-rich mylonitic amphibolite (AN01A)



5. DISCUSSIONS

In the following sections, we discuss how titanite record the tectonic history of the Anzola shear zone, and general implications these data provide in terms of microstructures and petrochronology in titanite grains.

5.1 Interpretation of titanite microstructure

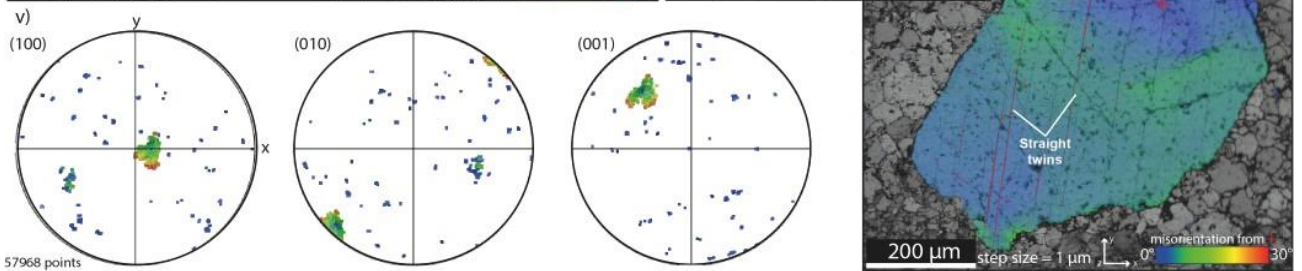
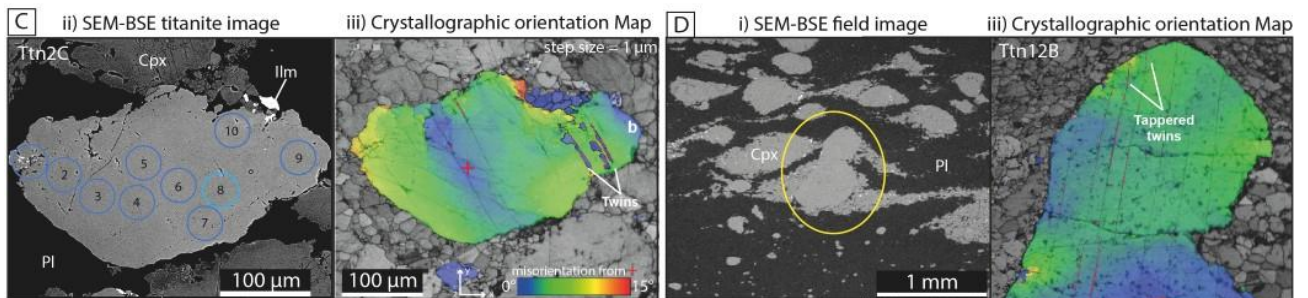
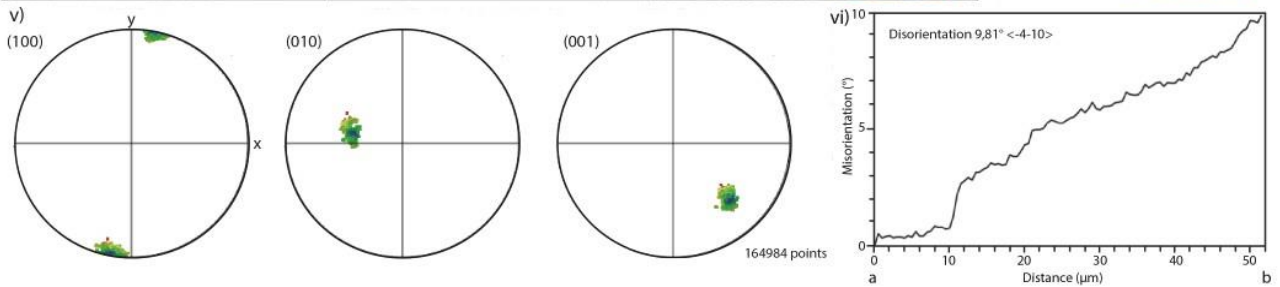
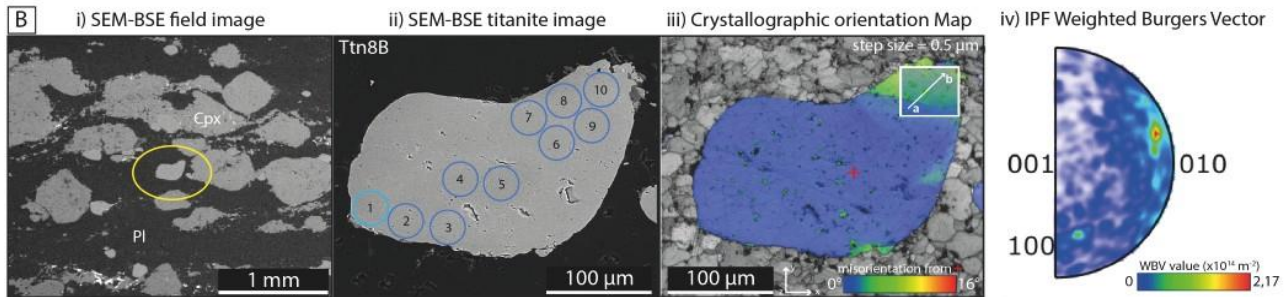
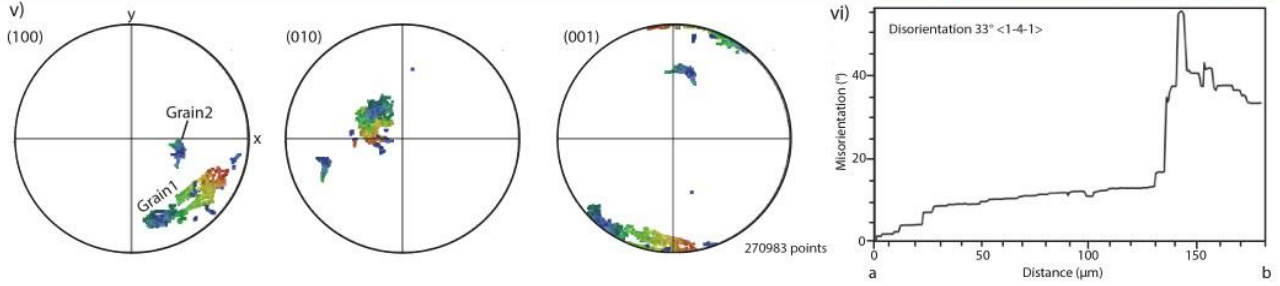
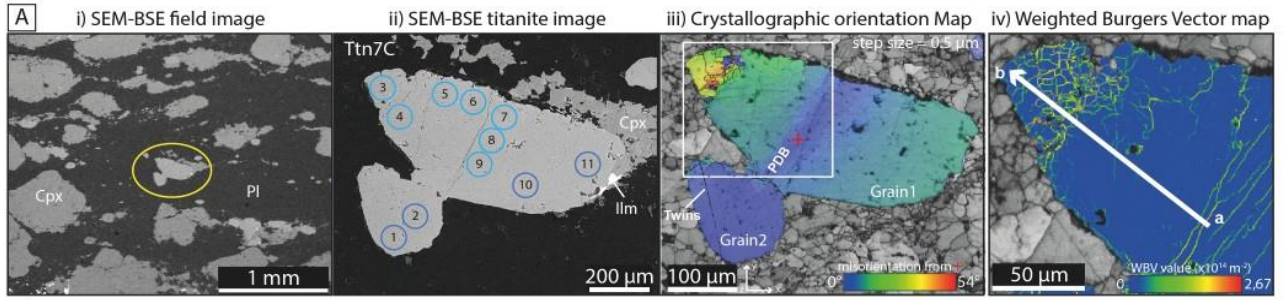
Until now, the studies concerning the microstructural features in titanite are limited. Granular texture, neoblastic microstructures and deformation twins are the main microstructural characteristics recognised in titanite, but their origin is firstly attributes as product of meteorite impact events (e.g., Papapavlou et al., 2017a, b, 2018; Timms et al., 2019; McGregor et al., 2021). Conversely, recent works (i.e., Gordon et al., 2021; Cavosie et al., 2022) revealed that neoblastic recrystallized titanite aggregates, including high angle grain boundaries and oscillatory/patchy zoning, can be traced in response to deformation during regional metamorphism.

In this work, detailed microstructural analyses show that titanite develops different textural and microstructural features at a distance of less than 30 cm and in dependence of the different mylonitic amphibolites' domains (Amph-rich; Pl/Cpx-rich; Fig. A.3.2A).

Titanites from the Amph-rich domain occur prevalently as elongated and sigmoidal shapes (average grain size 100-250x300-500 μm) and show good correlations between core-rim zoning and microstructural features (Figs. A.3.2-3). The irregular grain boundaries characterized by cusps and lobes together with gradational core-rim zoning, intracrystalline deformation (up to $\sim 25^\circ$) and incipient recrystallization of neoblastic grains pronounced towards the outermost rims of titanite grains, are clear evidence of partial recrystallization (Figs. A.3.2-3; Passchier and Trouw, 2005). Only few crystals show exceptional features consisting in a less accentuated core-rim zoning and a stronger intracrystalline distortion (Fig. A.3.2C, D) or in aggregate of multiple individual and different in size

Fig. A.3.4 - Representative textural and microstructural features of titanite from the mylonitic amphibolites Cpx/Pl-rich domain AN01D. i-ii) BSE panoramic images of analysed titanite grain location, textural zoning and features. The numbered circles in ii) represent the LASS spot analyses performed on titanite grains coloured according to the colour used to distinguish the different group of U-Pb data reported in Fig. 5 and tables 2. iii) Crystallographic orientation map showing degrees of misorientation across the grain and when present sets of twins. iv) Detailed Weighted Burgers Vector (WBV) map of region shown in iii). v) Pole figures for (100), (010), (001). Lower hemisphere, equal area projections in the sample x-y-z reference frame. The colours of point in pole figures reflect the colours of the misorientation map for titanite in iii). vi) Misorientation profile (a-b) across the grain shown in iii-iv).

Cpx/Pl-rich mylonitic amphibolite (AN01D)

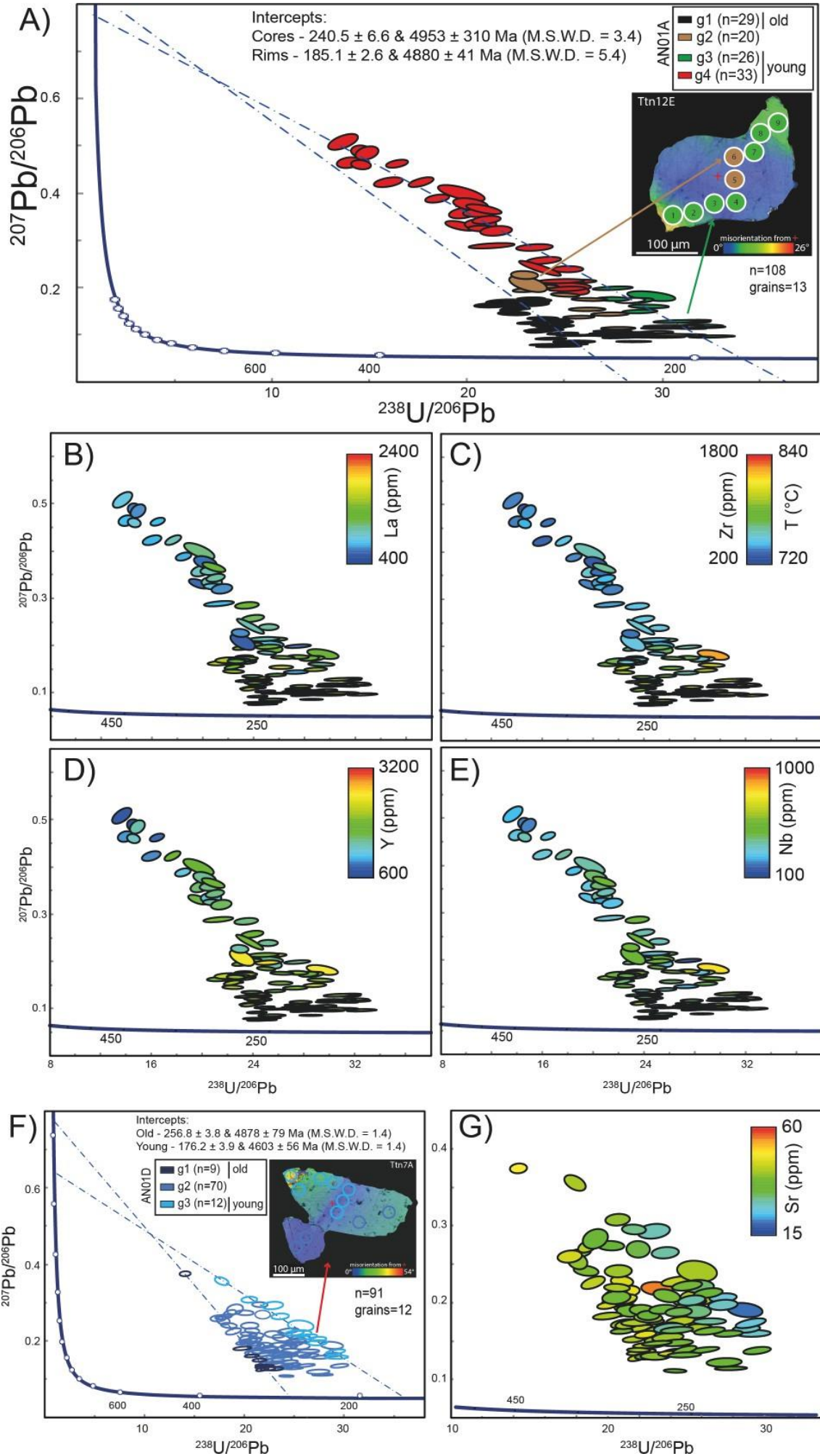


grains (Fig. A.3.3C). Similar observations are reported in Gordon et al., (2021) suggesting that such titanite aggregates may represent porphyroblasts associated with metamorphism and fluids, due to: i) growth of neoblastic titanite after older titanite, or ii) recrystallization of single titanite crystals affected by later tectonic processes.

Conversely, titanite from Cpx/Pl-rich domain, can be clearly distinguished in two different groups on the base of textural and microstructural features. The first includes small ($\sim 100 \times 250 \mu\text{m}$) elongated/sigmoidal titanite grains, which present irregular grain boundaries and lobated rims, zoning in accordance with tendentially abrupt misorientation changes (up to $15\text{-}50^\circ$) towards the outermost rims, locally shown by incipient recrystallization of subgrains (Fig. A.3.4A, B). Only one crystal displays absence of zoning but gradational core-rim misorientation up to 15° (Fig. A.3.4C). The second group, the predominant one, consists of large ($\sim 250 \times 500 \mu\text{m}$) subhedral wedge-shape titanite grains mainly characterized by absence of zoning or of patchy core-rim zoning and only little changes of crystallographic orientation (up to 12°) focused to the outermost rims (Fig. A.3.2H, I, 4).

In both sample domains, titanite crystals display a set of twins $\{111\}$ similar to previous studies (e.g., Papapavlou et al., 2018; Timms et al., 2019) and with a disorientation relationship from the host grain of $74^\circ / \langle -10-2 \rangle$ (Fig. A.3.3E, A.3.4D). Only in few crystals, twins appeared locally slightly kinked or/and tapered (Fig. A.3.4Diii). In Papapavlou et al., (2018), such twins are generally associated to three possible reasons: (a) by the presence of lattice defects during growth of a crystal (growth twins), (b) during phase transformations (transformation twins), (c) by the application of shear stresses on a crystal (deformation twins). In the present work, titanite are mostly syn-kinematic, formed during deformation and/or recrystallization, thus the third option of deformation twins would be the most suitable. However, the origin of $\{111\}$ deformation twins in titanite remains still unclear, and until now they are mostly interpreted as evidence of shock-induced deformation (Timms et al., 2019), that is an interpretation that is unsuitable for the titanite from the mylonitic amphibolites. What is sure is that further studies are needed to evaluate the formation conditions of $\{111\}$ set of twins in recrystallized titanite. Conversely, our microstructural observations suggest that titanite from mylonitic amphibolites deformed under tectono-metamorphic events related to the activity of the Anzola shear zone and so cannot be considered a diagnostic impact feature.

Summing up, detailed textural and microstructural results highlight that titanites from Amph-rich domain recorded the deformation processes better than the Cpx/Pl-rich layer, where undeformed



and unzoned titanites prevail. Overall, titanite grains from both domains don't show a pervasive intracrystalline deformation but a tendency to preserve an undeformed core in contrast with strongly recrystallization to the rims, suggesting that a partial recrystallization occurred during deformation. This heterogenous behaviour can be attributed as controlled by the bulk composition of the rock consisting of amphibolite (Amph-rich layer) versus calcsilicate (Cpx/Pl-rich layer), as demonstrated in Chapter 5. This last observation is interesting because may testify that even titanite microstructure (and not only the titanite chemistry) is controlled by composition and rheological behaviour of the rock.

Fig. A.3.5 - Tera-Wasserburg concordia plots summarising titanite U/Pb data yielded from this study, with representative correlations with trace elements concentrations and microstructural maps for: A) Amph-rich domain (AN01A). Chemical correlations are shown for: B) La (ppm), C) Zr (ppm) and derived Temperature (°C) from Hayden, (2008) calibration, D) Y (ppm), E) Nb (ppm). F) Cpx/Pl-rich domain (AN01D) and chemical correlation for G) Sr (ppm). Relationships with microstructural features within representative titanite grains for each domain is shown in A) and F). For A) and F) the regressions are made considering old or young analyses coloured as reported in the legend and Table 2. In A) the populations are distinguished also on the base of textural position and U-Pb data.

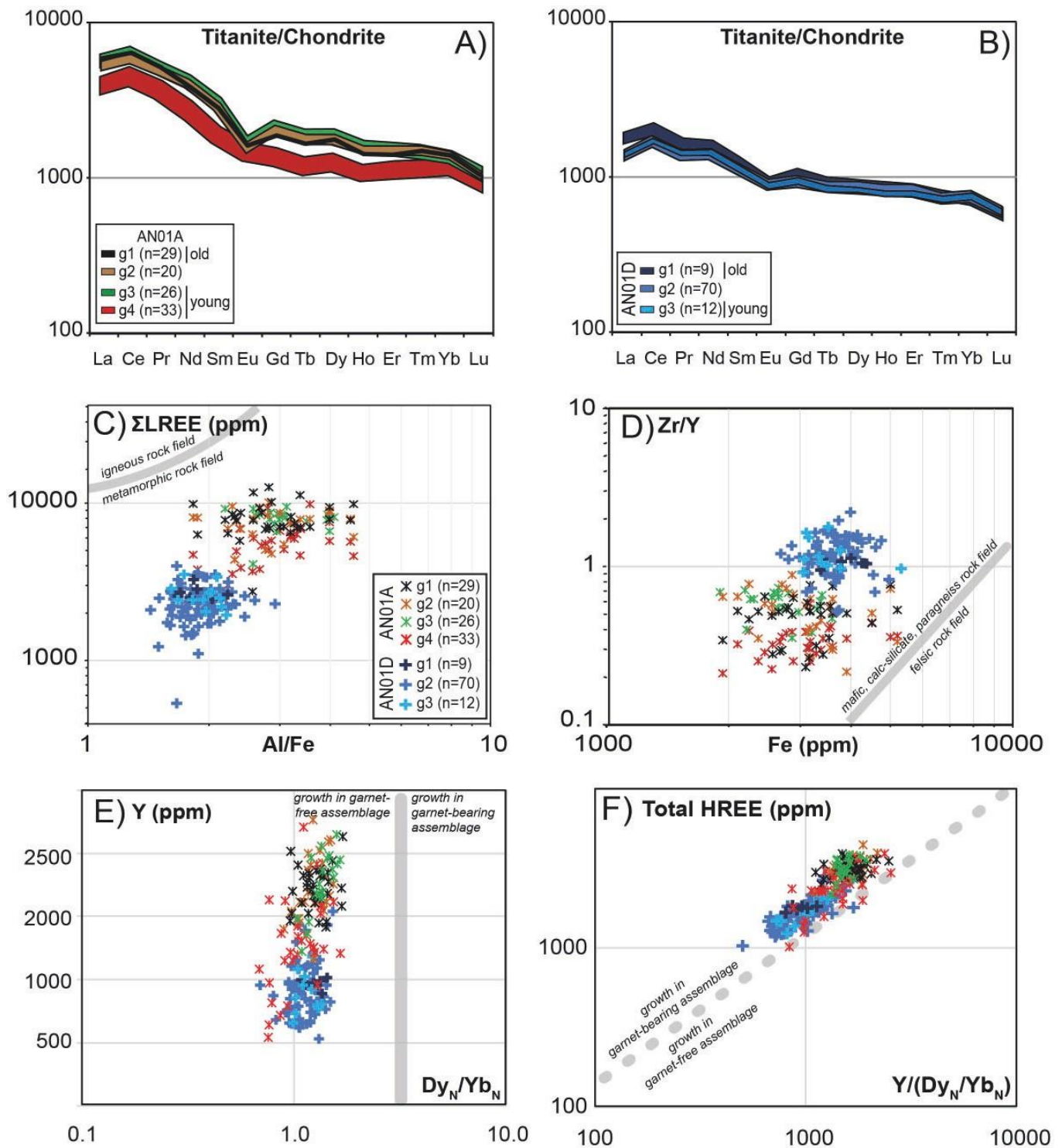


Fig. A.3.6 - Representative trace elements concentrations diagrams of titanite from mylonitic amphibolites (Amph-rich layer AN01A, Cpx/Pl-rich layer AN01D). A, B) Chondrite-normalised REE patterns of titanite in each sample: A) AN01A; B) AN01D. C) Al/Fe versus Σ LREE cross plot. D) Fe (ppm) versus Zr/Y cross plot. E) Y (ppm) versus Dy_N/Yb_N. F) Total HREE (ppm) versus Y/(Dy_N/Yb_N). Points and patterns are coloured according to population as reported in Figure 5 and distinguished on the base of the geochronological and microstructural relationships.

5.2 Titanite chemistry

As suggested by Scibiorski et al. (2019) and Scibiorski and Cawood, (2022), the trace element chemistry of titanite varies with host-rock lithology and especially the REE could be good petrogenetic indicators in metamorphic terranes in order to provide insight into the geochemical processes operating at the time of titanite (re)crystallisation (Fig. A.3.6). In particular, two geochemical correlations (i.e., Al/Fe versus Σ LREE; Fe versus Zr/Y contents) are identified as good discriminators for igneous and metamorphic titanite (Scibiorski and Cawood, 2022). In order to discriminate the possible origin of the studied titanite, we plotted Al/Fe versus Σ LREE and Fe versus Zr/Y contents whose results are shown in Fig. A.3.6C and A.3.6D, respectively. For what concern the Al/Fe versus Σ LREE diagram, titanites from the Anzola mylonitic amphibolite fall, with little changes in Σ LREE contents, in the field corresponding to the metamorphic titanite and especially coincides with the maximum density spectrum relative to the recrystallized metamorphic titanite grains (Al/Fe = 1-10; Σ LREE = 1000-10000). These results are in perfect accordance with our textural and microstructural observations. Even the Fe versus Zr/Y plot diagram support the petrographical observations confirming that the studied titanite derived from mafic (AN01A) or calc-silicates (AN01D) rocks (Fe = 1000-10000; Zr/Y= 1 for AN01D, Zr/Y = 0.1-1 for AN01A) in accordance with the previous observations made in Chapter 5. As suggested by Scibiorski and Cawood, (2022), these results are further in accordance with the absence of LREE-rich phases such as allanite or epidote in the studied rock, for what LREE are immobile in titanite. In contrast, major elements, Al and Fe, are more mobile during overprinting metamorphism or recrystallization because they can be incorporated into main phases such as clinopyroxene and/or Fe-bearing oxides such as ilmenite and/or magnetite (e.g., Gordon et al., 2021).

According to Scibiorski et al., (2019), the HREE can be further indicative of titanite (re)crystallisation relative to other mineral phases able to incorporate these elements. The authors suggest two diagrams in order to investigate the relationship between titanite and garnet HREE content. According to the authors, a Dy/Yb ratio (calculated from normalised values) higher to about 2 is indicative of titanite (re) crystallisation in presence of garnet. Our data are characterized always by values lower than 2 suggesting a garnet-free assemblage (Fig. A.3.6D). Actually, garnet is present as minor component within Cpx-rich mylonites (AN01D; Fig. A.3.2C, E). A further test for the relationship between garnet growth and HREE fractionation in titanite is the behaviour of Y in titanite (Fig. A.3.6E). A further diagram showing the total HREE against the ratio between Y and Dy/Yb can be useful in order to evaluate the relationship between

titanite and garnet (Fig. A.3.6F). Also, in this case all the data fall in the diagram side suggesting titanite growth in absence of garnet. This can be valid for samples with rare or minor amount of garnet and can be related to garnet-free microdomains within the samples (e.g., Scibiorski et al., 2019). This can be particularly the case for mylonites where different lithologies coexist at the thin section scale (see Chapter 5). According to the authors, titanite crystallising in garnet-bearing assemblages should be significantly HREE depleted since HREE are preferentially fractionated by garnet. It is likely that during titanite (re)crystallisation within mylonites the chemical system was open. From the REE patterns some interesting features can be highlighted (Fig. A.3.6A, B). Although titanite preferentially incorporates the MREE over the LREE and HREE (e.g., Tiepolo et al., 2002), the REE patterns of mylonitic amphibolites are characterised by an apparent LREE fractionation over MREE and HREE. This behaviour can be related to the availability of LREE within the system during titanite growth. Beside a major availability of LREE, in order to fractionate LREE over the M- and HREE need a change of the titanite behaviour. It has been demonstrated that intracrystalline deformation can promote intragrain chemical changes of highly resistant accessory minerals such as zircon (e.g., Piazzolo et al., 2016) as well as silicate porphyroclasts (e.g., Corvò et al., 2020). The LREE can be introduced to the system from external sources, or they can be added to the system by the breakdown of LREE bearing mineral phases during deformation. LREE can be abundant within accessory minerals such as monazite and epidotes (e.g., allanite). Monazite is non-compatible with the bulk chemistry whereas allanite is likely. However, allanite has never been found within mylonitic amphibolites whereas other epidotes are locally abundant. A possible internal source for LREE can be, thus, the breakdown of allanite.

5.3 U-Pb age interpretation and relationships with titanite microstructure and composition

Titanite U-Pb data can be affected by incorporation of significant amounts of common lead (Pb_c) during mineral (re-)crystallization (e.g., Kohn, 2017; Kirkland et al., 2018) and thus U-Pb isotopic data require correction before age calculations. The most commonly used method for correction is the ^{207}Pb -based correction (e.g., Spenser et al., 2013; Kirkland et al., 2016) which assumes that every data point lies on a mixing line between radiogenic lead ($0\%Pb_c$) and common lead ($100\%Pb_c$; Scibiorski et al., 2019). For a precise correction an appropriate $^{207}Pb/^{206}Pb$ composition for common lead must be used. One approach is to assume a Pb_c composition based on a global lead evolution model such as the model

proposed by Stacey and Kramers (1975), alternatively, in cases where the U-Pb data spread along the Pb_c -Pb mixing line, the approach is to regress the uncorrected data and then use the upper intercept as the common lead composition. The Tera-Wasserburg diagram is also useful in order to evaluate the Pb and/or U mobility that affected the analyses. U-Pb ages can be obtained by using these inverse isochrons (i.e., the Tera-Wasserburg plots) allowing to regress more radiogenic and less radiogenic measurements and providing lower intercept and upper intercept ages as indicative of crystallisation and Pb_c composition, respectively. In this work, titanite U-Pb data were determined without correction by using the lower and intercept ages of the data regression (Tera-Wasserburg diagrams).

It is interesting to note that only for the Amph-rich mylonitic layer (AN01A), titanite isotopic data can be clearly subdivided in populations (g1, g2, g3, g4) according to the spot position within the grain (Fig. A.3.5A). In particular, data from the titanite cores (g1) define a mixing line between Pb_c and radiogenic Pb with the oldest lower intercept ages; whereas the rims (g3, g4) of the grains yield an alignment characterised by higher amount of Pb_c and pointing to the youngest lower intercept age. These two populations define the boundary of the dataset which contains a several data related to intermediate position (g2) between rims and cores. The data suggest that during deformation Pb was lost from titanite cores or other U-bearing phases and was incorporated within the edges/rims (Kirkland et al., 2018). It is important to note that U-Pb data coinciding with the rims with the higher Pb_c content (g4) refer to total recrystallized titanite (Fig. A.3.3C) and are further broadly correlated with lower La, Nb, Y and Zr concentrations (Fig. A.3.5B-E). This can be explained by the fact that these late domains crystallised in a system where these elements were already fractionated within the former titanite domains by other minerals as effectively supported by the microstructural features (Fig. A.3.7B).

Titanite from the Cpx/Pl-rich mylonitic domain (AN01D) does not show clear correlation with the spot position resulting in accordance with the cloud of U-Pb data and with the weak textural and microstructural observations (Fig. A.3.7B, C). The only good correlation that was observed consisted in the U-Pb data, which define the younger lower intercept age, that show a weak correlation with Sr. Since these data are not strictly related to the external rims it is difficult to suggest a possible explanation. However, it is apparent that relationships between titanite chemistry and isotopic data are completely different from one sample to another in a close distance (a few centimetres; Fig. A.3.7A, B).

Therefore, it is highlight that even the U-Pb data, together with microstructure and chemistry,

recorded the different behaviour of titanite as strongly depended on the mineral assemblage and the bulk rock chemistry. Titanite from the Cpx/Pl-rich mylonitic domain (i.e., AN01D) lies, indeed, only preferentially on plagioclase and clinopyroxene rich layers that were interpreted as former calc-silicate levels (Chapter 5). Here, the correlation between U-Pb data and Sr could be explained by the petrographical and microstructural observations of calcite along the recrystallized tails of clinopyroxene porphyroclasts (Fig. A.3.7A). Conversely in the Amph-rich domain (AN01A), titanite are clearly core-rim zoned and deformation distortion and intracrystalline deformation become stronger. Thus, it is likely that titanite formed in association with clinopyroxene break down reactions: $\text{Cpx} + \text{Ilm} + \text{SiO}_2 + \text{H}_2\text{O} = \text{Ttn} + \text{Amph}$ (e.g., Harlov et al., 2006). To support this state are the textural observations from both sample domains, where titanite grains preferentially occur at contact with clinopyroxene porphyroclasts or embodied in the recrystallized plagioclase matrix, as well as the presence of ilmenite tails surrounding titanite grains.

5.4 Geochronology of Anzola shear zone and regional implications

A summary of U-Pb data from titanite of the mylonitic amphibolites of the Anzola shear zone is shown in Figure 7C. What is evident is that the U-Pb data are mainly distributed in the range of 260–180 Ma suggesting that the shear zone was active from Triassic to Early Jurassic (Fig. A.3.7C, D).

Since titanite is strongly reactive with the surrounded mineral phases and it can be subjected to rework during its history (e.g., Stearn et al., 2015), we cannot be totally sure that the old ages related to the “undeformed” core of titanite effectively coincides with the beginning of the shear zone activity (i.e., 260-240 Ma). Nevertheless, thanks to the petrochronology and the combination of U-Pb data with microstructures and geochemical features of titanite grains, we could hypothesises that the old ages could refer to an early deformation stage when probably the activity of shear zone started, metamorphic minerals became unstable and titanite started to react. This hypothesis can be partially supported by Ar-Ar radiometric dating of amphibole from the Anzola shear zone by Brodie et al., (1989), who provided a minimum age of about 247 Ma for unsheared mafic rocks and about 210-215 Ma for syn-kinematic amphibole grains. According to the authors, crustal extension started around 280 Ma, after the emplacement of the mafic intrusion, as further supported by other literature data from Ossola valley (Fig. A.3.7C; Carboniferous/Permian ages of mafic sills; U-Pb dating of zircon and/or monazite; Köppel, 1974; Klötzli et al., 2014; Kusiak et al., 2019) marking the beginning of a long-lasting

period of crustal thinning and cooling of more than 100 Myr. Therefore, on the base of our findings and those from Brodie et al., (1989), two hypotheses can explain the old ages (i.e., 260-240 Ma) found with U-Pb titanite from mylonitic amphibolites: i) titanite experienced cooling after the Variscan high temperature metamorphic and magmatic events (about 280-250 Ma); ii) titanite may have recorded heating stage due to the intrusion of undeformed Anzola gabbro in the early Triassic (i.e., 247 Ma; Brodie et al., 1989). Unfortunately, we didn't date gabbro due to the absence of datable minerals (i.e., zircon; as well as being beyond the aim of this work) and the only data available up to now is that relative the Ar-Ar dating on hornblende (i.e., 247 Ma) from Brodie et al., (1989). Therefore, we cannot say with certainty which of the two hypotheses is the more credible. Overall, according to Brodie et al., (1989), the considerably younger dates (215 and 210 Ma) obtained from sheared metabasic rocks (comparable to this work studied mylonitic amphibolites), suggest that cooling and mylonitic shearing may be related.

Conversely to the old ages, we can be totally sure on the fact that titanite petrochronology and microstructural features indicate when the shear zone activity stopped, namely around 190-180 Ma. Overlapping our results with those from Brodie et al., (1989) relative to the syn-kinematic hornblende (215-210 Ma), we can constrain a timing of deformation for the Anzola shear zone between 210-170 Ma under amphibolite facies (Fig. A.3.7D). This time interval coincides with the activity of the greenschist facies Pogallo Line (210–170 Ma; Fig. A.3.7D; Mulch et al., 2002; Wolff et al., 2012) and the activity of the granulite-facies shear zone from the northernmost sector of the IVZ (206-183 Ma; Boriani and Villa, 1997; Langone et al., 2018; Corvò et al., 2020). For both shear zone, the authors proposed that the shearing occurred during Late Triassic and ended during Early Jurassic in a time interval between 210-170 Ma (Fig. A.3.7D). Therefore, based on our new findings and existing geochronological studies, we can state that extensional shearing occurred simultaneously at different crustal levels within the studied sector of the IVZ (Fig. A.3.7D). In conclusion, this confirms the modern interpretations that attributed those ages linked to deformation which accommodate lower crustal extension and rifting processes which drove the Adriatic microplate evolution (e.g., Beltrando et al., 2015; Ewing et al., 2015; Langone et al., 2018; Petri et al., 2019; Corvò et al., 2020; Simonetti et al., 2021).

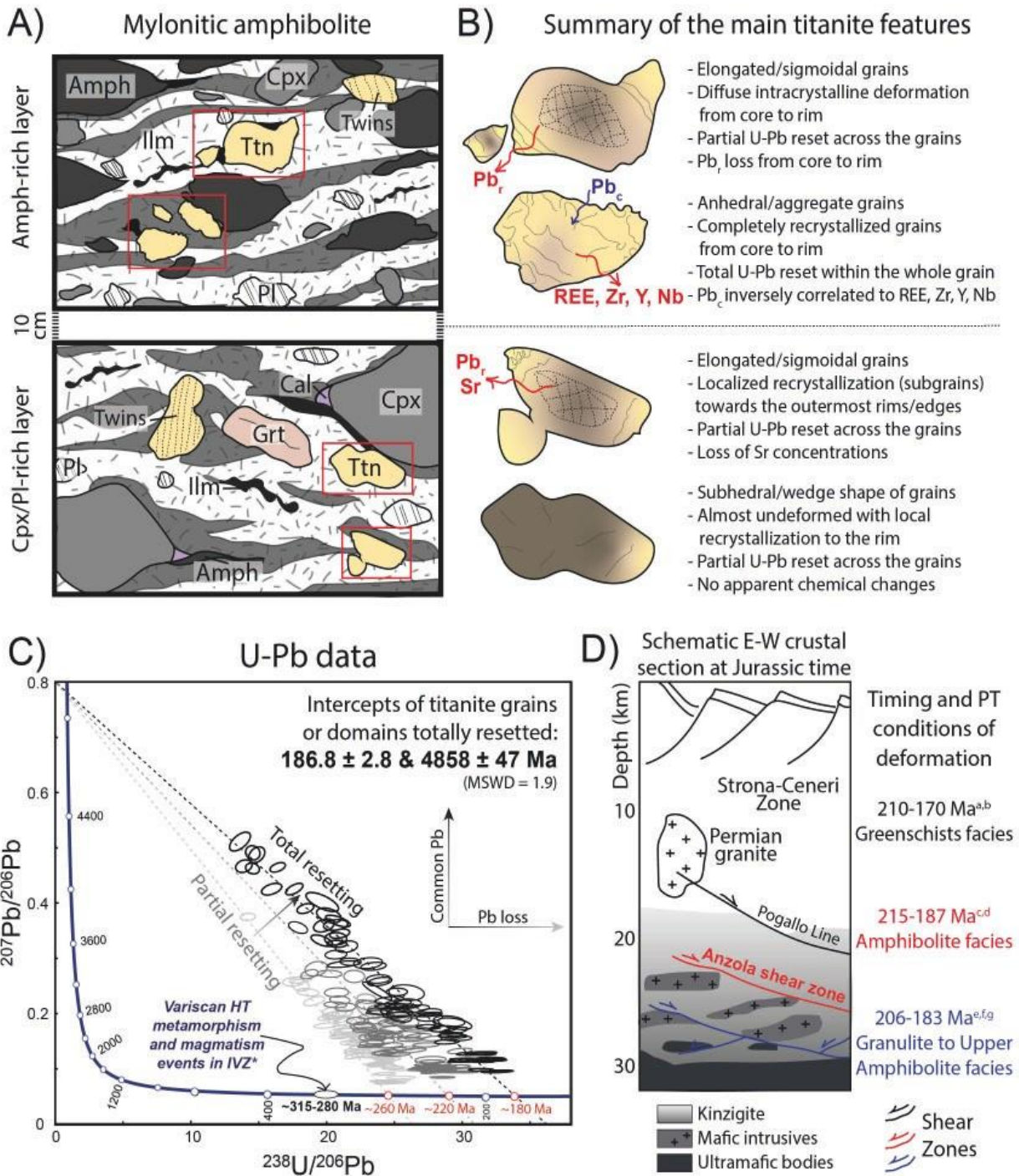


Fig. A.3.7 - Summary of petrochronology and textural/microstructural features of titanite and host rock of Anzola shear zone. A) Schematic representation of titanite and rock textures described in the text. The cartoons were drawn following thin sections viewed at the same scale, such that the grain size and mineralogical relationships are accurately represented. B) Summary of the main petrochronological, textural and microstructural titanite features from the studied sample. Titanite developed different features as function of deformation producing partial or total U-Pb reset and locally showing chemical changes with main mineral phases. Pb_r = radiogenic lead; Pb_c = common lead. C) Summary of U-Pb geochronological analysis of titanite on the studied samples (AN01A, AN01D). * = geochronological literature data from Koppel, (1974) and Klötzli et al., (2014). D) Schematic crustal section of the Jurassic passive continental margin in the Southern Alps (modified after Langone et al., 2018), showing the Anzola shear zone and other extensional faults at different crustal levels. Available timing and PT conditions of deformation are reported in a: Ar-Ar on white mica (Mulch et al., 2002); b: K-Ar on micas (Wolff et al., 2012); c: U-Pb on titanite (this work); d: Ar-Ar on hornblende (Brodie et al., on 1989); e: Ar-Ar on hornblende (Boriani and Villa, 1997); f: U-Pb on zircon (Langone et al., 2018); g: U-Pb on zircon (Corvò et al., 2020).

6. Conclusions

A petrochronological and microstructural study was performed on titanite grains from mylonitic amphibolites with the aim to testify the efficiency of its properties as petrochronometer and to constrain the activity of an important rift-related shear zone (i.e., the Anzola shear zone, IVZ).

The adopted multidisciplinary approach allowed to highlight that:

- Titanite develops different textural and microstructural features at the micro-scale (~10 μ m) in dependence of the different composition and rheological behaviour of the rock. Moreover, core-rim zoning, intracrystalline deformation, incipient recrystallization, deformation twins can be typical microstructural features attributable to deformation processes as recrystallization during the activity of a shear zone.
- Trace element concentrations in titanite allowed to confirm that its chemistry varies with host-rock lithology and especially Al/Fe versus Σ LREE and Fe versus Zr/Y contents proved that the studied titanite coincide with recrystallized metamorphic titanite grains derived from mafic and calc-silicate rocks as supported by petro-microstructural features. Conversely, Y versus Dy/Yb and Total HREE and Y/(Dy/Yb) revealed that titanite grew in absence of garnet, even if in one sample garnet is present. Nevertheless, this observation was attributable to the strong mobilization of chemical element occurring in heterogenous chemical and rheological microdomains of which the Anzola mylonitic amphibolites is constitute. This last aspect is further underlined by REE titanite patterns characterized by an apparent LREE fractionation over MREE and HREE usually due to open chemical system and thus intragrain chemical changes facilitated during titanite (re)crystallization processes and intracrystalline deformation.
- Even the isotopic data is strongly correlated to titanite chemistry and microstructures, which in turn differ from one sample to another in a close distance. In particular, the Amph-rich domain show a very nice correlation with spot position (old ages coincide with undeformed core, young ages recrystallized rims or total recrystallized titanite grains). Conversely, the Cpx/Pl-rich domain show a good correlation with chemistry (e.g., Sr) but it doesn't show clear correlation with textural and microstructural features.
- Overall, titanite from the mylonitic amphibolites of the Anzola shear zone likely recorded a

complex tectono-metamorphic history. Since its strong reactivity, indeed, it is not sure to define the start of the Anzola shear zone activity. However, what is certain is that deformation stopped in the Jurassic, around 185 Ma, according to the geochronological literature data available for the shear zones from other different crustal levels of the IVZ.

In conclusion, the adopted microstructural and petrochronological approach allowed to make interesting constrains not only on the role and behaviour of titanite as petrochronometer but also on the role of the Anzola shear zone during Triassic-Jurassic extension and exhumation.

References

- Aleinikoff, J. N., Wintsch, R. P., Tollo, R. P., Unruh, D. M., Fanning, C. M., & Schmitz, M. D., 2007. Ages and origins of rocks of the Killingworth dome, south-central Connecticut: Implications for the tectonic evolution of southern New England. *American Journal of Science*, 307(1), 63-118.
- Altenberger, U., 1997. Strain localization mechanisms in deep-seated layered rocks. *Geol. Rundsch.*, 86(1): 56-68.
- Beltrando, M., Stockli D.F., Decarlis A. and Manatschal G., 2015b. A crustal-scale view at rift localization along the fossil Adriatic margin of the Alpine Tethys preserved in NW Italy. *Tectonics*, 34: 1927-1951.
- Bestmann, M., Piazzolo, S., Spiers, C.J., Prior, D.J., 2005. Microstructural evolution during initial stages of static recovery and recrystallization: new insights from in-situ heating experiments combined with electron backscatter diffraction analysis. *J. Struct. Geol.* 27, 447-457.
- Boriani, A. and Villa I.M., 1997. Geochronology of regional metamorphism in the Ivrea-Verbanò Zone and Serie dei Laghi, Italian Alps. *Schweiz. Miner. Petrogr.*, 77: 381-402.
- Brodie, K.H., 1980. Variations in mineral chemistry across a phlogopite shear zone. *J. Struct. Geol.*, 2, 265-272.
- Brodie, K.H., 1981. Variation in amphibole and plagioclase composition with deformation. *Tectonophysics* 78, 385-402.
- Brodie, K.H. and Rutter E.H., 1987. Deep crustal extensional faulting in the Ivrea Zone of Northern Italy. *Tectonophysics*, 140: 193-212.
- Brodie, K.H., Rutter E.H. and Rex D., 1989. On the age of deep crustal extensional faulting in the Ivrea zone, Northern Italy. *Geol. Soc. London Spec. Publ.*, 45: 203-210.
- Brooks, K., 2019. Sphene (titanite). *Geology Today*, 35(5), 196-200.
- Carvalho, B.B., Bartoli, O., Ferri, F., Cesare, B., Ferrero, S., Remusat, L., Capizzi, L., and Poli, S., 2019. Anatexis and fluid regime of the deep continental crust: New clues from melt and fluid inclusions in metapelitic migmatites from Ivrea Zone (NW Italy). *Journal of Metamorphic Geology*, 37(7), 951-975.
- Cavosie, A. J., Spencer, C., Evans, N., Rankenburg, K., Thomas, R. J., & Macey, P. H., 2022. Granular titanite from the roter kamm crater in Namibia: Product of regional metamorphism, not meteorite impact. *Geoscience Frontiers*, 101350.
- Cherniak, D.J., 1993. Lead diffusion in titanite and preliminary results on the effects of radiation damage on Pb transport. *Chemical Geology* 110, 177-194.
- Cherniak, D. J., 2010. Diffusion in accessory minerals: zircon, titanite, apatite, monazite and xenotime. *Reviews in mineralogy and geochemistry*, 72(1), 827-869.
- Corvò, S., Langone, A., Padrón-Navarta, J.A., Tommasi, A. and Zanetti, A., 2020. Porphyroclasts: Source and sink of major and Trace Elements during deformation induced metasomatism (Finero, Ivrea-Verbanò Zone, Italy). *Geosciences*, 10: 196. <https://doi.org/10.3390/geosciences10050196>.
- Degli Alessandrini, G., 2018. Deformation mechanisms and strain localization in the mafic continental

- lower crust. PhD thesis, School Geogr. Earth Environ. Sci. Univ. Plymouth, 366 pp.
- Denyszyn, S. W., Fiorentini, M. L., Maas, R., & Dering, G., 2018. A bigger tent for CAMP. *Geology*, 46(9), 823-826.
- Erickson, T. M., Kirkland, C. L., & Timms, N. E. (2018, March). Deformation microstructures preserved in zircon and monazite from the Yarrabubba impact structure, Western Australia. In *Lunar and Planetary Science Conference* (No. 2083, p. 1764).
- Ewing, T.A., Hermann, J. and Rubatto, D., 2013. The robustness of the Zr-in-rutile and Ti-in-zircon thermometers during high-temperature metamorphism (Ivrea-Verbano Zone, Northern Italy). *Contrib. Miner. Petrol.*, 165: 757-779.
- Ewing T.A., Rubatto D., Beltrando M. and Hermann J., 2015. Con-straints on the thermal evolution of the Adriatic margin during Jurassic continental break-up: U-Pb dating of rutile from the Ivrea-Verbano Zone, Italy. *Contrib. Miner. Petrol.*, 169: 44.
- Frost, B. R., Chamberlain, K. R., & Schumacher, J. C., 2001. Sphene (titanite): phase relations and role as a geochronometer. *Chemical geology*, 172(1-2), 131-148.
- Garber, J.M., Hacker, B.R., Kylander-Clark, A.R.C., Stearns, M., Seward, G., 2017. Controls on Trace Element Uptake in Metamorphic Titanite: Implications for Petrochronology. *Journal of Petrology* 58 (6), 1031e1057
- Gordon, S. M., Kirkland, C. L., Reddy, S. M., Blatchford, H. J., Whitney, D. L., Teyssier, C., ... & McDonald, B. J., 2021. Deformation-enhanced recrystallization of titanite drives decoupling between U-Pb and trace elements. *Earth and Planetary Science Letters*, 560, 116810.
- Hayden, L.A., Watson, E.B., Wark, D.A., 2008. A thermobarometer for sphene (titanite). *Contributions to Mineralogy and Petrology* 155, 529e540.
- Hodges, K. V., & Fountain, D. M., 1984. Pogallo Line, South Alps, northern Italy: An intermediate crystal level, low-angle normal fault?. *Geology*, 12(3), 151-155.
- Karakas, O., Wotzlav, J.F., Guillong, M., Ulmer, P., Brack, P., Econo-mos, R., Bergantz, G.W., Sinigoi, S. and Bachmann, O., 2019. The pace of crustal-scale magma accretion and differentiation beneath silicic caldera volcanoes: *Geology*, 47: 719-723.
- Kirkland, C.L., Spaggiari, C.V., Johnson, T.E., Smithies, R.H., Danišák, M., Evans, N., Wingate, M.T.D., Clark, C., Spencer, C., Mikucki, E., McDonald, B.J., 2016. Grain size matters: Implications for element and isotopic mobility in titanite. *Precambrian Res.* 278, 283-302.
- Kirkland, C., Fougereuse, D., Reddy, S., Hollis, J., Saxey, D., 2018. Assessing the mechanisms of common Pb incorporation into titanite. *Chem. Geol.* 483, 558-566.
- Kirkland, C. L., Yakymchuk, C., Gardiner, N. J., Szilas, K., Hollis, J., Olierook, H., & Steenfelt, A., 2020. Titanite petrochronology linked to phase equilibrium modelling constrains tectono-thermal events in the Akia Terrane, West Greenland. *Chemical Geology*, 536, 119467.
- Kylander-Clark, A.R., Hacker, B.R., Cottle, J.M., 2013. Laser-ablation split-stream ICP petrochronology. *Chemical Geology* 345, 99e112.
- Kohn, M.J., 2017. Titanite petrochronology. *Reviews in Mineralogy and Geochemistry* 83 (1), 419e441.
- Klötzli, U. S., Sinigoi, S., Quick, J. E., Demarchi, G., Tassinari, C. C., Sato, K., & Günes, Z. (2014). Duration of igneous activity in the Sesia Magmatic System and implications for high-temperature metamorphism in the Ivrea-Verbano deep crust. *Lithos*, 206, 19-33.
- Kohn, M.J., 2017. Titanite petrochronology. *Review in Mineralogy & Geochemistry*, 83, 419-441.
- Köppel 1974. Isotopic U-Pb Ages of Monazites and Zircons from the Crust-Mantle Transition and Adjacent Units of the Ivrea and Ceneri Zones (Southern Alps, Italy). *Contr. Mineral. And Petrol.*, 43, 55-70.
- Kunz, B.E., Johnson, T.E., White, R.W. and Redler, C., 2014. Partial melting of metabasic rocks in Val Strona di Omegna, Ivrea Zone, Northern Italy. *Lithos*, 190-191, 1-12.
- Kusiak M.A., Kovaleva E., Wirth R., Klötzli U., Dunkley D.J., Yi K. and Lee S., 2019. Lead oxide nanospheres in seismically deformed zircon grains. *Geochim. Cosmochim. Acta*, 262: 20-30.

- Langone A., Zanetti A., Daczko N.R., Piazzolo S., Tiepolo M. and Mazzucchelli M., 2018. Zircon U-Pb dating of a lower crustal shear zone: A case study from the northern sector of the Ivrea-Verbanco Zone (Val Cannobina, Italy). *Tectonics*, 37: 322-342.
- Ludwig, K. R., 2003. *Isoplot 3.00: A Geochronological Toolkit for Microsoft Excel*. Berkeley Geochronology Center Special Publication No. 4.
- Manatschal, G., Müntener, O., Lavie, L. L., Minshull, T. A., & Péron-Pinvidic, G. (2007). Observations from the Alpine Tethys and Iberia–Newfoundland margins pertinent to the interpretation of continental breakup. *Geological Society, London, Special Publications*, 282(1), 291-324.
- McGregor, M., Erickson, T. M., Spray, J. G., & Whitehouse, M. J., 2021. High-resolution EBSD and SIMS U–Pb geochronology of zircon, titanite, and apatite: insights from the Lac La Moine impact structure, Canada. *Contributions to Mineralogy and Petrology*, 176(10), 1-25.
- Mohn, G., Manatschal, G., Beltrando, M., Masini, E. and Kuszniir, N., 2012. Necking of continental crust in magma-poor rifted margins: Evidence from the fossil Alpine Tethys margins: necking of continental crust. *Tectonics*, 31 (1): TC1012.
- Mottram, C. M., Cottle, J. M., & Kylander-Clark, A. R. (2019). Campaign-style U-Pb titanite petrochronology: along-strike variations in timing of metamorphism in the Himalayan metamorphic core. *Geoscience Frontiers*, 10(3), 827-847.
- Mulch, A., Cosca, M., & Handy, M., 2002. In-situ UV-laser $^{40}\text{Ar}/^{39}\text{Ar}$ geochronology of a micaceous mylonite: an example of defect-enhanced argon loss. *Contributions to Mineralogy and Petrology*, 142(6), 738-752.
- Oberti, R., Smith, D. C., Rossi, G., & Caucia, F., 1981. The crystal-chemistry of high-aluminium titanites. *European Journal of Mineralogy*, 777-792.
- Papapavlou, K., Darling, J. R., Moser, D. E., Barker, I. R., White, L. F., Lightfoot, P. C., ... & Dunlop, J., 2018. U–Pb isotopic dating of titanite microstructures: potential implications for the chronology and identification of large impact structures. *Contributions to Mineralogy and Petrology*, 173(10), 1-15.
- Passchier, C. W., & Trouw, R. A., 2005. *Microtectonics*. Springer Science & Business Media.
- Peressini, G., Quick J.E., Sinigoi S., Hofmann A.W. and Fanning M., 2007. Duration of a large mafic intrusion and heat transfer in the lower crust: a SHRIMP U-Pb Zircon study in the Ivrea-Verbanco Zone (Western Alps, Italy). *J. Petrol.*, 48: 1185-1218.
- Petri, B., Duret T., Mohn G., Schmalholz S.M., Karner G.D. and Müntener, O., 2019. Thinning mechanisms of heterogeneous continental lithosphere. *Earth Planet Sc. Lett.*, 512: 147–162.
- Piazzolo, S., La Fontaine, A., Trimby, P., Harley, S., Yang, L., Armstrong, R., & Cairney, J. M. (2016). Deformation-induced trace element redistribution in zircon revealed using atom probe tomography. *Nature communications*, 7(1), 1-7.
- Pittarello, L., Pennacchioni, G., & Di Toro, G., 2012. Amphibolite-facies pseudotachylytes in Premosello metagabbro and felsic mylonites (Ivrea Zone, Italy). *Tectonophysics*, 580, 43-57.
- Quick, J. E., Sinigoi, S., Snoke, A. W., Kalakay, T. J., Mayer, A., Peressini, G., 2003. Geological map of the southern Ivrea-Verbanco Zone, northwestern Italy. US Geological Survey.
- Redler, C., Johnson T.E., White R.W. and Kunz B.E., 2012. Phase equilibrium constraints on a deep crustal metamorphic field gradient: metapelitic rocks from the Ivrea Zone (NW Italy): Ivrea Zone metamorphic field gradient. *J. Metam. Geol.*, 30: 235-254.
- Rutter E.H., Brodie K.H. and Evans P.J., 1993. Structural geometry, lower crustal magmatic underplating and lithospheric stretching in the Ivrea-Verbanco zone, northern Italy. *J. Struct. Geol.*, 15: 647-662.
- Rutter, E., Brodie, K., James, T., Burlini, L., 2007. Large-scale folding in the upper part of the Ivrea-Verbanco zone, NW Italy. *Journal of Structural Geology*, 29, 1–17.
- Schmid, S.M., 1993. Ivrea zone and adjacent southern Alpine basement. In: J.F. Raumer and F. Neubauer (Eds.). *Pre-Mesozoic geology in the Alps*, Springer, Berlin, Heidelberg, p. 567-583.
- Schmid, R., and Wood, B.J., 1976. Phase relationships in granulitic metapelites from the Ivrea-Verbanco zone (Northern Italy). *Contrib. Miner. Petrol.*, 54: 255-279.
- Schmid, S.M., Zingg, A., Handy, M., 1987. The kinematics of movements along the Insubric Line and the

- emplacement of the Ivrea Zone. *Tectonophysics*, 135, 47–66.
- Scibiorski E., Kirkland C.L.C., Kemp A.I.S., Tohver E., Evans N.J. 2019. Trace elements in titanite: A potential tool to constrain polygenetic growth processes and timing. *Chemical Geology*, 509, 1-19.
- Scibiorski, E. A., & Cawood, P. A., 2022. Titanite as a petrogenetic indicator. *Terra Nova*.
- Scott, D. J., & St-Onge, M. R., 1995. Constraints on Pb closure temperature in titanite based on rocks from the Ungava orogen, Canada: Implications for U-Pb geochronology and PTt path determinations. *Geology*, 23(12), 1123-1126.
- Siegesmund, S., Layer P., Dunkl I., Vollbrecht A., Steenken A., Wemmer K. and Ahrendt H., 2008. Exhumation and deformation history of the lower crustal section of the Valstrona di Omega in the Ivrea Zone, southern Alps. *Geol. Soc. London Spec. Publ.*, 298: 45-68. <https://doi.org/10.1144/SP298.3>.
- Simonetti, M., Langone, A., Corvò, S., Bonazzi, M., 2021. Triassic-Jurassic rift-related deformation and temperature-time evolution of the fossil Adriatic margin: A review from Ossola and Strona di Omega valleys (Ivrea-Verbano Zone). *Ofioliti*, 46(2), 147-161.
- Smye A.J. and Stockli D.F., 2014. Rutile U-Pb age depth profiling: A continuous record of lithospheric thermal evolution. *Earth Planet. Sci. Lett.*, 408: 171-182.
- Smye A.J., Lavier L.L., Zack T. and Stockli D.F., 2019. Episodic heating of continental lower crust during extension: A thermal modeling investigation of the Ivrea-Verbano Zone. *Earth Planet. Sci. Lett.*, 521: 158-168.
- Spencer, K.J., Hacker, B.R., Kylander-Clark, A.R.C., Andersen, T.B., Cottle, J.M., Stearns, M.A., Poletti, J.E., Seward, G.G.E., 2013. Campaign-style titanite U-Pb dating by laser ablation ICP: Implications for crustal flow, phase transformations and titanite closure. *Chemical Geology* 341, 84e101. Kohn M.J., 2017. Titanite petrochronology. *Review in Mineralogy & Geochemistry*, 83, 419-441.
- Stacey, J.S., Kramers, J.D., 1975. Approximation of terrestrial lead isotope evolution by a two-stage model. *Earth Planet. Sci. Lett.* 26, 207–221.
- Stearns, M. A., Hacker, B. R., Ratschbacher, L., Rutte, D., & Kylander-Clark, A. R. C. (2015). Titanite petrochronology of the Pamir gneiss domes: Implications for middle to deep crust exhumation and titanite closure to Pb and Zr diffusion. *Tectonics*, 34(4), 784-802.
- Stünitz H., 1998. Syndeformational recrystallization - dynamic or compositionally induced? *Contrib. Mineral. Petrol.*, 131: 219–236
- Tiepolo, M., Oberti, R., Vannucci, R., 2002. Trace-element incorporation in titanite: constraints from experimentally determined solid/liquid partition coefficients. *Chem. Geol.* 191, 105–119.
- Timms, N. E., Pearce, M. A., Erickson, T. M., Cavosie, A. J., Rae, A. S., Wheeler, J., ... & Morgan, J. V., 2019. New shock microstructures in titanite (CaTiSiO₅) from the peak ring of the Chicxulub impact structure, Mexico. *Contributions to Mineralogy and Petrology*, 174(5), 1-23.
- Walters, J. B., & Kohn, M. J., 2017. Protracted thrusting followed by late rapid cooling of the Greater Himalayan Sequence, Annapurna Himalaya, Central Nepal: Insights from titanite petrochronology. *Journal of Metamorphic Geology*, 35(8), 897-917.
- Wheeler, J., Mariani, E., Piazzolo, S., Prior, D. J., Trimby, P., & Drury, M. R., 2009. The weighted Burgers vector: a new quantity for constraining dislocation densities and types using electron backscatter diffraction on 2D sections through crystalline materials. *Journal of microscopy*, 233(3), 482-494.
- Wolff R., Dunkl I., Kiesselbach G., Wemmer K., and Siegesmund S., 2012. Thermochronological constraints on the multiphase exhumation history of the Ivrea-Verbano Zone of the Southern Alps. *Tectonophysics*, 579: 104-117.
- Zanetti, A., Mazzucchelli, M., Sinigoi, S., Giovanardi, T., Peressini, G., & Fanning, M., 2013. SHRIMP U–Pb zircon Triassic intrusion age of the Finero mafic complex (Ivrea–Verbano Zone, Western Alps) and its geodynamic implications. *Journal of Petrology*, 54(11), 2235-2265.
- Zingg A., 1990. The Ivrea crustal cross-section (Northern Italy and Southern Switzerland). In: M.H. Salisbury and D.M. Fountain (Eds.), *Exposed cross-sections of the continental crust*. Springer Netherlands, Dordrecht, p. 1-19.

APPENDIX 4:
Microstructural characterization (SEM-EBSD)
of mylonitic amphibolites from the Anzola shear zone.

A.4 Microstructural characterization (SEM-EBSD) of mylonitic amphibolites from the Anzola shear zone.

In this paragraph, I briefly report the preliminary microstructural (SEM-EBSD) results performed on the mylonitic amphibolites from the Anzola shear zone (samples AN01; see chapter 5.6.2 for details). These data were obtained during the development of the work reported in chapter 5. They will be the object of another manuscript focused on the microstructural characterization of the mylonitic amphibolite of the Anzola shear zone and related deformation mechanisms. The results shown here were the object of a poster presentation at the SGI 2021 congress. The abstract is presented below.

Microstructural and petrological characterization of a major extensional shear zone in the middle crust (Val d'Ossola, Ivrea-Verbano Zone, Western Alps)

Stefania Corvò^{1,2*}, Matteo Maino^{1,2}, Antonio Langone², Sandra Piazzolo³

1 Dipartimento di Scienze della Terra e dell'Ambiente, Università degli studi di Pavia, Pavia, Italia

2 Istituto di Geoscienze e Georisorse di Pavia, C.N.R, Pavia, Italia

3 School of Earth and Environment, University of Leeds, Leeds, United Kingdom

Abstract

Shear zones localise most of deformation in narrow areas and provide efficient ways to mobilize significant volumes of fluids and melts up and down the crust. Deformation may localise if a specific domain focuses higher differential stress or strain rate with respect the host rocks. This concentration is commonly associated with variations in rock composition/texture, temperature/pressure conditions or presence of fluid/melts, which are even likely the dominant factor for weakening.

In this contribution, we investigate exhumed shear zone developed in the middle crust with the aim to decipher which heterogeneities promoted the strain localisation in a fully ductile regime. We present microstructural and petrological data to characterise the Pressure-Temperature- Deformation (*P-T-D*) path across a major extensional shear zone of the Ivrea-Verbano Zone (IVZ, Western Alps) exposed along the Ossola Valley, the Anzola shear zone (ASZ). The ASZ developed at the transition between amphibolite and granulite facies conditions and consists of metabasites rock showing mylonitic fabric alternating layers made mainly of clinopyroxene, amphibole and plagioclase porphyroclasts and in recrystallized grains. The SZ boundaries consist in undeformed gabbroic rocks to one side and felsic and mafic granulite to the other side. A calcsilicate layer occurs at the contact among the gabbroic

rocks and SZ. Our preliminary results suggest that deformation in the ASZ took place under granulite/amphibolite facies conditions at approximately between 650-800°C and confining pressures of around 8 kbar. Microstructural and textural data indicate that dissolution-precipitation creep is the dominant deformation mechanism. Evidence of synchronous deformation and mineral reactions of clinopyroxene suggests that metabasite become mechanically weak during the general transformation weakening process. This process was driven by melt flux deformation demonstrated by the occurrence of large amphibole porphyroclasts and interstitial ilmenite. Petrographic and textural observations suggest that the SZ was characterized by melt-rock interaction with the adjacent gabbroic and metamorphic wall rocks. In fact, our results show that the ASZ is extremely heterogeneous consisting by alternation of amphibolitic and calcsilicate layers, supported by the geochemical observations (e.g., occurrence of two different composition cpx: diopside and hedenbergite). The possible pre-existing heterogeneity (i.e., layering and grain-size variations) was probably the loci of concentrated shear deformation (Altenberger, 1997) and the magmatic fluids could be the source of clinopyroxene weakness and of the abundant amphibole. In this last case, geological interpretations already given (Brodie, 1981; Stünitz, 1998) require reappraisal.

References:

- Altenberger U., 1997. Strain localization mechanisms in deep-seated layered rocks. *Geol. Rundsch.*, 86(1): 56-68.
- Brodie, K.H., 1981. Variation in amphibole and plagioclase composition with deformation. *Tectonophysics* 78, 385–402.
- Stünitz H., 1998. Syndeformational recrystallization - dynamic or compositionally induced? *Contrib. Mineral. Petrol.*, 131: 219–236.

Textural and microstructural features, future work directions

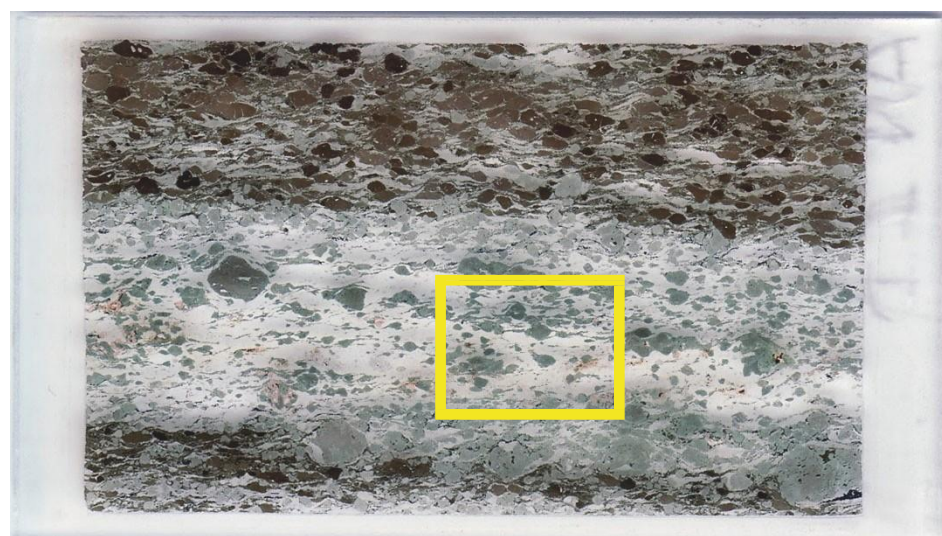
Two representative mylonitic amphibolites thin sections (amph-rich; cpx/pl-rich) from the Anzola shear zone were selected to better investigate the microstructural features of the main mineral phases. As demonstrated in chapter 5, the Anzola shear zone is characterized by a strong compositional variability even at the microscale. The aim of this microstructural investigation is to evaluate the rheological reply and the deformation mechanisms that develop as reply to the lithological heterogeneities. From the EBSD phase map is clear that the main mineral phases (i.e., clinopyroxene, plagioclase and amphibole) effectively have a different rheological reply to the deformation and that is also in dependence of the different compositional layering. In the first map is obtained from a zone

of the Amph-rich layer, clinopyroxene is mostly preserved as relict and is the less abundant phase. Plagioclase is completely recrystallized. Amphibole show two different textural features as mostly big rounded porphyroclast and as tails of recrystallized grains. The second phase map derives from the Cpx/Pl-rich layer. Here amphibole is completely absent, plagioclase predominate the matrix and is present mostly as recrystallized grains, even if few porphyroclasts are also observed. Clinopyroxene is present both as porphyroclasts and as tails of recrystallized grains. Further detailed microstructural investigations are needed, in order to better evaluate how at the microscale the main mineral phases differently reply to the compositional heterogeneities, which deformation mechanism develop in order to accommodate the strain localization and under which conditions these processes occur.

AN01E - Amph-rich

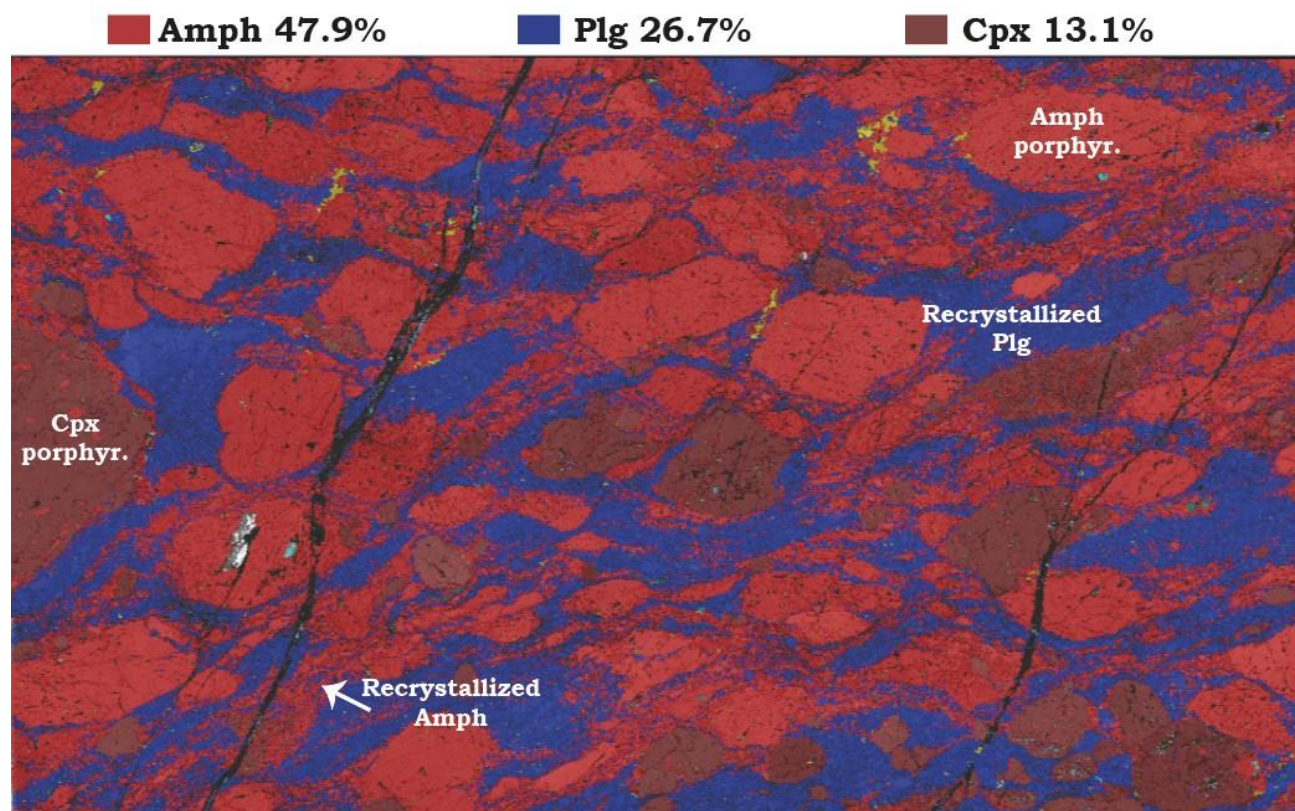


AN01D - Cpx/Pl-rich



Thin sections scans of the selected mylonitic amphibolites from the Anzola shear zone. The yellow boxes mark the area analysed by SEM-EBSD.

EBSO PHASE MAP MYLONITE AMPH-RICH



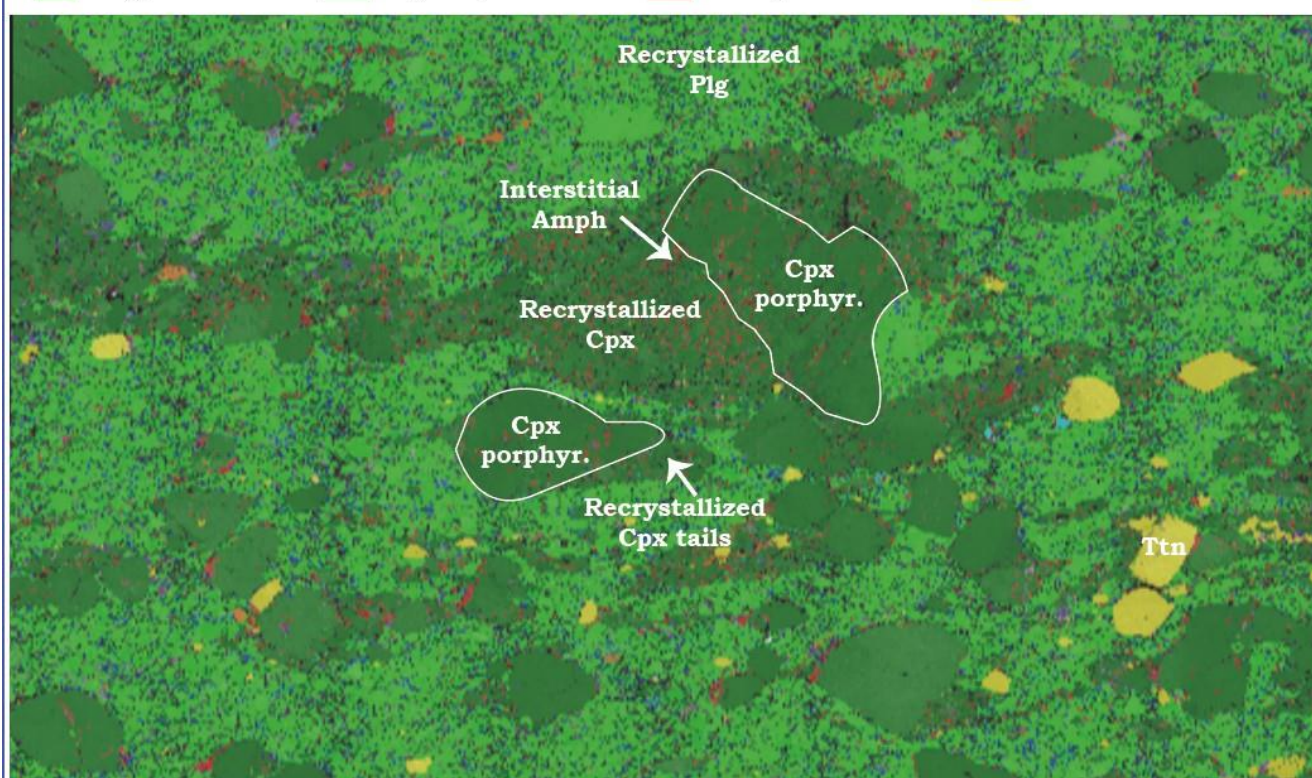
2 mm

Raster: 5725*10092

Step Size: 1 μ m

EBSO PHASE MAP MYLONITE PLG/CPX-RICH

■ Plg 49% ■ Cpx 26.3% ■ Amph 1.9% ■ Titanite 1.9%



1 mm

Raster: 6266*5692

Step Size: 1 μ m

APPENDIX 5

Thesis related manuscripts

A.5.1 Triassic-Jurassic rift related deformation and temperature-time evolution of the fossil Adriatic margin: A review from Ossola and Strona di Omegna valleys (Ivrea-Verbano Zone).

This manuscript presents a review of the Triassic-Jurassic geochronological and thermochronological data available for different sections of the Ivrea-Verbano Zone and discuss their implications for Mesozoic rifting-related tectonics and processes of lower crustal extension. It represents an important basis for further geochronological work relative to the evolution of the Ivrea-Verbano zone, or better of the Adriatic margin during the Late Triassic-Jurassic Tethyan rifting phase.

This paper was published open access on Ofioliti as Simonetti et al., (2021) on the Special section title: “Late Variscan to Alpine orogenic evolution: the role of rift inheritance”, dedicated to the memory of Marco Beltrando. Accepted in revised form 20 May 2021, available online 20 March 2021 and published online on 31 July 2021. This study was financed by the following project: PRIN2017 “Micro to Macro—how to unravel the nature of the large magmatic events; 20178LPCPWLangoneAntonio”.

For this work, the candidate collaborated with the team made by Matteo Simonetti (Servizio Geologico d’Italia, ISPRA), Mattia Bonazzi (University of Pavia) and Antonio Langone (Istituto di Geoscienze e Georisorse di Pavia) who conceptualized the work. All the authors equally contributed to the original initial draft and writing.

TRIASSIC-JURASSIC RIFT-RELATED DEFORMATION AND TEMPERATURE-TIME EVOLUTION OF THE FOSSIL ADRIATIC MARGIN: A REVIEW FROM OSSOLA AND STRONA DI OMEGNA VALLEYS (IVREA-VERBANO ZONE)

In “*Late Variscan to Alpine orogenic evolution: the role of rift inheritance*”.

Matteo Simonetti*, Antonio Langone ^{*,†}, Stefania Corvò^{***} and Mattia Bonazzi^{***}

* *Institute of Geosciences and Earth Resources, National Research Council (C.N.R.), Pavia, Italy.*

** *Department of Earth and Environmental Sciences, University of Pavia, Italy.*

[†] *Corresponding author, e-mail: langone@crystal.unipv.it*

Keywords: *geochronology; thermochronology; Ivrea-Verbano Zone; Anzola shear zone; Forno-Rosarolo shear zone; Tethyan rift; Adriatic Margin.*

ABSTRACT

The direct observation and investigation of rift-related structures at the mesoscale is uncommon. Hence, detailed constraints on the evolution of the main faults and shear zones developed during crustal extension are not always available.

The Ivrea-Verbano Zone, in the Italian Southern Alps, samples remnants of the former lower crust of the rifted margins surrounding the Alpine Tethys and therefore provides the opportunity to directly investigate rift-related tectonics. Here, several shear zones have been recognized and interpreted as related to Mesozoic rifting. However, even if there is a general agreement with this interpretation, the precise age of activity of many of those shear zones is not well constrained.

In this paper we present a review of the Triassic-Jurassic geochronological and thermochronological data available for two sections of the Ivrea-Verbano Zone, the Strona di Omezza and Ossola valleys, where at least two extensional shear zones are exposed. Ductile deformation occurred under amphibolite-facies conditions and it was alternatively attributed to late Variscan deformation or to Triassic-Jurassic rifting-related tectonics.

We discuss the available chronological data and the different interpretations provided for the shear zones considering also new geochronological studies on other lower crustal shear zones exposed in other sectors of the Ivrea-Verbano Zone. This review allows us to strengthen the more recent interpretations indicating that these shear zones are important tectonic structures related to Late Triassic-Jurassic deformation in the lower crust of the Adriatic margin.

INTRODUCTION

Several tectonic processes can lead to strain accumulation within the lithosphere. Strain is often localized into shear zones that show large variations in orientation, length, thickness, displacement, strain geometry, deformation regime and deformation mechanisms, all depending from the tectonic framework in which they form (e.g., Fossen and Cavalcante, 2017). Therefore, the study of shear zones may provide valuable information relevant to unravel the evolution of many geodynamic contexts. Because the complex nature of shear zones leads to a great variability in their evolution, a modern approach to the study of such structures requires the combination of many independent techniques, in order to unravel their kinematics, deformation temperatures, deformation regimes and strain geometry (see also Sibson, 1977; Law et al., 2004; Xypolias, 2010; Law, 2014). Furthermore, several geochronometers can be used to constrain the age and duration of deformation. Such multidisciplinary approach in the last years provided important constraints for new tectonic models in several collisional settings all over the world (Iacopini et al., 2008; Montomoli et al., 2013; Zhang et al., 2013; Iaccarino et al., 2015; Giorgis et al., 2017; Wu et al., 2017; Carosi et al., 2018; 2020; Parsons et al., 2018; Simonetti et al., 2020a; 2020b). The combination of geophysical, structural, geochronological and sedimentological studies also led to important advancement in understanding extensional tectonics, rift settings and related structures (Manatschal et al., 2007; Mohn et al., 2010; 2012; Beltrando et al., 2014; 2015;

Aravadinou and Xypolias, 2017; Langone et al., 2018; Real et al., 2018; Petri et al., 2019).

6WXGLHV RI ULIWHG PDUJLQV, LQ WKH ODVW GHFDGH, EHQHÀWHG from an increasing quantity of high-quality data from several disciplines. However, the direct observation and investigation of rift-related structures at the mesoscale is uncommon. Detailed constraints on the evolution of the main faults and shear zones developed during crustal extension are not always available even, if they would be fundamental data to elucidate this process and to constrain the rifting models.

Rift systems are generally subjected to shift in time and space within the evolving continental margins (Manatschal et al., 2007; Mohn et al., 2012; Beltrando et al., 2015). This is the case of the Mesozoic evolution of Southern Europe and North Africa where multiple rifting episodes characterize the Pangea breakup. Indeed, the Middle Triassic opening of the Meliata and Ionian Basins (Kozur, 1991; Speranza et al., 2012) was followed by the formation of the central Atlantic and the Alpine Tethys in the latest Triassic to Middle Jurassic times.

Extension-related tectonics began in the Late Triassic (Bertotti et al., 1993). During this epoch, extension of the upper crust was mainly controlled by major listric faults, such as the Lugano Val Grande fault, at the margins of Late Carboniferous-Early Permian basins. Subsequently, faulting around those centres gradually ceased and the site of extension shifted westwards towards the future site of crustal separation.

Manatschal et al. (2007), Mohn et al. (2012) and Beltrando et al. (2015) documented the rift-related evolution of the basement and the associated tectono-sedimentary record. According to their studies, three modes can be recognized during Tethyan rift localization. An initial stretching mode (mode 1) characterized by a ductile and diffused deformation of the middle and deep crust is followed by a thinning mode (mode 2) linked to initial rift localization and lithospheric WKLQQLQJ DQG, ÀQDOO, EÌ DQ H[KXPDWLRQ PRGH (PRGH 3) ZKHUH the crustal extension leads to a complete exhumation of the subcontinental mantle. During the three modes of Tethyan rift, several generations and types of extensional structures are formed, namely high-angle and low-angle normal faults, anastomosing shear-zones and decoupling horizons (Petri et al., 2019). Such structures accommodate the lateral extraction of mechanically stronger levels derived from the middle DQG ORZHU FUXVW. 7KH ÀUVV H[WHQVLRQDO GXFWLOH VKHDU JRQHV LQ the lower crust nucleates during the thinning mode (mode 2 of Manatschal et al. 2007) that is the less constrained stage among the three. Direct geological observations are not so common mainly because the fault systems and the sedimentary basins related to this mode are overprinted by subsequent, breakup-related deformation.

The Ivrea-Verbano Zone (IVZ) and the Serie dei Laghi (SdL) couple, in the Italian Southern Alps, samples remnants of the former Alpine Tethys rifted margin and therefore provides the opportunity to investigate rift-related tectonics across different crustal levels. In particular, the IVZ-SdL couple is interpreted as the Adriatic necking zone recording major thinning during Jurassic rifting (Decarlis et al., 2017). Instead, the Adriatic distal domain is preserved in the Canavese Zone, which shows evidence for subcontinental mantle H[KXPDWLRQ DW WKH VHDÁRRU (JHUUDQGR HW DO., 2004; %HOWUDQGR et al., 2015).

Several shear zones have been recognized in the IVZ (e.g., Rutter et al., 1993), where two major sets of structures are interpreted as related to Mesozoic rifting (Petri et al., 2019). 7KH ÀUVV VHW FRQVLRVW RI KLJK-WHPSHUDWXUH VKHDU JRQHV, whereas the second one consists of lower temperature fault structures. In the SdL, the Pogallo Line (PL), which in places marks the contact with the IVZ, is interpreted as a low-angle normal fault active under lower temperature conditions (Hodges and Fountain, 1984; Schmid et al., 1987; Zingg et al., 1990) compared to the shear zones within the IVZ (middle rift-related structures of Petri et al., 2019).

Even if there is a general agreement in considering all those structures linked to crustal extension, the precise age of activity of many of them is not well constrained and locally a detailed structural analysis is lacking. This leads to unclear correlations between similar structures that crops out in different localities of the IVZ and to the lack of precise structural and temporal constraints about the activity of such shear zones and faults. Because of these uncertainties, the reconstruction of exhumation and rifting processes is still limited and partly unclear.

7KH ÀUVV VVHS WRZDUG D FRPSOHWH XQGHUVVWDQGLQJ RI WKH UROH of the shear zones in the IVZ during rifting process is a complete revision of the geochronological and thermochronological data available in the literature. In this paper we present a detailed review and discussion of available geochronological and thermochronological data, with a focus on the Triassic-Jurassic time interval, for two sections of the IVZ exposed along the Strona di Omegna and Ossola valleys. Here, two shear zones, namely the Forno-Rosarolo and the Anzola shear zones respectively, are exposed. These two mylonitic

belts have been recently interpreted as belonging to the same system of shear zones affecting the northern sector of the IVZ, formed during the rifting process (middle rift-related structures of Petri et al., 2019). The aim of this paper is to verify which of the data already available in literature can be indicative of the period of activity of these structures, in order to strengthen their correlation and to better understand their role in the framework of Tethyan rifting.

GEOLOGICAL SETTING

The IVZ is located in northwestern Italy and belongs to the South Alpine domain (Fig. 1). It represents an exposed section of the pre-Alpine middle to lower continental crust that escaped a marked Alpine deformation overprint. It is separated from the Sesia Zone by the Insubric Line to the northwest and from the SdL by the Late-Variscan Cossato-Mergozzo-Brissago Line (CMB) and, in places, by the Pogallo Line (PL) to the southeast (Boriani et al., 1990). The CMB Line is crosscut by mylonites associated with the PL (Fig. 1), which is interpreted as a low-angle normal fault of Triassic-Jurassic age (Zingg et al., 1990) linked to crustal thinning (Hodges and Fountain, 1984). During the Alpine collision, the IVZ underwent exhumation and verticalization (Henk et al., 1997; Rutter et al., 2007; Wolff et al., 2012) together with the development of large-scale folds, such as the Proman antiform (Brodie and Rutter, 1987).

The IVZ is traditionally divided, from NW-SE, in three XQLVW: WKH PDQWOH SHULGRWLWHV, WKH ODÁF &RPSOH[DQG WKH Kinzigite Formation (Fig. 1). The main bodies of mantle peridotites are the Finero, Balmuccia, and Baldissero massifs that crop out close to the Insubric Line (Hartmann and :HGSRKO, 1993). 7KH ODÁF &RPSOH[ZDV HPSODFHG GXULQJ Permian (Peressini et al., 2007) with underplating relations and is coeval with the acid magmatism and volcanism recognized in the upper crust (Karakas et al., 2019). The bimodal magmatism is interpreted as an evidence for thinned lithospheric mantle (Schuster and Stüwe, 2008). The main phase of basic magmatism occurred at 288 ± 4 Ma (e.g., Peressini et al. 2007) and probably started largely before, as suggested EÌ WKH SUHVHQFH RI PDÁF VLOOV HPSODFHG GXULQJ &DUERQLIHUOUS (e.g., ~ 314; Klötzli et al., 2014). According to Klötzli et al. (2014), the overlapping ages, within error, between these old magmatic events and the high-temperature regional meta-PRUSKLVP (a 316 OD; (ZLQJ HW DO., 2013; 2015) GRFXPHQV D link between high grade metamorphism and magmatism. The Kinzigite Formation is made up of metasedimentary rocks with intercalated metabasic rocks (Zingg, 1990; Schmid, 1993). The metamorphic grade increases toward the NW (6FKPLG DQG :RRG, 1976; =LQJJ, 1983) IURP DPSKLEROLWH-to granulite-facies. In particular, the SE part of the Kinzigite Formation consists of micaschists that recorded amphibolite-facies metamorphism, intercalated with amphibolite layers, ZKHUHDV WRWKH 1: IHOVLF DQG PDÁF JUDQXOLWHV (DOVR NQRZQ DV stoneralites) are present. Lenses of calcisilicates and marbles are more abundant within the amphibolite-facies rocks but also occur within the granulites. Considering the changes in the mineral assemblage along the Strona di Omegna section, some authors introduced a further subdivision of the Kinzigite Formation with a transition zone between amphibolite- and granulite-facies metamorphic rocks (e.g., Redler et al., 2012; Kunz et al., 2014). In both the Ossola and Strona di Omegna valleys, the transition from amphibolite- to granulite-facies is PDUNHG EÌ PIORQLWLF JRQHV: WKH \$QJROD VKHDU JRQH (%URGLH

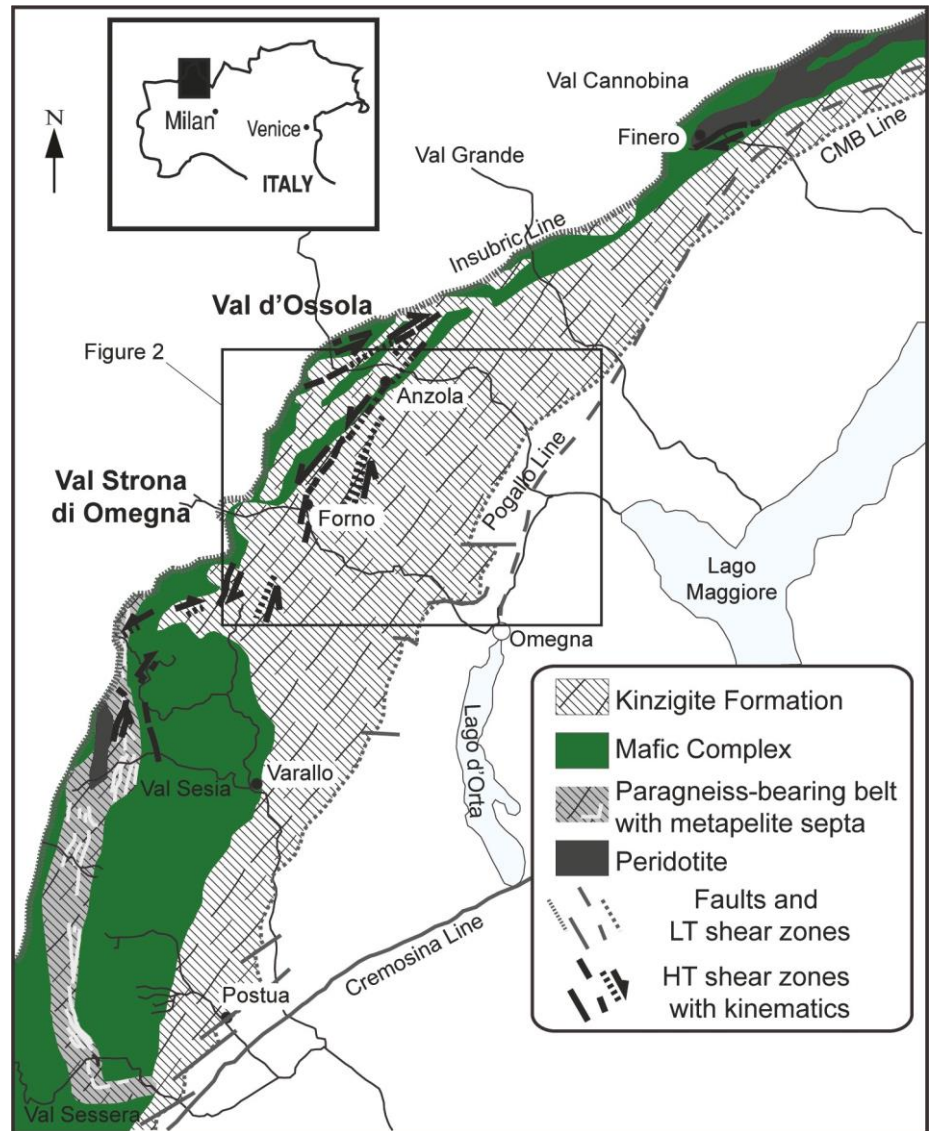


Fig. 1 - Geological sketch map of the central and northern IVZ (=Ivrea Verbano Zone, PRGLÄHG DIWHU (ZLQJ HW DO., 2015). 7KH ORFD-tions of high-temperature shear zones are after Rutter et al. (1993).

and Rutter, 1987) and the Rosarolo shear zone (Siegesmund et al., 2008), respectively. These structures were typically as-VRFLDWHG WR D VLQJOH IDXOW VVWHP QDPHG LQ GLIIHUHQW ZD: WKH Anzola-Rosarolo (Beltrando et al., 2015) or Anzola-Forno shear zone (Ewing et al., 2015). In this work, we refer to the high strain zone in the Ossola valley as the Anzola shear zone (Fig. 2A), whereas the high strain zone in the Strona di Omegna valley is referred to as Forno-Rosarolo shear zone (Fig. 2B).

From the structural point of view, the metamorphic foliation of the IVZ strikes NE-SW and is generally steeply inclined with a mineral lineation plunging toward SE. A system of large-scale superimposed folds linked to Variscan deformation is also recognized (Rutter et al., 2007). From the paleogeographic point of view, the IVZ was located to the western edge of the Adriatic Plate (Manatschal et al., 2007; Mohn et al., 2012; Beltrando et al., 2015). It was involved in a complex and polyphase episode of rift focusing in the Triassic-Jurassic interval that was investigated by integrating geochronological and thermochronological tools with available tectonostratigraphic records (Beltrando et al., 2015 and references therein).

THE LATE/POST VARISCAN HIGH-TEMPERATURE DEFORMATION

Following the Variscan orogeny, the IVZ was affected E\ SRVW-RURJHQLF H\WHQVLRQ (DV WHVWLÄHG E\ WKH DFWLYLW RI the CMB during Permian) and subsequently, in the Triassic-Jurassic time interval, by a complex and polyphase episode of rift focusing (Beltrando et al., 2015). The post-Variscan deformation was recognized since the earlier studies of the IVZ (Brodie and Rutter, 1987; Boriani et al., 1990; Rutter et al., 1993; 2007; Siegesmund et al., 2008; Garde et al., 2015). Crustal extension was accommodated by several shear zones active during different phases of rifting (Manatschal et al., 2007; Mohn et al., 2012) at different crustal levels (e.g., Beltrando et al., 2015). The uppermost rifting-related structure is the PL, which formed in the Kinzigite Formation and is interpreted as a low-angle shear zone with a normal kinematics (Hodges and Fountain, 1984) active between 210 and 170 Ma (Zingg, 1990; Wolff et al., 2012) under decreasing temperatures from amphibolite- to greenschist-facies conditions. New data about the extensional structures affecting the lower crust have been recently obtained from the northern sector of the

WLRQ ZLWKLQ DPSKLEROLWH-IDFLHV PDÄF URFNV DW PLGGOH/ORZHU FUXVWDO OHYHOV. %URGLH (1981) ZDV WKH ÄUVV DXWKRU IRFXVLQJ on the shear zone, and investigated the role of deformation during metamorphism and its effects on mineral and rock chemistry. The author demonstrated that the composition of amphibole and plagioclase, varies with deformation suggesting recrystallization under increasing temperature (prograde regional metamorphism). The microstructural and geochemical evolution of the shear zone was further investigated by Stünitz (1998). The Author showed that syn-tectonic recrystallization of clinopyroxene, amphibole and plagioclase produce compositional differences between porphyroclasts and UHFUVWDOOLJHG JUDLQV. .Q SDUWLFXODU, WKH \$XWKRU REVHUYHG WKDW: } recrystallized clinopyroxene is characterized by higher OJ# YDOXH (OJ/OJ + JH) DQG \$OFRQWHQW ZLWK UHVSHFW WR WKH porphyroclasts; ii) recrystallized grains of hornblende tend to have lower Ti content and higher Mg# value; iii) recrystallized plagioclase has lower anorthite and orthoclase components with respect to the rare plagioclase porphyroclasts. Combining microstructures with chemical changes Stünitz (1998) concluded that deformation took place during a retrograde P-T path under amphibolite-facies conditions (from ~ 650 WR 550 f &) DW SUHVXUHV RI SUREDEO\ OHVV WKDQ 8 NEDU. 7KH Anzola shear zone was studied also by Altenberger (1997) who revealed that the pre-existing heterogeneity (i.e., layering and grain-size variations) was the *locus* of concentrated shear deformation. As already documented by Brodie (1981), Altenberger (1997) further highlighted that mylonitic layers are richer in amphiboles than the wall rocks.

Despite the numerous studies on the microstructural and geochemical evolution of the shear zone the P-T conditions, i.e. prograde for Brodie (1981) and retrograde for Stünitz (1998), as well the timing are still unconstrained. The work RI %URGLH HW DO. (1989) LV WKH ÄUVV DWWHPSW WR FRQVWUDLQ WKH DJH of the deep crustal extensional episode in the Ossola valley. The authors provided Ar-Ar radiometric dating of hornblende from the undeformed gabbros and mylonites, their results are reported in the geochronological review section (IV.I; Table 1).

The Forno-Rosarolo shear zone

In the last decades the Strona di Omegna valley (Fig. 2B), has been widely studied from several point of view since it offers a spectacular exposure of continental crustal rocks for a thickness of ~ 14 km (the largest thickness of the Kinzigite Formation for the IVZ). Despite the high strain zone between Forno and Rosarolo villages was documented since Rutter et al. (1993) and subsequently studied by several authors (Rutter et al., 2007; Siegesmund et al., 2008; Garde et al., 2015), a complete characterization of the deformation characteristics and precise constraints about its geometry and internal structure are lacking. In addition, the deformation age was not directly constrained by *in situ* dating of syn-tectonic minerals DQG/RU RYHUJURZWKV. =LUFRQ JUDLQV IURP D PIORQLWLF VDPSON from the Forno-Rosarolo shear zone was dated by Kunz et al. (2018) and provided two age populations with an overall UDQJH RI 8-3E GDWHV IURP 316 WR 264 OD. +RZHYHU, VLQFH the dated zircon domains do not show evidence of deformation-induced recrystallization, these ages do not provide information about the timing of shearing. The lack of robust geochronological constraints prevents to frame the activity of this shear zone within the complex large-scale post-Variscan geodynamic context.

According to Siegesmund et al. (2008), the Forno-Rosa-

rolo shear zone can be described as a high-strain zone made up of a network of sub-parallel anastomosing shear zones variable from centimetric to metric scale. The authors proposed that the shear zone operated over a long-time span and that it initiated during the Early Permian magmatic underplating by accommodating extension in the lower crust under high-temperature conditions. Subsequently the shear zone was reactivated at different crustal levels during Mesozoic tectonics and was involved into Eocene tilting together with the whole IVZ (Siegesmund et al., 2008). During its long-lasting activity, the shear zone experienced both cataclastic and ductile deformation but due to the rheological contrast between individual layers made of different rock types, brittle and ductile deformation may have operated simultaneously, at least in some cases. Evidences of brittle deformation are cataclastic zones with centimetric to metric thickness oriented parallel to the shear zone boundary (Siegesmund et al., 2008).

The late stage of activity of the Forno-Rosarolo shear zone is documented by mylonitic foliation or, in places, form sills RULHQWHG SDUOOHO WR LW (6LHJHVXPQG HW DO., 2008). 7KHVH ÄQH-JUDLQHG PDÄF URFNV ZHUH UHFHQW\ LQWHUSUHWHG DV FDWDFODVLF injectites by Garde et al. (2015). According to these authors, cataclasis began with disperse general comminution followed by localized comminution, especially of garnet, and ÄXLGLJDWLRQ. 7KH ODWWHU LQGXFHG WKH IRUPDWLRQ RI YHU\ ÄQH-grained multi-layered dykes a few centimetres thick, which may cut back into the cataclastic fractures. Interestingly, the authors recognized that these brittle deformation features together with other evidences (such as pseudotachylites) were similar to impact-related structures observed in other contexts.

GEOCHRONOLOGICAL REVIEW: THE TEMPERATURE-TIME HISTORY

The available petrological, geochronological and thermochronological data (e.g., Siegesmund et al., 2008; Wolf et al., 2012; Ewing et al., 2013; 2015; Smye and Stockli, 2014; Smye et al., 2019). The Temperature-time (T-t) history is characterized by alternating cooling and (re)heating episodes linked to the main geodynamic events. In particular, the IVZ crustal section preserves thermal evidence for lithospheric thinning, Jurassic extension, continental breakup (e.g., Ewing et al., 2013; 2015; Smye and Stockli, 2014; Beltrando et al., 2015; Smye et al., 2019), as well as for exhumation of the crustal section in conjunction with the Alpine orogenesis (e.g., Zingg et al., 1990). Although these episodes are broadly recognized and even if there is a general agreement that the IVZ suffered exhumation, cooling and heating episodes during Jurassic, there are currently only a few constraints on the activity of ductile shear zones between Late Triassic and Early Jurassic in lower crustal rocks. In the following sections we summarize the available geochronological data (Fig. 3; Tables 1 and 2) for the shear zones and surrounding host rocks for both the Ossola and Strona di Omegna valleys. In the T-t diagrams of Fig. 3, the radiometric data and relative errors are coupled with temperatures as provided by the authors or as reported in previous T-t reconstructions (e.g., Schmid et al., 1987; Brodie et al., 1989; Zingg et al., 1990; Siegesmund et al., 2008; Smye and Stockli, 2014; Ewing et al., 2015).

Table 1 - Representative compilation of Triassic-Jurassic geochronological data available for the Ossola valley.

'DWLQJ PHWKRG	OLQHUDO	5RFN WISH	0HWDPRUSKLF IDFLHV	\$JH" HUURU (0D)	/RFDOLW\	5HHUHQFH
²⁰⁶ 3E/ ²³⁸ 8	JLUFHQ	PIORQLWLWF VWURQDOLWH	JUDQXOLWH	245" 10	3UHPRVHOOR	.XVLDN HW DO., 2019*
²⁰⁶ 3E/ ²³⁸ 8	JLUFHQ	PIORQLWLWF VWURQDOLWH	JUDQXOLWH	239" 4	3UHPRVHOOR	.XVLDN HW DO., 2019*
²⁰⁶ 3E/ ²³⁸ 8	JLUFHQ	PIORQLWLWF VWURQDOLWH	JUDQXOLWH	235" 10	3UHPRVHOOR	.XVLDN HW DO., 2019*
²⁰⁶ 3E/ ²³⁸ 8	JLUFHQ	PIORQLWLWF VWURQDOLWH	JUDQXOLWH	230" 10	3UHPRVHOOR	.XVLDN HW DO., 2019*
²⁰⁶ 3E/ ²³⁸ 8	JLUFHQ	PIORQLWLWF VWURQDOLWH	JUDQXOLWH	221" 3	3UHPRVHOOR	.XVLDN HW DO., 2019*
²⁰⁶ 3E/ ²³⁸ 8	JLUFHQ	PIORQLWLWF VWURQDOLWH	JUDQXOLWH	185" 6	3UHPRVHOOR	.XVLDN HW DO., 2019*
²⁰⁶ 3E/ ²³⁸ 8	JLUFHQ	PIORQLWLWF VWURQDOLWH	JUDQXOLWH	181" 3	3UHPRVHOOR	.XVLDN HW DO., 2019*
8±3E FRQFRUGLD DJH	UXWLOH	VWURQDOLWH	JUDQXOLWH	181" 4	/RUR	=DFN HW DO. 2011
²⁰⁶ 3E/ ²³⁸ 8	UXWLOH	VWURQDOLWH	JUDQXOLWH	184.4" 4.6	0HJROR	6PIH DQG 6WRFNOL, 2014
²⁰⁶ 3E/ ²³⁸ 8	UXWLOH	VWURQDOLWH	JUDQXOLWH	187.4" 7.6	0HJROR	6PIH DQG 6WRFNOL, 2014
²⁰⁶ 3E/ ²³⁸ 8	UXWLOH	VWURQDOLWH	JUDQXOLWH	171" 5	3UHPRVHOOR	(ZLQJ HW DO, 2015
²⁰⁶ 3E/ ²³⁸ 8	UXWLOH	VWURQDOLWH	JUDQXOLWH	155" 5	3UHPRVHOOR	(ZLQJ HW DO, 2015
²⁰⁶ 3E/ ²³⁸ 8	UXWLOH	VWURQDOLWH	JUDQXOLWH	187" 3-155" 12	\$QJROD	6PIH HW DO., 2019
²⁰⁶ 3E/ ²³⁸ 8	UXWLOH	VWURQDOLWH	JUDQXOLWH	187" 3-177" 3	/RUR	6PIH HW DO., 2019
⁴⁰ \$U± ³⁹ \$U	KRUQEOHQGH	PDILF JUDQXOLWH	JUDQXOLWH	284.27" 5.56	\$QJROD	%URGLH HW DO., 1989
⁴⁰ \$U± ³⁹ \$U	KRUQEOHQGH	JUDQXOLWH PDILF	JUDQXOLWH	224.11" 4.31	\$QJROD	%URGLH HW DO., 1989
⁴⁰ \$U± ³⁹ \$U	KRUQEOHQGH	JUDQXOLWH F	JUDQXOLWH	217.98" 4.15	\$QJROD	%URGLH HW DO., 1989
⁴⁰ \$U± ³⁹ \$U	ELRWLWH	PHWDSHOLWH PDILF	DPSKLEROLWH/JUHH QVKLVW	123.3" 7.2	0HUJRIJR	0XOFK HW DO., 2002
⁴⁰ \$U± ³⁹ \$U	PXVFRYLWH	PHWDSHOLWH	DPSKLEROLWH/JUHH QVKLVW	147.7" 5.1	0HUJRIJR	0XOFK HW DO., 2002
⁴⁰ \$U± ³⁹ \$U	PXVFRYLWH	PHWDSHOLWH	DPSKLEROLWH/JUHH QVKLVW	147.3" 6.5	0HUJRIJR	0XOFK HW DO., 2002
⁴⁰ \$U± ³⁹ \$U	PXVFRYLWH	PHWDSHOLWH	DPSKLEROLWH/JUHH QVKLVW	182.7" 2.4	0HUJRIJR	0XOFK HW DO., 2002
⁴⁰ \$U± ³⁹ \$U	PXVFRYLWH	PHWDSHOLWH	DPSKLEROLWH/JUHH QVKLVW	181.1" 2.2	0HUJRIJR	0XOFK HW DO., 2002
.±\$U	KRUQEOHQGH	VWURQDOLWH	JUDQXOLWH	208" 6	&XJIDJR	0FRZHOODQG6FKPLG, 1968
.±\$U	ELRWLWH	PHWDSHOLWH	DPSKLEROLWH	171" 5	%HWWROD	0FRZHOODQG6FKPLG, 1968
.±\$U	ELRWLWH	PHWDSHOLWH	DPSKLEROLWH	176" 5	\$OER	0FRZHOODQG6FKPLG, 1968
.±\$U	PXVFRYLWH	PHWDSHOLWH	DPSKLEROLWH	220" 11	&DQGRJOLD	+XQJLNHU, 1974
.±\$U	ELRWLWH	2 PLFDV JQHLLV	DPSKLEROLWH	190" 10	&DQGRJOLD	+XQJLNHU, 1974
.±\$U	ELRWLWH	PHWDSHOLWH	DPSKLEROLWH	184" 13	&DQGRJOLD	:ROII HW DO., 2012
.±\$U	ELRWLWH	VWURQDOLWH	JUDQXOLWH	163" 3	&XJIDJR	:ROII HW DO., 2012
5E±6U	ELRWLWH	PHWDSHOLWH	DPSKLEROLWH	172" 13	%HWWROD	-JHU HW DO., 1967
5E±6U	ELRWLWH	2 PLFDV JQHLLV	DPSKLEROLWH	253" 10	0HJRRIJR	+XQJLNHU 1974
5E±6U	ELRWLWH	VWURQDOLWH	JUDQXOLWH	187" 9	\$QJROD	+XQJLNHU 1974
5E±6U	ELRWLWH	VWURQDOLWH	JUDQXOLWH	185" 15	\$QJROD	+XQJLNHU 1974
5E±6U	ELRWLWH	ELRWLWH JQHLLV	DPSKLEROLWH	180" 7	7HJOLD	+XQJLNHU 1974
5E±6U	ELRWLWH	2 PLFDV JQHLLV	DPSKLEROLWH	185" 7	&DQGRJOLD	+XQJLNHU 1974
5E±6U	ELRWLWH	VWURQDOLWH	JUDQXOLWH	184	\$QJROD	*UDHVHU DQG +XQJLNHU, 1968
5E±6U	PXVFRYLWH	SHJPDWLWH	DPSKLEROLWH	180" 7	&DQGRJOLD	*UDHVHU DQG +XQJLNHU, 1968
5E±6U	PXVFRYLWH	SHJPDWLWH	DPSKLEROLWH	236" 10	&DQGRJOLD	*UDHVHU DQG +XQJLNHU, 1968

* \$JHV QRW UHSRUWHG LQ WKH ÅJXUHV 2 DQG/RU 3.

Table 2 - Representative compilation of Triassic-Jurassic geochronological data available for the Strona di Omega valley.

'DWLQJPHWKRG	0LQHUDO	5RFN WISH	0HWDPUSKLF	\$JHVHUUURU (0D)	/RFDOLW	5HIHUHQFH
6P±1G.VRFKURQ	ZKROHURFN, SODJLRFODVH, JDUQHW, RUWKRSURJQH	VWURQDOLWH	JUDQXOLWH	227° 3)RUQR	9RVKDJH HW DO., 1987*
ZHLJKHWHG-PHDQ ^{2063E/2388}	JLUFHQ	GXQLWH	JUDQXOLWH	200.5° 0.3	/D %DOPD- ORQWH&DSL	'HQ\ Q HW DO., 2018*
ZHLJKHWHG-PHDQ ^{2063E/2388}	JLUFHQ	SURJHQLWH	JUDQXOLWH	200.1° 0.5	/D %DOPD- ORQWH &DSL	'HQ\ Q HW DO., 2018*
^{2063E/2388}	UXWLOH	*DUQHWHLHURXV OHXFRVRPH	JUDQXOLWH	176° 4)RUQR	(ZLQJ HW DO., 2015
^{2063E/2388}	UXWLOH	*DUQHWHLHURXV OHXFRVRPH	JUDQXOLWH	163° 6)RUQR	(ZLQJ HW DO., 2015
^{2063E/2388}	UXWLOH	*DUQHWHLHURXV OHXFRVRPH	JUDQXOLWH	175° 4)RUQR	(ZLQJ HW DO., 2015
^{2063E/2388}	UXWLOH	*DUQHWHLHURXV OHXFRVRPH	JUDQXOLWH	175° 4)RUQR	(ZLQJ HW DO., 2015
^{2063E/2388}	UXWLOH	ODIHUHGPHWDSHOLWH UHWLWH DQG OHXFRVRPH	JUDQXOLWH	164° 3	3LDQD GL)RUQR	(ZLQJ HW DO., 2015
^{2063E/2388}	UXWLOH	ODIHUHGPHWDSHOLWH UHWLWH DQG OHXFRVRPH	JUDQXOLWH	140° 2	3LDQD GL)RUQR	(ZLQJ HW DO., 2015
^{2063E/2388}	UXWLOH	ODIHUHGPHWDSHOLWH UHWLWH DQG OHXFRVRPH	JUDQXOLWH	175° 5	3LDQD GL)RUQR	(ZLQJ HW DO., 2015
^{2063E/2388}	UXWLOH	ODIHUHGPHWDSHOLWH UHWLWH DQG OHXFRVRPH	JUDQXOLWH	159° 4	3LDQD GL)RUQR	(ZLQJ HW DO., 2015
^{2063E/2388}	UXWLOH	VWURQDOLWH	JUDQXOLWH	191-182° 2)RUQR	6P\H HW DO., 2019
^{40S-39S}	KRUQEOHQGH	PDILF JUDQXOLWH	JUDQXOLWH	201.7° 13	&DPSHOOR ORQWL	6LHJHVPXQG HW DO., 2008
^{40S-39S}	KRUQEOHQGH	PDILF JUDQXOLWH	JUDQXOLWH	210.3° 4.4	&DPSHOOR ORQWL	6LHJHVPXQG HW DO., 2008
^{40S-39S}	KRUQEOHQGH	PDILF JUDQXOLWH	JUDQXOLWH	206.1° 3	3LDQD GL)RUQR	6LHJHVPXQG HW DO., 2008
^{40S-39S}	KRUQEOHQGH	DPSKLEOLWHV	JUDQXOLWH	211.1° 7)RUQR	6LHJHVPXQG HW DO., 2008
^{40S-39S}	KRUQEOHQGH	DPSKLEOLWHV	JUDQXOLWH	222.7° 12.5	2WJD	6LHJHVPXQGHWO., 2008
^{40S-39S}	KRUQEOHQGH	DPSKLEOLWHV	JUDQXOLWH	221.6° 1.2	5RVDUROR	6LHJHVPXQG HW DO., 2008
^{40S-39S}	KRUQEOHQGH	DPSKLEOLWHV	DPSKLEROLWH	240° 20	5RVDUROR	6LHJHVPXQG HW DO., 2008
^{40S-39S}	KRUQEOHQGH	DPSKLEOLWHV	DPSKLEROLWH	239.3° 4.6	5RDG 5RVDUROR- ODUPR	6LHJHVPXQG HW DO., 2008
^{40S-39S}	KRUQEOHQGH	DPSKLEOLWHV	DPSKLEROLWH	250.4° 3.7)RUQHUR	6LHJHVPXQG HW DO., 2008
^{40S-39S}	KRUQEOHQGH	PDILF JUDQXOLWH	JUDQXOLWH	242° 1	3LDQD GL)RUQR	%RULDQL DQG 9LOOD, 1997
^{40S-39S}	KRUQEOHQGH	PDILF JUDQXOLWH	JUDQXOLWH	217° 1)RUQR	%RULDQL DQG 9LOOD, 1997
^{40S-39S}	KRUQEOHQGH	DPSKLEROLWH	DPSKLEROLWH	243° 1	ODUPR	%RULDQL DQG 9LOOD, 1997
.±\$U	ELRWLWH	VWURQDOLWH	JUDQXOLWH	156.3° 3.3	&DPSHOOR ORQWL	6LHJHVPXQG HW DO., 2008
.±\$U	ELRWLWH	VWURQDOLWH	JUDQXOLWH	159° 3.4	&DPSHOOR ORQWL	6LHJHVPXQGHWO., 2008
.±\$U	ELRWLWH	VWURQDOLWH	JUDQXOLWH	158.7° 3.3	5RDG &DPSHOOR ORQWL-3LDQD GL	6LHJHVPXQG HW DO., 2008
.±\$U	ELRWLWH	VWURQDOLWH	JUDQXOLWH	175.7° 3.7	2WJD	6LHJHVPXQGHWO., 2008
.±\$U	ELRWLWH	VWURQDOLWH	JUDQXOLWH	166.6° 3.5	5RVDUROR	6LHJHVPXQG HW DO., 2008
.±\$U	ELRWLWH	VWURQDOLWH	JUDQXOLWH	169.8° 3.6	5RVDUROR	6LHJHVPXQG HW DO., 2008
.±\$U	ELRWLWH	PHWDSHOLWH	DPSKLEROLWH	183.3° 3.8	5RDG 5RVDUROR- ODUPR	6LHJHVPXQG HW DO., 2008
.±\$U	ELRWLWH	PHWDSHOLWH	DPSKLEROLWH	167.3° 3.5	5RDG 5RVDUROR- ODUPR	6LHJHVPXQG HW DO., 2008
.±\$U	ELRWLWH	PHWDSHOLWH	DPSKLEROLWH	179.1° 3.8	ODUPR	6LHJHVPXQG HW DO., 2008
.±\$U	ELRWLWH	PHWDSHOLWH	DPSKLEROLWH	185.5° 3.9)RUQHUR	6LHJHVPXQG HW DO., 2008
.±\$U	ELRWLWH	PHWDSHOLWH	DPSKLEROLWH	201.7° 4.2	6WURQD	6LHJHVPXQG HW DO., 2008
.±\$U	ELRWLWH	PHWDSHOLWH	DPSKLEROLWH	200.3° 4.2	/RUHJOLD	6LHJHVPXQG HW DO., 2008
.±\$U	ELRWLWH	PHWDSHOLWH	DPSKLEROLWH	231.6° 4.8	/RUHJOLD	6LHJHVPXQG HW DO., 2008
5E±6U	ELRWLWH	VWURQDOLWH	JUDQXOLWH	193° 68)RUQR	+XQLNHU, 1974

* \$JHV QRW UHSRUWHG LQ WKH ÀXUHV 2 DQG/RU 3.

Ossola Valley

In the past decades, several radiometric studies were published for the basement rocks exposed in the Ossola valley (Fig. 3A). However, geochronological investigations dealing ZLWK 8-3E GDWLQJ RI JLUFQRQ DQG/RU PRQDJLWH DUH UDUH (.RSSHO, 1974; Klötzli et al., 2014; Kusiak et al., 2019) and there is a lack of sampling continuity along the crustal section. Gener-D00, ERWK JLUFQRQ DQG PRQDJLWH SURYLGHG &DUERQLIHURXV/3HUP-LDQ DJHV VXJJHVWLQJ WKDW PDÁF VLOOV ORFDOO LQWUXGHG GXULQJ Carboniferous (i.e., Albo sill of Klötzli et al., 2014; Fig. 2A) DQG WKDW PHWDPRUSKLF JURZWK/UHFU/VWDOOLJDWLRQ RI ERWK JLUFQRQ and monazite occurred during Early Permian as commonly found in rocks from IVZ (e.g., Vavra et al., 1999; Ewing et al., 2013; Klötzli et al., 2014). Despite the Anzola shear zone attracted many structural, microstructural, and geochemical studies (Brodie, 1981; Brodie et al., 1989; Brodie and Rutter, 1987; Altenberger, 1997; Stünitz, 1998; Rutter and Brodie, 1990; Rutter et al., 1993; 2007), the age of deformation is still poorly constrained.

Brodie et al. (1989) provided a direct attempt to date the Anzola shear zone by hornblende Ar-Ar dating. They obtained a minimum age of about 247 Ma for the unsheared metagabbro, whereas the shear zone provided two ages at 215±5 Ma, for the coarse-grained amphibole fraction, and 210±5 Ma, for the fine-grained amphibole fraction. The authors provided also closure temperature estimates for the radiometric data considering the grain sizes and two FRROLQJ UDWHV DW 1 DQG 10 f &/0D, UHVSHFWLYHO\ (LJ. 3\$). 7KH stated that their results are consistent with pre-existing age GHWHUPLQDWLRQ FRQLGHULQJ D FRROLQJ UDWH RI DERXW 4 f &/0D. According to Brodie et al. (1989), the obtained ages record cooling because the blocking temperature was interpreted to be grain-size dependent, i.e., younger ages were obtained IURP WKH ÀQH-JUDLQHG VQ-NLQHPDWLF KRUEOHQGH. 7KXV, DF-cording to the authors, the shearing was probably older than Late Triassic and likely it initiated prior to 280 Ma (i.e., prior to Early Permian). These Ar-Ar data were reinterpreted as possible evidence for an Late Triassic activity of the shear zone (Beltrando et al., 2015; Ewing et al., 2015).

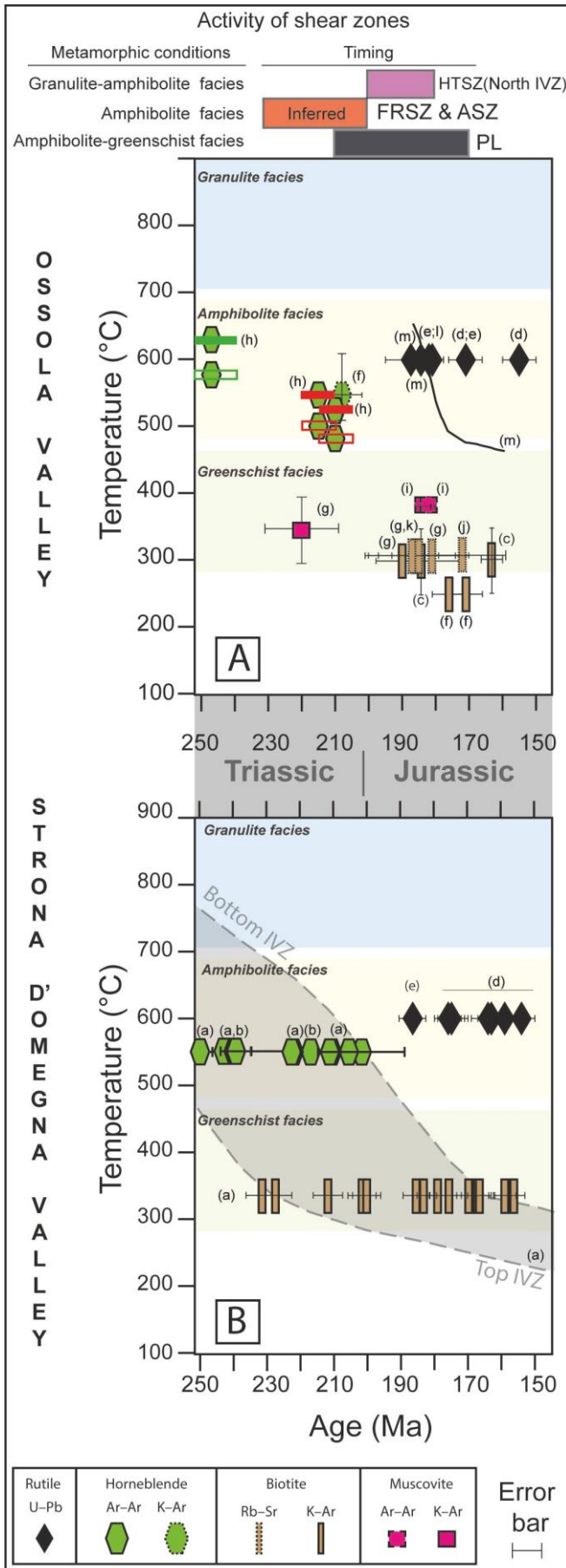


Fig. 3 - Triassic-Jurassic T-t diagrams based on published radiometric data for Ossola (A) and Strona di Omega (B) valleys. Both temperature and geochronological data are plotted according to the data as reported LQ WKH WHJW RU ÀXJUHV RI WKH UHODWLYH UHIHQFHV. Q (\$) VLQ \$U \$U KRUEOHQGH data with relative error bars are shown and refer to three analysed samples but calculated using closure temperature for Ar in hornblende at cooling UDWHV RI 1 (XQÀOOHG HUURU EDUV) DQG 10 f &/0D (ÀOOHG HUURU EDUV) DFFRUGLQJ WR Brodie et al. (1989); the data with green error bars refer to the undeformed gabbro whereas those with red error bars are associated to the hornblende from sheared metabasic rocks (for more details see Brodie et al., 1989). 7KH EODFN OLQH DVVRFLDWHG WR UXWLOH 83E GDWD UHSUHVHQWV WKH EHV-ÀW WKHUPDO KLVWRU EDVHG RQ 8-3E UXWLOH GHSWK SURÀOH GDWLQJ DIWHU 6PH DQG 6WRFNOL (2014). In (B), the light grey area encloses the thermal history from base to top of the IVZ, after Siegesmund et al. (2008) and was depicted based RQ KRUEOHQGH \$U \$U DQG ELRWLWH -\$U GDWD. 2Q WKH WRS RI WKH ÀXJUH WKH metamorphic conditions and timing for the activity of different shear zones LV VKRZQ: WKH KLJK-WHPSHUDWXUH VKHJU JROH (+76=) IURP QRUWK, 9= LV IURP Langone et al. (2018); the low grade Pogallo Line (PL) is after Wolff et al. (2012). For the Forno-Rosarolo (FRSZ) and Anzola (ASZ) shear zones the inferred timing is based on this geochronological review and is in agreement with previous studies (e.g., Ewing et al., 2015). 5HIHQHQFHV: D- 6LHJHVPXQG HW DO., 2008; E- %RULDQL DQG 9LOOD, 1997; F- Wolff et al., 2012; d- Ewing et al., 2015; e- Smye et al., 2019; f- McDowell DQG 6FKPLGW, 1968; j- +XQLNHU, 1974; k- %URGLH HW DO., 1989; l- 0XOFK HW DO., 2002; m- -JHU HW DO., 1967; n- *UDHYHU DQG +XQLNHU, 1968; o- =DFN HW DO., 2011; m- Smye and Stockli, 2014.

Other direct dating or (re)interpretations of mylonites from the Anzola shear zone are lacking. Nevertheless, we continue the review of the available geochronological-thermochronological data across the Ossola valley. Triassic ages in the Ossola valley are rare (Fig. 3A; Table 1). Rb-Sr cooling DJHV IRU PXVFRYLWH DW 243° 10 0D DQG 236° 10 0D ZHUH UH SRUWHG E\ +XQJLNHU (1974) DQG *UDHVHU DQG +XQJLNHU (1968), respectively, for pegmatites near Candoglia (Fig. 2A). These cooling ages relative to pegmatitic samples are not shown in Fig. 3A since do not represent metamorphic events. Other Late Triassic ages (Fig. 3A) are reported for a two-micas gneiss in Candoglia (K-Ar muscovite age at 220±11 Ma; Hunziker, 1974) and for a metabasite in granulite-facies conglwlrqv (KRUQEOHQGH .\$.U DJH DW 208° 6 0D; 0F'RZHOO DQG 6FKPLG, 1968). 6LQFH WKH ÁUVV UDGLRPHWULF VWXGLHV RQ WKH PHW-amorphic rocks, the (Early-Middle) Jurassic interval is more frequently represented with respect to Triassic one. Several Rb-Sr biotite dates are available for different rock types along the valley (Fig. 2A) and span from 187±9 to 172±13 Ma (Fig. 3\$; -JHU HW DO., 1967; *UDHVHU DQG +XQJLNHU, 1968; +XQJLNER, 1974). K-Ar dating of biotite within both amphibolite- and granulite-facies metapelites were carried out by several authors (0F'RZHOO DQG 6FKPLG, 1968; +XQJLNHU, 1974; ROII et al., 2012) and range from 190±10 to 171±5 Ma (Fig. 3A). The most recent K-Ar biotite ages are presented by Wolff et al. (2012) for metamorphic rocks showing both amphibolite- and granulite-facies metamorphism. Biotite in granulites JDYH DQDJH RI 163° 3 0D, ZKHUHDV ÉLRWLWH LQ DPSKLEROLWH-facies rocks resulted older than ~ 20 Myr (184±13 Ma). According to Wolff et al. (2012), these ages should represent the activity of the PL during Jurassic crustal thinning.

The PL was already investigated in detail by Mulch et al. (2002). They dated three distinct populations of muscovite by Ar-Ar method for a sample collected close to the Ossola valley (Fig. 2A). Separates of undeformed muscovite porphyroclasts formed an Ar-Ar age plateau of ~ 182 Ma (Fig. 3A). 'HIRUPHG PXVFRYLWH DQG ÁQH-JUDLQHG PXVFRYLWH SURYLGHG the same average age (148±5 and 147±7 Ma, respectively) by *in-situ* Ar-Ar analyses. In addition, the authors obtained a relatively young Ar-Ar biotite age of 123±7 Ma. According to Mulch et al. (2002), the radiometric data obtained for unghiruphg sruskurfovww uaháfw wkh djh ri juhhqvflkw-ídlhv piorqlwldwlrq (rffxuuhg dw derxw 380-400 f &) dorqj wkh 3/. The younger ages were interpreted by the authors as an evidence of slow cooling rate during the Late Jurassic and Early Cretaceous.

The Ossola valley was sampled several times in the last decade for rutile U-Pb thermochronological studies (Figs. 2A and 3A; Zack et al., 2011; Smye and Stockli, 2014; Ewing et al., 2015; Smye et al., 2019). Zack et al. (2011) provided LA-ICP-MS age of 181±4 Ma for a rutile collected in a stromalite near the Premosello village. Smye and Stockli (2014) reported LA-ICP-MS U-Pb rutile ages from two stromalites collected between Anzola and Premosello. The U-Pb ages for these samples point to 184±5 Ma and 187±8 Ma, respectively. Ewing et al. (2015) performed U-Pb SHRIMP analyses on rutile separates and obtained two different age populations at 171±5 and 155±5 Ma, respectively. The older population was dwwulexwhg E\ wkh dxwkruv wr d ÁUVV FRROLQJ HYHQW EHORZ 550-650 f &. 7KH SUHVHQFH RI D IRXQJHU SRSXODWLRQ ZDV LQWHUSUHWHG as rapid reheating followed by renewed cooling.

Kusiak et al. (2019) have recently studied zircon from high-grade felsic mylonitic metapelites near Premosello (Fig. 2A). The isotopic data indicate old detrital cores and Permian metamorphic ages (280±4 Ma). Interestingly, the

authors obtained also Triassic $^{206}\text{Pb}/^{238}\text{U}$ dates that they did not consider in the age calculations due to high common Pb. Kusiak et al. (2019) highlighted only the presence of one strongly deformed detrital core zircon yielding an apparent Jurassic U-Pb age (185 Ma) that they tentatively attributed to deformation.

Strona di Omega Valley

Several authors tried to depict the T-t evolution of the IVZ crustal section exposed in the Strona di Omega valley by collecting thermochronological data (e.g., Siegesmund et al., 2008). The well constrained tectono-metamorphic evolution RI WKH FUXVWDO VHFWRQ HJSRVHG DORQJ WKLV YDOOH EHQHÁWV DOVR of numerous and detailed geochronological studies (Henk et al., 1997; Vavra et al., 1999; Ewing et al., 2013; Guergouz et al., 2018; Kunz et al., 2018). Generally, U-Pb monazite data are clustered around 275-280 Ma (Henk et al., 1997; Guergouz et al., 2018) and, according to Henk et al. (1997) WKH EHFRPH VVWHPDWLFDOO\ IRXQJHU (IURP 292 WR 276 0D) towards the highest metamorphic grade.

A large age spread was documented for U-Pb zircon data, which provided useful information from prograde to retrograde metamorphic conditions (Vavra et al., 1999; Ewing et al., 2013; Klötzli et al., 2014; Guergouz et al., 2018; Kunz et al., 2018). Kunz et al. (2018) studied zircon grains from several samples (mostly metapelites and metapsammites) showing P-T conditions ranging from amphibolite- to granulite-facies. The authors obtained a spread of the U-Pb zircon dates > 60 0U, IURP DERXW 316 WR 240 0D. 7KHU UHFURJLJHG WKDW LQ granulite-facies rocks there is a general decoupling of zircon chemical and isotopic signatures, i.e. no correlations were observed EHWZHHQ 8-3É GDWHV DQG LQWHUQDO IHDWXUHV, 7K/8 UDWLR or Ti-in-zircon concentration. According to the authors, this decoupling is most likely due to the more intense thermal imprint (higher T for longer period) experienced by granulites with respect to amphibolite-facies samples. Noteworthy, the authors studied zircon grains from a mylonitic sample belonging to the Forno-Rosarolo shear zone. They recognized zircon internal features typical for growth at high temperature FRQGLWLRQV ZLWK ORFDO HYLGHQFH IRU ODWH-VWDJH ÁXLG-LQGXFHG UH-crystallization. This sample gave an overall range of U-Pb GDWHV IURP 316 WR 264 0D DQG, DFFRUGLQJ WR WKH DXWKRUV, LW was the only one showing a correlation between U-Pb dates and geochemical data. Other zircon bearing samples from Val Strona di Omega were studied by Vavra et al. (1999). They dated zircon grains from three different metapelitic samples representative of upper amphibolite- and granulite-facies zones and of the transition between these two sectors (Fig. 2B). Interestingly, the authors obtained a Late Permian age at 253±4 Ma for a high-U zircon domain from the transition zone and Early Triassic - Late Permian dates from altered zircon domains of both the transition zone (248±5 Ma, mean of 6 DQDO\HV) DQG WKH JUDQXOLWLF VDPSOH (246° 12 0D DQG 256° 9 Ma). According to these authors, since Pb-loss from high-U zircon domains is dominantly controlled by the susceptibility of the crystal lattice, the rejuvenated ages do not necessarily correspond to a geological event. However, the occurrence of several young apparent ages from U-rich domains also from other localities of the IVZ led the authors to suggest that they were the result of a near-complete resetting during an episode of annealing. Analogously, the youngest apparent ages from altered domains of zircon from the Strona di Omega valley coincide within error with those reported from altered domains in other valleys of the IVZ. According to the Vavra et

al. (1999), this coincidence and the fact that they are slightly younger than the youngest apparent ages from high-U domains would suggest that a major episode of zircon alteration DQG SDUWLDO UHVHWWLQJ RFFXUUHG EHFDXVH RI D VVURQJ WKHUPDO DQG/ or decompression event at 249 ± 7 Ma. This event was linked by the authors to the Permian post-collisional strike-slip tectonics, basin formation and volcanism. It is interesting to note that Vavra et al. (1999) reported also a further recrystallization SURFHVV LQGXFHG E\ ÁXLG LQJUHVVLRQ ZLWKLQ JLUFRQ JUDLQV from other localities of the IVZ. Zircon domains associated with WKL V ODWH VWDJH SURYLGHG /DWH 7ULDVLF/(DUO) -XUDVLF GDWHV DQG were associated with alkaline magmatism and hydrothermal activity due to the onset of continental breakup of Pangea.

Middle-Late Triassic ages were obtained also by Boriani and Villa (1997) dating hornblende (Ar-Ar method) IURP WKUHH PHWDEDVLWHV VKRZLQJ DPSKLEROLWH/JUDQXOLWH-IDFLHV conditions (Figs. 2B and 3B). According to the authors, two samples gave indistinguishable ages, i.e., at 243 and 242 ± 1 Ma, whereas the sample collected from an intermediate position between the other two (Fig. 2B), provided a younger date DW 217^o 1 OD, OLNHO\ UHODWHG WR ORFDO ÁXLG-LQGXFHG UHFUWVDO-lization. Ar-Ar amphibole dates ranging from late Permian to Late Triassic are also reported by Siegesmund et al. (2008) for samples collected along all the valley for both the IVZ and adjacent SdL unit (Figs. 2B and 3B). Hornblende ages showed an east-west age gradient decreasing from 257 ± 1 Ma, near the CMB Line, to 202 ± 3 Ma, close to the Insubric Line (Fig. 2B). Recently, Denyszyn et al. (2018) reported zircon U-Pb ages at the Triassic-Jurassic boundary (about 200 Ma) IRU WKH /D %DOPD-ORQWH &DSL R PÁF/XOWUDPÁF LQWUXVLRQ (Fig. 2B). The authors interpreted the age as indicative of a short-lived magmatic system associated with the Central Atlantic Magmatic Province, which is related to the opening of the central Atlantic Ocean and thus the breakup of Pangea. +RZHYHU, LW LV LQWHUHVWLQJ WR QRWH WKDW PÁF URFNV IURP WKH same locality (Monte Capio sill) were previously dated at Carboniferous (Klötzli et al., 2014). As reported by Berno et al. (2019) it cannot be excluded that the Triassic-Jurassic age obtained by Denyszyn et al. (2018) represents the product of zircon recrystallization rather than the age of magmatic crystallization. As highlighted by Berno et al. (2019) it has been demonstrated that the prolonged residence under high-temperature conditions for the deep sectors of the IVZ produced perturbation of the U-Pb isotope system in zircons, thereby leading to apparent age rejuvenation (e.g., Vavra et al. 1999; =DQHWWL HW DO., 2016; .XQJ HW DO., 2018).

Several thermochronological data based on U-Pb dating of rutile are available in the literature for granulite-facies metapelites from the base of the IVZ in the Strona di Omega valley (Ewing et al., 2013; 2015; Smye et al., 2019; Figs. 2B and 3B). Rutile crystallized during Permian granulite-facies conditions and provided Jurassic U-Pb ages indicating cool-LQJ WKURXJK 650-550 f & 5HFHQWO\, 6PH HW DO. (2019) GDWHG rutile from a garnet-rich metapelite that was already studied for geochemical characterization by Luvizotto et al. (2009). Rutile provided $^{206}\text{Pb}/^{238}\text{U}$ spot dates in the range of 182-191 OD. (ZLQJ HW DO. (2015) REWDLQHG WZR DJH SHDNV: WKH PDLQ RQH DW a 160 OD DQG D VXERUGLQDWH RQH DW a 175 OD (JLJ. 3%). \$FFRUGLQJ WR WKH DXWKRUV WKH IRXQJHU DJH FOXVWHU (a 160 OD) coincides with the exhumation of sub-continental mantle to WKH ÁRRU RI WKH \$OSLQH 7HWKIV DQG WKKV FDQ EH LQWHUSUHWHG DV regional cooling following a short heating episode recorded by the distal Adriatic margin. The ~ 175 Ma age was interpreted by the authors as the cooling in the footwall of rift-related faults and shear zones.

The rutile U-Pb ages (Ewing et al., 2013; 2015; Smye et al., 2019) partially overlap the biotite K-Ar ages obtained from the base of the IVZ by Siegesmund et al. (2008; Fig. 3B). These authors recognized that the biotite K-Ar dates GHFUHDVH IURP 230 WR 156 OD PRYLQJ WRZDUG ORZHU FUXVWDO levels, running subparallel to the hornblende ages but at lower temperatures (Fig. 3B). Siegesmund et al. (2008) did not REVHUYH DQ\ DEUXSW RIIWHV RI WKH GHFUHDVLRQ DJH SURÁOH DFURVV the two tectonic lineaments located in the lower part of the SURÁOH, L.H. WKH &0% DQG WKH 3/, VXJHVVWLQJ WKDW OHVJRJLF tectonics affected the entire basement pile in a uniform way.

DISCUSSIONS AND CONCLUSIONS

Timing of the Forno-Rosarolo and Anzola shear zones

As it concerns the deformation age of the Forno-Rosarolo shear zone, a robust interpretation is still lacking as well as direct attempts to date shearing. Siegesmund et al. (2008), following the work of Henk et al. (1997), reconstructed the T-t curves of both the IVZ and the adjacent SdL by using geochronological and thermochronological data collected along the Strona di Omega valley. As shown in the plot of the Ar-Ar hornblende data (Fig. 7 of Siegesmund et al., 2008), WKH LVRFKURQ DJHV VKRZ D ZHOOGHÁHQHG SURJUHVVLRQ becoming younger towards the Insubric Line. The authors reported that samples comprised between the Insubric Line and the Forno-Rosarolo shear zone did not provide a true plateau and that they were affected by a considerable amount of excess argon that makes the obtained ages unreliable. However, some of these samples provided well-GHÁHQHG LVRFKURQV ZLWK DQ DYHUDJH LVRFKURQ DJH RI 208^o 2 Ma that was not linked to the ductile deformation. Interestingly, Boriani and Villa (1997) also obtained a younger Ar-Ar hornblende date from the sample coming from the Forno-Rosarolo area with respect to the other two samples that they collected structurally above and below this sector. 7KH DXWKRUV LQWHUSUHWHG WKH IRXQJHU DJH DV GXH WR ORFDO ÁXLG-induced recrystallization of hornblende. It is interesting to QRWH WKDW WKUHH PÁF JUDQXOLWHV FROOHFWHG E\ 6LHJHVPXQG HW al. (2008) close to the Forno village (Fig. 2B) gave ages between 211 and 222 Ma comparable to the one obtained by Boriani and Villa (1997) in the same area (217 ± 1 Ma). Since the Boriani and Villa (1997) young age was interpreted as OLQNHG WR ÁXLG LQGXFHG UHFUWVDOOLJDWLVRQ, LW LV OLNHO\ WKDW WKL V SURFHVV LQÁXHQFHG DOVR WKH GDWD SURYLGHG E\ 6LHJHVPXQG HW al. (2008) from the same area, even if these latter authors did not discuss this hypothesis.

As reported in the review above, a direct attempt to date the Anzola shear zone was carried out by Brodie et al. (1989). According to the authors, the high temperature shear zone started prior to 280 Ma, probably around 300 Ma, and recorded a period of crustal thinning and cooling of more than 100 Myr of duration. Several authors provided an alternative interpretation for the Brodie et al. (1989) age dataset. According to Beltrando et al. (2015) and Ewing et al. (2015), a different scenario would be that the younger ages record Late Triassic deformation-induced recrystallisation and not diffusive loss of Ar. As already suggested by Boriani and Villa (1997), it appears that Ar-Ar ages of amphiboles in the IVZ are not controlled only by diffusive loss of Ar and that recrystallization of hornblende also plays an important role. Actually, the hypothesis suggested by Beltrando et al. (2015) and Ewing et al. (2015) was already proposed by Brodie and

data, it seems that the Jurassic heating event affected only the granulitic rocks comprised between the studied shear zones and the deepest levels of the continental crust (i.e., towards the Insubric Line). It is interesting to note that the same heating event has not been recorded at higher crustal levels (amphibolite-facies lithologies) otherwise a partial or total reset of other geochronometers and thermochronometers would be observed in these crustal portions. All these data indicate that the heating was recorded at regional scale (see Beltrando et al., 2015) but it probably affected mainly the high-grade rocks (stronalites), formerly at the base of the IVZ. A wider heating affecting also the amphibolite-facies rocks is not apparent from the thermochronological data available for these levels of the continental crust since the biotite and muscovite radiometric ages do not show a total or partial resetting (Fig. 3). Alternatively, the overlap between U-Pb rutile ages from granulites and thermochronological data (e.g., Rb-Sr, Ar-Ar and K-Ar of micas; Fig. 3) from upper crustal rocks would suggest a fast cooling during Jurassic induced by a rapid exhumation of the whole crustal section (e.g., Beltrando et al., 2015). This period of rapid exhumation of the IVZ broadly corresponds with the activity of shear zones at different crustal levels (Fig. 3). A fast exhumation process has been already suggested for the Adria lithosphere (e.g., Malenco area, Müntener et al., 2000).

In both the Strona di Omegna and Ossola valleys, the deformation is notably not limited to the Forno-Rosarolo and Anzola shear zones. Indeed, in the lowermost part of the FUXVWDO SURÀOHV RWKHU KLJK WHPHUDWXUH DQG SVHXGRWDFKIQWHLW-bearing mylonitic belts are exposed (e.g., Techmer et al., 1992). As suggested by Pittarello et al. (2012) such a deformation probably occurred during the early Mesozoic crustal extension, prior to the Alpine orogeny. Even if further studies are needed, it cannot be excluded that also the shear heating (e.g., Brun and Cobbold, 1980; Mako and Caddick, 2018) contributed at least partially to the temperature increment in this sector of the crust concurrently with other heat sources (L.H., DVWKHQRVSKHUH XSZHOOLQJ DQG KRW ÁXLGV; 6PIH HW DO., 2019). Hence, the potential effect of rift-related deformation and heating should be considered in the interpretation of thermochronological datasets of the IVZ, in particular for WKRVH VHFWRUV UHSUHVHQWLQJ SRUWLRQV RI WKH ORZHU FUXVW DQG/RU adjacent to shear zones. New detailed investigations and acquisition of new data able to directly constrain the timing and WHFWRQR-WKHUPDO DFWLYLW RI WKHVH VWUXFWXUHV ZRXOGFRQÀUP their role and possible hierarchy in crustal thinning processes during Tethyan rifting.

CONCLUSIONS

The present geochronological and thermochronological review allows to shed light on the evidences of Triassic-Jurassic rift-related deformation in the fossil Adriatic margin of the Alpine Tethys exposed along two valleys of the Ivrea-9HUEDQR =RQH. 7KH GDWD UHYLHZ KLJKLJKWHG WKDW: L) WKH WZR valleys have been sampled several times but with a different detail; ii) geochronological and thermochronological studies are rarely focused on shear zones; iii) the direct attempt to date deformation has been done by Ar-Ar method; iv) local HYLGHQFHV IRU ÁXLG-LQGXFHG UHFUJVVDOOLJDLWLRQ RI ERWK JHR- DQG thermo-chronometers during Late Triassic-Early Jurassic have been reported for both crustal sections; v) these recrystallization processes have been interpreted as evidence for rift-related deformation; v) granulites recorded Early-Middle

Jurassic heating and cooling events that apparently did not affect the lower grade metamorphic rocks of the upper crustal levels. We emphasise that more detailed investigations of the shear zones are needed in order to better understand the rifting processes that occurred at the fossil Adriatic margin during the Jurassic. We propose that the shear zones subject of this review must be investigated by applying a modern multidisciplinary approach FRPELQLQJ GHWDLQHG ÀHOGZRUN, PLFURVWUXFWXUDO DQDOVHV, SHW-rochronology and thermochronology.

ACKNOWLEDGEMENTS

This manuscript is dedicated to Marco Beltrando, a teacher to some, a colleague to others, certainly a great scientist and a friend to everyone. He dedicated part of his research activities on the shear zones presented here. This research ZDV IXQGHG E\ WKH IROORZLQJ SURMHFW: 35,12017 'OLFUR WR Macro - how to unravel the nature of the large magmatic events (20178LPCPW- Langone Antonio)". The manuscript has been conceptualized by L.A. and all the authors equally contributed to the original initial draft and writing. We thank Benoît Petri and an anonymous reviewer for their comments that improved the quality of the manuscript. We also thank the associate editor Riccardo Tribuzio for his comments and editing.

REFERENCES

- Altenberger U., 1995. Local disequilibrium of plagioclase in high-temperature shear zones of the Ivrea Zone, Italy. *J. Metam. *HRO.*, 13 (5): 553-558.
- Altenberger U., 1997. Strain localization mechanisms in deep-seat HG ODVHUHG URFNV. **HRO.* 5XQGVFK., 86 (1): 56-68.
- Aravadinou E. and Xypolias P., 2017. Evolution of a passive FUXVWDO-VFDOH GHWDFKPHQW (6IURV, SHJHDQ UHJLRQ): QVLJKWV IURP structural and petrofabric analyses in the hanging-wall. *J. Struct. *HRO.*, 103: 57-74. *KWWSV://GRL.RUJ/10.1016/M.MVJ.2017.09.008.*
- Beltrando M., Manatschal G., Mohn G., Dal Piaz G.V., Vitale Brovarone A. and Masini E., 2014. Recognizing remnants of PDJPD-SRRU ULIWHG PDUJLQV LQ KLJK-SUHVXUH RURJHOLF EHOWW: 7KH \$OSLQH FDVH VWXG. (DUWK. 6FL. 5HY., 131: 88-115. *KWWSV://GRL. RUJ/10.1016/M.HDUVFLUHY.2014.01.001.*
- Beltrando M., Stockli D.F., Decarlis A. and Manatschal G., 2015. A crustal-scale view at rift localization along the fossil Adriatic margin of the Alpine Tethys preserved in NW Italy. *Tectonics*, 34: 1927-1951. *KWWSV://GRL.RUJ/10.1002/2015T&003973.*
- Berno D., Tribuzio R., Zanetti A. and Hémond C., 2019. Evolution of the Ivrea-Verbano Zone, Northern Italy). *Contrib Min-HU. 3HWURO*, 175 (1): 1-28. *KWWSV://GRL.RUJ/10.1007/V00410-019-1637-8.*
- Bertotti G., Picotti V., Bernoulli D. and Castellarin A., 1993. From ULIWLQJ WR GULIWLQJ: WHFWRQLF HYROXWLRQ RI WKH 6RXWK-\$OSLQH XSSHU crust from the Triassic to the Early Cretaceous. *Sedim. Geol.*, 86: 53-76. *KWWSV://GRL.RUJ/10.1016/0037-0738(93)90133-3.*
- Boriani A. and Villa I.M., 1997. Geochronology of regional metamorphism in the Ivrea-Verbano Zone and Seri e dei Laghi, Italy. *Geol. Soc. Lond. Spec. Rep.*, 77: 381-402. *KWWSV://GRL. RUJ/10.5169/6(\$/6-58492.*
- Boriani A., Burlini L. and Sacchi R., 1990. The Cossato-Mergozzo-Brissago Line and the Pogallo Line (Southern Alps, Northern Italy) and their relationships with the late-Hercynian magmatic DQG PHWDPRUSKLF HYHQWV. *7HFWRQRSKVLFV*, 182: 91-102.

- Brodie K.H., 1981. Variation in amphibole and plagioclase composition. *Contributions to Mineralogy and Petrology*, 78: 385-402. [KWWSV://GRL.RUJ/10.1016/0040-1951\(81\)90021-4](https://doi.org/10.1007/BF01160040).
- Brodie K.H. and Rutter E.H., 1987. Deep crustal extensional faulting. *Journal of Metamorphic Geology*, 5: 193-212. [KWWSV://GRL.RUJ/10.1016/0040-1951\(87\)90229-0](https://doi.org/10.1016/0040-1951(87)90229-0).
- Brodie K.H., Rutter E.H. and Rex D., 1989. On the age of deep crustal extensional faulting in the Ivrea zone, Northern Italy. *Geological Magazine*, 146: 203-210. [KWWSV://GRL.RUJ/10.1144/GSL.SP.1989.045.01.11](https://doi.org/10.1017/S0016754700001144).
- Brun J.P. and Cobbold P.R., 1980. Strain heating and thermal softening. *Journal of Structural Geology*, 2: 149-158.
- Carosi R., Montomoli C. and Iaccarino S., 2018. 20 years of geological mapping of the metamorphic core across Central and Eastern Alps. *Journal of Metamorphic Geology*, 36: 124-138. [KWWSV://GRL.RUJ/10.1016/M.HDUVFLUHY.2017.11.006](https://doi.org/10.1016/j.jmg.2017.11.006).
- Carosi R., Petroccia A., Iaccarino S., Simonetti M., Langone A. and Montomoli C., 2020. Kinematics and timing constraints on the D₁ extensional unroofing of the Ivrea Zone. *Journal of Metamorphic Geology*, 38: 288-300. [KWWSV://GRL.RUJ/10.3390/JHRVFLHQFHV10080288](https://doi.org/10.1016/j.jmg.2019.10.005).
- Corvò S., Langone A., Padrón-Navarta J.A., Tommasi A. and Zanetti A., 2020. Kinematics and timing constraints on the D₁ extensional unroofing of the Ivrea Zone. *Journal of Metamorphic Geology*, 38: 288-300. [KWWSV://GRL.RUJ/10.3390/JHRVFLHQFHV10050196](https://doi.org/10.1016/j.jmg.2019.10.005).
- Decarlis A., Beltrando M., Manatschal G., Ferrando S. and Carosi R., 2017. Architecture of the distal Piedmont-Ligurian rifted margin. *Journal of Metamorphic Geology*, 35: 2388-2406. [KWWSV://GRL.RUJ/10.1002/2017J08004561](https://doi.org/10.1016/j.jmg.2017.08.004).
- Degli Alessandrini G., 2018. Deformation mechanisms and strain localization during extensional unroofing of the Ivrea Zone. *Journal of Metamorphic Geology*, 36: 366-380. [KWWSV://GRL.RUJ/10.1016/JHRVFLHQFHV.2018.09.005](https://doi.org/10.1016/j.jmg.2017.11.006).
- Denyszyn S.W., Fiorentini M.L., Maas R. and Dering G., 2018. A new zircon U-Pb age from the Ivrea Zone. *Journal of Metamorphic Geology*, 36: 823-826. [KWWSV://GRL.RUJ/10.1016/JHRVFLHQFHV.2018.09.005](https://doi.org/10.1016/j.jmg.2017.11.006).
- Ewing T.A., Hermann J. and Rubatto D., 2013. The robustness of zircon U-Pb ages from high-temperature metamorphic rocks. *Journal of Metamorphic Geology*, 31: 757-779. [KWWSV://GRL.RUJ/10.1007/s00410-012-0834-5](https://doi.org/10.1016/j.jmg.2012.12.002).
- Ewing T.A., Rubatto D., Beltrando M. and Hermann J., 2015. Constraints on the thermal evolution of the Adriatic margin during extensional unroofing. *Journal of Metamorphic Geology*, 33: 44-56. [KWWSV://GRL.RUJ/10.1007/V00410-015-1135-6](https://doi.org/10.1016/j.jmg.2014.12.002).
- Ferrando S., Bernoulli D. and Compagnoni R., 2004. The Canavese. *Journal of Metamorphic Geology*, 22: 237-256. [KWWSV://GRL.RUJ/10.1016/JHRVFLHQFHV.2004.02.002](https://doi.org/10.1016/j.jmg.2004.02.002).
- Fossen H. and Cavalcante G.C.G., 2017. Shear zones - A review. *Journal of Structural Geology*, 93: 434-455. [KWWSV://GRL.RUJ/10.1016/M.HDUVFLREV.2017.05.002](https://doi.org/10.1016/j.jsg.2017.05.002).
- Garde A.A., Boriani A. and Sørensen E.V., 2015. Crustal modelling of the Ivrea Zone. *Journal of Metamorphic Geology*, 33: 291-311. [KWWSV://GRL.RUJ/10.1016/JHRVFLHQFHV.2015.02.002](https://doi.org/10.1016/j.jmg.2014.12.002).
- Georgis S., Michels Z., Dair L., Braudy N. and Tikoff B., 2017. Kinematic and vorticity analyses of the western Idaho shear zone. *Journal of Metamorphic Geology*, 35: 223-234. [KWWSV://GRL.RUJ/10.1016/JHRVFLHQFHV.2017.08.004](https://doi.org/10.1016/j.jmg.2017.08.004).
- Giuntoli F., Menegon L., Warren C.J., Darlin, J. and Anderson M.W., 2020. Protracted shearing at mid-crustal conditions during large-scale extensional unroofing of the Ivrea Zone. *Journal of Metamorphic Geology*, 38: 267-280. [KWWSV://GRL.RUJ/10.1029/2020J026726](https://doi.org/10.1016/j.jmg.2019.10.005).
- *UDHVHU 6. DQG +XQJLNHU -, 1968. 5E-6U XQG 3E-, VRWRSHQ-%HVVLP-mungen an Gesteinen und Mineralien der Ivrea-Zone. *Schweizer Mineralogische und Petrographische Mitteilungen*, 48: 189-204.
- Guergouz C., Martin L., Vanderhaeghe O., Thébaud N. and Fiorentini M., 2018. Zircon and monazite petrochronologic record of prolonged amphibolite to granulite facies metamorphism in the Ivrea-Verbano and Strona-Ceneri Zones, NW Italy. *Lithos*, 158: 1-18. [KWWSV://GRL.RUJ/10.1016/M.OLWKR.2018.02.014](https://doi.org/10.1016/j.lithos.2018.02.014).
- Hartmann G. and Hans Wedepohl K., 1993. The composition of the Ivrea Zone. *Contributions to Mineralogy and Petrology*, 112: 1761-1782. [KWWSV://GRL.RUJ/10.1016/0016-7037\(93\)90112-5](https://doi.org/10.1007/BF01167037).
- Henk A., Franz L., Teufel S. and Oncken O., 1997. Magmatic unroofing of the Ivrea Zone. *Journal of Metamorphic Geology*, 15: 367-378. [KWWSV://GRL.RUJ/10.1086/515932](https://doi.org/10.1016/j.jmg.1997.05.002).
- Hodges K.V. and Fountain D.M., 1984. Pogallo Line, South Alps. *Journal of Metamorphic Geology*, 2: 151-155. [KWWSV://GRL.RUJ/10.1016/JHRVFLHQFHV.1984.02.002](https://doi.org/10.1016/j.jmg.1984.02.002).
- Hunziker J.C., 1974. Rb-Sr and K-Ar age determination and the Alpine tectonic history of the Western Alps. *Memorie di Geologia*, 8: 54.
- Iaccarino S., Montomoli C., Carosi R., Massonne H.-J., Langone A. and Visonà D., 2015. Pressure-temperature-time deformation path of kyanite-bearing migmatitic paragneiss in the Kali Gan- GDNL. *Journal of Metamorphic Geology*, 33: 103-121. [KWWSV://GRL.RUJ/10.1016/M.OLWKR.2015.06.005](https://doi.org/10.1016/j.jmg.2015.06.005).
- Iacopini D., Carosi R., Montomoli C. and Passchier C.W., 2008. Kinematics and timing constraints on the D₁ extensional unroofing of the Ivrea Zone. *Journal of Metamorphic Geology*, 26: 77-96. [KWWSV://GRL.RUJ/10.1016/M.tecto.2007.10.002](https://doi.org/10.1016/j.jmg.2007.10.002).
- JHU (., 1LJLJL (., DQG :HQN (., 1967. 5E-6U-\$OWHUVHVVWLPXQJHQ an Glimmern der Zentralalpen. *Beiträge zur Geologie der Schweiz*, NF 134: 67.
- Karakas O., Wotzlaw J.F., Guillong M., Ulmer P., Brack P., Economos R., Bergantz G.W., Sinigoi S. and Bachmann O., 2019. The pace of crustal-scale magma accretion and differentiation beneath the Ivrea Zone. *Journal of Metamorphic Geology*, 37: 719-723. [KWWSV://GRL.RUJ/10.1016/JHRVFLHQFHV.2019.08.004](https://doi.org/10.1016/j.jmg.2019.08.004).
- Kenkmann T., 2000. Processes controlling the shrinkage of porphyroblasts. *Journal of Metamorphic Geology*, 18: 471-487. [KWWSV://GRL.RUJ/10.1016/60191-8141\(99\)00177-7](https://doi.org/10.1016/j.jmg.2000.05.002).
- Kenkmann T. and Dresen G., 2002. Dislocation microstructure and phase distribution in a lower crustal shear zone - an example from the Ivrea Zone. *Journal of Metamorphic Geology*, 20: 445-458. [KWWSV://GRL.RUJ/10.1016/JHRVFLHQFHV.2002.05.002](https://doi.org/10.1016/j.jmg.2002.05.002).
- Klötzli U.S., Sinigoi S., Quick J.E., Demarchi G., Tassinari C.C.G., Sato K. and Günes Z., 2014. Duration of igneous activity in the Sesia Magmatic System and implications for high-temperature extensional unroofing. *Journal of Metamorphic Geology*, 32: 19-33. [KWWSV://GRL.RUJ/10.1016/JHRVFLHQFHV.2013.11.015](https://doi.org/10.1016/j.jmg.2013.11.015).
- Koppel V., 1974. Isotopic U-Pb ages of monazites and zircons from the crust-mantle transition and adjacent units of the Ivrea Zone. *Contributions to Mineralogy and Petrology*, 43: 55-70. [KWWSV://GRL.RUJ/10.1016/JHRVFLHQFHV.1974.05.002](https://doi.org/10.1007/BF01160040).
- Kozur H., 1991. The evolution of the Meliata-Hallstatt ocean and the Ivrea Zone. *Journal of Metamorphic Geology*, 9: 109-135. [KWWSV://GRL.RUJ/10.1016/0031-0182\(91\)90132-%](https://doi.org/10.1016/j.jmg.1991.03.002).
- Kunz B.E., Johnson T.E., White R.W. and Redler C., 2014. Partial melting of metabasic rocks in Val Strona di Omegna, Ivrea Zone. *Journal of Metamorphic Geology*, 32: 19-33. [KWWSV://GRL.RUJ/10.1016/M.lithos.2013.11.015](https://doi.org/10.1016/j.jmg.2013.11.015).
- Kunz B.E., Regis D. and Engi M., 2018. Zircon ages in granulite facies rocks from the Ivrea Zone. *Journal of Metamorphic Geology*, 36: 26-30. [KWWSV://GRL.RUJ/10.1007/V00410-018-1454-5](https://doi.org/10.1016/j.jmg.2017.11.006).
- Kusiak M.A., Kovaleva E., Wirth R., Klötzli U., Dunkley D.J., Yi K. and Lee S., 2019. Lead oxide nanospheres in seismically unroofed rocks from the Ivrea Zone. *Journal of Metamorphic Geology*, 37: 20-30. [KWWSV://GRL.RUJ/10.1016/JHRVFLHQFHV.2019.08.004](https://doi.org/10.1016/j.jmg.2019.08.004).
- Kylander-Clark A., Hacker B. and Cottle J.M., 2013. Laser ablation U-Pb zircon dating of the Ivrea Zone. *Journal of Metamorphic Geology*, 31: 99-112. [KWWSV://GRL.RUJ/10.1016/JHRVFLHQFHV.2012.12.002](https://doi.org/10.1016/j.jmg.2012.12.002).
- Langone A., Zanetti A., Daczko N.R., Piazzolo S., Tiepolo M. and Mazzucchelli M., 2018. Zircon U-Pb dating of a lower crustal granulite facies metamorphic rock from the Ivrea Zone. *Journal of Metamorphic Geology*, 36: 322-342. [KWWSV://GRL.RUJ/10.1002/2017J0804638](https://doi.org/10.1016/j.jmg.2017.11.006).

- Law R.D., 2014. Deformation thermometry based on quartz c-axis IDEULFV DQG UHFUIVWDOOLJDLWRQ PLFURVWUXFWXUHV: \$ UYHLZ. - 6WUXFW. *HRO., 66: 129-161. KWWWSV://GRL.RUJ/10.1016/M.MVJ.2014.05.023.
- Law R.D., Searle M.P. and Simpson R.L., 2004. Strain, deformation WLRQ WHPSHUDWXUHV DQG YRUWLFW RI ARZ DW WKH WRS RI WKH *UHDWHU Himalayan Slab, Everest Massif, Tibet. *J. Geol. Soc. London*, 161: 305-320.
- Luvizotto G.L., Zack T., Meyer H.P., Ludwig T., Triebel S., Kronz A., Munker C., Stockli D.F., Prowatke S., Klemme S., Jacob D.E. and von Eynatten H., 2009. Rutile crystals as potential trace element and isotope mineral standards for microanalysis. &KHP. *HRO., 261 (3-4): 346-369.
- Mako C.A. and Caddick M.J., 2018. Quantifying magnitudes of VKHDU KHDWLQJ LQ PHWDPRUSKLF VVWHPV. 7HFWRQRSKVLFV, 744: 499-517.
- Manatschal G., Müntener O., Lavier L.L., Minshull T.A. and Péron-Pinvic G., 2007. Observations from the Alpine Tethys and Iberia-Newfoundland margins pertinent to the interpretation of FRQWLQHQWDO EUHDNXS. *HRO. 6RF. /RQGRQ 6SHF. 3XEO., 282: 291-324. KWWWSV://GRL.RUJ/10.1144/63282.14.
- OF'RZHOO.: DQG 6FKPLG 5., 1968. 3RWDVVLPX-DUJRQDJHVIURP the Valle d'Ossola section of the Ivrea-Verbano Zone (Northern ,WDO). 6FKZHLJ. 0LQHU. 3HWURJU., 48: 205-210.
- Mohn G., Manatschal G., Beltrando M., Masini E. and Kuszner N., 2012. Necking of continental crust in magma-poor rifted mar- JLQV: (YLGHQFH IURP WKH IRVVLO \$OSLQH 7HWKIV PDUJLQV: QHFN- LQJ RI FRQWLQHQWDO FUXVW. 7HFWRQLFV, 31 (1): 7&1012. KWWWSV://GRL. RUJ/10.1029/20117&002961.
- Mohn G., Manatschal G., Müntener O., Beltrando M. and Masini E., 2010. Unravelling the interaction between tectonic and sedimentary processes during lithospheric thinning in the Alpine Tethys PDUJLQV. ,QW. -. (DUWK. 6FL., 99: 75-101. KWWWSV://GRL.RUJ/10.1007/ V00531-010-0566-6.
- Montomoli C., Iaccarino S., Carosi R., Langone A. and Visonà D., 2013. Tectonometamorphic discontinuities within the Greater +LPDODIDQ 6HTXHQFH LQ :HVWHUQ 1HSDO (&HQWUDO +LPDODID): ,Q- sights on the exhumation of crystalline rocks. *Tectonophysics*, 608: 1349-1370. KWWWSV://GRL.RUJ/10.1016/M.WHFWR.2013.06.006.
- Mulch A., Rosenau M., Dörr W. and Handy M.R., 2002. The age and structure of dikes along the tectonic contact of the Ivrea-Verbano and Strona-Ceneri Zones (Southern Alps, Northern ,WDO). 6ZLWJHUODQG. 6FKZHLJ. 0LQHU. 3HWURJU., 82: 55-76.
- Müntener O., Hermann J. and Trommsdorff V., 2000. Cooling history and exhumation of lower-crustal granulite and upper mantle (0DÖHQFR, HDVVHUQ FHQWUDO \$OSV). -. 3HWURO., 41: 175-200.
- Oriolo S., Wemmer K., Oyhantçabal P., Fossen H., Schulz B. and Siegesmund S., 2018. Geochronology of shear zones - A review. (DUWK 6FL. 5HY., 185: 665-683.
- Papapavlou K., Darling J.R., Storey C.D., Lightfoot P.C., Moser D.E. and Lasalle S., 2017. Dating shear zones with plastically GHIRUPHG WLWDLQWH: 1HZ LQVLJKW LQWR WKH RURJHQLF HYROXWLRQ RI the Sudbury impact structure (Ontario, Canada). *Precamb. Res.*, 291: 220-235. KWWWSV://GRL.RUJ/10.1016/M.SUHFDPUHV.2017.01.007. Parsons A.J., Coleman M.J., Ryan J.J., Zagorevski A., Joyce N.L., Gibson H.D. and Larson, K.P., 2018. Structural evolution of a crustal-scale shear zone through a decreasing temperature UHJLPH: 7KH <XNRQ 5LYHU VKHDU JRQH, <XNRQ-7DQDQD WHUUDQH, 1RUWKHUQ &RUGLOOHU. /LWKRVSKHUH, 10 (6): 760-782. KWWWSV://GRL. RUJ/10.1130/724.1.
- Peressini G., Quick J.E., Sinigoi S., Hofmann A.W. and Fanning M., 2007. 'XUDWLRQ RI D ODUJH PDÄF LQWUXVLRQ DQG KHDW WUDQVIHU LQ WKH ORZHU FUXVW: D 6+5,03 8-3E =LUFHQ VVXG\LQ WKH ,YUHD-9HUEDQR =RQH (:HVWHUQ \$OSV, ,WDO). -. 3HWURO., 48: 1185-1218. KWWWSV:// GRL.RUJ/10.1093/SHWURORJ/VHJP14.
- Petri B., Duret T., Mohn G., Schmalholz S.M., Karner G.D. and Müntener O., 2019. Thinning mechanisms of heterogeneous FRQWLQHQWDO OLWKRVSKHUH. (DUWK 3ODQHW 6FL. /HWW., 512: 147-162. KWWWSV://GRL.RUJ/10.1016/M.HSVO.2019.02.007.
- Pittarello L., Pennacchioni G. and Di Toro G., 2012. Amphibolite- facies pseudotachylytes in Premosello metagabbro and felsic mylonites (Ivrea Zone, Italy). *Tectonophysics*, 580, 43-57.
- Real C., Froitzheim N., Carosi R. and Ferrando S., 2018. Evidence of large-scale Mesozoic detachments preserved in the basement of the Southern Alps (northern Lago di Como area). Italy. *J. *HRVFL.*, 137: 283-293. KWWWSV://GRL.RUJ/10.3301/,-*.2018.15.
- Redler C., Johnson T.E., White R.W. and Kunz B.E., 2012. Phase HTXLOLEULXP FRQWUDLQVW RQD GHHS FUXVWDO PHWDPRUSKLF ÄHOQJUD- GLHQW: PHWDSHOLWLF URFNV IURP WKH ,YUHD =RQH (1: ,WDO). :YUHD =RQH PHWDPRUSKLF ÄHOQJUDGLHQW. -. 0HWDP.. *HRO., 30: 235-254. KWWWSV://GRL.RUJ/10.1111/M.1525-1314.2011.00965.[.
- Rutter E.H. and Brodie K.H., 1990. Some geophysical implications of the deformation and metamorphism of the Ivrea zone, North- HUQ ,WDO. 7HFWRQRSKVLFV, 182 (1-2): 147-160.
- Rutter E.H., Brodie K.H. and Evans P.J., 1993. Structural geometry, lower crustal magmatic underplating and lithospheric stretching LQ WKH ,YUHD-9HUEDQR JRQH, QRUWKHUQ ,WDO. -. 6WUXFW. *HRO., 15: 647-662. KWWWSV://GRL.RUJ/10.1016/0191-8141(93)90153-2.
- Rutter E.H., Brodie K.H., James T. and Burlini L., 2007. Large- scale folding in the upper part of the Ivrea-Verbano Zone, 1: ,WDO. -. 6WUXFW. *HRO., 29: 1-17. KWWWSV://GRL.RUJ/10.1016/M. MVJ.2006.08.013.
- Schaltegger U., Ulianov A., Müntener O., Ovtcharova M., Peytcheva I., Vonlanthen P., Vennemann T., Antognini M. and Girlanda F., 2015. Megacrystic zircon with planar fractures in miaskite-type nepheline pegmatites formed at high pressures in the lower crust (,YUHD =RQH, VRXWKHUQ \$OSV, 6ZLWJHUODQG). \$PHU. 0LQHU., 100: 83-94.
- Schmid S.M., 1993. Ivrea zone and adjacent southern Alpine base- PHQW. ,Q: -. 5DXPHU DQG. 1HXEDXHU ((GV.). 3UH-0HVRJRLF JHRORJ LQ WKH \$OSV, 6SULQJHU, %HUOLQ, +HLGHOEHUJ, S. 567-583.
- Schmid S.M., Aelbi H.R., Heller F. and Zingg A., 1989. The role of the Periadriatic Line in the tectonic evolution of the Alps. *Geol. 6RF. /RQGRQ 6SHF. 3XEO.*, 45 (1):135-171.
- 6FKPLG 5. DQG :RRG %.-., 1976. 3KDVH UHODWLRQV KLSV LQ JUDQXOLW- ic metapelites from the Ivrea-Verbano zone (Northern Italy). &RQWULE. 0LQHU. 3HWURO., 54: 255-279. KWWWSV://GRL.RUJ/10.1007/ BF00389407.
- Schmid S.M., Zingg A. and Handy M., 1987. The kinematics of movements along the Insubric Line and the emplacement of the ,YUHD =RQH. 7HFWRQRSKVLFV, 135 (1-3): 47-66.
- Schuster R., Stüwe K., 2008. Permian metamorphic event in WKH \$OSV. *HRORJ, 36: 603-606. KWWWSV://GRL.RUJ/10.1130/ G24703A.1.
- Sibson R.H., 1977. Fault rocks and fault mechanisms. *J. Geol. Soc. /RQGRQ*, 133: 191-213.
- Siegesmund S., Layer P., Dunkl I., Vollbrecht A., Steenken A., Wemmer K. and Ahrendt H., 2008. Exhumation and deformation history of the lower crustal section of the Valstrona di Omega in the Ivrea Zone, southern Alps. *Geol. Soc. London 6SHF. 3XEO.*, 298: 45-68. KWWWSV://GRL.RUJ/10.1144/63298.3.
- Simonetti M., Carosi R., Montomoli C., Corsini M., Petroccia A., Cottle J.M. and Iaccarino S., 2020a. Timing and kinematics RI ARZ LQ D WUDQVSUHVVLVYH GH[WUDO VKHDU JRQH, ODXUHV ODUVLI (6RXWKHUQ)UDQFH). ,QW. -. (DUWK. 6FL., 109: 2261-2285. KWWWSV:// GRL.RUJ/10.1007/V00531-020-01898-6.
- Simonetti M., Carosi R., Montomoli C., Cottle J.M. and Law R.D., 2020b. Transpressive deformation in the southern (XURSHDQ 9DULVFDQ %HOW: 1HZ LQVLJKW IURP WKH \$LXLOOHV 5RXJHV ODUVLI (:HVWHUQ \$OSV). 7HFWRQLFV, 39. KWWWSV://GRL. RUJ/10.1029/20207&00615.
- 6PH \$.-. DQG 6WRFNOL '.), 2014. 5XWLOH 8-3E DJH GHSWK SURÄO- LQ: \$ FRQWLQXRXV UHFUG RI OLWKRVSKHULF WKHUPO HYROXWLRQ. (DUWK 3ODQHW. 6FL. /HWW., 408: 171-182. KWWWSV://GRL.RUJ/10.1016/M. epsl.2014.10.013.
- Smye A.J., Lavier L.L., Zack T. and Stockli D.F., 2019. Episodic KHDWLQJ RI FRQWLQHQWDO ORZHU FUXVW GXULQJ H[WHQVLRQ: \$ WKHUPO modeling investigation of the Ivrea-Verbano Zone. *Earth Planet. 6FL. /HWW.*, 521: 158-168.
- Speranza F., Minelli L., Pignatelli A. and Chiappini M., 2012. The ,RQLDQ 6HD: 7KH ROGHVV LQ VLWX RFHQD IUDJPHQW RI WKH ZRUOG" Magnetic modelling of the Ionian Sea. *J. Geophys. Res. Solid (DUWK*, 117. KWWWSV://GRL.RUJ/10.1029/2012-%009475.

- Storey C.D., Brewer T.S. and Parrish R.R., 2004. Late-Proterozoic LF WHFWRQLFV LQ QRUWKZHVW 6FRWODQG: RQH FRQWUDFWLRQDO RURJHQ\ RU VHYHUDO" 3UHFDPEU. 5HV. 134 (3-4), 227-247. KWWWS://GRL.RUJ/10.1016/M.SUHFDPUHV.2004.06.004.
- Stünitz H., 1998. Syndeformational recrystallization - dynamic or FRPSRVLWLRQDO\ LQGXFHG" &RQWULE. 0LQHU. 3HWURO., 131: 219-236. KWWWSV://GRL.RUJ/10.1007/V004100050390.
- Techmer K.S., Ahrendt H. and Weber K., 1992. The development of pseudotachylyte in the Ivrea-Verbanio Zone of the Italian Alps. 7HFWRQRSK\VLV, 204: 307-322.
- Tillberg M., Drake H., Zack T., Kooijman E., Whitehouse M.J. DQG cVWUJP 0.(., 2020., Q VLWX 5E-6U GDWLQJ RI VOLFNHQÄEUHV LQ GHHS FUVWDOOLQH EDVHPHQW IDXOWV. 6FL 5HS 10: 562. KWWWSV://GRL.RUJ/10.1038/V41598-019-57262-5.
- Vavra G., Schmid R. and Gebauer D., 1999. Internal morphology, habit and U-Th-Pb microanalysis of amphibolite-to-granulite facies rocks from the Ivrea-Verbanio Zone of the Southern Alps. &RQWULE. 0LQHU. 3HWURO., 134(4): 380-404.
- Wolff R., Dunkl I., Kiesselbach G., Wemmer K. and Siegesmund S., 2012. Thermochronological constraints on the multiphase exhumation history of the Ivrea-Verbanio Zone of the Southern Alps. 7HFWRQRSK\VLV, 579: 104-117. KWWWSV://GRL.RUJ/10.1016/M.tecto.2012.03.019.
- Wu W., Liu J., Zhang L., Qi Y. and Ling C., 2017. Characterizing the tectonic evolution of the northern Ailao Shan-Red River shear zone, China. &RQWULE. 0LQHU. 3HWURO., 139: 95-114. KWWWSV://GRL.RUJ/10.1016/M.MVHDHV.2016.12.026.
- Zack T., Stockli D.F., Luvizotto G.L., Barth M.G., Belousova E., Wolfe M.R. and Hinton R.W., 2011. In situ U-Pb rutile dating of the Ivrea-Verbanio Zone. &RQWULE. 0LQHU. 3HWURO., 134: 515-530. KWWWSV://GRL.RUJ/10.1016/M.MVJ.2010.08.009.
- Zanetti A., Mazzucchelli M., Sinigoi S., Giovanardi T., Peressini G. and Fanning M., 2013. SHRIMP U-Pb zircon Triassic intrusion in the Ivrea-Verbanio Zone (Western Alps) and geodynamic consequences. &RQWULE. 0LQHU. 3HWURO., 134(11): 2235-2265.
- Zanetti A., Giovanardi T., Langone A., Tiepolo M., Wu F.-Y., Dallai I., and Fanning M., 2016. U-Pb zircon dating of the Ivrea-Verbanio Zone (Western Alps) and geodynamic consequences. &RQWULE. 0LQHU. 3HWURO., 134(11): 2235-2265.
- Zhang Q., Giorgis S. and Teyssier C., 2013. Finite strain analysis of the Zhangbaling metamorphic belt, SE China - Crustal thinning and extension. &RQWULE. 0LQHU. 3HWURO., 134(4): 380-404.
- Zingg A., 1980. Regional metamorphism in the Ivrea Zone (South-Alps). &RQWULE. 0LQHU. 3HWURO., 134(4): 380-404.
- Zingg A., 1983. The Ivrea and Strona-Ceneri zones (Southern Alps, Ticino and N-Italy) - a review. Schweiz Miner. Petrogr. Mitt., (2-3): 361-392.
- Zingg A., 1990. The Ivrea crustal cross-section (Northern Italy and Southern Alps). &RQWULE. 0LQHU. 3HWURO., 134(4): 380-404.
- Zingg A., Handy M.R., Hunziker J.C. and Schmid S.M., 1990. Tectonometamorphic history of the Ivrea Zone and its relationship to the crustal evolution of the Southern Alps. Tectonophysics, 182: 169-192. KWWWSV://GRL.RUJ/10.1016/0040-1951(90)90349-1.

Received, February 11, 2021

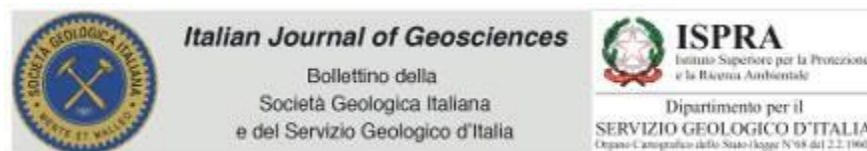
Accepted, May 19, 2021

A.5.2 Rift-related deformation in the middle continental crust: new microstructural and petrological insights from the Forno-Rosarolo shear zone (Ivrea-Verbano Zone, Western Alps)

In this work, a detailed study of the sheared rocks of the Forno-Rosarolo shear zone (FRSZ), a ductile shear zone exposed in the Strona di Omegna valley, was performed. The data obtained provide a detailed description and characterization of the sheared rocks of the FRSZ that allow to infer that it is a shear zone developed in an intermediate phase of the Tethyan rift. Our study also represents an indispensable starting point for future investigations about the exact age of deformation and for process-oriented investigations.

The content of this manuscript was submitted (19/10/2021) as original paper on the Italian Journal of Geosciences at the Special issue titled: and it is now under review. This study was financed by the following project: PRIN2017 “Micro to Macro—how to unravel the nature of the large magmatic events; 20178LPCPWLangoneAntonio”.

For this work, the candidate collaborated in field, samples preparation and lab work, and in writing paper with the team made by Matteo Simonetti (Servizio Geologico d’Italia, ISPRA), Mattia Bonazzi (University of Pavia), Antonio Langone (Istituto di Geoscienze e Georisorse di Pavia) and Matteo Maino (University of Pavia).



**Rift-related deformation in the middle continental crust:
new microstructural and petrological insights from the
Forno-Rosarolo shear zone (Ivrea-Verbano Zone, Western
Alps)**

Journal:	<i>Italian Journal of Geosciences</i>
Manuscript ID	IJG-2021-0993
Manuscript Type:	Original Article
Date Submitted by the Author:	19-Oct-2021
Complete List of Authors:	Simonetti, Matteo; ISPRa, Dipartimento per il Servizio Geologico d'Italia Langone, Antonio; National Research Council, Institute for Geosciences and Earth Resources Bonazzi, Mattia; Università degli Studi di Pavia Dipartimento di Scienze della Terra e dell'Ambiente Corvo, Stefania; Università degli Studi di Pavia Dipartimento di Scienze della Terra e dell'Ambiente, Maino, Matteo; Università degli Studi di Pavia, Dipartimento di Scienze della Terra

Abstract

The Ivrea-Verbano Zone, in the Italian Southern Alps, samples a complete section of lower continental crust recording the transition between the Variscan and the Alpine Tethys rift-related tectonics. We present the results of a structural, microstructural and petrographical study of one important tectonic structure developed in the Ivrea-Verbano zone at high-temperature conditions, i.e. the Forno-Rosarolo shear zone (FRSZ). The FRSZ is a NE-SW-oriented, subvertical mylonitic zone, developed within metapelites, amphibolites, calc-silicates and granulites. Metamorphic conditions of the wall rocks vary from the amphibolite to the granulite facies moving from the SE to the NW block across the shear zone. All kinematic indicators are indicative of a sinistral, top-to-the-SW sense of shear. Investigations on the kinematic of the flow in the mylonites revealed a non-coaxial deformation with a major component of pure shear acting together with simple shear. Estimations from the syn-tectonic mineral assemblages point to amphibolite facies condition during deformation (~650 °C and ~5.5 kbar). Although absolute dating is lacking, geological constraints indicate that the shear zone was active during the late Triassic – early Jurassic time. The data obtained in this work provide a detailed structural and microstructural description of the sheared rocks of the FRSZ that allow to infer that it is a shear zone developed in an intermediate phase of the Tethyan rift known as “thinning mode”.

A.5.1 Porphyroclasts: Source and Sink of Major and Trace Elements During Deformation-Induced Metasomatism (Finero, Ivrea-Verbano Zone, Italy)

This work deals with new petrological and geochemical data for mylonites from a meter-scale shear zone in mantle peridotites from the Finero massif (Ivrea-Verbano Zone). A complete dataset of major and trace element mineral chemistry is provided covering all the major lithologies of the Finero Phlogopite Peridotite mantle unit. These data allowed valuable constraints on the relationship between geochemistry and microstructural features in ultramafic shear zones.

This manuscript was the result of Master thesis and six months of scholarship at IGG-CNR of Pavia. It was published open access as original paper on MDPI geosciences as Corvò et al., (2020). Received 19 March 2020; Accepted 18 May 2020; Published 21 May 2020. This work received funds by the project PRIN2015 “Geochemical and isotopic budget of highly metasomatized sub-continental mantle in the Africa and Europe geodynamics systems: modern and fossil analogues”; by the PRIN2017 “Micro to Macro - how to unravel the nature of the large magmatic events (20178LPCPW- Langone Antonio)” and by a short post-graduation scholarship (2018; S. Corvò) at the IGG-CNR 718 (Pavia, Italy).

The PhD tenure for this study involved in particular the further acquisition and processing of new data, interpretation and writing of the manuscript. This work provides to the candidate the basic notions and skills for: geological setting of case study 2; the investigation of relationships between deformation and geochemical processes along shear zone, for the preparation and writing manuscript.

Article

Porphyroclasts: Source and Sink of Major and Trace Elements During Deformation-Induced Metasomatism (Finero, Ivrea-Verbano Zone, Italy)

Stefania Corvò ^{1,2,*} , Antonio Langone ^{2,*} , José Alberto Padrón-Navarta ³,
Andrea Tommasi ³  and Alberto Zanetti ^{2,*}

¹ Department of Earth and Environmental Sciences, University of Pavia, 27100 Pavia, Italy

² Institute of Geosciences and Earth Resources, National Research Council (C.N.R.), 27100 Pavia, Italy

³ Géosciences Montpellier, Univ. Montpellier & CNRS, 34090 Montpellier, France; padron@gm.univ-montp2.fr (J.A.P.-N.); andrea.tommasi@gm.univ-montp2.fr (A.T.)

* Correspondence: stefania.corvo01@universitadipavia.it (S.C.); langone@crystal.unipv.it (A.L.); zanetti@crystal.unipv.it (A.Z.)

Received: 13 March 2020; Accepted: 18 May 2020; Published: 21 May 2020



Abstract: Petrographic and geochemical data for mylonites from a metric-scale shear zone in mantle peridotites from the Finero massif (Southern Alps) record large mineralogical and geochemical modifications compared to surrounding coarse-grained ultramafic rocks, which were pervasively deformed in presence of hydrous melts. The mylonites are composed by olivine and orthopyroxene and, less frequently, clinopyroxene, phlogopite, and pargasite porphyroclasts enclosed in a fine-grained matrix of phlogopite and olivine, with subordinate amounts of orthopyroxene, clinopyroxene, pargasite, and chromite. P-T estimates indicate that deformation occurred under granulite- to upper-amphibolite facies conditions. Field relationships and U-Pb dating indicate that the shear zone was active during Lower Jurassic and/or later, in an extensional setting at the western margin of the Adria plate, which led to the opening of the Alpine Tethys. The major and trace element composition of the porphyroclasts in the mylonites significantly differ from those in the hosting coarse-grained ultramafics. Porphyroclasts were chemically active during deformation acting as source (diffusion-out) or sink (diffusion-in) for some trace elements. The chemical modifications were promoted by the interaction with aqueous fluids and the composition varied from mantle- (enriched in Ni, Co, Li, Na, REE, Y, and Sr) to crustal-derived (enriched in Zn, K, Al, Ti, and Fe).

Keywords: mantle peridotite; shear zone; major and trace elements; mylonite; porphyroclasts; Ivrea-Verbano Zone

1. Introduction

Shear zone evolution is commonly associated to bulk and mineral chemistry changes due to fluid–rock interaction [1–3], since shear zones provide important conduits for fluid movement through the crust [4] and lithospheric mantle [5,6]. Fluid focusing and high time-integrated fluid–rock ratios in shear zones allow mass transfer processes that can strongly modify the chemistry of deforming rocks. The P-T conditions and the chemical potential for certain components imposed by the external aqueous fluid dictate the mineral reactions and the stability of synkinematic mineral assemblages, controlling the balance between enrichment/depletion of major elements [7]. Moreover, deformation processes can locally accelerate chemical diffusion, promoting chemical heterogeneity and fractionation of trace elements [8,9].

The element behavior during deformation has mostly been the subject of research based on bulk chemistry and major-element mineral compositions [1,3–6,10–15]. These investigations point

to enhanced mobility at the bulk rock and mineral (major elements) scale. Trace-element mineral compositions are also modified by fluid–rock interactions, but the extent of modification and the relative roles of the nature of the fluids and of the deformation are poorly constrained. Available data suggest that trace element fractionation (i.e., REE and Y), in particular between clinopyroxene and amphibole, can be strongly affected by the stability of fine-grained accessory minerals precipitated in trace amounts from aqueous fluids percolating shear zones, independently on the deformation style (brittle vs. ductile) and/or to the alteration degree of mineral assemblages [3,13].

This work focuses on the evolution of major and trace element compositions in protomylonites and ultramylonites developed in a metric-scale shear zone crosscutting mantle peridotites from the Finero Phlogopite Peridotite unit (Ivrea-Verbano Zone). This shear zone has been the subject of previous microtextural and geochemical studies [1,2,14–16], which demonstrated that bulk compositions (major and trace elements) and mineral chemistry (major elements) underwent significant changes during shear deformation. Here, major and trace element composition of porphyroclasts in protomylonites and ultramylonites, as well as the major element composition of matrix-forming minerals are compared to the mineral compositions in the surrounding coarse-grained ultramafic rocks. Field evidence and zircon dating allowed us to constrain the timing of the shear zone activity and to address the mineralogical and geochemical changes in the frame of the geodynamic evolution of the northernmost part of the Ivrea-Verbano Zone.

2. Geological Setting

The Ivrea-Verbano Zone (IVZ) occupies the westernmost part of the Southern Alps. It consists of a lower continental crust sliver of the Adria plate, which escaped Alpine subduction, interleaved with remnants of the lithospheric mantle at different crustal levels [17–19]. Among these mantle remnants, the most important are the Finero, Balmuccia, and Baldissero peridotite massifs, which outcrop within the lowermost units of the crustal section close to the Insubric line [20].

The mantle peridotites of Finero (Figure 1a) have been thoroughly investigated due to their peculiar features: they consist of fully-metasomatized mantle rocks characterized by pervasive crystallization of significant amounts of pargasite and phlogopite, which may locally attain up to 25 vol.% [16]. The mantle rocks (also referred to as the Phlogopite Peridotite unit, Ph-Pd) crop out as a lens shaped body about 12 km long and 1.5 km wide with a SW-NE strike (Figure 1a,b). They are surrounded by mafic-ultramafic lithologies, which compose the Finero Mafic Complex. The latter is subdivided into three crustal units: (1) the Layered Internal Zone (LIZ), which is structurally the lowest unit, resulting in contact with the Ph-Pd; (2) the Amphibole Peridotite (Amph-Pd) and (3) the External Gabbro (EG). The EG is in contact with metamorphic rocks of the Kinzigite Formation (Figure 1a,b) [17–19,21–25]. The mantle unit and the Finero Mafic Complex are bounded at N-NW by the Insubric line (IL, Figure 1a), which marks the contact of the lower crust and mantle units of the Adria plate with an accretionary prism of the Alpine orogeny (the Austroalpine terrain).

The Ph-Pd unit is mostly composed by spinel harzburgites. Dunite, lherzolites, wehrlites, and pyroxenites are minor lithologies and occur mainly as layers/lenses. Pegmatites and pods with pargasite and phlogopite are common, as well as zircon-bearing felsic dykes that have been dated at Triassic–Jurassic time [26,27]. Chromite-rich layers/pockets mainly occur in dunite, where they are broadly parallel to the high-temperature (HT) foliation [19]. In recent decades, the deformation processes within the mantle peridotites (Ph-Pd) and mafic/ultramafic rocks of the Finero Mafic Complex were the subject of multiple microstructural [1,2,14–16,28–33] and geochemical/geochronological studies [17–25,27,33,34]. According to Tommasi et al. [16] the mantle peridotite experienced a pervasive HT deformation in the presence of hydrous melts with crystallization of pargasite at T of about 980–1080 °C and P < 2 GPa. The presence of hydrous melts strongly changed the deformation processes in the upper mantle resulting in rheological weakening, allowing pervasive deformation of the peridotites under low stress conditions (<10 MPa).

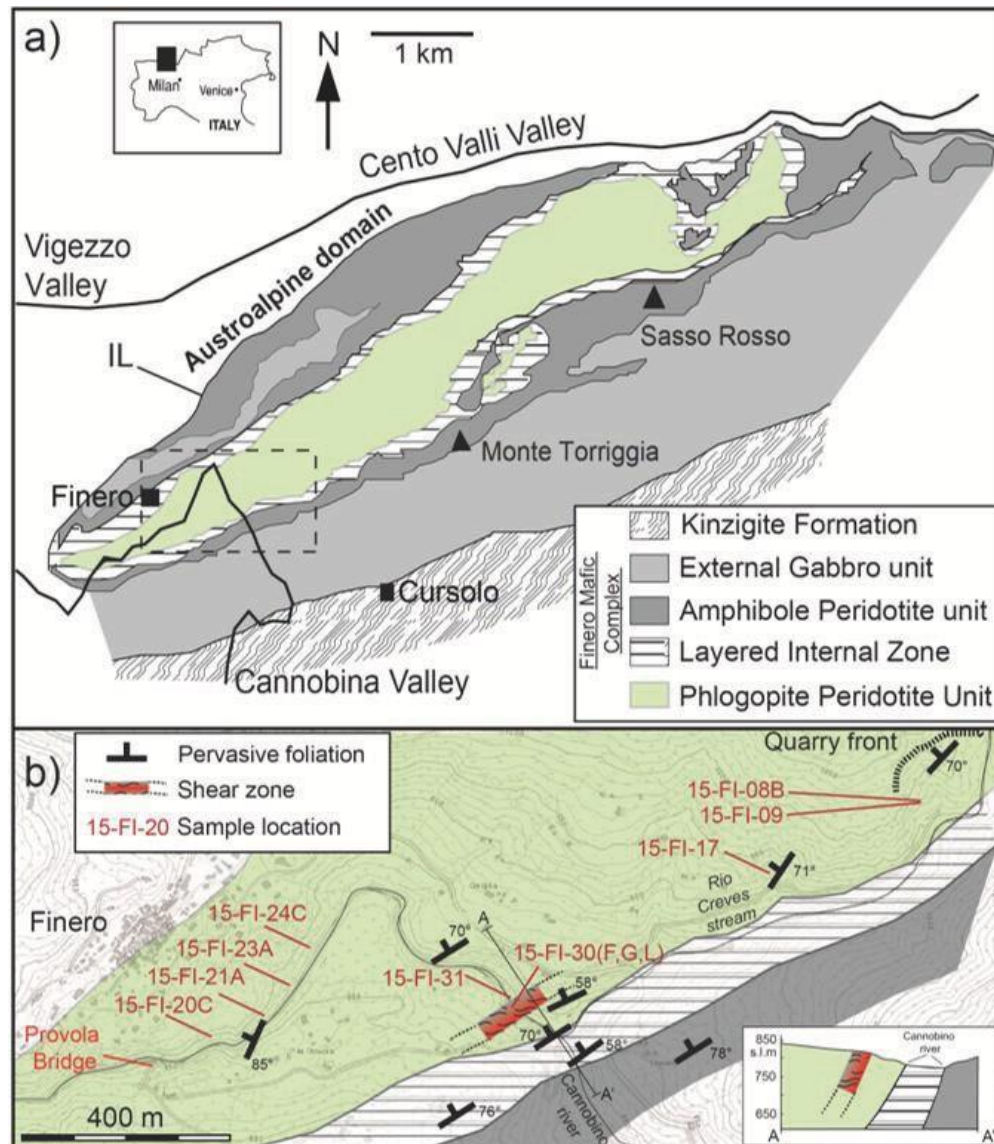


Figure 1. (a) Geological map of the northern sector of the Ivrea-Verbano zone showing the main units of the Finero Complex, as well as the Insubric Line (IL) and the Kinzigite Formation, which bounds it to the NW and SE, respectively. (b) Sketch map of the area east/northeast of Finero village showing representative attitudes of pervasive foliation and location of samples used for petrography, microstructures, and chemistry (red labels; modified after Tommasi et al. [16]). The studied shear zone is also shown as well as a schematic geological cross section (bottom right).

In addition to this pervasive low-stress deformation, the HT foliation of Finero peridotites is crosscut by many metric-scale shear zones (Figure 1b), recording localized deformation under subsolidus, higher stress conditions [16]. Most of these shear zones are subparallel to the pervasive HT foliation. Matysiak and Trepmann [32] focused on the deformation mechanisms of olivine from mylonitic peridotites from both the Finero Mafic Complex and the Ph-Pd body. They reported that mylonitic deformation occurred at least in two discrete cycles at decreasing temperature (from granulite- to amphibolite-facies) during the pre-Alpine exhumation. Brodie [1] and Altenberger [15] analyzed the bulk chemistry and major element compositions of minerals from mylonites/ultramylonites in the shear zone studied in this work. They argued that deformation was accompanied by mass transport and volume changes and proposed that changes in major element mineral chemistry tend to reflect the bulk chemical variations.

3. Results

3.1. Sampling and Petrography

Samples were collected in three different areas (see Figure 1b for sample location and Table 1; [16]). Coarse-grained ultramafics were sampled along the private road to a quarry front located on the right flank of the Creves stream valley (samples: 15-FI-08B, 15-FI-09, 15-FI-17) and along the Cannobino river, downstream of the Provola bridge (15-FI-20C, 15-FI-21A, 15-FI-23A, 15-FI-24C), whereas proto-ultramylonites were sampled in a metric-scale shear zone exposed close to the Cannobino-Creves confluence (15-FI-30F and 15-FI-30L ultramylonites, 15-FI-30G mylonite, and 2 meters away from the shear zone 15-FI-31 protomylonites). Selected samples are representative of the lithologic variability of the Ph-Pd unit (i.e., harzburgite, dunite, lherzolite, and pyroxenitic veins) and of the main microstructures across the shear zone (Figures 2–4). For the sake of simplicity, the samples will be hereafter indicated only by the last part of its label: e.g., 15-FI-30F will be reported as (30F).

Table 1. Labels, GPS coordinates (WGS84), lithologies of samples, and relative symbols used in diagrams.

GPS Coordinates	Sample Name	Lithology	Symbol
N46°06′17.88″/E8°32′36.22″	15-FI-30F	Ultramylonite porphyroclasts, matrix	○ ●
	15-FI-30L		● ●
	15-FI-30G		● ●
N46°06′18.79″/E8°32′35.70″	15-FI-31	Protomylonite	□
N46°06′22.44″/E8°32′18.16″	15-FI-24C	Harzburgite with pyroxenite vein	■
N46°06′16.38″/E8°32′08.57″	15-FI-20C		■
N46°06′19.79″/E8°32′16.29″	15-FI-23A	Dunite	+
N46°06′26.90″/E8°32′59.37″	15-FI-17		+
N46°06′17.51″/E8°32′12.99″	15-FI-21A	Ol. Websterite	×
N46°06′32.16″/E8°32′12.16″	15-FI-09	Wehrlite	◇
	15-FI-08B	Lherzolite	▲

3.1.1. Coarse-grained Ultramafics

The coarse-grained ultramafics (Figure 2) are equigranular. The harzburgite (e.g., sample 20C and 24C) is composed by olivine (60–90% vol.%), orthopyroxene (5–20% vol.%), clinopyroxene (0–10% vol.%), chromium-rich spinel (0–1% vol.%), pargasite (0–10% vol.%), and phlogopite (5–10% vol.%). The hydrous phases are distributed in a pervasive way but may also form local enrichments (pockets). Their orientation defines the HT foliation (Figure 2a,b). Phlogopite and amphibole-bearing orthopyroxenite (e.g., 20C, 24C) and Cr-diopside websterite lenses (mm to tens of cm-wide; e.g., 09, 21A) are associated with the harzburgite, defining a compositional layering parallel to the foliation. Locally, in the proximity of websterites, the ultramafics may have a lherzolitic composition (e.g., 08B). Dunites (e.g., 17, 23A) are present as tens of centimeters to several meters thick lens-shaped bodies, mainly elongated parallel to the harzburgite foliation [16]. Dunites may contain phlogopite veins/pods, phlogopite-bearing amphibole pyroxenites, pegmatoidal websterites, and chromitite layers [17–19]. Compared to the harzburgites, dunites are usually enriched in phlogopite (Figure 2b) and depleted in pargasite.

Olivine grains are euhedral to subhedral (Figure 2c), show undulose extinction, and often form triple junctions at 120°. The grain size in the ultramafics increases with olivine content, i.e., in dunites, olivine is very coarse-grained with polygonal and equiaxed shapes (5 mm on average), whereas in pargasite or phlogopite-rich harzburgites and lherzolites olivine crystals are smaller (1.7 mm on average).

Orthopyroxene has very irregular, interstitial-like shapes with cusp-like terminations at triple junctions (Figure 2d–f), except in the coarse websterite layers, where it shows a granular texture. Grain sizes are highly variable, from 50 μm to 1 cm. Coarse orthopyroxene grains may display kink bands and/or undulose extinction.

Clinopyroxene occurs as an interstitial, minor constituent of both harzburgites and dunites (Figure 2e), where it is usually heterogeneously distributed. The grain size is highly variable, from 100 μm to 5 mm. The clinopyroxene abundance tends to be inversely proportional to the amount of pargasite.

Pargasite is usually dispersed within the harzburgite but may also be enriched within diffuse lenses or layers elongated parallel to the harzburgite foliation. It occurs either as subhedral crystals or as more irregularly shaped grains. Grain sizes are on average around 800 μm but may vary from 140 μm to 3 mm.

Phlogopite usually occurs as large flakes, up to 5 mm long, aligned in the foliation (Figure 2e). Phlogopite content is highly variable, usually <5 vol.%. It is mostly undeformed, but locally phlogopite crystals may show undulose extinction, be bent, or display kinks outlined by the cleavages (Figure 2e).

Spinel occurs as an interstitial phase or as subhedral grains among major minerals. It is also a common inclusion within olivine, orthopyroxene, and phlogopite.

3.1.2. Sheared Peridotites

The studied shear zone is well exposed about 50 meters upstream to the confluence between the Cannobino river and Creves stream (Figure 1b). It has an asymmetric structure, being composed by a meter-thick ultramylonitic band and a ca. 3 m-thick mylonitic to protomylonitic zone (Figures 1b, 2 and 3a). Variably deformed felsic dykes were observed within the protomylonites (Figure 3b).

The present work focused on four samples representative of the protomylonites and ultramylonites from this shear zone (Figures 3 and 4). More petrographic and microstructural data from the same shear zone were reported by Brodie [1] and Altenberger [15].

The protomylonite (31), which was collected three meters away from the ultramylonitic zone, represents the less deformed sample. Recrystallization is limited and affects mainly olivine and orthopyroxene (see Figure 3c,d and Figure S1a). Olivine porphyroclasts show a strong shape-preferred orientation, undulose extinction, and closely spaced subgrains boundaries. The olivine recrystallized area fraction is around 21%, and recrystallized grain sizes are about 130 μm . Pyroxene porphyroclasts have irregular shapes and highly indented grain boundaries filled by olivine. Orthopyroxene also occurs as fine-grained interstitial crystals interleaved with recrystallized olivine. Pargasite is abundant (about 11 vol. %); phlogopite is less abundant (<2 vol. %). Both hydrous phases are weakly deformed; they show undulose extinction but no recrystallization (Figure 3c,d and Figure S1a).

The sample (30G) is representative of the transition from protomylonitic to ultramylonitic texture and is therefore heterogeneous at the thin section scale. Half of the thin section is a mylonite characterized by coarse-grained olivine, orthopyroxene, clinopyroxene, and chromite and is more enriched in phlogopite than the protomylonite (31). The other half is an ultramylonite characterized by large porphyroclasts of olivine and orthopyroxene or medium to coarse-grained mineral aggregates surrounded by a fine-grained matrix. Olivine porphyroclast dimensions vary from a hundred of micrometers to millimeters (Figures 3e and 4e). They are characterized by strong undulose extinction and closely spaced subgrains boundaries. The fine-grained matrix consists mainly of phlogopite and olivine with minor ortho- and clinopyroxene, chromite, and secondary antigorite (Figure 4a,b). Grain size in the matrix is in the range of 25–50 μm . Rarely, dolomite, calcite, and apatite were observed within the mylonitic matrix, interlayered with phlogopite and, within fractures of the porphyroclasts, together with serpentine (Figure S1b).

The ultramylonitic samples (30L and 30F) are characterized by rounded, sometimes angular, porphyroclasts of olivine, orthopyroxene, and, rarely, clinopyroxene embedded within a very fine-grained matrix. Both samples show local overprint of late brittle deformation. The number

of porphyroclasts is highly variable and their dimensions vary from a hundred of micrometers to millimeters (Figures 3g–l and 4). The fine-grained matrix surrounding the porphyroclasts has grain sizes in the range of 5–25 μm and is mainly made of phlogopite, olivine, orthopyroxene, clinopyroxene, and secondary antigorite, as well as minor chromite and amphibole (Figures 3g–l and 4).

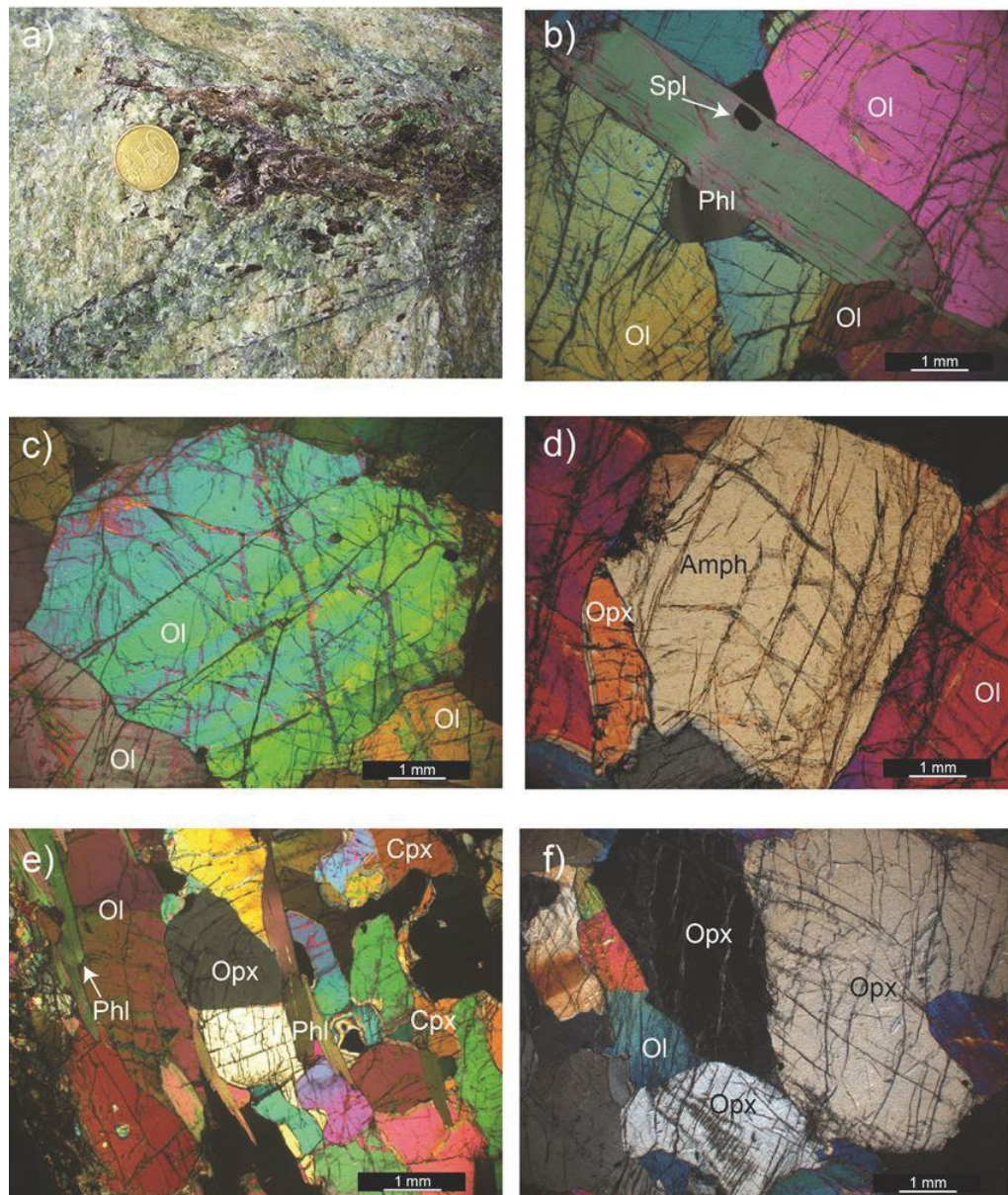


Figure 2. Petrographic and microstructural features in the coarse-grained ultramafic samples of the Ph-Pd unit (crossed polarizers). Mineral abbreviation after [35]. (a) Harzburgite at mesoscopic scale: pocket with large flakes of phlogopite (dark-brown), olivine (pale green), Cr-diopside (emerald green), and pargasite (dark spots); (b) Typical phlogopite (phl) elongated grain surrounded by olivine (ol) crystals in dunite (17); (c) Very coarse olivine grains with polygonal, equiaxed shape in dunite (17); (d) Very coarse amphibole grain with polygonal shape surrounded by olivine crystals in harzburgite (20C); (e) Mineral assemblage characterized by rounded crystals of orthopyroxene, olivine, and elongated phlogopite crystals, which mark the foliation in lherzolite (08B); (f) Anhedral orthopyroxene grain with cusp-like terminations in harzburgite (24C).

Under the optical microscope, the fine-grained matrix from ultramylonites shows an overall brownish colour characterized by alternating lighter and darker layers. Petrographic and chemical

observations by scanning electron microscopy (SEM) and electron microprobe analyses (EMPA) revealed that the widths of the layers vary from few μm up to 500 μm and that the darker layers are richer in phlogopite with respect to the lighter ones, which are mainly composed by olivine and orthopyroxene (Figure 4a–d).

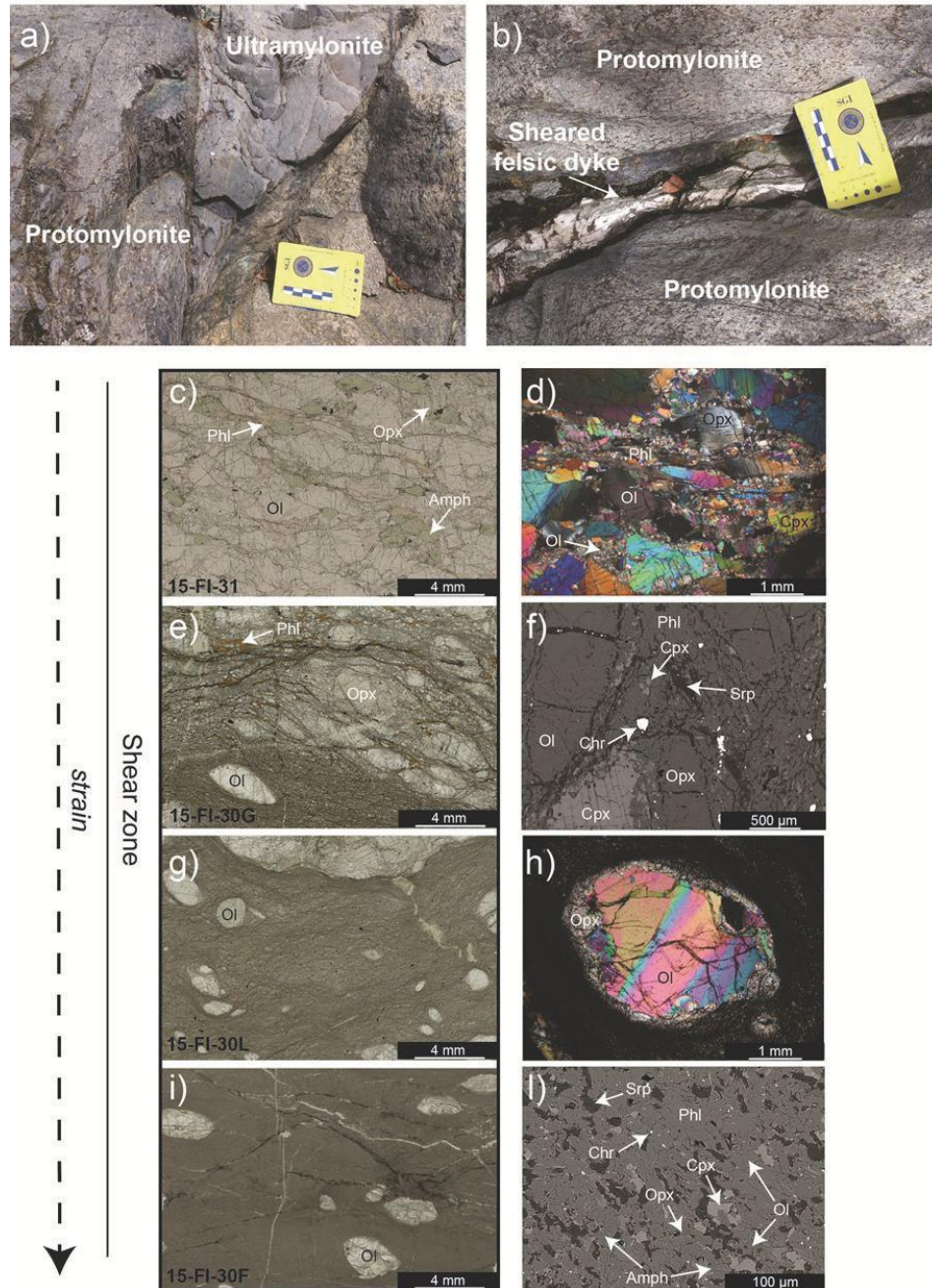


Figure 3. Shear zone macroscopic, petrographic, and microstructural features: (a) outcrop picture showing the textural variation from proto- to ultramylonite; (b) sheared felsic dyke within protomylonites; (c,e,g,i) Clippings of thin section natural light scans, the white box locates the higher resolution images presented on the right; (d) Cross-polarized light photomicrographs of protomylonitic harzburgite (31) characterized by elongated olivine and pyroxenes porphyroclasts surrounded by anastomosed seams of a fine-grained matrix; (f) Back-Scattered Electron (BSE) image of the mylonitic texture (30G); (h) Undulose extinction in a olivine porphyroblast surrounded by orthopyroxene recrystallized grains in the ultramylonite (30L); (j) BSE image of the ultramylonitic matrix (30F).

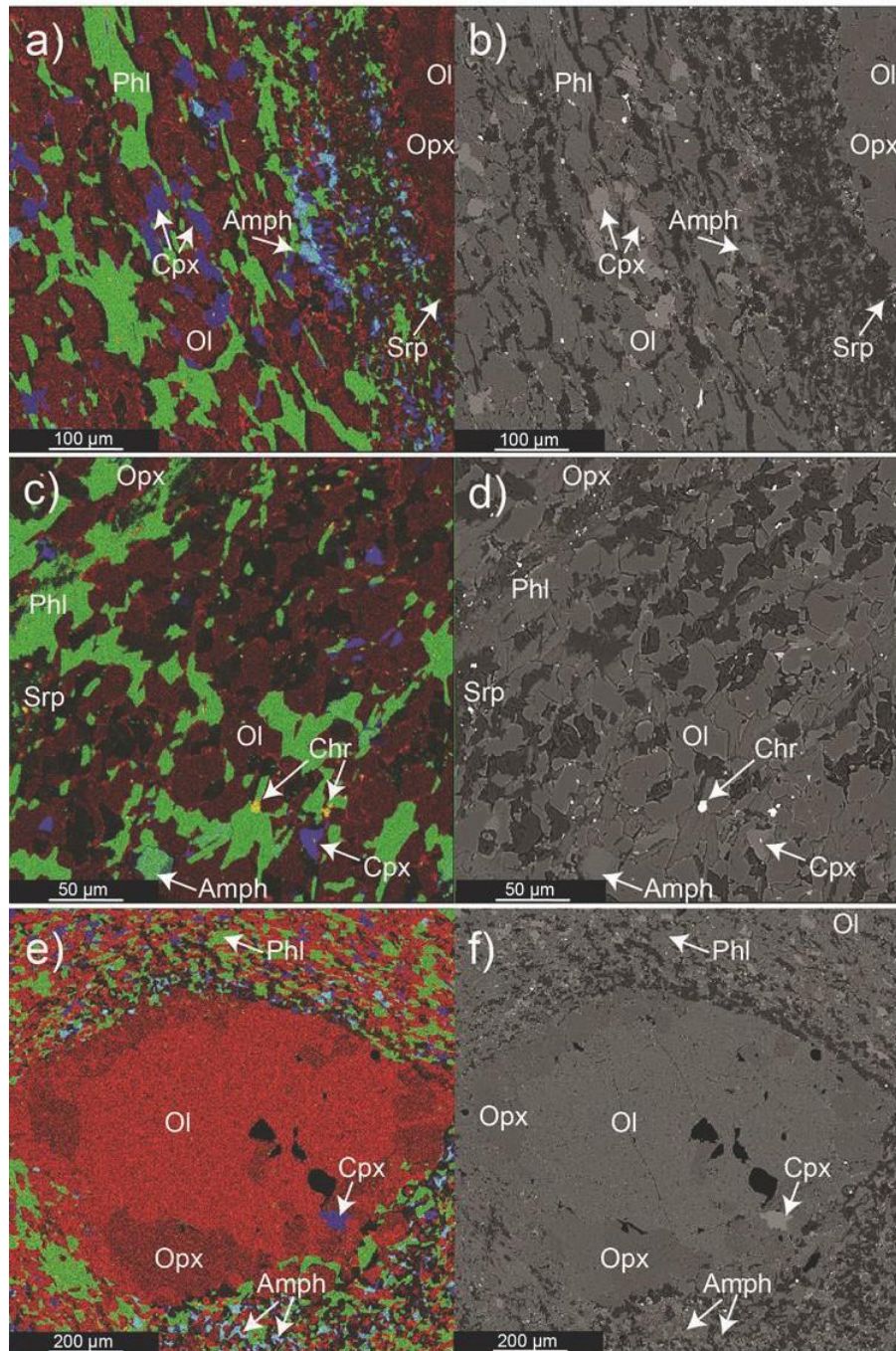


Figure 4. Red, green, and blue (RGB) compositional maps (left side) and BSE images (right side) showing the textures and major element distribution in mineral phases in mylonitic and ultramylonitic samples (30F, 30G, 30L). RGB map colours: Red = Fe; Green = Al and Blue = Ca. (a,b) texture variation in mylonite (30G) from olivine porphyroclast (on the right) to mylonitic matrix; (c,d) detail of ultramylonitic matrix (30F); (e,f) olivine porphyroclast embedded in the ultramylonitic matrix (30F).

Carbonates, apatite, talc, and pentlandite are accessory minerals observed in veins and fractures along the porphyroclasts and within the ultramylonitic matrix. Zircon was detected only within the fine-grained matrix of one ultramylonitic sample (30F). Except for low-temperature secondary minerals, such as talc and serpentine, all accessory minerals observed within both mylonites and ultramylonites have been already described as accessory within the host ultramafic rocks [17,26,36–40].

3.2. Mineral Chemistry

3.2.1. Major Elements

Combining field observations with textures and mineral assemblages, samples were subdivided into two main categories: samples from the shear zone and coarse-grained ultramafics. The shear zone (“shear zone” on diagrams) is further subdivided into a high strain zone, i.e., the ultramylonites (30L, 30F) and mylonite (30G) and a low strain zone, i.e., the protomylonitic sample (31), at the transition with coarse-grained harzburgites. The coarse-grained ultramafics are subdivided into: harzburgites (“harzb.” on diagrams; samples 20C, 24C) and “minor ultramafics”, which encompass the less abundant dunites, lherzolites, and pyroxenites (samples 08B, 09, 17, 21A, 23A). Data are reported in Table 2 and analytical details in Appendix A.

The forsterite content in olivine ranges between 89.5% and 91.5% (Figure 5a). The Mg# of orthopyroxene ($\text{Mg\#} = [\text{molar Mg}^{2+}/(\text{Mg}^{2+} + \text{Fe}^{2+}_{\text{tot}})]$) ranges between 0.90 and 0.92 (Figure 5b). Clinopyroxene is diopside with Mg# ranging from 0.93 to 0.95 (Figure 5c). The Mg# of clinopyroxene is inversely correlated with its modal abundance, i.e., lherzolite and olivine websterite show the lowest Mg#. Amphibole is dominantly pargasite with Mg# in the range of 0.89–0.92 (Figure 5d), in the sheared peridotites it shows higher edenite component and, locally, higher Cr₂O₃ becoming chromium-pargasite. Phlogopite occurring both as large deformed flakes and small grains within the were observed between core and rim analyses nor between porphyroclasts and matrix-forming grains. However, the Mg# of olivine and orthopyroxene from the ultramylonitic sample with less porphyroclasts (30F) are slightly lower than those reported for other rock types (Figure 5a,b) and even lower than the compositional field defined by previous studies of the shear zone [1,15] and of the coarse-grained ultramafics [17,25].

Spinel in the ultramylonites shows higher Cr# (0.7–0.8; $\text{Cr\#} = [\text{molar Cr}^{3+}/(\text{Cr}^{3+} + \text{Al}^{3+})]$) and lower Mg# (0.1–0.3) than less deformed protomylonite and coarse-grained harzburgites, which display Mg# and Cr# between 0.3 and 0.45 and 0.4 and 0.7, respectively (Figure 5f).

The Al₂O₃ content (wt.%) in orthopyroxene, clinopyroxene, amphibole, and phlogopite from the mylonite (30G) and ultramylonitic samples (30L, 30F) is distinctly lower than in the other rock types, i.e., the protomylonite (31) and coarse-grained harzburgites and minor ultramafics (Figure 6a,b). For instance, the Al₂O₃ content of orthopyroxene decreases from 1.0–1.5 wt.% to 0.3–0.5 wt.% (Figure 6a and Figure S2a). Amphibole and phlogopite within the protomylonite and coarse-grained harzburgites have Al₂O₃ contents in the range of 11–13 wt.% (Figure 6b) and 15–16 wt.% (Figure S2b), respectively. Within the shear zone, amphibole and phlogopite show lower Al₂O₃ contents in the range of 8–10 wt.% (Figure 6b) and 13–15 wt.% (Figure S2b), respectively.

TiO₂ (wt.%) contents of amphibole and phlogopite outside the high strain portion of the shear zone are in the range of 0.4–0.8 wt.% and 0.5–1.3 wt.%, respectively, distinctly lower than those measured in amphibole (0.6–1.2 wt.%) and phlogopite (1.5–1.7 wt.%) in the high strain zone (Figure 6c,d).

Cr₂O₃ content (wt.%) for orthopyroxene and amphibole from the high strain zone is on average slightly lower with respect to the same minerals within coarse-grained ultramafics (Figure S2e,f). The Cr₂O₃ concentration in orthopyroxene is generally in the range of 0.15–0.45 wt.% outside the high strain zone, whereas it is, on average, lower than 0.25 wt.% within it. The Cr₂O₃ content in amphibole also decreases within the high strain zone; it varies from 1.6–2.1 wt.% within coarse-grained ultramafics to 1.2–1.7 wt.% in the shear zone. Orthopyroxene and amphibole from the transition between the shear zone and coarse-grained harzburgites (i.e., sample 31) show a large variation of Cr₂O₃, overlapping values from both the shear zone samples and the coarse-grained ultramafics (Figure S2e,f). Clinopyroxene has Cr₂O₃ content in the range of 0.2–0.8 wt.% without clear variations among samples (Figure S2g). Phlogopite is characterized by a Cr₂O₃ content of 1.0–1.4 wt.% showing a weak decreasing trend from coarse-grained ultramafics towards the high strain domain of the shear zone (Figure S2h).

Na₂O and K₂O in amphibole vary significantly between the high strain domain of the shear zone and outside, showing opposite trends (Figure 6e,f). The Na₂O content of coarse-grained lithologies and of the protomylonite (31) is in the range of 2.0–2.5 wt.%, whereas within the high strain domain of the shear zone it is generally higher than 2.5 wt.%; with maximum values up to 3.0 wt.% in ultramylonite 30L (Figure 6e). The K₂O content of amphibole in the high strain zone is generally lower (0.4–0.7 wt.%) than the one measured in the protomylonite (31) and coarse-grained lithologies (0.5–1.1 wt.%, Figure 6f). Lower Na₂O and higher K₂O contents were obtained on average from phlogopite analyzed within the ultramylonite with less porphyroclast (30F) with respect to other samples from the shear zone and coarse-grained ultramafics (see Figure S2c,d).

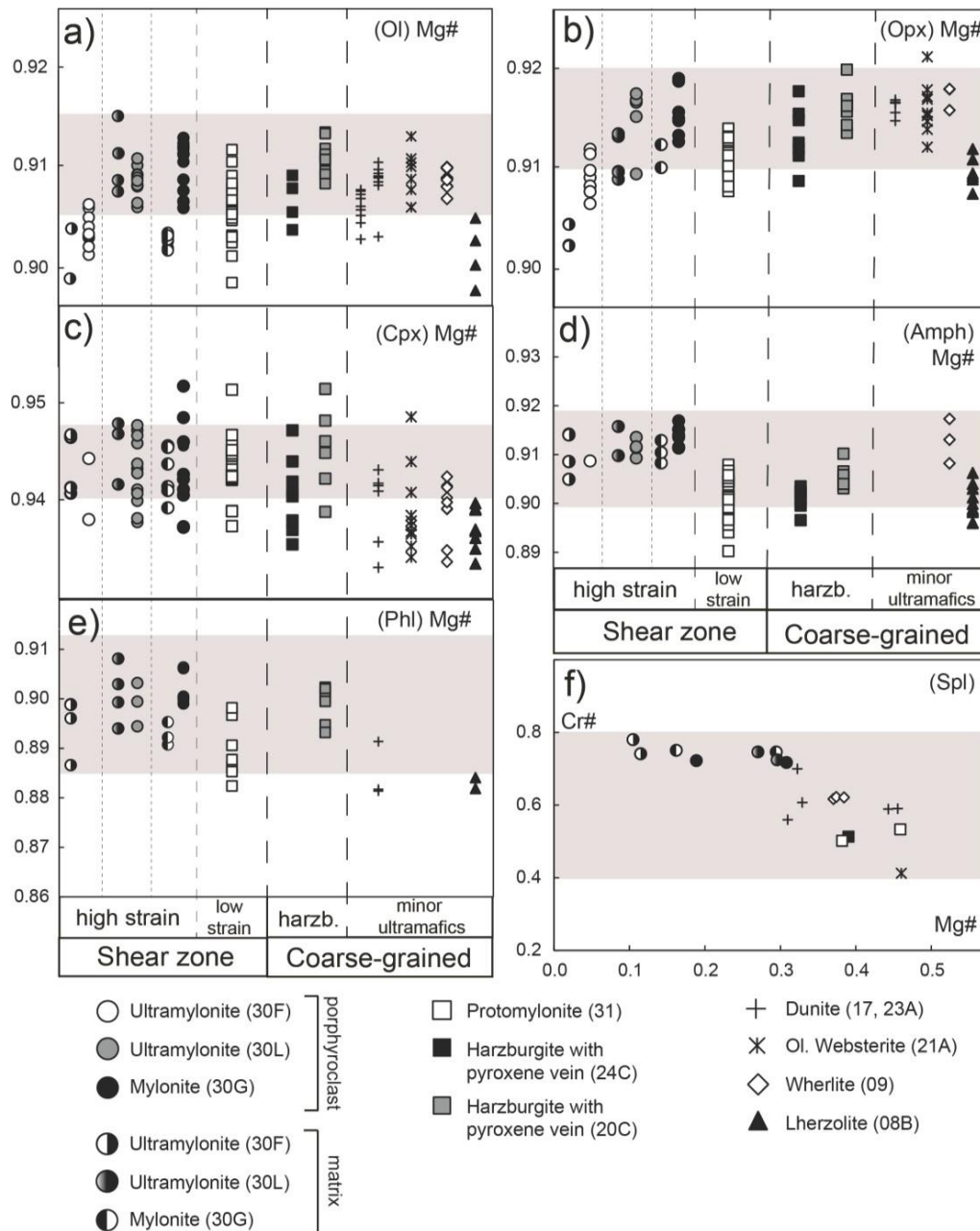


Figure 5. Major element ratios based on EMPA analyses of mineral phases of Finero Ph-Pd samples: Mg# in (a) olivine; (b) orthopyroxene; (c) clinopyroxene; (d) amphibole; (e) phlogopite; (f) Mg# (on x axis) vs Cr# (on y-axis) in Cr-spinel. The grey band refers to the range from literature data [1,15,17] on comparable Finero Ph-Pd samples.

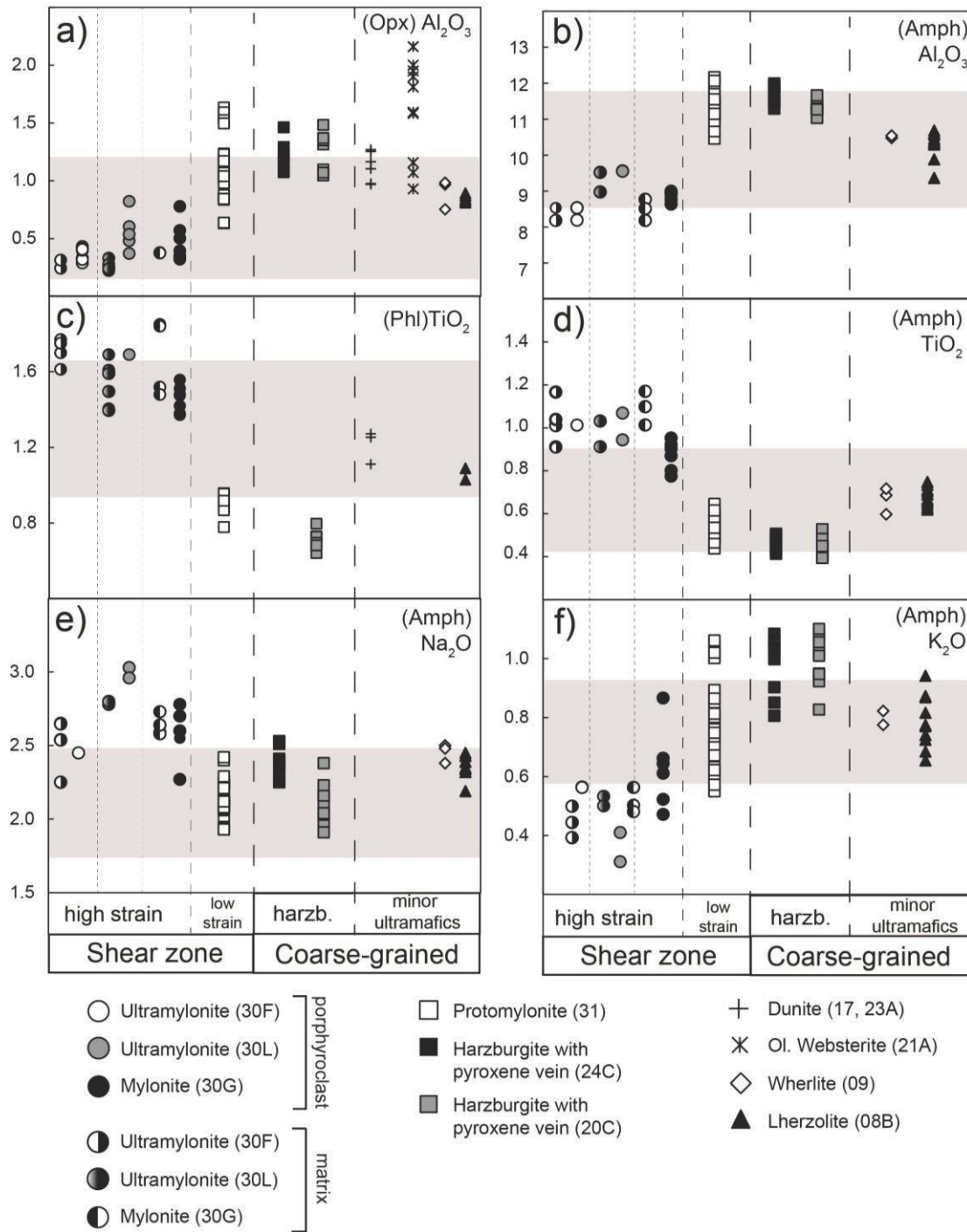


Figure 6. Major element content (wt.%) in mineral phases of Finero Ph-Pd samples: (a,b) Al₂O₃ in orthopyroxene and amphibole; (c,d) TiO₂ in phlogopite and amphibole; (e) Na₂O and K₂O (f) in amphibole. The grey band refers to the range from literature data [1,15,17].

Table 2. Average analyses for major elements (wt.%) of the mineral phases in the Finero ultramafic samples. (FeOt total iron oxide; σ line indicates the standard deviation; N is the number of analysis).

Sample/Lithotype	N	Phase	Texture	SiO ₂	TiO ₂	Al ₂ O ₃	Cr ₂ O ₃	FeO _(t)	MnO	NiO	MgO	CaO	Na ₂ O	K ₂ O	Total
15-FI-30F Ultramylonite	10	Ol	porphyroclast	40.55	0.02	0.00	0.01	9.40	0.11	0.40	49.39	0.01	0.01	0.00	99.91
		σ		0.425	0.022	0.007	0.012	0.190	0.041	0.050	0.480	0.006	0.012	0.004	
	3	Ol	matrix	40.92	0.03	0.00	0.02	9.46	0.15	0.40	48.68	0.01	0.01	0.01	99.70
		σ		1.068	0.030	0.008	0.022	0.042	0.025	0.057	1.669	0.014	0.006	0.005	
	7	Opx	porphyroclast	57.39	0.06	0.33	0.11	6.72	0.17	0.07	34.66	0.25	0.02	0.01	99.79
		σ		0.358	0.033	0.067	0.032	0.228	0.045	0.042	0.215	0.034	0.007	0.005	
	2	Opx	matrix	57.31	0.05	0.40	0.10	6.53	0.20	0.08	35.08	0.31	0.01	0.00	100.08
		σ		0.863	0.050	0.006	0.014	0.156	0.002	0.098	0.354	0.013	0.013	0.006	
	2	Cpx	porphyroclast	54.86	0.12	0.65	0.38	1.97	0.06	0.07	17.61	24.66	0.27	0.01	100.65
		σ		0.099	0.096	0.075	0.019	0.163	0.027	0.104	0.042	0.212	0.022	0.009	
	4	Cpx	matrix	54.57	0.05	0.36	0.27	1.88	0.04	0.03	17.67	24.61	0.26	0.01	99.76
		σ		0.168	0.048	0.056	0.061	0.107	0.012	0.023	0.178	0.172	0.032	0.003	
	1	Amph	porphyroclast	48.67	0.81	7.46	1.23	3.23	0.05	0.12	20.14	12.07	2.41	0.45	96.64
		σ		1.749	0.245	1.550	0.305	0.303	0.011	0.040	0.881	0.337	0.148	0.102	
	3	Amph	matrix	46.10	1.10	8.69	1.40	3.60	0.05	0.08	19.62	12.53	2.66	0.47	96.28
		σ		0.502	0.091	0.000	0.120	0.177	0.044	0.060	0.368	0.120	0.014	0.039	
	4	Phl	matrix	39.79	1.71	13.73	1.02	3.03	0.00	0.17	24.09	0.02	0.38	9.82	93.75
		σ		0.124	0.070	0.399	0.062	0.349	0.000	0.042	0.347	0.018	0.297	0.238	
2	Sp		0.10	0.29	9.25	43.74	39.34	0.58	0.11	2.72	0.03	0.03	0.03	96.23	
	σ		0.041	0.101	1.329	0.290	0.806	0.016	0.064	0.141	0.009	0.031	0.002		
15-FI-30L Ultramylonite	11	Ol	porphyroclast	40.45	0.02	0.02	0.02	8.92	0.11	0.47	49.58	0.02	0.02	0.01	99.64
		σ		0.435	0.030	0.016	0.025	0.150	0.023	0.071	0.355	0.021	0.013	0.008	
	5	Ol	matrix	40.65	0.01	0.00	0.01	9.48	0.15	0.44	48.92	0.01	0.02	0.01	99.68
		σ		0.373	0.016	0.007	0.021	2.211	0.056	0.097	2.206	0.009	0.016	0.007	
	5	Opx	porphyroclast	56.73	0.08	0.51	0.17	6.13	0.13	0.06	34.43	0.29	0.01	0.00	98.53
		σ		0.792	0.021	0.194	0.095	0.272	0.021	0.046	0.246	0.021	0.013	0.006	
	5	Opx	matrix	56.70	0.04	0.32	0.09	6.35	0.17	0.07	34.58	0.24	0.01	0.00	98.58
		σ		0.701	0.044	0.160	0.027	0.267	0.020	0.020	0.153	0.027	0.011	0.008	
	12	Cpx	porphyroclast	53.36	0.10	0.79	0.46	1.88	0.06	0.06	17.25	24.15	0.36	0.01	98.48
		σ		0.571	0.046	0.087	0.120	0.110	0.040	0.051	0.105	0.219	0.040	0.009	
	3	Cpx	matrix	53.82	0.09	0.62	0.43	1.84	0.07	0.07	17.49	24.22	0.36	0.01	99.02
		σ		0.491	0.054	0.252	0.206	0.121	0.036	0.046	0.709	0.199	0.077	0.011	
	3	Amph	porphyroclast	45.27	1.31	9.80	1.84	3.25	0.04	0.10	18.79	12.30	2.95	0.38	96.04
		σ		1.034	0.220	0.193	0.208	0.156	0.013	0.020	0.415	0.020	0.080	0.064	
	2	Amph	matrix	45.57	0.96	9.37	1.51	3.30	0.01	0.14	19.28	12.23	2.79	0.50	95.66
		σ		0.664	0.061	0.266	0.163	0.080	0.025	0.016	0.324	0.089	0.012	0.038	
	5	Phl	matrix	39.69	1.56	14.47	1.11	2.69	0.02	0.22	24.14	0.03	0.65	9.14	93.70
		σ		0.538	0.110	0.165	0.083	0.151	0.021	0.054	0.412	0.019	0.236	0.384	
2	Sp		0.01	0.32	11.89	49.26	30.88	0.24	0.19	6.84	0.00	0.03	0.01	99.63	
	σ		0.000	0.113	0.785	0.629	0.559	0.048	0.049	0.481	0.004	0.004	0.002		
15-FI-30G Mylonite	8	Ol	porphyroclast	40.80	0.02	0.00	0.01	9.13	0.14	0.40	49.65	0.01	0.01	0.00	100.16
		σ		0.359	0.016	0.006	0.010	0.395	0.035	0.045	0.293	0.011	0.007	0.006	
	14	Ol	matrix	41.15	0.01	0.01	0.01	8.84	0.12	0.42	49.32	0.01	0.01	0.01	99.91
		σ		0.261	0.017	0.013	0.010	0.426	0.029	0.046	0.880	0.017	0.014	0.006	
	5	Opx	porphyroclast	58.20	0.07	0.48	0.16	6.19	0.13	0.10	34.50	0.28	0.00	0.00	100.10
		σ		0.576	0.036	0.203	0.119	0.232	0.018	0.039	0.475	0.019	0.000	0.005	

Table 2. Cont.

Sample/Lithotype	N	Phase	Texture	SiO ₂	TiO ₂	Al ₂ O ₃	Cr ₂ O ₃	FeO _(t)	MnO	NiO	MgO	CaO	Na ₂ O	K ₂ O	Total
15-FI-31 Protomylonite	2	Opx σ	matrix	58.29	0.03	0.34	0.08	6.19	0.16	0.08	35.11	0.25	0.00	0.00	100.53
				0.382	0.003	0.028	0.021	0.092	0.033	0.060	0.342	0.033	0.008	0.001	
	9	Cpx σ	porphyroclast	54.50	0.10	0.63	0.39	1.94	0.06	0.06	17.37	24.50	0.32	0.00	99.88
				0.412	0.042	0.164	0.136	0.185	0.030	0.039	0.272	0.336	0.081	0.007	
	7	Cpx σ	matrix	55.22	0.06	0.60	0.43	1.73	0.07	0.07	17.34	24.80	0.27	0.00	100.59
				0.453	0.012	0.106	0.008	0.099	0.008	0.077	0.283	0.120	0.028	0.002	
	6	Amph σ	porphyroclast	47.09	0.90	8.87	1.61	3.25	0.04	0.09	19.43	12.48	2.61	0.61	96.97
				0.597	0.132	0.291	0.141	0.066	0.024	0.035	0.280	0.140	0.169	0.137	
	3	Amph σ	matrix	46.92	1.05	8.99	1.40	3.42	0.00	0.07	19.24	12.30	2.60	0.53	96.50
				0.191	0.061	0.092	0.082	0.007	0.004	0.045	0.311	0.035	0.007	0.043	
	6	Phl σ	porphyroclast	40.09	1.46	14.35	1.16	2.73	0.02	0.19	24.22	0.00	0.70	9.14	94.06
				0.238	0.229	0.641	0.075	0.503	0.015	0.041	0.422	0.015	0.276	0.112	
	4	Phl σ	matrix	40.12	1.60	14.30	1.12	2.94	0.01	0.21	24.06	0.02	0.63	9.10	94.11
				0.238	0.229	0.641	0.075	0.503	0.015	0.041	0.422	0.015	0.276	0.112	
	4	Sp σ		0.05	0.30	11.79	48.43	32.83	0.37	0.10	5.80	0.01	0.04	0.03	99.73
				0.061	0.035	1.190	1.724	2.535	0.127	0.067	1.900	0.009	0.023	0.046	
	24	Ol σ		41.64	0.01	0.00	0.02	8.89	0.14	0.41	47.96	0.01	0.01	0.01	99.10
				0.206	0.017	0.005	0.027	0.213	0.028	0.059	0.694	0.011	0.012	0.005	
	22	Opx σ		58.50	0.04	1.12	0.21	6.16	0.15	0.07	33.28	0.31	0.01	0.00	99.84
				0.382	0.031	0.294	0.110	0.117	0.028	0.042	0.434	0.111	0.008	0.005	
17	Cpx σ		55.74	0.06	0.90	0.27	1.81	0.08	0.05	16.86	24.64	0.17	0.00	100.58	
			0.308	0.037	0.186	0.113	0.105	0.025	0.038	0.322	0.156	0.034	0.010		
28	Amph σ		46.56	0.53	11.43	1.61	3.46	0.04	0.10	17.80	12.52	2.15	0.78	96.98	
			0.584	0.056	0.394	0.242	0.129	0.027	0.043	0.450	0.203	0.121	0.148		
7	Phl σ		40.53	0.90	16.17	1.14	2.78	0.00	0.23	22.44	0.01	0.66	9.17	94.03	
			0.405	0.061	0.402	0.113	0.146	0.006	0.061	0.529	0.011	0.065	0.093		
2	Sp σ		0.00	0.09	24.49	41.69	23.39	0.14	0.08	11.14	0.02	0.01	0.00	101.05	
			0.000	0.067	0.948	2.058	2.213	0.018	0.019	1.379	0.012	0.009	0.002		
4	Ol σ		41.63	0.01	0.01	0.01	8.89	0.12	0.39	48.31	0.02	0.01	0.00	99.41	
			0.126	0.012	0.011	0.021	0.178	0.029	0.031	0.698	0.012	0.012	0.001		
7	Opx σ		58.45	0.02	1.21	0.29	6.01	0.14	0.10	33.31	0.40	0.01	0.00	99.95	
			0.212	0.025	0.135	0.102	0.218	0.024	0.018	0.381	0.175	0.008	0.004		
8	Cpx σ		55.27	0.05	1.28	0.52	1.87	0.07	0.06	16.61	24.27	0.29	0.00	100.29	
			0.307	0.033	0.186	0.094	0.128	0.024	0.042	0.155	0.246	0.038	0.004		
8	Amph σ		46.00	0.45	11.76	1.87	3.46	0.04	0.10	17.68	12.42	2.38	0.97	97.13	
			0.287	0.035	0.245	0.150	0.081	0.034	0.055	0.185	0.117	0.101	0.105		
12	Ol σ		41.22	0.02	0.01	0.01	8.72	0.13	0.40	49.89	0.01	0.01	0.00	100.43	
			0.291	0.024	0.012	0.011	0.189	0.032	0.044	0.435	0.006	0.012	0.006		
8	Opx σ		57.81	0.03	1.26	0.27	6.00	0.13	0.08	34.51	0.37	0.03	0.01	100.50	
			0.539	0.020	0.166	0.058	0.135	0.027	0.037	0.286	0.060	0.025	0.008		
6	Cpx σ		54.75	0.07	1.12	0.38	1.79	0.07	0.03	17.33	24.31	0.19	0.00	100.02	
			0.367	0.043	0.275	0.137	0.128	0.014	0.027	0.334	0.413	0.031	0.005		
10	Amph σ		46.26	0.42	11.40	1.80	3.47	0.06	0.09	18.64	12.51	2.12	0.99	97.75	
			0.349	0.041	0.159	0.106	0.066	0.030	0.049	0.203	0.077	0.135	0.083		
8	Phl σ		40.03	0.70	16.30	1.17	2.68	0.00	0.24	23.80	0.01	0.69	9.16	99.86	
			0.370	0.050	0.150	0.050	0.090	0.010	0.040	0.340	0.020	0.020	0.210		
1	Sp		0.15	0.12	24.84	39.04	27.17	0.23	0.13	9.76	0.00	0.00	0.00	101.43	

Table 2. *Cont.*

Sample/Lithotype	N	Phase	Texture	SiO ₂	TiO ₂	Al ₂ O ₃	Cr ₂ O ₃	FeO _(t)	MnO	NiO	MgO	CaO	Na ₂ O	K ₂ O	Total
15-FI-23A Dunite	10	Ol		41.45	0.02	0.01	0.01	9.02	0.15	0.36	50.16	0.01	0.02	0.01	101.22
		σ		0.293	0.028	0.007	0.020	0.204	0.025	0.033	0.258	0.009	0.021	0.020	
	6	Opx		57.99	0.11	1.12	0.26	6.10	0.16	0.04	35.03	0.46	0.01	0.00	101.29
		σ		0.155	0.024	0.131	0.062	0.092	0.029	0.029	0.202	0.075	0.013	0.007	
	2	Cpx		55.20	0.16	1.07	0.35	1.95	0.06	0.04	17.72	24.61	0.19	0.02	101.36
		σ		0.042	0.133	0.137	0.072	0.064	0.023	0.049	0.078	0.085	0.012	0.010	
	4	Sp		0.14	0.68	19.65	41.60	29.04	0.22	0.14	10.11	0.00	0.03	0.00	101.60
		σ		0.141	0.058	1.015	2.762	4.372	0.054	0.061	1.732	0.002	0.036	0.008	
15-FI-17 Dunite	9	Ol		41.58	0.02	0.00	0.01	8.98	0.15	0.34	48.43	0.02	0.00	0.00	99.53
		σ		0.363	0.021	0.008	0.027	0.134	0.042	0.040	0.395	0.012	0.004	0.005	
	4	Cpx		55.52	0.09	0.95	0.64	1.97	0.07	0.03	16.72	23.95	0.43	0.00	100.39
		σ		0.273	0.011	0.157	0.155	0.151	0.049	0.041	0.134	0.308	0.099	0.000	
	3	Phl		40.88	1.21	15.30	1.51	2.96	0.00	0.17	22.72	0.00	0.83	9.15	94.73
		σ		0.550	0.088	0.186	0.076	0.127	0.003	0.065	0.297	0.000	0.100	0.229	
	1	Sp		0.04	0.45	13.99	48.68	29.02	0.20	0.11	7.75	0.00	0.04	0.00	100.28
		σ		0.04	0.45	13.99	48.68	29.02	0.20	0.11	7.75	0.00	0.04	0.00	100.28
15-FI-21A Ol. Websterite	8	Ol		41.34	0.02	0.00	0.00	8.86	0.12	0.42	49.65	0.02	0.01	0.00	100.45
		σ		0.364	0.026	0.004	0.007	0.224	0.017	0.048	0.515	0.010	0.014	0.005	
	10	Opx		57.82	0.03	1.62	0.32	6.10	0.15	0.05	34.44	0.33	0.01	0.01	100.86
		σ		0.393	0.025	0.429	0.144	0.294	0.039	0.032	0.532	0.067	0.013	0.005	
	10	Cpx		54.68	0.09	1.73	0.56	1.97	0.08	0.06	16.96	24.39	0.21	0.00	100.72
		σ		0.491	0.023	0.337	0.170	0.124	0.037	0.043	0.283	0.147	0.050	0.005	
15-FI-09 Wehrlite	1	Sp		0.05	0.20	31.15	32.60	24.81	0.17	0.15	11.87	0.01	0.03	0.00	101.05
		σ		0.05	0.20	31.15	32.60	24.81	0.17	0.15	11.87	0.01	0.03	0.00	101.05
	9	Ol		41.39	0.02	0.01	0.02	8.95	0.14	0.30	49.94	0.02	0.01	0.01	100.78
		σ		0.248	0.030	0.007	0.021	0.142	0.028	0.045	0.292	0.010	0.009	0.007	
	3	Opx		58.17	0.08	0.90	0.28	5.94	0.16	0.07	34.61	0.39	0.01	0.01	100.62
		σ		0.274	0.029	0.129	0.018	0.075	0.053	0.018	0.324	0.107	0.009	0.004	
	10	Cpx		55.17	0.06	1.12	0.59	2.03	0.07	0.04	17.52	23.71	0.36	0.00	100.67
		σ		0.388	0.033	0.069	0.126	0.158	0.032	0.044	0.544	0.608	0.031	0.007	
	3	Amph		47.14	0.65	9.99	1.96	3.24	0.06	0.11	19.09	12.41	2.45	0.58	97.68
		σ		1.318	0.063	1.074	0.196	0.111	0.009	0.031	0.447	0.361	0.064	0.385	
	3	Sp		0.05	0.28	18.52	45.07	27.58	0.27	0.06	9.33	0.01	0.01	0.01	101.18
		σ		0.038	0.092	0.214	0.428	0.349	0.026	0.024	0.174	0.011	0.010	0.012	
15-FI-8B Lherzolite	4	Ol		41.77	0.01	0.01	0.03	9.34	0.12	0.37	47.77	0.00	0.02	0.00	99.45
		σ		0.083	0.011	0.007	0.019	0.242	0.016	0.021	0.571	0.004	0.014	0.003	
	7	Opx		58.71	0.05	0.84	0.21	6.30	0.16	0.06	33.41	0.42	0.01	0.00	100.17
		σ		0.185	0.019	0.030	0.033	0.093	0.027	0.037	0.252	0.051	0.009	0.001	
	9	Cpx		56.05	0.08	0.95	0.50	1.99	0.08	0.05	16.71	24.31	0.32	0.00	101.04
		σ		0.373	0.040	0.137	0.147	0.049	0.042	0.052	0.240	0.110	0.042	0.003	
	10	Amph		47.14	0.67	10.40	1.80	3.56	0.04	0.11	18.02	12.39	2.36	0.78	97.27
		σ		0.490	0.045	0.383	0.162	0.112	0.025	0.035	0.317	0.078	0.075	0.090	
	2	Phl		40.84	1.06	15.53	1.29	2.96	0.01	0.20	22.30	0.00	0.82	9.12	94.12

3.2.2. Minor and Trace Elements Concentrations in Porphyroclasts

Trace element analyses of major rock-forming minerals were performed on all rock types and are shown following the rocks grouping defined before, i.e., shear zone (high strain and low strain domains), coarse-grained harzburgites, and coarse-grained minor ultramafics. Average values are reported in Table 3; the whole dataset is available as Supplementary Table S2 (see Appendix A for details in the data acquisition and processing). The small size of the matrix-forming minerals within the shear zone (<20 µm) hampered LA-ICP-MS analysis, which could only be performed on porphyroclasts from both protomylonites and ultramylonites. Single spot analyses were collected in core and rims of porphyroclasts. For selected grains, we also performed core-to-rim transects. Analyses were carried out on several porphyroclasts of olivine, orthopyroxene, and phlogopite but only on few clinopyroxene porphyroclasts due to their lower abundance.

Olivine porphyroclasts from different lithologies and textural types show significant variation in Li, Co, Ni, and Zn contents (Figure 7a–d; Table 3). All these elements have on average higher concentrations (up to three times) within the shear zone with respect to the coarse-grained ultramafics (Figure 7a–d). The concentration of Zn progressively increases towards the core of the shear zone, which is associated with a decrease of the number of olivine porphyroclasts (Figure 7d). The highest Zn values were obtained from the ultramylonitic sample containing only four olivine porphyroclasts (30F) in the studied thin section. In contrast, the maximum concentrations for Li are documented at the transition between the mylonite (30G) and the ultramylonite (30L), as previously documented also for Mg# and Na/K ratios.

In orthopyroxene porphyroclasts, as for olivine, the concentration of Li, Co, Ni, and Zn is on average higher in the protomylonites and ultramylonites than in the coarse-grained ultramafics (Table 3). Orthopyroxenes from the shear zone are also characterized by slightly lower values of Ca, Sc, V, and Cr (Figure 7e–h) but higher values of Ti (Table 3).

The Ti content of clinopyroxene porphyroclasts within the shear zone, especially in the ultramylonites, is significantly higher (>600 ppm) than in the coarse-grained ultramafics, which is <600 ppm. A similar trend is observed for Sc, which is higher (>50 ppm) in ultramylonites than in other rock types (<50 ppm; Figure 8b).

Amphibole porphyroclasts from the protomylonite (31) are characterized by higher Ba concentration (115 ppm on average) with respect to amphibole in the coarse-grained ultramafics (<100 ppm, Figure 8d). The trace element patterns mimic those reported for amphiboles from coarse-grained lithologies, but an overall enrichment in REE and Ba can be noticed (Figure S3). These geochemical features are consistent with those observed for clinopyroxene porphyroclasts (Figure S3) from the ultramylonites (30L and 30F) and the mylonite (30G). Amphibole from a coarse-grained harzburgite (24C) displays the highest Sc and V contents, whereas the lowest Sc and V concentrations are observed in amphiboles from the protomylonite (31; Figure 8c and Table 3). The minor and trace element characterization of phlogopite revealed some systematic variations among samples and textural sites. Phlogopite from the high-strain zone (mylonite 30G) showed the highest Li (up to six times the average values for other samples) and lowest Ba contents (Figure 8e,f).

In order to detect intragranular variations, trace element transects were performed across olivine and orthopyroxene porphyroclasts of samples from the high strain zone (Figure 9). Even though the LA-ICP-MS profiles are coarsely spaced (distance between two spots >100 µm), they show clear geochemical features. The Ni content across olivine porphyroclasts shows opposite trends between ultramylonites and mylonites (Figure 9a): it linearly decreases from core to rims in ultramylonites (30L and 30F) whereas it linearly increases towards the rims in (30G). In this sample (30G), Al and Ti decrease towards the rims (Figure S4). No other significant chemical variations within porphyroclasts from the ultramylonitic samples were observed except for Ti in sample 30F (Figure S4b). Orthopyroxene porphyroclasts in both the mylonite and the ultramylonites show only a weak intragranular chemical variation: Sc slightly decreases from core to the rims (Figure 9b) as well as Al, Ca, Ti, V, and Cr (Table 3).

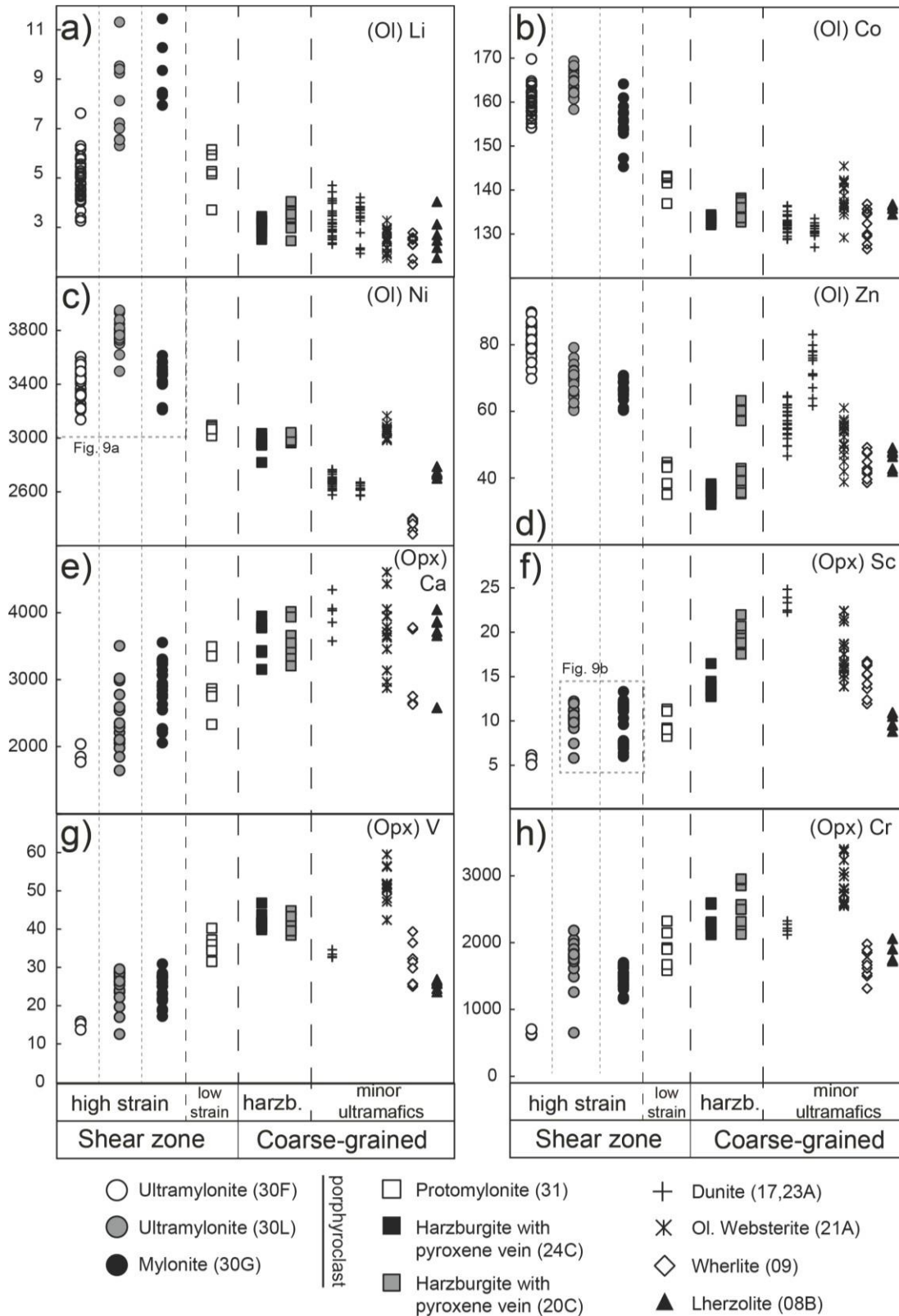


Figure 7. Trace-element concentrations (ppm) in mineral phases of Finero Ph-Pd samples. (a–d) Li, Co, Ni, Zn content in olivine; (e–h) Ca, Sc, V, Cr content in orthopyroxene. Dashed boxes in (c,f) refer to Figure 9a,b respectively.

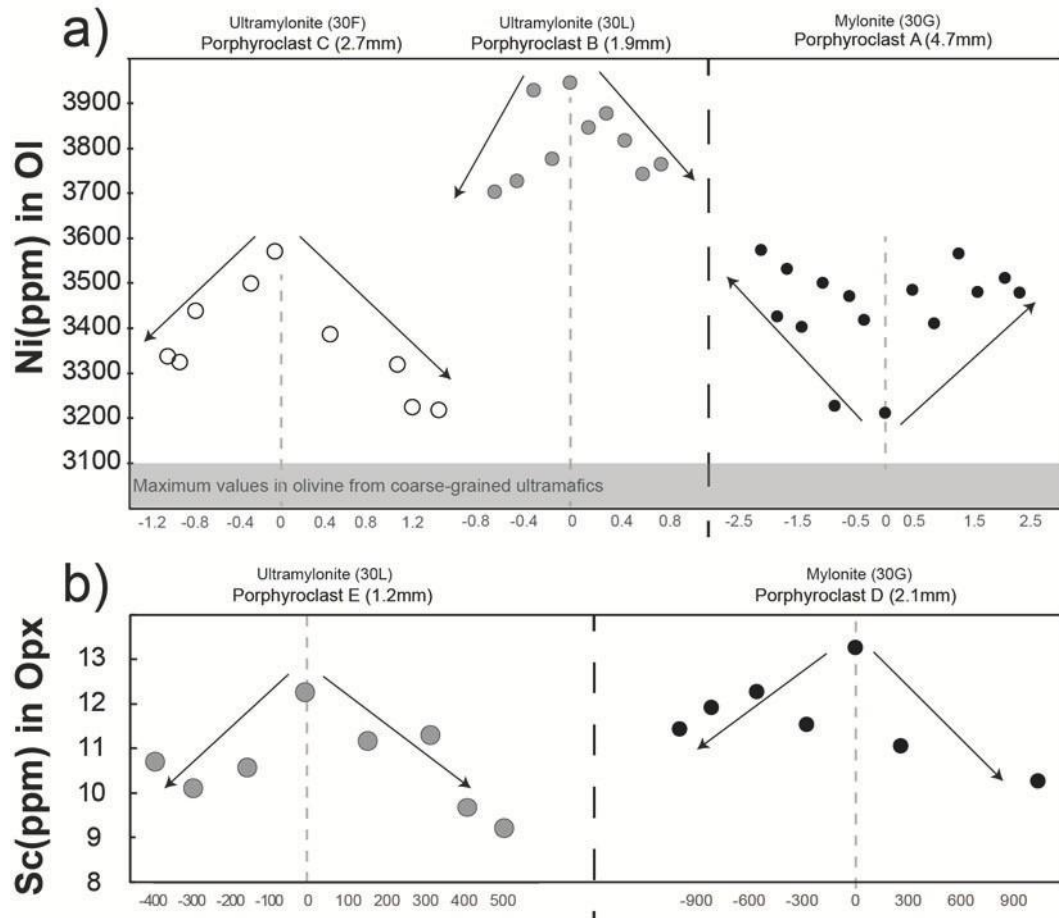


Figure 9. Trace element variation across porphyroclasts from the shear zone. (a) Ni (ppm) variation in olivine, and (b) Sc (ppm) in orthopyroxene, whose trends are underlined by arrows. X axes: approximate distance (mm in a and μm in b) from the core (0) towards the rims. The analytical points are largely spaced and not perfectly equidistant due to the presence of fractures and/or inclusions along the crystal avoided during the analytical procedure.

Table 3. Representative average trace element concentrations (ppm) of mineral phases in Finero ultramafic samples.

	Lithotype	Grain	Li	B	Al	Sc	Ti	V	Cr	Co	Ni	Cu	Zn	Rb	Sr	Y	Zr
15-FI-30F	Ultramylonite	Ol	4.8	17.2	2	1.8	10	0.4	16	158.4	3385	0.2	81.9	0.1	0.2	0.1	0.1
		Opx	1.4	15.4	1663	5.7	345	14.9	651	56.9	631	0.2	61.9	0.3	0.2	0.2	0.2
15-FI-30L	Ultramylonite	Ol	8.4	16.8	3	2.3	6	0.5	10	164.0	3770	1.2	68.9	0.1	0.4	0.1	0.2
		Opx	5.7	16.7	3235	10.1	489	24.5	1715	53.3	618	1.0	52.4	1.0	0.4	0.4	0.4
15-FI-30G	Mylonite	Cpx	24.7	4562	53.1	805	86.3	4424	18.8	334			12.0	224.7	8.3	16.3	0.0
		Ol	9.1	20.1	3	2.2	12	0.5	12	155.7	3454	0.6	65.5	0.1	0.1	0.1	0.1
		Opx	5.2	17.8	2800	9.8	539	24.7	1457	54.7	627	0.5	52.3	0.5	0.4	0.5	0.1
		Cpx	5.2	22.4	4141	56.6	662	95.4	4207	19.4	330	0.4	10.2	269.4	7.3	15.4	0.1
15-FI-31	Protomylonite	Phl	54.2	25.7	64486	7.9	6717	182.7	7790	47.1	1498	0.9	18.7	105.4	0.1	3.7	5.0
		Ol	5.1	9.4	14	1.2	8	0.4	13	142.7	3099		40.2				
		Opx	0.4	15.6	7262	9.6	250	35.7	1924	53.1	598	0.3	43.6		0.2	0.1	0.4
		Amph	1.9	15.3	49543	64.6	3040	281.1	12543	32.5	781	0.2	14.1	6.6	264.0	9.3	37.0
15-FI-24C	Harzburgite	Phl	4.5	16.4	72399	6.3	5291	180.2	7860	47.8	1618	0.2	16.7	584.7	85.3	0.0	2.3
		Ol	2.8	17.3	3	1.8	5	0.3	10	132.5	2926	0.5	35.5				
		Opx	1.2	16.5	7394	13.9	180	42.2	2313	51.1	601	0.3	37.1		0.2	0.1	0.9
		Cpx	3.3	18.6	7201	52.5	365	100.4	3552	17.1	304	4.7	6.4	0.0	130.4	1.8	17.9
15-FI-20C	Harzburgite	Amph	1.1	14.9	50698	99.2	2389	343.7	12637	31.2	763	3.9	12.7	8.6	294.6	5.1	73.7
		Ol	3.2	29.2	5	5.9	6	0.4	12	135.6	3003		45.8		0.0	0.0	0.1
		Opx	0.6	20.7	7776	19.5	236	41.8	2547	51.7	626		46.5		0.2	0.1	0.9
		Amph	0.9	29.3	44315	76.7	2373	293.1	12064	31.7	791		12.4	9.0	262.4	4.1	49.1
15-FI-23A	Dunite	Phl	2.0	36.3	64832	12.0	3841	189.4	8259	45.9	1572		20.8	723.4	94.9	0.0	3.7
		Ol	3.0	42.6	5	8.1	27	0.6	11	130.7	2622		73.3	0.1	0.0	0.0	0.1
		Opx	1.0	33.4	6544	23.4	576	33.2	2221	49.4	532		63.1	0.1	0.1	0.2	1.7
15-FI-17	Dunite	Ol	3.1	12.8	17	2.5	9	0.3	13	131.4	2703	0.2	58.5	0.1	0.0	0.0	0.0
		Phl	10.8	18.0	66804	9.7	6314	157.5	9408	45.0	1409	0.4	22.2	533.8	137.9	0.0	4.9
15-FI-21A	Ol.Websterite	Ol	2.2	29.6	11	1.8	10	0.4	8	140.6	3058	3.7	47.4		0.1		0.2
		Opx	1.2	27.7	9265	16.6	267	54.1	3036	56.0	669	0.6	40.9	0.0	0.7	0.1	1.3
		Cpx	2.3	24.9	10141	42.7	547	117.5	4295	20.6	366	0.5	9.7	0.1	99.5	2.4	18.9
		Amph	1.9	6.3	44527	81.3	2523	303.3	11769	30.9	750	1.0	13.2	10.7	279.9	6.3	57.6
15-FI-09	Wehrlite	Ol	2.1	34.0	19	5.5	12	0.7	13	132.0	2364		43.8	0.1	0.2	0.1	0.2
		Opx	1.8	40.3	4707	14.7	318	30.9	1674	49.9	469		42.2	1.8	5.0	1.0	1.7
		Cpx	1.9	35.6	6063	45.2	463	87.3	4180	19.9	278		9.1	0.1	156.5	1.8	6.9
15-FI-8B	Lherzolite	Ol	2.5	8.1	4	2.0	9	0.3	10	135.7	2729	0.5	45.8			0.0	0.1
		Opx	0.4	6.6	4788	9.9	297	25.2	1839	51.2	557	0.4	39.0		0.2	0.1	0.3
		Cpx	2.0	8.1	5625	40.7	448	78.8	4405	17.7	299	0.4	6.9		156.2	1.7	6.5
		Amph	1.0	7.2	43009	70.9	3195	253.1	12044	30.3	712	0.6	13.1	6.2	273.7	4.6	34.5
		Phl	1.5	7.7	62723	6.4	5581	158.3	8424	45.2	1451	0.6	17.0	502.5	88.6	0.1	2.0

4. Discussion

4.1. P-T Evolution and Geothermometry

Tommasi et al. [16] inferred that the coarse-grained peridotites of Finero (Ph-Pd) experienced a pervasive high temperature deformation in the presence of a hydrous melt (Figure 10) at $P < 2.0$ GPa and temperature in the range of 1050–1080 °C. These estimates were based on the stability field of pargasite + hydrous melt in the presence of spinel. The high temperature foliation of the peridotite is crosscut by several melanocratic to leucocratic dykes and veins. Giovanardi et al. [25,41], suggested equilibrium T for sapphirine-bearing gabbroic dykes mostly between 980 and 1030 °C at a pressure of 1.0 GPa.

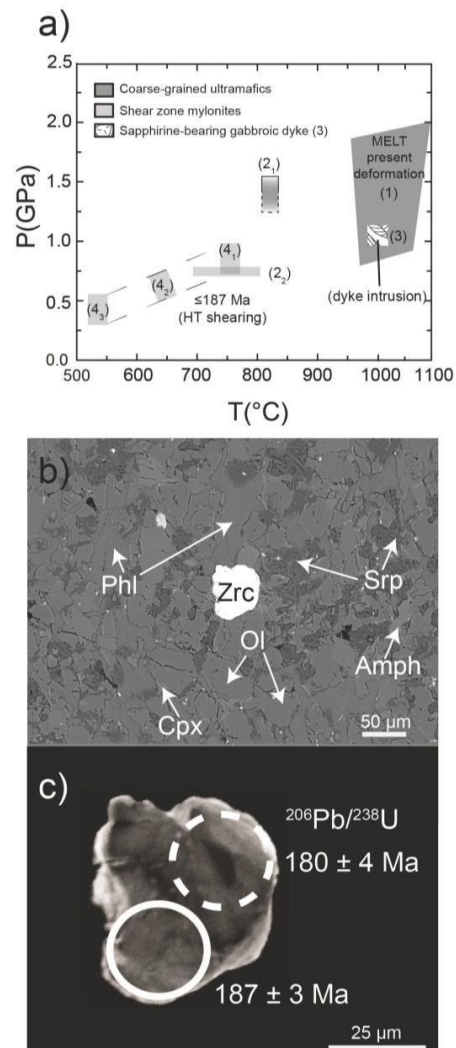


Figure 10. (a) Pressure–temperature diagram showing the main conditions for Finero mantle sequence lithologies: (1) the dark grey box defines the melt-present pervasive HT deformation for the coarse-grained ultramafics [16]; (2) P-T results from this study refer to: (2₁) subsolidus re-equilibration conditions for the coarse-grained ultramafics; (2₂) deformation in the shear zone based on synkinematic minerals; (3) P-T equilibrium conditions for sapphirine-bearing gabbroic dyke [25]; (4) shearing P-T conditions by [15], (4₁) = granulite facies; (4₂) = amphibolite facies; (4₃) = green-schists facies. See text for more details and Table 4. (b) BSE image showing the zircon grain within the fine-grained matrix of the ultramylonite (30F); (c) zircon CL image showing the zoning features and location of the two LA-ICP-MS pits yielding one concordant (white circle) and one discordant (dashed circle, $^{206}\text{Pb}/^{238}\text{U}$) age.

The pervasive high temperature deformation was followed by localized deformation events that occurred at lower temperatures from granulite to upper greenschist facies conditions (Figure 10a) [1,15,16,28,29,32,42]. The shear zone studied here was formed during one or more of these events, e.g., [15]. Temperatures for the studied samples were estimated by using geothermometers based on the pyroxene solvus. The calibration of Wells [43] for the two-pyroxene geothermometer was used for a direct comparison with existing T estimates for the mylonites obtained with the same calibration, i.e., Brodie [1] and Altenberger [15]. Results are listed in Table 4 and Table S4 and shown in Figure 10a. A pressure of 1.5 GPa (central value of the range proposed by Tommasi et al., [16]) was considered for the coarse-grained ultramafics, 0.75 GPa (from Altenberger [15]) for mylonites s.l. pairing synkinematic pyroxenes (Table 4, Figure 10a). By using the calibration of Wells [43], temperatures range from 815 to 830 °C for the coarse-grained ultramafics and from 680 to 810 °C for the proto- and ultramylonites (Table 4, Figure 10a). Temperatures were also constrained using the Ca-in-Opx geothermometer [44], which points to a smaller interval for the proto- and ultramylonites (670–690 °C; Table 4). Single-element geothermometers for olivine (i.e., Al-in, Cr-in, and V-in olivine geothermometers; [45,46]) systematically provide lower T than two-pyroxene geothermometers (Table 4), presumably as a consequence of a peculiar mineral-mineral partitioning due to the abundant modal amount of hydrous minerals in the Finero ultramafics that falls off the one used for the calibration of these single-element geothermometers.

Table 4. Geothermobarometry.

Sample	Lithology	P (GPa)	Temperature (°C)				
			Wells _(2px)	Ca-in opx ^a	Al-in ol ^b	Cr-in ol ^b	V-in ol ^c
15-FI-30F	Ultramylonite	0.75	750	672	632	551	559
15-FI-30L	Core	0.75	695	672	645	564	601
15-FI-30G	Mylonite Core	0.75	722	668	654	569	607
15-FI-31	Protomylonite	0.75	807	684	733	652	562
15-FI-30F	Ultramylonite	-	720	-	-	-	-
15-FI-30L	Matrix	-	723	-	-	-	-
15-FI-30G	Mylonite Matrix	-	679	-	-	-	-
15-FI-24C	Harzburgite with	1.5	817	767	683	556	506
15-FI-20C	pyroxene vein	1.5	831	787	707	620	558
15-FI-23A	Dunite	1.5	829	839	709	623	618
15-FI-17		1.5	-	-	739	645	543
15-FI-21A	Ol. Websterite	1.5	-	753	731	641	620
15-FI-09	Wehrlite	1.5	-	798	791	700	641
15-FI-08B	Lherzolite	1.5	830	816	696	609	534

Calibrations: Wells_(2px) = two-pyroxenes [43] at assumed P; ^a Nimis & Grutter, [44] at the assumed P,

^b De Hoog et al. [45]; at the assumed P; ^c Smith [46], pressure independent.

Summing up, the pervasive high-temperature deformation in the presence of a hydrous melt [16] of coarse-grained ultramafics was followed by thermal equilibration down to 750 °C. The obtained T values for mylonites s.l. are in agreement with the already published temperature estimates [1,15] indicating shearing under granulite- to upper-amphibolite facies conditions (mostly between 750 and 670 °C). These temperatures should be considered as a lower bound limit as the finer grain sizes of the mylonites will favour re-equilibration after deformation and might not record the deformation temperature.

4.2. Timing of Deformation

The Finero Complex was affected by different pre-Alpine tectonic events under granulite- to greenschist-facies conditions producing pervasive or localized foliations and isoclinal to open folds [1,15,16,28,29,32,41,47]. Discrete shear zones and pseudotachylites have received considerable attention over the past 40 years [1,15,16,29,33], but the age of the different deformation events is still debated. Altenberger [15] suggested that the shear zones were related to the Variscan cycle. Matysiak and Trepmann [33] argued that the development of mylonites was connected to extensional tectonics in Jurassic times by analogy with what was reported for other shear zones in the Ivrea-Verbano

Zone. The rare and unexpected occurrence of a single zircon grain within the fine-grained matrix of an ultramafic ultramylonitic sample (30F; Figure 10b,c) allowed us to discuss the age of activity of the shear zone. Zircon shows subround shape with lobate contours (Figure 10c). Under CL it is characterized a darker core, with a faint sector zoning, surrounded by an irregular thin rim with brighter CL emission (Figure 10c). Two LA-ICP-MS spots on this zircon provided one concordant U-Pb age at 187 ± 3 Ma (Figure 10c) and a second discordant one (3.5% discordance) with a $^{206}\text{Pb}/^{238}\text{U}$ age of 180 ± 4 Ma (Figure 10c and Table 5). Zircon has been observed as accessory in different lithologies within the Ph-Pd, i.e., chromitites [19,26,48] and leucocratic dykes/pods/pegmatites [26,27]. The studied zircon was possibly inherited from one of these lithologies affected by shearing.

Table 5. U-Pb zircon data.

Analyses	Isotopic Ratios						Age Estimates (Ma)						U-Pb Concordant Age (Ma)	
	$^{207}\text{Pb}/^{206}\text{Pb}$	$\pm 1\sigma$	$^{207}\text{Pb}/^{235}\text{U}$	$\pm 1\sigma$	$^{206}\text{Pb}/^{238}\text{U}$	$\pm 1\sigma$	$^{207}\text{Pb}/^{206}\text{Pb}$	$\pm 1\sigma$	$^{207}\text{Pb}/^{235}\text{U}$	$\pm 1\sigma$	$^{206}\text{Pb}/^{238}\text{U}$	$\pm 1\sigma$	Age	$\pm 2\sigma$
004SMPL	0.04788	0.00056	0.18710	0.00268	0.02835	0.00036	93	1	174	2	180	2		
005SMPL	0.04987	0.00056	0.20252	0.00272	0.02946	0.00034	189	2	187	3	187	2	187.2	3.3

The obtained U-Pb data perfectly overlaps the major age peak (about 187 Ma) of zircon from chromitite layers within the mantle peridotites interpreted as the timing of exhumation at crustal levels [19]. Triassic–Jurassic U-Pb zircon ages were also reported for other mantle chromitites [48] and leucocratic dykes (225 ± 13 Ma: [27]; 190–212 Ma: [34]); they were interpreted as due to prolonged formation and multistage zircon growth in the chromitites and the timing of intrusion for the dykes, respectively. It is difficult to constrain the origin of the zircon grain analyzed in the present study based only on the U–Pb data. Nevertheless: (i) the lack of abundant chromite/spinel associated with zircon in the fine-grained matrix (Figure 10b) and (ii) the occurrence of sheared leucocratic dykes in the shear zone (Figure 2b) led us to propose that the zircon grain was likely, and luckily, inherited from the leucocratic dykes. This would suggest that the shear zone activity post-dated the Triassic–Jurassic emplacement of these dykes.

The temperature estimates combined with geochemical and microstructural observations from the sheared peridotites suggest that the Ph-Pd unit was probably still at granulite/amphibolite-facies conditions during mylonitic deformation (Figure 10a). These conditions are not compatible with deformation events that occurred during the Alpine orogenic cycle, which formed low-T shear zones at depths of about 5–10 km or less [49]. Granulite-facies conditions have been also documented for mylonites in the crustal sequence of the Finero Complex at the boundary between gabbros and peridotites [50]. Geochronological surveys suggest that these mylonites formed over a large time interval at granulite-facies conditions (ca. 230–200 Ma, [50]), with deformation likely continuing at amphibolite-facies conditions down to 180 Ma [50]. A similar age interval for deformation was proposed for the Pogallo Line (210–170 Ma, [51]), an intermediate-crust extensional shear zone interpreted in literature as the main structure accommodating necking at the Adria margin during the opening of the Alpine Tethys [52,53].

Thus, the shear zone affecting the Ph-Pd unit is one of the youngest and deepest deformation structures so far documented of a large shear system which affected the lithospheric sequence at Triassic–Jurassic times, inducing an exceptional thinning of the northernmost tip of the Ivrea-Verbano Zone and governing the exhumation of the lowermost continental crust and of the upper mantle [18,19,50,52,53].

4.3. Mineral Chemistry vs. Deformation across Shear Zone

This work reveals the occurrence of marked geochemical variations, in both major and trace element concentrations, between mylonites s.l. in a metric-scale shear zone and their coarse-grained protoliths in the Finero Ph-Pd unit. Chemical variations were also observed among rocks showing different degrees of strain within the shear zone (Figure 11). By comparing the modal composition

of the ultramylonite matrix with that of coarse-grained phlogopite harzburgites, it is observed that shearing was accompanied by a pronounced increase in the phlogopite, a significant decrease in the olivine and amphibole, and a decrease of orthopyroxene modal abundance. Clinopyroxene remains at few vol.% level. The variation in modal composition clearly indicates bulk rock chemical changes due to the interaction with percolating fluids within the shear zone. According to the field evidence, the modal composition of sheared peridotites and the ubiquitous presence of orthopyroxene and olivine porphyroclasts in ultramylonites, we concluded that the shear zone affected mainly harzburgite; therefore, we directly compare the shear zone mineral chemistry with that of coarse-grained harzburgites.

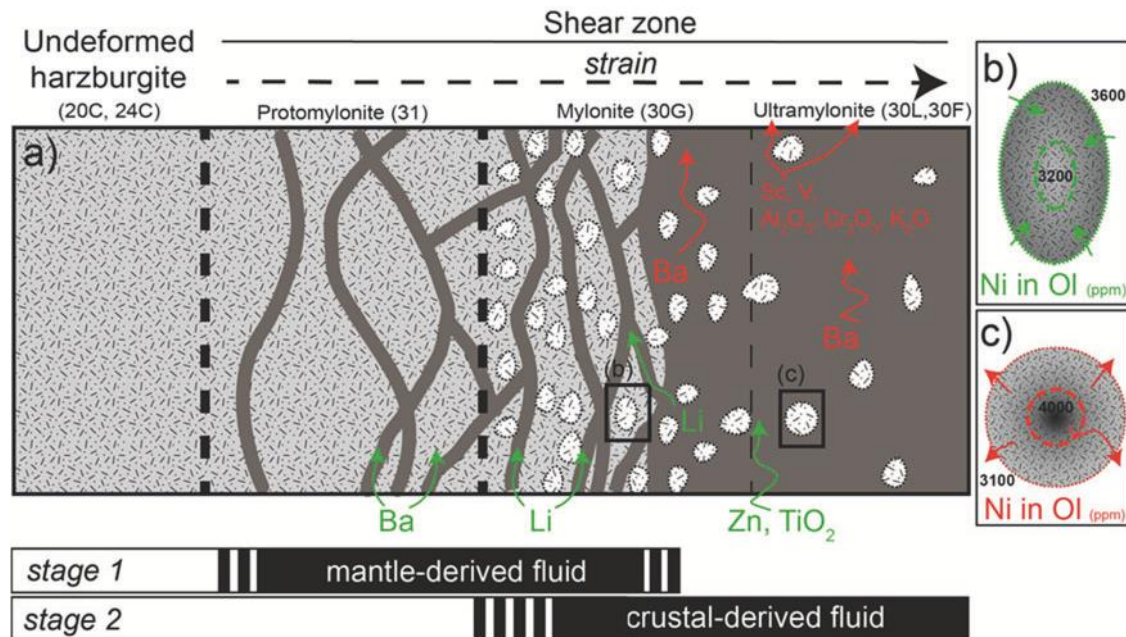


Figure 11. Cartoon summarizing the main observed variations in term of major and trace elements in the mineral phases: (a) Scheme of the transition from coarse-grained harzburgite to mylonite and ultramylonites. Arrows and text in red and green refer to enrichment and depletion, respectively, of elements within minerals and rocks. (b,c) Opposite chemical trends observed within olivine porphyroclasts from different sectors of the shear zone. The black bars on the bottom represent the domains of the shear zone affected by the different fluids.

4.3.1. Major Elements

In this section, the variation in major element contents of the different mineral phases from coarse-grained harzburgites to sheared peridotites is discussed, taking into account the information about the bulk rock chemistry of the studied shear zone provided [1,15]. According to these authors [1,15], the sheared peridotites experienced a gain in Al₂O₃, K₂O, and Na₂O.

Simple mass balance calculations, based on the average modal composition of coarse-grained harzburgite and the matrix composition of the ultramylonites, confirm an increase of Al₂O₃ in the bulk composition of the sheared peridotites. Considering that the Al₂O₃ content of silicates and spinel from the host coarse-grained harzburgites to the ultramylonitic domains decreases, it is suggested that the bulk gain in Al₂O₃ is the result of the profuse crystallisation (up to about 30 vol.% vs. <5 vol.% in coarse-grained harzburgites) of synkinematic phlogopite, which contains up to 14.5 wt.% Al₂O₃ (Figure S2b). The Al₂O₃ of silicates was probably also controlled by the stability of Al-bearing chromite, which is present as accessory phase within the fine-grained matrix. All these observations are consistent with the lower equilibrium T recorded by the sheared rocks (Figure 10a) promoting crystallisation hydrous minerals and chemical variation of mineral across the shear zone. In fact, it is common

wisdom that decreasing T reduces the diminishing of the substitution of Al^{3+} for Si^{4+} in tetrahedral sites of silicates (Tschermaks exchange). This decreases the capability to balance the incorporation of nondivalent elements (e.g., Al, Cr, Ti, Fe^{3+} , Mn^{3+}) in [8]-fold coordinated sites (e.g., REE^{3+} in M2 site of clinopyroxene and M4 site of amphibole; [54]), as well as the possibility of hosting Na and K in the [12]-fold coordinated sites of amphibole and phlogopite. A similar T-dependent behavior can be envisaged to explain the Cr_2O_3 content variation in mineral phases from the coarse-grained harzburgites to ultramylonites, as already proposed by Brodie [1] (Figure S2e–h).

Mass balance calculations and bulk chemistry data [1,15] also point to positive net gain of K, Na, and Ti for mylonites and ultramylonites with respect to coarse-grained harzburgites. Amphibole and phlogopite from sheared peridotites show different Na/K ratios and Na_2O and K_2O contents with respect to the coarse-grained harzburgites (Figure S2c,d). Na_2O and K_2O show opposite trends within amphibole: Na_2O increases, whereas K_2O decreases (Figure 6e,f). According to experimental investigation [55], the $\text{K}/(\text{K}+\text{Na})$ ratios may decrease in both amphibole and phlogopite at decreasing P and T conditions. Nevertheless, the observed variations would require changes in order of several GPa and/or hundreds of °C. Thus, it is argued that compositional variability of amphibole and phlogopite cannot be explained only by the estimated variation of P-T conditions between coarse-grained and sheared harzburgites.

Phlogopite and amphibole within the porphyroclast-poorest ultramylonite (30F) do not follow the chemical trends observed within the other sheared rocks. In particular, phlogopite is on average richer in TiO_2 , K_2O and has lower Na_2O (Figure 6c and Figure S2c,d). The latter is also consistently lower in amphibole. In this sample, the geochemical variations shown by phlogopite and amphibole are accompanied by on average lower Mg# of olivine and orthopyroxene with respect to all other Ph-Pd samples. Considering that we do not observe significant differences in terms of mineral assemblages and abundances among the sheared samples, two options can be envisaged: (i) an apparent change of P-T conditions of deformation and/or (ii) a variation of the fluid percolating this sector of the shear zone.

Summing up, the major element composition of minerals in different rocks and textural positions corroborates mass transfer processes within the shear zone and fractionation effects due to the crystallization of synkinematic major phases and/or accessories. Our results based on mineral chemistry are in agreement with the results of previously published data [1,15] confirming the open system nature of the shear zone, where the mineral chemistry was partially controlled by the evolving bulk composition, fluid chemistry, and P-T conditions that modified the mineral modal proportion.

4.3.2. Minor and Trace Elements

The minor and trace elements mineral composition provide further information about the petrochemical evolution of the shear zone. The trace element concentration of the porphyroclasts from the shear zone differs significantly from the same mineral phases in the coarse-grained ultramafics, independently on their modal composition. The observed chemical differences are more likely the result of fluid–rock interaction and re-equilibration during ductile deformation than due to the heterogeneity of protoliths. The major changes are documented for Li, Co, Ni, Zn in olivine, Sc, and V in orthopyroxene, Ti, Sc, REE, and Y in clinopyroxene, and Li and Ba in phlogopite, Ba in amphibole (Figures 7 and 8). Within the shear zone, the variation in concentration of some elements is correlated to the strain intensity (i.e., porphyroclasts/matrix ratios; Figure 11b,c): Ca, Sc, and V in orthopyroxene steadily decrease on average as strain increases (Figure 7e–g), whereas Zn in olivine increases (Figure 7d). A significant drop of Sc was also observed from core to rim of orthopyroxene porphyroclasts (Figure 7f) and for amphibole (Figure 8b) from the coarse-grained harzburgites (e.g., 24C and 20C) to the protomylonites (31).

The correlation of Sc, V, and Ca content in orthopyroxene suggests that their behavior can be mainly affected by decreasing T as already argued for Al_2O_3 and Cr_2O_3 . Scandium and V were likely partitioned in Al-rich silicates (clinopyroxene, amphibole, and the abundant phlogopite), whereas Cr was preferentially incorporated by spinel (Figure 5f) [56].

The progressive Zn enrichment within olivine porphyroclasts may be explained by an uptake of this element from the fluid phase by back diffusion. The availability of Zn in the fluids can be related to an external source and/or to breakdown of Zn-rich mineral phases during deformation. Olivine porphyroclasts also show a significant increase in Li, Co, and Ni from protomylonites to ultramylonites (Figure 7a–d). It is interesting to note that these elements in olivine from mantle peridotite show usually small concentration ranges being mainly partitioned by it [45].

Significant variations of Li in phlogopite and Ba in amphibole and phlogopite were observed across the shear zone even though these mineral phases are not always present as porphyroclasts in the ultramylonites (Figure 8g,h). The higher Li content of phlogopite (up to six times on average) within the high strain zone (30G) with respect to the protomylonites of the low strain zone and coarse-grained ultramafics may suggest a net in-flux of Li within the shear zone (Figure 11a). It should be noted that the highest Li contents in phlogopite and olivine were obtained from the sample of the high strain zone that represents the transition from ultramylonites to protomylonites (Figure 11a). Both phlogopite and amphibole show higher Ba contents in protomylonites with respect to those from coarse-grained protoliths and the phlogopite in the low strain zone. This highlights a net in-flux of Ba at the transition (i.e., sample 31) between the coarse-grained harzburgite and the ultramylonites.

Although clinopyroxene and amphibole porphyroclasts are not ubiquitous across the shear zone, they provide valuable insights about the geochemical evolution of the system. Amphibole composition suggests that only minor REE and HFSE changes affected the protomylonites (31); conversely, clinopyroxene porphyroclasts from mylonite (30G) and ultramylonite (30L) indicate that the high strain domain of the shear zone was significantly enriched in REE, Y, and Sr (Figure S3b). This was associated with a decrease of LREE/HREE fractionation and with an increase of REE/HFSE ratios.

Combining petrographic and microstructural features, together with the observed chemical variations, the percolation of solute-rich hydrous fluids under amphibolite/granulite facies conditions is envisaged. During such fluid-assisted shearing, porphyroclasts within the fine-grained matrix acted as both source or sink for several elements. It has been demonstrated that dislocations associated to crystal-plastic deformation are shortcuts promoting diffusion in and out of the porphyroclasts [57]. High-resolution EBSD analyses combined with further trace element mapping/profiles of the porphyroclasts are needed in order to better describe and quantify this process.

4.4. Evidence for Different Stages of Fluid–Rock Interaction

According to Altenberger [15], the shear zone experienced a long-term activity, which started under granulitic conditions, now represented by protomylonites, followed by amphibolite- to upper greenschist facies deformation event, well preserved in the ultramylonites.

Altenberger [15] demonstrated that the interaction between mylonites s.l. and fluids resulted in a modification of the whole rock chemistry by gain or loss of some elements. In the granulitic stage the shear zone suffered small volume changes, the addition of small amounts of fluids and a considerable gain of Ba, Na, Ti, and Cu, whereas other elements, such as Nb, F, and P were leached from the system [15]. Altenberger [15] also suggested that the fluid phase percolating during the granulitic stage of deformation derived probably from the upper mantle.

The trace element composition of the porphyroclasts provided in this work adds information about the origin of the fluid phase percolating during the granulitic event. The clinopyroxene porphyroclasts from the mylonitic domain of the (30G) and from ultramylonite (30L) are characterized by peculiar geochemical features. They show LREE-enriched convex-upward patterns and large REE/HFSE ratios (Figure S3b) that mimic those found in clinopyroxene from sapphirine-bearing gabbroic dykes discordantly cutting the Ph-Pd unit [17,25,41]. These magmatic products have been related to the late intrusion of mantle-derived alkali-rich melts, which promoted also metasomatic layers within the coarse-grained ultramafics. Altenberger [15] suggested a considerable whole rock gain of Ba during the granulite facies deformation. Coherently, we observe that amphibole and phlogopite from the protomylonite (31) are characterized by the highest Ba values.

An abrupt chemical change of the fluid component is documented by the low Ba values of phlogopite (<2500 ppm) from the mylonitic sector (sample 30G). These values are on average far from those reported for phlogopite within coarse-grained ultramafics, suggesting a leaching effect by the fluid. The sample (30G) represents the transition from protomylonites to ultramylonites, being composed of a mylonitic domain in contact with an ultramylonitic one. In this sample, olivine and phlogopite display the maximum values of Li. This enrichment is indicative of the presence of a recycled crustal component documented in magmatic olivine segregated from alkaline rocks, e.g., lamproites [58]. The sample (30G) is thus the transition from a sector recording the interaction with a mantle-derived fluid (i.e., protomylonites 31) and the ultramylonitic domain of the shear zone, where a crustal-derived fluid percolated and probably erased the fingerprints of a former mantle-derived fluid.

The crustal nature of this second fluid is also supported by the chemistry of olivine porphyroclasts from ultramylonites [59,60]. Olivine from these rocks show a decoupling of Zn with respect to Ni, Co, and Li, whose partitioning is governed by olivine. This suggests a net in flux of Zn within ultramylonites, coherently with bulk rock data [15]. Zn may be carried in the form of bisulfide complexes in deep, pH neutral to basic hydrothermal systems [58]. However, Zn concentration is very low in upper mantle sulfides, whose composition is dominated by Fe and Ni, with very subordinate Cu [61]. The lack of significant deposition of synkinematic sulfides within the ultramylonites does not support the large presence of S-complexes in the second fluid, suggesting alternatively the involvement of a silicate crustal component as source of the fluid. It has been demonstrated that Zn-bearing biotite and chlorite can host large amounts of bulk Zn content in siliciclastic metasedimentary rocks [62] and altered/metasomatized mafic rocks [63], respectively. In order to explain the Zn enrichment together with the large K, Al, Ti, and Fe content recorded by the most deformed sectors of the shear zone, it is argued that dissolution of crustal biotite more likely governed the composition of the second fluid phase.

As a whole, our data confirm that the shear zone acted as a metasomatic channel, where mobility of elements was promoted by large amounts of fluids and by the increase in reaction surfaces due to deformation-induced grain size reduction, e.g., [1,15]. The results of this study highlight the role of porphyroclasts as source or sink for some elements during the fluid-assisted deformation and emphasize how they provide valuable information to unravel the nature of percolating fluids (i.e., mantle vs. crustal). It is further suggested that the trace element chemistry of porphyroclasts should be taken into account for mass balance calculation of deformed rocks. The chemical modification across shear zones is usually explained by the chemistry of synkinematic minerals and gain or loss of elements, being porphyroclasts almost neglected (at least in terms of trace elements). Here, it is demonstrated that during granulite to amphibolite facies deformation, the composition of the porphyroclasts can be severely modified by the uptake of trace and minor elements, accommodating totally or partially the changes at the bulk rock scale. In other words, the mass gain/loss in sheared rocks cannot be entirely explained by the development of synkinematic mineral assemblages.

5. Conclusions

This work provides a complete dataset on major, minor, and trace element mineral chemistry covering all the major lithologies of the Finero Phlogopite Peridotite mantle unit. These data provide valuable constraints on the relationship between geochemistry and microstructural features in ultramafic shear zones. Remarkable chemical variations are observed both for major and trace elements.

The major and trace element composition of minerals from the proto- to ultramylonites that compose the shear zone and from the coarse-grained ultramafics that are their protoliths suggest that elements were exchanged at both outcrop and crystal scale. The shear zone acted as an open system where the combined effect of fluid-rock interaction, deformation, and recrystallization resulted in marked chemical variations. The LA-ICP-MS chemical data of porphyroclasts suggest that their trace element concentrations were severely modified during deformation and that they were either source or sink for some elements. The trace element composition study of porphyroclasts was crucial to gain

information about the composition of fluid flowing through mylonites. We propose that in order to understand the chemical variations across shear zones it is fundamental to study both synkinematic minerals and porphyroclasts in terms of major and trace elements. Our study indicates that the present-day compositions of the sheared peridotites are the result of the interplay between fluids with different compositions and/or proportion with respect to the solid component and rocks showing variable microstructures.

The P-T estimates together with geochemical and microstructural observations from the studied shear zone suggest that the Ph-Pd unit was still placed at moderate depth (i.e., >15 km) under granulitic-to amphibolite facies conditions during mylonitic deformation. These conditions are not compatible with deformation events that occurred during the Alpine orogenic cycle, which formed low-T shear zones at depths of about 5–10 km or less [53]. The occurrence of a single zircon grain within the fine-grained ultramylonitic matrix allowed us to constrain the timing of deformation at 187 Ma or younger. Zircon was likely (and luckily) inherited from nearby sheared leucocratic dykes that intruded within Ph-Pd unit from the late Triassic to the early Jurassic. The results of this study confirm that the Finero Complex represents a key area for the understanding of the Mesozoic tectono-magmatic events that ruled the extension of the western margin of the Adria plate leading to the opening of the Alpine Tethys.

Supplementary Materials: The following are available online at <http://www.mdpi.com/2076-3263/10/5/196/s1>, Figure S1:(a) EBSD map and (b) SEM observations, Table S1: Major elements, Figure S2: Extra major elements diagrams, Table S2: Trace elements, Figure S3: PM primitive mantle-normalized trace element patterns for (a) amphibole and, (b) clinopyroxene, Table S3: Porphyroclasts profiles, Figure S4: (a) Aluminium and (b) titanium in olivine porphyroclasts profiles, Table S4: Geothermometry, Table S5: U-Pb Zircon dating.

Author Contributions: Conceptualized the study and developed methodology, A.L.; performed the formal analysis, and data curation, S.C., A.L.; prepared the original initial draft and writing, S.C., A.L. and A.Z.; supervised and provided critical reviews and editing, A.L., A.Z., A.T., and J.A.P.-N. All authors have read and agreed to the published version of the manuscript.

Funding: This research was funded by the following projects: PRIN2015 “Geochemical and isotopic budget of highly metasomatized sub-continental mantle in the Africa and Europe geodynamics systems: modern and fossil analogues”; PRIN2017 “Micro to Macro – how to unravel the nature of the large magmatic events (20178LPCPW-Langone Antonio)”.

Acknowledgments: We thank the Assistant Editor Ashley Zhang and the reviewers for helpful comments that improved the manuscript. We would like to thank also the guest editors of the special issue. Part of the analyses were performed by Stefania Corvò during a short post-graduation scholarship (2018; S. Corvò) at the IGG-CNR (Pavia, Italy).

Conflicts of Interest: The authors declare no conflicts of interest.

Appendix A

Analytical methods. The major-element composition of mineral phases was determined by JEOL 8200 Electron Microprobe Analyses (EMPA) at the Dipartimento di Scienze della Terra “Ardito Desio”, University of Milan. Average data and standard deviations are reported in Table 2. For mylonitic samples some maps were produced by microprobe instrument in order to study in detail the porphyroclasts and matrix composition (e.g., Figure 4). Microchemical analyses and some Back-Scattered Electron (BSE) imaging on the matrix composition were also performed by Scanning Electron Microscopy (SEM) using a Tescan Mira3 XMU-series FESEM equipped with an EDAX-EDX (accelerating voltage 20 kV, beam intensity 16.5 nA, spot area 100×100 µm, counts of 100 s., analyses and working distance 15.8 mm; University of Pavia, Italy); data was processed with EDAX Genesis software using the ZAF algorithms the correction method (Figure S1). Trace element concentrations have been determined by means of the LA-ICP-MS (laser ablation inductively coupled plasma spectrometry) at the CNR-IGG of Pavia (Italy). Average values are reported in Table 3, the whole dataset is available as Supplementary Table S2. A PerkinElmer SCIEX ELAN DCR-e quadrupole ICP-MS was coupled with a 213nm Nd:YAG laser (NewWave Research). Helium was used as carrier gas and mixed with Ar downstream of the ablation cell. Laser spot size was calibrated between 50 and 60 µm and laser

beam fluency at 8–9 J/cm². Data reduction was performed with GLITTER software, using the reference synthetic glass NIST (SRM) 610, NIST612 as external standards. ²⁹Si was used as internal standards for olivine, orthopyroxene, phlogopite; ⁴⁴Ca for clinopyroxene, and amphibole (pargasite). Precision and accuracy were assessed via repeated analyses of basalt glass (BCR-2g) reference material, resulting better than ±10% at ppm concentration level. The uncertainties related to the trace element data is of 1σ. Detection limits were typically in the range of 100–500 ppb for Sc, 10–100 ppb for Sr, Zr, Ba, Gd and Pb, 1–10 ppb for Y, Nb, La, Ce, Nd, Sm, Eu, Dy, Er, Yb. Hf and Ta, and usually <1 ppb for Pr, Th, and U. Zircon grain was analyzed in situ by laser-ablation, inductively coupled, plasma mass spectrometry (LA-ICP-MS) on 30-µm-thick sections at the CNR-Istituto di Geoscienze e Georisorse U.O. Pavia (Italy). Analytical conditions are 25 µm in diameter of spot size, 8 J/cm² of energy density, and 5 Hz of repetition rate. Laser-induced elemental fractionation and mass bias were corrected using zircon standard (GJ1 zircon). Data reduction was carried out with GLITTER TM software. In order to better estimate the uncertainty affecting the ²⁰⁶Pb/²³⁸U, ²⁰⁷Pb/²³⁵U isotope ratios, the external reproducibility of the standard was propagated relative to individual uncertainties for the isotope ratios. After this error propagation, each analysis is accurate within the quoted errors. The ISOPLOT 3.0 software [64] was used for age calculation. Data are reported in Table 5.

References

1. Brodie, K.H. Variations in mineral chemistry across a phlogopite shear zone. *J. Struct. Geol.* **1980**, *2*, 265–272. [[CrossRef](#)]
2. Brodie, K.H. Variation in amphibole and plagioclase composition with deformation. *Tectonophysics* **1981**, *78*, 385–402. [[CrossRef](#)]
3. Rolland, Y.; Cox, S.; Boullier, A.M.; Pennacchioni, G.; Mancktelow, N. Rare earth and trace element mobility in mid-crustal shear zones: Insights from the Mont Blanc Massif (Western Alps). *Earth Planet. Sci. Lett.* **2003**, *214*, 203–219. [[CrossRef](#)]
4. McCaig, A.M. Deep fluid circulation in fault zones. *Geology* **1988**, *16*, 867–870. [[CrossRef](#)]
5. Hidas, K.; Tommasi, A.; Garrido, C.J.; Padrón-Navarta, J.P.; Mainprice, D.; Vauchez, A.; Barou, F.; Marchesi, C. Fluid-Assisted strain localization in the shallow subcontinental lithospheric mantle. *Lithos* **2016**, *262*, 636–650. [[CrossRef](#)]
6. Précigout, J.; Prigent, C.; Palasse, L.; Pochon, A. Water pumping in mantle shear zones. *Nat. Commun.* **2017**, *8*, 15736. [[CrossRef](#)]
7. Harlov, D.E.; Austrheim, H. *Metasomatism and the Chemical Transformation of Rock – The Role of Fluids in Terrestrial and Extraterrestrial Processes*; Lecture Notes in Earth System Sciences; Springer: Berlin, Germany, 2013; 800p.
8. Piazzolo, S.; La Fontaine, A.; Trimby, P.; Harley, S.; Yang, L.; Armstrong, R.; Cairney, J.M. Deformation-Induced trace element redistribution in zircon revealed using atom probe tomography. *Nat. Commun.* **2016**, *7*, 10490. [[CrossRef](#)]
9. Kovaleva, E.; Klötzli, U.; Habler, G.; Huet, B.; Guan, Y.; Rhede, D. The effect of crystal-plastic deformation on isotope and trace element distribution in zircon: Combined BSE, CL, EBSD, FEG-EMPA and NanoSIMS study. *Chem. Geol.* **2017**, *450*, 183–198. [[CrossRef](#)]
10. O’Hara, K.; Blackburn, W. Volume-Loss model for trace element enrichments in mylonites. *Geology* **1989**, *17*, 524–527. [[CrossRef](#)]
11. Condie, K.C.; Sinha, A.K. Rare earth and other trace element mobility during mylonitization: Comparison of the Brevard and Hope Valley shear zones in the Appalachia Mountains USA. *J. Metamorph. Geol.* **1996**, *14*, 213–226. [[CrossRef](#)]
12. Tursi, F.; Festa, V.; Fornelli, A.; Micheletti, F.; Spiess, R. Syn-Shearing mobility of major elements in ductile shear zones: State of the art for felsic deformed protoliths. *Period. Mineral.* **2018**, *87*, 289–308.
13. Goncalves, P.; Olliot, E.; Marquer, D.; Connolly, J.A.D. Role of chemical processes on shear zone formation: An example from the Grimsel metagranodiorite (Aar massif, Central Alps). *J. Metamorph. Geol.* **2012**, *30*, 703–722. [[CrossRef](#)]

14. Altenberger, U. The ductile deformation of the Ivrea Zone a study from micro to mesoscale. *Mitt. Geol. Inst.* **1991**, *239*, 91–92.
15. Altenberger, U. Long-Term deformation and fluid-enhanced mass transport in a Variscan peridotite shear zone in the Ivrea Zone, northern Italy: A microtextural, petrological and geochemical study of a reactivated shear zone. *Int. J. Earth Sci.* **1995**, *84*, 591–606.
16. Tommasi, A.; Langone, A.; Padrón-Navarta, J.A.; Zanetti, A. Hydrous melts weaken the mantle, hydrous minerals do not: Insights from a petrostructural study of the Finero pargasite and phlogopite-bearing peridotites, southern Alps. *Earth Planet. Sci. Lett.* **2017**, *477*, 59–72. [[CrossRef](#)]
17. Zanetti, A.; Mazzucchelli, M.; Rivalenti, G.; Vannucci, R. The Finero phlogopite-peridotite massif: An example of subduction-related metasomatism. *Contrib. Mineral. Petrol.* **1999**, *134*, 107–122. [[CrossRef](#)]
18. Zanetti, A.; Mazzucchelli, M.; Sinigoi, S.; Giovanardi, T.; Peressini, G.; Fanning, M. SHRIMP U-Pb zircon Triassic intrusion age of the Finero mafic com-plex (Ivrea-Verbano Zone, Western Alps) and its geodynamic implications. *J. Pet.* **2013**, *54*, 2235–2265. [[CrossRef](#)]
19. Zanetti, A.; Giovanardi, T.; Langone, A.; Tiepolo, M.; Wu, F.-Y.; Dallai, L.; Mazzucchelli, M. Origin and age of zircon-bearing chromitite layers from the Finero phlogopite peridotite (Ivrea-Verbano Zone, Western Alps) and geodynamic consequences. *Lithos* **2016**, *262*, 58–74. [[CrossRef](#)]
20. Hartmann, G.; Wedepohl, K.H. The composition of peridotite tectonites from the Ivrea complex, northern Italy: Residues from melt extraction. *Geochim. Cosmochim. Acta* **1993**, *57*, 1761–1782. [[CrossRef](#)]
21. Cawthorn, R.G. The amphibole peridotite-metagabbro complex, Finero, north-ern Italy. *J. Geol.* **1975**, *83*, 437–454. [[CrossRef](#)]
22. Coltorti, M.; Siena, F. Mantle tectonite and fractionated peridotite at Finero (Italian Western Alps). *Neues Jahrb. Mineral.* **1984**, *149*, 225–244.
23. Lu, M.; Hofmann, A.W.; Mazzucchelli, M.; Rivalenti, G. The mafic-ultramafic complex near Finero (Ivrea-Verbano Zone), I: Chemistry of MORB-like magmas. *Chem. Geol.* **1997**, *140*, 207–222. [[CrossRef](#)]
24. Lu, M.; Hofmann, A.W.; Mazzucchelli, M.; Rivalenti, G. The mafic-ultramafic complex near Finero (Ivrea-Verbano Zone), I: Geochronology and isotope geochemistry. *Chem. Geol.* **1997**, *140*, 223–235. [[CrossRef](#)]
25. Giovanardi, T.; Mazzucchelli, M.; Zanetti, A.; Langone, A.; Tiepolo, M.; Cipriani, A. Occurrence of phlogopite in the Finero mafic layered complex. *Open Geosci.* **2014**, *6*, 588–613. [[CrossRef](#)]
26. Grieco, G.; Ferrario, A.; von Quadt, A.; Köppel, V.; Mathez, A. The zircon-bearing chromitites of the phlogopite peridotite of Finero (Ivrea Zone, Southern Alps): Evidence and geochronology of a metasomatized mantle slab. *J. Petrol.* **2001**, *42*, 89–101. [[CrossRef](#)]
27. Stähle, V.; Frenzel, G.; Hess, J.C.; Saupé, F.; Schmidt, S.T.; Schneider, W. Permian metabasalt and Triassic alkaline dykes in the northern Ivrea Zone: Clues to the post-Variscan geodynamic evolution of the Southern Alps. *Schweiz. Mineral. Petrogr. Mitt.* **2001**, *81*, 1–21.
28. Garuti, G.; Friolo, R. Textural features and olivine fabrics of peridotites from the Ivrea-Verbano Zone (Italian Western Alps). *Mem. Sci. Géol.* **1979**, *33*, 111–125.
29. Kruhl, J.; Voll, G. Fabrics and metamorphism from the Monte Rosa Root Zone into the Ivrea Zone near Finero, southern margin of the Alps. *Schweiz. Mineral. Petrogr. Mitt.* **1976**, *56*, 627–633.
30. Kruhl, J.; Voll, G. Deformation and metamorphism of the western Finero Com-plex. *Mem. Sci. Géol.* **1979**, *33*, 95–104.
31. Langone, A.; Padrón-Navarta, J.A.; Wei-Qiang, J.; Zanetti, A.; Mazzucchelli, M.; Tiepolo, M.; Giovanardi, T.; Bonazzi, M. Ductile-Brittle deformation effects on crystal-chemistry and U-Pb ages of magmatic and metasomatic zircons from dyke of the Finero Mafic Complex (Ivrea-Verbano Zone, Italian Alps). *Lithos* **2017**, *284*, 493–511. [[CrossRef](#)]
32. Kenkmann, T.; Dresen, G. Dislocation microstructure and phase distribution in a lower crustal shear zone – An example from the Ivrea-Zone, Italy. *Int. J. Earth Sci.* **2002**, *91*, 445–458. [[CrossRef](#)]
33. Matysiak, A.K.; Trepmann, C.A. The deformation record of olivine in my-lonitic peridotites from the Finero Complex, Ivrea Zone: Separate deformation cycles during exhumation. *Tectonics* **2015**, *34*, 2514–2533. [[CrossRef](#)]
34. Schaltegger, U.; Ulianov, A.; Muntener, O.; Ovtcharova, M.; Peytcheva, I.; Vonlanthen, P.; Vennemann, T.W.; Antognini, M.; Giralanda, F. Megacrystic zircon with planar fractures in miaskite-type nepheline pegmatites formed at high pressures in the lower crust (Ivrea Zone, Southern Alps, Switzerland). *Am. Mineral.* **2015**, *100*, 83–94. [[CrossRef](#)]

35. Kretz, R. Symbols for rock-forming minerals. *Am. Mineral.* **1983**, *68*, 277–279.
36. Morishita, T.; Arai, S.; Green, D.H. Evolution of low-Al orthopyroxene in the Horoman Peridotite, Japan: An unusual indicator of metasomatizing fluids. *J. Petrol.* **2003**, *44*, 1237–1246. [[CrossRef](#)]
37. Morishita, T.; Arai, S.; Tamura, A. Petrology of an apatite-rich layer in the Finero Phlogopite-Peridotite massif, Italian Western Alps: Implications for evolution of a metasomatizing agent. *Lithos* **2003**, *69*, 37–49. [[CrossRef](#)]
38. Morishita, T.; Hattori, K.H.; Terada, K.; Matsumoto, T.; Yamamoto, K.; Takebe, M.; Ishida, Y.; Tamura, A.; Arai, S. Geochemistry of apatite-rich layers in the Finero phlogopite-peridotite massif (Italian Western Alps) and ion microprobe dating of apatite. *Chem. Geol.* **2008**, *251*, 99–111. [[CrossRef](#)]
39. Ferraris, C.; Grobety, B.; Früh-Green, G.L.; Wessicken, R. Intergrowth of graphite within phlogopite from Finero ultramafic complex (Italian Western Alps): Implications for mantle crystallization of primary-texture mica. *Eur. J. Mineral.* **2004**, *16*, 899–908. [[CrossRef](#)]
40. Matsumoto, T.; Morishita, T.; Masuda, J.; Fujioka, T.; Takebe, M.; Yamamoto, K.; Arai, S. Noble gases in the Finero phlogopite-peridotites, Italian Western Alps. *Earth Planet. Sci. Lett.* **2005**, *238*, 130–145. [[CrossRef](#)]
41. Giovanardi, T.; Zanetti, A.; Dallai, L.; Morishita, T.; Hémond, C.; Mazzucchelli, M. Evidence of subduction-related components in sapphirine-bearing gabbroic dykes (Finero phlogopite-peridotite): Insights into the source of Triassic-Jurassic magmatism at the Europe-Africa boundary. *Lithos* **2020**, *356–357*, 105366. [[CrossRef](#)]
42. Lensch, G. Die ultramafitite der zone von Ivrea und ihre geologische interpretation. *Schweiz. Mineral. Petrogr. Mitt.* **1968**, *48*, 91–102.
43. Wells, R.A. Pyroxene thermometry in simple and complex systems. *Contrib. Mineral. Petrol.* **1977**, *62*, 129–139. [[CrossRef](#)]
44. Nimis, P.; Grütter, H. Internally consistent geothermometers for garnet peridotites and pyroxenites. *Contrib. Mineral. Petrol.* **2010**, *159*, 411–427. [[CrossRef](#)]
45. De Hoog, J.C.M.; Gall, L.; Cornell, D.H. Trace-Element geochemistry of mantle olivine and application to mantle petrogenesis and geothermobarometry. *Chem. Geol.* **2010**, *270*, 196–215. [[CrossRef](#)]
46. Smith, D. Olivine thermometry and source constraints for mantle fragments in the Navajo Volcanic Field, Colorado Plateau, southwest United States: Implications for the mantle wedge. *AGU Geochem. Soc.* **2013**, *14*, 3. [[CrossRef](#)]
47. Steck, A.; Tieche, J.C. Carte géologique de l'antiforme peridotitique de Finero avec des observations sur les phases de déformation et de recristallisation. *Schweiz. Mineral. Petrogr. Mitt.* **1976**, *56*, 501–512.
48. Malitch, K.N.; Belousova, E.; Griffin, W.L.; Badanina, I.Y.; Knauf, V.V.; O'Reilly, S.Y.; Pearson, N.J. Laurite and zircon from the Finero chromitites (Italy): New insights into evolution of the subcontinental mantle. *Ore Geol. Rev.* **2019**, *90*, 210–225. [[CrossRef](#)]
49. Rutter, E.H.; Brodie, K.H.; Evans, P.J. Structural geometry, lower crustal magmatic underplating and lithospheric stretching in the Ivrea-Verbano zone, northern Italy. *J. Struct. Geol.* **1993**, *15*, 647–662. [[CrossRef](#)]
50. Langone, A.; Zanetti, A.; Daczko, N.; Piazzolo, S.; Tiepolo, M.; Mazzucchelli, M. Zircon U-Pb Dating of a lower Crustal Shear zone: A case study from the Northern Sector of the Ivrea-Verbano Zone (Val Cannobina, Italy). *Tectonics* **2018**, *37*, 322–342. [[CrossRef](#)]
51. Wolff, R.; Dunkl, I.; Kiesselbach, G.; Wemmer, K.; Siegesmund, S. Ther-Mochronological constraints on the multiphase exhumation history of the Ivrea-Verbano Zone of the Southern Alps. *Tectonophysics* **2012**, *579*, 104–117. [[CrossRef](#)]
52. Decarlis, A.; Beltrando, M.; Manatschal, G.; Ferrando, S.; Carosi, R. Architecture of the Distal Piedmont-Ligurian rifted margin in NW Italy: Hints for a flip of the rift system polarity. *Tectonics* **2017**, *36*, 2388–2406. [[CrossRef](#)]
53. Petri, B.; Duretz, T.; Mohn, G.; Schmalholz, S.M.; Karner, G.D.; Muntener, O. Thinning mechanisms of heterogeneous continental lithosphere. *Earth Planet. Sci. Lett.* **2019**, *512*, 147–162. [[CrossRef](#)]
54. Tiepolo, M.; Oberti, R.; Zanetti, A.; Vannucci, R.; Foley, S.F. Trace-Element partitioning between amphibole and silicate melt. *Rev. Mineral. Geochem.* **2007**, *67*, 417–45159. [[CrossRef](#)]
55. Konzett, J.; Ulmer, P. The stability of hydrous potassic phases in lherzolitic mantle— An experimental study to 9.5 GPa in simplified and natural bulk compositions. *J. Petrol.* **2001**, *40*, 629–652. [[CrossRef](#)]

56. Witt-Eickschen, G.; O'Neill, H.S.C. The effect of temperature on the equilibrium distribution of trace elements between clinopyroxene, orthopyroxene, olivine and spinel in upper mantle peridotite. *Chem. Geol.* **2005**, *221*, 65–101. [[CrossRef](#)]
57. Chakraborty, S. Diffusion in solid silicates: A tool to track timescales of processes comes of age. *Annu. Rev. Earth Planet. Sci.* **2008**, *36*, 153–190. [[CrossRef](#)]
58. Etschmann, B.; Liu, W.; Mayanovic, R.; Mei, Y.; Heald, S.; Gordon, R.; Brugger, J. Zinc transport in hydrothermal fluids: On the roles of pressure and sulfur vs. chlorine complexing. *Am. Mineral.* **2019**, *104*, 158–161. [[CrossRef](#)]
59. Foley, S.; Prelevic, D.; Rehfeldt, T.; Jacob, D. Minor and trace elements in olivines as probes into early igneous and mantle melting processes. *Earth Planet. Sci. Lett.* **2013**, *363*, 181–191. [[CrossRef](#)]
60. Sobolev, A.V.; Hofmann, A.W.; Kuzmin, D.V.; Yaxley, G.M.; Arndt, N.T.; Chung, S.L.; Danyushevsky, L.V.; Elliott, T.; Frey, F.A.; Garcia, M.O.; et al. The amount of recycled crust in sources of mantle-derived melts. *Science* **2007**, *316*, 412–417. [[CrossRef](#)]
61. Zhang, Z.; Hirschmann, M.M. Experimental constraints on mantle sulfide melting up to 8 GPa. *Am. Mineral.* **2016**, *101*, 181–192. [[CrossRef](#)]
62. Hammerli, J.; Spandler, C.; Oliver, N.H.S.; Sossi, P.; Dipple, G.M. Zn and Pb mobility during metamorphism of sedimentary rocks and potential implications for some base metal deposits. *Miner. Depos.* **2015**, *50*, 657–664. [[CrossRef](#)]
63. White, A.J.R.; Pearce, M.A.; Meadows, H.R. Distinguishing regional-and local-scale metasomatic systems at the Prairie Downs Zn-Pb deposit. *Lithos* **2016**, *262*, 247–265. [[CrossRef](#)]
64. Ludwig, K.R. Isoplot/Ex version 3.0. A geochronological toolkit for Microsoft Excel. *Berkeley Geochron. Center* **2003**, *4*, 1–70.



© 2020 by the authors. Licensee MDPI, Basel, Switzerland. This article is an open access article distributed under the terms and conditions of the Creative Commons Attribution (CC BY) license (<http://creativecommons.org/licenses/by/4.0/>).

APPENDIX 6

Side projects

A.6.1 HT-LP metamorphism and multi-stage anatexis of upper continental crust (N Sardinia, Italy)

In this paper, the evolution of a composite migmatitic complex exposed in the Variscan crust of northern Sardinia (Italy) is investigated. Pseudosection modelling, LA-ICP-MS U-Pb zircon and monazite dating of different anatectic melts, as well as pseudotachylite-bearing faults and ductile shear zones developed between the two anatectic events and provide quantitative information on the P - T - t path recorded by migmatites. The results are finally discussed in terms of the potential mechanisms triggering multi-stage anatexis and development of HT-LP conditions in the uppermost crust.

The content of this manuscript was submitted (16/11/2021) as original article on the Journal of Metamorphic Geology and it is now under review. John Wiley & Sons Ltd. All rights. For this work, the candidate collaborates for the learning, elaboration and interpretation of P - T pseudosections modelling.



HT-LP metamorphism and multi-stage anatexis of upper continental crust (N Sardinia, Italy)

Journal:	<i>Journal of Metamorphic Geology</i>
Manuscript ID	JMG-21-0111
Wiley - Manuscript type:	Original Article
Date Submitted by the Author:	16-Nov-2021
Complete List of Authors:	casini, leonardo; Universita degli Studi di Sassari Dipartimento di Chimica e Farmacia Maino, Matteo; Universita degli Studi di Pavia Dipartimento di Scienze della Terra e dell'Ambiente Langone, Antonio; Consiglio Nazionale delle Ricerche Oggiano, Giacomo; Universita degli Studi di Sassari Dipartimento di Chimica e Farmacia Corvò, Stefania; Universita degli Studi di Pavia Dipartimento di Scienze della Terra e dell'Ambiente Reche, Joan; Universitat Autònoma de Barcelona Departament de Geologia Liesa, Montserrat; Universitat de Barcelona
Keywords:	Variscan belt, diatexite, pseudosection modelling, pseudotachylite, monazite and zircon dating

Abstract

The Variscan high-grade metamorphic basement of northern Sardinia and southern Corsica record lower Carboniferous anatexis related to post-collisional decompression of the orogen. Migmatites exposed in the Punta Bianca locality (Italy), consist of quartz + biotite + plagioclase + K-feldspar orthogneisses, garnet and cordierite-bearing diatexite and metatexites, that is sillimanite/cordierite-bearing migmatites derived from metasediments. Field evidence, petrographic observations, ELAICP-MS zircon and monazite dating and pseudosection modelling suggest that anatexis was apparently episodic involving two main stages of partial melting. Pseudosection modelling indicates that the first stage of partial melting is in the upper amphibolite facies (~0.45 GPa at ~740°C). Cordierite overgrowths replacing sillimanite and the composition of plagioclase and K-feldspar suggest decompression followed cooling below the solidus at low pressures of ~0.3 GPa. The age of the first anatectic event is not precisely constrained because of extensive resetting of the isotopic systems during the second melting stage; yet few zircons preserve a lower Carboniferous age which is consistent with the regional dataset. This lower Carboniferous migmatitic fabric is offset by a network of pseudotachylite-bearing faults suggestive of cooling to greenschist-facies conditions. Garnet/cordierite-bearing diatexites incorporate fragments of pseudotachylite-bearing orthogneiss and metatexites. Pseudosection modelling indicates nearly isobaric re-heating up to ~750°C, followed by further cooling below the solidus. The inferred P–T path is consistent with decompression and cooling of the Variscan crust through post-collisional extension and collapse of the thickened orogenic crust, followed by nearly isobaric re-heating at low pressures (~0.3 GPa) yielding to a second melting stage under LP-HT conditions. U/Th-Pb monazite ages for diatexite migmatites indicate an upper bound of 316–310 Ma for the second melting stage, suggesting that the second melting stage is coincident with the regional phase of crustal shearing. The cause of the high geothermal gradient required for re-heating during the second melting stage is unknown but likely requires some heat source that was probably related to dissipation of mechanical work within crustal-scale shear zones. According to this interpretation, some upper Carboniferous peraluminous granites precursor of the Corsica-Sardinia Batholith could be the outcome rather than the cause of the late-Variscan high T metamorphism.

A.6.2 Petrological and geochronological constraints of a shallow intrusion into the Variscan medium-grade metamorphic sequence of the Asinara Island (Sardinia)

The candidate personally contributed to the development of the side project relative to the Variscan evolution of the Asinara island and of the related manuscript (in preparation) titled “Petrochronology of Late Variscan Castellaccio pluton (Asinara Isl., NW Sardinia, Italy)”. The data were object of a Master Thesis and of an oral presentation held by the candidate at “SIMP conference, Parma 2019” at the session: S19 The interplay between magmatic systems and tectonics: insights from multidisciplinary approaches.

A.4.2 Petrological and geochronological constraints of a shallow intrusion into the Variscan medium-grade metamorphic sequence of the Asinara Island (Sardinia)

Corvo' S.¹, Langone A.², Maino M.¹, Cuccuru S.³, Oggiano G.³, Seno S.¹

1 Dipartimento di Scienze della Terra, dell'Ambiente, Università di Pavia, Italy

2 Istituto di Geoscienze e Georisorse, C.N.R., Pavia, Italy

3 Dipartimento di Scienze della Natura e del Territorio, Università di Sassari, Italy

Abstract

The Asinara Island, NW Sardinia, is an exceptionally well-preserved segment of medium to high-grade metamorphic Variscan crust. Starting from the pioneering studies (Di Pisa et al., 1993; Del Moro et al., 1996; Carosi et al., 2004) describing the main features of the metamorphic and structural setting, we focus on petrology and geochronology of medium to low-grade metapelites surrounding the largest plutonic body of the island, i.e., the Castellaccio Pluton. The pluton consists of a small sill-shaped granodioritic body emplaced within a late-Variscan shear zone (Cuccurru et al., 2018). In this study, we show preliminary Pressure-Temperature-time (*P-T-t*) data from both the metapelites and the granodiorites of the Castellaccio Pluton. *P-T-t* paths are used to characterize the time-dependent thermal evolution of the Variscan upper crust. Close to the contact with granodiorites, the metapelites show HT-LP mineral assemblages (And+Bt+Ms) with local occurrence of fibrolite. Micaschists with cm-sized andalusite porphyroblasts contain also pinite pseudomorphs after cordierite. A few hundred meter far from the pluton, relicts of the Barrovian HT-MP mineral assemblage (St+Grt) can be still recognised and are partly overprinted by HT-LP mineral assemblages with And+Bt. Integrating

petrographic observation, thermo-barometric calculation and thermodynamic modelling (Perple_X) we provide estimations of the metamorphic conditions experienced by the host rocks. U-(Th-)Pb ages from zircon and monazite allow to determine the timing of the metamorphic evolution of this crustal segment, as well as to define the emplacement age of the Castellaccio Pluton. Finally, the new data are discussed in the frame of the Variscan evolution of the Corsica-Sardinia massif.

References:

- Carosi, R., Di Pisa, A., Iacopini, D., Montomoli, C., & Oggiano, G. 2004. The structural evolution of the Asinara Island (NW Sardinia, Italy). *Geodinamica Acta*, 17(5), 309–329.
- Cuccuru S., Casini L., Oggiano G. & Simula E.N. 2018. Structure of the Castellaccio Pluton (Asinara Island, Italy), *Journal of Maps*, 14:2, 293-302
- Del Moro A., Di Pisa A., Oggiano G., Pardini G. 1996. A syn-collisional variscan granitoid: the Cala d’Oliva Orthogneiss from Asinara island (Sardinia). *Plinius* 16 (1996) 96-98.
- Di Pisa A., Oggiano G., Talarico F. 1993. Post collisional tectono-metamorphic evolution in the axial zone of the Hercynian belt in Sardinia: the example from the Asinara island. *Orleans, Doc. B.R.G.M.* 219 (1993), 216-217.

**Curriculum vitae et studiorum
of Stefania Corvò**

Stefania Corvò

PhD Student in Earth and Environmental Sciences



© European Union, 1995-2021

PERSONAL INFORMATION

Email: stefania.corvo01@universitadipavia.it
Indirizzo: Viale Bligny 85 - 27100 Pavia, Italia
Telefono: (+39)3460283294
Data di nascita: 8 Mar, 1993
Nazionalità: Italiana
Link: https://www.researchgate.net/profile/Stefania_Corvo2



WORK INTERESTS

My main scientific interest focuses on the understanding of micro- and mesoscale processes and their link to macro-scale phenomena. To achieve this, it is essential the use of a multidisciplinary approach in order to observe, interpret and evaluate processes in the Earth. In particular, I work on high pressure and high temperature rocks from the lower crust from Western Alps localities. My studies concern geological processes occurring in correspondence of shear zones or of compositional and structural heterogeneous rock boundaries. Investigate the relationships between petrological and deformation processes is of great interest in my research.

CURRENT POSITION

Pavia, Italia
Ott 2018 - Dic 2021

PhD Student
Università Degli Studi Di Pavia, Department of Earth and Environmental Sciences

Project title: Determination of P-T-t-d paths from lithospheric shear zones: links between deformation, magmatism and metamorphism.
Supervisors: Dr. Matteo Maino, Dr. Antonio Langone, Prof. Sandra Piazzolo

ACCADEMIC CAREER

Mar 2018 - Set 2018

IGG-CNR Scholarship
Institute of Geosciences and Earth Resources, Pavia (IGG - CNR)

Geochemical characterisation (LA-ICPMS and FTIR) of nominally anhydrous minerals (NAMs) of peridotitic bodies in the Ivrea-Verbano zone (Southern Alps).
Supervisors: Dr. Alberto Zanetti, Dr. Antonio Langone, Dr. José Alberto Padrón-Navarta

Ott 2015 - Set 2017

Master Degree in Applied Earth Sciences to Civil and Environment Engineering
University of Pavia, Department of Earth and Environmental Sciences

Title of thesis: Water content in nominally anhydrous minerals (NAMs) from the Finero complex (Italy).
Supervisors: Dr. Alberto Zanetti, Dr. José Alberto Padrón-Navarta, Dr. Antonio Langone
Degree mark: 110/110 cum Laude

Ott 2012 - Ott 2015

Bachelor Degree in Earth Sciences
University of Genova Department of Earth and Environmental Sciences

Title of thesis: Determination of natural land values in the landslide area of Prato Casarile (Genova): environmental aspects in order to reinstate the site.
Supervisors: Prof. Pietro Marescotti, Dr. Geol. Eugenio Poggi, Prof. Gerardo Brancucci
Degree mark: 110/110 cum Laude

Set 2008 - Lug 2012

Liceo Scientifico
Leonardo da Vinci, Genova
Degree mark: 96/100

LINGUISTIC SKILLS

Francese

Livello intermedio. DELF B1

Inglese

Livello intermedio. First B2

GENERAL SKILLS

Geology

Metamorphic petrology

Microstructural geology

Tectonics and geodynamic

Field and lab work

Problem solving

Team working

Self-organization

TECHNICAL SKILLS

- Good knowledge in the thin sections and samples preparation (cutting, polishing, coating)
- Good knowledge in the use of specific instruments for petrographic, microstructural, geochemical and geochronological analysis, such as: ~~SEM-TESCAN VEGA~~ (scanning electron microscopy), ~~SEM-FEG~~ (field emission gun scanning electron microscopy), ~~EBS~~ (electron back-scattered diffraction), ~~LA-ICP-MS~~ (Laser Ablation Inductively Coupled Plasma Mass Spectrometry), ~~FTIR~~ (Fourier Transform InfraRed spectroscopy), ~~EMPA~~ (Electron Microprobe)

COMPUTER & MODELLING SOFTWARE SKILLS

- Good knowledge of Microsoft Office tools, Internet and e-mail.
- Operating systems (Windows and Linux)
- Applications (Word, Excel, Powerpoint Access; Adobe applications) Basic knowledge (video writing, graphics, sound, images, Photoshop, Illustrator, InDesign)
- Good knowledge of data processing and charts for publications (OPUS, Q-GIS, Matlab, Sigma Plot; MTEX)
- Good knowledge of specific software for data treatments and modelling (GLITTER, AztecICE, PerpleX)

PUBLICATIONS

- Simonetti M., Langone A., Corvò S., Bonazzi M., (2021). Triassic-Jurassic rift-related deformation and temperature-time evolution of the fossil Adriatic margin: A review from Ossola and Strona di Omegna valleys (Ivrea-Verbano Zone). *Ofioliti*, 46 (2), 147-161.
- Corvò, S., Maino, M., Langone, A., Schenker, F. L., Piazzolo, S., Casini, L., & Seno, S. (2021). Local variations of metamorphic record from compositionally heterogeneous rocks (Cima di Gagnone, Central Alps): Inferences on exhumation processes of (U) HPHT rocks. *Lithos*, 106126.
- Corvò, S., Langone, A., Padrón-Navarta, J.A.; Tommasi, A., Zanetti, A. (2020). Porphyroclasts: Source and Sink of Major and Trace Elements During Deformation-Induced Metasomatism (Finero, Ivrea-Verbano Zone, Italy). *Geosciences*, 10, 196.

REVIEWER EXPERIENCE

Arabian Journal of Geosciences

AWARDS

- Best Student Poster Presentation at the MSG-RIP-2021 meeting. Released by Mineralogical Society
- Grant award for the attendance at the SIMP-SGI-SoGel 2019 Parma. Released by SIMP society
- Giuseppe Schiavinato Award 2018 for the Best Italian Master Thesis in the Mineralogic Sciences field with links to petrological applications. Released by Accademia Nazionale dei Lincei, Rome

EXPERIENCES ABROAD

PhD Mobility Periods at University of Leeds (UK)

1°: February 2019 - March 2019 (two months); 2°: October 2019 - December 2019 (two months)

Tasks: Microstructural studies by the electron backscattered diffraction analysis (EBSD) and scanning electron microscope (SEM) on HP-HT metamorphic rock samples for the development of the PhD research.

Erasmus Traineeship at CNRS Geosciences, Montpellier (France)

March 2017 - July 2017 (4 months)

Tasks: Water content (OH) studies by means of FTIR technique in nominally anhydrous minerals (NAMs) such as olivine and pyroxene of Finero peridotite (Southern Alps, Italy)

BeGeoScientists 2021 1 Congresso Nazionale dei Giovani Geoscientisti (7-10/10/2021)

- Abstract submission (flash talk): A multidisciplinary approach to unravel the rocks heterogeneities: link between deformation and metamorphic processes from lithospheric crust;
- **Convener** of the Session Petrology to the rescue: multidisciplinary investigations from human activities to the Deep Earth

90th Conference of the Italian Geological Society (14-16/09/2021)

- Abstract submission (oral): Local variations of metamorphic record from compositionally heterogeneous rocks: Inferences on exhumation processes of HP rocks from the Adula-Cima Lunga unit
- Abstract submission (poster): Microstructural and petrological characterization of a major extensional shear zone in the middle crust (Val d'Ossola, Ivrea-Verbano Zone, Western Alps)

3rd European Mineralogical Conference (29-02/08-09/2021)

- Abstract submission (oral): Titanite as powerful petrochronometer for unravelling the evolution of a major extensional shear zone in the middle crust (Val d'Ossola, Ivrea-Verbano Zone, Western Alps)

Waiting for Yorsget (Young Research in Structural geology and Tectonics (21-22/06/2021))

- Abstract submission (poster): Local variations of metamorphic record from compositionally heterogeneous rocks: Inferences on exhumation processes of continental (U)HP-HT unit (Cima di Gagnone, Central Alps)
- Abstract submission (poster): Evolution of a major extensional shear zone in the middle crust (Val d'Ossola, Ivrea-Verbano Zone, Western Alps)

Metamorphic Studies Group 40th anniversary Meeting Research in Progress (29-31/03/2021) organized by the Mineralogical Society.

- Abstract submission (poster): Unravelling the evolution of a major extensional shear zone from middle crust (Val d'Ossola, Ivrea-Verbano Zone, Western Alps, Italy)

EGU General Assembly 2020 (04-08/05/2020)

- Abstract submission (oral): Timing of HP/HT alpine metamorphism: new data from Cima di Gagnone (Central Alps)

***/20 (*UXSSR GL /DYRUR VXOOH 2ILROLWL 0HGLWHUUDQHH) 0HHWLQJ - 7RULQR (30/01/2020)**

- \$EVWUDFW VXEPLVLRQ (RUDO): 'DWLQJ RI +3/+7 DOSLQH PHWDPRUSKLV: 1HZ SHWURORJLFDO, FKURQRORJLFDO DQG PLFUR- VVUXFWXUDO GDWD IURP &LPD GL *DJQRQH (&HQWUDO \$OSV).

Oral presentation to the group seminar on the PhD project (2° mobility period in Leeds, 22/11/2019)

- Entitled Determination of P-T-t-d paths from lithospheric shear zones: Links between deformation, magmatism and metamorphism.

International School entitled Structure and Composition of the Lower Continental Crust (7-10/10/2019) organized by University of Pavia, in collaboration with IGG-CNR, GNP, SIMP.

- Abstract submission (poster): Timing and deformation features of shear zones at different crustal levels (Val d'Ossola, Ivrea-Verbano Zone, Western Alps).

Il tempo del pianeta Terra e il tempo dell'uomo: Le geoscienze fra passato e futuro (16-19/09/2019) organised by: Società Geologica Italiana (SGI) e Società Italiana di Mineralogia e Petrografia (SIMP), Istituto Nazionale di Geofisica e Vulcanologia (INGV).

- Abstract submission (oral presentation): Determination of P-T-t-d path in a high-grade shear zone: petro-chronological and microstructural study from the Cima di Gagnone (Adula-Cima Lunga nappe, Central Alps).
- Abstract submission (oral presentation): Petrological and geochronological constraints of a shallow intrusion into the Variscan medium-grade metamorphic sequence of the Asinara Island (Sardinia).

The 14th Emile Argand Conference on Alpine Geological Studies (04-08/09/2019) organised by University of Lausanne and held in Sion

- Abstract submission (poster): "Dating of HP/HT Alpine metamorphism: petro-chronological and micro-structural study from the Cima di Gagnone (Cima Lunga unit, Central Alps).

Geosciences for the environment natural hazards and cultural heritage (12-14/09/2018) organised by: Società Geologica Italiana (SGI) e Società Italiana di Mineralogia e Petrografia (SIMP), Istituto Nazionale di Geofisica e Vulcanologia (INGV).

- Abstract submission: Water content in nominally anhydrous minerals (NAMs) from subcontinental mantle bodies of the Ivrea-Verbano Zone (Southern Alps)

EMAW2018 3rd European Mantle Workshop (26-28/06/2018) organised by: IGG - CNR, SIMP, GNP, INGV, SGI, UNIPV.

- Abstract submission (poster): A geochemical characterisation (EMPA and LAICPMS) of Finero peridotite (Southern Alps, Italy).
- Abstract submission (poster): Water content in nominally anhydrous minerals (NAMs) from peridotite bodies of the Ivrea-Verbano zone (Southern Alps, Italy).

IGG-days (29-30/05/2018) organised by: Institute of Geosciences and Earth Resources (IGG - CNR).

- Abstract submission (oral presentation): 'Hydrogen content in nominally anhydrous minerals (NAMs) from upper mantle: petrological and geophysical implications'.

Geosciences: a tool in a changing world (06/09/2017) organised by: Società Geologica Italiana (SGI) e Società Italiana di Mineralogia e Petrografia (SIMP), Istituto Nazionale di Geofisica e Vulcanologia (INGV).

- Abstract submission (oral presentation): 'Hydrogen content in nominally anhydrous minerals from Finero peridotite (Italy)'.

EDUCATION COURSES

- 1 February 2021 - Scientific Writing course held by Dr. Cristina Persano and organized by the PhD Program in Earth and Environmental Sciences of the University of Pavia.
- 2-3 December 2020 - PTt trajectory of metamorphic processes from a combination of pseudosection calculations, nucleation and growth simulations, and diffusion modelling using different approaches workshop organised by Geochemical Society.
- 6 November 2020 - La bellezza nel piccolo. Fotografare al microscopio presented by Bernardo Cesare. Organised by Museo Alto Garda (MAG).
- 17-20 February 2020 - Microtectonics Course held by Cees Passchier at Johannes Gutenberg University of Mainz.
- 20-23 January 2020 - Principles of geological numerical modelling. Held by Dr. Leonardo Casini. Organised by Department of Environment and Earth Sciences of Pavia.
- 19-21 July 2019 - Field trip Course in the Western Alps, Chenaillet-Monginevre. Organised by Department of Environment and Earth Sciences of Pavia.
- 7-10 October 2019 - International School "Structural and Composition of the Lower Continental Crust". Organised by University of Pavia.
- 27 May 2019 - Frontiers in ICP-MS/MS Application in Earth and Environmental Sciences Course. Organised by Department of Environment and Earth Sciences and IGG-CNR of Pavia.
- 23-24 May 2019 - Vajont landslide: The meaning of a disaster field course. Organised by Department of Environment and Earth Sciences of Pavia.
- 6 November 2019 - Sulfide Differentiation at the Upper Mantle and Lower Crust: Ocean Research and Potential Implications for the Crust-Mantle Boundary in the Ivrea Zone presented by Jakub Ciazela. Organised by Department of Environment and Earth Sciences of Pavia.
- October 2019 - Science communication course for the realization of scientific report and video. Organised by Department of Environment and Earth Sciences of Pavia in collaboration with Università Statale di Milano.
- October 2018 - January 2019 - Physical properties of minerals and rocks held by Ross Angel (48 h) at Department of Environment and Earth Sciences of Pavia.

TEACHING & MENTORING EXPERIENCE

TUTORING

March 2022 - June 2020:

- Tutoring (25h), for Bachelor degree course in Petrography and microscopy laboratory for rock thin sections identification. Supervisor: Prof. Riccardo Tribuzio
- Tutoring (15h), for Bachelor degree course in Geological survey. Supervisor: Prof. Giovanni Toscani

March 2021 - June 2021:

- Tutoring (20h), for Bachelor degree course in Petrography and microscopy laboratory for rock thin sections identification. Supervisor: Prof. Riccardo Tribuzio
- Tutoring (20h), for Bachelor degree course in Geological survey. Supervisor: Prof. Giovanni Toscani
- Tutoring in the field trip DW (OEDLVODQGRIWKHODVWHUFRXUVH6HLVPLFLQWHUSUHWDWLRQDQGJHRORJLFDO PRGHOOQJ. Supervisor: Dr. Giovanni Toscani, Dr. Matteo Maino

March 2020 - June 2020:

- Tutoring (30h), for Bachelor degree course in Petrography and microscopy laboratory for rock thin sections identification. Supervisor: Prof. Riccardo Tribuzio

March 2019 - June 2019:

- Tutoring (20h), for Bachelor degree course in Petrography and microscopy laboratory for rock thin sections identification. Supervisor: Prof. Riccardo Tribuzio
- Tutoring in the field trip DW/DJR GL&RPR of the Master course 6HLVPLFLQWHUSUHWDLRQDQGJHRORJLFDO PRGHOOOLQJ. Supervisor: Dr. Giovanni Toscani, Dr. Matteo Maino

THESIS COSUPERVISOR

2021

- Bachelor Degree Co-tutor of Noemi Tosi, Bachelor Thesis: Variazioni geochemiche della Titanite attraverso una sezione di crosta continentale (Val d'Ossola; Zona Ivrea-Verbano)

2020

- Bachelor Degree Co-tutor of Matilda Soldano, Bachelor Thesis: Analisi degli elementi maggiori dei granati e caratterizzazione petrografica del complesso metamorfico in Val D'Ossola (Zona Ivrea-Verbano).
- Master Degree Co-tutor of Eleonora Zangara, Master thesis: Petrological and geochronological constraints of a shallow intrusion into the Variscan medium-grade metamorphic sequence of the Asinara Island (Sardinia).

2019

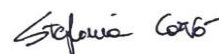
- Bachelor Degree Co-tutor of Maria Vittoria Betuschi, Bachelor Thesis: Caratterizzazione petrografica del complesso metamorfico in Val DOssola (zona Ivrea-Verbano): indagini geocronologiche preliminari.

ACADEMIC ACTIVITY AND MEMBERSHIPS

- Attendance as presenter at the Settimana del Pianeta Terra 2021 - Maratona delle Geoscienze Pavia (9a edition 3rd-10th October 2021)
- Attendance as sharper at the Sharper Night 2021 in Pavia (24th September 2021)
- Occasional service assignment (130h) for activities related to the Scientific Degree Plan (Piano Lauree Scientifiche PLS - 2021)
- Membership with a collaboration assignment to the Institute of Geosciences and Earth Resources, Pavia (IGG - CNR) (2019-2021; 2021-2023)
- Member of the Earth and Environmental Science Department council of Pavia as PhD students delegate (2018-2020; 2020-2022)
- Member of the Earth and Environmental Science Department council of Genova as Bachelor students delegate (2013-2015)
- Membership of Società Italiana di Mineralogia e Petrologia: SIMP
- Membership of Metamorphic Studies Group - Mineralogical Society
- Membership of Società Geologica Italiana: SGI
- Membership of European Association of Geochemistry: EAG

'DWH 24/12/2021

6LJQDWXUH



Enjoy Life Always

There is a world outside to discover!

